At the precipice of the Great Oxygen Crash:

Redox-sensitive metal geochemistry in the Paleoproterozoic Onega Basin

by

Kaarel Mänd

A thesis submitted in partial fulfillment of the requirements for the degree of

Doctor of Philosophy

Department of Earth and Atmospheric Sciences

University of Alberta

Abstract

The middle Paleoproterozoic era (~2200–1800 million years ago) was host to some of the most significant perturbations in Earth's elemental cycles, including the largest ever excursion of carbon isotope ratios in sedimentary rocks, known as the Lomagundi-Jatuli Event. This event has been linked to a contemporaneous "overshoot" in atmospheric oxygen concentrations to near-modern values, as recorded by geochemical redox proxies in rocks from this time. After ~2060 million years ago the Lomagundi-Jatuli isotope excursion waned and, closely thereafter, the O_2 overshoot receded. However, there are several competing explanations as to the mechanisms underpinning these global events, and their effect on the evolution of life remains tentative.

One of the most complete successions to record the Lomagundi-Jatuli Event and its termination is the Onega Basin in NW-Russia. Geochemical data from this succession features prominently in global redox studies but have produced contradictory interpretations due to uncertainty regarding local basinal configuration and redox conditions. In this thesis, I use redox-sensitive metal concentration and isotope ratio analyses of Onega Basin sedimentary rocks to provide constraints on the local depositional setting, assess proxy evidence for global redox conditions, and explore their implications for the mechanisms governing global carbon and oxygen cycle shifts, and the emergence of eukaryotic life forms.

Mudstone iron isotope analyses in the upper Zaonega Formation, middle part of the Onega Basin sedimentary succession, are consistent with the operation of an ancient benthic Fe shuttle,

implying restricted hydrographic conditions and redox stratification. Though this implies basinal modulation of trace metal cycling, high metal concentrations and isotope signatures of occasional oxic iron drawdown attest to replenishment of the basin with oxidized water masses, allowing the sediments to record signals of global marine chemistry.

Molybdenum, uranium, and rhenium concentrations in the upper Zaonega Formation, as well as uranium isotope ratios, are the highest reported from organic-rich mudstones older than the Neoproterozoic. To explain such values, the contemporaneous oceans must have been highly oxygenated. Given that the Zaonega Formation post-dates the end of the Lomagundi-Jatuli Event by several million years, it means that the carbon isotope excursion and the O_2 overshoot were to some extent decoupled. This finding disagrees with the most-cited explanation for these events, which invokes a pulse of elevated organic carbon burial, and urges consideration of alternative mechanisms.

Finally, fractionated chromium isotope ratios are found throughout a >2400 m thick section of the Onega Basin sedimentary rocks. Since chromium isotope fractionations require appreciable levels of atmospheric O_2 to form, these findings mean that stable, high-pO_2 conditions must have been the norm throughout the entire period during which this succession accumulated. This stands in contrast to the following mid-Proterozoic time period, which is characterized by low and unstable levels of pO_2. The acquisition of the mitochondria in eukaryotic organisms has commonly been linked to atmospheric oxygenation, but despite the long period of stable oxygenation discovered here, diverse eukaryote fossils only become

common in the mid-Proterozoic. Therefore, intrinsic biological factors must have controlled the timing of mitochondrial acquisition, instead of background redox levels.

Preface

This papers-based dissertation and includes the collaborative work of several co-authors in chapters 2 through 4. These chapters constitute independent journal articles on the metal geochemistry of the Onega Basin, one of which has already been published and two of which are in the final stages of revision prior to submission. I am the lead author of all the chapters included here and was intimately involved in every aspect of their production from conceptualization, field work, material and data collection, analysis, interpretation, and writing. This work was supervised by Dr. Kurt O. Konhauser at the University of Alberta, Dr. Aivo Lepland at the Norwegian Geological Survey, and Dr. Kalle Kirsimäe at the University of Tartu, Estonia.

Chapter 2 has been prepared as a manuscript for submission as: Mänd, K., Lalonde, S. V., Paiste, K., Thoby, M., Lumiste, K., Robbins, L. J., Kirsimäe, K., Lepland, A., Konhauser., K. O. "Iron isotopes reveal a benthic iron shuttle in the Paleoproterozoic Zaonega Formation: Basinal restriction, euxinia, and the effect on global paleoredox proxies." My contribution to this chapter involved the majority of the laboratory analyses, the interpretation of the results, and the writing. The study was designed by myself, S. V. Lalonde, M. Thoby, K. Kirsimäe, A. Lepland, and K. O. Konhauser. M. Thoby, S. V. Lalonde, and K. Kirsimäe supervised and assisted in the laboratory analyses, and K. Lumiste assisted in statistical analyses. S. V. Lalonde, K. Paiste, K. Kirsimäe, and A. Lepland helped refine the interpretation of the results. The manuscript was written with input from all authors.

Chapter 3 is published as: Mänd, K., Lalonde, S. V., Robbins, L. J., Thoby, M., Paiste, K., Kreitsmann, T., Paiste, P., Reinhard, C. T., Romashkin, A. E., Planavsky, N. J., Kirsimäe, K., Lepland, A., Konhauser, K. O., 2020. "Palaeoproterozoic oxygenated oceans following the Lomagundi–Jatuli Event." *Nature Geoscience 13*, 302–306. I was involved in the design of the study, performed the majority of the laboratory analyses, interpreted the results, and led the writing of the manuscript. Additional study designers were S. V. Lalonde, N. J. Planavsky, K. Kirsimäe, A. Lepland, K. O. Konhauser. Laboratory analyses were also provided by S. V. Lalonde, M. Thoby, K. Paiste, T. Kreitsmann, P. Paiste, K. Kirsimäe. A. E. Romashkin provided the field descriptions and the material. All authors contributed to the writing of the manuscript.

Chapter 4 has been prepared as a manuscript for submission as: Mänd, K., Planavsky, N. J., Robbins, L. J., Wang, C., Kreitsmann, T., Paiste, K., Paiste, P., Romashkin, A. E., Kirsimäe, K., Lepland, A., Konhauser, K. O. "A hundred million years of oxygen abundance in the mid-Paleoproterozoic." I was a contributor to the study design, led the data acquisition and interpretation, and wrote the majority of the manuscript. The study was designed by myself, N. J. Planavsky, K. Kirsimäe, A. Lepland, and K. O. Konhauser. Laboratory analyses were contributed also by N. J. Planavsky, C. Wang, T. Kreitsmann, K. Paiste, P. Paiste, and K. Kirsimäe. A. E. Romashkin contributed the material and core descriptions and all co-authors were involved in the writing of the manuscript.

Acknowledgments

The list of people who helped me reach this point is too long to include here fully. My foremost thanks goes to my supervisors and good friends Kurt Konhauser, Aivo Lepland, and Kalle Kirsimäe, who have always looked out for my best interests and have worked tirelessly to elevate me. They are a better and more inspiring supervisory team than I could have dreamed of. I also thank my supervisory committee members and mentors Karlis Muehlenbachs, Murray Gingras, Daniel Alessi, and Long Li, whose advice and insights I treasure.

The years went by fast due to the good times we had with my extended lab group in Edmonton, to whom I still owe many beers, and my home team of friends and colleagues in Tartu. Furthermore, I was very lucky to be able to travel to McGill in Montreal, Canada, IUEM in Brest, France, Argonne National Laboratory in Chicago, USA, Yale University in New Haven, USA, El Tatio in Chile, and NGU in Trondheim, Norway. I remember all these places especially fondly thanks to all the help and welcome I received from colleagues there; I'm dying to see you all again at the next conference.

This thesis would not have been possible without the support of my generous funders, the Archimedes Foundation, the Estonian Research Council, the Natural Sciences and Engineering Research Council of Canada, UAlberta North, and the University of Alberta.

Finally, I am grateful to all my friends and family for sticking by me. Most of all, I am in debt to my wife Rahel, who was my staunchest ally throughout this entire long journey.

Table of contents

List of tables

List of figures

Chapter 1: Earth and Life in the middle Paleoproterozoic

1.1 Paradise lost: The Lomagundi-Jatuli Event and the O_2 overshoot

In the story of how Earth's surface environment became oxygen-rich, the Proterozoic eon (2500–541 million years ago; Ma) takes centre stage. Whereas the primordial, Archean Earth hosted only minor and transient oxygen in its atmosphere and oceans, the Great Oxidation Event (GOE) at the beginning of the Proterozoic upended the situation (Figure 1.1a; MacGregor 1927; Cloud 1972; Holland 1984; 2002; 2006; Lyons et al. 2014; defined in this dissertation as the period which saw the loss of mass-independent sulphur fractionation in the rock record). This event is marked by the disappearance of the oxygen-sensitive, detrital minerals pyrite and uraninite from surface sediments (MacGregor 1927; Ramdohr 1958; Holland 1962; Roscoe 1969; Rasmussen and Buick 1999; Johnson et al. 2014), the appearance of oxidized "red beds" (Cloud 1965, 1968; Holland 1984, 2006), the retention of iron (Fe) in paleosols (Cloud 1965; Holland and Beukes 1990; Rye and Holland 1998), and a peak in the deposition of banded iron formations (Cloud 1968, 1973; Roscoe 1969; Bekker et al. 2010; Konhauser et al. 2017). The "smoking gun" that signifies the GOE, however, is the loss of mass-independent fractionation of sulphur isotopes (MIF-S) from sediments after ~2320 Ma (Figure 1.1b; Farquhar et al. 2000; Bekker et al. 2004), or even by ~2502–2434 Ma (Warke et al. 2020). The creation and preservation of MIF-S depends on photochemical reactions with gaseous sulphur (S) phases and UV-light in the atmosphere. The disappearance of MIF-S in the sedimentary record signifies the onset of an ozone layer, which blocked much of the UV flux, implying that oxygen levels must have risen

and remained above 10^{-5} times the present atmospheric level, the threshold required for the formation of the ozone layer (Farquhar et al. 2000; Pavlov and Kasting 2002; Farquhar et al. 2011). However, the age that the GOE ushered in was not one of continuity; instead what followed were some of the most dramatic fluctuations in Earth's coupled oxygen, carbon, and nutrient cycles.

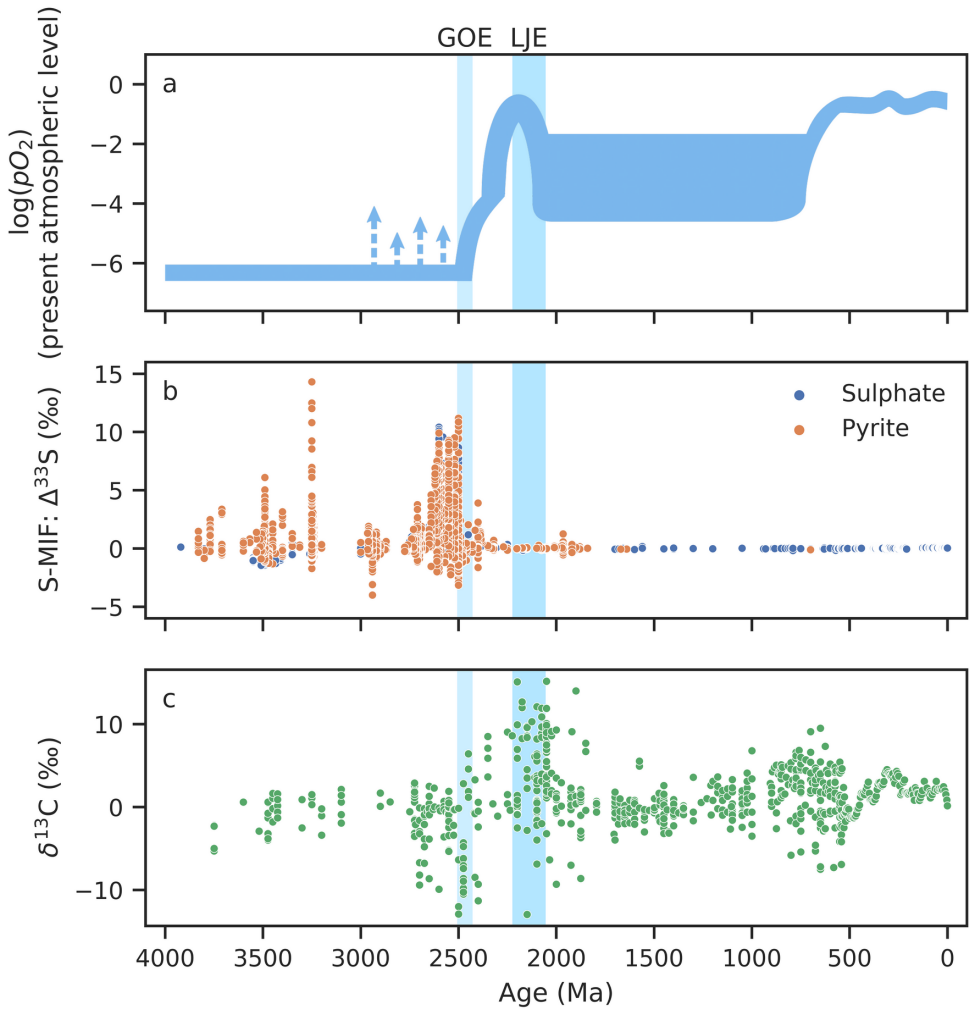

Figure 1.1: Foundational proxies for the modern view on atmospheric oxygenation through Earth history. (a) Interpretation of atmospheric oxygen history by Lyons et al. (2014). (b) Mass-

independent fractionation of sulphur in sedimentary S phases, data from Havig et al. (2017). (c) Carbonate carbon isotope composition, data from Krissansen-Totton et al. (2015). Vertical bars mark the latest constraints on the Great Oxidation Event (GOE; Warke et al. 2020) and the Lomagundi-Jatuli Event (LJE; Martin et al. 2013).

The most conspicuous of these shifts is the Lomagundi-Jatuli Event (LJE), the Earth's longest-lasting and most positive carbonate carbon isotope ($\delta^{13}C$) excursion, which occurred shortly following the GOE (Figure 1.1b, Schidlowski et al. 1976; Karhu and Holland 1996; Bekker and Holland 2012). This event is of marked significance since for most of Earth's history, the carbon (C) cycle remained relatively unperturbed, as evidenced by stable $\delta^{13}C$, varying primarily between -5‰ and 5‰ (Schidlowski et al. 1983; Strauss 1996; Shields and Veizer 2002). Only few major deviations from this trend exist, the LJE being one of them: between ~2220 and 2060 Ma (Karhu and Holland 1996; Melezhik et al. 2007; Martin et al. 2013) carbonate $\delta^{13}C$ ranged from 5‰ to 15‰, reaching as high as 28‰ (Bekker et al. 2003). Despite conflicting data and a sparse carbonate rock record, leading to problems with precisely bracketing the LJE (e.g., Guo et al. 2009; Bekker and Holland 2012; Martin et al. 2015; Martindale et al. 2015; Bekker et al. 2016; Kerr et al. 2016; Bauer et al. 2019), ^{13}C-enriched carbonates co-occur for ~160 Myrs on all contemporary cratons (Martin et al. 2013). This suggests that the LJE must have represented a profound and global perturbation of Earth's carbon cycle.

The canonical explanation for the LJE relies on carbon burial mass balance. Since the $\delta^{13}C$ value of carbon input into the oceans is thought to be linked to the primordial mantle $\delta^{13}C$ value

of ~−5‰ (Deines 1992), $\delta^{13}C$ of the marine dissolved inorganic carbon pool should then be governed primarily by the balance between the burial of carbonate minerals and organic carbon (C_{org}). While carbonate precipitation does not impart a significant fractionation (Schrag et al. 2013), a preference for ^{12}C in C-fixing enzymatic reactions results in a ~−27‰ offset (Craig 1953; Park and Epstein 1960; Freeman 2001). An increase in the proportion of C_{org} burial can, therefore, drive the residual marine pool towards more positive $\delta^{13}C$ values. Such a C_{org} burial pulse could have been induced by rapid weathering of detrital pyrite following the GOE (Johnson et al. 2014; Hartmann et al. 2017). The resulting acid rock drainage could have mobilized nutrients and enhanced bioproduction in the oceans (Konhauser et al. 2011) to the point of shifting the C_{org}–carbonate burial ratio. Since every mole of C_{org} that is buried—and therefore made unavailable to respiration—results in the net release of a mole of O_2, a mass balance calculation shows that excess C_{org} buried over the duration of the LJE could have resulted in the release of 12–22 times the modern atmospheric O_2 content (Karhu 1993).

This interpretation of the LJE is strengthened by abundant evidence for a significant accumulation of atmospheric O_2 during the time of the LJE—so much that an "O_2-overshoot" has been proposed (Bekker and Holland 2012). Amongst the clearest evidence for this is the deposition of sulphate evaporites and expanded sulphur isotope ($\delta^{34}S$) fractionation, both pointing to a large marine sulphate pool, which is stable only in oxygenated oceans (e.g. Schröder et al. 2008; Planavsky et al. 2012a; Scott et al. 2014; Blättler et al. 2018). Furthermore, the concentrations of many minor elements that are mobilized in oxidative conditions increase in sedimentary rocks during the GOE and LJE—this is seen, for example, in the molybdenum

(Mo), uranium (U), chromium (Cr), rhenium (Re), iodine (I), and selenium (Se) records (Scott et al. 2008; Konhauser et al. 2011; Partin et al. 2013a, 2013b; Hardisty et al. 2014; Kipp et al. 2017; Sheen et al. 2018). Even more evidence is found in the Mo isotope composition of shales deposited at this time (Asael et al. 2018), and in an increase in the proportion of oxidized Fe burial compared to total Fe (e.g., Bekker and Holland 2012; Canfield et al. 2013). Even the mantle was affected: U contents in igneous rocks during this time period are markedly elevated due to the oxic mobilization of U into subducting oceanic crust leading to larger U melt fluxes (Liu et al. 2019). The LJE and signs of oxygenation are ultimately tied together through sedimentary multiple oxygen isotope records which suggest that the O_2 overshoot coincided with a major increase in global biological productivity (Crockford et al. 2019).

Despite this seemingly comprehensive set of evidence, issues persist with the canonical explanation for the LJE. For one, the volumes of O_2 implied by Karhu (1993) to have been generated through C_{org} burial are difficult to reconcile with our understanding of the C and O cycles (e.g., Hayes and Waldbauer 2006; Bachan and Kump 2015; Shields and Mills 2017; Miyazaki et al. 2018; Crockford et al. 2019; Geyman and Maloof 2019). Furthermore, there is a paucity of C_{org}-rich sediments deposited at the time of the LJE, whereas such sediments feature prominently in the immediately post-LJE period (termed the “Shunga Event”; Melezhik et al. 1999b), associated with normal-marine $\delta^{13}C_{carb}$ values (Črne et al. 2014; Kreitsmann et al. 2019, 2020)—exactly the opposite of what would be expected had excess C_{org} burial led to the LJE (Melezhik et al. 2005).

Consequently, an increasing number of alternative hypotheses are being proposed to explain the LJE through means other than C_{org} burial. First, strong shifts in carbonate $\delta^{13}C$ are seen in marine sediments during early diagenesis (Ahm et al. 2018; Higgins et al. 2018) and changes in prevailing sea levels and tectonic settings may affect their expression, leading to temporal variations in $\delta^{13}C$ (Immenhauser et al. 2003; Swart 2008; Geyman and Maloof 2019). As such, the LJE has been re-interpreted as alternatively reflecting a facies effect, and being disconnected from fluctuations in the global pool of dissolved inorganic C (Bakakas Mayika et al. 2020). Second, Hayes and Waldbauer (2006) and Cadeau et al. (2020) have speculated that the LJE $\delta^{13}C$ excursion reflected an increased prevalence of ^{13}C-enriched diagenetic carbonate formed via methanogenesis in sediments (though see rebuttals in Planavsky et al. 2012b; Bekker and Holland, 2012). Third, it is possible to generate large C isotope excursions by varying the amount of carbonate burial without affecting C_{org} burial by, for example, suppressing carbonate weathering (Shields and Mills 2017). Fourth, the onset of modern-style tectonics has been proposed to coincide with the GOE—if subduction efficiency increased massively at this time, the decoupling of subducted carbonate and C_{org} through preferential melting may have led to a transient increase in the $\delta^{13}C$ of volcanic gases (Eguchi et al. 2020). Finally, a recent C, O, and S cycle modeling study by Miyazaki et al. (2018) found that, by taking into account the recycling of sedimentary isotope anomalies and by making C_{org} oxidation vary with pO_2, it is possible to generate a sustained positive $\delta^{13}C$ excursion with only mild increases in relative C_{org} burial.

Overall, there is a dawning realization that the causes and mechanisms behind the Earth's largest C cycle perturbation are, essentially, unconstrained. New geochemical data from sedimentary rocks is, therefore, needed to evaluate competing hypotheses.

1.2 The Great O_2 Crash

Regardless of the mechanisms underlying the LJE, the corresponding period of high pO_2 came to a close as the Lomagundi-Jatuli $\delta^{13}C$ excursion waned. There is substantial evidence suggesting a step change in O_2 abundance between the >2100 and <1800 Ma periods, leading into the generally oxygen-depleted mid-Proterozoic (Canfield 1998; Planavsky et al. 2018a). Redox-sensitive elements such as I, Se, and U, which are more soluble in oxic waters, decrease in concentration in post-2100 Ma carbonates, shales, and iron formations, reflecting a potential deoxygenation of the oceans (Partin et al. 2013a, 2013b; Hardisty et al. 2014; Hardisty et al. 2017; Kipp et al. 2017). Sulphate abundance, again tied to ocean oxygenation, displays a similar trend. In the final stages of the LJE, ~2100–2000 Ma sedimentary sulphate species are ^{34}S-enriched, a potential sign of a shrinking marine sulphate pool (Planavsky et al. 2012b). The same is suggested by a decrease in sulphate minerals in evaporite sequences (Pope and Grotzinger 2003; Schröder et al. 2008), a proliferation of anoxic basins as suggested by increased burial of reduced Fe and C_{org} (Melezhik et al. 1999b; Bekker and Holland 2012; Strauss et al. 2013), and a decreased U melting flux (Liu et al. 2019). Finally, triple oxygen isotope ratios in sulphate minerals retain large mass independent anomalies after 2000 Ma, suggesting a drop in biological productivity (Crockford et al. 2018; Hodgskiss et al. 2019).

The reasons and the precise timing of this decline are, however, poorly constrained, due to a paucity of focused redox studies of the time period and the ambiguity of the results reported to date. Most geochemical data from this era come from only two extensively studied sedimentary successions—the Onega Basin in NW-Russia and the Francevillian Basin in Gabon. In a seminal study, Kump et al. (2011) discovered a two-step negative $\delta^{13}C$ excursion in carbonates and organic matter of the Zaonega Formation (ZF) in the Onega Basin, immediately post-dating the LJE. Correlating this to a similar two-step negative excursion in the Francevillian Basin, these authors proposed a global $\delta^{13}C$ excursion representing the oxidation of organic matter laid down during the LJE that exerted a downward forcing on O_2 abundance. In subsequent studies of these basins, more evidence for a return to anoxic conditions has surfaced. Mudstones in the ZF and the Francevillian Basin contain some of the least positive $^{98/95}Mo$ isotope ratios reported so far for the Proterozoic, suggesting a near absence of oxic Mo burial in the oceans (Asael et al. 2013; Canfield et al. 2013; Asael et al. 2018; Ossa Ossa et al. 2018). A sharp shift in Se isotope ratios and a decrease in overall abundance of Se in the ZF and Francevillian Basin, compared to older sedimentary successions, has also been interpreted as a resurgence in strictly anoxic water masses (Kipp et al. 2017). Scott et al. (2014) suggested an O_2 and seawater sulphate crash immediately following the LJE due to the presence of highly elevated pyrite $\delta^{34}S$ ratios that correlated negatively with $\delta^{13}C$ in the ZF. Similar data were later obtained from the Francevillian Basin with the conclusion that this shift was global in nature (Ossa Ossa et al. 2018).

On the other hand, such inferences have not been without challenge. Later studies have suggested that strongly negative $\delta^{13}C$ in the ZF and Francevillian Basin does not reflect global

deoxygenation, but local hydrothermal overprint and methanotrophy (Qu et al. 2012, 2018; Črne et al. 2014; Kreitsmann et al. 2019; Bakakas Mayika et al. 2020; Kreitsmann et al. 2020), whereas the high $\delta^{34}S$ values in the ZF have been reinterpreted to be the result of anomalously high local sulphate drawdown in a semi-restricted, highly bioproductive basin (Paiste et al. 2018; Paiste et al. 2020b). Still other redox proxies suggest the persistence of oxic or LJE-type signals in these sections: total As concentration and the proportion of As deposited as oxidized As(V) do not seem to decline in Francevillian Basin and ZF samples compared to earlier Paleoproterozoic material (Chi Fru et al. 2019). Similarly, there is no evidence for decreased Mo concentrations following the LJE (Scott et al. 2008). In fact, negative cerium (Ce) anomalies in ZF apatite and carbonate require that coeval seawater was at least partially oxic (Joosu et al. 2015; Kreitsmann et al. 2020), whereas elevated $\delta^{238}U$ values in ZF shales are difficult to reconcile with deeply anoxic ocean conditions (Asael et al. 2013; Yang et al. 2017). Hence, while it is clear that O_2 abundance declined into the mid-Proterozoic, redox proxies disagree on its timing and extent.

These contradictions can be partially reconciled by invoking a poorly-redox buffered mid-Proterozoic Earth that saw frequent fluctuations in redox states (e.g., Sperling et al. 2014; Canfield et al. 2018; Diamond and Lyons 2018; Planavsky et al. 2018b; Cole et al. 2020; Planavsky et al. 2020). The best illustration for this is seen in North American successions from ~1900–1800 Ma: massive deposition of iron formations during this period attests to shallow-water anoxia (Rasmussen et al. 2012; Konhauser et al. 2017), supported by unfractionated Cr and Mo isotopes in some sections (Frei et al. 2009; Partin et al. 2015), and a lack of negative Ce anomalies (Bellefroid et al. 2018). Yet, many other North American intervals of similar age

record metal isotope fractionations, requiring robust oxidative element cycling (Frei et al. 2009; Frei and Polat 2013; Fralick et al. 2017; Planavsky et al. 2018b). To elucidate the patterns of oxygenation in the late Paleoproterozoic, therefore, requires assessment of redox stability at long time scales over the Paleoproterozoic.

1.3 The cradle of complex life

The major redox transformations in the Paleoproterozoic may have been echoed in the evolutionary history of life. One of the more impactful developments of the Proterozoic and of all Earth history was the emergence of the eukaryotic cell—i.e., eukaryogenesis—which heralded in an entirely new magnitude of biological complexity (Lane and Martin 2010). Yet, the when, how, and why of eukaryogenesis has been the subject of intense debate for more than half a century (Sagan 1967), owing to a sparse Proterozoic fossil record (Butterfield 2015), the difficulty in preserving taxonomically informative cellular structures in the rock record, and a lack of extant prokaryote-eukaryote intermediaries (although see Zaremba-Niedzwiedzka et al. 2017).

Eukaryogenesis was a prolonged process that involved several major evolutionary leaps, the most significant being the acquisition of the mitochondria (Lane and Martin 2010; Porter 2020). While there is an uncertainty of more than a billion years in the timing of these various transformations, much evidence places the first mitochondria in the early Proterozoic, in range of the redox transitions explored below. Molecular biomarkers of eukaryotes in the form of eukaryote-specific sterols, however, are only preserved in Neoproterozoic or younger rocks

(Brocks et al. 2017), implying either the ecological marginalization of pre-Neoproterozoic eukaryotes (Brocks et al. 2017) or a late origin of sterol synthesis (Porter 2020). Molecular clocks, which combine the genetic diversity of extant eukaryotes with genetic divergence rates calibrated through fossil evidence, mostly place the last eukaryotic common ancestor (LECA) in the Late Paleoproterozoic or the Mesoproterozoic (Chernikova et al. 2011; Shih and Matzke 2013), while others allow for the emergence of the LECA >1800 Ma (Sánchez-Baracaldo et al. 2017; Betts et al. 2018). It should, however, be noted that errors in molecular clocks are large and the results are strongly affected by the fossil interpretations used for calibration (Porter 2020).

The clearest evidence for the early appearance of eukaryotes is instead found in the fossil record (Butterfield 2015; Javaux and Lepot 2018). *Bangiomorpha pubescens*, an eukaryotic fossil from Arctic Canada, possibly of red algal affinity, provides evidence for the divergence of crown group eukaryotes before 1047 Ma (Butterfield 2000; Gibson et al. 2018), whereas the oldest red algae-like fossils date to ~1600 Ma (Bengtson et al. 2017b). Large acritarchs with complex cell walls, evocative of cytoskeleton-bearing total-group eukaryotes, are seen much earlier in several 1900–1600 Ma successions in North China, Australia, and Russia (e.g., Lamb et al. 2009; Javaux and Lepot 2018). Unfortunately, the inherent incompleteness of the fossil record makes it entirely plausible that the divergence of the eukaryotic lineage from their archaean ancestors predated even that. For instance, differentiated, macroscopic, and even motile fossils found in the ~2100 Ma Francevillian Group, Gabon (El Albani et al. 2019), and structures evoking fungal affinity seen in the ~2400 Ma Ongeluk Formation, South Africa (Bengtson et al.

2017a), may point to an early evolution of complex microorganisms similar to eukaryotes. An important nuance in these age estimates is that eukaryogenesis was likely a drawn-out process over a time period of up to a billion years (Porter 2020). It is thus plausible that many of the earliest fossils represent the eukaryote stem group that predated LECA, which would explain the discrepancy between some fossil and molecular clock data (Butterfield 2015; Porter 2020). In summation, evidence is increasingly pointing towards the origin of eukaryotes in the Paleoproterozoic.

A tantalizing possibility then arises where the O_2 overshoot and subsequent crash played a role in triggering the early evolution of eukaryotes—the existence of an environmental forcing is, perhaps, suggested by the apparently singular appearance of endosymbiotic eukaryote-like organisms in Earth history (Zachar and Szathmáry 2017). Although it has been maintained that no specific environmental forcing was needed (e.g., Lane and Martin 2010), many have speculated that rising pO_2 following the GOE may have favoured eukaryotic organisms (e.g., Imachi et al. 2020). In general, O_2 and nutrient-rich conditions are more conducive to complex organisms, such as eukaryotes (Reinhard et al. 2020). Support for this hypothesis is given by phylogenetic analyses that confirm the ability for aerobic respiration in the mitochondrial ancestor (Wang and Wu 2014) and contested interpretations that several of the unique eukaryotic characteristics, such as sterol synthesis, sexual reproduction, and endosymbiosis, are adaptations to oxidative stress (Galea and Brown 2009; Gross and Bhattacharya 2010; Hörandl and Speijer 2018). Oxygen-dependence in eukaryotes may also explain the temporal coincidence between a

Neoproterozoic rise in oxygen levels and the emergence of eukaryotic algae-dominated ecosystems (Brocks et al. 2017).

On the other hand, mitochondria retain ancestral anaerobic metabolic pathways (Mentel and Martin 2008), suggesting that anoxic conditions were commonly encountered during early eukaryote evolution. Furthermore, despite the energetic benefits of aerobic respiration over anaerobic alternatives, Zimorski et al. (2019) questioned whether this outweighed the energetic costs of synthesizing relatively reduced cellular components in a higher-O_2 environment. If so, oxygenated environments were not necessarily a boon for eukaryotes. In fact, the opposite may be true: Brasier and Lindsay (1998) argued that mitochondrial acquisition was a result of a billion-year period of low-nutrient conditions in the mid-Proterozoic. Furthermore, as the mid-Proterozoic is now known to have hosted highly fluctuating redox states, these conditions may also have favoured more versatile (endo)symbiotic forms of life that were able to combine two different metabolic strategies from the host and the symbiont (Zachar and Szathmáry 2017). Clearly, constraints on the redox background in which eukaryogenesis took place are necessary to aid in resolving this ongoing debate.

1.4 The Onega Basin as a testing ground

1.4.1 Basin development

There remains much uncertainty regarding the nature and causes of Paleoproterozoic redox shifts and their effects on the biosphere. In order to test these competing hypotheses, well-grounded geochemical proxy data from contemporaneous sedimentary successions are needed. Given that

only a handful of suitable successions are known, however, it is crucial that we understand their evolution fully and can deconvolute the roles played by both local and global processes in assembling the geochemical proxy records found within.

A unique source of geochemical data for the end-LJE period, and the focus of this thesis, is the Onega Basin in NW-Russia (Figure 1.2, 1.3). The geology, petrography, basinal development, and the metamorphic and diagenetic history of the Onega Basin, as well as aspects of its geochemistry, have been extensively studied over the past decades. Most of the groundwork has been laid in Russian-language literature, beginning in the 1950s (Yakovleva and Gilyarova 1960), but these results are summarized and built upon in the many overviews by Victor A. Melezhik (e.g., Melezhik et al. 1999a, 1999b, 2001, 2004, 2005, 2009, 2015), in the the 3-volume FAR-DEEP book series (Melezhik et al. 2013a), and publications stemming from related projects (Ojakangas et al. 2001; Brasier et al. 2011; Kump et al. 2011; Reuschel et al. 2012; Qu et al. 2012, 2018; Asael et al. 2013, 2018; Scott et al. 2014; Črne et al. 2014, Lepland et al. 2014; Joosu et al. 2015; Blättler et al. 2018; Paiste et al. 2018, 2020a, 2020b; Kreitsmann et al. 2019, 2020; Kipp et al. 2020). A brief overview of the development of the basin follows.

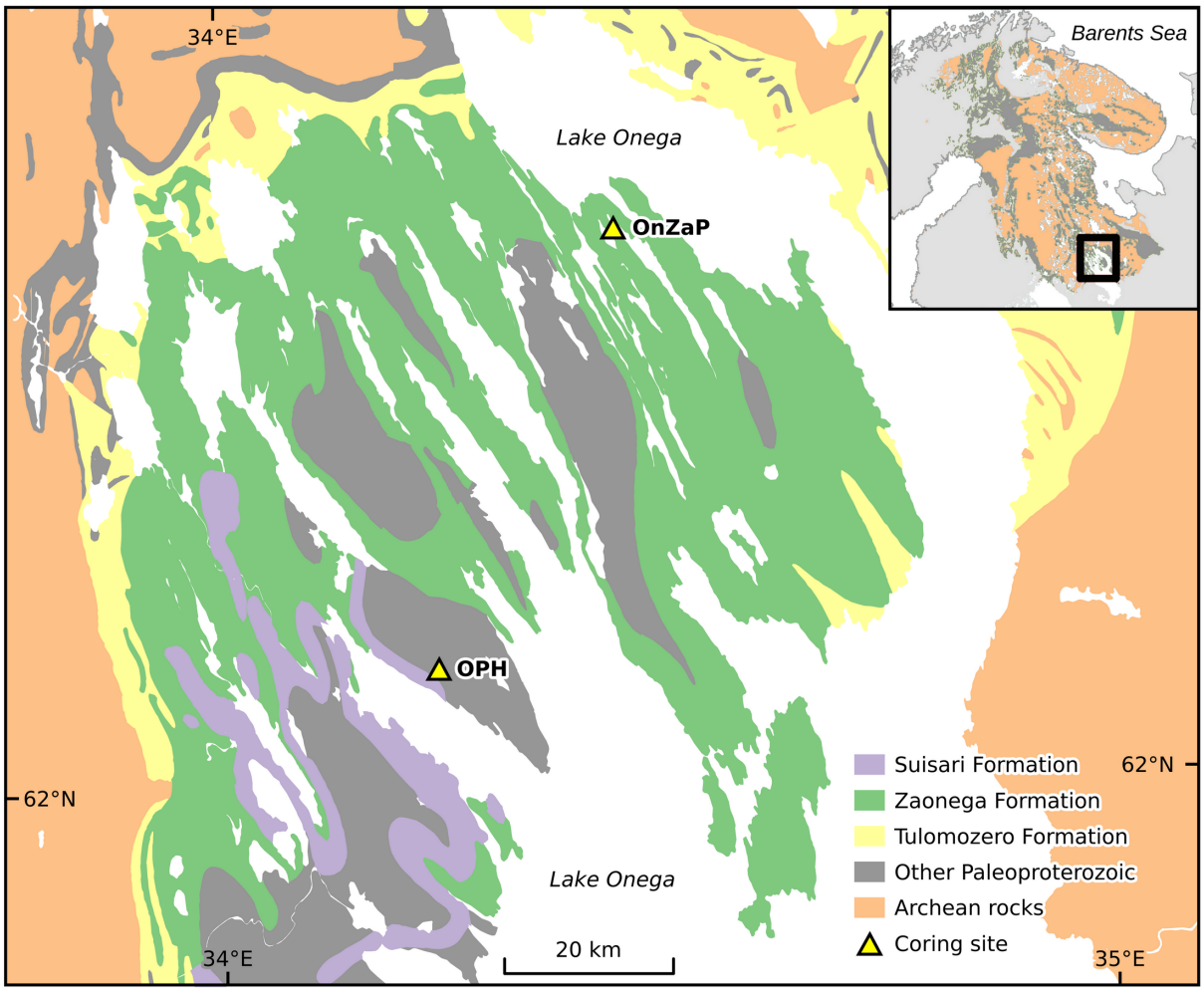

Figure 1.2: Geological map of the Onega Basin showing the exposures of the studied sedimentary successions, as well as the drilling sites of the Onega Parametric Hole (OPH), and OnZaP-1 and -3.

The Onega Basin hosts a diverse ~5-km-thick Paleoproterozoic volcano-sedimentary succession, a preserved fragment of supracrustal cover developed on Archean granites and gneisses of the eastern Fennoscandian Shield, Karelian block (Figure 1.2). The Paleoproterozoic evolution of the Fennoscandian shield started with rifting action that was initiated prior to ~2505

Ma, possibly related and the breakup of the Kenorland supercontinent (Strand and Köykkä 2012). Subsequent development proceeded in periods of rifting and sediment accumulation alternating with uplift and erosion. As regional plume-related rifting and volcanism intensified, an active continental margin was established by 2440 Ma in the Onega Basin area (Melezhik and Hanski, 2013). Deposition in the basin begins in a subaerial rift environment in the northwestern part of the basin, transitions to shallow-marine, and includes thin greywacke and arkosic sandstones alternating with extensive basaltic andesite to andesite lava flows that constitute the Glubokozero and Kumsa formations (Melezhik et al. 2013b; Figure 1.3), the latter forming part of extensive flood basalts deposited throughout the Fennoscandian region (Melezhik and Hanski, 2013).

Plume-related underplating and crustal thickening subsequently led to a long period of uplift, repeated rifting, and deep erosion on the Fennoscandian shield, expressed in wide-spread weathering surfaces (Ojakangas et al. 2001; Daly et al. 2006). The tectonic setting resulted in a highly variable rift and erosional valley topography (Melezhik and Hanski, 2013). In this time period, Fennoscandia was also affected by the global Huronian “Snowball Earth” glactionation (Evans et al. 1997). Despite most likely being located near low latitudes (e.g., Mertanen et al. 1999), diamictites and dropstones are wide-spread on the shield (Ojakangas et al. 2001). In the northern and western part of the Onega Basin, this time period is expressed in the Paljeozero Formation (Figure 1.3), which contains polymict conglomerates and subordinate sandstones and shales of highly variable thickness and lithological heterogeneity (Melezhik et al. 2013b). These

rocks were later peneplenized and deeply chemically weathered (Kump et al., 2013), likely reflecting a tropical climate (Marmo 1992; Torsvik and Meert, 1995).

Between 2200–2100 Ma, major north-west to south-east trending rift systems developed on the Kola craton to the north of the Karelian block, and the incipient Svecofennian sea to the south (Melezhik and Hanski, 2013). Deposition restarted in the Onega Basin in an intracrustal setting with the thin Jangozero and Medvezhegorsk formations, consisting of fluvial arkosic sandstones, gritstones, siltstones, and quartz conglomerates interspersed with subaerial basalt flows (Figure 1.3; Melezhik et al. 2013b). The area between the Kola and Svecofennian rifts subsequently developed into a vast epeiric sea, host to a shallow-water carbonate platform with positive $\delta^{13}C_{carb}$ values reflecting the 2200–2060 Ma LJE (Karhu and Holland 1996; Melezhik et al. 1999a). Sediments from this phase are widely developed throughout the Onega Basin as the Tulomozero Formation and show large lateral facies changes. Arid and semi-restricted settings led to the variable deposition of red beds, mudstones, massive evaporites, evaporitic dolostones, and shallow-water stromatolitic dolostones with sparse basalt flows (Figure 1.3, 1.4h-j; Melezhik et al., 2013b). Overall the sedimentary environment transitioned from peritidal and shallow-water tidal environments to deeper intertidal settings co-extant with sabkhas and playas, then returned to intertidal marine conditions (Melezhik et al. 1999a). This was followed by emergence and partial erosion, though a discontinuity is apparent only in some parts of the basin (Melezhik et al. 2013b).

By ~2100 Ma, the Fennoscandian blocks were fully split as the Kola rift to the north of the Onega basin developed into the Kola Ocean (Daly et al. 2006) and, after ~2060 Ma, so did the

rift to the south-west of the basin, such that the Onega Basin became part of the margin of the Svecofennian Sea, and eventually, the Jormua Ocean (Karhu, 1993; Melezhik and Hanski, 2013). Concurrent with this, a rift opened in the Onega Basin, resulting in a volcanically active and relatively deeper-water depositional environment (Melezhik and Hanski, 2013). Sediments and volcanic rocks of this time period form the Zaonega Formation, the most areally extensive of the formations in the Onega Basin, containing siliciclastic turbidites and fine-grained, parallel-laminated, highly C_{org}-rich mudstones intercalated with (calcitized) dolostones (Figure 1.3, 1.4c-g). Most of the thickness of the formation is, however, made up of mafic sills, lavas, and tuffs (Melezhik et al. 1999b). The western part of the basin was subsequently filled with several hundreds of meters of Suisari Formation tuffs and ultramafic lavas/sills deposited in deep-water conditions, with minor tuffaceous mudstone layers (Figure 1.3, 1.4a, b; Melezhik et al. 2013b); the formation is considered to be a remnant of one of the oldest continental flood basalts (Puchtel et al. 1998).

After the deposition of the Suisari Formation, the Svecofennian Sea began to close; a ~100 Myr period followed during which the Karelian block underwent collision with several island arcs in a north-east direction, forming the Svecofennian orogen (Lahtinen et al. 2009). During this period, the sediments in the Onega Basin were uplifted and eroded, but as the rift reactivated, a lacustrine basin reformed (Melezhik and Hanski, 2013). Rocks from this time are poorly studied and difficult to correlate in the Onega Basin, but the central part of the basin includes thick successions of turbiditic greywackes, and polymict sandstones and siltstones, comprising the Kondopoga Formation (Figure 1.3; Melezhik et al. 2013b). The lack of sulphide

minerals, but abundant diagenetic ankerites and siderites has been interpreted as evidence for iron fixation in a sulphide-depleted lacustrine setting (Melezhik et al. 2009). The formation also hosts pyrobitumen clasts, interpreted to be redeposited from surface oil seeps, ultimately derived from Zaonega Formation source rock (Melezhik et al. 2009). Deposition in the basin terminated with the Vashozero Formation, comprised of greywackes, cross-bedded sandstones, siltstones, and mudstones, but also some stromatolitic dolostones, tentatively interpreted as reflecting shallow-water, high-energy supratidal environments (Melezhik et al. 2013b).

Following deposition, between ~1890–1790 Ma, the building of the Svecofennian orogen forced the Onega Basin into a series of parallel, northwest–southeast oriented folds, dipping towards the south-east, with shallow synclines but steep anticlines, further complicated by parallel faults (Melezhik et al. 2013b). Regional metamorphism proceeded to greenschist facies, as shown by the formation of talc from dolomite and quartz in the Tulomozero and Zaonega formations (but only rare presence of tremolite; Melezhik et al. 1999a), and chlorite–actinolite–epidote paragenesis corresponding to ~350°C in the Zaonega Formation (Melezhik et al. 1999b). Following this, the basin has enjoyed a tectonically quiescent regime (Melezhik et al. 2013b).

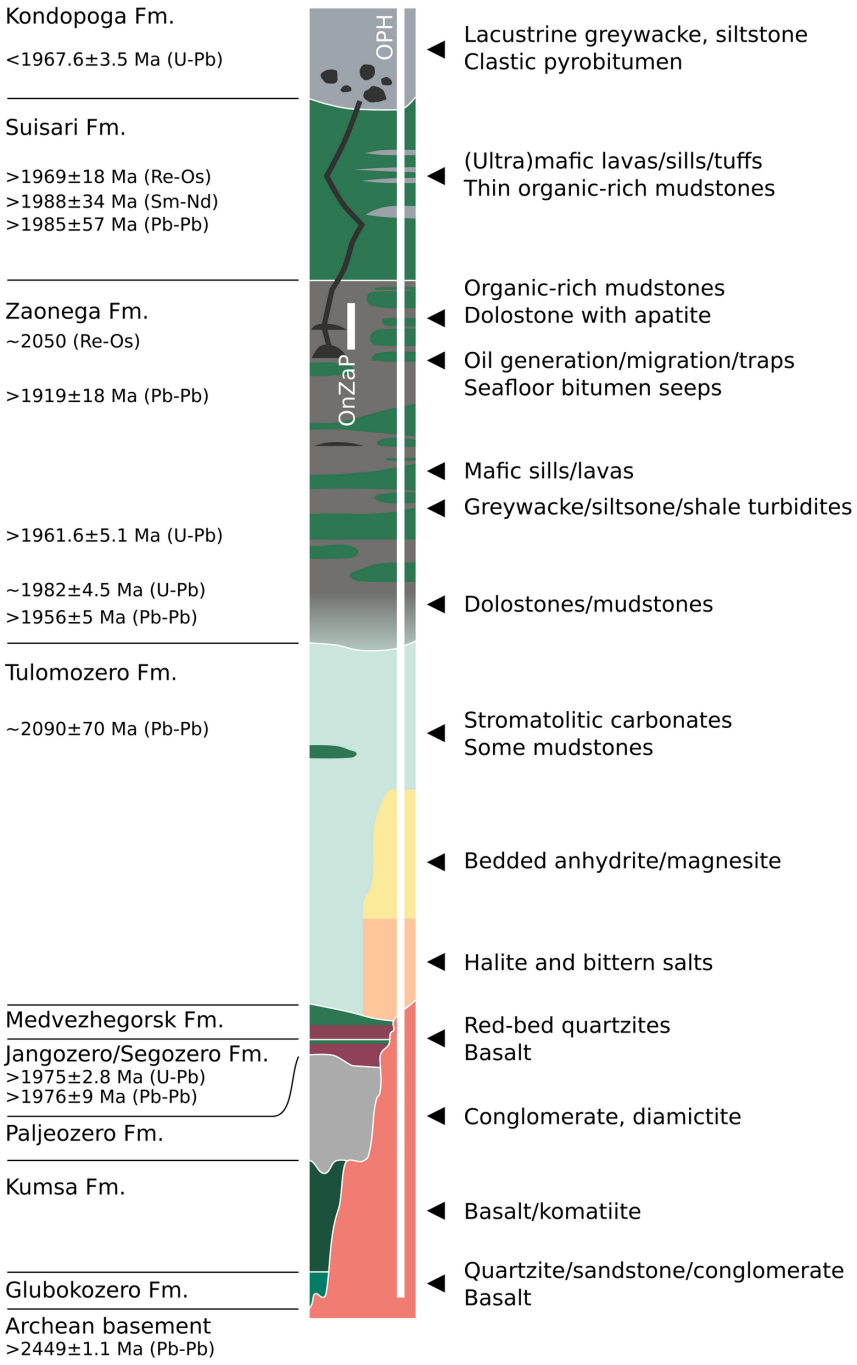

Figure 1.3: Simplified stratigraphic column of the Onega Basin sedimentary succession showing formation boundaries, age constraints, predominant geological features, and drill cores (OPH =

Onega Parametric Hole). Age constraints are explained in text and in Martin et al. (2015). Modified from Melezhik et al. (2015) and Paiste (2018).

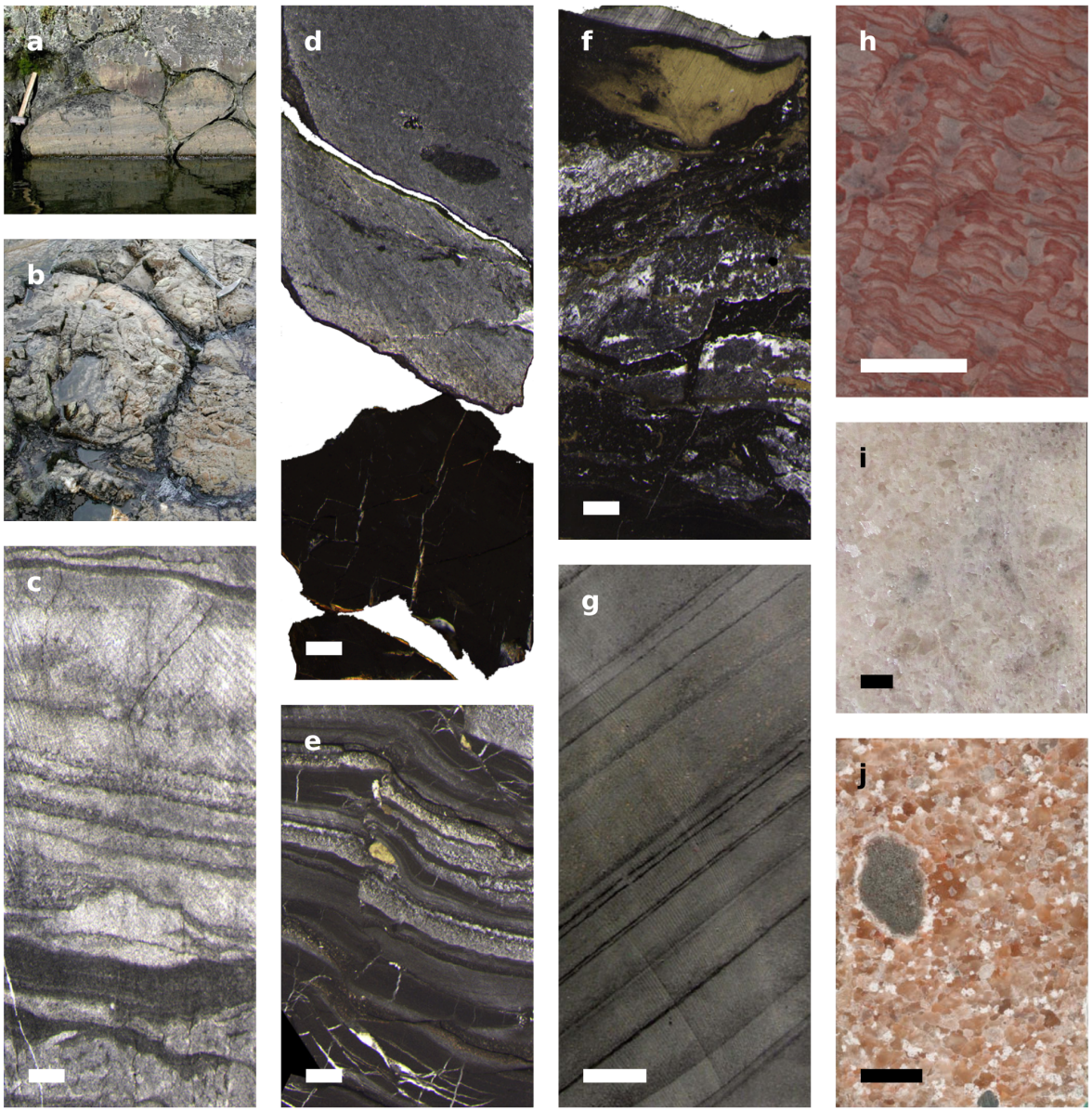

Figure 1.4: Photographs illustrating common rock types in the studied section of the Onega Basin. (a, b) Mafic pillow lavas of the Suisari Formation in outcrops on the western shore of

Lake Onega. Hammer heads in both images are ~15 cm across. Reproduced from Melezhik et al. (2013b). (c-g) Drill core photographs of the Zaonega Formation. (c) Laminated fine-grained dolomite in the upper part of the formation, at 13 m depth in the OnZaP section (Paiste et al. 2018). (d) Contact between phosphorus-hosting massive dolostone and highly organic-rich mudstone hosting pyrobitumen veinlets at 53 m in the OnZaP section, used for basin-wide correlation (Paiste et al. 2020a). (e) Laminated organic- and sulphide-rich mudstone displaying soft-sediment deformation as well as quartz-mica and pyrobitumen veining, 63 m in the OnZaP section (Paiste et al. 2018). (f) Highly silicified mudstone displaying deformation, intense veining, and secondary pyrite, 77 m in the OnZaP section (Paiste et al. 2018). (g) Rhythmically bedded greywacke-siltstone in the lower Zaonega Formation, 282 m depth in the FAR-DEEP 12AB drill cores (Melezhik et al. 2013b). (h-j) Drill core photographs of the Tulomozero Formation. (h) Pink dolostones composed of columnar stromatolites, with dolarenite filling inter-columnar areas, 303 m depth in drill core 7 (Melezhik et al. 2013b). (i) Massive, coarse-crystalline anhydrite in the middle part of the formation in the southern Onega Basin, at 2510 m in the Onega Parametric Hole (Melezhik et al. 2015). (j) Brown-pink, massive, coarse-grained halite with felted anhydrite and magnesite intraclasts and accessory bittern salts. Lower part of the Tulomozero Formation, 2854 m in the Onega Parametric Hole (Blättler et al. 2018). Scale bars are 1 cm across.

1.4.2 Tulomozero Formation

This thesis focuses on the Tulomozero, Zaonega, and Suisari formations, which are described in more detail below. There is significant vertical and lateral lithofacies variation in the ~800-m-

thick Tulomozero Formation. The south-western part of the Tulomozero Formation lies on Archean crust and begins with a ~200-meters-thick unit of massive brown, pink, and grey halite with accessory bittern salts (e.g., sylvine) and clasts of magnesite (Figure 1.4j), then passing into ~300 m of massive anhydrite-magnesite (Figure 1.4i; Blättler et al. 2018) interbedded with shales. This suggests a restricted, lagoonal setting transitioning into a sabkha environment (Melezhik et al. 2015). However, the basin must still have been open to seawater replenishment in order to sustain the accumulation of thick salt deposits (Blättler et al. 2018). By contrast, in other parts of the basin, the succession begins with cyclical red sandstones, dolarenites, and siltstones suggesting deposition in fluvial settings transitioning into peritidal, or fining-upward dolarenite and mudstone cycles, interpreted as carbonate platform slope settings (Melezhik et al. 2015). On top of these lie sediments indicating the growth of a spatially heterogeneous shallow-water carbonate platform, where dolomite-dominated carbonate is the predominant lithology. In simplified succession, these are biostromal and biohermal columnar dolomite stromatolites (Figure 1.4h), as well as re-sedimented dolostones, reflecting low-energy shallow-water intertidal environments, barred evaporitic lagoons and peritidal evaporitic environments. These are followed by red, flat-laminated, dolomitic and magnesite stromatolites formed in evaporative ephemeral ponds and coastal sabkhas. Marine influence is interpreted to be highest in the topmost part of the formation (Melezhik et al. 2005). Lateral heterogeneity is exemplified through the common presence of shale lenses and interbeds in some upper Tulomozero Formation drill cores, but not others (Melezhik et al. 2013b). Arid conditions throughout the depositional period are revealed by desiccated carbonate and mudstone beds with tepees, abundant magnesite interlayers, dissolution breccias, quartz or dolomite pseudomorphs after

halite and Ca-sulphate minerals (lath-shaped or swallow-tail-terminating crystals and cauliflower nodules and lenses), and chicken-wire fabric in both mudstone and dolostone intervals, suggesting alternating playa lake and coastal sabkhas environments (Melezhik et al. 2005, Reuschel et al. 2012; Blättler et al. 2018). Nearly all lithologies in the Tulomozero Formation are tinged brown, red, or pink, indicating the presence of oxygen during deposition (Melezhik et al. 2015). A ~20-m-thick basalt flow is present in the upper part of the formation throughout the basin (Melehzik et al. 2013b).

The rocks of the Tulomozero Formation were all affected by regional greenschist metamorphism, as is evidenced by the presence of talc, ostensibly formed through the reaction of dolomite with quartz in metamorphic conditions (Melezhik et al. 2015). The metamorphism caused the recrystallization of much of the dolomite—there is very little preserved micritic dolomite, which is replaced by granular, crystalline and micro-sparitic dolomite, or with sparitic dolomite in later-stage void fillings. Some discolouring of the dolomite suggests epigenetic fluid flow. Major features of bedding and lamination, however, remain readily visible (Melezhik et al. 2015), and the $\delta^{13}C$ record is interpreted to not have been significantly affected (Melezhik et al. 1999a, 2001, 2015). In contrast to carbonate lithologies, the evaporite succession is likely to have remained largely pristine, aside from recrystallization, due to the retention of halite and bittern salts, which would have been readily dissolved had large amounts of fluids moved through the section (Blättler et al. 2018). Moreover, seismic reflectance data suggests that the salts have not undergone significant mass flowage (Blättler et al. 2018).

The Tulomozero Formation is famous as one of the type sections of the LJE—it contains $\delta^{13}C_{carb}$ values up to 18‰, which potentially reflect local amplification of a globally positive dissolved inorganic C pool (Schidlowski et al. 1975; Karhu 1993; Melezhik et al. 1999a). Furthermore, the abundance of evaporitic sulphate minerals, the overall succession of evaporite mineralogy, and the S and Ca isotopic composition of the sulphate phases have been taken as evidence of a large marine sulphate pool, perhaps >20% of modern levels (Melezhik et al. 2005; Reuschel et al. 2012; Blättler et al. 2018). This indicates highly oxidized ocean conditions during the deposition of the Tulomozero Formation.

1.4.3 Zaonega Formation

The overlying Zaonega Formation is a ~1500-m-thick volcano-sedimentary package with a controversial relationship to the Tulomozero Formation. Melezhik et al. (2013b) most recently highlighted a significant (even angular) unconformity in parts of the basin, with the implication of a time gap made more significant by uplift and erosion of the Tulomozero Formation (Melezhik et al. 2013b). The lower part of the Zaonega Formation begins with ~200 m of rhythmically interbedded feldspar-quartz sandstones and siltstones (mica and pyrite are also common; Figure 1.4g) with thin dolomite interlayers and dark, carbonaceous quartz-sericite-chlorite-carbonate shales with disseminated pyrite. Overlying these are ~100 meters of sandstones, siltstones, and shales, including distinctively coloured, thinly laminated, marly rhythmitites that are a marker horizon throughout the basin. These are topped by horizontally-bedded quartz-feldspar sandstones and quartz-sericite-chlorite shales (Krupenik and Sveshnikova 2011; Melezhik et al. 2013b). The upper part of the Zaonega Formation includes the prior

lithologies, but is dominated by highly C_{org}-rich siliciclastic mudstones (Figure 1.4e) and abundant mafic sills, tuffs, and lavas. It begins with a ~200-m-thick member of cyclically interbedded greywackes and mudstones displaying Bouma sequences characteristic of turbidity currents, with minor carbonate beds (mostly dolomitic), conglomerates, some C_{org}-rich rocks, and amygdaloidal mafic lava flows and gabbro sills (with peperitic textures). These are topped by a 300-m-thick member of Bouma-sequence greywacke, and highly C_{org}-rich siltstone and mudstone (locally termed shungite; up to >80 wt.% C_{org}), interbedded with massive dark grey carbonates (calcite to dolomite) and black silica-rich veins and layers. The member also hosts (in a laterally heterogeneous manner) amygdaloidal and pillow basalts with peperite contacts. This is topped by 200–300 m of siltstones, tuffite, quartz–biotite–chlorite and biotite–albite–quartz schists, and variably C_{org}-bearing dolostones (Figure 1.4c; Melezhik et al. 2013b). The upper half of the formation is also rich in disseminated and nodular to massive sulphides, primarily pyrite (Figure 1.5a; Paiste et al. 2018), but also pyrrhotite (Asael et al. 2013).

The depositional environment of the Zaonega Formation is poorly constrained (Melezhik et al. 1999a, 2013b). An abundance of intruded magma bodies and lavas throughout the formation attests to a volcanically active basin. The igneous bodies are distributed in a laterally heterogeneous manner: in the northern part of the basin, ~35% of the succession's thickness is constituted by igneous rocks, whereas the number increases to as much as 70% in the southwestern part (Melezhik et al. 2013b). Abundant sulphides suggest a marine-dominated setting and generally fine-grained textures together with Bouma-sequence rhythmitites attest to a deep-water environment. However, cross-bedding is common in dolostones and mudstones of

the upper part of the formation (Paiste et al. 2018). The complexity of the depositional setting is attested to by common soft-sediment deformation (Figure 1.4e), slumped beds, boudinage, sedimentary dykes (containing pyrobitumen and calcite) and intraformational conglomerates (Črne et al. 2013a, 2013b). Overall, the formation is consistent with deposition in a volcanically active and laterally heterogeneous rift basin developed on the margin of the Svecofennian Sea (Melezhik et al. 2013b).

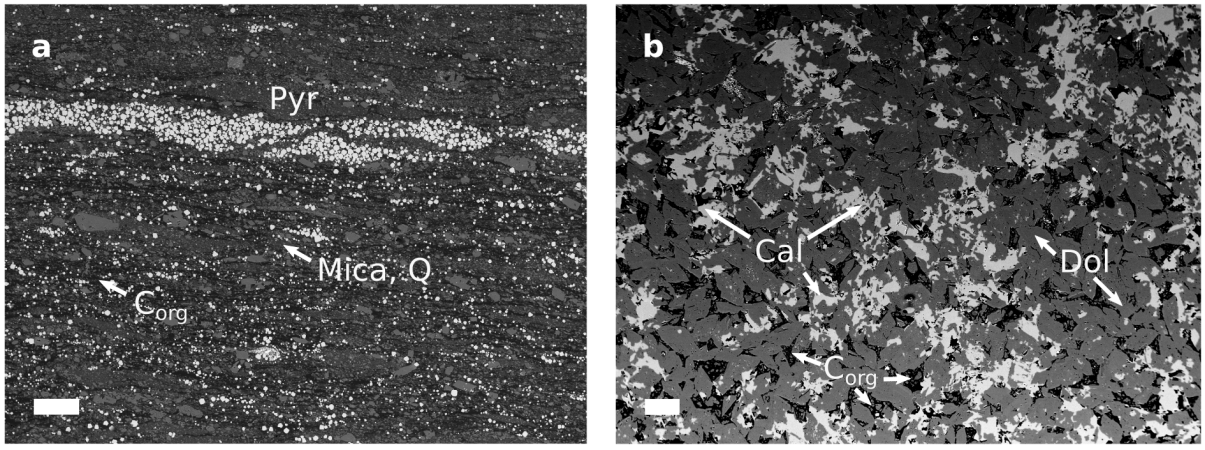

Figure 1.5: Representative scanning electron microscope images of upper Zaonega Formation rocks. (a) Organic-rich mudstone with alternating layers of organic C (C_{org}) and mica-quartz (Q) with early-diagenetic pyrite (Pyr) layers and clusters; 1116 m depth in the Onega Parametric Hole drill cores (courtesy of K. Paiste). (b) Dolostone sample containing planar-e dolomite (Dol, dark grey) crystals that have been partially dedolomitized to calcite (Cal, light grey) in an organic C matrix. From 1112 m in the Onega Parametric Hole (Kreitsmann et al. 2019). Scale bars are 100 μm across.

Post-depositional processes are extensively studied in the Zaonega Formation. Greenschist-facies metamorphism resulted in chlorite–actinolite–epidote mineral paragenesis (Melezhik et al. 1999b). Abundant sills with peperitic contacts, associated with explosion-expulsion breccias, show intrusion of magma bodies into as-of-yet unconsolidated sediments (Črne et al. 2013a, 2013b). This drove extensive hydrothermal circulation and oil generation in the basin, exemplified by common mica-quartz and pyrobitumen veins, as well as silicification of sedimentary intervals (Figure 1.4f; Melezhik et al. 2013b; Paiste et al. 2018). One result of this is that carbonate beds in the upper Zaonega Formation were affected by secondary dedolomitization. Carbonate bed centers are composed predominantly of planar-e to planar-s >300 μm dolomite with C_{org} or mica filling the pore space, but in bed margins, calcite dominates, often present as pseudomorphosed dolomite crystals together with quartz, mica, and talc (Figure 1.5b). This change in mineralogy was accompanied by lowering of $\delta^{18}O$ and $\delta^{13}C$ values (both down to −16‰; Črne et al. 2014; Kreitsmann et al. 2019, 2020). Fluid movement has also resulted in the dissolution of some early diagenetic, fine-grained, disseminated pyrites (Figure 1.5a) and the precipitation of pyrrhotite (Asael et al. 2013), and large secondary vein- or void-filling pyrite concretions (Figure 1.4f; Paiste et al. 2018). Oil migration is seen in numerous 0.1 to 5-cm-wide pyrobitumen veins and veinlets cross-cutting the formation (Figure 1.4d, e; Melezhik et al. 2004), which are most abundant in contact zones with igneous bodies (Qu et al. 2012). Vesicles inside the veins, sometimes filled with secondary minerals, attest to cracking and degassing of oil. High-resolution $\delta^{13}C$ stratigraphy suggests that most oil migration distances remain in the few centimeters to couple meters range (Qu et al. 2012). Some oil traps (up to 95 wt.% C_{org}), however, occur in the upper part of the basin between brecciated dolostones,

sandstones or bedded between C_{org}-rich mudstones and dolostones (Qu et al. 2012, Strauss et al. 2013, Paiste et al. 2018). Massive, unbedded, dark grey Si- and C_{org}-rich rocks, locally termed maksovite, occur as distinctive lensoidal bodies up to >100-m-thick, associated with breccias in the host rocks; these have been interpreted as fossil seeps of oil and fluidized sediments to the seafloor (Qu et al. 2012, Strauss et al. 2013). Clastic pyrobitumen, interpreted as remnants of oil seeps, are also found in the overlying Kondopoga Formation (Melezhik et al. 2008).

Dolostone layers in the lower part of the Zaonega Formation record positively fractionated $\delta^{13}C$ values, indicative of the final stages of the LJE. Upper Zaonega Formation carbonate rocks, on the other hand, host negatively fractionated $\delta^{13}C_{carb}$ (<−16‰), associated with <−40‰ $\delta^{13}C$ organic matter, and were interpreted by Kump et al. (2011) to reflect a global episode of black shale weathering. However, these low values have been reinterpreted to reflect methane methanotrophy (Qu et al. 2012, 2018) and recrystallization of carbonate minerals in the presence of methane- and organic-C-derived dissolved inorganic C (Črne et al. 2014; Melezhik et al. 2015; Kreitsmann et al. 2019, 2020). The most pristine among dolostone intervals of the upper Zaonega Formation display slightly negative to normal-marine $\delta^{13}C$ values and likely reflect post-LJE deposition. The upper Zaonega Formation also contains mudstone and dolostone layers enriched in apatite (Figure 1.4d), associated with highly C_{org}-rich intervals, making it one of the world's oldest deposits of phosphate-rich rocks. High pyrite contents (Paiste et al. 2018), a background of intensive methane generation (Qu et al. 2012), and putative fossil methane and sulphur cycling microbial communities have led to the interpretation that apatite precipitation resulted from biotic phosphate pumping by methane and sulphur-cycling microorganisms under

variable sediment redox conditions (Lepland et al., 2014). Variable and often heavy pyrite $\delta^{34}S$ values in the Zaonega Formation have been interpreted as recording a diminished global marine sulphate pool (Scott et al., 2014), or anomalously high local sulphate demand by microorganisms (Paiste et al. 2018, 2020a, 2020b), whereas authigenic rare earth element patterns in apatite and dolomite suggest deposition in a hydrothermally active and semi-restricted basin under and oxidative atmosphere (Joosu et al. 2015; Kreitsmann et al. 2020).

1.4.4 Suisari Formation

The Suisari Formation, which overlies the Zaonega Formation, is the least studied of the three and comprises a ~700-m-thick package of mafic to ultramafic volcanic or volcaniclastic rocks and sills. Overall, the succession hosts thick and numerous high-MgO mafic lava flows displaying variolitic and amygdaloidal textures and pillow structures (Figure 1.4a, b), as well as mafic pyroclastic flows. Packages of lava flows are separated by sometimes rhythmical parallel-to-cross-bedded basaltic tuffs, which together comprise ~100 m of stratigraphy. The Suisari Formation is also intruded by a large amount of basaltic and doleritic dykes and sills. Abundant pillow basalts and pyroclastic flows attest to the importance of both subaqueous and subaerial volcanism. Parallel-bedded and rhythmical pyroclastic flows and tuffs suggest deep-water and redepositional sedimentation (Melezhik et al. 2013b). Given radiometric, lithostratigraphic, and geochemical constraints linking the basalts to coeval ones in other parts of the Fennoscandian shield, Puchtel et al. (1998, 1999) interpreted the Suisari Formation to reflect one of the earliest continental flood basalts, derived from a single large mantle plume.

1.4.5 Age constraints

Age constraints on the Onega Basin sedimentary succession are sparse and generally imprecise (Figure 1.3). As a maximum bound on the earliest deposition in the basin, a 2449±1.1 Ma Pb–Pb age was acquired using ID-TIMS from a pluton that cross-cuts the Archean basement, on which the sedimentary succession rests (Amelin et al. 1995). The first syn-depositional bound is from early diagenetic dolomites of the upper Tulomozero Formation, which yielded a 2090±70 Ma Pb–Pb age (Ovchinnikova et al. 2007). In the lower Zaonega Formation, Martin et al. (2015) reported a single-zircon U–Pb age of ~1982±4.5 Ma from a tuff layer, whereas preliminary Re–Os isochrons of ~2050 Ma have been reported for upper Zaonega Formation C_{org}-rich mudstones (Hannah et al. 2008; Bauer et al. 2019). The ages of the Tulomozero Formation and the lower Zaonega Formation are, furthermore, constrained by their positive $\delta^{13}C_{carb}$ values (e.g., Melezhik et al. 2015), which attest to their deposition during the LJE, bracketed between ~2200 and ~2060 Ma in Fennoscandia (Martin et al. 2013). In the Suisari Formation, gabbro sills, interpreted to be coeval with the platformal lavas, have been dated at 1988±34 using Sm–Nd systematics on combined whole-rock and clinopyxene samples; 1985±57 Ma using whole-rock and plagioclase Pb–Pb dating; and 1969±18 Ma by a Re-Os isochron from whole-rock peridotite/gabbro, ilmenite, and ulvöspinel (Puchtel et al. 1999). Finally, a sandstone in the Kondopoga Formation yielded a detrital zircon Pb–Pb age of 1967±3.5 Ma (Martin et al. 2015).

A suite of cross-cutting dykes in the Onega Basin provide minimum age constraints. A mafic sill in the Jangozero Formation (incorrectly labeled as a lava flow by Martin et al. 2015, see Kipp et al. 2020) has yielded U–Pb zircon and baddeleyite ages of 1976±9 Ma (Puchtel et al.

1998) and 1975.3 ± 2.8 Ma (Martin et al. 2015). Dolerite sills in the Zaonega Formation have given Pb–Pb zircon ages of 1956±5 Ma from the lower part of the formation (Stepanova et al. 2014), 1961±5.1 Ma from the middle part (Martin et al. 2015) and 1919±18 Ma from the upper part (Priyatkina et al. 2014). Since many among such sills display peperitic contacts (Črne et al. 2013a, 2013b), implying emplacement into unconsolidated sediments, it is possible that these ages approach the time of sediment deposition (Melezhik et al. 2013).

Therefore, while dates remain imprecise, the Onega Basin offers an almost unique opportunity to assess geochemical O_2 proxies in a single, thick sedimentary succession that records the height of the LJE, its termination and the immediate aftermath.

1.4.6 Studied material

Though the Onega Basin is a keystone in our understanding of redox development during the middle Paleoproterozoic, it is a highly complex sedimentary setting which has led to much controversy over the origins and meaning of the proxy records contained in the basin's sediments. In order to provide further geochemical constraints, samples were acquired from three drill cores of the Onega Basin: OnZaP-1 and OnZaP-3, which together form a 102-m-thick composite section of the upper Zaonega Formation, and the Onega Parametric Hole that sections >2400 meters of LJE to post-LJE sedimentary rocks of the Tulomozero, Zaonega, and Suisari Formations.

The OnZaP-1 and -3 cores were drilled in 2012 near the Shunga village, (65.5870N 34.9310E and 65.5920N 34.9280E, respectively). A lithological description of the full composite

section, as well as discussion on pyrite paragenesis and sulphur isotope systematics, is given by Paiste et al. (2018). Carbonate petrography and geochemistry in the same section are expanded on by Kreitsmann et al. (2020). Briefly, the lower part of the section from 102 to 53 m depth hosts shales with high C_{org} (up to 70 wt.%) and pyrite contents, increasing towards the top of the interval. Interbedded between them are dark grey dolomite–calcite beds. Between 53 and 44 m depth a massive dolostone layer occurs, hosting apatite. Mica–quartz and pyrobitumen veins are abundant from 102 to 53 m. Above 44 m, shales with much lower C_{org} and pyrite contents are interbedded with carbonates containing dolomite, siderite, and ankerite, and displaying cross-bedding features. Pyrobitumen veins are markedly rarer in this interval.

Two sets of samples were acquired from the OnZaP section: set MSP0001, containing 134 samples, aimed to cover the whole section at ~1 m intervals, whereas lithological transitions were sampled at a higher resolution. Sample set MSP0010, consisting of 78 samples, focused specifically on C_{org}-rich mudstone intervals with the aim of studying mechanisms of trace metal enrichment.

The OPH core was drilled ~80 km south-southwest of the OnZaP cores (62.1559 N 34.4073E) in 2007–2009. A full lithological description of the OPH core is only available in Russian-language literature (Krupenik and Sveshnikova 2011), but a partial English-language summary is given by Melezhik et al. (2013b). Blättler et al. (2018) further describe the lower, evaporitic part of the Tulomozero Formation in the OPH core, whereas Melezhik et al. (2015) focus on carbonate petrography and geochemistry in the Tulomozero and Zaonega formations, and Kreitsmann et al. (2019) in the upper Zaonega Formation. The recovered core begins with

the Tulomozero Formation: from 2940 to 2833 m depth is a unit of massive halite with anhydrite, magnesite, and mudstone interclasts, as well as ~10 wt.% of bittern salts. This is followed from 2833 to 2330 m by interlayered meter-scale cycles of anhydrite, magnesite and laminated mudstone. From 2330 to 2115 m depth, pink to tan microbially laminated dolostone predominates, but red magnesite-hosting mudstone and magnesite layers are also common. Above 2115 m depth starts the Zaonega Formation, beginning with interlayered shale and dolomite, then transitioning to tuffaceous shales with rhythmic bedding above 2035 m depth. Above 1866 m depth, the formation is dominated by dolerite and basalt sills. C_{org}-rich mudstone and carbonate intervals occur at 1789–1713 m, 1597–1583 m, 1546–1535 m, 1439–1426 m, 1419–1379 m, and 1358–1348 m. A much longer section of highly C_{org}-rich mudstones interbedded with dolostones occurs from 1226–1069 m, host to an apatite-rich mudstone–dolostone contact at 1112 m, which has been correlated to the OnZaP section based on lithological similarity, and C and S isotope stratigraphy (Paiste et al. 2020a, 2020b). Further (tuffaceous) mudstone layers, typically lower in C_{org} and pyrite content, are present at 1034–1012 m, 949–945 m, 913–876 m, 818–813 m, and 798–790 m. Above 790 m is the Suisari Formation, dominated by MgO-rich mafic to ultramafic lavas, sills, and pyroclastic flows. Tuffaceous mudstone layers occur at 6 separate intervals between the start of the formation and the end of the recovered OPH core at 530 m depth, constituting ~47 m of stratigraphy.

Three sets of samples were taken from the OPH core: set “NGU” consisted of 140 samples, taken to explore changes in chemical composition, cover the Zaonega and Suisari formation sedimentary packages, with a particular focus on the 1226–1069 m interval. Sample set “ACME”

(40 samples) was intended to provide increased resolution for trace metal studies in the 1124–1080 m interval, especially near bed contacts. Sample set “Yale” (73 samples), intended specifically for Cr isotope analyses, aimed to uniformly cover the entire OPH sedimentary succession, including the Tulomozero Formation, except for increased resolution between 1226–1069 m.

1.5 Metal geochemistry

The methodology of this dissertation centres on the geochemistry of a suite of metals in the Onega Basin. Redox-sensitive metals are widely utilized as proxies for oceanic and atmospheric redox changes through Earth history due to their contrasting chemical behaviours in oxygen-rich, oxygen-poor, and sulphide-rich conditions. Many trace metals, such as Mo, U, Re, and Cr (Fe acts in the opposite manner), are present at higher concentrations under elevated oxidation states in oxygen-rich conditions, where they form highly soluble complexes (Morford and Emerson 1999; Tribovillard et al. 2006; Robbins et al. 2016; Robbins et al. 2020). In contrast, these metals occur in highly insoluble or particle-reactive forms in oxygen-rich settings, resulting in efficient loss to sediments. Accordingly, it is possible to assess local water column redox conditions based on the efficiency of trace metal drawdown into underlying sediments (e.g., Jones and Manning 1994; Algeo and Liu 2020). As a corollary, the size of the global dissolved trace metal pools, i.e., their average seawater concentration, is highly dependent on the ratio of oxidized to anoxic depositional conditions. Since trace metal concentrations in anoxic sediments scale with aqueous concentrations in the overlying water column (Algeo and Lyons 2006), it is possible to assess changes in global oceanic redox balance by comparing metal concentrations in anoxic

sedimentary rocks through time (e.g., Scott et al. 2008; Partin et al. 2013a; Reinhard et al. 2013; Sheen et al. 2018).

More nuanced redox inferences can be gleamed through the isotope composition of such metals. In this work, I focus on Fe, Mo, U, and Cr isotopes. Secular shifts in sediment Fe isotope compositions (δ^{56}Fe; Beard and Johnson 1999) over the Neoarchean and Paleoproterozoic are indicative of large-scale changes in Earth system redox conditions, but δ^{56}Fe had already stabilized by the time sediments in the Onega Basin were deposited (Rouxel et al. 2005). More often, δ^{56}Fe in anoxic sediments is used as a nuanced tracer of local redox settings and hydrographic conditions, as δ^{56}Fe fractionations can be the result of changes in the size and drawdown efficiencies in the local dissolved Fe(II) pool, the availability of sulphide, microbial Fe redox cycling, or basinal Fe shuttling (Rouxel et al. 2005; Severmann et al. 2008; Dauphas et al. 2017; Mansor and Fantle 2019).

Molybdenum isotope compositions in seawater (δ^{98}Mo) are a widely used global redox proxy, most significantly affected by adsorption to manganese(IV) oxides precipitating under oxic conditions (Barling et al. 2001, Siebert et al. 2003; Arnold et al. 2004). These reactions preferentially remove ^{95}Mo from seawater, inducing a large, −3.3‰ fractionation (Siebert et al. 2003) and driving residual seawater δ^{98}Mo to more positive values. As a result, the relative abundance of oxic depositional conditions, where manganese(IV) cycling can occur, largely determines average seawater δ^{98}Mo composition. Molybdenum isotope ratios in sediments deposited under anoxic and sulphidic conditions can be inherited from seawater with only minor

fractionation and can therefore be considered proxies for the global seawater redox state (Arnold et al. 2004; Kendall et al. 2017).

An opposite mechanism controls the U isotope composition of seawater ($\delta^{238}U$): the largest fractionations are associated with incorporation into anoxic, organic-rich sediments, which strongly prefer ^{238}U, driving residual seawater $\delta^{238}U$ values more negative (Weyer et al. 2008; Tissot and Dauphas 2015). More positive seawater and sediment $\delta^{238}U$ values are, therefore, seen in oxygenated oceans where anoxic conditions are scarce (Kendall et al. 2015; Andersen et al. 2017; Wang et al. 2018).

In contrast to the marine-focused Fe, Mo and U systems, foremost Cr isotope fractionations ($\delta^{53}Cr$; Ellis et al. 2002) are imparted in continental settings, during the oxic weathering of igneous Cr(III)-hosting minerals (Frei et al. 2009). The most significant oxidant strong enough to convert insoluble Cr(III) to Cr(VI) is Mn(IV)-oxides, which require appreciable atmospheric O_2 availability. Upon reaction with Cr(III), they induce a major positive fractionation in the resulting soluble Cr(VI) phase (Schauble et al. 2004). As most other subsequent aqueous fractionation processes require Cr(VI), the presence of fractionated Cr in sediments is evidence of an oxidizing atmosphere (Frei et al. 2009; Crowe et al. 2013; Wei et al. 2020). A complication in this framework is the discovery that photochemical reactions with UV light (Liu et al. 2020) and anoxygenic photosynthesis (Daye et al. 2019) are also capable of oxidizing Mn(II), which may. Furthermore, organic ligands are capable of solubilizing Cr(III) while producing vaying $\delta^{53}Cr$ fractionations (Saad et al. 2017). It remains unclear to which extent these processes are capable of leading to large-scale $\delta^{53}Cr$ fractionations in marine sediments—after all, such

processes must have been operational over the Archean and Proterozoic, yet the Precambrian δ^{53}Cr record remains highly distinct from the Phanerozoic one (Saad et al. 2017)—but the possibility must be considered.

1.6 Summary and aims

There is considerable interest in understanding the major environmental transformations of the Paleoproterozoic. However, much of the canonical interpretations pertaining to rising and falling O_2 levels, the mechanisms behind major perturbations of the element cycles, and their combined effect on the evolution of life, have recently been challenged based on competing theoretical frameworks of elemental cycling and more complex models of basinal evolution. This is particularly the case for the Onega Basin, a pillar for the modern understanding of post-GOE redox shifts (e.g, Paiste et al. 2020a). As a result, the mechanisms behind these Paleoproterozoic environmental transformations, amongst the most consequential in Earth history, are still unconstrained.

The aim of this thesis, therefore, is to constrain the redox and hydrographical conditions of key sections of the Onega Basin, particularly the upper Zaonega Formation, in order to provide a well-founded assessment of oceanic and atmospheric redox development through the LJE and immediate post-LJE time periods. For this purpose, I utilize a suite of local and global redox proxies consisting of trace metal concentrations, as well as Fe, Mo, U, and Cr isotope characteristics on the OnZaP and OPH drill cores.

Specifically, chapter 2 aims to provide constraints on the basinal configuration and redox structure of the Onega Basin using Fe isotope ratios in mudstones of the upper ZF. Anticorrelation between authigenic Fe abundance and ^{56}Fe-enrichment attests to the presence of a benthic Fe shuttle (Severmann et al. 2008), which, in turn, requires basinal restriction and a redox-stratified basin to facilitate redox cycling of Fe and its quantitative capture in anoxic sediments (Wijsman et al. 2001; Anderson and Raiswell 2004). However, contrasting hints of oxic Fe drawdown in some samples, which display positive covariation between Fe abundance and δ^{56}Fe values, point to occasional influxes of oxidized water from the open ocean (Scholz et al. 2014). These results reveal a picture of a restricted Onega Basin that nevertheless retained a connection to the open ocean and thus was able to record geochemical signals of global element cycling—however, these signals were likely to be significantly modulated by basin-scale processes.

Chapter 3, using data from the same section of the upper ZF, centres on the abundances of redox-sensitive trace metals Mo, U, and Re, as well as Mo and U isotope ratios, in order to constrain global metal redox cycling in the aftermath of the LJE. Extremely high redox-sensitive metal concentrations require that the ZF acted as an efficient trace metal drawdown "pump," which was regularly replenished from a sizeable, oxidized dissolved trace metal reservoir in the open ocean. Even more exceptional U isotope ratios, likewise, suggest efficient U drawdown in a highly bioproductive basin, capturing the isotope signal of a globally oxidized seawater U pool (Andersen et al. 2014). The overall picture is that of a substantially oxygen-rich global ocean. Intriguingly, this section of the ZF likely post-dates the LJE by several to tens of millions of

years, showing that the end of the LJE did not necessarily correspond to a deoxygenation. This contradicts the "standard" narrative of the LJE, which invokes an increased C_{org} burial flux to explain both the C isotope excursion and the O_2 overshoot (Bekker and Holland 2012).

Chapter 4 expands the scope of the rocks studied to include most of the 2400-m-thick sedimentary succession of the Onega Basin, from evaporites and carbonates recording the height of the LJE to post-LJE organic-rich mudstones and carbonates. Chromium isotope measurements reveal fractionated Cr throughout this section, persisting over several facies shifts. Since fractionated Cr in seawater and sediments is best explained through oxidative weathering of Cr on land (Frei et al. 2009), requiring appreciable levels of pO_2, these results suggest that not only the oceans, but also the atmosphere remained stably oxidized throughout a potentially >100 million-year depositional period. This contrasts strikingly with the following mid-Proterozoic, which is seen as a time of generally low pO_2 and substantial redox instability (e.g., Toma et al. 2019). One implication of this finding is that, contrary to expectations, such a period of stable oxygenation did not immediately result in the emergence of a complex and diverse eukaryotic biosphere, as seen in the fossil record of the time (Butterfield 2015).

The final chapter concludes with an outline of future avenues for research. Among these are a focused study on the mechanisms behind anomalously high trace metal enrichment and hydrothermal alteration in the ZF using microscale X-ray adsorption fine structure analysis which can reveal the chemical speciation of Mo. Likewise, rare earth element patterns in ZF mudstones will be analysed to assess changes in sediment provenance over the section, potentially revealing shifts in basin configuration and further constraining the mechanisms of

metal enrichment. To expand the scope, lacustrine Kondopoga Formation mudstones in the Onega Basin, overlying the section studied in this dissertation (Melezhik et al. 2013b), are an intriguing target due to the presence of large acritarchs in that formation (Javaux and Lepot 2018). Local-scale redox proxies combined with refined paleontological methods may be used to constrain the environmental backdrop and evolutionary significance of this assemblage. Finally, at the broadest scale, the reasons behind the overlapping environmental transitions of the Paleoproterozoic will be investigated from the perspective of globally shifting weathering regimes and mineralogies, using a database of 21 compiled paleosol sequences. These proposed works are outlined in more detail in the concluding chapter.

Chapter 2: Iron isotopes reveal a benthic iron shuttle[1]

2.1 Introduction

The Proterozoic eon (2500–554 Ma) hosted some of the most fundamental global environmental transitions in Earth's history, including the multi-step rise of oxygen in the atmosphere (Lyons et al. 2014). The most pronounced amongst these are the Great Oxidation Event (2502–2320 Ma; Bekker et al. 2004; Warke et al. 2020), the Lomagundi Event, which has been proposed to coincide with an "O_2 overshoot" (~2200–2060 Ma; Karhu and Holland 1996; Bekker and Holland 2012; Martin et al. 2013), and the terminal oxygenation of the atmosphere in the Neoproterozoic Oxidation Event (~800–550 Ma; Och and Shields-Zhou 2012). Intermixed with these positive shifts in atmospheric O_2 fugacity is a proposed retrograde redox shift—an "O_2 crash"—that follows the Lomagundi Event and the O_2 overshoot (Kump et al. 2011; Canfield et al. 2013; though see contradictory view in Ohmoto et al. 2014). The timing, extent, and environmental significance of this O_2 crash are contentious, largely due to conflicting interpretations based on different geochemical redox proxies (Kump et al. 2011; Canfield et al. 2013; Scott et al. 2014; Ossa Ossa et al. 2018; Paiste et al. 2018; Kreitsmann et al. 2020; Mänd et al. 2020; Paiste et al. 2020b). Resolving the redox dynamics of the post-Lomagundi time period requires new geochemical proxy data from the sedimentary rock record to be placed in a

[1] A version of this chapter is prepared for submission as Mänd, K., Lalonde, S. V., Paiste, K., Thoby, M., Lumiste, K., Robbins, L. J., Kirsimäe, K., Lepland, A., and Konhauser, K. O. "Iron isotopes reveal a benthic iron shuttle in the Paleoproterozoic Zaonega Formation: Basinal restriction, euxinia, and the effect on global paleoredox proxies."

framework which takes into account both global and local elemental cycling (e.g., Paiste et al. 2020a).

The Paleoproterozoic Zaonega Formation comprises a sedimentary succession that records the end of the Lomagundi Event and the O_2 overshoot (Melezhik et al. 1999b). As such, it has been the target of a number of attempts to assess global redox conditions using a variety of geochemical proxies, such as carbon and nitrogen isotopes (Kump et al. 2011; Kreitsmann et al. 2019; Kreitsmann et al. 2020), rare earth element patterns (Joosu et al. 2015; Kreitsmann et al. 2020), sulphur isotopes (Scott et al. 2014), selenium isotopes (Kipp et al. 2020), and the abundances and isotopes of several redox-sensitive metals (Scott et al. 2008; Asael et al. 2013; Partin et al. 2013a; Scott et al. 2014; Asael et al. 2018; Mänd et al. 2020). Many of the interpretations in those previous studies rely on the assumption that the Zaonega Formation faithfully records chemical signals from the global ocean, so that inferences from these rocks may be extrapolated to assess global conditions. This assumption, however, is being increasing challenged on the basis that the Zaonega Formation was influenced by significant syn-depositional magmatic activity resulting in hydrothermal circulation, hydrocarbon generation and seepage, basinal reconfiguration and restriction, as well as local modulation of both the sulphur and carbon cycles (Qu et al. 2012; Črne et al. 2014; Joosu et al. 2015; Paiste et al. 2018; Kreitsmann et al. 2019; Kreitsmann et al. 2020; Paiste et al. 2020b).

The redox structure of the basin and its hydrographical openness are especially crucial in interpreting the redox-sensitive element record, since trace metal drawdown rates are dependent on water column oxygen or sulphide fugacity, with restricted conditions in anoxic basins

resulting in drawdown and distillation of the trace metal pool (Robbins et al. 2016; Robbins et al. 2020). Yet, recently published interpretations of the Zaonega Formation do not agree in this regard. On one hand, sulphur isotope modeling results (Paiste et al. 2018; Paiste et al. 2020b) and persistent positive europium anomalies (Joosu et al. 2015; Kreitsmann et al. 2020) seem to suggest a basin with poor access to the open ocean, but where anoxia and sulphidic conditions were restricted mostly to pore waters. On the other hand, selenium isotopes and trace metal abundances in the Zaonega Formation seem to require more anoxic and less restricted conditions (Asael et al. 2013; Scott et al. 2014; Kipp et al. 2020; Mänd et al. 2020).

In this study we report iron (Fe) elemental ratios and isotopes from a 102-meters-thick section of the Zaonega Formation in the northern Onega Basin—the same section previously investigated by Paiste et al. (2018), Mänd et al. (2020), and Kreitsmann et al. (2020)—in order to resolve issues surrounding the interpretation of paleoenvironmental depositional conditions. Due to its redox sensitivity and importance to microbial processes, Fe geochemistry is a powerful proxy for water column redox structure, sediment biogeochemistry, and basinal configuration (Poulton and Canfield 2005; Dauphas et al. 2017), and provides key insights into the Paleoproterozoic Zaonega Formations and its attendant controversies.

2.2 The Fe isotope paleoredox proxy

Iron is the most abundant redox-sensitive element in Earth's sedimentary environments and its geochemistry has been routinely used in assessments of paleoredox conditions from ancient sediments. To investigate Fe redox cycling, a variety of chemical indices have been proposed.

For example, positive deviations in the ratio of bulk Fe to bulk aluminum (Al)—a redox-insensitive element hosted in the detrital fraction of sediments—from the detrital mean (0.472±0.302 wt.% wt.%$^{-1}$; Cole et al. 2017) can indicate authigenic enrichment of Fe in sediments, whereas negative deviations may indicate microbial Fe(III) reduction and mobilization (Lyons et al. 2003; Raiswell et al. 2018). The Fe/Al ratio is commonly elevated under anoxic water masses, where Fe(II) can be drawn down into sediments through capture in sulphide minerals, so that a trend towards higher Fe/Al ratios is observed moving from shallower oxic facies to deeper anoxic ones (e.g., Severmann et al. 2008).

The most frequently utilized Fe-based redox proxy is the sequential Fe extraction method and the speciation data that it yields (Raiswell and Canfield 1998; Poulton and Canfield 2005). Based on calibrations in modern anoxic basins (i.e., the Black Sea), the ratio of highly reactive Fe to total Fe is indicative of redox conditions in the water column overlying the sediments. Under oxic conditions, the upper limit for this ratio is 0.22, and the lower limit for firmly anoxic conditions is 0.38 (Poulton and Canfield 2011). Values between these thresholds are considered equivocal, since water column iron enrichments could be masked by high sedimentation rates or transformation of unsulphidised highly reactive iron into sheet silicates (Raiswell et al. 1994; Poulton and Canfield 2011; Clarkson et al. 2014). Furthermore, if the fraction of pyrite-bound Fe within the total reactive Fe pool exceeds 0.7–0.8, the overlying water column may also have been sulphidic (Poulton and Canfield 2005, 2011), indicating prevailing euxinic conditions.

However, these relatively simple frameworks are complicated by factors such as bathymetry, sedimentation rate, and local terrigenous and hydrothermal inputs that can

significantly affect the distribution of Fe within sediments (Scholz 2018; Scholz et al. 2019), but which are rarely resolvable for ancient sedimentary basins. In addition, studies of modern environments have shown that Fe distribution in sediments may reflect the influence of a strong redoxcline rather than the whole water column (Rico and Sheldon 2019). The effects of post-depositional processes on Fe distribution patterns in sedimentary rocks are also important aspects to be considered, since diagenesis and metamorphism readily mobilise Fe and generate proxy signatures that are unrelated to environmental redox conditions (Clarkson et al. 2014; Slotznick et al. 2018). Thus, pairing Fe speciation with other proxies (e.g., mineralogy, petrography, trace elements, and isotope characteristics) is necessary for a more scrutinous interpretation of paleoenvironmental redox conditions.

Iron isotopes provide a particularly powerful tool in assessing Fe redox and precipitation processes (Dauphas et al. 2017; Johnson et al. 2020). The Fe isotope composition of a sample is commonly expressed as the permil deviation of the ratio ^{56}Fe over ^{54}Fe from that of the reference standard IRMM-014:

$$\delta^{56}Fe = ((^{56}Fe/^{54}Fe)_{sample}/(^{56}Fe/^{54}Fe)_{IRMM\text{-}014} - 1) \times 1000‰$$

Redox cycling produces the most substantial Fe isotope fractionations, since ^{56}Fe is preferentially enriched in Fe(III) over Fe(II). Equilibrium fractionation factors between aqueous Fe(II) and Fe(III)-bearing phases, such as ferrihydrite ($Fe[OH]_3$), goethite (FeO[OH]), or magnetite (Fe_3O_4), have been estimated to be between ~+3‰ and ~+1‰ (e.g., Beard et al. 2010; Wu et al. 2011; Frierdich et al. 2014a, 2014b). This means that sediments rich in authigenic Fe(III) commonly

have high δ^{56}Fe values—for example, ferrihydrite produced from aqueous Fe(II) by anoxygenic iron-based photosynthesis (also known as photoferrotrophy) is enriched in ^{56}Fe and results in a δ^{56}Fe shift of ~+1.5‰ (Croal et al. 2004). Furthermore, if a substantial fraction of dissolved Fe(II) is drawn down by Fe(III) precipitation, this can drive the residual Fe(II) pool towards negative δ^{56}Fe values, both on a basin scale (e.g., Planavsky et al. 2012b), and globally (Rouxel et al. 2005).

By contrast, redox cycling within sediments produces ^{56}Fe-depleted Fe(II)—most commonly this occurs through DIR, which couples microbial Fe(III) reduction with the oxidation of organic carbon. The generated Fe(II) hosts δ^{56}Fe values ~−1.3‰ to −2.6‰ lower than the Fe(III) substrate and can subsequently precipitate as magnetite, siderite ($FeCO_3$) or pyrite (FeS_2), or escape into the water column (Beard et al. 1999; Icopini et al. 2004; Crosby et al. 2007). In fact, DIR is such a dominant process in modern sediments that it supplies a substantial portion of ^{56}Fe-depleted dissolved Fe(II) into the oceans along with hydrothermal venting (where δ^{56}Fe tends to be ~−0.5–0.1‰) (Fung et al. 2000; Conway and John 2014).

Authigenic Fe(II) drawdown through sulphide precipitation in anoxic and sulfidic waters or sediments with no redox change can also induce a fractionation. This process occurs through several steps involving aqueous FeS and greigite (Fe_3S_4) and commonly results in the formation of pyrite (Luther 1991; Rickard 1997). The net fractionation factor for this process is typically considered to be negative, producing δ^{56}Fe shifts from 0.5‰ to −2‰ (Guilbaud et al. 2011; Rolison et al. 2018). Given that equilibrium and kinetic fractionations in pyrite precipitation produce opposing isotope effects, the sign and extent of fractionation depends on the extent and

rate of Fe(II) precipitation: late-stage pyrite precipitating slowly can evolve to positive values (Mansor and Fantle 2019).

While using pyrite δ^{56}Fe values recorded in ancient organic-rich shales to set constraints on local and global Fe cycling is possible (Dauphas et al. 2017), different influences on the Fe isotope budget often produce similar δ^{56}Fe shifts, making the interpretation of this record at times challenging. For example, if pyrite precipitates in the water column, δ^{56}Fe values can vary based on how much of the dissolved Fe(II) pool has previously been drawn down by Fe oxidation, which preferentially removes ^{56}Fe (e.g., Planavsky et al. 2012a). For pyrite produced diagenetically in the sediments through DIR, a detrital Fe(III) source will produce more negative δ^{56}Fe pyrite values than an authigenic Fe(III) source. Finally, since the resulting fractionation is governed by the rate of pyrite precipitation, both local sulphide and Fe(II) availability can modulate precipitation rates and, therefore, net fractionation (Mansor and Fantle 2019).

A highly diagnostic pattern in pyrite δ^{56}Fe is present in anoxic and sulphidic basins, such as the modern Black Sea. There, a "benthic Fe shuttle" delivers Fe(II) derived through DIR from suboxic sediments on basin margins towards deeper, more anoxic parts of the basins where it is deposited nearly quantitatively as pyrite (Anderson and Raiswell 2004; Severmann et al. 2008). Since biological reduction preferentially mobilizes ^{54}Fe, this results in a gradient towards higher authigenic iron abundance (Fe/Al) and more negative δ^{56}Fe from shelf to basin. For example, while oxic shelf sediments in the Black Sea carry δ^{56}Fe values averaging +0.16±0.02‰, sulphidic sediments further off-shore average −0.13±0.04‰ (Severmann et al. 2008). This mechanism has similarly been applied to sediments deposited during ancient oceanic anoxic

events (Duan et al. 2010). Crucially, the presence of such a trend has been shown to depend on several parameters, including the redox structure of the basin and the shelf-to-basin ratio, that are closely related to the degree of hydrographic openness (Scholz 2018). In more open settings than the Black Sea, even a positive sedimentary δ^{56}Fe–Fe/Al trend is possible as smaller fractions of dissolved Fe(II) are oxidatively recaptured in suboxic conditions (Scholz et al. 2014). Using the robust body of work on Fe-cycling processes in modern anoxic and suboxic analogue settings, it is possible to reconstruct ancient Fe cycling regimes based on pyrite δ^{56}Fe data.

2.3 Geological background

The Zaonega Formation forms part of the sedimentary succession within the >1200-km^2 Paleoproterozoic Onega Basin in northwestern Russia, on the northern shore of Lake Onega (Figure 1.2). The Onega Basin succession begins in the early Paleoproterozoic with the deposition of packets of terrigenous clastic sediments interlayered with lava flows in a continental rift setting (Melezhik et al. 2013b). Stabilization and shallowing of the basin led to the deposition of >800 m of evaporites and evaporitic carbonates of the Tulomozero Formation (Melezhik et al. 1999a). Following a deepening of the basin, >1500 m of shales, dolostones, and mafic lavas of the Zaonega Formation were deposited during a period of high volcanic activity (Melezhik et al. 1999b). The basin was subsequently filled by accumulation of hundreds of meters of mafic lavas and tuffs of the Suisari Formation (Puchtel et al. 1999). Deposition terminated with the emplacement of lacustrine siliciclastics of the Kondopoga Formation (Melezhik et al. 2013b). Subsequently, during the 1890–1790 Ma Svecofennian orogeny, the

basin was metamorphosed to greenschist facies and deformed into a series of northwest–southeast-oriented folds (Melezhik et al. 2013b).

The lithology of the Zaonega Formation is dominated by interbedded organic-rich shales and dolostones—the latter forming a larger portion in the lower and upper part of the succession, the former dominant in the middle portion—as well as turbidites and a smaller number of tuffs (Paiste et al. 2020a). Mudstones in the formation can be exceptionally rich in organic carbon (up to 70 wt.% in some layers; Melezhik et al. 1999b) and pyrite (up to 16.5%; Črne et al. 2013a, 2013b; Scott et al. 2014). The more organic-rich layers contain some of Earth's earliest phosphorus-rich sediments (Lepland et al. 2014). These results attest to a biologically productive basinal ecosystem and dissimilatory metabolic processes that led to sharp and fluctuating redox gradients in the sediments and water column (Lepland et al. 2014).

Additionally, >35% of the formation in the northern part of the basin, and ~70% in the southern part, is comprised of mafic volcanic rocks and intrusions, attesting to a strong volcanic influence on the sedimentary environment (Melezhik et al. 2013b). Some of the dykes and sills have peperitic contacts with the sedimentary layers, indicating syn-depositional emplacement (Melezhik et al. 2004). The resulting thermal gradient led to syn-depositional oil and gas generation, in turn fueling basin-wide methanotrophy in the sediments or the water column (Qu et al. 2012; Strauss et al. 2013), and resulting in oil spills (Melezhik et al. 1999b). The generation of hydrothermal fluids further led to emplacement of silicic veins that permeate the rock in the middle part of the Zaonega Formation (Paiste et al. 2018), and have led to dedolomitization and re-equilibration of the carbon and oxygen isotope compositions on carbonate beds, whereas

internal parts of some beds have remained largely intact (Črne et al. 2014; Kreitsmann et al. 2019; Kreitsmann et al. 2020).

Age constraints for the Zaonega Formation are given by a 2090±70 Ma dolomite Pb–Pb age in the underlying Tulomozero Formation (Ovchinnikova et al. 2007), and by $\delta^{13}C$ stratigraphy: the lower Zaonega Formation records the termination of the positive Lomagundi carbon isotope excursion (Melezhik et al. 2015), which has previously been dated to ~2060 Ma in Fennoscandia (Martin et al. 2013). The minimum depositional age is given by several cross-cutting dykes, some of which were syn-depositional, and have U–Pb ages of 1919±18 Ma (Priyatkina et al. 2014), 1956±5 Ma (Stepanova et al. 2014) and 1961±5.1 Ma (Martin et al. 2015). Volcanics in the overlying Suisari Formation have been dated to 1969±18 Ma (Re–Os; Puchtel et al. 1999)) and 1988±34 Ma (Pb–Pb; Puchtel et al. 1998). Additionally, a single zircon from a tuff layer in the lower Zaonega Formation yielded a U–Pb age of 1982 ± 4.5 Ma (Martin et al. 2015), whereas preliminary Re–Os dates constrain the upper Zaonega Formation to ~2050 Ma (Hannah et al. 2008; Bauer et al. 2019). Ultimately, these age constraints place the deposition of the Zaonega Formation between ~2050–1988 Ma.

2.4 Materials and methods

2.4.1 Sample material

The material for this study comes from drill cores OnZaP-1 and OnZaP-3, drilled 500 m apart in the northern Onega Basin near Shunga village (62.5870 N, 34.9310 E, and 62.5920 N, 34.9280 E, respectively). Using a P-rich dolomite marker horizon that occurs throughout the Onega

Basin, Paiste et al. (2018) correlated the two cores to form a 102 m thick combined section. The lower part of the section from the base at 102 m to 53 m is dominated by increasingly organic- and pyrite-rich shales, interbedded with some dolomite-calcite beds that are cross-cut by a suite of quartz, mica, and pyrobitumen veins. At 53 m, a layer of phosphorus-rich shale occurs and is overlain by a massive dolomite bed up to 44 m with thin shale interlayers and tens-of-centimeters to several-meters-thick black silica veins. Above 33 m, the section is dominated by relatively organic- and pyrite-poor shales and carbonates, which show cross-bedding features. See Paiste et al. (2018) for a detailed lithological description.

Two sets of samples were chosen for chemical analyses: set MSP0001 (n = 134) and set MSP0010 (n = 78). Part of the elemental concentration data and methodology reported here is adapted from Paiste et al. (2018) and Mänd et al. (2020).

2.4.2 Element concentrations

Total organic carbon content for sample set MSP0001 was determined from powdered samples at the Geological Survey of Norway in Trondheim using a LECO SC-444 analyzer. The detection limit was 0.1 wt.% and precision exceeded 10%. Similar data for sample set MSP0010 was measured by loss on ignition at the European Institute for Marine Studies (IUEM) in Brest, France. Approximately 0.5 g per each sample was dried and pulverised, then loaded into ceramic beakers and combusted at 500 °C for 24 hours, after which the mass loss was measured. Repeat measurements of 7 samples determined that the error was typically <1 wt.%.

Element concentrations for sample set MSP0001 were determined at Acme Labs, Bureau Veritas Commodities Canada Ltd. First, the samples were pulverised and organic carbon was removed through combustion. For major element analysis, the samples were fused in a $LiBO_2$ flux, digested, and analysed using inductively coupled plasma optical emission spectrometry (ICP-OES). Minor element analysis was done on samples fully digested in HNO_3, $HClO_4$, and HF, using inductively coupled plasma mass spectrometry (ICP-MS). The average relative standard deviation was <5% for all elements.

Elemental concentrations and Fe isotope compositions for sample set MSP0010 were measured at IUEM in Brest, France. Samples were powdered using a tungsten carbide crusher and an agate mill. To remove organic carbon, ~0.5 g of each sample was combusted at 500 °C for 24 hours. For major element analysis, samples were digested overnight at 80 °C in concentrated HF and HNO_3, and neutralized with boric acid to retain Si. Concentrations were measured on a Jobin Yvon Horiba Ultima 2 ICP-OES. External accuracy was monitored using a suite of 8 reference materials; measured values were within 2% of recommended values in all cases and relative standard deviation between repeat measurements was <2%.

Sample preparation for minor element and Fe isotope analysis of sample set MSP0010 was done in a class 1000 clean laboratory at IUEM using only purified acids from a TFE sub-boiling distillation system. All samples were handled in acid-washed TFE and PFA beakers and vials. First, 1.5 mL of concentrated HF and 1.5 mL of concentrated HNO_3 was added to the samples, heated to 80 °C overnight, then allowed to evaporate at 80 °C. Second, 3.3 mL of concentrated HCl and 0.7 mL of concentrated HNO_3 (i.e., *aqua regia*) was added, heated to 35 °C for 3 h, and

allowed to evaporate at 80 °C once more. Finally, samples were taken up in 4 mL of 6N HCl and stored in PFA vials.

To measure elemental concentrations, 100 mg of each sample solution was diluted in 4 mL 2% HNO_3 and spiked with indium, which was monitored to correct for instrument drift. Concentrations were measured on a Thermo Scientific Element 2 sector field ICP-MS, and external precision was assessed against BHVO-2, ShTX-1, and ShWYO-1 geostandards. For the elements discussed here, reference material measurements were within 20% of known values and relative standard deviation between repeats was <12%.

2.4.3 Iron isotopes

Iron isotope measurements were performed at IUEM and IFREMER (Brest, France) on aliquots of fully digested samples (described above) following the protocol developed by Rouxel et al. (2008b). First, Fe in dissolved samples was separated from other elements using column chromatography: the samples were passed through polypropylene columns loaded with 2.0 mL (wet volume) AG1-X8 anion-exchange resins. Prior to sample loading, the columns were washed with ~10 mL 3N HNO_3, ~10 mL ultrapure (18 MΩ cm^{-1}) water, and ~10 mL 0.24N HCl, then conditioned with 4 mL of 6N HCl. An aliquot of each fully dissolved sample calculated to contain ~40 µg of Fe was then loaded onto the columns, after which the matrix was eluted with the addition of 22 mL 6N HCl. Iron was then eluted with the addition of 16 mL of 0.24N HCl and captured in TFE beakers. The eluted Fe solution was evaporated at 90 °C and the Fe re-dissolved in 4 mL of 0.28N HNO_3.

Iron isotope compositions were determined at IFREMER using a Thermo-Scientific Neptune multicollector ICP-MS in medium or high-resolution mode. Prior to analysis, each purified Fe sample was doped with 0.02 mL of a 100 μg g^{-1} Ni solution with a known isotope composition. During Fe isotope measurements, Ni isotopes were monitored to correct for matrix effects (Malinovsky et al. 2003; Poitrasson and Freydier 2005). Furthermore, instrumental mass bias was monitored and corrected for using sample-standard-bracketing, wherein each sample analysis was bookended by measurement of an IRMM-014 standard solution (Belshaw et al. 2000). Repeat Fe isotope measurements of the IRMM-014 (n = 107) reference material gave an internal reproducibility of 0.07 to 0.08‰ (2SD). Measurements of the geostandards BHVO-2 (n = 5) and IF-G (n = 3) gave average δ^{56}Fe values of +0.12±0.07‰ and +0.64±0.08‰, respectively, which agree within error with previously reported values (Jochum et al. 2005).

2.4.4 Principal component analysis

Principal component analysis (PCA) was performed using the *factoextra* package for the R programming language (Kassambara and Mundt 2020). The analysis was performed using 19 chemical variables, including proxies for detrital material (Al, Ti, Si, Li, Fe), hydrothermal input (Si, $(Eu/Eu^*)_{SN}$), carbonate content (Ca, Mg, Mn, Li), phosphate (Ca, P), anoxia (TOC, V_{EF}, Mo_{EF}, U_{EF}, Re_{EF}), and iron cycling (Fe, Fe/Al, δ^{56}Fe). All variables were centered and normalized by their standard deviation in order to standardize their variances. Six samples from the altered 77–70 m and 53–44 m intervals (see below) were excluded from PCA analyses. Six further outliers were iteratively removed from PCA analysis, for a final total of 24 samples used.

Data analysis and visualization employed the *pandas* (McKinney 2010), *pyrolite* (Williams et al. 2020), *matplotlib* (Hunter 2007), *mpltern* (Ikeda et al. 2019), and *seaborn* (Waskom et al. 2020) packages for the Python programming language.

2.5 Results

2.5.1 Geochemical data

The results of select geochemical analyses of the OnZaP core are displayed in Figure 2.1.

Iron content ranges between 0.0 and 33.8 wt.%, with a median value of 3.2 wt.% (n = 212). Both TOC and vanadium (V) contents—commonly used as redox indicators (Algeo and Li 2020)—are highly elevated. Total organic carbon varies between 0.1 and 70.5 wt.%, with a median of 8.6 wt.% (n = 210). Values reaching 10 wt.% are common in the bottom of the section to ~30 m, and the high point is reached in the ~55 m shale interval. Above 30 m, TOC values are generally lower at a couple wt.%.

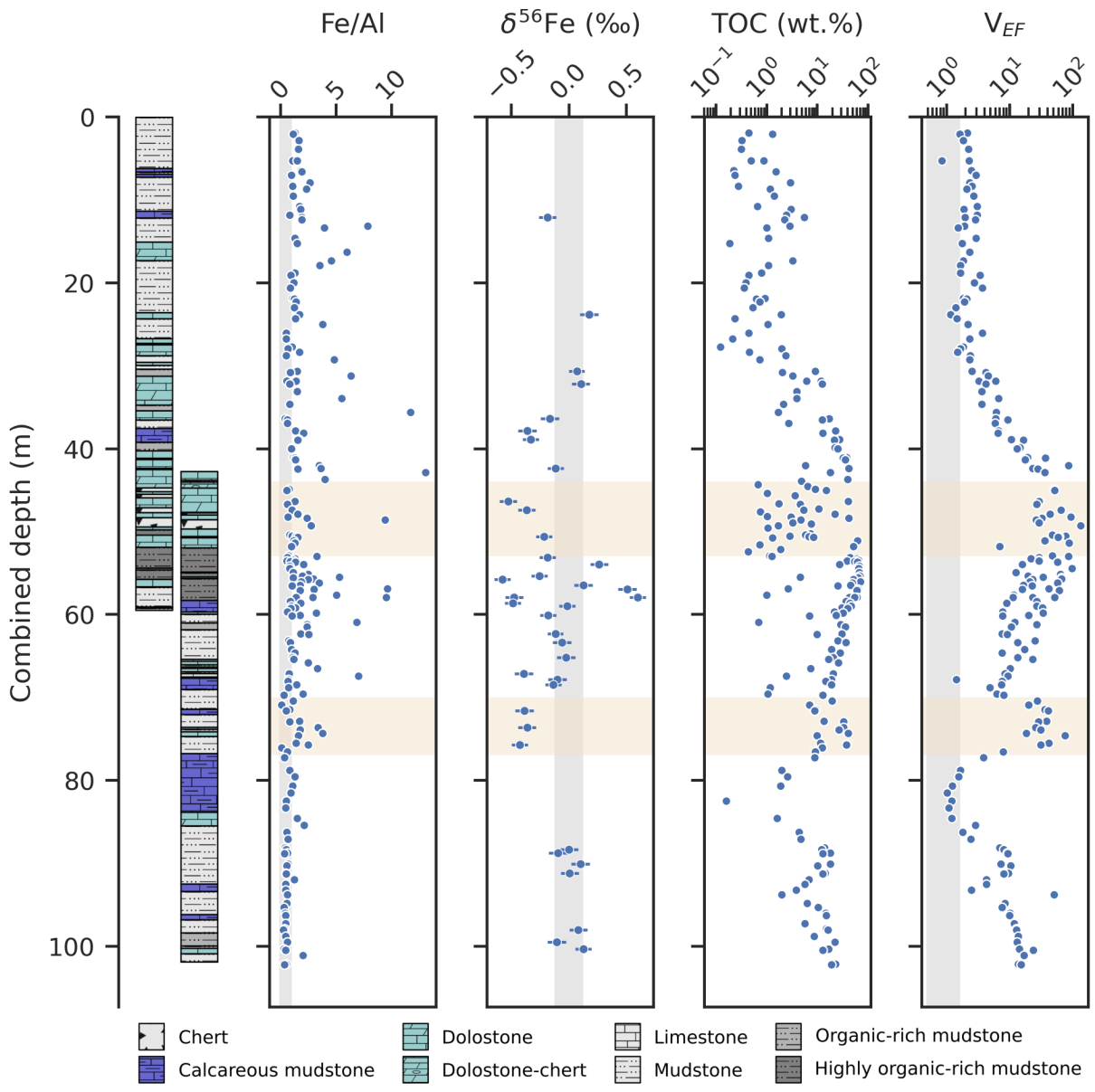

Figure 2.1: Geochemical indicators of Fe redox cycling in the OnZaP drill cores—authigenic Fe excess (Fe/Al) and Fe isotope composition (δ^{56}Fe)—with other redox indicators: total organic carbon (TOC) and the vanadium enrichment factor (V_{EF}). Grey vertical spans denote average crustal composition (Rudnick and Gao 2014; Cole et al. 2017), yellow horizontal spans denote

zones of secondary silicification (Paiste et al. 2018). Note the logarithmic scales on the TOC and V_{EF} *axes.*

Vanadium varies between 7 and 3018 μg g^{-1} and has a median value of 245 μg g^{-1} (n = 206). In order to correct for the fluctuating influence of the detrital sediments, authigenic V content can be represented through enrichment factors (Tribovillard et al. 2006). To calculate enrichment factors, the element in question is normalized to an immobile element (commonly Al), and the ratio is further normalized to a proxy composition for the average detrital sediment (here the upper continental crust; Rudnick and Gao 2014):

$$X_{EF} = (X/Al)_{sample}/(X/Al)_{crust}$$

Vanadium enrichment factors vary between 0.8 and 133.4, with a median of 9.7 (n = 192), and show tight stratigraphic trends. From the bottom of the section to ~80 m, there is a decrease from values at ~10 to ~1, followed by a gradual rise to >100 at 50 m, then a gradual drop to ~2 at ~30 m, after which values stay constant until the top of the core. A sharp increase in comparison to this overall trend occurs in the silicified 77–70 m interval, with values exceeding 40.

Authigenic iron abundance likewise increases in the middle of the section. The Fe/Al ratio varies from 0.09 to 33.50, and has a median of 1.23 (n = 198). Values far exceeding crustal levels are common between 77 and 40 m, and are especially elevated from 60 to 53 m, where many samples surpass a ratio of 4. An overall shift in baseline Fe/Al values from ~0.5 to ~1 is seen from the bottom of the core towards the top.

Iron isotope ratios in the OnZaP section range from −0.58±0.07‰ to +0.60±0.07‰ δ^{56}Fe (errors for individual measurements are given as 2σ) and display a median value of −0.12‰ (n = 38). Below 80 m and above 35 m, values are close to the crustal mean of ~0‰, but in the middle of that range, δ^{56}Fe becomes more variable and negative. Values significantly above the crustal mean are concentrated in a short interval from 60 to 53 m.

Positive europium (Eu) anomalies are associated with the input of high-temperature hydrothermal fluids, and can be recorded in authigenic phases in sedimentary rocks. Europium anomalies are commonly calculated based on concentrations normalized to Post-Archean Australian Shale (subscript "SN"; Taylor and McLennan 1985), and use the normalized concentrations of neighbouring rare earth elements as the expected Eu abundance (Eu*):

$$(Eu/Eu^*)_{SN} = Eu_{SN} / (0.67 \times Sm_{SN} + 0.33 \times Tb_{SN})$$

In unfiltered samples of the Zaonega Formation, $(Eu/Eu^*)_{SN}$ ranges from 0.54 to 2.98, with a median of 1.25 (n = 180).

2.5.2 Principal component analysis

Principal component analysis is commonly used for dimension reduction in high-dimensionality datasets so as to find overarching trends in the data and to explore relationships between variables (e.g., Iwamori et al. 2017). The results for the first four principal components (PCs), which collectively account for 83% of variability, are shown on Figure 2.2 and in Table 1. Among the parameters studied here, the highest amount of variability (35%, PC 1) can be

ascribed to a contrast between Ti, P, Li, Al, Mn, Mg, Fe, and Ca on the one hand, and Si and $(Eu/Eu^*)_{SN}$ on the other. In other words, this component describes contrast of detrital components and some authigenic phases, like carbonate and phosphate, against Si-richness and hydrothermal influence. A few metal enrichment factors (V_{EF}, Re_{EF}) and $\delta^{56}Fe$ display some covariance with Si.

Table 2.1: Loadings placed on variables by the first four principal components (PC). See text for details on variables.

Column	PC1	PC2	PC3	PC4
Si	-0.38	0.11	-0.11	-0.01
$(Eu/Eu^*)_{SN}$	-0.27	0.07	-0.29	0.11
Re_{EF}	-0.24	-0.14	-0.39	-0.11
$\delta^{56}Fe$	-0.16	0.09	0.03	0.61
V_{EF}	-0.12	-0.37	-0.19	-0.22
U_{EF}	-0.07	-0.41	-0.10	-0.10
Mo_{EF}	-0.05	-0.42	-0.10	-0.05
TOC	0.02	-0.43	0.06	0.00
Fe/Al	0.17	-0.36	0.03	0.18
Ca	0.19	-0.13	-0.18	0.51
Fe	0.24	-0.29	0.24	0.21
Mg	0.27	0.08	-0.42	-0.08
Mn	0.27	0.03	-0.35	0.33
Al	0.29	0.00	0.41	-0.12
Li	0.33	0.20	-0.13	-0.15
P	0.33	0.08	-0.31	-0.13
Ti	0.33	-0.04	-0.12	-0.18

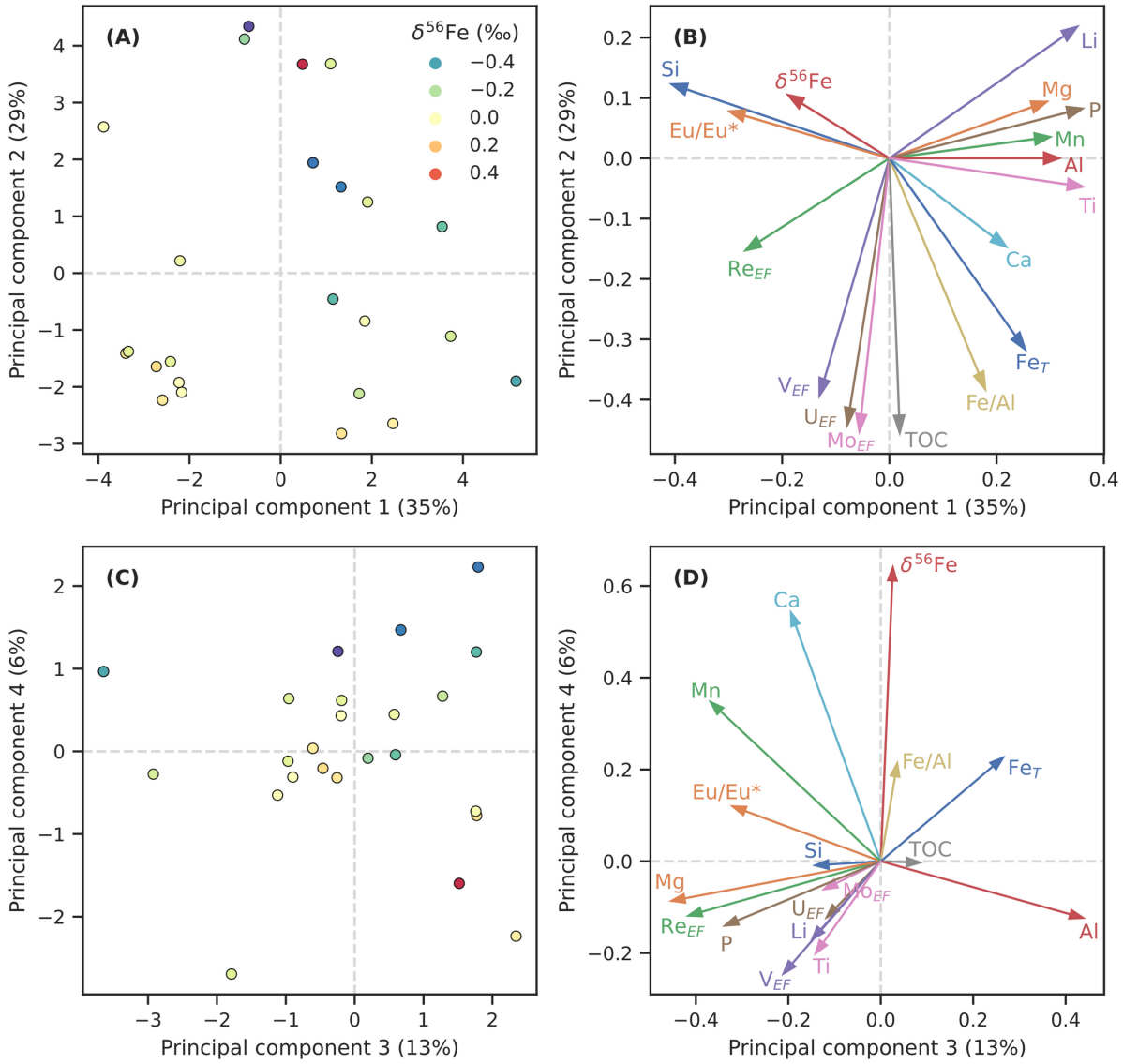

Figure 2.2: The results of principal component analysis on selected variables of the OnZaP dataset. Panels (A) and (C) show individual sample scores for components 1 and 2, and 3 and 4, respectively (color scale reflects iron isotope composition, $\delta^{56}Fe$). Panels (B) and (D) show the loadings that the respective principal components place on the analysed chemical variables.

Loadings placed on variables by the first four principal components (PC). See text for details on variables.

Principal component 2 (29% of variability) is strongly controlled by indicators of anoxia and reductive element drawdown, such as TOC, metal enrichment factors (Mo_{EF}, U_{EF}, and V_{EF}), and Fe accumulation (Fe, Fe/Al), with minor opposite contributions from Li, Si, and δ^{56}Fe. The third principal component (13% of variability) includes major contributions from Al and Fe, and opposite ones from Mg, Mn, P, Re_{EF}, V_{EF}, P, $(Eu/Eu^*)_{SN}$, and Ca, possibly representing a contrast between clay-rich and carbonate lithologies. The fourth component (6% of variability) is strongly controlled by δ^{56}Fe, together Ca, Mn, Fe, and Fe/Al, which contrast modestly with Ti, Li, P, Al and metal enrichment factors.

2.6 Discussion

2.6.1 Post-depositional alteration

Pyrite—the dominant Fe phase in much of the OnZaP section (Paiste et al. 2018)—is typically considered to be resistant to metamorphic resetting of δ^{56}Fe (Mansor and Fantle 2019). Yet, previous studies of Fe geochemistry in the Zaonega Formation have revealed post-depositional alteration of pyrite and Fe-rich carbonates (Asael et al. 2013; Paiste et al. 2018), likely related to thermal gradients and hydrothermal circulation driven by the emplacement of magma bodies into partially unlithified Zaonega Formation sediments (Qu et al. 2012). Therefore, in order to glean paleoredox insights from the data reported here, the effect of alteration on the preserved proxies must first be assessed.

Asael et al. (2013) studied the Fe geochemistry of a section from the FAR-DEEP 13A drill core, collected ~300 m from the OnZaP 1 and 3 drill sites. The FAR-DEEP 13A core has been correlated with the OnZaP section based on lithology and C isotope stratigraphy (Paiste et al. 2020a), so that the top of the section studied by Asael et al. (2013) (130–175 m depth in the 13A core), corresponds to ~40 m below the bottom of the OnZaP section. In that study, a significant amount of pyrrhotite ($Fe_{0.8–1}S$) was inferred based on Fe speciation, a phase commonly associated with pyrite metamorphism (Rickard and Luther 2007). The relative pyrite to pyrrhotite content correlated with the S/Fe ratio, suggesting that pyrrhotite formed through thermal breakdown of pyrite and the loss of S, whereas the Fe pool remained immobile and no shifts in the bulk δ^{56}Fe were expected (Asael et al. 2013).

In the OnZaP cores, as studied by Paiste et al. (2018), very little pyrrhotite was detected by XRD, suggesting only minor S mobility, though some acid-volatile sulphide, commonly associated with Fe monosulphides (e.g., pyrrhotite and sphalerite), was liberated during HCl-digestion. Still, other evidence for local Fe remobilization is present, at least in the carbonate beds. Dolomites in the OnZaP section contain up to 10 wt.% Fe, while secondary calcites formed through dedolomitization are devoid of Fe. Carbonate beds also host large (>100 μm) inclusion-rich euhedral pyrite, likely of late diagenetic or metamorphic origin, which may partially account for the Fe remobilized during dedolomitization, or which may have formed from the recrystallization of previously disseminated pyrite. Pyrite in shale beds, on the other hand, is commonly smaller in size (typically ~10 μm), more disseminated, and likely early diagenetic in nature (though larger, late-stage pyrite crystals have also been observed). The strongest evidence

for fluid alteration in the OnZaP section was seen in the visibly altered silica-rich 77–70 m interval, and in the 53–44 m dolomite interval, which hosts thick silica veins (Paiste et al. 2018).

Overall, Fe alteration in the Zaonega Formation likely occurred in a closed system and resulted in the redistribution of Fe between different mineral phases with little net Fe gain or loss. This means that little change in bulk-sample Fe/Al and δ^{56}Fe are expected, especially in shale intervals. Iron speciation, however, is known to have been significantly affected by Fe redistribution in the carbonate beds (Paiste et al. 2018), and potential S mobility (Asael et al. 2013).

We performed a series of checks to reduce the potential effects that alteration may have on our analyses and interpretations. First, the MSP0010 sample set (from which all δ^{56}Fe values were measured) was chosen specifically from shale intervals, avoiding conspicuous mono-mineral clusters and silicate veins. Second, we removed data points from the silicified 77–70 m and 53–44 m intervals from further paleoenvironmental consideration. Although no anomalous Fe/Al ratios are observed in these silicified intervals, they host uniformly low δ^{56}Fe values (<0.2‰), which is consistent with the possible input of ^{56}Fe-depleted dissolved Fe(II) during hydrothermal alteration (Figure A1 in Appendix 1). Third, we focus the discussion below primarily on bulk rock proxies, rather than mineral phase-specific indices (i.e., Fe speciation) since the former are less susceptible to diagenetic/metamorphic repartitioning of elements. This conservative approach allows us to conclude that secondary alteration is unlikely to have resulted in the wholesale overprint of primary δ^{56}Fe signals in the OnZaP section, although it may have contributed to slightly increased scatter in the relationships explored below. We do note that the

potential effects of hydrocarbon migration on Fe phases and δ^{56}Fe signals in the Zaonega Formation remain unconstrained as we are not aware of any study which has investigated such effects in natural or experimental settings.

2.6.2 The principal influences on iron geochemistry

Principal component analysis (Figure 2.2, Table 2.1) reveals that the chemistry of the Zaonega Formation sedimentary rocks is most significantly controlled (PC 1) by variability in Si-richness, which seems to coincide with $(Eu/Eu^*)_{SN}$, an indicator of hydrothermal influence (see next section). The second component (PC2) is dominated by TOC, and authigenic Fe and trace metal enrichments and potentially describes the extent of anoxia, or conditions which are conducive to the development of authigenic metal enrichments. The third component (PC 3) may describe an aspect of carbonate richness, whereas PC 4, accounting for only 6% of variance, is most affected by δ^{56}Fe.

Iron chemistry contributes most significantly to PCs 2 and 4, suggesting that redox conditions during deposition played a role in determining Fe distribution patterns. Curiously, δ^{56}Fe has only weak contributions to the first two PCs, and a strong contribution to PC 4, meaning that variations in δ^{56}Fe do not coincide strongly with variations in other geochemical parameters. The first two PCs place a weak loading on δ^{56}Fe, with the most conspicuous opposite loading placed on Fe and Fe/Al. This implies a potential anticorrelation between these variables, whereas unidirectional covariation between the same components is seen on PC 4. This may also suggest that δ^{56}Fe data is affected by several different mechanisms resulting in opposing trends—

PCA generally fails to deconvolute such overlapping trends (Iwamori et al. 2017). Given these interpretations, we approach our subsequent discussion on Fe geochemistry from the perspective of hydrothermal influence, detrital composition, and redox conditions.

2.6.3 Detrital versus authigenic iron sources

We investigate the influence of the detrital composition on δ^{56}Fe in Figure 2.3. There is significant variability in the Si/Al ratio that seems to exert some influence on δ^{56}Fe—only relatively Al-rich samples host fractionated δ^{56}Fe (Figure 2.3a,b). Possibly, the Si-rich and unfractionated end-member represents a sandy or silty detrital component, as opposed to a more clay-rich component with higher Al content. Coarser grain size would imply a shallower paleoenvironmental setting with higher rates of deposition and a lower likelihood of developing anoxia, given that equilibrium would have been maintained with a weak to mildly oxidizing atmosphere, that could limit non-quantative Fe redox cycling and the generation of fractionated δ^{56}Fe. Clay deposition, on the other hand, occurs at lower rates and is associated with higher rates of organic matter loading, which may be characteristic of deposition beneath a chemocline, and in turn facilitate the development of anoxia and redox driven Fe cycling. However, grain size variation in the OnZaP section is not very large and what little variation there is may largely be controlled by turbidite deposition (Paiste et al. 2018). Alternatively, if Si-richness describes hydrothermal influence, the association of Si-rich samples with non-fractionated δ^{56}Fe implies that hydrothermal fluids did not host fractionated Fe.

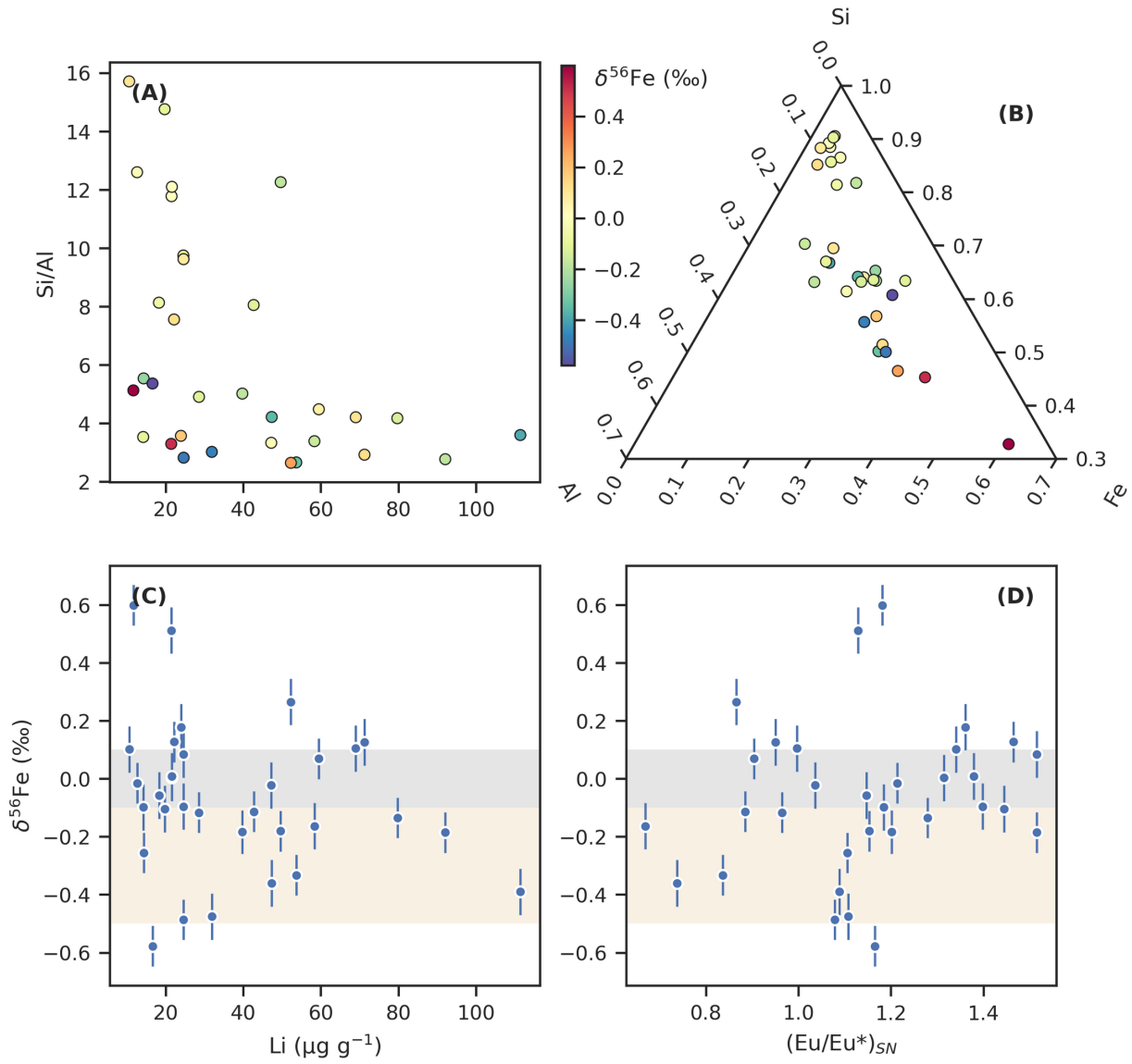

Figure 2.3: The influence of detrital composition and hydrothermal influence on the iron isotope ratio ($\delta^{56}Fe$). (A) Lithium (Li) concentrations plotted against the ratio of silica (Si) to aluminium (Al) reveal different Si and Li-rich detrital components. (B) Ternary plot showing the relative Al, Si, and Fe composition of individual samples. Note that the scales are truncated. Color scale on panels A and B indicates $\delta^{56}Fe$ values; fractionated Fe is present in relatively Al- and Fe-rich,

but Si- and Li-poor samples. (C) $\delta^{56}Fe$ plotted against Li shows that Li-rich samples tend towards negative $\delta^{56}Fe$ values. (D) $\delta^{56}Fe$ shown against the europium anomaly $(Eu/Eu^*)_{SN}$, a proxy for hydrothermal influence. No clear covariation is discernible.

Samples with high Li contents denote another clearly distinguishable detrital component, which associates with Al-richness. This relationship may develop as a result of Li being concentrated in clay minerals (e.g., Chan et al. 2006). Figure 2.3c reveals that the most Li-rich sediments tend to host negative δ^{56}Fe values, and likely represent the weathering product of an uncommonly ^{56}Fe-depleted parent rock.

2.6.4 Hydrothermal iron

Iron isotope variability is often studied in relation to authigenic Fe enrichments, proxied by Fe/Al, as the highest fractionations are associated with redox or precipitation processes resulting in authigenic Fe accumulation in sediments (Dauphas et al. 2017). A link between these two variables is also implied by the PCA results. When viewed on a regression plot (Figure 2.4a), there appears to be a general trend towards lower δ^{56}Fe values as Fe/Al rises, though the correlation is weak (R^2 = 0.15). There is, however, significant scatter and several samples that display an opposite trend towards positive δ^{56}Fe at higher Fe/Al.

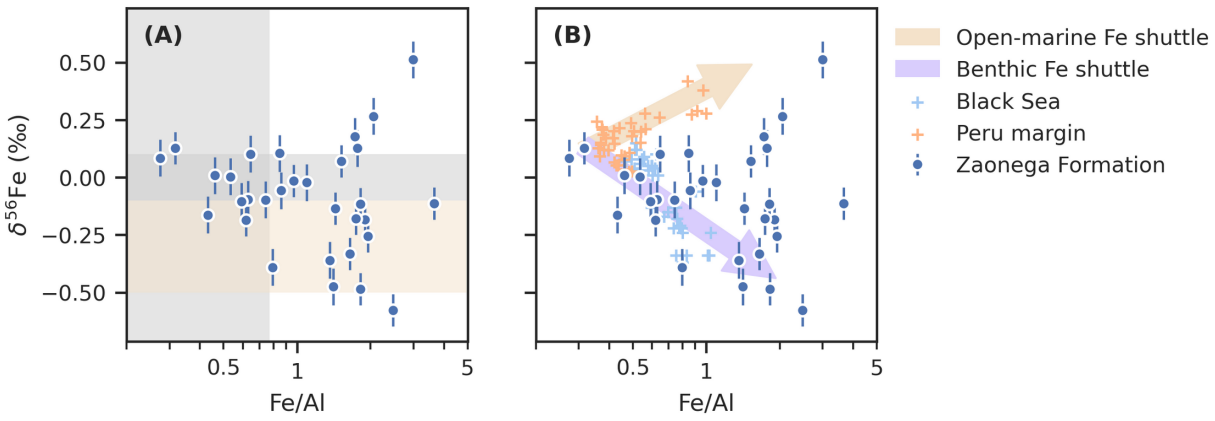

Figure 2.4: Iron isotope values from the Zaonega Formation plotted against Fe/Al ratios, a proxy for both the diagenetic loss of Fe and authigenic Fe input (notice the logarithmic scale on the horizontal axis). Panel (A) shows the data against typical crustal Fe/Al ratios (vertical grey span; Cole et al. 2017), and δ^{56}Fe range (grey horizontal span; Beard et al. 2003), as well as the hydrothermal δ^{56}Fe range (yellow horizontal span; Severmann et al. 2004; Rouxel et al. 2008a). Panel (B) presents an interpretation in which the trends in δ^{56}Fe values are explained through a benthic Fe shuttle (similar to the Black Sea; Severmann et al. 2008), and an open-marine authigenic Fe shuttle component (similar to the Peru margin; Scholz et al. 2014).

One possible interpretation for the main negative trend relates to Fe(II) delivered to the Onega basin from hydrothermal vents. High-temperature dissolution of Fe typically results in δ^{56}Fe compositions lower than the igneous background and the δ^{56}Fe of such Fe(II), therefore, trends towards negative values (from −0.67‰ to −0.09‰, more commonly between −0.5‰ and −0.1‰; Severmann et al. 2004; Rouxel et al. 2008a). Since most δ^{56}Fe values in the Zaonega Formation lie within the reported ranges of δ^{56}Fe for crustal and hydrothermal Fe (Severmann et

al. 2004; Rouxel et al. 2008a), it is possible that δ^{56}Fe was controlled by a mixing relationship between detrital Fe dominated by crustal isotope compositions and Fe(II) derived from basinal hydrothermal input.

A commonly used proxy for tracking the influence of hydrothermal fluids is the europium anomaly ($(Eu/Eu^*)_{SN}$; Figure 2.3d). Unlike neighbouring rare earth elements, Eu can be reduced to a divalent state in acidic, high-temperature fluids, in which case it complexes with chlorides and remains highly soluble compared to other rare earth elements (Bau 1991). Hydrothermal vents, therefore, commonly display relative enrichments in Eu, and while the anomaly is quickly diluted in modern open ocean away from the venting sites, it is a useful proxy for hydrothermal influence in more restricted basins (Bau 1991).

Strong Eu anomalies have previously been reported from authigenic apatite and carbonates in the Zaonega Formation (Joosu et al. 2015; Kreitsmann et al. 2020). Interestingly though, when we plot $(Eu/Eu^*)_{SN}$ against δ^{56}Fe in the Zaonega Formation sediments we find no discernible relationship (Figure 2.3d). This is, however, not a strictly robust use of the bulk sediment $(Eu/Eu^*)_{SN}$ proxy, as no filtering was done to deconvolute detrital background values (e.g., Kreitsmann et al. 2020), and $(Eu/Eu^*)_{SN}$ anomalies may also result from high-temperature Eu disproportionation between plagioclase and other igneous components (Weill and Drake 1973). Yet, authigenic Fe sulphides and oxides, if precipitating from hydrothermally influenced seawater, are known to preserve significant Eu anomalies (Bau 1991; Mills and Elderfield 1995). If δ^{56}Fe variations are driven mainly by varying proportions of hydrothermal Fe(II) input, at least a tendency towards higher Eu anomalies with lower δ^{56}Fe values may be expressed. No such

tendency is seen in the Zaonega Formation sediments—rather, δ^{56}Fe fractionations seem to be associated specifically with samples that display very little to no Eu anomaly (Figure 2.3d). Furthermore, hydrothermal input cannot explain the subset of samples displaying positive δ^{56}Fe (Figure 2.4). Therefore, we do not consider a hydrothermal control on δ^{56}Fe to be dominant and favour alternative explanations that seem more likely.

2.6.5 Iron redox-shuttling

A common mechanism responsible for covariation between Fe/Al and δ^{56}Fe in modern anoxic basins is the benthic Fe shuttle (Wijsman et al. 2001; Anderson and Raiswell 2004; Severmann et al. 2008). Dissimilatory Fe reduction occurs widely in shelf sediments and is a major source for Fe(II) into the ocean as much of the resulting Fe(II) can escape from pore water into the bottom water (Moore and Braucher 2008; Conway and John 2014). In modern redox-stratified and (semi-)restricted basins—most notably the Black Sea (Severmann et al. 2008)—there is a net transfer of this reactive Fe from the shelf into the basin (Wijsman et al. 2001). Deep currents transport DIR-derived Fe as colloids or fine particulates to the deeper, anoxic parts of the basin (Lenstra et al. 2019), where it is quantitatively captured as pyrite upon reaction with dissolved sulphide (Wijsman et al. 2001). The end result is that sediments in the anoxic basin become enriched in authigenic Fe relative to the continental crust (elevated Fe/Al ratios), whereas shelf sediments become comparatively depleted (depleted Fe/Al) (Anderson and Raiswell 2004). In parallel, since DIR preferentially mobilizes ^{54}Fe, the shelf sediments will tend to become more positive in δ^{56}Fe. Partial reoxidation of dissolved Fe(II) during basin-wards transport will preferentially remove even more of the ^{56}Fe, leading to significant negative authigenic δ^{56}Fe

inputs into basinal sediments (Severmann et al. 2008). Anticorrelation between Fe/Al and δ^{56}Fe has also been detected in Phanerozoic (e.g., Duan et al. 2010) and Neoproterozoic (e.g., Kunzmann et al. 2017) drill core data, reflecting a facies change from oxidized shelves to anoxic deep basins, settings conducive to benthic Fe shuttling.

On Figure 2.4b, data from the Zaonega Formation is plotted next to Black Sea data from Severmann et al. (2008). Broadly, these datasets lay out a similar trend, suggesting that a benthic Fe shuttle may be responsible for much of the variation in δ^{56}Fe. A major difference with the Black Sea dataset is the much-expanded Fe/Al range. This may be due to higher Fe(II) concentrations in the deep Proterozoic oceans, given the likelihood that they remained pervasively anoxic—although in Mänd et al. (2020) previously argued that redox-sensitive metal accumulations and isotope ratios in the Zaonega Formation suggest that large parts of the oceans, in this sense surface waters, were oxidized at the time these rocks were deposited. The shift in Fe/Al may alternatively imply an unusually high Fe/Al ratio of background detritus—average Fe/Al ratios reach ~1 in the upper part of the OnZaP section, though this is more likely the result of authigenic ankerite/siderite accumulation (see below; Figure 2.1). Finally, the shift may be due to a more vigorous benthic Fe shuttle in the Zaonega Formation compared to the Black Sea.

A subset of relatively Fe/Al-rich samples plot on an opposite trend and constitute the highest δ^{56}Fe component (Figure 2.4). While the small number of samples (~5) makes any conclusion tentative, the coherence of the trend and the position of these samples in a relatively thin stratigraphic horizon between 54 and 58 m (Figure 2.1) hints at a probable paleoenvironmental significance to the trend. Mansor and Fantle (2019) suggested that positive

sediment δ^{56}Fe fractionations can reflect late-stage pyrites formed at slow rates of precipitation, possibly due to low sulphate or iron concentrations, in which case the positive equilibrium isotope fractionation factor inherent in pyrite precipitation overwhelms the negative kinetic isotope effect. However, sulphur isotope systematics of the OnZaP section have previously been used to argue that pyrite precipitation occurred rapidly due to high rates of organic carbon remineralization in the sediments (Paiste et al. 2018; Paiste et al. 2020b).

Authigenic accumulation of ^{56}Fe-enriched Fe is perhaps more likely to be the result of partial Fe(II) oxidation and precipitation as Fe(III) phases, which commonly host positive δ^{56}Fe signatures (Beard et al. 2010; Wu et al. 2011; Frierdich et al. 2014a, 2014b). In fact, a positive Fe/Al–δ^{56}Fe trend has been noted in sediments deposited on the lower boundary of the anoxic wedge on the hydrographically open Peru margin (Scholz et al. 2014). In the Peru margin oxygen minimum zone, DIR produces a reductive Fe(II) flux which leaks from sediments; as the dissolved Fe(II) migrates towards the suboxic margins of the oxygen minimum zone, a fraction of that Fe(II) will be oxidized and precipitated, producing sediments with Fe/Al enrichments and positive δ^{56}Fe values. The data from Scholz et al. (2014) that define this mechanism have been added for comparison purposes to Figure 2.4b. Compared to the Peru margin data, the positive sub-trend in the Zaonega Formation is again shifted towards markedly higher Fe/Al ratios, likely for the same reasons as the main negative trend.

Iron oxide precipitation can, in principle, account for both positively fractionated Fe oxides in the intial stage, and negatively fractionated phases in later stages through isotope distillation of the Fe(II) pool (Rouxel et al. 2005). However, distillation implies drawdown of the Fe pool

and lower authigenic Fe contents in the negative δ^{56}Fe end-member, inconsistent with the Zaonega Formation data, where both positively and negatively fractionated samples are associated with higher Fe/Al ratios. Instead, mixing of Fe from authigenic Fe oxides and benthic shuttle-derived authigenic sulphides can better explain the data, including the scatter observed between δ^{56}Fe and Fe/Al, despite most Fe likely having been subsequently converted to pyrite during diagenesis. A simultaneous influence of both of these two mechanisms, depending on the location of the sampling site relative to the oxygen-minimum zone and the deep basin, was noted by Scholz et al. (2019) in the modern Guaymas basin in the Gulf of California. Namely, sediments in the oxygen-minimum zone were depleted in Fe/Al and slightly enriched in ^{56}Fe, suggesting Fe(II) release during DIR and loss into the water column. Slight accumulation of Fe(III)-hydroxides in sites below the oxygen-minimum zone noted through elevated Fe/Al and δ^{56}Fe. Sites in the deeper basin, where most of the released Fe(II) ended up accumulating, displayed higher Fe/Al together with less positive δ^{56}Fe. We suggest that, similarly to the Guaymas basin, the Fe cycle in the Zaonega Formation was influenced by both partial Fe(III) precipitation and Fe(II) scavenging.

2.6.6 Redox development in the upper Zaonega Formation

The OnZaP section records a depositional setting that likely passed through facies shifts and experienced changes in basin chemistry and hydrographical conditions as the sediments accumulated. The bottom of the section (up to ~80 m) records δ^{56}Fe values close to 0‰, as well as low Fe/Al ratios, (~0.5; Figure 2.1). However, both TOC and trace metal enrichment is very high in that interval, implying a predominantly anoxic environment, and arguing against high

detrital deposition rates that could diminish authigenic Fe accumulation. Furthermore, XRD-based Fe speciation results imply that most Fe in that interval is hosted within pyrite, arguing against sulphide limitation (Paiste et al. 2018). In a basin hosting a benthic Fe shuttle, these types of sediments would be expected to capture Fe relatively efficiently. That they do not seems to suggest that the basin experienced diminished suboxic cycling and benthic Fe flux at that time. Possibly, this interval marks a period of more open hydrographic conditions, such that the benthic Fe flux ensuing from shelf areas was diluted over the open ocean. Scholz (2018) identified basinal restriction as one of the most important parameters for determining if sediments capture a benthic Fe shuttle. The lack of a clear benthic Fe shuttle trend is also noted in a section of the FAR-DEEP 13A drill core by Asael et al. (2013), stratigraphically below the OnZaP section. This suggests that the conditions preventing a benthic Fe flux from being recorded persisted through much of the middle Zaonega Formation succession.

The shift to clearly more variable and negative δ^{56}Fe above 80 m coincides with an increase in metal enrichment factors and TOC (Figure 2.1), as well as pyrite abundance (Paiste et al. 2018). In short, the depositional site became more conducive to Fe drawdown via reaction with sulphide. Whether this sulphide was present in the open water column or confined to sediments is a matter of debate—high Mo concentrations (as reported in Mänd et al. 2020) are usually associated with sulphidic conditions (Algeo and Lyons 2006), whereas S isotope systematics in the Zaonega Formation are more easily explained through the confinement of sulphidic conditions to the pore waters (Paiste et al. 2018; Paiste et al. 2020b).

The interval between 60–53 m hosts the highest values for many redox indicators, which corresponds to efficient Fe drawdown, and explains why the interval has some of the highest Fe/Al ratios and the most negative δ^{56}Fe values (Figure 2.1). However, a small number of samples in this interval display markedly positive δ^{56}Fe values and may imply partial Fe oxide drawdown, which can only occur under an oxidizing water column. This discrepancy may potentially result from highly variable redox conditions, where a sharp sulphidic-oxic redoxcline fluctuated between the water column and the sediments. This is consistent with previous interpretations in Lepland et al. (2014) including phosphate rich sediments and putative fossilized sulphur oxidizing microbial communities in a nearby correlative outcrop that were interpreted to have formed in sediments with a rapidly fluctuating sulphidic–suboxic redox boundary. Likewise, dramatically elevated trace metal enrichments previously identified in this interval are consistent with a fluctuating redox setting that is especially conducive to trace metal drawdown (Mänd et al. 2020), where oxidative pulses supply the trace elements and sulphidic episodes sequester those trace metals efficiently.

Above 35 m, δ^{56}Fe values rise again to near 0‰, concomitant with a drop in TOC and metal enrichment factors. In this interval, putative evaporite mineral pseudomorphs together with cross-bedding have been interpreted to reflect a shallowing depositional setting, whereas the decrease in relative pyrite and highly reactive Fe abundance have been interpreted to reflect waning anoxic conditions (Paiste et al. 2018). The overall baseline Fe/Al still remains elevated at ~1, on account of increasing Fe-rich dolomite, ankerite, and siderite content. The presence of these minerals implies high levels of dissolved Fe(II), but limited sulphide content (i.e.,

ferruginous conditions) at the depositional site, which is consistent with the lack of a benthic Fe shuttle isotope signature in this section. Further, deviations in δ^{56}Fe from the crustal mean persist (−0.18 to +0.18‰), suggesting Fe isotope fractionation during partial Fe(II) drawdown.

2.6.7 The Onega Basin paleoenvironment

The initiation of benthic Fe shuttling in the Zaonega Formation (in the interval between 80 and 30 m) has implications for the basinal redox structure and hydrographic setting that can, in turn, affect the interpretation of trace element proxies and global redox conditions.

A benthic Fe shuttle comes with two principal requirements—a strong redox gradient ensuring Fe release and capture efficiencies in different parts of the basin, and a degree of basinal restriction. On the redox side, a benthic Fe shuttle first requires the presence of suboxic settings in shallower parts of the basin that allows for the accumulation of biologically available Fe(III) phases in the sediments that can then subsequently be converted through DIR to Fe(II) (Severmann et al. 2008), and so that Fe(II) diffusing out of the sediments would not be quantitatively scavenged upon reaching the water column (Anderson and Raiswell 2004; Duan et al. 2010). Secondly, euxinia is usually invoked to explain how the resulting Fe(II) flux ends up being quantitatively trapped in the deeper basin (Lyons and Severmann 2006; Severmann et al. 2008). Both of these settings would need to have been simultaneously present in the Zaonega Formation to explain the overall δ^{56}Fe–Fe/Al relationship.

Arguably more important than the redox condition is the shelf-to-basin ratio, which is closely tied to the degree of hydrographic restriction (Scholz 2018). Specifically, the larger the

areal ratio of the Fe source (the suboxic shelf) to the Fe sink (the euxinic basin), the more pronounced the signature of the benthic Fe flux will be, relative to lithogenic detrital Fe. For example, the modern Black Sea and the Guaymas basin, both of which host a benthic Fe shuttle, have very large shelf to basin ratios, a result of their restricted settings (Anderson and Raiswell 2004; Scholz et al. 2019). Conversely, the Peru Margin that opens to the Pacific Ocean does not display substantial accumulations of ^{56}Fe-depleted Fe (Scholz et al. 2014). The δ^{56}Fe data presented here suggests basinal restriction during deposition of the Zaonega Formation, in agreement with previous interpretations based on S isotope systematics (Paiste et al. 2018), and tectonic reconstructions in which the Onega Basin is viewed as a rift basin with the potential for a large shelf-to-basin ratio (Melezhik et al. 1999b).

It is difficult to understand why Fe/Al ratios in the middle of the OnZaP section are so highly elevated ($\gg$1). This may point either to high detrital Fe/Al ratios (unlikely, as Fe/Al below 80 m is generally ~0.5), a change in sediment provenance, or an especially effective benthic Fe shuttle. The latter may result from the unusually high bioproductivity and organic carbon loading rates in the Zaonega Formation (up to 70% wt.% TOC; Mänd et al. 2020). On the sink side, biomass can contribute to high Fe/Al by directly scavenging Fe (e.g., Shawar et al. 2018), or indirectly by encouraging the establishment of anoxia in sediments and the conversion of sulphate to sulphide, leading to more efficient Fe capture. On the source side, organic carbon loading can also drive increased rates of DIR in shallower settings, as has been noted in the modern Black Sea (Lenstra et al. 2019).

In contrast to the prevailing negative δ^{56}Fe trends, the positive δ^{56}Fe values in the 60–53 m interval imply the episodic presence of suboxia, which can partially draw down the dissolved Fe(II) pool resulting in positive fractionations via partial Fe(II) oxidation (Scholz et al. 2014). This implies a highly variable redox structure possibly driven by varying organic matter loading, or periodic influxes of oxic water into the deeper basin (Figure 2.5). While the low number of highly positive δ^{56}Fe samples make this conclusion tentative, strong support is provided by numerous other geological and geochemical inferences: the accumulation of hundreds of meters of massive halites and anhydrites in the Tulomozero Formation, which underlies the Zaonega Formation in the Onega Basin, requires both restriction in order to effect evaporation, and constant replenishment in order to sustain salt accumulation for hundreds of meters (Blättler et al., 2018). Similar cycles of restriction and openness are implied in the Zaonega Formation by the Se and N isotope record (Kipp et al., 2020) and by extremely elevated authigenic trace metal concentrations (Mänd et al., 2020). A modern analogue for such cycles is seen in Baltic Sea anoxic deeps, which see bi-decadal influxes of oxic water, which replenish the local trace metal pool and also lead to especially pronounced sedimentary trace metal enrichments (Scholz et al. 2013, 2018).

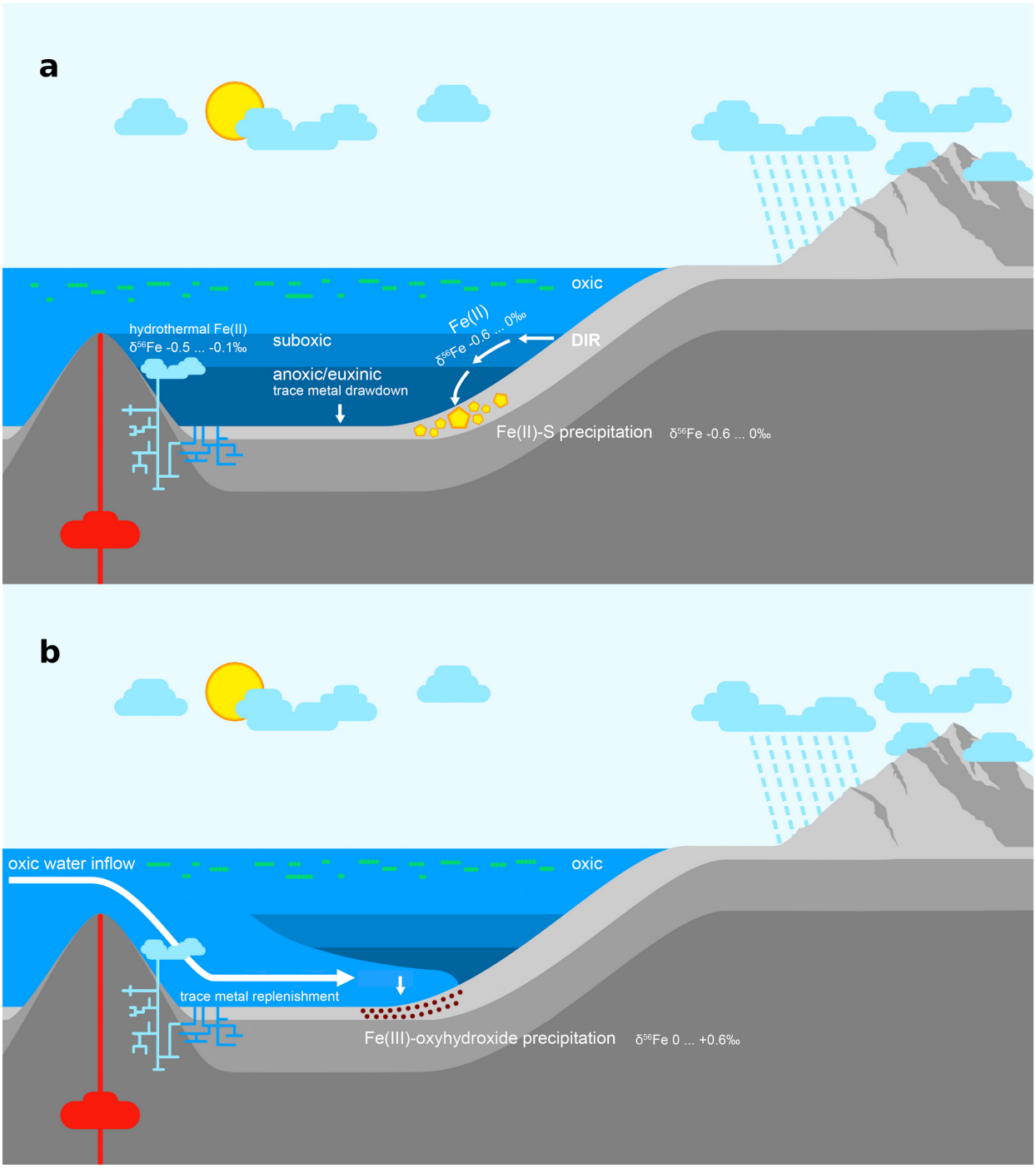

Figure 2.5: An interpretation of the hydrographic and redox conditions in the Onega Basin during the deposition of the upper Zaonega Formation. (a) Hydrographic restriction rendered

the basin redox-stratified. Dissimilatory iron reduction (DIR) converted detrital Fe(III) phases in reducing sediments into Fe(II) with negative δ^{56}Fe values. Dissolved Fe(II) with negative δ^{56}Fe values may also have been contributed by hydrotherms. If overlain by suboxic waters, some of this Fe(II) flux escaped into the water column, was transported into deeper, anoxic waters, and deposited as Fe(II)-sulphides. (b) Periodically, the basin experienced oxic water inflow events, which caused dissolved Fe(II) in the basin to be oxidized, precipitating Fe(III)-oxyhydroxides with sometimes positive (up to +0.6‰) δ^{56}Fe values.

Overall, the Fe record in the Zaonega Formation is consistent with other records of the middle Paleopoterozoic—a time of elevated oxygen levels compared to the preceding Archean eon and the subsequent Mesoproterozoic (Bekker and Holland 2012; Lyons et al. 2014). Pyrite δ^{56}Fe in black shales of this time period has been shown to be elevated (−0.5‰ to +1‰), compared to those from the Archean and Mesoproterozoic (Rouxel et al. 2005; Heard and Dauphas 2020). Rouxel et al. (2005) interpreted this as being the result of high rates of sulphate input into seawater (Konhauser et al. 2011; Blättler et al. 2018), which drove extensive pyrite precipitation, leading to the preferential removal of ^{54}Fe from seawater. Zaonega Formation δ^{56}Fe data fits squarely within that range. Significantly, the ~1‰ variation in δ^{56}Fe within the Zaonega Formation suggests a relatively small dissolved Fe reservoir in which Fe cycling proceeded largely quantitatively, contrasting with δ^{56}Fe isotope data from both the Archean (Heard and Dauphas 2020) and Neoproterozoic (Kunzmann et al. 2017).

2.7 Conclusions and implications

In this study we measured Fe isotopes throughout a section of the Zaonega Formation, which were found to vary between −0.58‰ and +0.60‰. While some of the observed variation was driven by changes in the composition of detrital material, the bulk reflects two competing processes that led to authigenic Fe accumulation. Most of the negatively fractionated Fe, prevailing between 80–30 m in the OnZaP section, can be ascribed to a benthic Fe shuttle, akin to that seen in the modern Black Sea (Severmann et al. 2008). This Fe shuttle requires a redox gradient from oxidizing shallow to anoxic and sulphidic deep waters, consistent with the inference that the deep Onega Basin at the time represented a predominantly anoxic basin in a generally oxygenated world. This finding agrees best with the results of Paiste et al. (2018), who stressed the importance of basinal restriction on S isotope characteristics—only in restricted settings will a distinctive Fe shuttle signature be recorded (Scholz 2018).

Positive δ^{56}Fe values in the 60–53 m interval, however, attest to the episodic delivery of authigenic Fe(III) to the sediments, requiring periodic influxes of oxidized waters into the predominantly anoxic basin. Hence, restriction was not total, and intermittent connection with the open ocean persisted. These types of redox fluctuation-driven drawdown–replenishment cycles are especially conducive to the generation of high sedimentary enrichments of certain trace metals, explaining their extreme accumulations reported previously in the Zaonega Formation (Kipp et al. 2020; Mänd et al. 2020).

In totality, the Onega Basin can be seen as a complex sedimentary system affected to a large degree by local processes and conditions, such as high rates of organic matter loading and basinal restriction. Nevertheless, this basin remained in communication with the open ocean, and was thus able to incorporate global signals of element cycling. Therefore, the geochemistry of the Zaonega Formation can be used to deduce global environmental conditions in the Paleoproterozoic, but doing so requires nuanced assessment of the coupled effects of local and global redox and hydrographic conditions.

Chapter 3: Oxygenated oceans following the Lomagundi-Jatuli Event[2]

3.1 Introduction

The Paleoproterozoic era (2500–1600 Ma) witnessed the longest positive carbon isotope ($\delta^{13}C_{carb}$) excursion in Earth's history, recorded in marine carbonates deposited worldwide between ~2220–2060 Ma—the Lomagundi-Jatuli Event (LJE) (Karhu and Holland 1996; Martin et al. 2013). Marine carbonates are generally characterized by $\delta^{13}C_{carb}$ values that vary between −5‰ to 5‰ for most of Earth's history, whereas peak LJE $\delta^{13}C_{carb}$ values reach 10–15‰ (Karhu and Holland 1996). There is ongoing debate regarding the processes that led to the LJE. The standard and most commonly accepted interpretation invokes increased burial of ^{13}C-depleted organic carbon (C_{org}), leading to the ^{13}C-enrichment of the dissolved inorganic carbon pool and positive $\delta^{13}C_{carb}$ (Karhu and Holland 1996; Bekker and Holland 2012). This acceleration in C_{org} burial may have been the result of an increase in oxidative weathering and nutrient delivery to the oceans (Bekker and Holland 2012). Using a simple isotope mass balance, it has been estimated that between $5–9\times10^{20}$ mol of C_{org} was buried over 100 Ma, corresponding to the release of O_2 equivalents representing 12–22 times the present O_2 atmospheric pool. An ensemble of evidence points to atmospheric O_2 accumulation during the LJE, including proxies

[2] A version of this chapter was published as Mänd, K., Lalonde, S. V., Robbins, L. J., Thoby, M., Paiste, K., Kreitsmann, T., Paiste, P., Reinhard, C. T., Romashkin, A. E., Planavsky, N. J., Kirsimäe, K., Lepland, A., and Konhauser, K. O., (2020) "Palaeoproterozoic oxygenated oceans following the Lomagundi–Jatuli Event." *Nature Geoscience 13,* 302–306.

indicating growth of the marine sulphate reservoir (Planavsky et al. 2012b; Scott et al. 2014; Blättler et al. 2018), elevated concentrations of redox sensitive elements (RSE) (Konhauser et al. 2011; Partin et al. 2013a; Kipp et al. 2017), and evidence for locally oxic conditions (Bekker and Holland 2012; Canfield et al. 2013). However, others have argued that the "standard" interpretation of the LJE is difficult to reconcile with our understanding of the C and O cycles (Bachan and Kump 2015; Miyazaki et al. 2018), and that there is a notable paucity of C_{org}-rich deposits at this time (Melezhik et al. 1999a), the most basic tracer of enhanced organic carbon burial. Further, the carbon isotope dynamics during and after the positive excursion are currently debated, and there are multiple interpretations of the LJE positive $\delta^{13}C_{carb}$ values that do not invoke elevated rates of organic carbon burial and oxygen release (Miyazaki et al. 2018; Eguchi et al. 2020). Therefore, additional constraints on carbon and oxygen cycling are clearly needed to refine our view of this time interval.

The "standard" interpretation suggests that oxygen release due to C_{org} burial must have significantly slowed down in the aftermath of the LJE. In order to test this, we present new redox tracer data from two correlative sections (OnZaP and OPH sections; see Methods) of the upper Zaonega Formation (ZF), a post-LJE mudstone-dolostone succession. We provide some of the most straightforward evidence for Proterozoic surface oxygenation. In fact, current redox proxy records are most consistent with increasing oxygenation in the aftermath of the LJE—forcing a re-evaluation of our basic view of this turbulent interval of Earth's history.

3.2 Age and geochemical signatures of the Zaonega Formation

According to the latest U-Pb age constraints on a tuff horizon within the lower ZF, the formation was deposited at ~1980 Ma, ~80 Myrs after the proposed termination of the LJE (Martin et al. 2015). This age model is consistent with $\delta^{13}C_{carb}$ stratigraphy. In the Onega Basin, $\delta^{13}C_{carb}$ values in the lowermost ZF and underlying Tulomozero Formation are characterized by typical LJE values of ≥8‰ (Melezhik et al. 2015), with $\delta^{13}C_{carb}$ in preserved carbonate strata returning to normal marine values of ~0‰ further upsection (Kreitsmann et al. 2019). In the OPH core, the studied section occurs after several hundred meters of stratigraphy—including cumulatively ~210 meters of mudstone-dominated sediments—and contains carbonates bearing a normal marine (and therefore post-LJE) $\delta^{13}C_{carb}$ signal (Kreitsmann et al. 2019). Assuming a reasonable range of deposition rates for the mudstones—e.g., 1–100 m Myr^{-1} (Sadler 1999)—the studied section of the ZF was deposited millions of years after the termination of the LJE in the Onega Basin.

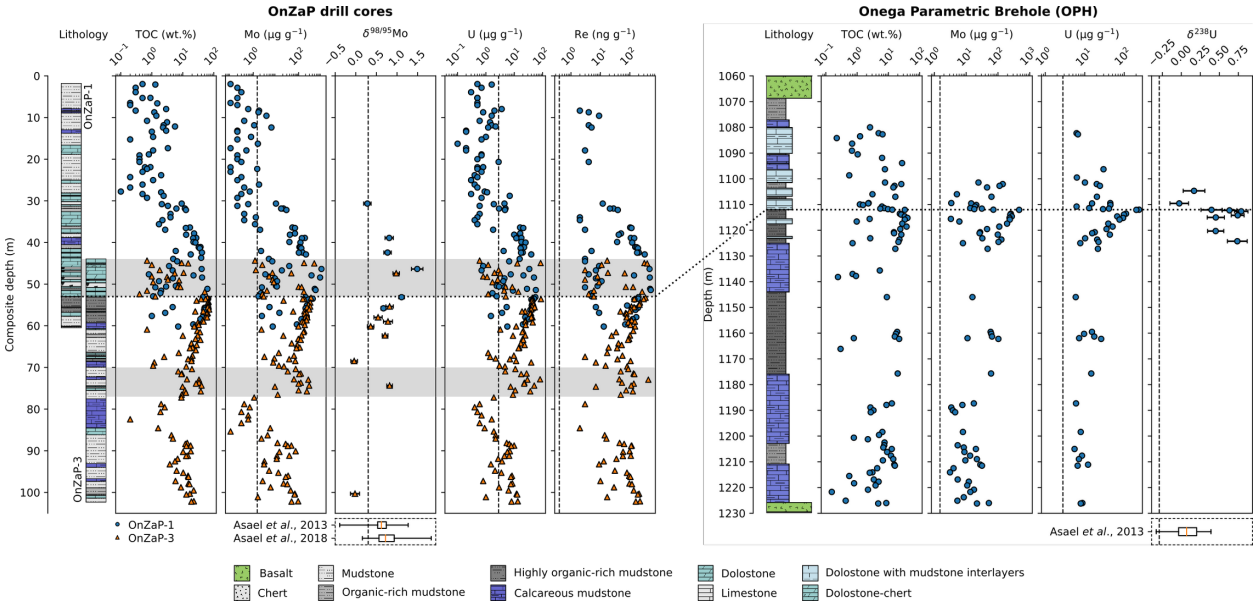

Figure 3.1: Lithology and geochemistry of the Zaonega Formation. Total organic carbon (TOC) and redox sensitive metal (RSE) profiles (errors contained within symbols), and Mo and U isotope ratios (δ^{98}Mo and δ^{238}U, error bars are 2×SE) are shown for the OnZaP and OPH sections. Vertical dashed lines are average crustal values (McLennan 2001; Andersen et al. 2017; Kendall et al. 2017) and the dotted horizontal line is the phosphorus-rich mudstone–dolostone contact used for intra-basinal correlation (see Methods and Appendix 2). Boxplots below the Mo and U isotope plots represent the distribution of previously published ZF data from lower in the succession (see Appendix 2) (Asael et al. 2013; Asael et al. 2018). Grey horizontal bands are partly silicified and calcified intervals due to fluid alteration (Paiste et al. 2018). While these imply the presence of secondary fluids that could have mobilized RSE, microscale RSE distribution confirms the primary nature of the RSE enrichments (see Appendix 2).

The section is rich in total organic carbon (TOC), with average values of 27.4±18.5 wt.% in mudstones of the OnZaP section, and 14.5±9.9 wt.% in OPH mudstones (Figure 3.1). These values are roughly comparable to the most organic-rich modern marine sediments (e.g., up to 21.3 wt.% on the Peru margin; Böning et al. 2004). We focus specifically on molybdenum (Mo), uranium (U), and rhenium (Re) enrichments, as these metals have previously provided robust evidence for major shifts in Earth's redox state (Partin et al. 2013a; Reinhard et al. 2013; Sheen et al. 2018). In the Zaonega mudstones Mo, U, and Re are significantly elevated relative to other Proterozoic black shales (Partin et al. 2013a; Reinhard et al. 2013; Sheen et al. 2018), averaging 130±142 μg g^{-1}, 19±15 μg g^{-1}, and 116±84 ng g^{-1}, respectively, in OnZaP mudstones. In the OPH section, Mo and U average 71±92 μg g^{-1} and 37±50 μg g^{-1}, whereas overall maximum Mo, U, and Re concentrations across both sites are 1009 μg g^{-1}, 238 μg g^{-1}, and 516 ng g^{-1}, respectively. In the OnZaP section, δ^{98}Mo is on average 0.67±0.81‰, with a maximum of 1.49±0.14‰. Uranium isotope values (δ^{238}U) in the OnZaP section range from −0.03 to 0.79‰, with an average of 0.47‰. The maximum value is the most ^{238}U-enriched shale measurement that has been reported to date (Yang et al. 2017; Wang et al. 2018).

The primary source of these RSE (in the rest of this manuscript, RSE refers specifically to Mo, U, and Re) to the oceans is the oxidative weathering of terrestrial RSE-bearing minerals (e.g., pyrite, uraninite), and subsequent riverine transport as aqueous oxyanions (Dunk et al. 2002; Miller et al. 2011). Hydrothermal inputs, while not fully constrained at present, are expected to be of less significance to the cycling of these RSE (Miller et al. 2011; Reinhard et al. 2013). The most important RSE sink is sequestration into marine sediments, which is influenced

by the redox state of the depositional setting (Crusius et al. 1996; Dunk et al. 2002). In oxic seawater, RSE are present as recalcitrant species that tend to accumulate in the water column (Anderson et al. 1989; Miller et al. 2011), although Mo adsorbs to Mn(IV)-oxides under oxic conditions and can then be released in pore waters following the reductive dissolution of Mn(IV)-oxides in anoxic sediments (Algeo and Lyons 2006). In anoxic environments, the RSE are progressively converted into particle-reactive species resulting in efficient drawdown through authigenic sulphide precipitation or adsorption to organic matter (Anderson et al. 1989; Crusius et al. 1996). With regards to Mo, it has been found that most efficient Mo sequestration takes place under euxinic waters with >11 μM of sulphide (HS^-) (Helz et al. 1996). In a broad sense, the contrasting behaviour of these elements in oxic and anoxic conditions ensures that the drawdown and marine reservoir sizes are governed by global ocean redox—large RSE reservoirs develop in an oxic ocean, which leads to large local sedimentary RSE enrichments under anoxic conditions (Reinhard et al. 2013; Sheen et al. 2018).

The U and Mo isotope systems, similar to RSE enrichments, respond to the global marine redox landscape. There is consensus that well-oxygenated oceans are characterized by high Mo and U isotope values (Andersen et al. 2017; Kendall et al. 2017). It is, however, difficult to gauge when a sedimentary archive captures seawater U and Mo isotope values. For instance, seawater Mo isotope values are most likely to be captured in shales deposited in isolated basins with high HS^- levels (Dickson 2017). However, non-quantitative reduction of Mo in euxinic marine basins results in negative fractionation and shale δ^{98}Mo values that are lower than seawater (Kendall et al. 2017), and therefore, δ^{98}Mo in euxinic shales is often interpreted as a

minimum estimate for seawater δ^{98}Mo (Canfield et al. 2013). Uranium isotope values in shales will be closest to seawater values in oxic sediments and up to ~1‰ heavier than seawater in anoxic and high productivity settings (see Appendix 2 for detailed discussion on Mo and U isotope values; Andersen et al. 2017). Using this framework, our data points to well-oxygenated global oceans with high rates of primary productivity during deposition of the locally anoxic Zaonega Formation.

3.3 Marine RSE inventory

RSE enrichments in the ZF far exceed anything known from pre-Neoproterozoic black shales (Figure 3.2). Similar values are found only in the Phanerozoic, where they have been taken as evidence for an expanded seawater RSE inventory, the direct result of pervasive ocean-atmosphere oxygenation (Partin et al. 2013a; Reinhard et al. 2013; Sheen et al. 2018). We believe that the ZF, likewise, contains evidence of a large global marine RSE inventory that strongly suggests a relatively oxidized ocean–atmosphere system with a robust terrestrial oxic RSE weathering flux, in which the drawdown of RSE was limited by the relative scarcity of anoxic conditions on the seafloor. Further, U and Re enrichments—which, unlike Mo, are also drawn down in ferruginous waters (Tribovillard et al. 2006)—suggest that this was an episode of thorough water column oxygenation on continental shelves, rather than just a restriction of euxinic deposition, >1400 Myr before terminal oceanic oxygenation during the Neoproterozoic (Och and Shields-Zhou 2012).

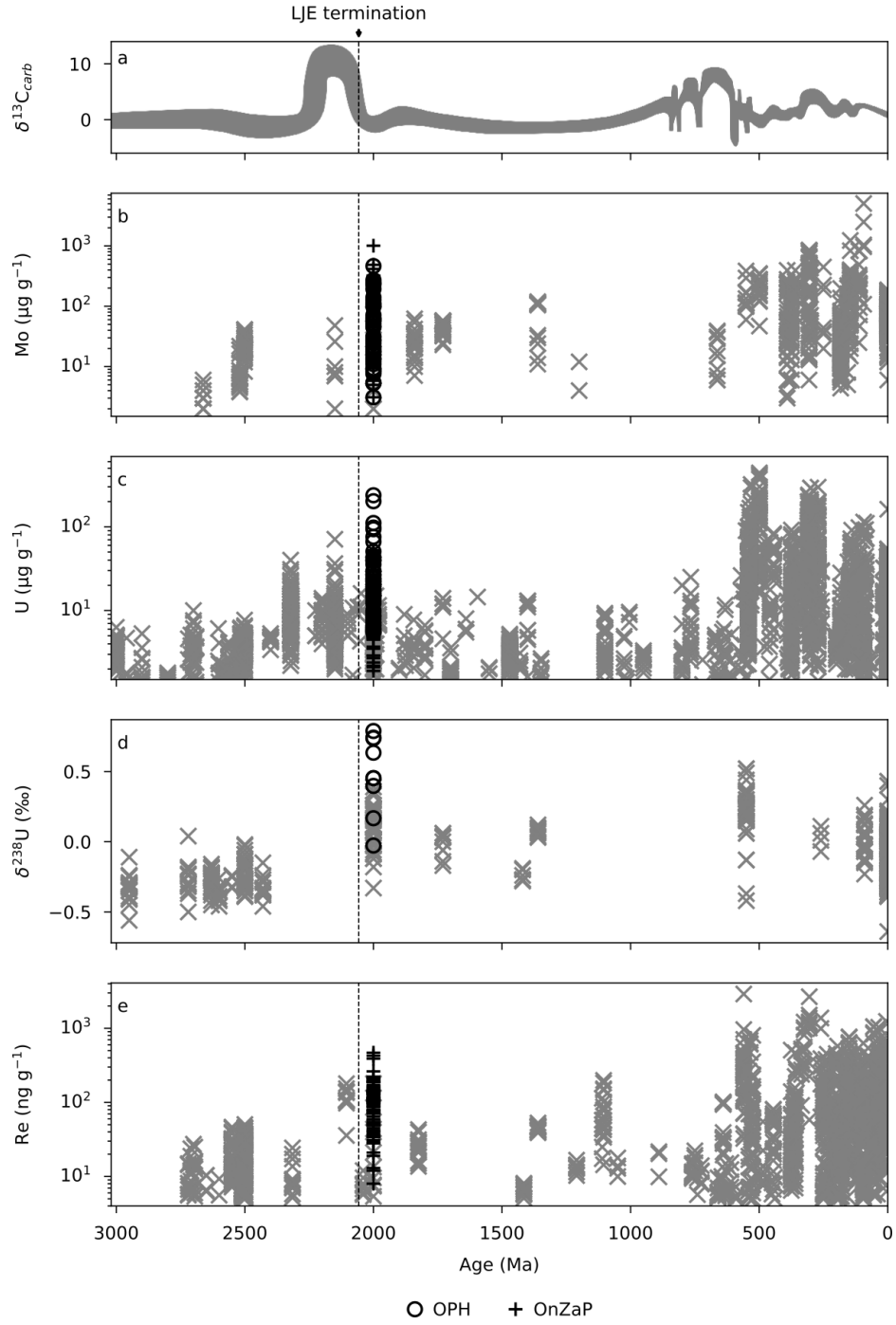

Figure 3.2: Secular trends in redox sensitive element concentrations from anoxic shales. Zaonega Formation data (plus and circle symbols) are plotted on compilations from literature

(X symbols). (a) Changes in $\delta^{13}C_{carb}$ ratio through time, modified from Karhu (1999). (b) Molybdenum concentrations from Robbins et al. (2016). (c) Uranium concentrations from Partin et al. (2013a). (d) Uranium isotope ratios from Wang et al. (2018) and Yang et al. (2017). (e) Rhenium concentrations from (Sheen et al. 2018). Concentration errors are within symbols; for $\delta^{238}U$ and age errors, refer to Figure 3.1, Appendix 2, and compilation data sources.

While low Mo in black shales could be explained by either a small marine Mo pool, basinal restriction leading to localized Mo depletion (Algeo and Lyons 2006), or inefficient Mo scavenging under low HS^- conditions (Helz et al. 1996), there are limited ways to explain elevated RSE concentrations in black shales of the ZF (i.e., up to several hundreds of μg g^{-1} of Mo throughout the >160 km-wide basin). One possibility is anomalously low sedimentation rates, which have previously been invoked to explain high TOC in U-rich black shales of the Miocene Monterey Formation, USA (Föllmi et al. 2005). Although low sedimentation rates may have played a role in concentrating TOC and RSE in the ZF, the magnitude of the RSE enrichment—consistent with Phanerozoic levels (Figure 3.2)—makes it unlikely sedimentation rate alone could account for it. A more plausible explanation is that the ZF was also a highly efficient, likely anoxic RSE sink that had reliable access to a large oceanic RSE inventory (see Appendix 2 for additional discussion on factors controlling RSE accumulation; Algeo and Lyons 2006).

The U isotope values provide an independent confirmation of highly oxygenated oceans—as noted above they are the most positive shale $\delta^{238}U$ values measured to date (Figure 3.2), requiring both high seawater $\delta^{238}U$ values (likely comparable to the modern value of ~−0.4‰)

and a near full expression of the equilibrium ~1.2‰ fractionation during U reduction. High seawater values only develop when oxic U burial is a major U burial flux in well-oxygenated oceans (Andersen et al. 2014). In addition, a significant positive U isotope fractionation ($\geqslant$0.6‰) strongly suggests U reduction in the water column instead of within the sediment pile (Andersen et al. 2017). Uranium reduction rates appear to scale with sulphate (or iron) reduction rates (Barnes and Cochran 1993)—providing a link between amounts of organic matter loading in a marine system and the isotope fractionation that occurs during U burial. For reference, there is limited water column sulphate reduction in the modern Black Sea and Cariaco Basin because of low rates of productivity and maximum sediment δ^{238}U is only ~0.8‰ and ~0.6‰ higher than seawater, respectively (Andersen et al. 2014). In contrast, high productivity in the ZF is consistent with the anomalous organic carbon enrichments. Therefore, the strongly positive U isotope values in the ZF, along with the RSE enrichments, are most readily explained by invoking both globally well-oxygenated oceans and a locally anoxic basin with markedly elevated rates of primary productivity, the latter of which would tend to enhance the expression of isotope effects associated with U reduction.

3.4 Conflicting views on oxygenation during ZF deposition

Our interpretation that the ZF records well-oxygenated global ocean conditions is ostensibly in conflict with previous interpretations derived from C, S, and Mo isotope records proposed to reflect global deoxygenation. However, much of this data can plausibly be explained through local rather than global processes. First, Kump et al. (2011) postulated a post-LJE global negative δ^{13}C excursion based on depleted δ^{13}C in ZF carbonates. This was interpreted to result

from the widespread oxidation of organic-rich shales, which would have favoured suppressed, rather than elevated, O_2 levels. However, negative $\delta^{13}C$ in the ZF has subsequently been reinterpreted to reflect basin-wide methanotrophy and secondary overprinting of carbonate rocks (Qu et al. 2012). Second, Scott et al. (2014) argued that highly ^{34}S-enriched pyrites in the upper ZF reflect a global collapse of the marine sulphate reservoir due to deoxygenation. In contrast, Paiste et al. (2018) explained the same trends through basin-specific processes involving quantitative uptake of sulphate. Third, Asael et al. (2013) and Asael et al. (2018) inferred an ~0.7‰ seawater $\delta^{98}Mo$ value from two other cores in the upper ZF, identical to the average in the OnZaP section. Mn-oxides, which form in oxic waters, preferentially scavenge ^{95}Mo and drive seawater $\delta^{98}Mo$ to higher values. If one assumes a modern riverine input value of ~0.7‰ for the Paleoproterozoic (Kendall et al. 2017), a seawater value of ~0.7‰ suggests limited Mn-oxide precipitation and, thus, little O_2 in the global oceans. However, the sequestration of Mo in anoxic settings like the Zaonega Formation commonly imparts a negative $\delta^{98}Mo$ fractionation, except in highly restricted euxinic basins where nearly all Mo is drawn down (Kendall et al. 2017). This highlights that the highest Mo isotope values of ~1.4‰ represent a minimum seawater $\delta^{98}Mo$ estimate (see Appendix 2; Canfield et al. 2013) and that the Mo isotope data does not necessarily preclude widespread oxic conditions.

3.5 Implications of oxygenated oceans at approximately 2000 Ma

RSE-replete global conditions during the deposition of the ZF have important implications for Earth's global C and O cycles during the Paleoproterozoic. Tracking the evolution of Earth's redox history is also critical for understanding early eukaryote evolution. The late rise to

prevalence of eukaryotes in the Neoproterozoic is thought to be linked to widespread anoxic and nutrient-poor conditions that favoured prokaryotic metabolisms (Brocks et al. 2017). Given the extent of ocean oxygenation and nutrient abundance inferred from the ZF (Bekker and Holland 2012; Lepland et al. 2014), conditions favourable to eukaryotic diversification could have been present for much of the middle Paleoproterozoic. It is curious, then, that molecular clock analyses and microfossil evidence of eukaryote origin tend to converge after ~1900 Ma (Parfrey et al. 2011; Betts et al. 2018). In the simplest sense this discrepancy supports the central importance of a unique endosymbiosis event for the emergence of eukaryotes, rather than removal or lessening of an environmental barrier.

The ZF is part of a well-recognized overall trend towards elevated RSE concentrations at ~2400–2000 Ma that has been linked to well-oxygenated oceanic–atmospheric conditions (Partin et al. 2013a; Kipp et al. 2017; Sheen et al. 2018). Surprisingly, our ZF data extend this trend past the termination of the LJE. Furthermore, the extreme RSE enrichments hint that, instead of being in decline, atmospheric O_2 abundance could still have been high perhaps several tens of Myrs after the canonical end of the LJE (Martin et al. 2015). In the modern, well-oxygenated world, the geologic O_2 response time is on the order of ~2 Myrs (Kasting and Canfield 2012), whereas the residence times of Mo, U, and Re in the oceans are ~440, ~400, and ~780 kyrs, respectively (Anderson et al. 1989; Miller et al. 2011). Therefore, if the LJE decline is linked to a decrease in O_2 production as the result of diminishing C_{org} burial by the end of the LJE, then O_2 would be expected to be significantly attenuated by this time. Instead, our data suggest the opposite.

Our observations provide empirical evidence for models (e.g., Miyazaki et al. 2018) that decouple the strongly positive carbonate carbon isotope values of the LJE from enhanced organic carbon burial. Further, given the likelihood that highly oxidized conditions continued up to ~2000 Ma, this highlights the importance of exploring alternative interpretations of the carbon isotope record and the need for refined chemostratigraphic and geochronological studies focused on this key interval of Earth's history.

3.6 Methods

3.6.1 Materials

The material for this study comes from drill cores in the Onega Basin that intersect the ZF—a relatively well-preserved 1500 m-thick succession of organic-rich mudstones and carbonates, interlayered and intersected with igneous units including lavas, tuffs, and sills (see Appendix 2 for a detailed geological setting; Melezhik et al. 1999b). The 60 m long cores OnZaP-1 and OnZaP-3 were drilled 500 m apart in the northeastern part of the Onega Basin near Shunga village, close to drill core FAR-DEEP 13A (Paiste et al. 2018). The OnZaP-1 and OnZaP-3 cores are partly overlapping and combined provide a 102 m thick OnZaP section. The 3500 m long OPH core that intersects the entire supracrustal succession of the Onega Basin was drilled ~60 km to the south. Paiste (2018) correlated the upper ZF OnZaP and OPH sections based on C isotopes, trace metal enrichments, P concentrations, and a distinct massive P-rich dolomite unit that occurs throughout the Onega Basin.

The lithology of this section is characterized by alternating dolomite to calcite-rich carbonates and exceptionally organic-rich mudstones that are intersected by silica or pyrobitumen veins (Figure 3.1). In the OnZaP section, the interval from the bottom of the section to 53 m depth is dominated by highly organic-rich mudstones with relatively few carbonate beds; the 53–33 m interval is mostly dolostone and contains a distinctive dolomite unit; and the 33–1.7 m interval consists of grey mudstones and marly carbonate beds (Paiste et al. 2018). Two sets of samples from the OnZaP section were analyzed in this study. Set MSP0001 consists of 135 samples that were taken at roughly 1 m intervals and is identical to that used in Paiste et al. (Paiste et al. 2018). Set MSP0010 contains 79 samples that more specifically targeted RSE and organic-rich intervals. A set of 89 samples were analyzed from the 1060–1230 m interval of the OPH core that is roughly equivalent to the OnZaP section.

3.6.2 Elemental concentrations

Total organic carbon content of the MSP0001 and OPH samples were adapted from Paiste et al. (2018) and were measured from powdered aliquots using a LECO SC-444 analyzer at the Geological Survey of Norway (NGU), Trondheim, Norway. Detection limit was 0.1 wt.% and precision better than 10%. For the MSP0010 set, TOC was measured at the Pôle Spectrométrie Océan, European Institute for Marine Studies (IUEM), Brest, France. Dried and powdered samples were combusted in ceramic beakers at 500 °C for 24h and loss of mass on ignition was determined. Repeat measurements of 7 samples generally differed by <1 wt.%.

Major and trace element compositions of MSP0001 samples were determined at Acme Labs, Bureau Veritas Commodities Canada Ltd. The samples were first pulverized and combusted to remove organic carbon. For major elements, the sample was fused in $LiBO_2$ flux, then digested, whereas minor elements were analyzed from full digests in HNO_3, $HClO_4$, and HF. Measurements utilized inductively coupled plasma optical emission spectrometry (ICP-OES) or mass spectrometry (ICP-MS). Average relative standard deviation was less than 5% for all elements. MSP0010 element composition was determined at IUEM. Samples were pulverized in a tungsten carbide crusher and an agate mill, then combusted at 500 °C for 24h to remove organic carbon. Major element concentrations were measured on a Jobin Yvon Horiba Ultima 2 ICP-OES after digestion overnight at 80 °C in concentrated HF and HNO_3 and neutralization with boric acid to retain Si. For trace element concentrations, digestion was performed in a class 1000 clean laboratory, using distilled acids—samples mixed with concentrated HF and HNO_3 were heated to 80 °C overnight, then allowed to evaporate; this digestion was then repeated with concentrated *aqua regia*, after which the sample was taken up in 6M HCl. Trace element concentrations were measured on a Thermo Scientific Element 2 ICP-MS calibrated against commercial multi-element standards and digested geostandards (e.g., BHVO-2). OPH major and trace elements were measured on a Philips PW 1480 X-ray fluorescence spectrometer (XRF) equipped with a Rh X-ray tube at the Geological Survey of Norway. For major elements 0.6 g of ground and combusted (1000 °C) sample was fused into a bead in a CLAISSE FLUXER-BIS together with 4.2 g of $Li_2B_4O_7$. For trace elements 2.4 g of Hoechst wax was mixed with 9.6 g of sample in a Spex Mixer/Mill and pressed into a pellet using a Herzog pelletizing press. Major

element detection limits were 0.01% (P_2O_5, CaO), 0.5% (SiO_2), 0.02% (Al_2O_3), or 0.02% (MgO) and precision (1σ) was typically ~2%. Detection limits for trace elements were ≤10 μg g^{-1}.

Samples with a ratio of $(CaO+MgO)/(SiO_2+Al_2O_3)$ > 0.2—approximating >20 wt.% carbonate content—were excluded when calculating Mo, U, and Re averages, since compilations of RSE in black shales generally only include shale samples (Partin et al. 2013a; Reinhard et al. 2013; Sheen et al. 2018). An exception was made for samples with >5 wt.% TOC, since such sediments would have played a role in trace metal cycling regardless of their mineralogical composition.

3.6.3 Mo isotopes

Mo isotopes were measured from fully digested OnZaP MSP0010 samples that were purified via column chromatography according to Asael et al. (2013). A ^{97}Mo–^{100}Mo double spike was employed (Siebert et al. 2001) and the isotopes were measured on a Thermo Scientific Neptune multi-collector ICP-MS at IFREMER, Brest, France. Data is expressed relative to NIST SRM 3134 = 0.25‰ (Nägler et al. 2014). Detailed methodology is provided in Appendix 2.

3.6.4 U Isotopes

Samples for U isotopes were sequentially digested in a mixture of 3 mL HNO_3 and 1 mL HF at 100 °C for 24h, then *aqua regia* at 95 °C for 24h. Following each digestion step the sample was evaporated to dryness. Sample residues were taken up in 5 mL of 3M HNO_3 at 70 °C. All sample preparation was performed in a Pico-trace clean lab at the Yale Metal Geochemistry Center.

Uranium isotope values were measured on a Thermo Neptune Multi-collector ICP-MS following the method in Wang et al. (2018) using the IRMM-3636 233/236 U double spike. Accuracy and precision were monitored with concentration matched CRM112, CRM129a, and Ricca geostandards. Error was less than 0.15‰. Detailed methodology is provided in Appendix 2.

Chapter 4: Protracted oxygenation in the Paleoproterozoic did not result in proliferation of mitochondrial organisms[3]

4.1 Introduction

Free O_2 in the atmosphere, the result of oxygenic photosynthesis, shapes ecology on the global scale. Understanding Earth's oxygenation is therefore paramount to understanding the evolution and history of life. One of the more contentious parts of this history relates to the emergence of eukaryotes in the Paleoproterozoic eon. Today most eukaryotes require O_2 levels of at least 1% of present atmospheric levels (i.e., the Pasteur Point; Fenchel and Finlay 1995; though see Stolper et al. 2010), and as such it has been argued that periods of high atmospheric O_2 concentrations (pO_2) were necessary for the emergence and radiation of mitochondria-bearing eukaryotes (e.g., Catling et al. 2005). Yet, an alternative viewpoint maintains that inferred pO_2 shifts do not correspond well with the evolutionary history of complex life (e.g., Butterfield 2009), with the implication that fortuitously timed biotic novelties (cf. Erwin) control when

[3] A version of this chapter is prepared for submission as Mänd, K., Planavsky, N. J., Porter, S., Robbins, L. J., Wang, C., Kreitsmann, T., Paiste, K., Paiste, P., Romashkin, A. E., Kirsimäe, K., Lepland, A., and Konhauser, K. O. "Protracted oxygenation in the Paleoproterozoic did not result in proliferation of mitochondrial organisms"

groups of organisms rise to ecological dominance, independent of environmental triggers (e.g., Betts et al. 2018).

Over the last two decades, a consensus has emerged regarding Archean and Proterozoic redox evolution. The disappearance of mass-independent sulphur isotope fractionations signifies the oxygenation of the atmosphere by ~2501 to 2302 Ma (Bekker et al. 2004; Warke et al. 2020). This change is colloquially known as the Great Oxidation Event (GOE; Holland 2002). The Rhyacian period (2300–2050 Ma) is notable for signals of highly elevated sulfate including the deposition of massive evaporites (e.g., Blättler et al. 2018) and sedimentary sulphur isotope signatures (Planavsky et al. 2012b) that point to a robust marine sulfate pool. Although signals for sulfate rise are typically taken as evidence for high atmospheric oxygen levels, there is little direct evidence constraining pO_2.

The Orosirian period (2050 to 1800 Ma), and more generally the mid-Proterozoic (2000 to 800 Ma), is thought to be characterized by low levels of oxygen, as evidenced by the loss of iron from paleosols (e.g., Mitchell and Sheldon 2010), and muted sedimentary RSE concentrations (Partin et al. 2013a; Reinhard et al. 2013). However, there is also increasing evidence for substantial redox variability throughout this time period (e.g., Tang et al. 2017). One the one hand, biomass with strongly negative carbon isotope ratios coupled to positive sulphur isotope ratios of pyrite and muted Mo isotope fractionations have been interpreted to reflect a rapid decrease in O_2 at ~2000 Ma (Kump et al. 2011; Asael et al. 2013; Canfield et al. 2013; Scott et al. 2014). Worldwide deposition of shallow water iron formations between 1880–1850 Ma is further evidence for shallow-water anoxia in large parts of the ocean (Canfield 2005; Konhauser

et al. 2017). On the other hand, oxidative redox-sensitive metal cycling persists through this time period (Frei et al. 2009; Fralick et al. 2017; Planavsky et al. 2018b). Collectively it is becoming clear that redox proxies point away from a traditionally envisioned unidirectional oxygenation following the GOE, and point towards spatially and temporally variable redox conditions (e.g., Toma et al. 2019).

Evidence for inhibited Cr oxidation, from Cr isotopes, has been a key argument for low mid-Proterozoic surface oxygen levels (Planavsky et al. 2014; Cole et al. 2016; Colwyn et al. 2019). Although the Cr isotope record may suggest redox variability and intervals of oxygenation throughout the middle Proterozoic (Gilleaudeau et al. 2016; Canfield et al. 2018) there is intriguingly no evidence for Paleoproterozoic oxygenation from Cr isotopes—when it has been commonly proposed from other proxies that it was a high-oxygen interval (Bekker and Holland 2012; Canfield et al. 2013; Blättler et al. 2018). Thus with current records it is fair to say that different proxies present varying views of Earth's oxygenation, hindering attempts to link oxygenation to shifts in ecosystem structure.

A key location for studying the Orosirian transition is the Onega Basin in the Karelian Republic, Russia. It comprises a ~3-km-thick Paleoproterozoic succession of evaporites, carbonates, and siliciclastics, including organic-rich mudstones, intercalated with mafic igneous rocks (Figure 4.1). Geochemical signals in evaporites and carbonates from the lower part of this succession have previously been tied to elevated ocean sulfate and oxygen levels (Blättler et al. 2018) and the Lomagundi-Jatuli carbon isotope excursion, which has been associated with excess organic carbon burial and O_2 release (Melezhik et al. 1999a). The overlying organic-rich

mudstones have variably been argued to record a decline in O_2 levels (Kump et al. 2011, Scott et al. 2014) or inversely, be indicative of continued oxygenated conditions (Kipp et al. 2020; Kreitsmann et al. 2020; Mänd et al. 2020). However, what has never been attempted before is an integrated assessment of the redox state and redox stability throughout the entire succession hosted in the Onega Basin—nor has such a large-scale assessment, to our knowledge, been attempted for any other succession from this period. In this study, we present new bulk-rock chromium isotope data (δ^{53}Cr) from evaporites, carbonates, and organic-rich mudstones from a ~2400-m-thick volcano-sedimentary section of the Onega Basin. We find that substantially fractionated sedimentary δ^{53}Cr values persist throughout the Onega Basin succession. This suggests that the Onega Basin records a protracted time period—possibly more than 100 Myrs—that was host to a fundamentally stable and oxygen-rich ocean-atmosphere system providing a platform to revisit the links between oxygen and eukaryote divergence.

4.2 Geological background

The Onega Basin succession begins with the deposition of coarse-grained siliciclastics and lava flows onto a basement of Archean granites and gneisses (Melezhik et al. 2013b). These are overlain by the ~800-m-thick Tulomozero Formation made up of evaporites and dolomites (Melezhik et al. 1999a). The Zaonega Formation follows as a ~1500-m-thick volcano-sedimentary package consisting of dolostones, siliciclastic turbidites, and mudstones intercalated with mafic igneous rocks (Melezhik et al. 1999a). On top of that lies the ~500-m-thick Suisari Formation comprising mainly tuffs and mafic lavas/sills (Puchtel et al. 1999). The section is capped by fluvial-lacustrine siliciclastics of the Kondopoga Formation (Melezhik et al. 2013b).

Following deposition, the Onega Basin underwent greenschist-facies metamorphism during the ~1890–1790 Ma Svecofennian orogeny, which deformed the succession into a series of northwest–southeast trending folds (Melezhik et al. 2013b).

This study focuses on the Tulomozero, Zaonega, and Suisari formations that constitute the middle and upper part of the Onega Basin succession. There is significant lithofacies variation in the Tulomozero Formation—in the northern part of the basin, along with the western and eastern margins, the formation consists mainly of dolostone with varying amounts of magnesite and Ca-sulphate pseudomorphs, and siliciclastic layers. By contrast, the formation in the southern part of the basin, as recorded by the drill core of the Onega Parametric Hole, begins with a ~600-meters-thick halite and anhydrite-magnesite unit that grades upwards into a dolomite dominated unit. It is likely that in its present northern extent the formation was deposited in a low-energy intertidal, sabkha or playa lake environment with fluvial influences, whereas the southern part of the basin was more restricted and evaporitic, but still experienced consistent seawater influx that sustained the accumulation of hundreds of meters of evaporites (Melezhik et al. 2013b). Carbonates of the Tulomozero Formation are characterized by strongly positive carbon isotope ratios ($\delta^{13}C_{carb}$), with values as high as 18‰ that potentially reflect local amplification of a globally ^{13}C-enriched bicarbonate pool (e.g., Karhu 1993; Melezhik et al. 1999a). As such, it is one of the type sections for the Lomagundi-Jatuli carbon isotope excursion (Karhu and Holland 1996). The mineralogy of the halite and Ca-sulphate succession, together with their S and Ca isotope composition, have been taken as evidence of a large marine sulphate pool (Reuschel et al. 2012), constituting >30% of modern levels (Blättler et al. 2018).

The overlying Zaonega Formation was, in contrast, deposited in alternating shallow and deeper water conditions, possibly in a rift basin developed on a highly active continental margin (Melezhik et al. 1999b). Between 35–70% of the succession is composed of mafic sills and lavas, often emplaced into unconsolidated sediments (Melezhik et al. 2013b). The lowermost Zaonega Formation is dominated by mudstones with common dolostone interbeds which transition into deeper-water mixed mudstones, dolostones, and siliciclastic rhythmitites further upsection. The formation is notable for containing extremely high organic carbon content (up to 70 wt.%), the earliest known oil field (Melezhik et al. 1999b; Qu et al. 2012), highly elevated RSE concentrations (Mänd et al. 2020), and one of the earliest sedimentary phosphorus enrichments (Lepland et al. 2014). Variable and often high pyrite $\delta^{34}S$ values have been interpreted as recording a diminished global marine sulphate pool (Scott et al. 2014) or alternatively anomalously high local sulphate demand by microorganisms (Paiste et al. 2018; Paiste et al. 2020b). In the lower part of the Zaonega Formation, dolostones enriched in ^{13}C record the Lomagundi-Jatuli excursion (Melezhik et al. 2015), but the best-preserved carbonates of the upper Zaonega Formation have normal-marine $\delta^{13}C$ values (Črne et al. 2014; Kreitsmann et al. 2019; Kreitsmann et al. 2020). Strongly negative $\delta^{13}C$ values in carbonates and organic matter from the middle part of the Zaonega Formation were earlier thought to reflect a global negative C isotope excursion (Kump et al. 2011) but are now viewed as artifacts of hydrothermal de-dolomitization (Kreitsmann et al. 2019) and the incorporation of methanotrophic biomass (Qu et al. 2012). The deposition of the Zaonega Formation was followed by the Suisari Formation, signifying a slowdown of subsidence and the infilling of the basin with hundreds-of-meters-thick subaqueous lavas containing interspersed thin mudstone beds (Melezhik et al. 2015).

The age of the Onega Basin remains imprecisely constrained. The most robust anchor for the older age boundary is given by Pb–Pb ages of 2449 ± 1.1 Ma for a sill crosscutting the Archean basement (Amelin et al. 1995). The Tulomozero Formation is additionally constrained by an imprecise dolomite Pb–Pb age of 2090 ± 70 Ma (Ovchinnikova et al. 2007) and by virtue of it recording the Lomagundi-Jatuli isotope excursion (along with the lowermost Zaonega Formation), which terminated in Fennoscandia at ~2060 Ma (Martin et al. 2013). A single zircon from a tuff layer in the lower Zaonega Formation yielded a U–Pb age of 1982 ± 4.5 Ma (Martin et al. 2015). In terms of the younger age boundary, a suite of cross-cutting dykes in the Tulomozero and Zaonega Formations yield ages of 1919 ± 18 Ma (Priyatkina et al. 2014), 1956 ± 5 Ma (Stepanova et al. 2014), and 1961 ± 5.1 Ma (Martin et al. 2015), some of which have peperitic contacts, implying that the sediments were still wet and unconsolidated at the time of intrusion. Sills of the Suisari Formation are dated 1969 ± 18 Ma (Puchtel et al. 1998) and 1988 ± 34 Ma (Puchtel et al. 1999). Re-Os dates on Zaonega Formation mudstones yield an age of ~2050 Ma (Bauer et al. 2019). In summary, while dates are imprecise, deposition of the ~2300-m-thick succession comprising the Tulomozero, Zaonega, and Suisari formations likely spanned several tens of millions and possibly over a hundred million years; provisionally, we constrain the age of the succession between ~2090–1961 Ma.

4.3 Materials and methods

4.3.1 Drill core

Drill core samples were obtained from the ~3500-m-long Onega Parametric Hole (OPH), drilled in 2008–2009 in the southern Onega Basin (62.1559 N, 34.4073 E; Figure 1.2; Krupenik and Sveshnikova 2011). The drill core intersects ~800 m of the Tulomozero Formation, ~1500 m of the Zaonega Formation, and ~500 m of the Suisari Formation. Samples for this study were obtained from all of the aforementioned formations and constitute three sample sets: "NGU" (140 samples), "ACME" (40 samples), and "Yale" (73 samples). Care was taken to remove any macroscopically visible veins or monocrystalline mineral grains from rock slabs, especially for the "Yale" samples from which Cr isotope compositions were measured.

4.3.2 X-ray diffraction

The mineralogical composition of the samples was studied using X-ray diffractometry (XRD) at the University of Tartu, Estonia. Rock samples were ground to a fine powder, pressed into un-oriented tablets and scanned on a Bruker D8 Advance diffractometer, where a copper *Kα* X-ray source and a LynxEye positive sensitive detector were used to generate diffractograms in a 2–70° 2Θ range. Quantitative mineral abundances were modeled using the Rietveld algorithm-based Topaz software suite. The relative error for major mineral components (>5 wt.%) was ~10% and ~20% for minor mineral components (<5 wt.%).

4.3.3 Element abundances

Total organic carbon (TOC) content was measured at the Geological Survey of Norway (NGU) using a LECO SC-444 analyser ("NGU" samples; Paiste et al. 2020a) and at the University of Alberta via loss on ignition ("ACME" and "Yale" samples). Sample aliquots weighing between 0.5 and 2 g were loaded into ceramic beakers and combusted at 500 °C for 8–12 h, and the change in mass was recorded. Element concentrations for sample set "NGU" were determined at NGU with a Philips PW 1480 X-ray fluorescence spectrometer equipped with a rhodium X-ray tube. For major elements, 0.6 g of powdered sample aliquots and 4.2 g of $Li_2B_4O_7$ were heated to 1000°C and fused into a bead using a CLAISSE FLUXER-BIS. For minor elements, samples were prepared by mixing 9.6 g of powdered sample with 2.4 g of Hoechst wax in a Spex Mixer/ Mill and pressing them into a pellet using a Herzog press. The detection limits for major elements were generally below 0.02% and the typical precision (1σ) was ~2%. For minor elements, detection limits were ≤10 μg g^{-1}. Calibration of the XRF was done using a set of ~120 internationally certified natural rock standards as well as ~20 artificial standards provided by the XRF manufacturer.

Element concentrations for sample set "ACME" were determined at ACME Laboratories, Bureau Veritas Commodities Canada Ltd. The samples were powdered and then heated to mineralize organic carbon. Major elements were analyzed via inductively coupled plasma optical emission spectroscopy (ICP-OES) from aliquots fused into a $LiBO_2$ bead. Minor elements were digested using a mix of HNO_3, $HClO_4$, and HF and analyzed via inductively coupled plasma

mass spectrometry (ICP-MS). Average relative standard deviation was less than 5% for all elements; accuracy was monitored using the OREAS 25a and OREAS 45e reference materials.

Element concentrations of sample set "Yale" were measured at the Yale Metal Geochemistry Center (YMGC). The samples were pulverized in an agate mill, combusted in ceramic crucibles at 500°C for 8h to remove organic carbon and digested in a class ten Pico-trace clean laboratory using a succession of concentrated, Teflon-distilled acids. Digestions were initiated with the addition of 3 ml of HNO_3 and 1 ml of HF, then heated at 100 °C for 24h in closed Teflon vials, before being evaporated to dryness. Once dry, 3 ml HCl and 1 ml of HNO_3 were added to each sample, and samples were heated at 95 °C for 24h before being dried down. Final residues were then taken up in 5 mL of 3N HNO_3 solution at 70 °C for 1h. Prior to analyses by ICP-MS, samples were diluted 200:1 in 5% Teflon-distilled HNO_3 spiked with 1 ng g^{-1} indium (In). All samples were measured on a Thermo Scientific Element XR high-resolution ICP-MS. The In spike was used to correct for instrumental drift over the analytical session. Five dilutions of a customized internal laboratory standard were measured at the end and beginning of the analyses and several times throughout the run. Repeat analysis on the laboratory standard yielded a relative standard deviation (1σ) for all elements (excepting Na) of ≤8%, averaging ~4% across the analytical session. External accuracy was assessed by measuring the geostandard BHVO-2; relative difference between measured and known values for all elements was 8.3% on average and generally below 10%. Particularly, the Cr and Ti values for BHVO-2 were within the 95% confidence interval for accepted values (Jochum et al. 2005). For all sample sets, Cr was

normalized to the detrital tracer element titanium to assess authigenic enrichments, as suggested by Cole et al. (2017).

4.3.4 Isotope ratios

Oxygen isotope ratios of carbonates from micro-drilled samples were measured at the University of Tartu using a Thermo Scientific Delta V Advantage continuous flow isotope ratio mass spectrometer and include data published in Kreitsmann et al. (2019). The precision of the measurements was 0.2‰ (2σ) and the long-term reproducibility exceeded ±0.2‰ (2σ). The compositions are expressed as the ratio of ^{18}O over ^{16}O, normalized to the Vienna Pee Dee Belemnite (VPDB) reference standard as $\delta^{18}O$:

$$\delta^{18}O = [(^{18}O/^{16}O)_{sample} / (^{18}O/^{16}O)_{VPDB} - 1] \times 1000‰$$

A correction was applied for the differing phosphoric acid fractionation factor of dolomite and calcite (Rosenbaum and Sheppard 1986) according to the mineralogy of individual samples. Oxygen isotope compositions of bulk samples are presented here as an average of several micro-drilled sub-samples (1–7 micro-drilled measurements per bulk sample).

Chromium isotope compositions were determined for the “Yale” sample set at the YMGC from solutions prepared for elemental concentration analysis (see above). Sample preparation adapted the methods of Schoenberg et al. (2008) and Reinhard et al. (2014). An aliquot of each sample, containing ~200 ng of Cr, was diluted in 2 ml of 6N HCl and a ^{50}Cr–^{54}Cr double spike was added at a spike/sample ratio of ~0.5, in order to correct for isotope fractionation during

sample processing and measurement (e.g., Schoenberg et al. 2008). The samples were purified chromatographically to remove mass interference from ^{54}Fe, ^{50}Ti, and ^{50}V. First, samples were passed through columns containing AG1-X8 anionic resin, where the matrix was eluted by addition of 0.2N HCl and Cr was subsequently collected with 2N HNO_3. Second, samples were loaded on microcolumns filled with AG1-X8 resin to remove all remaining Fe, and Cr was eluted with 6N HCl. In the final step, Ti was removed using the cationic resin AG50W-X8: the matrix was eluted with 0.5N HNO_3, 0.5N HF, and 1N HCl and Cr was subsequently released with 1.8N HCl. Residues were taken up in 5% HNO_3 and analyzed on a Thermo-Finnigan Neptune Plus multicollector ICP-MS. To correct for remaining interferences, the samples were run in high-resolution mode and Fe, Ti, and V were monitored. Standard-sample bracketing with the NIST SRM 979 reference standard was employed to correct for instrumental drift. Instrumental mass bias and fractionation during sample preparation was corrected for using the Cr double-spike through the data reduction model of Siebert et al. (2001). The Cr isotope compositions are normalized to the composition of the reference material NIST SRM 979, and reported as:

$$\delta^{53}Cr = [(^{53}Cr/^{52}Cr)_{sample} / (^{53}Cr/^{52}Cr)_{SRM979} - 1] \times 1000‰.$$

The internal precision was calculated based on 20 duplicate analyses of NIST SRM 979 and reported as 2σ uncertainty. Geostandards BHVO-2B and Nod-1-a were used to monitor the external precision; the measured values were between −0.10‰ to −0.13‰ and 0.09‰ to 0.04‰, respectively, which is within error of previously reported measurements (Cole et al. 2016).

4.3.5 *In-situ* element mapping

In-situ element mapping of two polished samples (OPH-1572 and OPH-4081) from representative lithologies was conducted at the University of Tartu. Mapping involved parallel laser scans perpendicular to bedding from areas containing secondary silicate veins and anhydrite. Scans were performed with a Cetac LSX-213 G2+ laser system with a HelEx II fast-washout two-volume large-format cell using 800 ml min^{-1} helium as carrier gas. A square 65 μm laser spot moving left-to-right at 65 μm s^{-1} at 10 Hz and a power of 3.45 J cm^{-2} was used. The total duty cycle was 0.2 s. For sample OPH-4081, ^{24}Mg, ^{27}Al, ^{28}Si, ^{31}P, ^{34}S, ^{39}K, ^{43}Ca, ^{49}Ti, ^{51}V, ^{52}Cr, ^{55}Mn, ^{56}Fe, ^{60}Ni, ^{63}Cu, ^{66}Zn, ^{88}Sr, ^{89}Y, ^{137}Ba, ^{140}Ce, and ^{238}U were measured at a dwell time of 7 ms. For sample OPH-1572, ^{13}C, ^{27}Al, ^{28}Si, ^{31}P, ^{34}S, ^{43}Ca, ^{47}Ti, ^{51}V, ^{52}Cr, ^{55}Mn, ^{56}Fe, ^{60}Ni, ^{63}Cu, ^{66}Zn, ^{95}Mo, ^{140}Ce, and ^{238}U were measured at a dwell time of 8 ms. The composition of the volatilized material was analyzed using an Agilent 8800 quadrupole ICP-MS in single quad mode. Maps are presented as relative abundances in counts per second.

4.4 Results

4.4.1 Mineralogy

Based on the results of 147 XRD analyses, the samples were divided into three main lithotypes: (1) evaporites (containing >10 wt.% halite, magnesite and/or anhydrite) which mainly occur below 2330 m depth; (2) carbonates (containing >50 wt.% dolomite, calcite, magnesite and/or siderite) above 2330 m depth that are dominated by dolomite and magnesite in the Tulomozero Formation, and dolomite-calcite in the Zaonega Formation; and (3) mudstone which first appear

above 2330 m, but become dominant in the Zaonega Formation, where they contain mostly quartz, feldspars, micas and chlorite. See Appendix 3 for a more detailed description. For some mudstone and carbonate samples, mineralogical data was not available. For classification, the carbonate content of these samples was estimated using elemental abundances and the formula (Ca + Mg) / (Si + Al), with values >0.5 being considered carbonates.

4.4.2 Element abundance

The total organic carbon content was measured mainly in the Zaonega and Suisari formations, where it ranges between 0 and 57.1 wt.%, with an average of 10.7±12.4 wt.% (n = 173; here and after, the reported variance for averages is 1σ). The largest spike in TOC, to an average of ~26.1 wt.%, comes in the phosphorus (P)-rich Zaonega Formation mudstone interval between 1125 m and 1112 m, below a silicified dolostone interval which is a marker horizon within the Onega Basin (Paiste et al. 2020a). Chromium concentrations range between 0.3 and 2283.1 μg g^{-1}, with an average of 150.8±240.4 μg g^{-1} (n = 253). Authigenic Cr abundances, expressed as Cr/Ti, range between 0.002 and 0.694 (μg g^{-1}/μg g^{-1}; Fig. 2), with an average of 0.070±0.085 (n = 253). In the Tulomozero Formation evaporites, Cr/Ti is between 0.002 and 0.366, with an average of 0.102±0.104 (n = 16); in the Tulomozero and Zaonega Formation carbonates it ranges between 0.008 and 0.694 and averages 0.083±0.100 (n = 93). In mudstones, Cr/Ti ranges between 0.003 and 0.554, averaging 0.058±0.069 (n = 144). The most consistently enriched interval in terms of Cr overlaps with that of TOC, below the P-rich mudstone-dolostone contact at 1115–1108 m (average 0.118).

4.4.3 Isotope ratios

Carbonate oxygen isotope compositions range between −17.2 and −4.8‰ $\delta^{18}O$, with an average of −11.0±2.7‰ (n = 45; Figure A7). In the lower Tulomozero Formation, a stratigraphic trend from ~−17‰ to >−10‰ $\delta^{18}O$ is expressed from ~2900 m to ~2300 m, after which values fall to generally >−10‰ into the lower Zaonega Formation. A rising trend from ~−14‰ to >−10‰ is also observed in the 1140 to 1090 m interval of the Zaonega Formation.

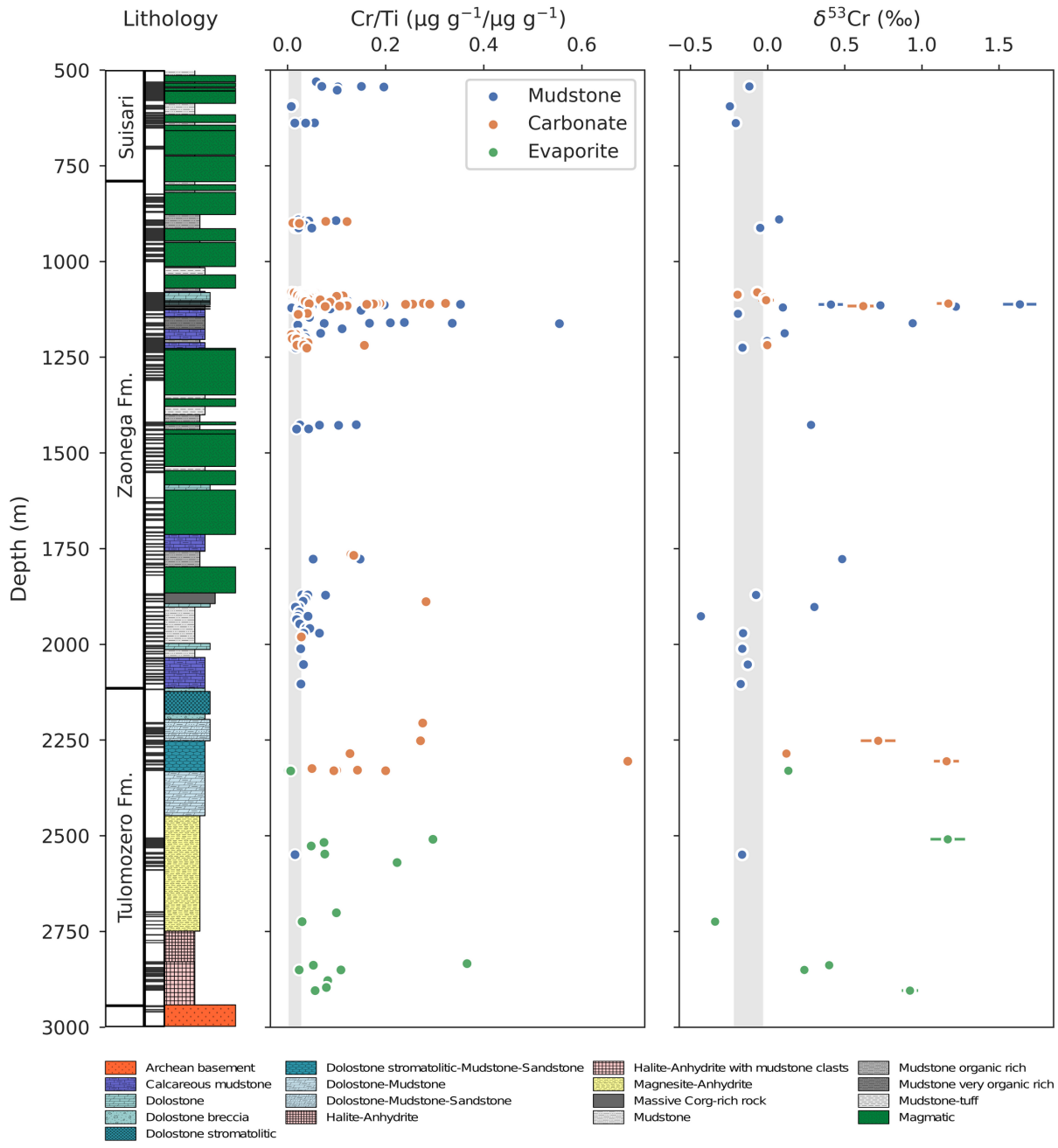

Figure 4.1: Chromium geochemistry in the Onega Parametric Hole drill core. Columns show the lithology, abundance of authigenic chromium (Cr/Ti), and its isotope composition (δ^{53}Cr). Color

of datapoints corresponds to lithology. Crustal averages, vertical grey bars, are taken from Cole et al. (2017) and Schoenberg et al. (2008).

Chromium isotope ratios vary between −0.43±0.03‰ and +1.64±0.10‰ δ^{53}Cr, with an average of +0.24±0.51‰ (n = 41); their lithological association is shown in Figure 4.2. In the Tulomozero Formation evaporites, δ^{53}Cr ranges between −0.34 and +1.17‰ (average +0.42±0.55; n = 6); in dolostones from the Tulomozero and Zaonega formations the values range between −0.20 and +1.17‰ (average +0.20±0.50‰; n = 14). Mudstone samples vary from −0.43 to +1.64‰ and average +0.22±0.52‰ (n = 21). Fractionated δ^{53}Cr values are present throughout the studied section, with the exception of low-Cr/Ti samples between 2100 and 1900 m, and above 600 m depth. The extent of fractionation, however, varies: the highest values are seen in the lower Tulomozero Formation, below 2200 m (up to +1.17±0.11‰), and in the 1230–1080 m mudstone-dolostone interval of the Zaonega Formation (up to +1.63±0.11‰), whereas a relatively poorly fractionated interval (up to +0.48±0.03%) occurs between 2200–1250 m.

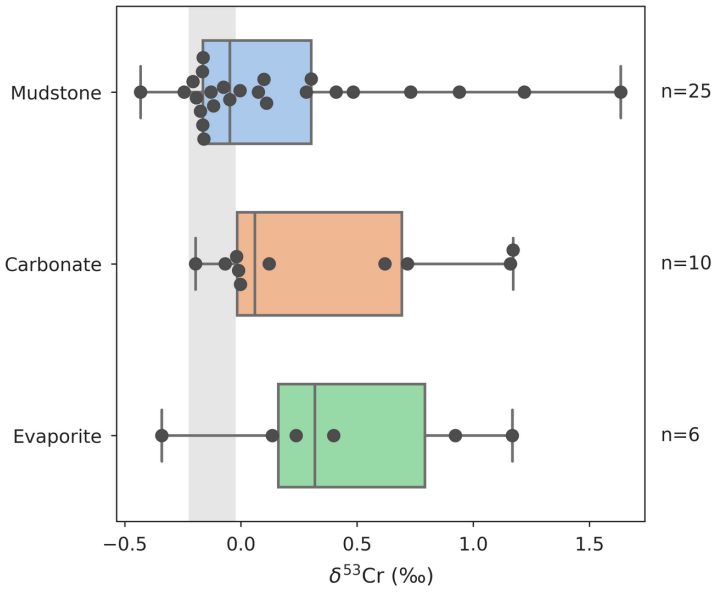

Figure 4.2: Chromium isotope ratios per lithology. Boxplots show medians, 25/75th quantiles, and the full range; superimposed black circles are individual samples. Grey bar denotes average crustal composition from Schoenberg et al. (2008).

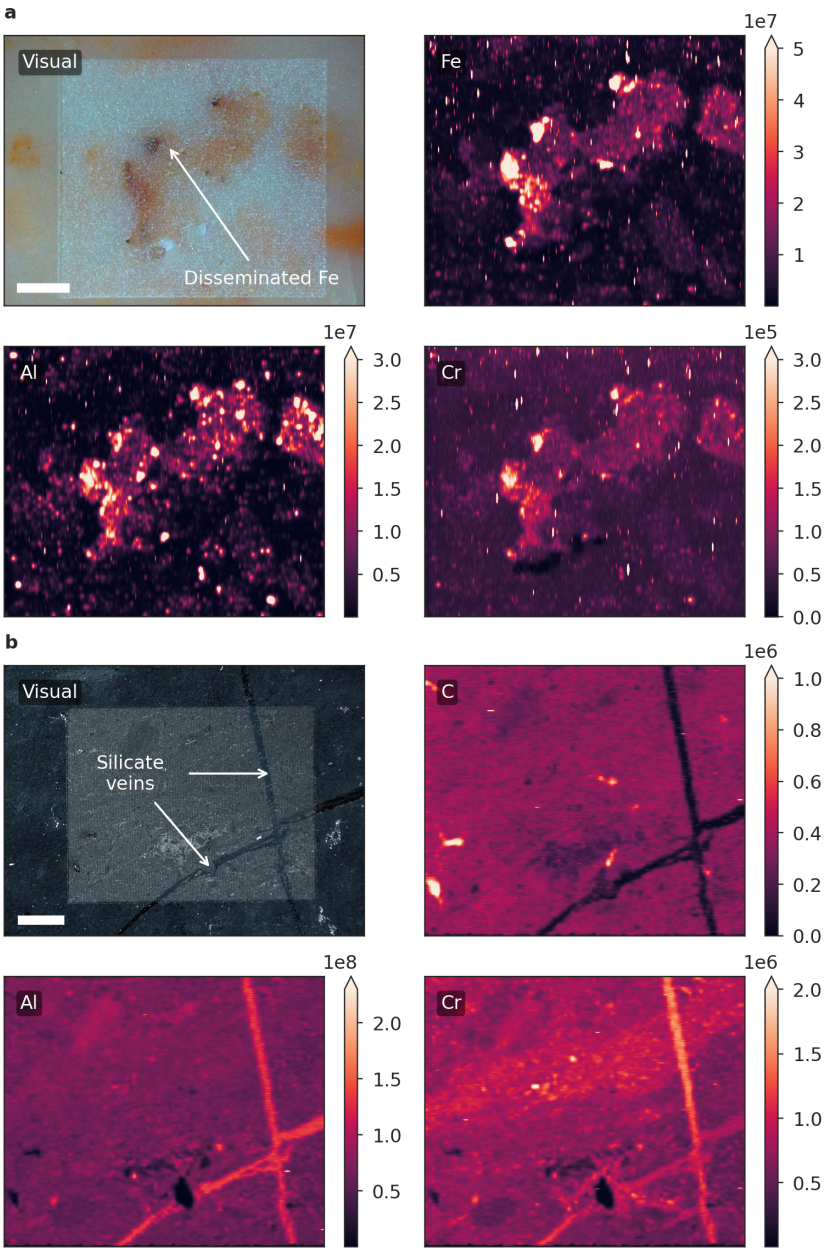

Figure 4.3: In-situ element maps for representative Onega Basin samples. Optical micrographs and relative carbon, aluminum, iron, and chromium abundance maps (reported in counts per second) were determined through laser-ablation mass-spectrometry from representative lithologies in the OPH core. (a) Evaporitic carbonate sample OPH-4081 (depth 2305.25 m,

$\delta^{53}Cr$ = 1.16±0.08), composed mainly of dolomite–magnesite, hosts disseminated Fe-rich phases, in which Cr is preferentially concentrated. (b) C_{org}-rich mudstone sample OPH-1572 (depth 1112.08 m, $\delta^{53}Cr$ 1.63±0.11‰) displays C_{org}-rich sedimentary laminae and Al-rich cross-cutting mica veins. Cr is concentrated both in the laminae and veins. Scale bars are 1 mm. Note difference in scale.

4.4.4 *In-situ* element mapping

Figure 4.3 shows optical and SEM-BSE micrographs, as well as LA-ICP-MS element mapping results. Slab OPH-4081, a dolomite-magnesite-rich evaporitic carbonate sample, shows Cr concentrated within reddish Fe-rich phases that are disseminated throughout the dolomite–magnesite matrix (Figure 4.3a). In slab OPH-1572, which is a C_{org}-rich mudstone, Cr is concentrated in both the C_{org}-rich laminae, but also in the cross-cutting mica (Al-rich) veins (Figure 4.3b). Mica veins display the highest Cr concentrations where they intersect the Cr-rich laminae.

4.5 Discussion

4.5.1 Chromium as a paleoredox proxy

The utility of Cr as a paleoredox proxy is due to its contrasting solubilities in oxygen-rich and oxygen-poor environments and the distinctive isotope fractionations associated with redox transitions. Chromium occurs in igneous rocks as insoluble Cr(III), with an isotope composition of −0.12±0.10‰ δ^{53}Cr (e.g., Schoenberg et al. 2008), but can be converted to soluble Cr(VI)

through reactions with manganese(IV) oxides in terrestrial weathering environments (e.g., Frei et al. 2009). Since the main pathway for Mn(IV) oxide formation requires molecular oxygen, and Cr(III) oxidation with Mn(IV) oxides induces a strong positive fractionation, theoretically ~+6‰, but lower in natural environments (e.g., Schauble et al. 2004; Wei et al. 2020), the presence of fractionated Cr in aqueous environments indirectly attests to the availability of free oxygen in the atmosphere. Chromium isotope fractionation is amplified by redox reactions occurring in rivers (e.g., Ellis et al. 2002) and oceans (e.g., Scheiderich et al. 2015), producing δ^{53}Cr values that vary between +0.3‰ and +1.6‰ in modern seawater. Such fractionated δ^{53}Cr signals can be captured by sediments that scavenge dissolved Cr, so that the presence or absence of fractionated Cr in sediments can be used to track atmospheric oxygen levels through Earth history (e.g., Frei et al. 2009; Wei et al. 2020). Similarly, since concentrations of soluble Cr(VI) in seawater scale with the generation of Mn(IV) oxides in terrestrial settings and with the abundance of oxygen-rich settings in the oceans, Cr concentration trends in anoxic sediments (which readily scavenge dissolved Cr) have also been tied to fluctuations in the extent of anoxic and euxinic seafloor area. For example, Reinhard et al. (2013) reported a shift from ~0.017 μg g^{-1}/μg g^{-1} Cr/Ti ratios in the mid-Proterozoic mudstones to ~0.05 from the Neoproterozoic, corresponding to expected shifts in atmospheric oxygen levels over the Proterozoic.

A complication is that photochemical and photosynthetic processes have recently been shown to be capable of oxidizing Mn, challenging the idea that only oxygen-rich environments can produce Cr fractionations (Daye et al. 2019; Liu et al. 2020). Similarly, Saad et al. (2017) showed that ligand-based non-redox Cr(III) solubilization may affect both positive and negative

δ^{53}Cr fractionation in a similar magnitude to redox processes. Yet, it is still unclear whether such mechanisms can explain robust Cr weathering and marine burial fluxes, and the survival of fractionated δ^{53}Cr signals until Cr deposition in marine sediments (Anbar and Holland, 1992; Saad et al. 2017; Wei et al., 2020).

Organic-rich mudstones, such as those of the Onega Basin, can quantitatively capture marine δ^{53}Cr due to the fast kinetics of Cr(VI) reduction in anoxic waters, as has been demonstrated in the anoxic Cariaco Basin (e.g., Reinhard et al. 2014). Carbonates, while a much less efficient sink, capture Cr with an induced negative fractionation in biogenic carbonates (e.g., Farkaš et al. 2018), but possibly minimal fractionation in abiogenic ones (Rodler et al. 2015). Therefore, δ^{53}Cr values in carbonates can be considered a minimum boundary on seawater values. Evaporites are the least studied, but existing work on groundwater-derived evaporites in the Atacama Desert suggests that Cr was captured quantitatively in chromate salts (Pérez-Fodich et al. 2014). The presence of bittern salts in the Tulomozero Formation implies almost complete seawater evaporation in the basin, which strongly supports nearly quantitative capture of all seawater components. This is confirmed by element mapping of the most ^{53}Cr-enriched evaporite sample which shows that chromium is hosted in diffuse, likely authigenic iron phases that are disseminated throughout the dolomite-magnesite matrix (Figure 4.3a). The elevated mudstone Cr/Ti ratios averaging 0.059±0.068 and sedimentary δ^{53}Cr values reaching a Paleoproterozoic maximum of +1.63±0.11‰ are difficult to explain through the currently-known oxygen-independent processes. For instance, ligand-based Cr(III) solubilization occurs at significantly lower rates than proton-driven solubilization (Saad et al. 2017), UV-based Mn photo-oxidation

was, by the time of the middle Paleoproterozoic, hampered by the ozone layer (Liu et al. 2020), and Mn oxides produced through anoxygenic photosynthesis in reduced surface settings (Daye et al. 2019) would have been vulnerable to back-reduction prior to diffusing to subsurface Cr weathering environments (Anbar and Holland, 1992). Therefore, the data most likely reflect elevated redox potentials during the deposition of the Tulomozero and Zaonega formations (see Appendix 3 for more discussion).

4.5.2 Post-depositional alteration of chromium

Due to its complex geological history, secondary processes within the Onega Basin succession may have altered some geochemical signals. For example, stromatolitic carbonates in the Tulomozero Formation have undergone pervasive dolomite/magnesite recrystallization with micritic fabrics being destroyed, though most samples have retained recognizable bedding and lamination (e.g., Melezhik et al. 1999a; Reuschel et al. 2012; Melezhik et al. 2015). Zaonega Formation carbonates, where dolomite is the primary phase, have in large part been secondarily de-dolomitized to calcite, with a concomitant decrease in both their $\delta^{18}O$ and $\delta^{13}C$ values, though this has primarily affected the margins of dolomite beds (Črne et al. 2014; Kreitsmann et al. 2019; Kreitsmann et al. 2020). Furthermore, there are pervasive quartz-mica veins in the mudstones of the Zaonega Formation that were emplaced due to syn-depositional hydrothermal activity triggered by the emplacement of mafic lavas and sills or during later greenschist facies metamorphism (Paiste et al. 2018). Elemental mapping of mudstone samples shows that Cr is enriched both in C_{org}-rich laminae, as well as in microscale mica veins, suggesting some Cr mobilization into percolating fluids (Figure 4.3b). Finally, there was significant hydrocarbon

migration in the Zaonega Formation (Qu et al., 2012); although Cr accumulation or fractionation through oil migration has not been studied, oils are plausible source fluids for transition metal ore formation (Migdisov et al. 2017) and mobilization into hydrocarbons is known to fractionate some transition metals (e.g., Gao et al. 2018).

Despite the evidence above for post-depositional fluid alteration, several factors suggest that this process cannot explain the positively fractionated δ^{53}Cr values in the Onega Basin. First, conspicuous veins, mono-mineral clusters, and altered margins of carbonate beds were carefully screened and avoided during sample selection. Second, igneous-derived Cr from hydrothermal sources is expected to host negative δ^{53}Cr ratios (Schoenberg et al. 2008), and remobilization of primary Cr(III) is likely to drive residual sediment δ^{53}Cr values more negative (Ellis et al. 2002), yet our samples have positive δ^{53}Cr values. The lack of alteration is also evident by Cr mapping —concentrations in mica veins are highest in the areas where they cross Cr-rich laminae (Figure 4.3b), suggesting adjacent laminae as the source of Cr. Third, Cr abundance trends in the OPH drill core correspond to those of other redox-sensitive metals with comparable chemical behaviour to molybdenum and uranium, which have previously been found to be unaffected by secondary mobilization (Mänd et al. 2020). This implies that the bulk of the authigenic Cr and its isotope systematics remain undisturbed. Fourth, wholesale Cr alteration through hydrocarbon migration is hampered by the generally short migration distances in the Zaonega Formation (centimeter-to-meter scale; Qu et al., 2012), and the sub-μg g^{-1} Cr concentrations in oils implying limited capacity for Cr mobilization (Ventura et al. 2015). Finally, the evaporite section of the lower Tulomozero Formation is composed of minerals, such as halite and bittern salts,

which are highly susceptible to fluid alteration. Their persistence implies that no substantial fluid movement has occurred in these rocks.

Carbonates in the Onega Basin deserve further assessment since this lithology has a high propensity for diagenetic recrystallization. For example, fractionated δ^{53}Cr values in mid-Proterozoic carbonate rocks (up to +1.77‰) (Gilleaudeau et al. 2016) have been suggested to have formed through cryptic diagenesis (e.g., Planavsky et al. 2018b). The influence of diagenetic processes on δ^{53}Cr can be assessed by tracking the oxygen isotope composition, which is a sensitive indicator of diagenetic overprint in carbonate rocks, with more pervasive diagenesis leading to lower δ^{18}O values (Banner and Hanson 1990). Figure 4.4 shows the correlation between δ^{53}Cr and δ^{18}O, with the least-altered samples tending to have more fractionated Cr compositions, suggesting that secondary processes decreased, not increased the δ^{53}Cr.

The best illustration that Cr geochemistry in the Onega Basin reflects primary processes is Figure 4.5a, which relates Cr/Ti to δ^{53}Cr in all three lithologies. That nearly all samples lie on a general positive trend suggests that δ^{53}Cr variance throughout the Onega Basin can largely be explained through the mixing of two components—an unfractionated detrital source and a fractionated seawater source—without needing to invoke secondary overprint (e.g., Planavsky et al. 2014).

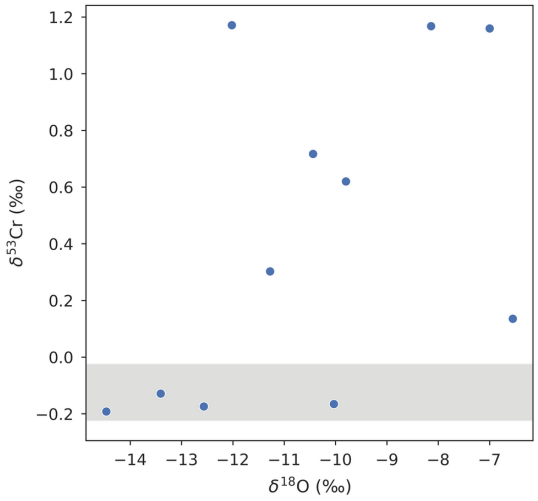

Figure 4.4: Alteration of isotope ratios. Chromium isotope ratios ($\delta^{53}Cr$) are plotted against oxygen isotope ratios ($\delta^{18}O$); in the latter case, lower values are indicative of stronger alteration of carbonates.

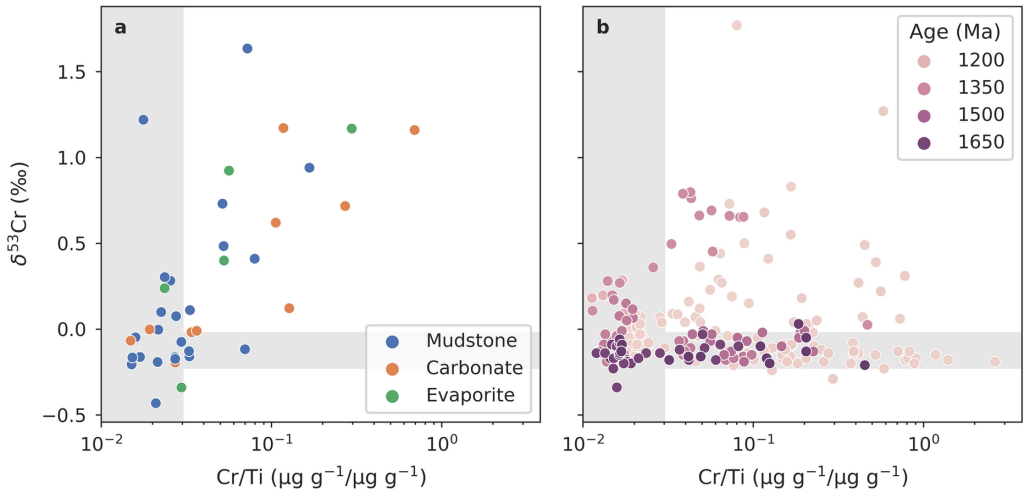

Figure 4.5: Authigenic chromium abundances (Cr/Ti) plotted against isotope ratios ($\delta^{53}Cr$). (a) Onega Basin data from this study, coloured per lithology. (b) Published data from mid-Proterozoic sections of various lithologies, coloured according to age (1950–1000 Ma). A

positive trend, as opposed to a horizontal one, suggests Cr(VI) cycling and the presence of atmospheric oxygen (e.g., Planavsky et al. 2014). Data for panel b is from Frei and Polat (2013), Planavsky et al. (2014), Cole et al. (2016), Gilleaudeau et al. (2016), and Canfield et al. (2018).

4.5.3 Basin controls on the dissolved chromium pool

Even if the authigenic δ^{53}Cr reflects a seawater signal, it is possible that elevated δ^{53}Cr was only a local phenomenon, and not representative of global Cr cycling. There is strong evidence for basin restriction in the Onega Basin that would allow such a scenario—evaporite mineralogy and sedimentary textures indicative of shallow deposition abound in the Tulomozero Formation (Melezhik et al. 1999a; Blättler et al. 2018). Furthermore, the sulphur isotope record in the Zaonega Formation has been interpreted to reflect varying levels of restriction (Paiste et al. 2020b). In this case, distillation of the dissolved Cr pool by preferential drawdown of ^{52}Cr (i.e., Rayleigh fractionation) could have driven δ^{53}Cr more positive. Alternatively, positive values may have resulted from an anomalously positive riverine source of Cr.

However, Cr concentrations consistently reach hundreds of μg g^{-1} over the hundreds of meters of mudstone-carbonate stratigraphy in the Zaonega and Suisari formations making it unlikely that a single point source could have provided this Cr. Distillation of the Cr pool is also unlikely, as that implies a substantial diminution of the dissolved Cr—it is far more parsimonious to invoke a fractionated open marine Cr source (e.g., Mänd et al. 2020). Conversely, in the lower Tulomozero Formation, the precipitation of bittern salts implies that seawater evaporation and Cr drawdown likely proceeded nearly to completion, again suggesting

that the global marine δ^{53}Cr signal was captured. While the shallow-water upper Tulomozero Formation carbonates present the highest likelihood of δ^{53}Cr distillation, the low efficiency of Cr incorporation into carbonates (Reinhard et al. 2013) again precludes strong distillation.

Variable Cr abundances and isotope ratios attest to differences in Cr cycling and drawdown across the Onega Basin succession (Figure 4.1). For example, the highest average Cr/Ti ratios and δ^{53}Cr values are present in the ~1230–1080 m interval. This same interval hosts extremely high TOC content (up to >70 wt.%), authigenic apatite, and fossilized sulphur cycling microbial ecosystems which are interpreted as having been formed in a highly biologically productive setting with fluctuating sulfidic–suboxic redox boundaries close to sediment surface that are especially conducive to redox-sensitive metal drawdown (Lepland et al. 2014; Mänd et al. 2020). Additionally, since the interval was also host to a degree of hydrocarbon migration (Qu et al. 2012), secondary Cr accumulation or isotope fractionation may have contributed to these maximum values. On the other hand, marl samples from the transition zone of the Tulomozero and Zaonega formations (between 2100–1920 m) and in the Suisari Formation (above 500 m) host unfractionated Cr at low authigenic concentrations. In these latter cases, high levels of plagioclase (up to 53.2%), and the presence of amphibole and titanite, suggest that the sediments may have experienced substantial volcanic ash input that delivered unfractionated, igneous Cr. Since almost all samples lie on a generally positive trend between δ^{53}Cr and Cr/Ti (Figure 4.5a), variation in both of these parameters can be sufficiently explained through variable Cr drawdown efficiencies leading to differing ratios of authigenic to detrital Cr. While it remains possible that

waters in the Onega Basin experienced basin-specific Cr cycling, the presence of isotopically fractionated Cr demands an oxygenated ocean–atmospheric system that can host Cr(VI)-cycling.

4.5.4 Atmospheric–oceanic redox in the Paleoproterozoic

The Rhyacian period has been proposed as a time of elevated oxygen abundance in the middle Paleoproterozoic, sandwiched between times of comparatively lower oxygen abundance (Bekker and Holland 2012). Oxygenated conditions are evidenced by evaporite mineralogy together with calcium and sulphur isotope records that indicate elevated marine sulfate levels (Blättler et al. 2018), consistent with high redox-sensitive element concentrations and isotope ratios (Konhauser et al. 2011; Partin et al. 2013a; Robbins et al. 2016; Asael et al. 2018; Mänd et al. 2020). This period of O_2 abundance was originally tied to the Lomagundi-Jatuli carbon isotope excursion through the mechanism of excess organic carbon burial (Karhu and Holland 1996; Bekker and Holland 2012), although this interpretation has become increasing challenged (e.g,. Melezhik et al. 1999b; Bakakas Mayika et al. 2020; Mänd et al. 2020).

Intriguingly, the Rhyacian rock record is characterized by very minor sedimentary Cr isotope anomalies, despite this proxy being frequently cited as evidence for atmospheric oxygenation (Wei et al. 2020). Previous reports of positively fractionated Cr in the Paleoproterozoic do exist (Figure 4.6), particularly in the ~1850 Ma Gunflint iron formation (Frei et al. 2009; Fralick et al. 2017), coupled with negatively fractionated Cr in the ~1900 Ma Schreiber Beach paleosol (Frei and Polat 2013), both indicative of Cr(VI) solubilization and transport into oceans. However, with the exception of meteorically derived diagenetic carbonate

cements in the Gunflint Formation (Fralick et al. 2017), these fractionations barely extend beyond the crustal mean (maximum of +0.21‰), and are even surpassed by δ^{53}Cr data from the Neoarchean that are indicative of only locally oxygenated conditions in a predominantly anoxic world. Furthermore, δ^{53}Cr values of Rhyacian iron formations are even less fractionated (up to +0.03‰) (Frei et al. 2009). The anomalous feature of the later Paleoproterozoic δ^{53}Cr record is high positive fractionations (up to +2.34‰) in the ~1900 Ma Flin Flon and Beaverlodge Lake paleosols (Babechuk et al. 2017; Toma et al. 2019), constituting the opposite of the expected isotope effect of oxic Cr weathering.

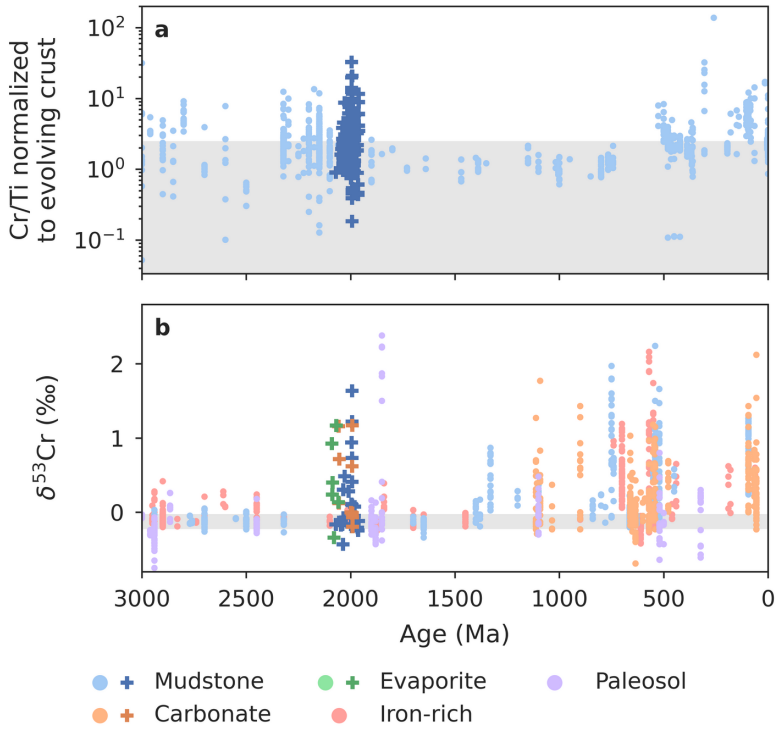

Figure 4.6: Authigenic chromium abundances (using Cr/Ti as proxy) in shales (a) and δ^{53}Cr values in various geological archives (b) through time. Differently coloured pastel dots represent

previously published data of different lithological affinities. Saturated cross symbols are data from this study. Cr/Ti data is from Reinhard et al. (2013) and Robbins et al. (2016); δ^{53}Cr data is from the compilation of Wei et al. (2020). Since Cr concentrations in the crust have decreased through geological time due to a decreasing prevalence of Cr-rich ultramafic igneous rocks, samples have been normalized to changes in crustal abundance according to Condie (1993). Grey bars represent average crustal compositions as in Figure 2.

Collectively, these data have been used to suggest a late Paleoproterozoic to Mesoproterozoic Cr cycle highly distinct from the modern—variable atmospheric pO_2 produced, in an alternating fashion, localized positively fractionated Cr runoff related to Mn oxide cycling (Frei and Polat 2013; Fralick et al. 2017) or negatively fractionated runoff related to ligand- or acid-based solubilization (Babechuk et al. 2017; Toma et al. 2019). The oceans, meanwhile, are implied to have remained predominantly anoxic, with relatively minor fractionated Cr runoff diluted within an unfractionated marine reservoir.

In contrast to this mid-Proterozoic scenario, illustrated by a general lack of correlation between Cr/Ti and δ^{53}Cr at this time (Figure 4.5b), our data from the ~2090–1961 Ma Onega Basin suggest a distinctly modern Cr cycle in the Rhyacian to the early Orosirian: nearly all samples follow a positive trend between Cr/Ti and δ^{53}Cr (Figure 4.5a) that is a telltale sign of oxidative Cr(VI) cycling coupled to Mn(II) oxidation (Planavsky et al. 2014). Whereas Fe(II) oxidation occurs at circumneutral pH at near 0 mV potential, high-potential redox reactions ($\gg$500 mV) are required to oxidize Mn^{2+} under the same conditions. Although it remains unresolved how much, and for how long, oxygen levels would have to rise above the ~0.1% PAL

required for coupled Mn-Cr oxidation (Planavsky et al. 2014), highly fractionated δ^{53}Cr values coupled to high authigenic Cr enrichments imply globally elevated pO_2 levels sufficient to induce efficient Mn(IV)-oxide-driven Cr(III) solubilization (see discussion on alternative Mn oxidation and Cr fractionation mechanisms in Appendix 3). This Cr(VI) then accumulated in predominantly oxic oceans, where the oxyanion was stable. The large, positively fractionated marine Cr pool was then further subjected to biochemical Cr redox cycling in the photic zone (e.g., Scheiderich et al. 2015).

Most significant is that the fractionated δ^{53}Cr values persist for nearly the entirety of the ~2300-m-thick sampled succession, across facies that transition from a shallow evaporative setting to a deeper water turbidite system, and most likely representing several tens to potentially more than a hundred Myrs of time (Figure 4.1, 4.6). Most parsimoniously, the data suggest that Earth's atmospheric oxygenation remained above the ~0.1% pO_2 threshold for Cr(III) oxidation and transport to the oceans (e.g., Planavsky et al. 2014) for the entirety of this time period. These findings provide a striking contrast to what is increasingly seen as a highly variable mid-Proterozoic redox landscape (e.g., Tang et al. 2017; Planavsky et al. 2018b). In this light, the Orosirian period perhaps witnessed a momentous transition from a well-buffered to a poorly-buffered atmospheric–oceanic redox state.

4.5.5 Implications for eukaryote evolution

The emergence of the eukaryotic cell was likely to have been a complex and drawn out process over potentially a billion years of Earth history (Butterfield 2015; Porter 2020). It is generally

accepted that the first eukaryote common ancestor (FECA) diverged from archaea, as was recently illustrated by the discovery of the archeon *Asgardarcaheota* with genomic characteristics closely linking it to eukaryotes (Zaremba-Niedzwiedzka et al. 2017; Imachi et al. 2020). It is unclear which metabolism FECA utilized, but most commonly it is considered to be anaerobic. The signal event in eukaryote evolution was the subsequent endosymbiotic acquisition of the mitochondria, an organelle which allows for aerobic respiration in all modern aerobic eukaryotes, as well as the last eukaryote common ancestor (LECA) (Wang and Wu 2014). This may have marked an increase in the metabolic energy available to cells by several magnitudes, expanding the potential for genomic innovation and leading to rapid evolution in the eukaryote lineage (Lane and Martin 2010), though see counterarguments in Szathmáry (2015) and Zachar and Szathmáry (2017).

The timing of this event is the central debate in the study of eukaryote emergence. One model suggests that early non-mitochondrial eukaryote precursors first developed a complex cell prior to ingesting the mitochondrial precursor, whereas the competing one invokes a preexisting symbiotic relationship between two prokaryotes that co-evolved into an endosymbiosis (Speijer 2020). In terms of absolute timing, due the association of the mitochondria with aerobic respiration, its acquisition has often been tied to the rise in pO_2 following the GOE (e.g., Gross and Bhattacharya 2010; Imachi et al. 2020). This is also supported by recent modeling work which shows that O_2-rich conditions—that allow higher nutrient availability in aqueous environments—can more readily support complex organisms such as eukaryotes (Reinhard et al. 2020). However, mitochondria retain ancestral anaerobic metabolic pathways (Mentel and

Martin 2008), leading others to argue that pO_2 was not a critical factor in the development of mitochondrial endosymbiosis (e.g., Zachar and Szathmáry 2017; Zimorski et al. 2019).

Ultimately, the firmest evidence for the timing of eukaryote evolution comes from fossils. The most unambiguous sign of early divergences within crown-group, mitochondrial eukaryotes is the ~1047 Ma *Bangiomorpha pubescens*, a purported red algae fossil from Arctic Canada (Butterfield 2000). Red algae-like fossils have recently been found even further back in time, at ~1600 Ma (Bengtson et al. 2017b), and so have diverse assemblages of large organic structures with complex cell walls evocative of cytoskeleton-bearing eukaryotes, which appear simultaneously in several 1800–1600 Ma successions in North China and Australia (e.g., Lamb et al. 2009; Javaux and Lepot 2018). Molecular clocks, which combine fossil evidence with the genetic diversity of extant eukaryotes and genetic divergence rates, generally agree with this record. Most place the LECA, and by inference the acquisition of the mitochondria, in the Late Paleoproterozoic or the Mesoproterozoic (e.g., Chernikova et al. 2011; Shih and Matzke 2013), with only a minority allowing for >1600 Ma dates (e.g., Sánchez-Baracaldo et al. 2017; Betts et al. 2018). The totality of the present evidence, therefore, suggests mitochondrial acquisition in the Late Paleoproterozoic to Mesoproterozoic.

Our study provides us with an unparallelled opportunity to contribute to the debate on whether pO_2 abundance played a role in the emergence of the mitochondria by juxtaposing the present fossil record with the long-term record of Paleoproterozoic oxygenation revealed here (tens to more than a hundred Myrs). In short, the lack of substantial evidence for eukaryotes during this time period means that, unless the Rhyacian and Orosirian periods were improbably

biased against preservation of eukaryotic fossils, stable and high O_2 levels during this time period did not result in the appearance of mitochondrial eukaryotes, or at least in them exerting a significant influence over contemporary ecosystems. Combined with the appearance of such fossil assemblages in the poorly oxygenated and O_2-buffered mid-Proterozoic, this strongly suggests that high pO_2 was not the critical factor in the acquisition of mitochondrial organisms and/or their ecological proliferation. Instead, the combined geochemical and fossil record seems to point more readily towards the importance of a fortuitous evolutionary singularity in mitochondrial acquisition (Butterfield 2015).

As a final complicating factor in this discussion, there are scattered reports of even older structures evoking eukaryote affinity. For example, the ~2100 Ma Franceville Group, Gabon, hosts a putative assemblage of differentiated, macroscopic, and even motile pyritized fossils (El Albani et al. 2010, 2019). Furthermore, Bengtson et al. (2017a) reported fungi-like filamentous structures from basalt vesicles in the ~2400 Ma Ongeluk Formation, South Africa. If these fossils represent early mitochondrial eukaryotes, their absence from the Onega Basin suggests that early eukaryote evolution was highly localized or that other factors facilitated their preservation only in the above-mentioned settings. The contrast between relatively singular finds such as the Franceville biota and the Ongeluk fungi, and the less complex, ~1600 Ma eukaryote assemblages that have been described from several continents prompts skepticism that the former represent direct ancestors to extant eukaryote lineages (Javaux and Lepot 2018). We concede, however, that the Proterozoic fossil record is incompletely studied, and new findings may vindicate the Franceville and Ongeluk biota in the future.

4.6 Conclusions

Onega Basin rocks constitute the earliest known sedimentary rock succession that hosts substantially and persistently fractionated Cr isotopes. Thus, the time of sedimentary deposition in the Onega Basin, provisionally ~2090 to ~1961 Ma, is the earliest known period of substantial length when oxygen levels remained persistently above the thereshold for oxidative Cr cycling. While it was previously known that the mid-Proterozoic contrasted with the earlier Paleoproterozoic in terms of the average oxygenation, we show that this retrograde redox transition also coincided with a major shift in the stability of redox environments.

The absence of evidence for diverse fossil assemblages of eukaryotes in the identified long-term window of oxygenation, contrasting with the relatively oxygen-poor mid-Proterozoic, strongly suggests that mitochondrial acquisition, or at least the proliferation of mitochondrial organisms, did not occur in this time frame. This disagrees with the widely held assumption that mitochondria evolved and became wide-spread as a response to the rise of oxygen in the past. We urge renewed paleontological work in rocks dating from the middle Paleoproterozoic period of high pO_2, as only fossil evidence has the potential to conclusively resolve these central debates in the emergence of complex life.

Chapter 5: Conclusions

5.1 The redox-sensitive metal record in the Onega Basin

The rise and fall of atmospheric–oceanic O_2 levels across the Paleoproterozoic coincided with major shifts in tectonics, weathering regimes, and C cycling, but the mechanisms that governed these transformations are still debateable. Geochemical data from the Onega Basin, which straddles the LJE and its termination, may hold the key to explaining these processes, but competing interpretations of proxy data from this sedimentary succession have led to contradictory conclusions about global redox conditions, largely because the effects of modulating processes on the local scale are poorly understood.

This dissertation aims to arrive at a firmer interpretation of Onega Basin geochemistry by first assessing secondary overprint and the basinal redox and hydrographic structure, before reaching for global redox inferences. Iron isotopes in the upper ZF, owing to an anticorrelation between Fe/Al and δ^{56}Fe, reveal the presence of a benthic iron shuttle, which requires a large shelf-to-basin areal ratio, meaning a restricted basin, and basinal redox stratification (Severmann et al. 2008). Hints of oxidative Fe drawdown in some samples hosting high Fe/Al and δ^{56}Fe suggest the occasional influx of oxic water masses capable of oxidizing dissolved Fe(II) (Scholz et al. 2014)—a finding consistent with earlier inferences based on cycles of evaporite deposition lower in the Onega Basin stratigraphy (Blättler et al. 2018) and Se and N geochemistry (Kipp et al., 2020). Iron isotopes also reveal that the basin configuration was variable in time—e.g., the lower part of the ZF, though anoxic, does not host the signature of a benthic Fe shuttle (as seen

also in the section studied by Asael et al. 2013). This is most parsimoniously explained by an increase in hydrographic restriction in the middle part of the section, leading to more quantitative Fe(II) drawdown. These changes corresponded to positive shifts in metal drawdown efficiency: Mo values rise to 1009 μg g^{-1}, U to 238 μg g^{-1}, Re to 516 ng g^{-1}, and V to 3018 μg g^{-1} in this interval. Furthermore, the most positive Mo and U isotope ratios are recorded here, up to +1.49‰ and +0.79‰, respectively, implying more quantitative trace metal drawdown. Metal drawdown was facilitated by local anoxia and robust levels of bioproduction, as seen in the high TOC content (>70 wt.%; Melezhik et al. 1999b), the presence of active methane-sulfide cycling microbial communities (Qu et al. 2012; Lepland et al. 2014), and a full expression of the seawater–sediment U fractionation factor, which requires efficient biological U reduction at the sediment–water interface (Andersen et al. 2014). The middle part of the ZF section exposed in the OnZaP cores, therefore, can be considered an uncommonly efficient anoxic redox-sensitive metal trap, possibly similar to anoxic deeps in the modern Baltic Sea, which witness bi-decadal influxes of oxygenated, metal-rich water replenishing the dissolved metal pool and leading to high sedimentary metal concentrations (Scholz et al. 2018).

Despite the basinal restriction and active biological element cycling that complicate the interpretation of C and S isotopes (Paiste et al. 2020a), the extension of the redox inferences studied here into a global scale is greatly aided by the presence of nearly-unprecedented redox-sensitive trace metal richness and fractionation. Whereas low concentrations of redox-sensitive metals and small fractionations from the mean are commonly seen in sediments deposited in times of global O_2 abundance, due to a variety of modulating processes (e.g., Algeo and Lyons

2006; Kendall et al. 2017), it is generally difficult to explain large sedimentary concentrations and substantially fractionated isotope ratios without invoking a large, oxidized open ocean trace metal inventory. This is certainly the case for Mo, U, Cr, and Re concentrations, as well as the Mo, U, and Cr isotope systems (Scott et al. 2008; Partin et al. 2013a; Reinhard et al. 2013; Andersen et al. 2017; Kendall et al. 2017; Sheen et al. 2018; Wei et al. 2020). Overall, the most parsimonious explanation for the trace metal record in the Onega Basin is that the sediments were deposited in a locally mostly anoxic basin, but at a time of elevated oxygenation in both the global atmosphere and the oceans, with oxic conditions in the ocean commonly present throughout the full water column, at least on the continental shelf.

This finding evokes the work of Kump et al. (2011), who interpreted the ZF C and nitrogen (N) isotope records to reflect the peak and final culmination of the Paleoproterozoic oxygen-rich period (though their proposed global-scale black shale oxic weathering pulse has subsequently been challenged; Qu et al. 2012; Kreitsmann et al. 2019). Certainly, the Onega Basin metal concentrations are higher than in other mudstone sections of the Paleoproterozoic, and the U and Cr isotope values are the only substantially fractionated ones reported in this period so far. However, establishing absolute changes in O_2 levels across the Paleoproterozoic based on redox-sensitive metal data is not straightforward, and lies outside the scope of this dissertation.

More definitely, these findings argue against several common conceptions regarding Paleoproterozoic redox development. For one, the ZF has previously been interpreted as a time of rapidly falling O_2 levels, based on Mo, S, and C isotope systematics (Asael et al. 2013; Scott et al. 2014; Asael et al. 2018). However, subsequent work on S isotopes in the ZF (Paiste et al.

2018; Paiste et al. 2020b) has challenged that view, and now the trace metal results from this PhD project seem to suggest almost the opposite. It is, therefore, uncertain when the high-pO_2 conditions characteristic of the middle Paleoproterozoic truly ended, especially since the mid-Proterozoic redox state is now seen to be highly unstable and prone to hosting contradictory proxy records (e.g., Toma et al. 2019). Only the emplacement of numerous iron formations on continental shelves beginning at ~1880 Ma is convincing evidence for the expansion of anoxia on a global scale (Rasmussen et al. 2012; Canfield et al. 2013; Konhauser et al. 2017).

High concentrations of trace metals have been reported previously in the ZF and used to infer high levels of ocean–atmospheric oxygenation, but mostly in global-scale compilations (e.g., Partin et al. 2013a; Reinhard et al. 2013; Sheen et al. 2018). In these studies, the uncertainties in the deposition date of the ZF have allowed these data to be categorized with other LJE-aged successions. As such, Onega Basin geochemistry from stratigraphically equivalent intervals has been used simultaneously and contradictorily to support both an O_2 overshoot during the LJE, and a subsequent crash following the termination of the LJE (Paiste et al. 2020a). However, it is clear from the $\delta^{13}C$ stratigraphy of the Onega Basin (Melezhik et al. 2015) that redox proxy records reported herein post-date the end of the LJE at least by several million years. Short of overturning the entire conception of a globally synchronous LJE (e.g., Bakakas Mayika et al. 2020), perhaps the best way to interpret this record is to concede that oxygen-rich conditions post-dated the end of the LJE by a substantial amount of time. This is in direct contradiction of the most widely-cited mechanism for the LJE, which evokes an elevated rate of C_{org} burial, possibly the result of increased nutrient fluxes following the GOE, to explain

both the $\delta^{13}C$ excursion and the O_2 overshoot (Karhu and Holland 1996; Bekker and Holland 2012). Ultimately, other proposed explanations for the LJE must then come to the forefront (e.g., Hayes and Waldbauer 2006; Miyazaki et al. 2018; Eguchi et al. 2020).

Finally, the period of high and stable oxygen levels revealed here bears upon the evolution of life in the Proterozoic. Specifically, many researchers since Sagan (1967) have speculated that mitochondrial acquisition was a direct consequence of the oxygenation of Earth's surface environments, as inferred from the mitochondria's modern role as the oxygen-metabolizing organelle. A careful reading of the fossil record and the latest molecular clocks, however, does not support the initial proliferation of mitochondrial organisms during the tens to >100 Myrs long period studied in this dissertation; rather, evidence seems to converge on the ~1700–1600 Ma period, which hosts the first diverse and wide-spread eukaryotic fossil communities (e.g., Butterfield 2015; Porter 2020). If the stable and O_2-rich middle-Paleoproterozoic Earth state did not result in the appearance of diverse eukaryote communities in the fossil record, it questions the notion that mitochondrial acquisition was necessarily triggered by oxygen abundance. Alternatively, if mitochondrial endosymbiosis did occur in this time period, it did not result in a rapid evolutionary change in microbial communities as preserved in the rock record. This would contradict the influential view of Lane and Martin (2010) that the emergence of mitochondria-hosting cells, owing to their ability to support markedly larger genomes, led to rapid evolutionary innovation. In any case, the retrograde transition from a stable, high-pO_2 world in the middle Paleoproterozoic to an unstable, low-pO_2 world in the mid-Proterozoic is important backdrop to further debate regarding the conditions and mechanisms of eukaryogenesis.

5.2 Future work

This thesis opens up further avenues for research both into the Onega Basin specifically, and the Paleoproterozoic in general. First, it is necessary to delve deeper into the mechanisms which led to the unusually high trace metal enrichments in the ZF, surpassing all other known organic-rich mudstones prior to the Neoproterozoic. This is especially crucial since the incorporation mechanisms of trace metals, such as Mo, into sediments underlying anoxic water masses are as-of-yet unclear. For example, a strong covariation between Mo and TOC in anoxic sediments points to Mo drawdown through adsorption/incorporation to organic matter (Algeo and Lyons 2006). This is confirmed by X-ray adsoprtion fine structure (XAFS) analyses of sediment Mo, which have found evidence for the association of sedimentary Mo with organic compounds (e.g., Dahl et al. 2017). However, other XAFS results have argued for a dominant role of inorganic Fe-Mo-S phases (e.g., Vorlicek et al. 2018); in that case, the TOC–Mo covariation may be a coincidence of the dependence of dissolved sulphide levels on local bioproductivity (Helz and Vorlicek 2019). The up to 1009 μg g^{-1} Mo concentrations in the ZF make it an ideal test case for assessing which of these proposed pathways accounts for exceptionally high sedimentary Mo enrichments. Microscale XAFS measurements across the Mo K-edge have already been performed on ZF rocks in the Advanced Photon Source synchrotron facility of the Argonne National Laboratory, IL, USA.

Shifts in sediment provenance, basin hydrogeography, and water chemistry, which collectively control metal drawdown in anoxic sediments can be further constrained using rare earth element (REE) patterns. For example, anomalously low Ce concentrations are indicative of

oxic conditions along the source-to-sink path of REEs (Bau and Dulski 1996), whereas hydrothermal fluids host anomalously high Eu contents (Bau 1991). Statistical analysis of REE patterns can also be used to deconvolute different clastic sediment sources (e.g., Wang et al. 2019). Previous studies on authigenic phosphate (Joosu et al. 2015) and carbonate minerals (Kreitsmann et al. 2020) have identified negative Ce and positive Eu anomalies, indicating, respectively, oxidative element cycling and hydrothermal input into the Onega Basin. Unfortunately, these interpretations were limited by the small sample numbers that passed screening for contaminated and altered intervals. In order to provide a more robust assessment of REE patterns, the full mudstone-dominated ZF dataset can be used. This comes with added complexity, since the upper ZF contains many different lithologies, and has seen significant hydrothermal alteration, all of which and are known to affect REE partitioning differently. As a result, REE patterns in the ZF display considerably more scatter than is seen in more uniform shale sections. In order to untangle these influences and produce a robust REE-based record of changing seawater composition through the ZF, statistical methods such as principal component analysis and clustering can be used to assess factors controlling REE partitioning and to identify primary signals of marine chemistry.

In keeping with the turn towards biological tie-ins explored in chapter 4, further work could target the lacustrine mudstones of the ~1900 Ma Kondopoga Formation, which overlie the Suisari Formation and constitute the topmost part of the Onega Basin. The reason is that these rocks host some of the earliest known acritarchs (Javaux and Lepot 2018). The fossil affinity of these structures is unknown, though many other complex acritarchs of the Proterozoic have been

interpreted as unambiguous eukaryotes (e.g., Lamb et al. 2009). In any case, the appearance of acritarchs in the fossil record may herald an increase in the complexity of Earth's ecosystems in the Proterozoic. It is intriguing that the Kondopoga structures immediately overlie the section studied in this dissertation, which is marked by high levels of atmospheric oxygenation. As such, it is worth assessing the environmental settings of the Kondopoga Formation and/or global redox during its deposition, as this may provide clues to the conditions conducive to the emergence of complex Proterozoic ecosystems. Lacustrine sediments present a challenge for interpretation of geochemical proxies, since many isotope systems are developed for marine settings in mind. However, work on other lacustrine sediments of the Proterozoic paves the way (e.g., Rico et al. 2019). Molybdenum and Fe isotopes can be used to provide constraints on local redox settings, and Cr isotope fractionations work as global redox proxies even in lacustrine sediments, given that major Cr fractionations are imparted in continental weathering settings.

Finally, the implications of this dissertation have been to question the veracity of earlier hypotheses about the LJE and Paleoproterozoic redox development. Yet, new hypotheses must also be brought forward to explain the LJE, the O_2 overshoot, and the return to low-pO_2 conditions by the mid-Proterozoic. One potential avenue through which to investigate these transitions is through the chemistry of continental weathering environments. For this purpose, a chemical database from 21 complete paleosols—ancient preserved soils—covering the Precambrian has already been compiled. Using chemical indices developed for this purpose—currently under review at *Nature Communications* (Hao *et al.*)—it is possible to assess changes in the original content of the clay mineral kaolinite across the Paleoproterozoic. Preliminary

results show a significant increase in estimated kaolinite richness over the Paleoproterozoic, which may indicate an acid weathering pulse due to rapid oxidation of detrital pyrite following the GOE (Konhauser et al. 2011). Acid weathering of nutrient-bearing minerals would the help explain the inferred increase in bioproductivity following the GOE (Crockford et al. 2019), and concurrently high levels of pO_2. Furthermore, this paleosol database can be used to probe the relationship between Cr leaching and Mn oxide precipitation in weathering environments to elucidate the anomalous features of the Paleoproterozoic paleosol δ^{53}Cr record (e.g., Toma et al. 2019).

In summary, the Paleoproterozoic remains an enigmatic period that was nevertheless key in the transformation of the Earth into an oxygen-rich world host to a highly complex biosphere. To solve the puzzles that this era holds, new geochemical data is sorely needed, but these must be firmly rooted in an understanding of local depositional environments.

Bibliography

Ahm, A.-S.C., Bjerrum, C.J., Blättler, C.L., Swart, P.K., and Higgins, J.A. (2018) Quantifying early marine diagenesis in shallow-water carbonate sediments. Geochimica Et Cosmochimica Acta, 236, 140–159.

Algeo, T.J., and Li, C. (2020) Redox classification and calibration of redox thresholds in sedimentary systems. Geochimica Et Cosmochimica Acta, 287, 8–26.

Algeo, T.J., and Liu, J. (2020) A re-assessment of elemental proxies for paleoredox analysis. Chemical Geology, 540, 119549.

Algeo, T.J., and Lyons, T.W. (2006) Mo–total organic carbon covariation in modern anoxic marine environments: Implications for analysis of paleoredox and paleohydrographic conditions. Paleoceanography, 21, PA1016.

Amelin, Yu.V., Heaman, L.M., and Semenov, V.S. (1995) U Pb geochronology of layered mafic intrusions in the eastern Baltic Shield: Implications for the timing and duration of Paleoproterozoic continental rifting. Precambrian Research, 75, 31–46.

Anbar, A.D., and Holland, H.D. (1992) The photochemistry of manganese and the origin of banded iron formations. Geochimica et Cosmochimica Acta, 56, 2595–2603.

Andersen, M.B., Romaniello, S., Vance, D., Little, S.H., Herdman, R., and Lyons, T.W. (2014) A modern framework for the interpretation of 238U/235U in studies of ancient ocean redox. Earth and Planetary Science Letters, 400, 184–194.

Andersen, M.B., Stirling, C.H., and Weyer, S. (2017) Uranium Isotope Fractionation. Reviews in Mineralogy and Geochemistry, 82, 799–850.

Anderson, R.F., Fleisher, M.Q., and LeHuray, A.P. (1989) Concentration, oxidation state, and particulate flux of uranium in the Black Sea. Geochimica Et Cosmochimica Acta, 53, 2215–2224.

Anderson, T.F., and Raiswell, R. (2004) Sources and mechanisms for the enrichment of highly reactive iron in euxinic Black Sea sediments. American Journal of Science, 304, 203–233.

Arnold, G.L., Anbar, A.D., Barling, J., and Lyons, T.W. (2004) Molybdenum isotope evidence for widespread anoxia in mid-Proterozoic oceans. Science, 304, 87–90.

Asael, D., Tissot, F.L.H., Reinhard, C.T., Rouxel, O., Dauphas, N., Lyons, T.W., Ponzevera, E., Liorzou, C., and Chéron, S. (2013) Coupled molybdenum, iron and uranium stable isotopes as oceanic paleoredox proxies during the Paleoproterozoic Shunga Event. Chemical Geology, 362, 193–210.

Asael, D., Rouxel, O., Poulton, S.W., Lyons, T.W., and Bekker, A. (2018) Molybdenum record from black shales indicates oscillating atmospheric oxygen levels in the early Paleoproterozoic. American Journal of Science, 318, 275–299.

Babechuk, M.G., Kleinhanns, I.C., and Schoenberg, R. (2017) Chromium geochemistry of the ca. 1.85 Ga Flin Flon paleosol. Geobiology, 15, 30–50.

Bachan, A., and Kump, L.R. (2015) The rise of oxygen and siderite oxidation during the Lomagundi Event. Proceedings of the National Academy of Sciences of the United States of America, 112, 6562–6567.

Bakakas Mayika, K., Moussavou, M., Prave, A.R., Lepland, A., Mbina, M., and Kirsimäe, K. (2020) The Paleoproterozoic Francevillian succession of Gabon and the Lomagundi-Jatuli event. Geology.

Banner, J.L., and Hanson, G.N. (1990) Calculation of simultaneous isotopic and trace element variations during water-rock interaction with applications to carbonate diagenesis. Geochimica Et Cosmochimica Acta, 54, 3123–3137.

Barling, J., Arnold, G.L., and Anbar, A.D. (2001) Natural mass-dependent variations in the isotopic composition of molybdenum. Earth and Planetary Science Letters, 193, 447–457.

Barnes, C.E., and Cochran, J.K. (1993) Uranium geochemistry in estuarine sediments: Controls on removal and release processes. Geochimica Et Cosmochimica Acta, 57, 555–569.

Bau, M. (1991) Rare-earth element mobility during hydrothermal and metamorphic fluid-rock interaction and the significance of the oxidation state of europium. Chemical Geology, 93, 219–230.

Bau, M., and Dulski, P. (1996) Distribution of yttrium and rare-earth elements in the Penge and Kuruman iron-formations, Transvaal Supergroup, South Africa. Precambrian Research, 79, 37–55.

Bauer, A.M., Rooney, A.D., Lepland, A., Cole, D.B., and Planavsky, N.J. (2019) The dynamics of the Lomagundi-Jatuli carbon isotope excursion and implications for early life. In Geobiology 2019 Conference Proceedings. Presented at the 2nd Geobiology Society Conference, Banff, Canada.

Beard, B.L., and Johnson, C.M. (1999) High precision iron isotope measurements of terrestrial and lunar materials. Geochimica et Cosmochimica Acta, 63, 1653–1660.

Beard, B.L., Johnson, C.M., Cox, L., Sun, H., Nealson, K.H., and Aguilar, C. (1999) Iron Isotope Biosignatures. Science, 285, 1889–1892.

Beard, B.L., Johnson, C.M., Damm, K.L.V., and Poulson, R.L. (2003) Iron isotope constraints on Fe cycling and mass balance in oxygenated Earth oceans. Geology, 31, 629–632.

Beard, B.L., Handler, R.M., Scherer, M.M., Wu, L., Czaja, A.D., Heimann, A., and Johnson, C.M. (2010) Iron isotope fractionation between aqueous ferrous iron and goethite. Earth and Planetary Science Letters, 295, 241–250.

Bekker, A., and Holland, H.D. (2012) Oxygen overshoot and recovery during the early Paleoproterozoic. Earth and Planetary Science Letters, 317–318, 295–304.

Bekker, A., Karhu, J.A., Eriksson, K.A., and Kaufman, A.J. (2003) Chemostratigraphy of Paleoproterozoic carbonate successions of the Wyoming Craton: Tectonic forcing of biogeochemical change? Precambrian Research, 120, 279–325.

Bekker, A., Holland, H.D., Wang, P.-L., Rumble, D., Stein, H.J., Hannah, J.L., Coetzee, L.L., and Beukes, N.J. (2004) Dating the rise of atmospheric oxygen. Nature, 427, 117–20.

Bekker, A., Slack, J.F., Planavsky, N., Krapež, B., Hofmann, A., Konhauser, K.O., and Rouxel, O.J. (2010) Iron Formation: The Sedimentary Product of a Complex Interplay among Mantle, Tectonic, Oceanic, and Biospheric Processes. Economic Geology, 105, 467–508.

Bekker, A., Krapež, B., Müller, S.G., and Karhu, J.A. (2016) A short-term, post-Lomagundi positive C isotope excursion at c. 2.03 Ga recorded by the Wooly Dolomite, Western Australia. Journal of the Geological Society, 173, 689–700.

Bellefroid, E.J., Hood, A.v.S., Hoffman, P.F., Thomas, M.D., Reinhard, C.T., and Planavsky, N.J. (2018) Constraints on Paleoproterozoic atmospheric oxygen levels. Proceedings of the National Academy of Sciences of the United States of America, 115, 8104–8109.

Belshaw, N.S., Zhu, X.K., Guo, Y., and O'Nions, R.K. (2000) High precision measurement of iron isotopes by plasma source mass spectrometry. International Journal of Mass Spectrometry, 197, 191–195.

Bengtson, S., Rasmussen, B., Ivarsson, M., Muhling, J., Broman, C., Marone, F., Stampanoni, M., and Bekker, A. (2017a) Fungus-like mycelial fossils in 2.4-billion-year-old vesicular basalt. Nature Ecology & Evolution, 1, 1–6.

Bengtson, S., Sallstedt, T., Belivanova, V., and Whitehouse, M. (2017b) Three-dimensional preservation of cellular and subcellular structures suggests 1.6 billion-year-old crown-group red algae. PLOS Biology, 15, e2000735.

Betts, H.C., Puttick, M.N., Clark, J.W., Williams, T.A., Donoghue, P.C.J., and Pisani, D. (2018) Integrated genomic and fossil evidence illuminates life's early evolution and eukaryote origin. Nature Ecology & Evolution, 2, 1556.

Blättler, C.L., Claire, M.W., Prave, A.R., Kirsimäe, K., Higgins, J.A., Medvedev, P.V., Romashkin, A.E., Rychanchik, D.V., Zerkle, A.L., Paiste, K., and others (2018) Two-billion-year-old evaporites capture Earth's great oxidation. Science, 360, 320–323.

Böning, P., Brumsack, H.-J., Böttcher, M.E., Schnetger, B., Kriete, C., Kallmeyer, J., and Borchers, S.L. (2004) Geochemistry of Peruvian near-surface sediments. Geochimica Et Cosmochimica Acta, 68, 4429–4451.

Brasier, A.T., Fallick, A.E., Prave, A.R., Melezhik, V.A., and Lepland, A. (2011) Coastal sabkha dolomites and calcitised sulphates preserving the Lomagundi-Jatuli carbon isotope signal. Precambrian Research, 189, 193–211.

Brasier, M.D., and Lindsay, J.F. (1998) A billion years of environmental stability and the emergence of eukaryotes: New data from northern Australia. Geology, 26, 555–558.

Brocks, J.J., Jarrett, A.J.M., Sirantoine, E., Hallmann, C., Hoshino, Y., and Liyanage, T. (2017) The rise of algae in Cryogenian oceans and the emergence of animals. Nature, 548, 578–581.

Butterfield, N.J. (2000) Bangiomorpha pubescens n. Gen., n. Sp.: Implications for the evolution of sex, multicellularity, and the Mesoproterozoic/Neoproterozoic radiation of eukaryotes. Paleobiology, 26, 386–404.

Butterfield, N.J. (2009) Oxygen, animals and oceanic ventilation: An alternative view. Geobiology, 7, 1–7.

Butterfield, N.J. (2015) Early evolution of the Eukaryota. Palaeontology, 58, 5–17.

Cadeau, P., Jézéquel, D., Leboulanger, C., Fouilland, E., Le Floc'h, E., Chaduteau, C., Milesi, V., Guélard, J., Sarazin, G., Katz, A., and others (2020) Carbon isotope evidence for large methane emissions to the Proterozoic atmosphere. Scientific Reports, 10, 18186.

Canfield, D.E. (1998) A new model for Proterozoic ocean chemistry. Nature, 396, 450–453.

Canfield, D.E. (2005) The early history of atmospheric oxygen: Homage to Robert M. Garrels. Annual Review of Earth and Planetary Sciences, 33, 1–36.

Canfield, D.E., Ngombi-Pemba, L., Hammarlund, E.U., Bengtson, S., Chaussidon, M., Gauthier-Lafaye, F., Meunier, A., Riboulleau, A., Rollion-Bard, C., Rouxel, O., and others (2013) Oxygen dynamics in the aftermath of the Great Oxidation of Earth's atmosphere. Proceedings of the National Academy of Sciences of the United States of America, 110, 16736–16741.

Canfield, D.E., Zhang, S., Frank, A.B., Wang, X., Wang, H., Su, J., Ye, Y., and Frei, R. (2018) Highly fractionated chromium isotopes in Mesoproterozoic-aged shales and atmospheric oxygen. Nature Communications, 9, 1–11.

Catling, D.C., Glein, C.R., Zahnle, K.J., and McKay, C.P. (2005) Why O2 Is Required by Complex Life on Habitable Planets and the Concept of Planetary "Oxygenation Time". Astrobiology, 5, 415–438.

Chan, L.-H., Leeman, W.P., and Plank, T. (2006) Lithium isotopic composition of marine sediments. Geochemistry, Geophysics, Geosystems, 7.

Chernikova, D., Motamedi, S., Csürös, M., Koonin, E.V., and Rogozin, I.B. (2011) A late origin of the extant eukaryotic diversity: Divergence time estimates using rare genomic changes. Biology Direct, 6, 26.

Chi Fru, E., Somogyi, A., Albani, A.E., Medjoubi, K., Aubineau, J., Robbins, L.J., Lalonde, S.V., and Konhauser, K.O. (2019) The rise of oxygen-driven arsenic cycling at ca. 2.48 Ga. Geology, 47, 243–246.

Clarkson, M.O., Poulton, S.W., Guilbaud, R., and Wood, R.A. (2014) Assessing the utility of Fe/Al and Fe-speciation to record water column redox conditions in carbonate-rich sediments. Chemical Geology, 382, 111–122.

Cloud, P.E. (1965) Significance of the Gunflint (Precambrian) Microflora: Photosynthetic oxygen may have had important local effects before becoming a major atmospheric gas. Science (New York, N.Y.), 148, 27–35.

Cloud, P.E. (1968) Atmospheric and Hydrospheric Evolution on the Primitive Earth. Science, 160, 729–736.

Cloud, P.E. (1972) A working model of the primitive Earth. American Journal of Science, 272, 537–548.

Cloud, P.E. (1973) Paleoecological Significance of the Banded Iron-Formation. Economic Geology, 68, 1135–1143.

Cole, D.B., Reinhard, C.T., Wang, X., Gueguen, B., Halverson, G.P., Gibson, T., Hodgskiss, M.S.W., McKenzie, N.R., Lyons, T.W., and Planavsky, N.J. (2016) A shale-hosted Cr isotope record of low atmospheric oxygen during the Proterozoic. Geology, 44, 555–558.

Cole, D.B., Zhang, S., and Planavsky, N.J. (2017) A new estimate of detrital redox-sensitive metal concentrations and variability in fluxes to marine sediments. Geochimica Et Cosmochimica Acta, 215, 337–353.

Cole, D.B., Mills, D.B., Erwin, D.H., Sperling, E.A., Porter, S.M., Reinhard, C.T., and Planavsky, N.J. (2020) On the co-evolution of surface oxygen levels and animals. Geobiology, 00, 1–22.

Colwyn, D.A., Sheldon, N.D., Maynard, J.B., Gaines, R., Hofmann, A., Wang, X., Gueguen, B., Asael, D., Reinhard, C.T., and Planavsky, N.J. (2019) A paleosol record of the evolution of Cr redox cycling and evidence for an increase in atmospheric oxygen during the Neoproterozoic. Geobiology, 17, 579–593.

Condie, K.C. (1993) Chemical composition and evolution of the upper continental crust: Contrasting results from surface samples and shales. Chemical Geology, 104, 1–37.

Conway, T.M., and John, S.G. (2014) Quantification of dissolved iron sources to the North Atlantic Ocean. Nature, 511, 212–215.

Craig, H. (1953) The geochemistry of the stable carbon isotopes. Geochimica et Cosmochimica Acta, 3, 53–92.

Croal, L.R., Johnson, C.M., Beard, B.L., and Newman, D.K. (2004) Iron isotope fractionation by Fe(II)-oxidizing photoautotrophic bacteria 11Associate editor: D. E. Canfield. Geochimica Et Cosmochimica Acta, 68, 1227–1242.

Crockford, P.W., Hayles, J.A., Bao, H., Planavsky, N.J., Bekker, A., Fralick, P.W., Halverson, G.P., Bui, T.H., Peng, Y., and Wing, B.A. (2018) Triple oxygen isotope evidence for limited mid-Proterozoic primary productivity. Nature, 559, 613–616.

Crockford, P.W., Kunzmann, M., Bekker, A., Hayles, J., Bao, H., Halverson, G.P., Peng, Y., Bui, T.H., Cox, G.M., Gibson, T.M., and others (2019) Claypool continued: Extending the isotopic record of sedimentary sulfate. Chemical Geology, 513, 200–225.

Crosby, H.A., Roden, E.E., Johnson, C.M., and Beard, B.L. (2007) The mechanisms of iron isotope fractionation produced during dissimilatory Fe(III) reduction by Shewanella putrefaciens and Geobacter sulfurreducens. Geobiology, 5, 169–189.

Crowe, S.A., Døssing, L.N., Beukes, N.J., Bau, M., Kruger, S.J., Frei, R., and Canfield, D.E. (2013) Atmospheric oxygenation three billion years ago. Nature, 501, 535–8.

Crusius, J., Calvert, S., Pedersen, T., and Sage, D. (1996) Rhenium and molybdenum enrichments in sediments as indicators of oxic, suboxic and sulfidic conditions of deposition. Earth and Planetary Science Letters, 145, 65–78.

Črne, A.E., Melezhik, V.A., Prave, A.R., Lepland, A., Romashkin, A.E., Rychanchik, D.V., Hanski, E.J., and Luo, Z.-Y. (2013a) Zaonega Formation: FAR-DEEP hole 13A. In V.A. Melezhik, A.R. Prave, A.E. Fallick, E.J. Hanski, A. Lepland, L.R. Kump, and H. Strauss, Eds., Reading the Archive of Earth's Oxygenation Vols. 1-3, Vol. 2: The Core Archive of the Fennoscandian Arctic Russia - Drilling Early Earth Project, pp. 1008–1046. Springer, Berlin Heidelberg.

Črne, A.E., Melezhik, Victor A., Prave, A.R., Lepland, A., Romashkin, A.E., Rychanchik, D.V., Hanski, E.J., and Luo, Zh.-Y. (2013b) Zaonega Formation: FAR-DEEP Holes 12A and 12B, and neighbouring quarries. In V.A. Melezhik, A.R. Prave, A.E. Fallick, E. Hanski, A. Lepland, L.R. Kump, and H. Strauss, Eds., Reading the Archive of Earth's Oxygenation Vols. 1-3, Vol. 2: The Core Archive of the Fennoscandian Arctic Russia - Drilling Early Earth Project, pp. 946–1007. Springer, Berlin Heidelberg.

Črne, A.E., Melezhik, V.A., Lepland, A., Fallick, A.E., Prave, A.R., and Brasier, A.T. (2014) Petrography and geochemistry of carbonate rocks of the Paleoproterozoic Zaonega Formation, Russia: Documentation of 13C-depleted non-primary calcite. Precambrian Research, 240, 79–93.

Dahl, T.W., Chappaz, A., Hoek, J., McKenzie, C.J., Svane, S., and Canfield, D.E. (2017) Evidence of molybdenum association with particulate organic matter under sulfidic conditions. Geobiology, 15, 311–323.

Daly, J.S., Balagansky, V.V., Timmerman, M.J., and Whitehouse, M.J. (2006) The Lapland-Kola orogen: Palaeoproterozoic collision and accretion of the northern Fennoscandian lithosphere. Geological Society, London, Memoirs, 32, 579–598.

Dauphas, N., John, S.G., and Rouxel, O. (2017) Iron Isotope Systematics. Reviews in Mineralogy and Geochemistry, 82, 415–510.

Daye, M., Klepac-Ceraj, V., Pajusalu, M., Rowland, S., Farrell-Sherman, A., Beukes, N., Tamura, N., Fournier, G., and Bosak, T. (2019) Light-driven anaerobic microbial oxidation of manganese. Nature, 576, 311–314.

Deines, P. (1992) Mantle carbon: Concentration, mode of occurrence, and isotopic composition. In Early Organic Evolution pp. 133–146. Springer.

Diamond, C.W., and Lyons, T.W. (2018) Mid-Proterozoic redox evolution and the possibility of transient oxygenation events. Emerging Topics in Life Sciences, ETLS20170146.

Dickson, A.J. (2017) A molybdenum-isotope perspective on Phanerozoic deoxygenation events. Nature Geoscience, 10, 721–726.

Duan, Y., Severmann, S., Anbar, A.D., Lyons, T.W., Gordon, G.W., and Sageman, B.B. (2010) Isotopic evidence for Fe cycling and repartitioning in ancient oxygen-deficient settings:

Examples from black shales of the mid-to-late Devonian Appalachian basin. Earth and Planetary Science Letters, 290, 244–253.

Dunk, R.M., Mills, R.A., and Jenkins, W.J. (2002) A reevaluation of the oceanic uranium budget for the Holocene. Chemical Geology, 190, 45–67.

Eguchi, J., Seales, J., and Dasgupta, R. (2020) Great Oxidation and Lomagundi events linked by deep cycling and enhanced degassing of carbon. Nature Geoscience, 13, 71–76.

El Albani, A., Bengtson, S., Canfield, D.E., Bekker, A., Macchiarelli, R., Mazurier, A., Hammarlund, E.U., Boulvais, P., Dupuy, J.-J., Fontaine, C., and others (2010) Large colonial organisms with coordinated growth in oxygenated environments 2.1 Gyr ago. Nature, 466, 100–104.

El Albani, A., Mangano, M.G., Buatois, L.A., Bengtson, S., Riboulleau, A., Bekker, A., Konhauser, K., Lyons, T., Rollion-Bard, C., Bankole, O., and others (2019) Organism motility in an oxygenated shallow-marine environment 2.1 billion years ago. Proceedings of the National Academy of Sciences, 116, 3431–3436.

Ellis, A.S., Johnson, T.M., and Bullen, T.D. (2002) Chromium Isotopes and the Fate of Hexavalent Chromium in the Environment. Science, 295, 2060–2062.

Evans, D.A., Beukes, N.J., and Kirschvink, J.L. (1997) Low-latitude glaciation in the Palaeoproterozoic era. Nature, 386, 262–266.

Farkaš, J., Frýda, J., Paulukat, C., Hathorne, E.C., Matoušková, Š., Rohovec, J., Frýdová, B., Francová, M., and Frei, R. (2018) Chromium isotope fractionation between modern seawater and biogenic carbonates from the Great Barrier Reef, Australia: Implications for the paleo-seawater δ^{53}Cr reconstruction. Earth and Planetary Science Letters, 498, 140–151.

Farquhar, J., Bao, H., and Thiemens, M. (2000) Atmospheric Influence of Earth's Earliest Sulfur Cycle. Science, 289, 756–758.

Farquhar, J., Zerkle, A.L., and Bekker, A. (2011) Geological constraints on the origin of oxygenic photosynthesis. Photosynthesis Research, 107, 11–36.

Fenchel, T., and Finlay, B.J. (1995) Ecology and evolution in anoxic worlds. Oxford; New York: Oxford University Press, 1995.

Föllmi, K.B., Badertscher, C., de Kaenel, E., Stille, P., John, C.M., Adatte, T., and Steinmann, P. (2005) Phosphogenesis and organic-carbon preservation in the Miocene Monterey Formation at Naples Beach, California - The Monterey hypothesis revisited. Bulletin of the Geological Society of America, 117, 589–619.

Fralick, P., Planavsky, N., Burton, J., Jarvis, I., Addison, W.D., Barrett, T.J., and Brumpton, G.R. (2017) Geochemistry of Paleoproterozoic Gunflint Formation carbonate: Implications for hydrosphere-atmosphere evolution. Precambrian Research, 290, 126–146.

Freeman, K.H. (2001) Isotopic Biogeochemistry of Marine Organic Carbon. Reviews in Mineralogy and Geochemistry, 43, 579–605.

Frei, R., and Polat, A. (2013) Chromium isotope fractionation during oxidative weathering—Implications from the study of a Paleoproterozoic (ca. 1.9Ga) paleosol, Schreiber Beach, Ontario, Canada. Precambrian Research, 224, 434–453.

Frei, R., Gaucher, C., Poulton, S.W., and Canfield, D.E. (2009) Fluctuations in Precambrian atmospheric oxygenation recorded by chromium isotopes. Nature, 461, 250–253.

Frierdich, A.J., Beard, B.L., Scherer, M.M., and Johnson, C.M. (2014a) Determination of the Fe(II)aq–magnetite equilibrium iron isotope fractionation factor using the three-isotope method and a multi-direction approach to equilibrium. Earth and Planetary Science Letters, 391, 77–86.

Frierdich, A.J., Beard, B.L., Reddy, T.R., Scherer, M.M., and Johnson, C.M. (2014b) Iron isotope fractionation between aqueous Fe(II) and goethite revisited: New insights based on a multi-direction approach to equilibrium and isotopic exchange rate modification. Geochimica Et Cosmochimica Acta, 139, 383–398.

Fung, I.Y., Meyn, S.K., Tegen, I., Doney, S.C., John, J.G., and Bishop, J.K.B. (2000) Iron supply and demand in the upper ocean. Global Biogeochemical Cycles, 14, 281–295.

Galea, A.M., and Brown, A.J. (2009) Special relationship between sterols and oxygen: Were sterols an adaptation to aerobic life? Free Radical Biology and Medicine, 47, 880–889.

Gao, Y., Casey, J.F., Bernardo, L.M., Yang, W., and Bissada, K.K. (Adry) (2018) Vanadium isotope composition of crude oil: effects of source, maturation and biodegradation. In M. Lawson, M.J. Formolo and J.M. Eiler, Eds., From Source to Seep: Geochemical Applications in Hydrocarbon Systems. Geological Society of London, London.

Geyman, E.C., and Maloof, A.C. (2019) A diurnal carbon engine explains ^{13}C-enriched carbonates without increasing the global production of oxygen. Proceedings of the National Academy of Sciences of the United States of America, 116, 24433–24439.

Gibson, T.M., Shih, P.M., Cumming, V.M., Fischer, W.W., Crockford, P.W., Hodgskiss, M.S.W., Wörndle, S., Creaser, R.A., Rainbird, R.H., Skulski, T.M., and others (2018) Precise age of Bangiomorpha pubescens dates the origin of eukaryotic photosynthesis. Geology, 46, 135–138.

Gilleaudeau, G.J., Frei, R., Kaufman, A.J., Kah, L.C., Azmy, K., Bartley, J.K., Chernyavskiy, P., and Knoll, A.H. (2016) Oxygenation of the mid-Proterozoic atmosphere: Clues from chromium isotopes in carbonates. Geochemical Perspectives Letters, 2, 178–187.

Gross, J., and Bhattacharya, D. (2010) Uniting sex and eukaryote origins in an emerging oxygenic world. Biology Direct, 5, 53.

Guilbaud, R., Butler, I.B., Ellam, R.M., Rickard, D., and Oldroyd, A. (2011) Experimental determination of the equilibrium Fe isotope fractionation between Fe_{aq}^{2+} and Fe_{Sm} (mackinawite) at 25 and 2°C. Geochimica Et Cosmochimica Acta, 75, 2721–2734.

Guo, Q., Strauss, H., Kaufman, A.J., Schröder, S., Gutzmer, J., Wing, B., Baker, M.A., Bekker, A., Jin, Q., Kim, S.-T., and others (2009) Reconstructing Earth's surface oxidation across the Archean-Proterozoic transition. Geology, 37, 399–402.

Hannah, J.L., Stein, H.J., Zimmerman, A., Yang, G., Melezhik, V.A., Filippov, M.M., Turgeon, S.C., and Creaser, R.A. (2008) Re-Os geochronology of shungite: A 2.05 Ga fossil oil field in

Karelia. In Goldschmidt Conference Abstracts p. A351. Presented at the 33rd International Geological Congress, Oslo, Norway.

Hardisty, D.S., Lu, Z., Planavsky, N.J., Bekker, A., Philippot, P., Zhou, X., and Lyons, T.W. (2014) An iodine record of Paleoproterozoic surface ocean oxygenation. Geology, 42, 619–622.

Hardisty, D.S., Lu, Z., Bekker, A., Diamond, C.W., Gill, B.C., Jiang, G., Kah, L.C., Knoll, A.H., Loyd, S.J., Osburn, M.R., and others (2017) Perspectives on Proterozoic surface ocean redox from iodine contents in ancient and recent carbonate. Earth and Planetary Science Letters, 463, 159–170.

Hartmann, J., Li, G., and West, A.J. (2017) Running out of gas: Zircon 18O-Hf-U/Pb evidence for Snowball Earth preconditioned by low degassing. Geochemical Perspectives Letters, 41–46.

Havig, J.R., Hamilton, T.L., Bachan, A., and Kump, L.R. (2017) Sulfur and carbon isotopic evidence for metabolic pathway evolution and a four-stepped Earth system progression across the Archean and Paleoproterozoic. Earth-Science Reviews, 174, 1–21.

Hayes, J.M., and Waldbauer, J.R. (2006) The carbon cycle and associated redox processes through time. Philosophical Transactions of the Royal Society of London B: Biological Sciences, 361, 931–950.

Heard, A.W., and Dauphas, N. (2020) Constraints on the coevolution of oxic and sulfidic ocean iron sinks from Archean–Paleoproterozoic iron isotope records. Geology, 48, 358–362.

Helz, G.R., and Vorlicek, T.P. (2019) Precipitation of molybdenum from euxinic waters and the role of organic matter. Chemical Geology, 509, 178–193.

Helz, G.R., Miller, C.V., Charnock, J.M., Mosselmans, J.F.W., Pattrick, R.A.D., Garner, C.D., and Vaughan, D.J. (1996) Mechanism of molybdenum removal from the sea and its concentration in black shales: EXAFS evidence. Geochimica Et Cosmochimica Acta, 60, 3631–3642.

Higgins, J.A., Blättler, C.L., Lundstrom, E.A., Santiago-Ramos, D.P., Akhtar, A.A., Crüger Ahm, A.-S., Bialik, O., Holmden, C., Bradbury, H., Murray, S.T., and others (2018) Mineralogy, early marine diagenesis, and the chemistry of shallow-water carbonate sediments. Geochimica Et Cosmochimica Acta, 220, 512–534.

Hodgskiss, M.S.W., Crockford, P.W., Peng, Y., Wing, B.A., and Horner, T.J. (2019) A productivity collapse to end Earth's Great Oxidation. Proceedings of the National Academy of Sciences of the United States of America, 116, 17207–17212.

Holland, H.D. (1962) Model for the evolution of the Earth's atmosphere. In A.E.J. Engel, H.I. James, and B.F. Leonard, Eds., Petrologic studies: a volume to honor AF Buddigington. Geological Society of America.

Holland, H.D. (1984) The Chemical Evolution of the Atmosphere and Oceans, 600 p. Princeton University Press, Princeton, NJ.

Holland, H.D., and Beukes, N.J. (1990) A paleoweathering profile from Griqualand West, South Africa: evidence for a dramatic rise in atmospheric oxygen between 2.2 and 1.9 bybp. American Journal of Science, 290, 1–34.

Holland, H.D. (2002) Volcanic gases, black smokers, and the great oxidation event. Geochimica Et Cosmochimica Acta, 66, 3811–3826.

Holland, H.D. (2006) The oxygenation of the atmosphere and oceans. Philosophical Transactions of the Royal Society of London. Series B, Biological Sciences, 361, 903–15.

Hörandl, E., and Speijer, D. (2018) How oxygen gave rise to eukaryotic sex. Proceedings of the Royal Society B: Biological Sciences, 285, 20172706.

Hunter, J.D. (2007) Matplotlib: A 2D Graphics Environment. Computing in Science Engineering, 9, 90–95.

Icopini, G.A., Anbar, A.D., Ruebush, S.S., Tien, M., and Brantley, S.L. (2004) Iron isotope fractionation during microbial reduction of iron: The importance of adsorption. Geology, 32, 205–208.

Ikeda, Y., Grabowski, B., and Körmann, F. (2019) Mpltern: Ternary plots as projections of Matplotlib. Zenodo.

Imachi, H., Nobu, M.K., Nakahara, N., Morono, Y., Ogawara, M., Takaki, Y., Takano, Y., Uematsu, K., Ikuta, T., Ito, M., and others (2020) Isolation of an archaeon at the prokaryote–eukaryote interface. Nature, 577, 519–525.

Immenhauser, A., Porta, G.D., Kenter, J.A.M., and Bahamonde, J.R. (2003) An alternative model for positive shifts in shallow-marine carbonate δ13C and δ18O. Sedimentology, 50, 953–959.

Iwamori, H., Yoshida, K., Nakamura, H., Kuwatani, T., Hamada, M., Haraguchi, S., and Ueki, K. (2017) Classification of geochemical data based on multivariate statistical analyses: Complementary roles of cluster, principal component, and independent component analyses. Geochemistry, Geophysics, Geosystems, 18, 994–1012.

Javaux, E.J., and Lepot, K. (2018) The Paleoproterozoic fossil record: Implications for the evolution of the biosphere during Earth's middle-age. Earth-Science Reviews, 176, 68–86.

Jochum, K.P., Nohl, U., Herwig, K., Lammel, E., Stoll, B., and Hofmann, A.W. (2005) GeoReM: A New Geochemical Database for Reference Materials and Isotopic Standards. Geostandards and Geoanalytical Research, 29, 333–338.

Johnson, C., Beard, B., and Weyer, S. (2020) Iron Geochemistry: An Isotopic Perspective. Springer International Publishing, Cham.

Johnson, J.E., Gerpheide, A., Lamb, M.P., and Fischer, W.W. (2014) O2 constraints from Paleoproterozoic detrital pyrite and uraninite. GSA Bulletin, 126, 813–830.

Jones, B., and Manning, D.A.C. (1994) Comparison of geochemical indices used for the interpretation of palaeoredox conditions in ancient mudstones. Chemical Geology, 111, 111–129.

Joosu, L., Lepland, A., Kirsimäe, K., Romashkin, A.E., Roberts, N.M.W., Martin, A.P., and Črne, A.E. (2015) The REE-composition and petrography of apatite in 2 Ga Zaonega Formation, Russia: The environmental setting for phosphogenesis. Chemical Geology, 395, 88–107.

Karhu, J.A. (1993) Paleoproterozoic evolution of the carbon isotope ratios of sedimentary carbonates in the Fennoscandian Shield, 87 p. Geologian tutkimuskeskus, Espoo.

Karhu, J.A. (1999) Carbon isotopes. In C.P. Marshall and R.W. Fairbridge, Eds., Encyclopedia of Geochemistry pp. 67–73. Kluwer Academic Publishers, Boston.

Karhu, J.A., and Holland, H.D. (1996) Carbon isotopes and the rise of atmospheric oxygen. Geology, 24, 867–870.

Kassambara, A., and Mundt, F. (2020) Factoextra: Extract and Visualize the Results of Multivariate Data Analyses.

Kasting, J.F., and Canfield, D.E. (2012) The Global Oxygen Cycle. In A.H. Knoll, D.E. Canfield, and K.O. Konhauser, Eds., Fundamentals of Geobiology pp. 93–104. John Wiley & Sons, Chichester, UK.

Kendall, B., Komiya, T., Lyons, T.W., Bates, S.M., Gordon, G.W., Romaniello, S.J., Jiang, G., Creaser, R.A., Xiao, S., McFadden, K., and others (2015) Uranium and molybdenum isotope evidence for an episode of widespread ocean oxygenation during the late Ediacaran Period. Geochimica Et Cosmochimica Acta, 156, 173–193.

Kendall, B., Dahl, T.W., and Anbar, A.D. (2017) The stable isotope geochemistry of molybdenum. Reviews in Mineralogy and Geochemistry, 82, 683–732.

Kerr, G.B., Prave, A.R., Martin, A.P., Fallick, A.E., Brasier, A.T., and Park, R.G. (2016) The Palaeoproterozoic global carbon cycle: Insights from the Loch Maree Group, NW Scotland. Journal of the Geological Society, 173, 170–176.

Kipp, M.A., Stüeken, E.E., Bekker, A., and Buick, R. (2017) Selenium isotopes record extensive marine suboxia during the Great Oxidation Event. Proceedings of the National Academy of Sciences of the United States of America, 114, 875–880.

Kipp, M.A., Lepland, A., and Buick, R. (2020) Redox fluctuations, trace metal enrichment and phosphogenesis in the ~2.0 Ga Zaonega Formation. Precambrian Research, 343, 105716.

Konhauser, K.O., Lalonde, S.V., Planavsky, N.J., Pecoits, E., Lyons, T.W., Mojzsis, S.J., Rouxel, O.J., Barley, M.E., Rosìere, C., Fralick, P.W., and others (2011) Aerobic bacterial pyrite oxidation and acid rock drainage during the Great Oxidation Event. Nature, 478, 369–373.

Konhauser, K.O., Planavsky, N.J., Hardisty, D.S., Robbins, L.J., Warchola, T.J., Haugaard, R., Lalonde, S.V., Partin, C.A., Oonk, P.B.H., Tsikos, H., and others (2017) Iron formations: A global record of Neoarchaean to Palaeoproterozoic environmental history. Earth-Science Reviews, 172, 140–177.

Kreitsmann, T., Külaviir, M., Lepland, A., Paiste, K., Paiste, P., Prave, A.R., Sepp, H., Romashkin, A.E., Rychanchik, D.V., and Kirsimäe, K. (2019) Hydrothermal dedolomitisation of

carbonate rocks of the Paleoproterozoic Zaonega Formation, NW Russia — Implications for the preservation of primary C isotope signals. Chemical Geology, 512, 43–57.

Kreitsmann, T., Lepland, A., Bau, M., Prave, A., Paiste, K., Mänd, K., Sepp, H., Martma, T., Romashkin, A.E., and Kirsimäe, K. (2020) Oxygenated conditions in the aftermath of the Lomagundi-Jatuli Event: The carbon isotope and rare earth element signatures of the Paleoproterozoic Zaonega Formation, Russia. Precambrian Research, 347, 105855.

Krissansen-Totton, J., Buick, R., and Catling, D.C. (2015) A statistical analysis of the carbon isotope record from the Archean to Phanerozoic and implications for the rise of oxygen. American Journal of Science, 315, 275–316.

Krupenik, V., and Sveshnikova, K. (2011) Correlation of the Onega Parametric Hole with the reference sections of the Onega Structure. In L. Glushanin, N. Sharov, and V. Shchiptsov, Eds., The Onega Palaeoproterozoic Structure (Geology, Tectonics, Deep Structure and Minerogeny) pp. 190–195. Institute of Geology, Karelian Research Centre of the Russian Academy of Sciences.

Kump, L.R., Junium, C., Arthur, M.A., Brasier, A., Fallick, A., Melezhik, V., Lepland, A., Črne, A.E., and Luo, G. (2011) Isotopic evidence for massive oxidation of organic matter following the Great Oxidation Event. Science, 334, 1694–1696.

Kump, L.R., Kirsimäe, K., Melezhik, V.A., Brasier, A.T., Fallick, A.E., and Salminen, P.E. (2013) Terrestrial Environments. In V.A. Melezhik, A.R. Prave, E.J. Hanski, A.E. Fallick, A. Lepland, L.R. Kump, and H. Strauss, Eds., Reading the Archive of Earth's Oxygenation Vol. 3:

Global Events and the Fennoscandian Arctic Russia-Drilling Early Earth Project, pp. 1407–1456. Springer Berlin Heidelberg, Berlin, Heidelberg.

Kunzmann, M., Gibson, T.M., Halverson, G.P., Hodgskiss, M.S.W., Bui, T.H., Carozza, D.A., Sperling, E.A., Poirier, A., Cox, G.M., and Wing, B.A. (2017) Iron isotope biogeochemistry of Neoproterozoic marine shales. Geochimica Et Cosmochimica Acta, 209, 85–105.

Lahtinen, R., Korja, A., Nironen, M., and Heikkinen, P. (2009) Palaeoproterozoic accretionary processes in Fennoscandia. Geological Society, London, Special Publications, 318, 237–256.

Lamb, D.M., Awramik, S.M., Chapman, D.J., and Zhu, S. (2009) Evidence for eukaryotic diversification in the ∼1800 million-year-old Changzhougou Formation, North China. Precambrian Research, 173, 93–104.

Lane, N., and Martin, W. (2010) The energetics of genome complexity. Nature, 467, 929–934.

Lenstra, W.K., Hermans, M., Séguret, M.J.M., Witbaard, R., Behrends, T., Dijkstra, N., van Helmond, N.A.G.M., Kraal, P., Laan, P., Rijkenberg, M.J.A., and others (2019) The shelf-to-basin iron shuttle in the Black Sea revisited. Chemical Geology, 511, 314–341.

Lepland, A., Joosu, L., Kirsimäe, K., Prave, A.R., Romashkin, A.E., Črne, A.E., Martin, A.P., Fallick, A.E., Somelar, P., Üpraus, K., and others (2014) Potential influence of sulphur bacteria on Palaeoproterozoic phosphogenesis. Nature Geoscience, 7, 20–24.

Liu, H., Zartman, R.E., Ireland, T.R., and Sun, W. (2019) Global atmospheric oxygen variations recorded by Th/U systematics of igneous rocks. Proceedings of the National Academy of Sciences of the United States of America, 201902833.

Liu, W., Hao, J., Elzinga, E.J., Piotrowiak, P., Nanda, V., Yee, N., and Falkowski, P.G. (2020) Anoxic photogeochemical oxidation of manganese carbonate yields manganese oxide. Proceedings of the National Academy of Sciences, 117, 22698–22704.

Luther, G.W. (1991) Pyrite synthesis via polysulfide compounds. Geochimica Et Cosmochimica Acta, 55, 2839–2849.

Lyons, T.W., and Severmann, S. (2006) A critical look at iron paleoredox proxies: New insights from modern euxinic marine basins. Geochimica Et Cosmochimica Acta, 70, 5698–5722.

Lyons, T.W., Werne, J.P., Hollander, D.J., and Murray, R.W. (2003) Contrasting sulfur geochemistry and Fe/Al and Mo/Al ratios across the last oxic-to-anoxic transition in the Cariaco Basin, Venezuela. Chemical Geology, 195, 131–157.

Lyons, T.W., Reinhard, C.T., and Planavsky, N.J. (2014) The rise of oxygen in Earth's early ocean and atmosphere. Nature, 506, 307–15.

MacGregor, A.M. (1927) The problem of the Precambrian atmosphere. South African Journal of Science, 24, 115.

Malinovsky, D., Stenberg, A., Rodushkin, I., Andren, H., Ingri, J., Öhlander, B., and C. Baxter, D. (2003) Performance of high resolution MC-ICP-MS for Fe isotope ratio measurements in sedimentary geological materials. Journal of Analytical Atomic Spectrometry, 18, 687–695.

Mansor, M., and Fantle, M.S. (2019) A novel framework for interpreting pyrite-based Fe isotope records of the past. Geochimica Et Cosmochimica Acta, 253, 39–62.

Marmo, J.S. (1992) The Lower Proterozoic Hokkalampi Paleosol in North Karelia, Eastern Finland. In M. Schidlowski, S. Golubic, M.M. Kimberley, D.M. McKirdy, and P.A. Trudinger, Eds., Early Organic Evolution: Implications for Mineral and Energy Resources pp. 41–66. Springer Berlin Heidelberg, Berlin, Heidelberg.

Martin, A.P., Condon, D.J., Prave, A.R., and Lepland, A. (2013) A review of temporal constraints for the Palaeoproterozoic large, positive carbonate carbon isotope excursion (the Lomagundi–Jatuli Event). Earth-Science Reviews, 127, 242–261.

Martin, A.P., Prave, A.R., Condon, D.J., Lepland, A., Fallick, A.E., Romashkin, A.E., Medvedev, P.V., and Rychanchik, D.V. (2015) Multiple Palaeoproterozoic carbon burial episodes and excursions. Earth and Planetary Science Letters, 424, 226–236.

Martindale, R.C., Strauss, J.V., Sperling, E.A., Johnson, J.E., Van Kranendonk, M.J., Flannery, D., French, K., Lepot, K., Mazumder, R., Rice, M.S., and others (2015) Sedimentology, chemostratigraphy, and stromatolites of lower Paleoproterozoic carbonates, Turee Creek Group, Western Australia. Precambrian Research, 266, 194–211.

Mänd, K., Lalonde, S.V., Robbins, L.J., Thoby, M., Paiste, K., Kreitsmann, T., Paiste, P., Reinhard, C.T., Romashkin, A.E., Planavsky, N.J., and others (2020) Palaeoproterozoic oxygenated oceans following the Lomagundi–Jatuli Event. Nature Geoscience, 13, 302–306.

McKinney, W. (2010) Data Structures for Statistical Computing in Python. In S. van der Walt and J. Millman, Eds., Proceedings of the 9th Python in Science Conference pp. 56–61.

McLennan, S.M. (2001) Relationships between the trace element composition of sedimentary rocks and upper continental crust: Trace element composition and upper continental crust. Geochemistry, Geophysics, Geosystems, 2, 1021.

Melezhik, V.A., Fallick, A.E., Medvedev, P.V., and Makarikhin, V.V. (1999a) Extreme $^{13}C_{carb}$ enrichment in ca. 2.0 Ga magnesite–stromatolite–dolomite–'red beds' association in a global context: A case for the world-wide signal enhanced by a local environment. Earth-Science Reviews, 48, 71–120.

Melezhik, V.A., Fallick, A.E., Filippov, M.M., and Larsen, O. (1999b) Karelian shungite—an indication of 2.0-Ga-old metamorphosed oil-shale and generation of petroleum: Geology, lithology and geochemistry. Earth-Science Reviews, 47, 1–40.

Melezhik, V.A., Fallick, A.E., Medvedev, P.V., and Makarikhin, V.V. (2001) Palaeoproterozoic magnesite: lithological and isotopic evidence for playa/sabkha environments. Sedimentology, 48, 379–397.

Melezhik, V.A., Filippov, M.M., and Romashkin, A.E. (2004) A giant Palaeoproterozoic deposit of shungite in NW Russia: Genesis and practical applications. Ore Geology Reviews, 24, 135–154.

Melezhik, V.A., Fallick, A.E., Rychanchik, D.V., and Kuznetsov, A.B. (2005) Palaeoproterozoic evaporites in Fennoscandia: Implications for seawater sulphate, the rise of atmospheric oxygen and local amplification of the $\delta^{13}C$ excursion. Terra Nova, 17, 141–148.

Melezhik, V.A., Huhma, H., Condon, D.J., Fallick, A.E., and Whitehouse, M.J. (2007) Temporal constraints on the Paleoproterozoic Lomagundi-Jatuli carbon isotopic event. Geology, 35, 655–658.

Melezhik, V.A., Fallick, A.E., Filippov, M.M., Lepland, A., Rychanchik, D.V., Deines, Y.E., Medvedev, P.V., Romashkin, A.E., and Strauss, H. (2009) Petroleum surface oil seeps from a Palaeoproterozoic petrified giant oilfield. Terra Nova, 21, 119–126.

Melezhik, V.A., Prave, A.R., Fallick, A.E., Kump, L.R., Strauss, H., Lepland, A., and Hanski, E.J., Eds. (2013a) Reading the Archive of Earth's Oxygenation, 490 p. Vols. 1-3, Vol. 1: The Palaeoproterozoic of Fennoscandia As Context for the Fennoscandian Arctic Russia-Drilling Early Earth Project. Springer, Berlin Heidelberg.

Melezhik, V.A., and Hanski, E.J. (2013) Palaeotectonic and Palaeogeographic Evolution of Fennoscandia in the Early Palaeoproterozoic. In Victor A. Melezhik, A.R. Prave, A.E. Fallick, L.R. Kump, H. Strauss, A. Lepland, and Eero J. Hanski, Eds., Reading the Archive of Earth's Oxygenation: Volume 1: The Palaeoproterozoic of Fennoscandia as Context for the

Fennoscandian Arctic Russia - Drilling Early Earth Project pp. 111–178. Springer, Berlin, Heidelberg.

Melezhik, V.A., Fallick, A.E., Filippov, M.M., Deines, Y.E., Črne, A.E., Lepland, A., Brasier, A.T., and Strauss, H. (2013a) Giant Palaeoproterozoic petrified oil field in the Onega Basin. In Reading the Archive of Earth's Oxygenation Vols. 1-3, Vol. 3: Global Events and the Fennoscandian Arctic Russia - Drilling Earth Project, pp. 1202–1273. Springer, Berlin Heidelberg.

Melezhik, V.A., Medvedev, P.V., and Svetov, S.A. (2013b) The Onega Basin. In V.A. Melezhik, A.R. Prave, A.E. Fallick, L.R. Kump, H. Strauss, A. Lepland, and E.J. Hanski, Eds., Reading the Archive of Earth's Oxygenation Vols. 1-3, Vol. 1: The Palaeoproterozoic of Fennoscandia As Context for the Fennoscandian Arctic Russia - Drilling Early Earth Project, pp. 387–490. Springer, Berlin Heidelberg.

Melezhik, V.A., Fallick, A.E., Brasier, A.T., and Lepland, A. (2015) Carbonate deposition in the Palaeoproterozoic Onega basin from Fennoscandia: A spotlight on the transition from the Lomagundi-Jatuli to Shunga events. Earth-Science Reviews, 147, 65–98.

Mentel, M., and Martin, W. (2008) Energy metabolism among eukaryotic anaerobes in light of Proterozoic ocean chemistry. Philosophical Transactions of the Royal Society B: Biological Sciences, 363, 2717–2729.

Mertanen, S., Halls, H.C., Vuollo, J.I., Pesonen, L.J., and Stepanov, V.S. (1999) Paleomagnetism of 2.44 Ga mafic dykes in Russian Karelia, eastern Fennoscandian Shield — implications for continental reconstructions. Precambrian Research, 98, 197–221.

Migdisov, A.A., Guo, X., Williams-Jones, A.E., Sun, C.J., Vasyukova, O., Sugiyama, I., Fuchs, S., Pearce, K., and Roback, R. (2017) Hydrocarbons as ore fluids. Geochemical Perspectives Letters, 5, 47–52.

Miller, C.A., Peucker-Ehrenbrink, B., Walker, B.D., and Marcantonio, F. (2011) Re-assessing the surface cycling of molybdenum and rhenium. Geochimica Et Cosmochimica Acta, 75, 7146–7179.

Mills, R.A., and Elderfield, H. (1995) Rare earth element geochemistry of hydrothermal deposits from the active TAG Mound, 26°N Mid-Atlantic Ridge. Geochimica Et Cosmochimica Acta, 59, 3511–3524.

Mitchell, R.L., and Sheldon, N.D. (2010) The ∼1100Ma Sturgeon Falls paleosol revisited: Implications for Mesoproterozoic weathering environments and atmospheric CO2 levels. Precambrian Research, 183, 738–748.

Miyazaki, Y., Planavsky, N., Bolton, E.W., and Reinhard, C.T. (2018) Making sense of massive carbon isotope excursions with an inverse carbon cycle model. Journal of Geophysical Research: Biogeosciences, 123, 2485–2496.

Moore, J.K., and Braucher, O. (2008) Sedimentary and mineral dust sources of dissolved iron to the world ocean. Biogeosciences, 5, 631–656.

Morford, J.L., and Emerson, S. (1999) The geochemistry of redox sensitive trace metals in sediments. Geochimica Et Cosmochimica Acta, 63, 1735–1750.

Nägler, T.F., Anbar, A.D., Archer, C., Goldberg, T., Gordon, G.W., Greber, N.D., Siebert, C., Sohrin, Y., and Vance, D. (2014) Proposal for an international molybdenum isotope measurement standard and data representation. Geostandards and Geoanalytical Research, 38, 149–151.

Och, L.M., and Shields-Zhou, G.A. (2012) The Neoproterozoic oxygenation event: Environmental perturbations and biogeochemical cycling. Earth-Science Reviews, 110, 26–57.

Ohmoto, H., Watanabe, Y., Lasaga, A.C., Naraoka, H., Johnson, I., Brainard, J., and Chorney, A. (2014) Oxygen, iron, and sulfur geochemical cycles on early Earth: Paradigms and contradictions.

Ojakangas, R.W., Marmo, J.S., and Heiskanen, K.I. (2001) Basin evolution of the Paleoproterozoic Karelian Supergroup of the Fennoscandian (Baltic) Shield. Sedimentary Geology, 141–142, 255–285.

Ossa Ossa, F., Eickmann, B., Hofmann, A., Planavsky, N.J., Asael, D., Pambo, F., and Bekker, A. (2018) Two-step deoxygenation at the end of the Paleoproterozoic Lomagundi Event. Earth and Planetary Science Letters, 486, 70–83.

Ovchinnikova, G.V., Kuznetsov, a.B., Melezhik, V.A., Gorokhov, I.M., Vasil’eva, I.M., and Gorokhovskii, B.M. (2007) Pb-Pb age of Jatulian carbonate rocks: The Tulomozero Formation of southeast Karelia. Stratigraphy and Geological Correlation, 15, 359–372.

Paiste, K. (2018) Reconstructing the Paleoproterozoic sulfur cycle: Insights from the multiple sulfur isotope record of the Zaonega Formation, Karelia, Russia. PhD Thesis, University of Tromsø – The Arctic University of Norway, Tromsø, Norway.

Paiste, K., Lepland, A., Zerkle, A.L., Kirsimäe, K., Izon, G., Patel, N.K., McLean, F., Kreitsmann, T., Mänd, K., Bui, T.H., and others (2018) Multiple sulphur isotope records tracking basinal and global processes in the 1.98 Ga Zaonega Formation, NW Russia. Chemical Geology, 499, 151–164.

Paiste, K., Lepland, A., Zerkle, A.L., Kirsimäe, K., Kreitsmann, T., Mänd, K., Romashkin, A.E., Rychanchik, D.V., and Prave, A.R. (2020a) Identifying global vs. basinal controls on Paleoproterozoic organic carbon and sulfur isotope records. Earth-Science Reviews, 207, 103230.

Paiste, K., Pellerin, A., Zerkle, A.L., Kirsimäe, K., Prave, A.R., Romashkin, A.E., and Lepland, A. (2020b) The pyrite multiple sulfur isotope record of the 1.98 Ga Zaonega Formation: Evidence for biogeochemical sulfur cycling in a semi-restricted basin. Earth and Planetary Science Letters, 534, 116092.

Parfrey, L.W., Lahr, D.J.G., Knoll, A.H., and Katz, L.A. (2011) Estimating the timing of early eukaryotic diversification with multigene molecular clocks. Proceedings of the National Academy of Sciences of the United States of America, 108, 13624–13629.

Park, R., and Epstein, S. (1960) Carbon isotope fractionation during photosynthesis. Geochimica et Cosmochimica Acta, 21, 110–126.

Partin, C.A., Bekker, A., Planavsky, N.J., Scott, C.T., Gill, B.C., Li, C., Podkovyrov, V., Maslov, A., Konhauser, K.O., Lalonde, S.V., and others (2013a) Large-scale fluctuations in Precambrian atmospheric and oceanic oxygen levels from the record of U in shales. Earth and Planetary Science Letters, 369–370, 284–293.

Partin, C.A., Lalonde, S.V., Planavsky, N.J., Bekker, A., Rouxel, O.J., Lyons, T.W., and Konhauser, K.O. (2013b) Uranium in iron formations and the rise of atmospheric oxygen. Chemical Geology, 362, 82–90.

Partin, C.A., Bekker, A., Planavsky, N.J., and Lyons, T.W. (2015) Euxinic conditions recorded in the ca. 1.93 Ga Bravo Lake Formation, Nunavut (Canada): Implications for oceanic redox evolution. Chemical Geology, 417, 148–162.

Pavlov, A.A., and Kasting, J.F. (2002) Mass-independent fractionation of sulfur isotopes in Archean sediments: Strong evidence for an anoxic Archean atmosphere. Astrobiology, 2, 27–41.

Pérez-Fodich, A., Reich, M., Álvarez, F., Snyder, G.T., Schoenberg, R., Vargas, G., Muramatsu, Y., and Fehn, U. (2014) Climate change and tectonic uplift triggered the formation of the Atacama Desert's giant nitrate deposits. Geology, 42, 251–254.

Planavsky, N.J., Rouxel, O.J., Bekker, A., Hofmann, A., Little, C.T.S., and Lyons, T.W. (2012a) Iron isotope composition of some Archean and Proterozoic iron formations. Geochimica Et Cosmochimica Acta, 80, 158–169.

Planavsky, N.J., Bekker, A., Hofmann, A., Owens, J.D., and Lyons, T.W. (2012b) Sulfur record of rising and falling marine oxygen and sulfate levels during the Lomagundi event. Proceedings of the National Academy of Sciences of the United States of America, 109, 18300–18305.

Planavsky, N.J., Reinhard, C.T., Wang, X., Thomson, D., McGoldrick, P., Rainbird, R.H., Johnson, T., Fischer, W.W., and Lyons, T.W. (2014) Low Mid-Proterozoic atmospheric oxygen levels and the delayed rise of animals. Science, 346, 635–638.

Planavsky, N.J., Cole, D.B., Isson, T.T., Reinhard, C.T., Crockford, P.W., Sheldon, N.D., and Lyons, T.W. (2018a) A case for low atmospheric oxygen levels during Earth's middle history. Emerging Topics in Life Sciences, 2, 149–159.

Planavsky, N.J., Slack, J.F., Cannon, W.F., O'Connell, B., Isson, T.T., Asael, D., Jackson, J.C., Hardisty, D.S., Lyons, T.W., and Bekker, A. (2018b) Evidence for episodic oxygenation in a weakly redox-buffered deep mid-Proterozoic ocean. Chemical Geology, 483, 581–594.

Planavsky, N.J., Robbins, L.J., Kamber, B.S., and Schoenberg, R. (2020) Weathering, alteration and reconstructing Earth's oxygenation. Interface Focus, 10, 20190140.

Poitrasson, F., and Freydier, R. (2005) Heavy iron isotope composition of granites determined by high resolution MC-ICP-MS. Chemical Geology, 222, 132–147.

Pope, M.C., and Grotzinger, J.P. (2003) Paleoproterozoic Stark Formation, Athapuscow Basin, Northwest Canada: Record of Cratonic-Scale Salinity Crisis. Journal of Sedimentary Research, 73, 280–295.

Porter, S.M. (2020) Insights into eukaryogenesis from the fossil record. Interface Focus, 10, 20190105.

Poulton, S.W., and Canfield, D.E. (2005) Development of a sequential extraction procedure for iron: Implications for iron partitioning in continentally derived particulates. Chemical Geology, 214, 209–221.

Poulton, S.W., and Canfield, D.E. (2011) Ferruginous conditions: A dominant feature of the ocean through Earth's history. Elements, 7, 107–112.

Priyatkina, N., Khudoley, A.K., Ustinov, V.N., and Kullerud, K. (2014) 1.92 Ga kimberlitic rocks from Kimozero, NW Russia: Their geochemistry, tectonic setting and unusual field occurrence. Precambrian Research, 249, 162–179.

Puchtel, I.S., Arndt, N.T., Hofmann, A.W., Haase, K.M., Kröner, A., Kulikov, V.S., Kulikova, V.V., Garbe-Schönberg, C.-D., and Nemchin, A.A. (1998) Petrology of mafic lavas within the Onega plateau, central Karelia: Evidence for 2.0 Ga plume-related continental crustal growth in the Baltic Shield. Contributions to Mineralogy and Petrology, 130, 134–153.

Puchtel, I.S., Brügmann, G.E., and Hofmann, A.W. (1999) Precise Re–Os mineral isochron and Pb–Nd–Os isotope systematics of a mafic–ultramafic sill in the 2.0 Ga Onega plateau (Baltic Shield). Earth and Planetary Science Letters, 170, 447–461.

Qu, Y., Črne, A.E., Lepland, A., and van Zuilen, M.A. (2012) Methanotrophy in a Paleoproterozoic oil field ecosystem, Zaonega Formation, Karelia, Russia. Geobiology, 10, 467–78.

Qu, Y., Lepland, A., van Zuilen, M., Whitehouse, M., Črne, A.E., and Fallick, A.E. (2018) Sample-scale carbon isotopic biosignatures of diverse biomass in the Paleoproterozoic Zaonega Formation, Russia. Precambrian Research, 315, 222–231.

Raiswell, R., and Canfield, D.E. (1998) Sources of iron for pyrite formation in marine sediments. American Journal of Science, 298, 219–245.

Raiswell, R., Canfield, D.E., and Berner, R.A. (1994) A comparison of iron extraction methods for the determination of degree of pyritisation and the recognition of iron-limited pyrite formation. Chemical Geology, 111, 101–110.

Raiswell, R., Hardisty, D.S., Lyons, T.W., Canfield, D.E., Owens, J.D., Planavsky, N.J., Poulton, S.W., and Reinhard, C.T. (2018) The iron paleoredox proxies: A guide to the pitfalls, problems and proper practice. American Journal of Science, 318, 491–526.

Ramdohr, P. (1958) New observations of the ores of the Witwatersrand in South Africa and their genetic significance. Geological Society of South Africa Transactions, 61, 1–50.

Rasmussen, B., and Buick, R. (1999) Redox state of the Archean atmosphere: Evidence from detrital heavy minerals in ca. 3250–2750 Ma sandstones from the Pilbara Craton, Australia. Geology, 27, 115–118.

Rasmussen, B., Fletcher, I.R., Bekker, A., Muhling, J.R., Gregory, C.J., and Thorne, A.M. (2012) Deposition of 1.88-billion-year-old iron formations as a consequence of rapid crustal growth. Nature, 484, 498–501.

Reinhard, C.T., Planavsky, N.J., Robbins, L.J., Partin, C.A., Gill, B.C., Lalonde, S.V., Bekker, A., Konhauser, K.O., and Lyons, T.W. (2013) Proterozoic ocean redox and biogeochemical stasis. Proceedings of the National Academy of Sciences of the United States of America, 110, 5357–5362.

Reinhard, C.T., Planavsky, N.J., Wang, X., Fischer, W.W., Johnson, T.M., and Lyons, T.W. (2014) The isotopic composition of authigenic chromium in anoxic marine sediments: A case study from the Cariaco Basin. Earth and Planetary Science Letters, 407, 9–18.

Reinhard, C.T., Planavsky, N.J., Ward, B.A., Love, G.D., Hir, G.L., and Ridgwell, A. (2020) The impact of marine nutrient abundance on early eukaryotic ecosystems. Geobiology, 18, 139–151.

Reuschel, M., Melezhik, V.A., Whitehouse, M.J., Lepland, A., Fallick, A.E., and Strauss, H. (2012) Isotopic evidence for a sizeable seawater sulfate reservoir at 2.1 Ga. Precambrian Research, 192–195, 78–88.

Rickard, D. (1997) Kinetics of pyrite formation by the H2S oxidation of iron (II) monosulfide in aqueous solutions between 25 and 125°C: The rate equation. Geochimica Et Cosmochimica Acta, 61, 115–134.

Rickard, D., and Luther, G.W. (2007) Chemistry of Iron Sulfides. Chemical Reviews, 107, 514–562.

Rico, K.I., and Sheldon, N.D. (2019) Nutrient and iron cycling in a modern analogue for the redoxcline of a Proterozoic ocean shelf. Chemical Geology, 511, 42–50.

Rico, K.I., Sheldon, N.D., Gallagher, T.M., and Chappaz, A. (2019) Redox Chemistry and Molybdenum Burial in a Mesoproterozoic Lake. Geophysical Research Letters, 46, 5871–5878.

Robbins, L.J., Lalonde, S.V., Planavsky, N.J., Partin, C.A., Reinhard, C.T., Kendall, B., Scott, C., Hardisty, D.S., Gill, B.C., Alessi, D.S., and others (2016) Trace elements at the intersection of marine biological and geochemical evolution. Earth-Science Reviews, 163, 323–348.

Robbins, L.J., Mänd, K., Planavsky, N.J., Alessi, D.S., and Konhauser, K.O. (2020) Trace Metals. In M. Gargaud, W.M. Irvine, R. Amils, H.J. Cleaves, D. Pinti, J. Cernicharo Quintanilla, and M. Viso, Eds., Encyclopedia of Astrobiology pp. 1–5. Springer, Berlin, Heidelberg.

Rodler, A., Sánchez-Pastor, N., Fernández-Díaz, L., and Frei, R. (2015) Fractionation behavior of chromium isotopes during coprecipitation with calcium carbonate: Implications for their use as paleoclimatic proxy. Geochimica Et Cosmochimica Acta, 164, 221–235.

Rolison, J.M., Stirling, C.H., Middag, R., Gault-Ringold, M., George, E., and Rijkenberg, M.J.A. (2018) Iron isotope fractionation during pyrite formation in a sulfidic Precambrian ocean analogue. Earth and Planetary Science Letters, 488, 1–13.

Roscoe, S.M. (1969) Huronian rocks and uraniferous conglomerates in the Canadian Shield. Geological Survey of Canada.

Rosenbaum, J., and Sheppard, S.M.F. (1986) An isotopic study of siderites, dolomites and ankerites at high temperatures. Geochimica Et Cosmochimica Acta, 50, 1147–1150.

Rouxel, O., Shanks, W.C., Bach, W., and Edwards, K.J. (2008a) Integrated Fe- and S-isotope study of seafloor hydrothermal vents at East Pacific Rise 9–10°N. Chemical Geology, 252, 214–227.

Rouxel, O., Sholkovitz, E., Charette, M., and Edwards, K.J. (2008b) Iron isotope fractionation in subterranean estuaries. Geochimica Et Cosmochimica Acta, 72, 3413–3430.

Rouxel, O.J., Bekker, A., and Edwards, K.J. (2005) Iron Isotope Constraints on the Archean and Paleoproterozoic Ocean Redox State. Science, 307, 1088–1091.

Rudnick, R.L., and Gao, S. (2014) Composition of the Continental Crust. In Treatise on Geochemistry pp. 1–51. Elsevier, Amsterdam.

Rye, R., and Holland, H.D. (1998) Paleosols and the evolution of atmospheric oxygen; a critical review. American Journal of Science, 298, 621–672.

Saad, E.M., Wang, X., Planavsky, N.J., Reinhard, C.T., and Tang, Y. (2017) Redox-independent chromium isotope fractionation induced by ligand-promoted dissolution. Nature Communications, 8, 1–10.

Sadler, P.M. (1999) The influence of hiatuses on sediment accumulation rates. GeoResearch Forum, 5, 15–40.

Sagan, L. (1967) On the origin of mitosing cells. Journal of Theoretical Biology, 14, 225–IN6.

Sánchez-Baracaldo, P., Raven, J.A., Pisani, D., and Knoll, A.H. (2017) Early photosynthetic eukaryotes inhabited low-salinity habitats. Proceedings of the National Academy of Sciences, 114, E7737–E7745.

Schauble, E., Rossman, G.R., and Taylor, H.P. (2004) Theoretical estimates of equilibrium chromium-isotope fractionations. Chemical Geology, 205, 99–114.

Scheiderich, K., Amini, M., Holmden, C., and Francois, R. (2015) Global variability of chromium isotopes in seawater demonstrated by Pacific, Atlantic, and Arctic Ocean samples. Earth and Planetary Science Letters, 423, 87–97.

Schidlowski, M., Eichmann, R., and Junge, C.E. (1975) Precambrian sedimentary carbonates: carbon and oxygen isotope geochemistry and implications for the terrestrial oxygen budget. Precambrian Research, 2, 1–69.

Schidlowski, M., Eichmann, R., and Junge, C.E. (1976) Carbon isotope geochemistry of the Precambrian Lomagundi carbonate province, Rhodesia. Geochimica Et Cosmochimica Acta, 40, 449–455.

Schidlowski, M., Hayes, J.M., and Kaplan, I.R. (1983) Isotopic inferences of ancient biochemistries-Carbon, sulfur, hydrogen, and nitrogen. In J.W. Schopf, Ed., Earth's Earliest Biosphere: Its Origin and Evolution pp. 149–186. Princeton University Press, Princeton, N.J.

Schoenberg, R., Zink, S., Staubwasser, M., and von Blanckenburg, F. (2008) The stable Cr isotope inventory of solid Earth reservoirs determined by double spike MC-ICP-MS. Chemical Geology, 249, 294–306.

Scholz, F. (2018) Identifying oxygen minimum zone-type biogeochemical cycling in Earth history using inorganic geochemical proxies. Earth-Science Reviews, 184, 29–45.

Scholz, F., McManus, J., and Sommer, S. (2013) The manganese and iron shuttle in a modern euxinic basin and implications for molybdenum cycling at euxinic ocean margins. Chemical Geology, 355, 56–68.

Scholz, F., Severmann, S., McManus, J., and Hensen, C. (2014) Beyond the Black Sea paradigm: The sedimentary fingerprint of an open-marine iron shuttle. Geochimica Et Cosmochimica Acta, 127, 368–380.

Scholz, F., Baum, M., Siebert, C., Eroglu, S., Dale, A.W., Naumann, M., and Sommer, S. (2018) Sedimentary molybdenum cycling in the aftermath of seawater inflow to the intermittently euxinic Gotland Deep, Central Baltic Sea. Chemical Geology, 491, 27–38.

Scholz, F., Schmidt, M., Hensen, C., Eroglu, S., Geilert, S., Gutjahr, M., and Liebetrau, V. (2019) Shelf-to-basin iron shuttle in the Guaymas Basin, Gulf of California. Geochimica Et Cosmochimica Acta, 261, 76–92.

Schrag, D.P., Higgins, J.A., Macdonald, F.A., and Johnston, D.T. (2013) Authigenic carbonate and the history of the global carbon cycle. Science, 339, 540–543.

Schröder, S., Bekker, A., Beukes, N.J., Strauss, H., and Niekerk, H.S.V. (2008) Rise in seawater sulphate concentration associated with the Paleoproterozoic positive carbon isotope excursion: Evidence from sulphate evaporites in the ∼2.2–2.1 Gyr shallow-marine Lucknow Formation, South Africa. Terra Nova, 20, 108–117.

Scott, C., Lyons, T.W., Bekker, A., Shen, Y., Poulton, S.W., Chu, X., and Anbar, A.D. (2008) Tracing the stepwise oxygenation of the Proterozoic ocean. Nature, 452, 456–459.

Scott, C., Wing, B.A., Bekker, A., Planavsky, N.J., Medvedev, P., Bates, S.M., Yun, M., and Lyons, T.W. (2014) Pyrite multiple-sulfur isotope evidence for rapid expansion and contraction of the early Paleoproterozoic seawater sulfate reservoir. Earth and Planetary Science Letters, 389, 95–104.

Severmann, S., Johnson, C.M., Beard, B.L., German, C.R., Edmonds, H.N., Chiba, H., and Green, D.R.H. (2004) The effect of plume processes on the Fe isotope composition of hydrothermally derived Fe in the deep ocean as inferred from the Rainbow vent site, Mid-Atlantic Ridge, 36°14′N. Earth and Planetary Science Letters, 225, 63–76.

Severmann, S., Lyons, T.W., Anbar, A., McManus, J., and Gordon, G. (2008) Modern iron isotope perspective on the benthic iron shuttle and the redox evolution of ancient oceans. Geology, 36, 487–490.

Shawar, L., Halevy, I., Said-Ahmad, W., Feinstein, S., Boyko, V., Kamyshny, A., and Amrani, A. (2018) Dynamics of pyrite formation and organic matter sulfurization in organic-rich carbonate sediments. Geochimica Et Cosmochimica Acta, 241, 219–239.

Sheen, A.I., Kendall, B., Reinhard, C.T., Creaser, R.A., Lyons, T.W., Bekker, A., Poulton, S.W., and Anbar, A.D. (2018) A model for the oceanic mass balance of rhenium and implications for the extent of Proterozoic ocean anoxia. Geochimica Et Cosmochimica Acta, 227, 75–95.

Shields, G., and Veizer, J. (2002) Precambrian marine carbonate isotope database: Version 1.1. Geochemistry, Geophysics, Geosystems, 3, 1 of 12–12 of 12.

Shields, G.A., and Mills, B.J.W. (2017) Tectonic controls on the long-term carbon isotope mass balance. Proceedings of the National Academy of Sciences of the United States of America, 201614506.

Shih, P.M., and Matzke, N.J. (2013) Primary endosymbiosis events date to the later Proterozoic with cross-calibrated phylogenetic dating of duplicated ATPase proteins. Proceedings of the National Academy of Sciences, 110, 12355–12360.

Siebert, C., Nägler, T.F., and Kramers, J.D. (2001) Determination of molybdenum isotope fractionation by double-spike multicollector inductively coupled plasma mass spectrometry. Geochemistry, Geophysics, Geosystems, 2, 1032.

Siebert, C., Nägler, T.F., von Blanckenburg, F., and Kramers, J.D. (2003) Molybdenum isotope records as a potential new proxy for paleoceanography. Earth and Planetary Science Letters, 211, 159–171.

Slotznick, S.P., Eiler, J.M., and Fischer, W.W. (2018) The effects of metamorphism on iron mineralogy and the iron speciation redox proxy. Geochimica Et Cosmochimica Acta, 224, 96–115.

Speijer, D. (2020) Debating Eukaryogenesis—Part 1: Does Eukaryogenesis Presuppose Symbiosis Before Uptake? BioEssays, 42, 1900157.

Sperling, E.A., Rooney, A.D., Hays, L., Sergeev, V.N., Vorob'eva, N.G., Sergeeva, N.D., Selby, D., Johnston, D.T., and Knoll, A.H. (2014) Redox heterogeneity of subsurface waters in the Mesoproterozoic ocean. Geobiology, 12, 373–386.

Stepanova, A., Samsonov, A., and Larionov, A. (2014) The final episode of middle Proterozoic magmatism in the Onega structure: Data on trans-Onega dolerites. Transactions of the Karelian Research Centre of the Russian Academy of Sciences, Precambrian Geology Series, 1, 3–16.

Stolper, D.A., Revsbech, N.P., and Canfield, D.E. (2010) Aerobic growth at nanomolar oxygen concentrations. Proceedings of the National Academy of Sciences, 107, 18755–18760.

Strand, K., and Köykkä, J. (2012) Early Paleoproterozoic rift volcanism in the eastern Fennoscandian Shield related to the breakup of the Kenorland supercontinent. Precambrian Research, 214–215, 95–105.

Strauss, H., Des Marais, D.J., Hayes, J.M., and Summons, R.E. (1992) The carbon-isotopic record. In J.W. Schopf and C. Klein, Eds., The Proterozoic biosphere: A multidisciplinary study pp. 117–127. Cambridge University Press.

Strauss, H., Melezhik, V.A., Lepland, A., Fallick, A.E., Hanski, E.J., Filippov, M.M., Deines, Y.E., Illing, C.J., Črne, A.E., and Brasier, A.T. (2013) Enhanced accumulation of organic matter: The Shunga Event. In V.A. Melezhik, A.R. Prave, E.J. Hanski, A.E. Fallick, A. Lepland, L.R. Kump, and H. Strauss, Eds., Reading the Archive of Earth's Oxygenation Vols. 1-3, Vol. 3: Global Events and the Fennoscandian Arctic Russia - Drilling Earth Project, pp. 1195–1273. Springer, Berlin Heidelberg.

Swart, P.K. (2008) Global synchronous changes in the carbon isotopic composition of carbonate sediments unrelated to changes in the global carbon cycle. Proceedings of the National Academy of Sciences, 105, 13741–13745.

Szathmáry, E. (2015) Toward major evolutionary transitions theory 2.0. Proceedings of the National Academy of Sciences, 112, 10104–10111.

Tang, D., Shi, X., Ma, J., Jiang, G., Zhou, X., and Shi, Q. (2017) Formation of shallow-water glaucony in weakly oxygenated Precambrian ocean: An example from the Mesoproterozoic Tieling Formation in North China. Precambrian Research, 294, 214–229.

Taylor, S.R., and McLennan, S.M. (1985) The continental crust: Its composition and evolution. Blackwell Scientific Pub., Palo Alto, CA.

Tissot, F.L.H., and Dauphas, N. (2015) Uranium isotopic compositions of the crust and ocean: Age corrections, U budget and global extent of modern anoxia. Geochimica Et Cosmochimica Acta, 167, 113–143.

Toma, J., Holmden, C., Shakotko, P., Pan, Y., and Ootes, L. (2019) Cr isotopic insights into ca. 1.9 Ga oxidative weathering of the continents using the Beaverlodge Lake paleosol, Northwest Territories, Canada. Geobiology, 17, 467–489.

Torsvik, T.H., and Meert, J.G. (1995) Early Proterozoic palaeomagnetic data from the Pechenga Zone (north-west Russia) and their bearing on Early Proterozoic palaeogeography. Geophysical Journal International, 122, 520–536.

Tribovillard, N., Algeo, T.J., Lyons, T., and Riboulleau, A. (2006) Trace metals as paleoredox and paleoproductivity proxies: An update. Chemical Geology, 232, 12–32.

Ventura, G.T., Gall, L., Siebert, C., Prytulak, J., Szatmari, P., Hürlimann, M., and Halliday, A.N. (2015) The stable isotope composition of vanadium, nickel, and molybdenum in crude oils. Applied Geochemistry, 59, 104–117.

Vorlicek, T., Helz, G.R., Chappaz, A., Vue, P., Vezina, A., and Hunter, W. (2018) Molybdenum burial mechanism in sulfidic sediments: Iron-Sulfide pathway. ACS Earth and Space Chemistry, 2, 565−576.

Wang, L., Han, X., Ding, S., Liang, T., Zhang, Y., Xiao, J., Dong, L., and Zhang, H. (2019) Combining multiple methods for provenance discrimination based on rare earth element geochemistry in lake sediment. Science of The Total Environment, 672, 264–274.

Wang, X., Planavsky, N.J., Hofmann, A., Saupe, E.E., De Corte, B.P., Philippot, P., LaLonde, S.V., Jemison, N.E., Zou, H., Ossa, F.O., and others (2018) A Mesoarchean shift in uranium isotope systematics. Geochimica Et Cosmochimica Acta, 238, 438–452.

Wang, Z., and Wu, M. (2014) Phylogenomic Reconstruction Indicates Mitochondrial Ancestor Was an Energy Parasite. PLOS ONE, 9, e110685.

Warke, M.R., Rocco, T.D., Zerkle, A.L., Lepland, A., Prave, A.R., Martin, A.P., Ueno, Y., Condon, D.J., and Claire, M.W. (2020) The Great Oxidation Event preceded a Paleoproterozoic “snowball Earth.” Proceedings of the National Academy of Sciences, 117, 13314–13320.

Waskom, M., Botvinnik, O., Gelbart, M., Ostblom, J., Hobson, P., Lukauskas, S., Gemperline, D.C., Augspurger, T., Halchenko, Y., Warmenhoven, J., and others (2020) Mwaskom/seaborn: Statistical data visualization. Zenodo.

Wei, W., Klaebe, R., Ling, H.-F., Huang, F., and Frei, R. (2020) Biogeochemical cycle of chromium isotopes at the modern Earth's surface and its applications as a paleo-environment proxy. Chemical Geology, 541, 119570.

Weill, D.F., and Drake, M.J. (1973) Europium Anomaly in Plagioclase Feldspar: Experimental Results and Semiquantitative Model. Science, 180, 1059–1060.

Weyer, S., Anbar, A.D., Gerdes, A., Gordon, G.W., Algeo, T.J., and Boyle, E.A. (2008) Natural fractionation of 238U/235U. Geochimica Et Cosmochimica Acta, 72, 345–359.

Wijsman, J.W.M., Middelburg, J.J., and Heip, C.H.R. (2001) Reactive iron in Black Sea Sediments: Implications for iron cycling. Marine Geology, 172, 167–180.

Williams, M.J., Schoneveld, L., Mao, Y., Klump, J., Gosses, J., Dalton, H., Bath, A., and Barnes, S. (2020) Pyrolite: Python for geochemistry. Journal of Open Source Software, 5, 2314.

Wu, L., Beard, B.L., Roden, E.E., and Johnson, C.M. (2011) Stable Iron Isotope Fractionation Between Aqueous Fe(II) and Hydrous Ferric Oxide. Environmental Science & Technology, 45, 1847–1852.

Yakovleva, V.V., and Gilyarova, M.A. (1960) The Middle Proterozoic. The north-western Onega area. In K.O. Kratz, Ed., Geology of the USSR. Karelian ASSR, vol. 37, pp. 138–152.

Yang, S., Kendall, B., Lu, X., Zhang, F., and Zheng, W. (2017) Uranium isotope compositions of mid-Proterozoic black shales: Evidence for an episode of increased ocean oxygenation at 1.36Ga and evaluation of the effect of post-depositional hydrothermal fluid flow. Precambrian Research, 298, 187–201.

Zachar, I., and Szathmáry, E. (2017) Breath-giving cooperation: Critical review of origin of mitochondria hypotheses. Biology Direct, 12, 19.

Zaremba-Niedzwiedzka, K., Caceres, E.F., Saw, J.H., Bäckström, D., Juzokaite, L., Vancaester, E., Seitz, K.W., Anantharaman, K., Starnawski, P., Kjeldsen, K.U., and others (2017) Asgard archaea illuminate the origin of eukaryotic cellular complexity. Nature, 541, 353–358.

Zimorski, V., Mentel, M., Tielens, A.G.M., and Martin, W.F. (2019) Energy metabolism in anaerobic eukaryotes and Earth's late oxygenation. Free Radical Biology and Medicine, 140, 279–294.

Appendix 1: Supplementary information to chapter 2

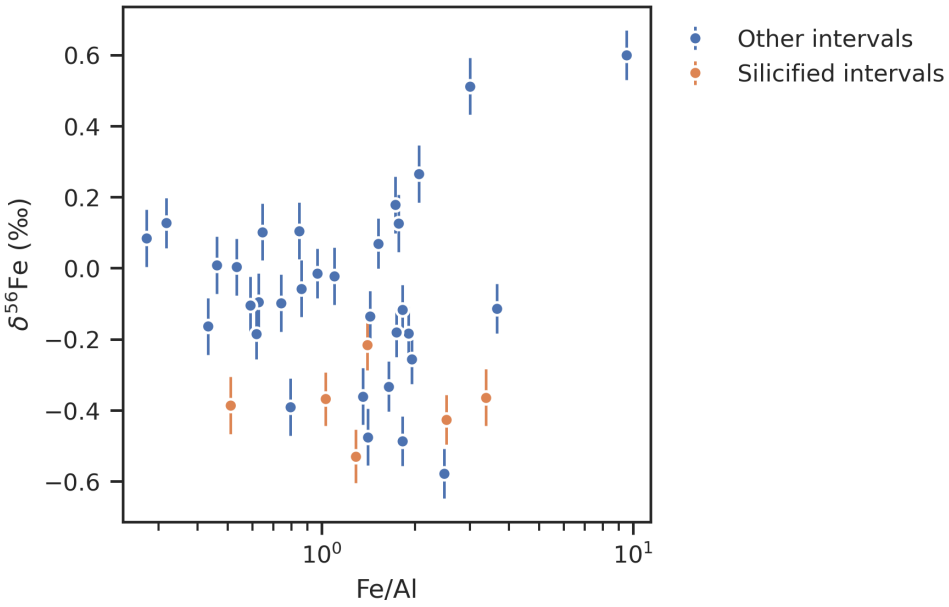

Figure A1: Cross-plot of Fe isotope ratios (δ^{56}Fe) and authigenic Fe enrichment (Fe/Al), highlighting samples from silicified intervals (77–70 m and 53–44 m).

Appendix 2: Supplementary information to chapter 3

Geological setting

The Zaonega Formation (ZF) is part of the Paleoproterozoic volcano-sedimentary succession of the Onega Basin in Karelia, northwestern Russia (Figure 1.1). It formed on the rifted margin of the Karelian craton in the Svecofennian Ocean and lies unconformably on Archean granites and gneisses (Melezhik et al. 1999b; Melezhik et al. 2013). The basin underwent regional greenschist facies metamorphism during the 1890–1790 Ma Svecofennian orogeny (Melezhik et al. 1999b). The ZF lies above the Tulomozero Formation, a shallow water ^{13}C-enriched carbonate and evaporite succession that records oxygenated seawater conditions (Melezhik et al. 1999a; Blättler et al. 2018), and is overlain by the basalts of the Suisari Formation (Melezhik et al. 1999b).

The ZF itself consists of a 1500 m-thick succession of graded greywackes, organic-rich mudstones, and carbonates interbedded and intersected by lava flows, tuff layers, and gabbro intrusions (Melezhik et al. 1999b; Črne et al. 2013). Sedimentation occurred in a rift basin of mixed shallow- and deep-water conditions and was punctuated by abundant turbidity current deposits (Črne et al. 2013, 2014; Melezhik et al. 2015). Synsedimentary volcanic activity—exemplified by peperite contacts of mafic intrusions into unconsolidated, wet sediments—resulted in localized contact metamorphism and initiated hydrocarbon generation and migration (Melezhik et al. 2004; Qu et al. 2012; Melezhik et al. 2013). The associated high nutrient flux fuelled an exceptionally productive microbial ecosystem that produced one of the oldest

phosphorites and one of the largest Paleoproterozoic organic carbon deposits (Melezhik et al. 2004; Lepland et al. 2014). While organic matter in most of the ZF has $\delta^{13}C$ values of ~−25‰ that are characteristic of CO_2 fixation, a section of the middle-to-upper ZF displays $\delta^{13}C_{org}$ values between −25‰ and −40‰, indicative of biomass contribution from methanotrophy (Qu et al. 2012, 2018). Distinctly positive $\delta^{34}S$ values of pyrite in the upper ZF have been interpreted as resulting from high microbial sulphate demand in an intermittently restricted basin (Paiste et al. 2018).

Age constraints of the Zaonega Formation

The upper bound for the age of the ZF canonically relies on the occurrence of ^{13}C-enriched carbonate rocks in the underlying Tulomozero Formation and the lowermost ZF (Melezhik et al. 1999a, 2015). These are viewed as recording the Lomagundi-Jatuli Event (LJE), which terminated in Fennoscandia at ~2060 Ma (Karhu and Holland 1996; Martin et al. 2013). The lower constraint is provided by cross-cutting dykes, dated 1919±18 Ma (Priyatkina et al. 2014), 1956±5 Ma (Stepanova et al. 2014), and 1961±5.1 Ma (Martin et al. 2015), as well as gabbro sills of the overlying Suisari Formation, dated to 1969±18 Ma (Puchtel et al. 1998) and 1988±34 Ma (Puchtel et al. 1999). The depositional age constraint on the ZF was recently provided by Martin et al. (2015), who dated a tuff in the lower part of the ZF to 1982±4.5 Ma. Although this new date has yet to be independently confirmed, we provisionally adopt a ~1980 Ma age for the ZF.

Fluid alteration effects

If RSE concentrations in the ZF are to be used to make global inferences about the paleoredox conditions contemporaneous to deposition, it must be determined if these enrichments are primary (i.e., representative of seawater) or the result of a secondary diagenetic/metamorphic overprinting. Many of the samples with the highest RSE concentrations in the OnZaP section are found in the 77–70 m and 53–44 m intervals (Figure 3.1). These intervals show evidence of alteration, including features characteristic of soft-sediment deformation, veining, and silicification (Paiste et al. 2018). Furthermore, hydrocarbon generation and migration is known to have occurred in the ZF (Melezhik et al. 1999b; Qu et al. 2012, 2018; Črne et al. 2013). These modifications occurred shortly following deposition, triggered by syn-depositional magmatic activity and the emplacement of gabbro sills into unlithified, wet sediments (Qu et al. 2012; Črne et al. 2013).

Nonetheless, there are a number of lines of evidence that these secondary processes had a limited effect on the inventory of RSE. First, the highest Mo enrichments correspond to the highest Mo isotope ratios (1.49±0.14‰; Figure 3.1) which is inconsistent with Mo being introduced by hydrothermal fluids that are characterized by low δ^{98}Mo values of 0.04±1.04‰ (Breillat et al. 2016; Kendall et al. 2017). Second, oil is generally depleted in Mo (Bell 1960; Migdisov et al. 2017) and migrating hydrocarbons in the upper ZF have been shown to be locally sourced (Qu et al. 2012, 2018), indicating only a minor effect on larger-scale RSE trends. Third, Mo and U enrichments within the confined interval in the upper ZF extend over the breadth of the Onega Basin, and are present in both the OnZaP and OPH sections that are separated by 60

km (Figures 1.2, 3.1). This clearly points to a basin-wide enrichment, instead of localized hydrothermal systems. Mo enrichments have also been reported from core C-175 studied by Asael et al. (2018) and cores FAR-DEEP 13A and 12AB studied by Lepland et al. (2014), all of which can be correlated to the studied OnZaP and OPH sections (Paiste et al. 2020). The most parsimonious explanation for the basin-wide enrichments, therefore, is a depositional event initiated by the establishment of transient water column conditions that were conducive to the sequestration of RSE.

In-situ microscale RSE mapping of rock slabs from the OnZaP section was used to further determine the potential role of hydrothermal and pyrobitumen veining on RSE distribution in the upper ZF. Microscale X-ray fluorescence (μXRF) mapping shows that Mo in RSE-replete horizons of the upper ZF is predominantly associated with laminated mudstone comprising the host rock, with individual laminae having variable concentrations (Figure A2a). Cross-cutting quartz and phyllosilicate veins permeate the sediments and occasionally act to concentrate Mo at vein margins, but have a negligible effect on bulk Mo concentration. Moreover, mudstones show Mo depletion at contacts to silicate veins, suggesting that any Mo mobilized was locally derived from the host mudstone and subsequently redistributed.

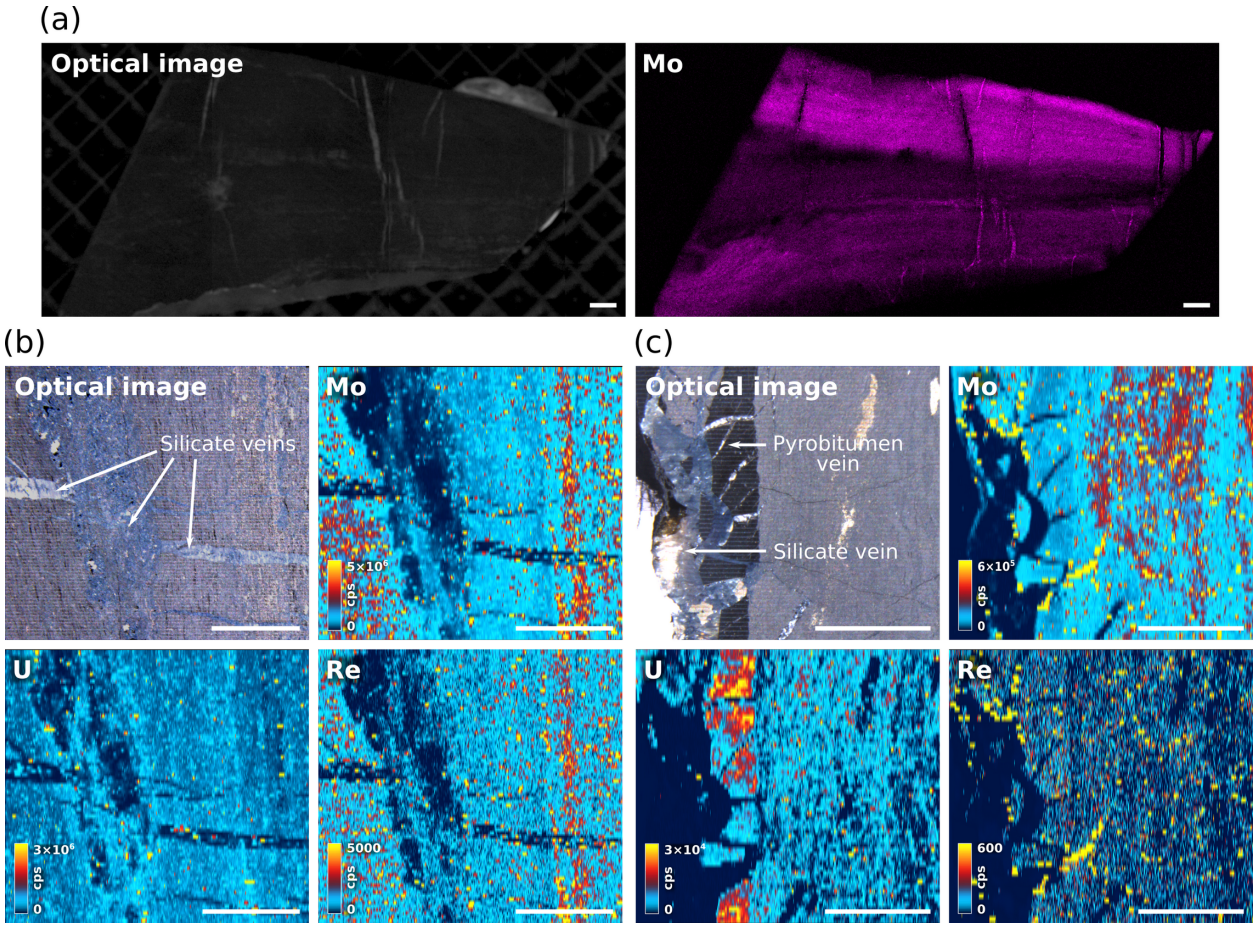

Figure A2: Distribution of RSE in Zaonega Formation mudstones and cross-cutting veins. (a) Optical microscope image and μXRF Mo abundance map of sample 4000943 slab (depth 46.36 m in the OnZaP section). (b) Optical microscope image and corresponding LA-ICP-MS abundance maps of Mo, U, and Re of sample 4000943 slab (depth 46.36 m in OnZaP section); bulk abundance 1009 μg g^{-1} of Mo, 34 μg g^{-1} of U, and 468 μg g^{-1} of Re. (c) Optical microscope image and corresponding LA-ICP-MS abundance maps of sample 4000988 slab (depth 74.35 m in OnZaP section); bulk abundance 291 μg g^{-1} of Mo, 50 μg g^{-1} of U, and 111 μg g^{-1} of Re. Scale bars represent 2 mm.

Laser ablation inductively coupled plasma mass spectrometry (LA-ICP-MS) mapping corroborates the observations from μXRF (Figure A2b,c). Mo is predominantly present in laminated sediments and seems to be much less abundant in silicate veins (though some minor concentration is observed on vein edges). Pyrobitumen veins are devoid of Mo, yet seem to concentrate U. Re follows a similar pattern to Mo, but shows a slight preference to pyrobitumen, compared to Mo (Figure A2b,c). Overall, these data preclude a significant role of veining on RSE distribution in the ZF (with the possible exception of U), even on a per-sample basis. Therefore, we suggest that Mo and U concentrations >100 μg g^{-1}, and Re >100 ng g^{-1}, can likely be regarded as primary environmental signals.

Factors controlling RSE accumulation in sediments

As a consequence of RSE reactivity under different redox conditions (Anderson et al. 1989; Miller et al. 2011), black shales effectively sequester Mo, U, and Re proportionally to their concentration in the overlying water column, which is in turn tied to the relative global proportion of marine oxic to anoxic water column conditions (Algeo and Lyons 2006; Partin et al. 2013; Sheen et al. 2018). This inference has led to several large-scale temporal surveys of RSE in black shales that generally supported a four-stage history of ocean oxygenation (Scott et al. 2008; Figure 3.2; Partin et al. 2013; Sheen et al. 2018). Low trace metal abundances in the Archean (generally <10 μg g^{-1} Mo and U, as well as <30 ng g^{-1} Re) point to prevailing anoxia with possible transient O_2. Moderate increases in RSE concentrations in the Paleoproterozoic (up to 100 μg g^{-1} Mo, 60 μg g^{-1} U, and 180 ng g^{-1} Re) are followed by a decline in the mid-Proterozoic, interpreted to reflect the rise and then a decline of ocean–atmosphere O_2 levels

(Konhauser et al. 2011; Partin et al. 2013; Reinhard et al. 2013). A conspicuous increase in RSE in black shales starting in the Neoproterozoic (up to thousands of μg g^{-1} Mo, 500 μg g^{-1} U, and 1000 ng g^{-1} Re) is consistent with the rise of O_2 to near-modern levels and the terminal oxygenation of the oceans (Och and Shields-Zhou 2012; Sahoo et al. 2012).

While compilations such as these rely on averaging of local conditions over many sections, it is important for our study to consider alternative mechanisms that can affect local RSE abundance. For instance, there are several factors that can explain low RSE concentrations without the need to invoke a predominantly anoxic ocean. Firstly, poor connectivity of the basin to the open ocean can lead to local drawdown of RSE—in the isolated Black Sea, euxinic conditions have resulted in highly efficient Mo drawdown leaving only ~0.3 nM of Mo in the bottom water and relatively low Mo concentrations of <40 μg g^{-1} in the topmost sediments (Algeo and Lyons 2006). Secondly, local RSE abundance is dependent on the uniformity or heterogeneity of RSE concentrations throughout the oceans, which is ensured in the modern by RSE residence times exceeding the mean ocean mixing time (Morford and Emerson 1999; Henderson and Anderson 2003; Miller et al. 2011). Poorly oxygenated oceans, however, must have lowered RSE residence times, which may have resulted in anomalously low sedimentary RSE concentrations where local RSE drawdown exceeded lateral input, even if the local basin wasn't strictly isolated. Third, inefficient Mo scavenging under low HS^- conditions can lead to low sedimentary Mo concentrations even in open-marine conditions (Helz et al. 1996).

In contrast, it is much more difficult to explain elevated RSE concentrations in black shales in a way that does not rely on the presence of a large global marine RSE pool. Nevertheless, one

important factor to consider is sedimentation rate—a longer residence time of sediments in the zone of RSE diffusion near the sediment-water interface will allow for higher accumulation of RSE (Andersen et al. 2014). For example, low sedimentation rates have been linked to high TOC accumulation in the U-rich black shales of the Miocene Monterey Formation, USA (Föllmi et al. 2005). While it is possible that low sedimentation rates enhance TOC and RSE accumulation in the ZF, it is unlikely that they were the primary control—the magnitude of RSE enrichment, rivalling Phanerozoic levels (Figure 3.2), requires an oxygenated, RSE-rich marine pool to draw upon. This is independently confirmed by highly enriched $\delta^{238}U$ data that require low rates of global anoxic U drawdown (Figure 3.2) (Andersen et al. 2014). Another remote possibility is that, if the Onega Basin was highly restricted, the local RSE pool could have been enriched by the weathering flux from a proximal RSE-rich ore body. However, given that the RSE-enriched horizon, several tens of meters thick, extends throughout the ~200 km diameter basin, it is implausible for the implied volumes of RSE to be supplied by a single point weathering source. Furthermore, the highest $\delta^{98}Mo$ values occur in the parts of the section that have highest Mo concentrations (Figure 3.1). Had most of the Mo in that interval been derived from the weathering of a proximal Mo-rich ore body, $\delta^{98}Mo$ would instead be expected to correspond to values around ~0.3‰ that are characteristic of igneous Mo-bearing sulphide minerals (Breillat et al. 2016). A more likely explanation for RSE enrichment, then, is that the ZF was a highly efficient RSE sink that had reliable access to a large oceanic RSE inventory (though some modest restriction was required to sequester appreciable amounts of Mo; Algeo and Lyons (2006); Sahoo et al. (2012)].

Redox evolution in the upper ZF

Primary changes in RSE abundance through the upper ZF should reflect changes in redox and hydrographic conditions during deposition. Indeed, RSE trends through the OnZaP and OPH sections agree well with independent studies on the redox evolution of the upper ZF (Melezhik et al. 2004; Qu et al. 2012, 2018; Melezhik et al. 2013; Lepland et al. 2014; Paiste et al. 2018). Based on petrological and sedimentological features, such as intermittent turbidites, peperite contacts marking the emplacement of mafic intrusions in wet, unconsolidated sediments, pyrobitumen veining, and phosphorite layers, the ZF is thought to mostly represent deep water deposition in a magmatically active basin that experienced hydrocarbon generation/seepage (Melezhik et al. 2004; Melezhik et al. 2013) and redox fluctuations. Paiste et al. (2018) has shown that these conditions extend to the 102–44 m interval in the OnZaP section and that the interval was also host to an active methane and S-cycling microbial community (Qu et al. 2012, 2018; Lepland et al. 2014; Paiste et al. 2018).

Our RSE data support this interpretation, with Mo, U, and Re all following similar trends. Mo concentrations, for example, remain below 95 μg g^{-1} in the lower part of the OnZaP section until ~80 m depth, above which they increase gradually up to ~400 μg g^{-1} at 53 m, consistent with the onset of anoxia and more efficient RSE drawdown (Figure 3.1). While the presence of early-diagenetic pyrite in the form of 30–100 μm-sized ellipsoidal clusters suggests that HS^- was restricted primarily to shallow pore waters throughout most of the OnZaP section (Paiste et al. 2018), highly enriched and variable RSE content in the 53–44 m interval (Mo concentrations vary between ~20−1000 μg g^{-1} and reach their highest value at 46 m depth) shows that redox

conditions became significantly more variable. This is supported by the occurrence of phosphorite layers in the same interval (Figure A6)—correlative samples form a nearby outcrop have been shown to bare putative indication of phosphogenic S-cycling microbes inhabiting a fluctuating sulphidic–(sub)oxic redoxcline close to the water–sediment interface (Lepland et al. 2014). Variable redox conditions may have been the result of intermittent basin restriction, similar to modern anoxic basins (Scholz et al. 2018), where periodic inputs of oxic water replenish RSE that are then sequestered in sediments when euxinia develops during stagnant periods. Above 44 m depth, TOC and pyrite abundance gradually decreases, until petrographic markers of potentially shallower and more restricted hydrographic conditions become present at 33 m (Paiste et al. 2018). Furthermore, increasing $\delta^{13}C_{org}$ and $\delta^{34}S$ values have been used to suggest a change to variable (sub)oxic conditions (Paiste et al. 2018). This shift is also borne out by decreasing Mo and U abundances that approach crustal levels above 33 m (Mo concentrations fall to below 10 μg g^{-1}; Figure 3.1), whereas Re, which also accumulates in suboxic conditions, remains partially enriched above 2 ng g^{-1} (Morford et al. 2005). Collectively, redox conditions in the OnZaP section were most favourable for the drawdown of RSE during the deposition of organic-rich mudstones intercalated with dolostone beds at depths between 76–44 m.

Molybdenum isotopes

The Mo isotope system provides additional constraints on marine Mo cycling and ocean redox conditions (Siebert et al. 2003). The most significant input of Mo to the oceans is riverine transport of dissolved MoO_4^{2-}, which has a modern average $\delta^{98}Mo$ of ~0.2‰ (Siebert et al. 2003; Voegelin et al. 2012). Amongst the sinks, Mo adsorption to Mn(IV)-oxides in oxic environments

is the most consequential, as it imparts the largest isotope fractionation at about −3.3‰ (Barling et al. 2001; Siebert et al. 2003). However, in strongly euxinic environments, Mo removal into sediments is often near-quantitative with only minor fractionation (Barling et al. 2001; Siebert et al. 2003; Arnold et al. 2004; Neubert et al. 2008). Intermediate redox conditions lead to variable Mo fractionation from seawater to sediment; an average of about −0.7‰ is commonly assumed (Poulson et al. 2006; Siebert et al. 2006; Poulson Brucker et al. 2009; Goldberg et al. 2012; Dickson et al. 2014). Due to widespread oxic conditions in modern oceans and the large fractionation imparted by adsorption onto Mn(IV)-oxides, the residual marine pool has been enriched to 2.36‰ δ^{98}Mo (Barling et al. 2001; Siebert et al. 2003; Nakagawa et al. 2012). Accordingly, less oxidized marine conditions in the Proterozoic would have been characterized by lower seawater δ^{98}Mo values (Arnold et al. 2004). It also follows that strongly sulphidic sediments, where Mo removal is quantitative, can faithfully record this signal, allowing the use of black shale δ^{98}Mo as a paleoredox proxy (Barling et al. 2001; Arnold et al. 2004; Neubert et al. 2008; Kendall et al. 2017).

Despite the ZF being predominantly a black shale succession, interpreting the Mo isotope record in the OnZaP section is difficult for several reasons. Under euxinic conditions with HS^- <11 μM, fractionation between intermediate thiomolybdate species can result in significant offsets between seawater and sediment δ^{98}Mo (Tossell 2005; Neubert et al. 2008; Nägler et al. 2011; Wagner et al. 2017), and verifying euxinia in the upper ZF section has proven difficult. Fe speciation, the most-accepted method for tracking euxinic conditions (Poulton and Canfield 2005, 2011), can be affected by Fe mobilization and (re-)precipitation (Slotznick et al. 2018). Fe

speciation is biased in the upper ZF due to the presence of Fe-rich carbonates and secondary pyrrhotite (Asael et al. 2013; Paiste et al. 2018). Early diagenetic pyrite, evident as 30–100 μm-sized ellipsoidal clusters, have been taken as evidence for the restriction of HS^- to pore waters (Paiste et al. 2018), and so has phosphorite accumulation in the same interval (Figure 3.1; Lepland et al. 2014). Modern phosphorites do not accumulate in euxinic basins, but rather in suboxic ones with euxinia confined to the immediate subsurface, as is preferred by polyphosphate-cycling microorganisms (Crosby and Bailey 2012). In contrast, enriched $\delta^{238}U$ values suggest euxinia, as such values require U reduction in the water column; the latter of which likely scales with S reduction rates (Barnes and Cochran 1993; Andersen et al. 2014).

The second prerequisite for quantitative Mo drawdown is the establishment of a restricted basin (Algeo and Lyons 2006; Kurzweil et al. 2015; Dickson 2017; Lu et al. 2017). The $\delta^{98/95}Mo$ of modern seawater (2.36‰) is only captured in sediments of the heavily restricted Black Sea (Algeo and Lyons 2006; Neubert et al. 2008), while sediments in the less restricted, but HS^--replete Cariaco Basin are fractionated by about −0.7‰ from seawater values (Arnold et al. 2004; Algeo and Lyons 2006). Partial restriction of the Onega basin has been suggested to explain S-isotope systematics in the ZF (Paiste et al. 2018), and some restriction is required to capture non-trivial amounts of Mo in sediments (Algeo and Lyons 2006). However, as discussed above, tens of meters of sediment with a Mo concentration over several hundred μg g^{-1} could not have accumulated in a Black Sea-like setting without relatively frequent deep water replenishment. Furthermore, Kurzweil et al. (2015) suggested that a negative correlation between $\delta^{98}Mo$ and Mo concentrations would be indicative of a Mo drawdown regime favourable for quantitative

capture, but the reverse is observed in the OnZaP section—Mo isotope ratios show a positive tendency with increasing Mo concentrations (Figure A3), suggesting that Mo was not quantitatively sequestered in the ZF. Accordingly, the sedimentary δ^{98}Mo recorded in the upper ZF should be somewhat depleted relative to seawater (Dickson 2017).

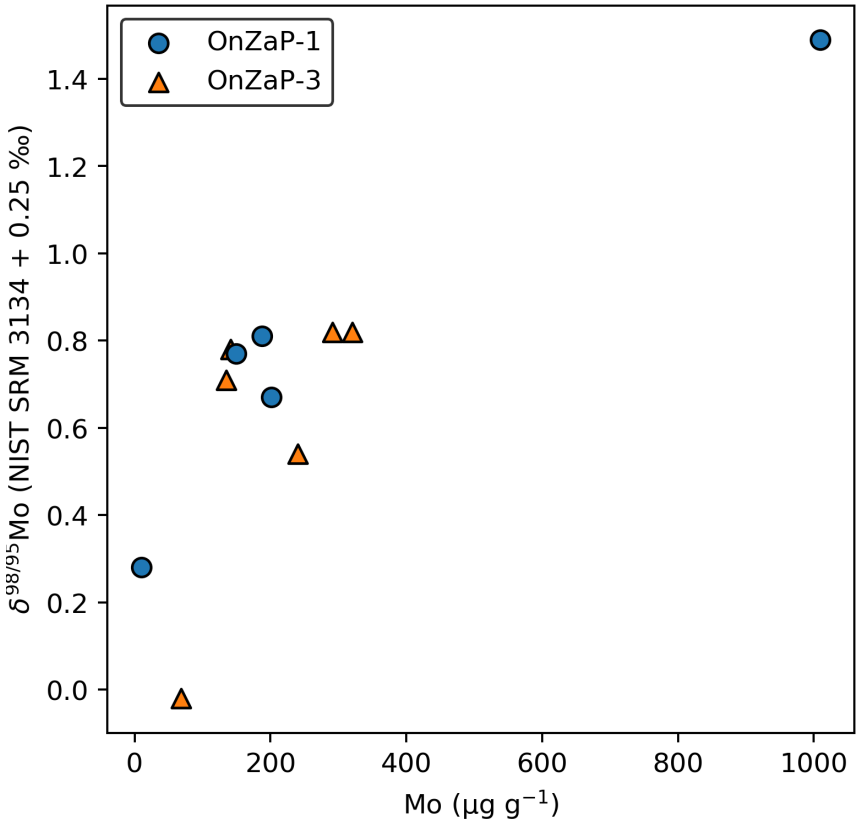

Figure A3: Crossplot of Mo concentration and δ^{98}Mo in the OnZaP section.

Given that almost all known Mo fractionation processes lead to the depletion of ^{98}Mo in sediments (Kendall et al. 2017), the δ^{98}Mo data presented here can be considered a minimum estimate for seawater at ~2000 Ma. In the OnZaP section, average δ^{98}Mo is relatively low at 0.67±0.81‰, but reaches a maximum of 1.49±0.14‰ at 46.36 m (Figure 3.1). While this isolated

maximum value could be anomalous, similar values have been reported from the ZF interval ~50 m below the OnZaP section in the core FAR-DEEP 13A (as correlated via a P-rich dolostone marker horizon; Paiste et al. 2020), drilled 200 m from the OnZaP drilling sites (Asael et al. 2013). Though samples from euxinic intervals in Asael et al. (2013) had a similarly low average δ^{98}Mo of 0.73±0.21‰, three measurements exceeded 1‰, with a maximum value of 1.29±0.11‰. Likewise, Asael et al. (2018) examined the C-175 and C-5190 cores (drilled ~20 and ~40 km from the OnZaP site, respectively, and possibly representing a stratigraphic section of the upper ZF beginning >300 m below the OnZaP section and extending to its lower half; Paiste et al. 2020), where samples from euxinic intervals had an average δ^{98}Mo of 0.70±0.21‰, with eight measurements surpassing 1‰, and some reaching as high as 1.83±0.11‰. These authors considered averages of samples from euxinic intervals representative of seawater δ^{98}Mo with the highest values attributed to distillation effects in a temporarily restricted basin (Asael et al. 2013).

Alternatively, we propose that the requisite conditions for quantitative capture of seawater δ^{98}Mo were effectively absent during deposition of the upper ZF, either due to relatively open-marine conditions, insufficient water column HS^-, or Mn(IV)-oxide cycling. Given this view, the small number samples in the ZF that record values ≥1.4‰ likely represent periods of more quantitative capture of seawater values that may be attributed to increased basinal restriction or transient increases in water column HS^-. A minimum seawater δ^{98}Mo value of ~1.4‰ is comparable to other Proterozoic successions, including those deposited during the LJE (Partin et al. 2015; Asael et al. 2018), but is modest compared to Phanerozoic seawater. Thus, the Mo

isotope record in the ZF is compatible with an oxygenated ocean but cannot itself preclude anoxic conditions.

Uranium isotopes

Redox processes in marine environments have been found to induce significant U isotope fractionation (Weyer et al. 2008), allowing the U isotope system to become widely utilized in paleoredox studies. Oceanic $\delta^{238}U$ in the modern world is −0.39±0.01‰ (Tissot and Dauphas 2015) and varies little in the open ocean, as U is present in oxic seawater as uranyl $[U(VI)O_2]^{2+}$ that forms highly stable carbonate complexes; as such, the residence time of U in seawater is in the order of ~400 kyrs (Ku et al. 1977), far exceeding the ~1 kyr ocean mixing time (Sarmiento and Gruber 2006). Seawater $\delta^{238}U$ reflect the balance between the riverine U source, and between different sedimentary U sinks. Rivers, being the major U input into oceans (Dunk et al. 2002), carry a mean $\delta^{238}U$ value of ~−0.34‰ (Andersen et al. 2016), within error of estimates of the −0.29±0.03‰ continental crust (Tissot and Dauphas 2015). Amongst major sinks, anoxic sediments and euxinic sediments prefer ^{238}U, leaving residual seawater depleted in comparison to riverine inputs (Andersen et al. 2017). Mn- and Fe-oxides bury isotopically light U, but this is a relatively minor sink (Andersen et al. 2017). Incorporation into carbonates formed in the water column is generally thought to impart only minor fractionation on U isotopes (Romaniello et al. 2013). Hydrothermal processes operating at mid-ocean ridges cycle seawater U through hot, highly reducing, deep mafic rocks, where U is reduced and incorporated into altered oceanic crust. This can be quantitative or impart a positive $\delta^{238}U$ fractionation (Andersen et al. 2015; Noordmann et al. 2016). Sediments underlying fully anoxic waters have the great potential to

shape seawater $\delta^{238}U$ values. These constitute the most effective U sinks per unit of area (Dunk et al. 2002) and effect the highest fractionation from seawater $\delta^{238}U$. Modern anoxic basin sediments contain values between −0.2‰ and 0.4‰; even larger fractionations are possible when reduction happens in the water column instead of the sediment pile (Andersen et al. 2017). The marine U pool is highly sensitive to the extent of strongly anoxic basins and at times in Earth history where the anoxic sink was increased in prevalence—e.g., at times of lower oxygenation in the Precambrian—seawater $\delta^{238}U$ is expected to have been lower.

Therefore, there has been extensive research targeting the U isotope composition of ancient sediments that can record seawater $\delta^{238}U$ as a proxy for the oxygenation of the ocean–atmosphere system (see Andersen et al. 2017). The first sedimentary $\delta^{238}U$ enrichments are reported from the Meso- and Neoarchean, suggesting oxic weathering, local U burial in anoxic sediments, and at least locally depleted $\delta^{238}U$ compared to modern seawater values (Kendall et al. 2013; Wang et al. 2018). $\delta^{238}U$ values increase in the Paleoproterozoic (Wang et al. 2018), whereas the mid-Proterozoic record is, as of yet, sparse: carbonates from the time period display $\delta^{238}U$ values similar to modern seawater, implying limited marine euxinia (Gilleaudeau et al. 2019), while shale $\delta^{238}U$ allow for more anoxic conditions (Yang et al. 2017). A near-modern seawater U balance is thought to have been established by the Ediacaran (Kendall et al. 2015), with some fluctuations associated with Phanerozoic anoxic events (e.g, Dahl et al. 2014).

Aside from carbonates, many studies utilize anoxic shales as $\delta^{238}U$ archives. Uranium fractionation in anoxic sediments is imparted during the reduction of uranyl to U(IV) that, given the slow kinetics, is thought to occur mainly in sediment pore waters, catalyzed by microbial

enzymes (Anderson et al. 1989). Experimental and modelling studies suggest that the equilibrium fractionation factor in U reduction is ~1.2‰ (Abe et al. 2008; Stirling et al. 2015; Andersen et al. 2017), yet given diffusion limitations into the sediments, the effective fractionation is normally half of that (Andersen et al. 2014). Interpretation of shale $\delta^{238}U$ is complicated by several factors. (1) The extent of fractionation from seawater to anoxic shales is highly dependent on the specific redox state of the depositional environment, i.e., the depth of oxygen penetration into sediments or the redox state of the bottom waters (Andersen et al. 2014). (2) Basinal restriction, like in the modern Black Sea (Noordmann et al. 2015), can lead to significant bottom water U drawdown and modulation of local seawater $\delta^{238}U$ due to back-diffusion of depleted sediment pore water. The result is significant difference between the effective and intrinsic fractionation (Andersen et al. 2017). (3) If sedimentation rates are high, detrital or carbonate contamination may play a large part in the sediment U budget and isotope composition; methods have been developed to correct for such contamination (Asael et al. 2013; Andersen et al. 2016). (4) In the Precambrian, the prevalence of anoxic basins might have resulted in effective U drawdown and short seawater U residence times (Partin et al. 2013); due to the $\delta^{238}U$ variability of local riverine input (−0.70 to 0.06‰ in the modern; Andersen et al. 2016), seawater $\delta^{238}U$ might then have become heterogeneous, and could have ceased to reflect global, as opposed to local, U cycling (Andersen et al. 2017). In summation, there are several possible non-unique ocean redox states for most shale $\delta^{238}U$ values.

That the ZF contains anomalously high U concentrations (up to 238 μg g^{-1}, rivalling even modern sediments in anoxic settings), however, imposes significant constraints on these

uncertainties. These concentrations require that the Onega Basin retained reliable access to an extensive marine U pool during ZF deposition, which precludes the possibility of the local marine $\delta^{238}U$ being affected either by ocean U heterogeneity or local water column U depletion. Significant detrital or carbonate contamination is, likewise, negated by the high total U content. The average U content of our $\delta^{238}U$ samples is 55±41 μg g^{-1}, whereas the upper crust, a proxy for detrital material, only contains 2.7 μg g^{-1} of U on average (Rudnick and Gao 2014) and primary carbonates ~1 μg g^{-1} (Romaniello et al. 2013)—hence, only a minor fraction of U could be derived from contamination in these samples.

The U isotope composition in the ZF is, therefore, a product of local water column and sediment redox conditions and the balance of marine U sinks, i.e., global marine redox conditions. Our average $\delta^{238}U$ is 0.48±0.28‰, whereas the highest values, up to 0.79‰, are anomalous in the shale $\delta^{238}U$ record (Figure 3.2). The typical fractionation between anoxic water columns and the underlying sediments is 0.6–0.8‰ (Andersen et al. 2014), and subtracting that from our data, we would arrive at an average estimated seawater $\delta^{238}U$ between −0.32 to −0.12‰. These values are somewhat higher, but comparable, to the modern −0.39‰ seawater value and imply a near-modern or lesser significance of anoxic basins as a marine U sink. However, it is not possible to explain the highest $\delta^{238}U$ values of nearly 0.8‰ merely by modulating the extent of ocean anoxia—one would arrive at seawater $\delta^{238}U$ values exceeding the average crustal source of −0.29‰ (Tissot and Dauphas 2015), which is considered highly unlikely in the current understanding of marine U systematics (Andersen et al. 2017). Instead, the effective fractionation between anoxic seawater and the underlying sediments must have

exceeded the typical values (Andersen et al. 2014), likely due to a shift in the locus of U reduction into the water column, as is observed in Unit II of the Black Sea (Andersen et al. 2014). Water column U reduction requires high organic matter loading and high water column sulphate reduction rates. This conclusion is not unexpected—the ZF is known for extraordinary C_{org} abundance that must, in part, be attributed to a highly productive local ecosystem (Qu et al. 2012; Lepland et al. 2014; Paiste et al. 2018). Further, the ZF $\delta^{238}U$ data require seawater $\delta^{238}U$ values not substantially lower than the modern value, which in turn requires a prevalence of euxinic conditions on the seafloor similar to, or lower than, the modern world.

The ZF $\delta^{238}U$ record has previously been studied by Asael et al. (2013) from a section of the FAR-DEEP 13A core (drilled close to the OnZaP coring sites, but ~50 m lower in stratigraphy; Figure 1.2; Paiste et al. 2020). These data, despite being significantly more depleted, are consistent with our findings—even though their measured $\delta^{238}U$ averaged only 0.07±0.18‰, this was likely due to the significantly lower U concentrations in their samples, on average 5±3 μg g^{-1}. In such a case, the detrital component could exert a large effect on sample $\delta^{238}U$ composition. After being corrected for detritus, the average shifted to 0.35±0.22‰, placing these values well within the uncertainty expected for different burial U isotope fractionations. Further, given the low enrichments in the FAR-DEEP 13A core, U(VI) reduction almost certainty occurred within the sediment pile leading to a muted fractionation.

RSE normalized to organic carbon content

Total organic carbon in the OnZaP section and the studied OPH section is amongst the highest of all sections included in RSE compilations (Scott et al. 2008; Partin et al. 2013; Sheen et al. 2018), and as such, RSE concentrations in the upper ZF are slightly muted when normalized to TOC. Even so, the normalized RSE abundances still rank among the highest before the Neoproterozoic, supporting our interpretations of a large marine RSE inventory (Figure A4).

A linear relationship between sediment Mo and TOC content has been observed in many modern and ancient euxinic basins, a result of the importance of organic phases in scavenging Mo from anoxic waters (Algeo and Lyons 2006; Chappaz et al. 2014; Dahl et al. 2017; Wagner et al. 2017). A seminal study by Algeo and Lyons (2006) found that in restricted anoxic basins, Mo/TOC ratios in organic-rich sediments scale with deep water Mo concentration, allowing for its use in constraining local hydrographic and redox conditions. Deep water Mo concentration has a first-order dependency on the size of the marine Mo pool, but is modulated by the degree of deep water restriction because if water exchange is limited, anoxic Mo scavenging rates can exceed the replenishment rates, leading to depletion of dissolved Mo (Algeo and Lyons 2006). The highest sediment Mo/TOC was found in weakly restricted basins with intermittently or weakly euxinic bottom waters, where deep water flushing events are sufficiently common that Mo is not drawn down significantly, but where HS^- could still accumulate enough to convert MoO_4^{2-} to particle-reactive $MoO_xS_{4-x}^{2-}$ phases (Helz et al. 1996; Algeo and Lyons 2006). This effect is amplified by the efficient operation of the Mn(IV)-oxide shuttle in mildly or intermittently euxinic conditions (Emerson and Huested 1991; Crusius et al. 1996; Morford and

Emerson 1999; Algeo and Lyons 2006; Algeo and Tribovillard 2009). Since the oxidation state of the oceans is poorly constrained in the Precambrian, Mo/TOC serves mainly as a proxy of deep water Mo concentrations, which can be related to the size of the global marine Mo pool only if local basinal restriction can be constrained via independent means.

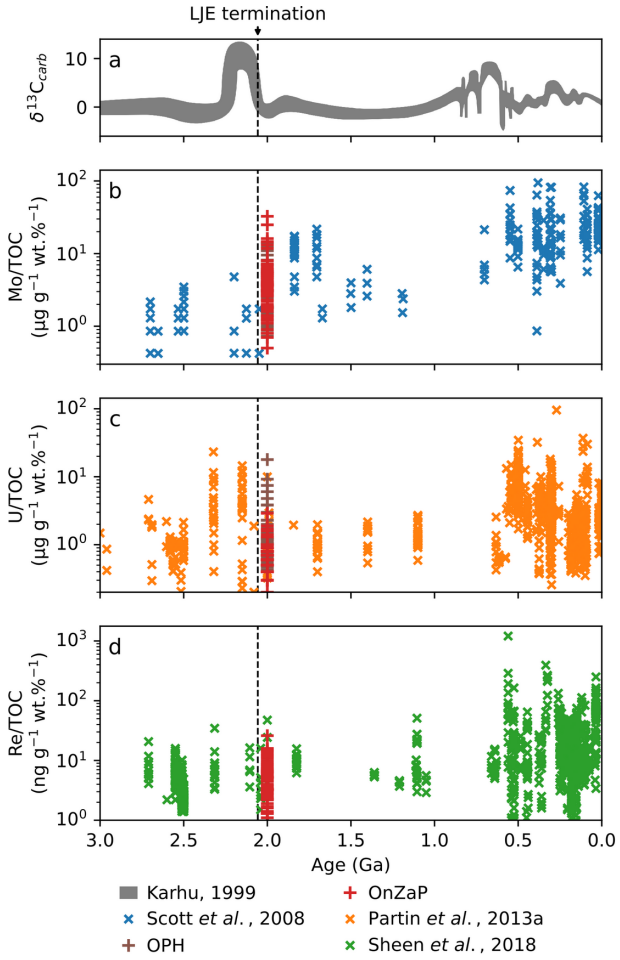

Figure A4: Secular trends in $\delta^{13}C_{carb}$, as well as Mo/TOC, U/TOC and Re/TOC ratios of anoxic shales. Data from Karhu (1999), Scott et al. (2008), Partin et al. (2013), and Sheen et al. (2018), respectively, along with measurements from this study.

The average slope of Mo/TOC covariation in non-carbonate/organic-rich samples of the ZF is 5.11 μg g^{-1} wt.%$^{-1}$, comparable to the modern Black Sea, in which deep water Mo is 0.2–0.3 nM, ~20–30 times less than the open ocean on a salinity-normalized basis (Figure A5; Algeo and Lyons 2006). The exceptions are the 78–70 m and 53–44 m intervals of the OnZaP section, and the 1125–1100 m interval in the OPH core, where Mo/TOC reaches maximum values of 32.6 μg g^{-1} wt.%$^{-1}$ and 13.85 μg g^{-1} wt.%$^{-1}$, respectively. These relatively enriched intervals could represent periods when the ZF entered the type of hydrographic conditions most susceptible to Mo scavenging i.e., mild and intermittent deep water restriction and a fluctuating and weak euxinia. This is supported by the co-occurrence of the highly variable Mo concentrations in that same interval (Figure 3.1).

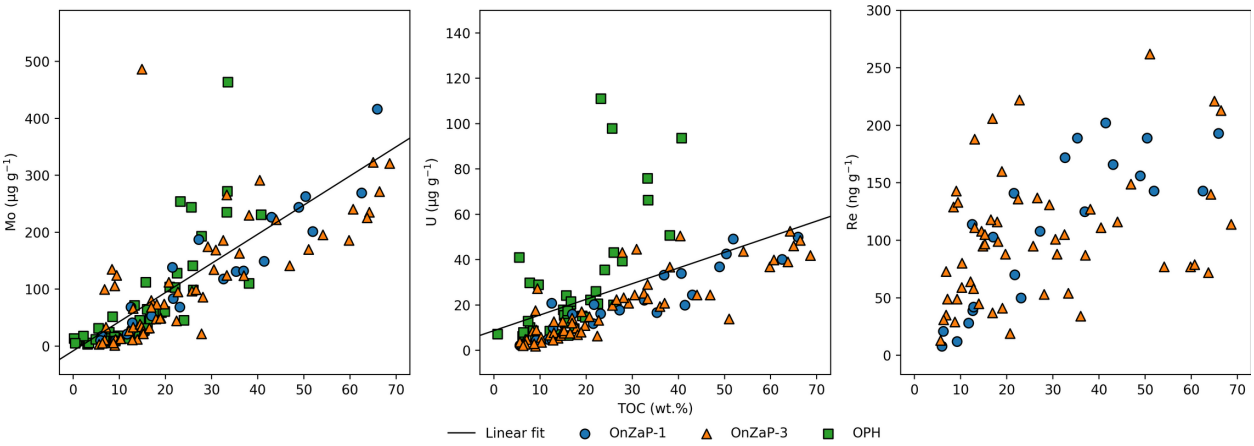

Figure A5: Covariation of total organic carbon (TOC) and RSE concentrations in the OnZaP section and OPH core.

Despite these intervals of high values, the dominant Mo/TOC trend of 5.11 μg g^{-1} wt.%$^{-1}$ is modest, in a puzzling contrast to the extremely high Mo concentrations. There are several

potential explanations for this discrepancy. First, it is possible that upper ZF sediments, containing >60 wt.% TOC, were sufficiently efficient at scavenging trace metals to deplete the local deep water of dissolved Mo even under conditions of only modest restriction. Further work on the applicability of the Mo/TOC proxy in situations of high organic matter accumulation is needed to test this; Algeo and Lyons (2006) only calibrated their proxy up to 20 wt.% TOC. Second, if the Onega basin had a relatively unrestricted connection to the ocean, rapid water mixing would have made water column HS^- accumulation rare, precluding the presence of particle reactive Mo phases. The unrestricted modern Namibian shelf, for example, has a sediment Mo/TOC ratio of only ~6±3 μg g^{-1} $wt.\%^{-1}$, despite abundant deep water Mo (Algeo and Lyons 2006). This interpretation is supported by Paiste et al. (2018), who, based on pyrite petrography, argued that HS^- in the ZF was confined mostly to pore waters. Third, the applicability of the Mo/TOC proxy to Precambrian sediments is questionable in itself. Algeo and Lyons (2006) considered that a wholesale drawdown of the trace metal inventory during global anoxia might fundamentally change the Mo–TOC relationship, so that their calibration might not hold. Furthermore, the average composition of marine organic matter and how it was processed in the sediment pile might have been somewhat different in the Paleoproterozoic, affecting its reactivity to trace metals.

Enrichment factors

Enrichment factors (EF) are way of presenting RSE content that corrects for the effects of detrital input and facilitates comparison between different elements (Algeo and Tribovillard 2009). The RSE concentrations are corrected for the Al concentration of the sample and the

average content of the upper continental crust (Taylor et al. 2001) using the formula $X_{EF} = (X/Al)_{sample}/(X/Al)_{crust}$. In the studied section of the ZF, EFs confirm the high authigenic enrichment of RSE and tightly correspond to TOC and RSE concentrations. Whereas a substantial authigenic enrichment starts at X_{EF} >10 (Algeo and Tribovillard 2009), Mo_{EF} in the ZF reaches a maximum of 2019, U_{EF} up to 1425, and Re_{EF} up to 6770 (Figure A6).

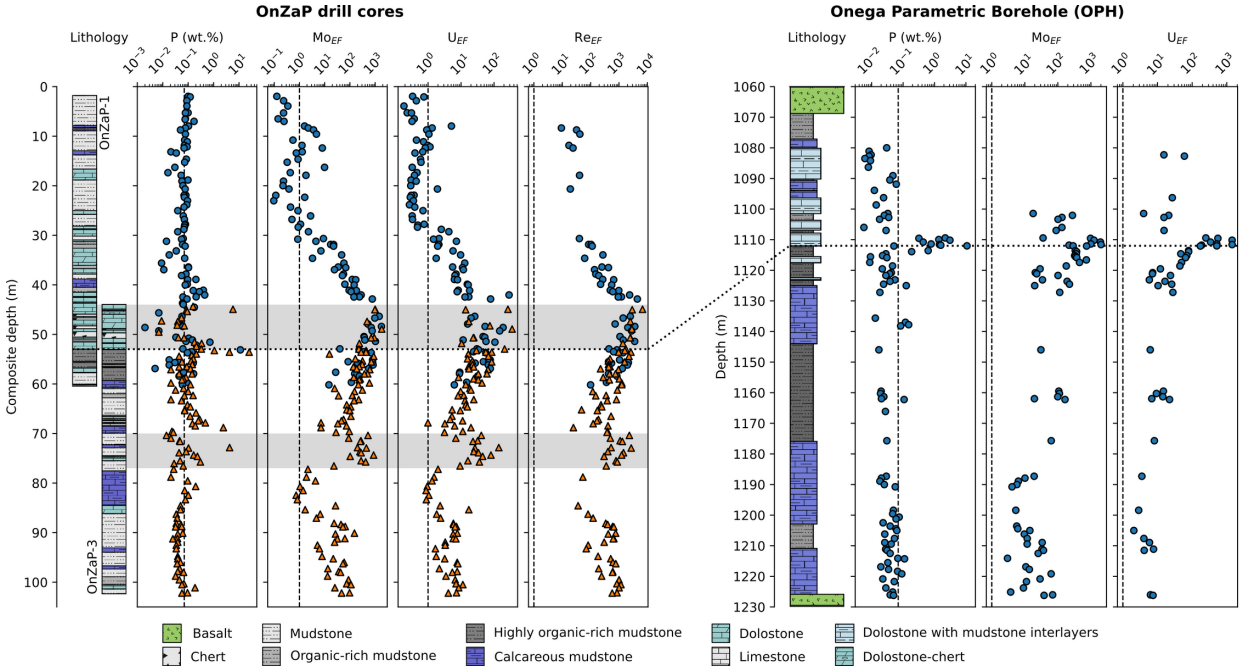

Figure A6: Phosphorus concentrations and redox-sensitive metal enrichment factors. Phosphorus content illustrates the P-rich mudstone-dolostone contact that is used for intra-basinal correlation. For reference to plot elements see caption of Figure 3.1.

Supplementary methods

Mo isotopes

Mo isotopes were measured from digested OnZaP MSP0010 samples and all preparation was done in a class 1000 clean laboratory using Mo-free chemicals and equipment. Samples were doped with a ^{97}Mo–^{100}Mo double spike in a constant ratio of spike/sample in order to track any isotope fractionation during sample purification and to correct for instrumental mass bias (Siebert et al. 2001). Mo was purified via two-stage column chromatography adapting from the protocol of Asael et al. (2013), using Biorad AG 1-X8 anion exchange resin and Biorad AG 50W-X8 cation exchange resin. The purified Mo solution was measured for isotope composition in the Pôle Spectrométrie Océan, IFREMER, Brest, France, using a Thermo Scientific Neptune multicollector ICP-MS. δ^{98}Mo was obtained through the double spike deconvolution method of Siebert et al. (2001). Each sample was bracketed with and corrected to measurements of the in-house standard Mo-SPEX that demonstrated a 2SD reproducibility of 0.13‰. Data were acquired relative to Mo-SPEX and expressed relative to NIST SRM 3134 = 0.25‰ (Nägler et al. 2014), as per the following equations:

$\delta^{98}Mo_{Mo\text{-}SPEX} = \delta^{98}Mo_{RochMo2} - 0.05 \pm 0.06$‰ (Asael et al. 2013);

$\delta^{98}Mo_{RochMo2} = \delta^{98}Mo_{SRM3134} - 0.34 \pm 0.05$‰ (Goldberg et al. 2013).

U isotopes

Uranium isotopes of samples from the OPH drill core were measured at the Yale Metal Geochemistry Center, Yale University, USA. Sample digestion, U separation, and isotope measurements were performed in a Pico-trace clean laboratory. The samples were digested in a mixture of 3 ml concentrated HNO_3 and 1 ml HF at 100°C for 24 hours, evaporated to dryness, then digested in aqua regia at 95°C for another 24 hours, evaporated to dryness, and taken up in 5 ml 3M HNO_3 at 70°C. Uranium separation and isotope measurement followed the method outlined in Wang et al. (2018). To monitor instrumental mass bias and potential fractionation during laboratory treatment, the samples were doped with proper amounts of IRMM-3636 233/236 U double spike to yield a $^{238}U/^{236}U$ ratio of ~30 (following Weyer et al. 2008). Uranium was separated from matrix elements chromatographically, in columns of UTEVA ion exchange resin (with two stages of column chemistry; based on Weyer et al. 2008). Isotope values were measured on a Thermo Neptune Plus MC-ICP-MS, with every set of three samples bracketed by concentration matched CRM 112a standard (New Brunswick Laboratory, USA Dept. of Energy) in order to check for instrumental drift. Accuracy and precision were further monitored with routine measurements of concentration matched standards: CRM129a (New Brunswick Laboratory, USA Dept. of Energy) was −1.71±0.13‰ (2SD, n=27), and in-house Ricca ICP solution was −0.22±0.11‰ (2SD, n=25). These standard measurements agree with the results of previous studies (Zhang et al. 2018a, 2018b, 2019). Instrumental error was found to be less than 0.15‰ in all samples. U isotope ratios are reported in relation to the CRM-112a standard, defined as $\delta^{238}U = 0‰$.

In-situ RSE measurements

μXRF elemental maps were acquired from polished slabs at IUEM, Brest, France using a Bruker Tornado M4 μXRF system equipped with a Si drift detector and a Rh source operating at 50kV and 600 μA. A spot size of 20 μm was employed with a dwell time of 6 ms per pixel, and mapping was performed under vacuum. Image processing included spectral deconvolution and 3-pixel averaging.

LA-ICP-MS measurements were taken from polished slabs in the University of Tartu, Estonia on an Agilent 8800 ICP-MS in single quad mode coupled to a Cetac LSX-213 G2+ laser ablation unit with a HelEx II fast-washout two-volume large-format cell using 800 ml min^{-1} He as carrier gas. Relative element abundance maps of sample 4000943 were interpolated from parallel scans moving left to right at 65 μm s^{-1} with a 65 μm square spot at 10 Hz and laser power of 3.3 J cm^{-2}. Isotopes of ^{13}C, ^{27}Al, ^{28}Si, ^{34}S, ^{47}Ti, ^{51}V, ^{52}Cr, ^{57}Fe, ^{59}Co, ^{60}Ni, ^{63}Cu, ^{66}Zn, ^{75}As, ^{78}Se, ^{95}Mo, and ^{238}U were collected with a dwell time of 8 ms and ^{185}Re with a dwell time of 13 ms, corresponding to a total duty cycle of 0.2 s. Sample 4000988 was, instead, scanned at 33 μm s^{-1} with a 65 μm square spot at 5 Hz and a laser power of 1.65 J cm^{-2}. Isotopes of ^{27}Al, ^{28}Si, ^{34}S, ^{47}Ti, ^{51}V, ^{52}Cr, ^{57}Fe, ^{95}Mo, and ^{238}U were collected with a dwell time of 16 ms and ^{185}Re with a dwell time of 20 ms, corresponding to a total duty cycle of 0.2 s. Maps are presented in counts per second.

References

Abe, M., Suzuki, T., Fujii, Y., Hada, M., and Hirao, K. (2008) An ab initio molecular orbital study of the nuclear volume effects in uranium isotope fractionations. The Journal of Chemical Physics, 129, 164309.

Algeo, T.J., and Lyons, T.W. (2006) Mo–total organic carbon covariation in modern anoxic marine environments: Implications for analysis of paleoredox and paleohydrographic conditions. Paleoceanography, 21, PA1016.

Algeo, T.J., and Tribovillard, N. (2009) Environmental analysis of paleoceanographic systems based on molybdenum–uranium covariation. Chemical Geology, 268, 211–225.

Andersen, M.B., Romaniello, S., Vance, D., Little, S.H., Herdman, R., and Lyons, T.W. (2014) A modern framework for the interpretation of 238U/235U in studies of ancient ocean redox. Earth and Planetary Science Letters, 400, 184–194.

Andersen, M.B., Elliott, T., Freymuth, H., Sims, K.W.W., Niu, Y., and Kelley, K.A. (2015) The terrestrial uranium isotope cycle. Nature, 517, 356–359.

Andersen, M.B., Vance, D., Morford, J.L., Bura-Nakić, E., Breitenbach, S.F.M., and Och, L. (2016) Closing in on the marine 238U/235U budget. Chemical Geology, 420, 11–22.

Andersen, M.B., Stirling, C.H., and Weyer, S. (2017) Uranium Isotope Fractionation. Reviews in Mineralogy and Geochemistry, 82, 799–850.

Anderson, R.F., Fleisher, M.Q., and LeHuray, A.P. (1989) Concentration, oxidation state, and particulate flux of uranium in the Black Sea. Geochimica Et Cosmochimica Acta, 53, 2215–2224.

Arnold, G.L., Anbar, A.D., Barling, J., and Lyons, T.W. (2004) Molybdenum isotope evidence for widespread anoxia in mid-Proterozoic oceans. Science, 304, 87–90.

Asael, D., Tissot, F.L.H., Reinhard, C.T., Rouxel, O., Dauphas, N., Lyons, T.W., Ponzevera, E., Liorzou, C., and Chéron, S. (2013) Coupled molybdenum, iron and uranium stable isotopes as oceanic paleoredox proxies during the Paleoproterozoic Shunga Event. Chemical Geology, 362, 193–210.

Asael, D., Rouxel, O., Poulton, S.W., Lyons, T.W., and Bekker, A. (2018) Molybdenum record from black shales indicates oscillating atmospheric oxygen levels in the early Paleoproterozoic. American Journal of Science, 318, 275–299.

Barling, J., Arnold, G.L., and Anbar, A.D. (2001) Natural mass-dependent variations in the isotopic composition of molybdenum. Earth and Planetary Science Letters, 193, 447–457.

Barnes, C.E., and Cochran, J.K. (1993) Uranium geochemistry in estuarine sediments: Controls on removal and release processes. Geochimica Et Cosmochimica Acta, 57, 555–569.

Bell, K.G. (1960) Uranium and other trace elements in petroleums and rock asphalts. Geological Survey Professional Paper, 356 B, 44–65.

Blättler, C.L., Claire, M.W., Prave, A.R., Kirsimäe, K., Higgins, J.A., Medvedev, P.V., Romashkin, A.E., Rychanchik, D.V., Zerkle, A.L., Paiste, K., and others (2018) Two-billion-year-old evaporites capture Earth's great oxidation. Science, 360, 320–323.

Breillat, N., Guerrot, C., Marcoux, E., and Négrel, Ph. (2016) A new global database of δ98Mo in molybdenites: A literature review and new data. Journal of Geochemical Exploration, 161, 1–15.

Chappaz, A., Lyons, T.W., Gregory, D.D., Reinhard, C.T., Gill, B.C., Li, C., and Large, R.R. (2014) Does pyrite act as an important host for molybdenum in modern and ancient euxinic sediments? Geochimica Et Cosmochimica Acta, 126, 112–122.

Crosby, C.H., and Bailey, J.V. (2012) The role of microbes in the formation of modern and ancient phosphatic mineral deposits. Frontiers in Microbiology, 3, 241.

Crusius, J., Calvert, S., Pedersen, T., and Sage, D. (1996) Rhenium and molybdenum enrichments in sediments as indicators of oxic, suboxic and sulfidic conditions of deposition. Earth and Planetary Science Letters, 145, 65–78.

Črne, A.E., Melezhik, V.A., Prave, A.R., Lepland, A., Romashkin, A.E., Rychanchik, D.V., Hanski, E.J., and Luo, Zh.-Y. (2013) Zaonega Formation: FAR-DEEP Holes 12A and 12B, and neighbouring quarries. In V.A. Melezhik, A.R. Prave, A.E. Fallick, E. Hanski, A. Lepland, L.R. Kump, and H. Strauss, Eds., Reading the Archive of Earth's Oxygenation Vols. 1-3, Vol. 2: The Core Archive of the Fennoscandian Arctic Russia - Drilling Early Earth Project, pp. 946–1007. Springer, Berlin Heidelberg.

Črne, A.E., Melezhik, V.A., Lepland, A., Fallick, A.E., Prave, A.R., and Brasier, A.T. (2014) Petrography and geochemistry of carbonate rocks of the Paleoproterozoic Zaonega Formation, Russia: Documentation of 13C-depleted non-primary calcite. Precambrian Research, 240, 79–93.

Dahl, T.W., Boyle, R.A., Canfield, D.E., Connelly, J.N., Gill, B.C., Lenton, T.M., and Bizzarro, M. (2014) Uranium isotopes distinguish two geochemically distinct stages during the later Cambrian SPICE event. Earth and Planetary Science Letters, 401, 313–326.

Dahl, T.W., Chappaz, A., Hoek, J., McKenzie, C.J., Svane, S., and Canfield, D.E. (2017) Evidence of molybdenum association with particulate organic matter under sulfidic conditions. Geobiology, 15, 311–323.

Dickson, A.J. (2017) A molybdenum-isotope perspective on Phanerozoic deoxygenation events. Nature Geoscience, 10, 721–726.

Dickson, A.J., Cohen, A.S., and Coe, A.L. (2014) Continental margin molybdenum isotope signatures from the early Eocene. Earth and Planetary Science Letters, 404, 389–395.

Dunk, R.M., Mills, R.A., and Jenkins, W.J. (2002) A reevaluation of the oceanic uranium budget for the Holocene. Chemical Geology, 190, 45–67.

Emerson, S.R., and Huested, S.S. (1991) Ocean anoxia and the concentrations of molybdenum and vanadium in seawater. Marine Chemistry, 34, 177–196.

Föllmi, K.B., Badertscher, C., de Kaenel, E., Stille, P., John, C.M., Adatte, T., and Steinmann, P. (2005) Phosphogenesis and organic-carbon preservation in the Miocene Monterey Formation at

Naples Beach, California - The Monterey hypothesis revisited. Bulletin of the Geological Society of America, 117, 589–619.

Gilleaudeau, G.J., Romaniello, S.J., Luo, G., Kaufman, A.J., Zhang, F., Klaebe, R.M., Kah, L.C., Azmy, K., Bartley, J.K., Zheng, W., and others (2019) Uranium isotope evidence for limited euxinia in mid-Proterozoic oceans. Earth and Planetary Science Letters, 521, 150–157.

Goldberg, T., Archer, C., Vance, D., Thamdrup, B., McAnena, A., and Poulton, S.W. (2012) Controls on Mo isotope fractionations in a Mn-rich anoxic marine sediment, Gullmar Fjord, Sweden. Chemical Geology, 296-297, 73–82.

Goldberg, T., Gordon, G., Izon, G., Archer, C., Pearce, C.R., McManus, J., Anbar, A.D., and Rehkämper, M. (2013) Resolution of inter-laboratory discrepancies in Mo isotope data: An intercalibration. Journal of Analytical Atomic Spectrometry, 28, 724–735.

Helz, G.R., Miller, C.V., Charnock, J.M., Mosselmans, J.F.W., Pattrick, R.A.D., Garner, C.D., and Vaughan, D.J. (1996) Mechanism of molybdenum removal from the sea and its concentration in black shales: EXAFS evidence. Geochimica Et Cosmochimica Acta, 60, 3631–3642.

Henderson, G.M., and Anderson, R.F. (2003) The U-series Toolbox for Paleoceanography. Reviews in Mineralogy and Geochemistry, 52, 493–531.

Karhu, J.A. (1999) Carbon isotopes. In C.P. Marshall and R.W. Fairbridge, Eds., Encyclopedia of Geochemistry pp. 67–73. Kluwer Academic Publishers, Boston.

Karhu, J.A., and Holland, H.D. (1996) Carbon isotopes and the rise of atmospheric oxygen. Geology, 24, 867–870.

Kendall, B., Brennecka, G.A., Weyer, S., and Anbar, A.D. (2013) Uranium isotope fractionation suggests oxidative uranium mobilization at 2.50Ga. Chemical Geology, 362, 105–114.

Kendall, B., Komiya, T., Lyons, T.W., Bates, S.M., Gordon, G.W., Romaniello, S.J., Jiang, G., Creaser, R.A., Xiao, S., McFadden, K., and others (2015) Uranium and molybdenum isotope evidence for an episode of widespread ocean oxygenation during the late Ediacaran Period. Geochimica Et Cosmochimica Acta, 156, 173–193.

Kendall, B., Dahl, T.W., and Anbar, A.D. (2017) The stable isotope geochemistry of molybdenum. Reviews in Mineralogy and Geochemistry, 82, 683–732.

Konhauser, K.O., Lalonde, S.V., Planavsky, N.J., Pecoits, E., Lyons, T.W., Mojzsis, S.J., Rouxel, O.J., Barley, M.E., Rosìere, C., Fralick, P.W., and others (2011) Aerobic bacterial pyrite oxidation and acid rock drainage during the Great Oxidation Event. Nature, 478, 369–373.

Ku, T.-L., Knauss, K.G., and Mathieu, G.G. (1977) Uranium in open ocean: Concentration and isotopic composition. Deep Sea Research, 24, 1005–1017.

Kurzweil, F., Wille, M., Schoenberg, R., Taubald, H., and Van Kranendonk, M.J. (2015) Continuously increasing δ98Mo values in Neoarchean black shales and iron formations from the Hamersley Basin. Geochimica Et Cosmochimica Acta, 164, 523–542.

Lepland, A., Joosu, L., Kirsimäe, K., Prave, A.R., Romashkin, A.E., Črne, A.E., Martin, A.P., Fallick, A.E., Somelar, P., Üpraus, K., and others (2014) Potential influence of sulphur bacteria on Palaeoproterozoic phosphogenesis. Nature Geoscience, 7, 20–24.

Lu, X., Kendall, B., Stein, H.J., Li, C., Hannah, J.L., Gordon, G.W., and Ebbestad, J.O.R. (2017) Marine redox conditions during deposition of Late Ordovician and Early Silurian organic-rich mudrocks in the Siljan ring district, central Sweden. Chemical Geology, 457, 75–94.

Martin, A.P., Condon, D.J., Prave, A.R., and Lepland, A. (2013) A review of temporal constraints for the Palaeoproterozoic large, positive carbonate carbon isotope excursion (the Lomagundi–Jatuli Event). Earth-Science Reviews, 127, 242–261.

Martin, A.P., Prave, A.R., Condon, D.J., Lepland, A., Fallick, A.E., Romashkin, A.E., Medvedev, P.V., and Rychanchik, D.V. (2015) Multiple Palaeoproterozoic carbon burial episodes and excursions. Earth and Planetary Science Letters, 424, 226–236.

Melezhik, V.A., Fallick, A.E., Medvedev, P.V., and Makarikhin, V.V. (1999a) Extreme 13Ccarb enrichment in ca. 2.0 Ga magnesite–stromatolite–dolomite–‘red beds’ association in a global context: A case for the world-wide signal enhanced by a local environment. Earth-Science Reviews, 48, 71–120.

Melezhik, V.A., Fallick, A.E., Filippov, M.M., and Larsen, O. (1999b) Karelian shungite—an indication of 2.0-Ga-old metamorphosed oil-shale and generation of petroleum: Geology, lithology and geochemistry. Earth-Science Reviews, 47, 1–40.

Melezhik, V.A., Filippov, M.M., and Romashkin, A.E. (2004) A giant Palaeoproterozoic deposit of shungite in NW Russia: Genesis and practical applications. Ore Geology Reviews, 24, 135–154.

Melezhik, V.A., Medvedev, P.V., and Svetov, S.A. (2013) The Onega Basin. In V.A. Melezhik, A.R. Prave, A.E. Fallick, L.R. Kump, H. Strauss, A. Lepland, and E.J. Hanski, Eds., Reading the Archive of Earth's Oxygenation Vols. 1-3, Vol. 1: The Palaeoproterozoic of Fennoscandia As Context for the Fennoscandian Arctic Russia - Drilling Early Earth Project, pp. 387–490. Springer, Berlin Heidelberg.

Melezhik, V.A., Fallick, A.E., Brasier, A.T., and Lepland, A. (2015) Carbonate deposition in the Palaeoproterozoic Onega basin from Fennoscandia: A spotlight on the transition from the Lomagundi-Jatuli to Shunga events. Earth-Science Reviews, 147, 65–98.

Migdisov, A.A., Guo, X., Williams-Jones, A.E., Sun, C.J., Vasyukova, O., Sugiyama, I., Fuchs, S., Pearce, K., and Roback, R. (2017) Hydrocarbons as ore fluids. Geochemical Perspectives Letters, 5, 47–52.

Miller, C.A., Peucker-Ehrenbrink, B., Walker, B.D., and Marcantonio, F. (2011) Re-assessing the surface cycling of molybdenum and rhenium. Geochimica Et Cosmochimica Acta, 75, 7146–7179.

Morford, J.L., and Emerson, S. (1999) The geochemistry of redox sensitive trace metals in sediments. Geochimica Et Cosmochimica Acta, 63, 1735–1750.

Morford, J.L., Emerson, S.R., Breckel, E.J., and Kim, S.H. (2005) Diagenesis of oxyanions (V, U, Re, and Mo) in pore waters and sediments from a continental margin. Geochimica Et Cosmochimica Acta, 69, 5021–5032.

Nakagawa, Y., Takano, S., Firdaus, M.L., Norisuye, K., Hirata, T., Vance, D., and Sohrin, Y. (2012) The molybdenum isotopic composition of the modern ocean. Geochemical Journal, 46, 131–141.

Nägler, T.F., Neubert, N., Böttcher, M.E., Dellwig, O., and Schnetger, B. (2011) Molybdenum isotope fractionation in pelagic euxinia: Evidence from the modern Black and Baltic Seas. Chemical Geology, 289, 1–11.

Nägler, T.F., Anbar, A.D., Archer, C., Goldberg, T., Gordon, G.W., Greber, N.D., Siebert, C., Sohrin, Y., and Vance, D. (2014) Proposal for an international molybdenum isotope measurement standard and data representation. Geostandards and Geoanalytical Research, 38, 149–151.

Neubert, N., Nägler, T.F., and Böttcher, M.E. (2008) Sulfidity controls molybdenum isotope fractionation into euxinic sediments: Evidence from the modern Black Sea. Geology, 36, 775–778.

Noordmann, J., Weyer, S., Montoya-Pino, C., Dellwig, O., Neubert, N., Eckert, S., Paetzel, M., and Böttcher, M.E. (2015) Uranium and molybdenum isotope systematics in modern euxinic basins: Case studies from the central Baltic Sea and the Kyllaren fjord (Norway). Chemical Geology, 396, 182–195.

Noordmann, J., Weyer, S., Georg, R.B., Jöns, S., and Sharma, M. (2016) 238U/235U isotope ratios of crustal material, rivers and products of hydrothermal alteration: New insights on the oceanic U isotope mass balance. Isotopes in Environmental and Health Studies, 52, 141–163.

Och, L.M., and Shields-Zhou, G.A. (2012) The Neoproterozoic oxygenation event: Environmental perturbations and biogeochemical cycling. Earth-Science Reviews, 110, 26–57.

Paiste, K. (2018, November 8) Reconstructing the Paleoproterozoic sulfur cycle: Insights from the multiple sulfur isotope record of the Zaonega Formation, Karelia, Russia. PhD Thesis, University of Tromsø – The Arctic University of Norway, Tromsø, Norway.

Paiste, K., Lepland, A., Zerkle, A.L., Kirsimäe, K., Izon, G., Patel, N.K., McLean, F., Kreitsmann, T., Mänd, K., Bui, T.H., and others (2018) Multiple sulphur isotope records tracking basinal and global processes in the 1.98 Ga Zaonega Formation, NW Russia. Chemical Geology, 499, 151–164.

Paiste, K., Lepland, A., Zerkle, A.L., Kirsimäe, K., Kreitsmann, T., Mänd, K., Romashkin, A.E., Rychanchik, D.V., and Prave, A.R. (2020) Identifying global vs. Basinal controls on Paleoproterozoic organic carbon and sulfur isotope records. Earth-Science Reviews, 207, 103230.

Partin, C.A., Bekker, A., Planavsky, N.J., Scott, C.T., Gill, B.C., Li, C., Podkovyrov, V., Maslov, A., Konhauser, K.O., Lalonde, S.V., and others (2013) Large-scale fluctuations in Precambrian atmospheric and oceanic oxygen levels from the record of U in shales. Earth and Planetary Science Letters, 369–370, 284–293.

Partin, C.A., Bekker, A., Planavsky, N.J., and Lyons, T.W. (2015) Euxinic conditions recorded in the ca. 1.93 Ga Bravo Lake Formation, Nunavut (Canada): Implications for oceanic redox evolution. Chemical Geology, 417, 148–162.

Poulson Brucker, R.L., McManus, J., Severmann, S., and Berelson, W.M. (2009) Molybdenum behavior during early diagenesis: Insights from Mo isotopes. Geochemistry, Geophysics, Geosystems, 10, Q06010.

Poulson, R.L., Siebert, C., McManus, J., and Berelson, W.M. (2006) Authigenic molybdenum isotope signatures in marine sediments. Geology, 34, 617–620.

Poulton, S.W., and Canfield, D.E. (2005) Development of a sequential extraction procedure for iron: Implications for iron partitioning in continentally derived particulates. Chemical Geology, 214, 209–221.

Poulton, S.W., and Canfield, D.E. (2011) Ferruginous conditions: A dominant feature of the ocean through Earth's history. Elements, 7, 107–112.

Priyatkina, N., Khudoley, A.K., Ustinov, V.N., and Kullerud, K. (2014) 1.92 Ga kimberlitic rocks from Kimozero, NW Russia: Their geochemistry, tectonic setting and unusual field occurrence. Precambrian Research, 249, 162–179.

Puchtel, I.S., Arndt, N.T., Hofmann, A.W., Haase, K.M., Kröner, A., Kulikov, V.S., Kulikova, V.V., Garbe-Schönberg, C.-D., and Nemchin, A.A. (1998) Petrology of mafic lavas within the Onega plateau, central Karelia: Evidence for 2.0 Ga plume-related continental crustal growth in the Baltic Shield. Contributions to Mineralogy and Petrology, 130, 134–153.

Puchtel, I.S., Brügmann, G.E., and Hofmann, A.W. (1999) Precise Re–Os mineral isochron and Pb–Nd–Os isotope systematics of a mafic–ultramafic sill in the 2.0 Ga Onega plateau (Baltic Shield). Earth and Planetary Science Letters, 170, 447–461.

Qu, Y., Črne, A.E., Lepland, A., and van Zuilen, M.A. (2012) Methanotrophy in a Paleoproterozoic oil field ecosystem, Zaonega Formation, Karelia, Russia. Geobiology, 10, 467–78.

Qu, Y., Lepland, A., van Zuilen, M., Whitehouse, M., Črne, A.E., and Fallick, A.E. (2018) Sample-scale carbon isotopic biosignatures of diverse biomass in the Paleoproterozoic Zaonega Formation, Russia. Precambrian Research, 315, 222–231.

Reinhard, C.T., Planavsky, N.J., Robbins, L.J., Partin, C.A., Gill, B.C., Lalonde, S.V., Bekker, A., Konhauser, K.O., and Lyons, T.W. (2013) Proterozoic ocean redox and biogeochemical stasis. Proceedings of the National Academy of Sciences of the United States of America, 110, 5357–5362.

Romaniello, S.J., Herrmann, A.D., and Anbar, A.D. (2013) Uranium concentrations and 238U/235U isotope ratios in modern carbonates from the Bahamas: Assessing a novel paleoredox proxy. Chemical Geology, 362, 305–316.

Rudnick, R.L., and Gao, S. (2014) Composition of the Continental Crust. In Treatise on Geochemistry pp. 1–51. Elsevier, Amsterdam.

Sahoo, S.K., Planavsky, N.J., Kendall, B., Wang, X., Shi, X., Scott, C., Anbar, A.D., Lyons, T.W., and Jiang, G. (2012) Ocean oxygenation in the wake of the Marinoan glaciation. Nature, 489, 546–549.

Sarmiento, J.L., and Gruber, N. (2006) Ocean Biogeochemical Dynamics, 526 p. Princeton University Press.

Scholz, F., Baum, M., Siebert, C., Eroglu, S., Dale, A.W., Naumann, M., and Sommer, S. (2018) Sedimentary molybdenum cycling in the aftermath of seawater inflow to the intermittently euxinic Gotland Deep, Central Baltic Sea. Chemical Geology, 491, 27–38.

Scott, C., Lyons, T.W., Bekker, A., Shen, Y., Poulton, S.W., Chu, X., and Anbar, A.D. (2008) Tracing the stepwise oxygenation of the Proterozoic ocean. Nature, 452, 456–459.

Sheen, A.I., Kendall, B., Reinhard, C.T., Creaser, R.A., Lyons, T.W., Bekker, A., Poulton, S.W., and Anbar, A.D. (2018) A model for the oceanic mass balance of rhenium and implications for the extent of Proterozoic ocean anoxia. Geochimica Et Cosmochimica Acta, 227, 75–95.

Siebert, C., Nägler, T.F., and Kramers, J.D. (2001) Determination of molybdenum isotope fractionation by double-spike multicollector inductively coupled plasma mass spectrometry. Geochemistry, Geophysics, Geosystems, 2, 1032.

Siebert, C., Nägler, T.F., von Blanckenburg, F., and Kramers, J.D. (2003) Molybdenum isotope records as a potential new proxy for paleoceanography. Earth and Planetary Science Letters, 211, 159–171.

Siebert, C., McManus, J., Bice, A., Poulson, R., and Berelson, W.M. (2006) Molybdenum isotope signatures in continental margin marine sediments. Earth and Planetary Science Letters, 241, 723–733.

Slotznick, S.P., Eiler, J.M., and Fischer, W.W. (2018) The effects of metamorphism on iron mineralogy and the iron speciation redox proxy. Geochimica Et Cosmochimica Acta, 224, 96–115.

Stepanova, A., Samsonov, A., and Larionov, A. (2014) The final episode of middle Proterozoic magmatism in the Onega structure: Data on trans-Onega dolerites. Transactions of the Karelian Research Centre of the Russian Academy of Sciences, Precambrian Geology Series, 1, 3–16.

Stirling, C.H., Andersen, M.B., Warthmann, R., and Halliday, A.N. (2015) Isotope fractionation of 238U and 235U during biologically-mediated uranium reduction. Geochimica Et Cosmochimica Acta, 163, 200–218.

Taylor, A.P., Barry, J.C., and Webb, R.I. (2001) Structural and morphological anomalies in magnetosomes: Possible biogenic origin for magnetite in ALH84001. Journal of Microscopy, 201, 84–106.

Tissot, F.L.H., and Dauphas, N. (2015) Uranium isotopic compositions of the crust and ocean: Age corrections, U budget and global extent of modern anoxia. Geochimica Et Cosmochimica Acta, 167, 113–143.

Tossell, J.A. (2005) Calculating the partitioning of the isotopes of Mo between oxidic and sulfidic species in aqueous solution. Geochimica Et Cosmochimica Acta, 69, 2981–2993.

Voegelin, A.R., Nägler, T.F., Pettke, T., Neubert, N., Steinmann, M., Pourret, O., and Villa, I.M. (2012) The impact of igneous bedrock weathering on the Mo isotopic composition of stream waters: Natural samples and laboratory experiments. Geochimica Et Cosmochimica Acta, 86, 150–165.

Wagner, M., Chappaz, A., and Lyons, T.W. (2017) Molybdenum speciation and burial pathway in weakly sulfidic environments: Insights from XAFS. Geochimica Et Cosmochimica Acta, 206, 18–29.

Wang, X., Planavsky, N.J., Hofmann, A., Saupe, E.E., De Corte, B.P., Philippot, P., LaLonde, S.V., Jemison, N.E., Zou, H., Ossa, F.O., and others (2018) A Mesoarchean shift in uranium isotope systematics. Geochimica Et Cosmochimica Acta, 238, 438–452.

Weyer, S., Anbar, A.D., Gerdes, A., Gordon, G.W., Algeo, T.J., and Boyle, E.A. (2008) Natural fractionation of 238U/235U. Geochimica Et Cosmochimica Acta, 72, 345–359.

Yang, S., Kendall, B., Lu, X., Zhang, F., and Zheng, W. (2017) Uranium isotope compositions of mid-Proterozoic black shales: Evidence for an episode of increased ocean oxygenation at 1.36Ga and evaluation of the effect of post-depositional hydrothermal fluid flow. Precambrian Research, 298, 187–201.

Zhang, F., Xiao, S., Kendall, B., Romaniello, S.J., Cui, H., Meyer, M., Gilleaudeau, G.J., Kaufman, A.J., and Anbar, A.D. (2018a) Extensive marine anoxia during the terminal Ediacaran Period. Science Advances, 4, eaan8983.

Zhang, F., Romaniello, S.J., Algeo, T.J., Lau, K.V., Clapham, M.E., Richoz, S., Herrmann, A.D., Smith, H., Horacek, M., and Anbar, A.D. (2018b) Multiple episodes of extensive marine anoxia linked to global warming and continental weathering following the latest Permian mass extinction. Science Advances, 4, e1602921.

Zhang, F., Xiao, S., Romaniello, S.J., Hardisty, D., Li, C., Melezhik, V., Pokrovsky, B., Cheng, M., Shi, W., Lenton, T.M., and others (2019) Global marine redox changes drove the rise and fall of the Ediacara biota. Geobiology, 17, 594–610.

Appendix 3: Supplementary information to chapter 4

X-ray diffraction results

The Tulomozero Formation samples are dominated by halite below ~2800 m (averaging 49.2±31.7 wt.%; errors for averages are given in 1σ), with abundant magnesite and anhydrite (11.9±12.1 wt.% and 26.2±23.3 wt.%, respectively), and accessory evaporite minerals like hexahydrite, pentahydrite, starkeyite, kieserite, bloedite, leonite, langbeinite, kainite, and picomerite (all below 10 wt.%). Quartz is relatively common (averaging 10.4±10.0 wt.%), whereas other detritally derived minerals (e.g., K-feldspar, chlorite, hematite), talc, and dolomite are all present below 7.2 wt.%. From ~2800 to ~2330 m, halite gives way to evaporitic magnesite and anhydrite (averaging 44.6±28.2 wt.% and 25.9±18.9 wt.%, respectively), with major inputs of glauberite (5.5±15.6 wt.%), gypsum (2.0±4.0 wt.%), quartz (8.2±8.2 wt.%), and dolomite (3.6±11.4 wt.%) and an increased prevalence of aluminosilicates like plagioclase (up to 20.1 wt.%), K-feldspar, micas, and chlorite. From ~2330 m depth in the upper Tulomozero Formation to ~2100 m depth in the lower Zaonega Formation, the major mineral is dolomite (averaging 56.9±29.9 wt.%) with abundant magnesite interbeds (up to 68.1 wt.%), occasional quartz-feldspar-mica-chlorite-hematite layers (which contain up to ~30 wt.% of quartz and plagioclase), and accessory talc (below 3.0 wt.%). From ~2100 to 1700 m the mineralogy is similar, but quartz (averaging 16.1±8.9 wt.%) and aluminosilicates (25.5±23.4 wt.% plagioclase, 20.8±15.5 wt.% micas) tend to dominate over dolomite (17.4±26.2 wt.%). The sedimentary interval from 1230 to 1080 m is dominated by alternating dolomite-calcite (averaging 34.6±39.2

wt.% and 11.5±18.5 wt.%, respectively) and quartz-aluminosilicate assemblages (12.9±17.7 wt. % quartz, 15.7±18.2 wt.% micas, and 9.5±11.6 wt.% K-feldspar), the latter being more prevalent below 1112 m and the former above 1112 m. In this interval, pyrite and apatite are also common (3.8±5.2 wt.%, and 0.3±0.9 wt.%, respectively), especially near the 1112 m boundary. Sedimentary layers above this section, at 980–913 m, ~635 m, and ~590–530 m, contain mostly quartz, K-feldspar, plagioclase, and chlorite (averaging 23.7±20.1, 7.5±4.4, 30.1±16.3, and 20.6±18.0 wt.%, respectively).

Oxygen isotope ratios

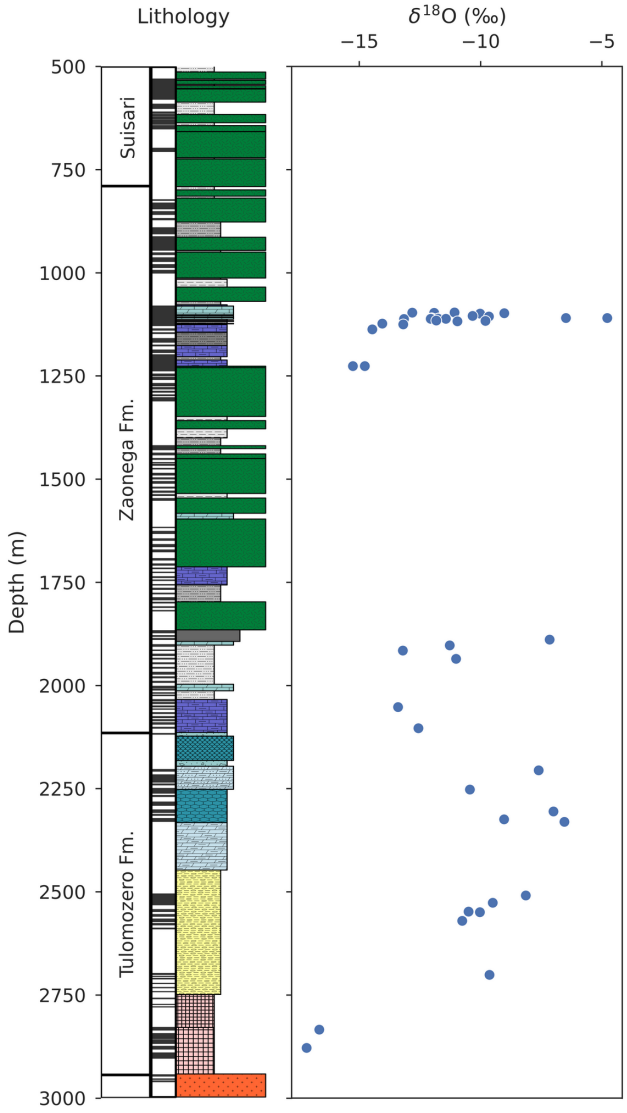

Figure A7: Carbonate oxygen isotope ratios ($\delta^{18}O$) in the Onega Parametric Hole drill core.

Other processes that may affect δ^{53}Cr

Variation in sedimentary δ^{53}Cr can be explained through a variety of processes, the first of which is local post-depositional mobilization of Cr by hydrothermal fluids, as discussed in chapter 4. Alternatively, negative fractionations have been observed in Cr adsorption onto organic matter (e.g., Jamieson-Hanes et al. 2012; Semeniuk et al. 2016); the expression of isotope fractionation in sediments can then be modulated through a variable mixing relationship between different Cr hosting phases, or by diagenetic redistribution of Cr (Frank et al. 2020). Furthermore, the Zaonega Formation was characterized by highly variable redox conditions (Lepland et al. 2014; Paiste et al. 2018; Mänd et al. 2020), which may also induce δ^{53}Cr variation: while Cr drawdown in anoxic waters is close to quantitative (Kim et al. 2001), in suboxic conditions the locus of reduction shifts into the sediments, so that a distilled, positively-fractionated Cr(VI) phase can escape back into the water column, leaving the sediments depleted in ^{53}Cr (Reinhard et al. 2014). Finally, the highly biologically productive local ecosystem in the Zaonega Formation (Qu et al. 2012; Lepland et al. 2014; Paiste et al. 2020) may, too, have induced δ^{53}Cr variability in the water column, as the photobiochemical reduction of Cr results in substantial δ^{53}Cr variation in oceanic depth gradients (Scheiderich et al. 2015). However, all these processes require first that Cr(VI) be present—the implication is oxidative weathering of Cr on land.

Significantly, an increasing number of recent studies have found alternative pathways of Mn oxidation and Cr fractionation that do not require the presence of free O_2. For example, Liu et al. (2020), described anoxic and abiotic oxidation of Mn(II) carbonates (rhodochrosite) which can take place under UV radiation, producing Mn(III)-oxides potentially capable of driving Cr-

isotope fractionation. Daye et al. (2019) reported that anoxygenic photosynthetic organisms are also capable of oxidizing Mn(II) to Mn(III) and Mn(IV) without the presence of oxygen (see also Johnson et al. 2013). Finally, Saad et al. (2017) showed that ligand-based solubilization of Cr(III) can produce isotope fractionations of a magnitude and direction that are difficult to predict.

Although UV-dependent Mn oxidation is potentially relevant for the Archean, deposition of the Tulomozero and Zaonega rocks postdates the disappearance of S-MIF (and the formation of a UV-shielding ozone layer) by at least 200 Myr. (Martin et al. 2015; Warke et al. 2020). Further, the abundance of authigenic Cr accumulation in the Zaonega Formation is most easily explained through a large dissolved marine Cr(VI) pool, which requires vigorous Cr solubilization on land, its riverine transfer into oceans, and the presence of oxic settings in the oceans so that Cr(VI) could accumulate. All of this is consistent with other proxy records in the Paleoproterozoic, which purport a fundamentally oxidized surface world (e.g., Bekker and Holland 2012; Partin et al. 2013; Hardisty et al. 2014; Blättler et al. 2018). Conversely, it is still unclear whether the relatively lower rates of ligand-based, non-redox Cr(III) solubilization can account for the necessary Cr fluxes (Saad et al. 2017), or whether likely short-lived Mn oxides generated through photochemical or photosynthetic processes on the surface in light-replete conditions are capable of affecting Cr oxidation at scale (Anbar and Holland, 1992). Fundamentally, while all of these alternative processes are expected to have been in operation since the Archean, the highly fractionated Cr record in the Onega Basin is vastly different from anything in the Archean

or early Mesoproterozoic. We contend, therefore, that O_2-driven Mn(IV) oxide generation is the best explanation for the Onega Basin data (Frei et al. 2009; Wei et al. 2020).

References

Anbar, A.D., and Holland, H.D. (1992) The photochemistry of manganese and the origin of banded iron formations. Geochimica et Cosmochimica Acta, 56, 2595–2603.

Bekker, A., and Holland, H.D. (2012) Oxygen overshoot and recovery during the early Paleoproterozoic. Earth and Planetary Science Letters, 317–318, 295–304.

Blättler, C.L., Claire, M.W., Prave, A.R., Kirsimäe, K., Higgins, J.A., Medvedev, P.V., Romashkin, A.E., Rychanchik, D.V., Zerkle, A.L., Paiste, K., and others (2018) Two-billion-year-old evaporites capture Earth's great oxidation. Science, 360, 320–323.

Daye, M., Klepac-Ceraj, V., Pajusalu, M., Rowland, S., Farrell-Sherman, A., Beukes, N., Tamura, N., Fournier, G., and Bosak, T. (2019) Light-driven anaerobic microbial oxidation of manganese. Nature, 576, 311–314.

Frank, A.B., Klaebe, R.M., Löhr, S., Xu, L., and Frei, R. (2020) Chromium isotope composition of organic-rich marine sediments and their mineral phases and implications for using black shales as a paleoredox archive. Geochimica Et Cosmochimica Acta, 270, 338–359.

Frei, R., Gaucher, C., Poulton, S.W., and Canfield, D.E. (2009) Fluctuations in Precambrian atmospheric oxygenation recorded by chromium isotopes. Nature, 461, 250–253.

Hardisty, D.S., Lu, Z., Planavsky, N.J., Bekker, A., Philippot, P., Zhou, X., and Lyons, T.W. (2014) An iodine record of Paleoproterozoic surface ocean oxygenation. Geology, 42, 619–622.

Jamieson-Hanes, J.H., Gibson, B.D., Lindsay, M.B.J., Kim, Y., Ptacek, C.J., and Blowes, D.W. (2012) Chromium Isotope Fractionation During Reduction of Cr(VI) Under Saturated Flow Conditions. Environmental Science & Technology, 46, 6783–6789.

Johnson, J.E., Webb, S.M., Thomas, K., Ono, S., Kirschvink, J.L., and Fischer, W.W. (2013) Manganese-oxidizing photosynthesis before the rise of cyanobacteria. Proceedings of the National Academy of Sciences, 110, 11238–11243.

Kim, C., Zhou, Q., Deng, B., Thornton, E.C., and Xu, H. (2001) Chromium(VI) Reduction by Hydrogen Sulfide in Aqueous Media: Stoichiometry and Kinetics. Environmental Science & Technology, 35, 2219–2225.

Lepland, A., Joosu, L., Kirsimäe, K., Prave, A.R., Romashkin, A.E., Črne, A.E., Martin, A.P., Fallick, A.E., Somelar, P., Üpraus, K., and others (2014) Potential influence of sulphur bacteria on Palaeoproterozoic phosphogenesis. Nature Geoscience, 7, 20–24.

Liu, W., Hao, J., Elzinga, E.J., Piotrowiak, P., Nanda, V., Yee, N., and Falkowski, P.G. (2020) Anoxic photogeochemical oxidation of manganese carbonate yields manganese oxide. Proceedings of the National Academy of Sciences, 117, 22698–22704.

Martin, A.P., Prave, A.R., Condon, D.J., Lepland, A., Fallick, A.E., Romashkin, A.E., Medvedev, P.V., and Rychanchik, D.V. (2015) Multiple Palaeoproterozoic carbon burial episodes and excursions. Earth and Planetary Science Letters, 424, 226–236.

Mänd, K., Lalonde, S.V., Robbins, L.J., Thoby, M., Paiste, K., Kreitsmann, T., Paiste, P., Reinhard, C.T., Romashkin, A.E., Planavsky, N.J., and others (2020) Palaeoproterozoic oxygenated oceans following the Lomagundi–Jatuli Event. Nature Geoscience, 13, 302–306.

Paiste, K., Lepland, A., Zerkle, A.L., Kirsimäe, K., Izon, G., Patel, N.K., McLean, F., Kreitsmann, T., Mänd, K., Bui, T.H., and others (2018) Multiple sulphur isotope records tracking basinal and global processes in the 1.98 Ga Zaonega Formation, NW Russia. Chemical Geology, 499, 151–164.

Paiste, K., Pellerin, A., Zerkle, A.L., Kirsimäe, K., Prave, A.R., Romashkin, A.E., and Lepland, A. (2020) The pyrite multiple sulfur isotope record of the 1.98 Ga Zaonega Formation: Evidence for biogeochemical sulfur cycling in a semi-restricted basin. Earth and Planetary Science Letters, 534, 116092.

Partin, C.A., Bekker, A., Planavsky, N.J., Scott, C.T., Gill, B.C., Li, C., Podkovyrov, V., Maslov, A., Konhauser, K.O., Lalonde, S.V., and others (2013) Large-scale fluctuations in Precambrian atmospheric and oceanic oxygen levels from the record of U in shales. Earth and Planetary Science Letters, 369–370, 284–293.

Qu, Y., Črne, A.E., Lepland, A., and van Zuilen, M.A. (2012) Methanotrophy in a Paleoproterozoic oil field ecosystem, Zaonega Formation, Karelia, Russia. Geobiology, 10, 467–78.

Reinhard, C.T., Planavsky, N.J., Wang, X., Fischer, W.W., Johnson, T.M., and Lyons, T.W. (2014) The isotopic composition of authigenic chromium in anoxic marine sediments: A case study from the Cariaco Basin. Earth and Planetary Science Letters, 407, 9–18.

Saad, E.M., Wang, X., Planavsky, N.J., Reinhard, C.T., and Tang, Y. (2017) Redox-independent chromium isotope fractionation induced by ligand-promoted dissolution. Nature Communications, 8, 1–10.

Scheiderich, K., Amini, M., Holmden, C., and Francois, R. (2015) Global variability of chromium isotopes in seawater demonstrated by Pacific, Atlantic, and Arctic Ocean samples. Earth and Planetary Science Letters, 423, 87–97.

Semeniuk, D.M., Maldonado, M.T., and Jaccard, S.L. (2016) Chromium uptake and adsorption in marine phytoplankton – Implications for the marine chromium cycle. Geochimica Et Cosmochimica Acta, 184, 41–54.

Warke, M.R., Rocco, T.D., Zerkle, A.L., Lepland, A., Prave, A.R., Martin, A.P., Ueno, Y., Condon, D.J., and Claire, M.W. (2020) The Great Oxidation Event preceded a Paleoproterozoic "snowball Earth." Proceedings of the National Academy of Sciences, 117, 13314–13320.

Wei, W., Klaebe, R., Ling, H.-F., Huang, F., and Frei, R. (2020) Biogeochemical cycle of chromium isotopes at the modern Earth's surface and its applications as a paleo-environment proxy. Chemical Geology, 541, 119570.

Appendix 4: Data

Table A1a: Element concentration data for drill cores OnZaP-1 and OnZaP-3.

Sample ID	Drill site	Core depth (m)	Comb. depth (m)	Sample set	Lithology	Ag (ppm)	Al (ppm)	As (ppm)	Ba (ppm)	Be (ppm)	Bi (ppm)	Ca (ppm)	Cd (ppm)	Ce (ppm)
4000319	OnZaP-1	1.96	1.96	MSP0001	Mudstone	0.03	42,200	0.7	150	1	0.29	700	0.07	7.65
4000921	OnZaP-1	2.08	2.08	MSP0010	Mudstone		61,367	0.8	205			743	0.15	73.51
4000320	OnZaP-1	2.85	2.85	MSP0001	Mudstone	0.05	45,500	0.3	129		0.19	900	0.06	12.69
4000321	OnZaP-1	3.92	3.92	MSP0001	Mudstone	0.04	46,300	2.5	142	2	0.22	900	0.11	7.46
4000922	OnZaP-1	5.28	5.28	MSP0010	Mudstone		61,531	3.8	208			799	0.10	28.94
4000322	OnZaP-1	5.31	5.31	MSP0001	Mudstone	0.03	45,700	0.5	141	1	0.26	700	0.04	8.18
4000323	OnZaP-1	6.50	6.50	MSP0001	Mudstone	0.03	37,700	0.4	90	1	0.31	800	0.07	6.59
4000923	OnZaP-1	6.60	6.60	MSP0010	Mudstone		50,874		139			589		
4000324	OnZaP-1	7.01	7.01	MSP0001	Mudstone	0.03	43,800	2.0	153	3	0.61	6,200	0.04	12.05
4000332	OnZaP-1	7.96	7.96	MSP0001	Mudstone	0.03	20,200	1.0	81	1	0.06	123,600	0.07	19.01
4000336	OnZaP-1	8.35	8.35	MSP0001	Mudstone	0.09	43,200	0.8	174	4	0.33	14,400	0.07	15.07
4000342	OnZaP-1	8.74	8.74	MSP0001	Mudstone	0.12	25,200	1.3	101		0.27	133,100	0.05	18.33
4000345	OnZaP-1	9.58	9.58	MSP0001	Mudstone	0.11	43,300	2.0	171	2	0.42	17,500	0.05	21.65
4000346	OnZaP-1	10.79	10.79	MSP0001	Mudstone	0.06	38,700	0.6	122	2	0.20	1,000	0.04	4.28
4000924	OnZaP-1	11.13	11.13	MSP0010	Mudstone		55,179	1.0	193			968	0.08	61.32
4000347	OnZaP-1	11.86	11.86	MSP0001	Mudstone	0.07	46,700	0.6	181	3	0.20	700	0.08	17.52
4000925	OnZaP-1	12.15	12.15	MSP0010	Mudstone		55,134	1.3	190			1,640	0.15	95.03
4000348	OnZaP-1	12.39	12.39	MSP0001	Mudstone	0.14	41,900	2.8	143	2	1.20	1,000	0.08	11.34
4000349	OnZaP-1	13.16	13.16	MSP0001	Mudstone	0.03	8,300	0.7	12		0.09	156,200	1.75	13.19
4000351	OnZaP-1	13.40	13.40	MSP0001	Mudstone	0.03	14,300	0.7	23		0.10	120,000	0.04	11.52
4000358	OnZaP-1	14.65	14.65	MSP0001	Mudstone	0.09	48,600	1.5	138	2	1.67	1,000	0.04	4.69
4000362	OnZaP-1	15.26	15.26	MSP0001	Mudstone	0.04	32,800	3.4	106	1	0.05	82,100	0.05	26.18
4000368	OnZaP-1	16.29	16.29	MSP0001	Mudstone	0.03	8,700	0.8	25			145,200	0.08	5.08
4000376	OnZaP-1	17.36	17.36	MSP0001	Mudstone	0.03	12,400	1.9	35		0.07	149,100	0.04	7.28
4000383	OnZaP-1	17.90	17.90	MSP0001	Mudstone	1.42	14,800	3.6	43		0.08	138,100	0.15	11.68
4000926	OnZaP-1	18.85	18.85	MSP0010	Mudstone		65,737	1.7	203			15,385	0.09	86.70
4000392	OnZaP-1	19.08	19.08	MSP0001	Mudstone	2.45	46,000	0.9	194	2	0.05	1,200	0.09	20.92
4000393	OnZaP-1	19.99	19.99	MSP0001	Mudstone	0.79	48,000	0.8	163	2	0.46	800	0.08	12.18
4000394	OnZaP-1	20.66	20.66	MSP0001	Mudstone	0.13	41,800	0.6	202	2	0.36	700	0.06	26.74
4000927	OnZaP-1	21.91	21.91	MSP0010	Mudstone		60,897	2.4	217			13,421	0.10	85.37
4000395	OnZaP-1	21.94	21.94	MSP0001	Mudstone	0.03	46,300	0.6	173	2	0.08	5,600	0.04	28.76
4000396	OnZaP-1	22.33	22.33	MSP0001	Mudstone	0.04	49,600	0.7	166	2	0.23	8,500	0.04	24.77
4000398	OnZaP-1	23.03	23.03	MSP0001	Mudstone	0.04	55,800	0.5	171	1	0.20	25,700	0.05	30.87
4000928	OnZaP-1	23.84	23.84	MSP0010	Mudstone		42,146	1.8	148			90,824	0.06	33.94
4000403	OnZaP-1	24.31	24.31	MSP0001	Mudstone	0.06	36,300	1.1	163	1	0.13	68,800	0.04	29.02

Sample ID	Drill site	Core depth (m)	Comb. depth (m)	Sample set	Lithology	Ag (ppm)	Al (ppm)	As (ppm)	Ba (ppm)	Be (ppm)	Bi (ppm)	Ca (ppm)	Cd (ppm)	Ce (ppm)
4000406	OnZaP-1	25.03	25.03	MSP0001	Mudstone	0.05	12,300	1.0	49			157,400	0.04	12.62
4000412	OnZaP-1	26.09	26.09	MSP0001	Mudstone	0.05	34,800	0.5	180	4	0.10	3,400	0.05	14.04
4000413	OnZaP-1	26.80	26.80	MSP0001	Mudstone	0.05	42,400	0.5	205	4	0.20	12,300	0.04	22.19
4000414	OnZaP-1	27.77	27.77	MSP0001	Mudstone	0.08	34,000	6.1	173	2	0.18	89,800	0.08	38.44
4000929	OnZaP-1	27.95	27.95	MSP0010	Mudstone		64,710	10.6	284			26,599	0.17	107.78
4000421	OnZaP-1	28.36	28.36	MSP0001	Mudstone	0.06	18,000	5.3	89	1	0.06	148,900	0.07	22.96
4000930	OnZaP-1	28.80	28.80	MSP0010	Mudstone		78,575	24.0	396			7,242	0.28	131.78
4000429	OnZaP-1	29.28	29.28	MSP0001	Carbonate	0.05	4,700	1.5	32			176,100	0.04	7.77
4000931	OnZaP-1	30.66	30.66	MSP0010	Mudstone		60,082	70.7	373			1,016	0.31	118.61
4000436	OnZaP-1	30.79	30.79	MSP0001	Mudstone	0.2	37,300	31.6	220	4	0.22	2,000	0.13	18.86
4000442	OnZaP-1	31.21	31.21	MSP0001	Carbonate	0.03	2,400	1.6	9			173,300	0.04	5.40
4000932	OnZaP-1	31.85	31.85	MSP0010	Mudstone		66,223	61.3	495			603	0.35	111.17
4000447	OnZaP-1	31.86	31.86	MSP0001	Mudstone	0.39	40,400	69.1	293	3	0.34	700	0.15	11.28
4000933	OnZaP-1	32.19	32.19	MSP0010	Mudstone		68,962	82.6	476			687	0.34	101.21
4000455	OnZaP-1	33.15	33.15	MSP0001	Carbonate	0.04	3,000	3.0	15			196,200	0.05	4.49
4000466	OnZaP-1	33.96	33.96	MSP0001	Carbonate	0.1	1,500	5.1	10			218,300	0.10	4.72
4000471	OnZaP-1	34.64	34.64	MSP0001	Carbonate	0.07	6,500	2.5	35			192,700	0.07	6.30
4000478	OnZaP-1	35.61	35.61	MSP0001	Mudstone	0.12	1,100	11.1	5			205,500	0.07	3.68
4000934	OnZaP-1	36.40	36.40	MSP0010	Mudstone		82,644	78.6	664			1,175	3.35	187.83
4000483	OnZaP-1	36.52	36.52	MSP0001	Mudstone	0.98	53,800	92.4	388	4	0.39	1,300	2.04	33.33
4000484	OnZaP-1	36.94	36.94	MSP0001	Carbonate	0.06	4,400	0.9	18			204,400	0.27	9.23
4000935	OnZaP-1	37.83	37.83	MSP0010	Mudstone		65,920	176.0	555			877	2.14	190.65
4000491	OnZaP-1	38.13	38.13	MSP0001	Mudstone	1.6	43,600	204.8	307	3	0.52	1,000	2.91	41.42
4000936	OnZaP-1	38.91	38.91	MSP0010	Mudstone		81,186	258.2	585			5,677	5.05	278.80
4000492	OnZaP-1	38.97	38.97	MSP0001	Mudstone	1.86	43,500	258.7	153	3	0.50	9,400	3.68	35.21
4000493	OnZaP-1	39.88	39.88	MSP0001	Mudstone	2.24	33,100	331.9	99	1	0.32	101,000	3.46	37.96
4000937	OnZaP-1	40.02	40.02	MSP0010	Carbonate		43,619	148.5	268			43,616	4.99	67.32
4000938	OnZaP-1	41.09	41.09	MSP0010	Mudstone		62,286	231.5	377				3.65	55.91
4000494	OnZaP-1	41.15	41.15	MSP0001	Mudstone	2.25	35,100	313.4	251	2	0.57	1,800	5.92	22.83
4000939	OnZaP-1	41.38	41.38	MSP0010	Mudstone		62,876	276.0	440			2,582	4.07	78.70
4000500	OnZaP-1	42.04	42.04	MSP0001	Carbonate	0.05	400	2.5	5			203,800	0.12	5.22
4000940	OnZaP-1	42.42	42.42	MSP0010	Mudstone		33,273	361.8	149			2,965	3.43	68.95
4000504	OnZaP-1	42.45	42.45	MSP0001	Mudstone	1.76	37,800	223.5	128	1	0.46	36,300	2.62	36.79
4000941	OnZaP-1	42.86	42.86	MSP0010	Carbonate		14,490	438.0	24			75,713	4.74	40.43
4000942	OnZaP-1	43.69	43.69	MSP0010	Carbonate		33,898		66			8,032		
4000516	OnZaP-1	43.94	43.94	MSP0001	Carbonate	0.04		4.9	4			171,800	0.14	0.11
4000005	OnZaP-3	2.10	44.37	MSP0001	Carbonate	0.07		1.1	4			170,500	0.29	
4000521	OnZaP-1	44.53	44.53	MSP0001	Carbonate	0.07		4.7	4			172,400	0.14	0.07
4000953	OnZaP-3	2.68	44.93	MSP0010	Carbonate		9,236	97.8	10			172,457	3.92	38.12
4000954	OnZaP-3	2.77	45.02	MSP0010	Mudstone		26,653	270.3	26			509	1.28	1.47
4000015	OnZaP-3	3.12	45.39	MSP0001	Carbonate	0.05		2.6	3			187,900	0.42	0.18
4000529	OnZaP-1	45.65	45.65	MSP0001	Carbonate	0.05		7.0	4			191,200	0.10	0.13
4000943	OnZaP-1	46.36	46.36	MSP0010	Mudstone		37,475	1187.4	60			855	12.05	15.17
4000030	OnZaP-3	4.38	46.65	MSP0001	Carbonate	0.04		7.7	2			165,200	0.32	0.08
4000536	OnZaP-1	46.70	46.70	MSP0001	Mudstone	0.21	1,000	15.1	2			300	0.38	0.04

Sample ID	Drill site	Core depth (m)	Comb. depth (m)	Sample set	Lithology	Ag (ppm)	Al (ppm)	As (ppm)	Ba (ppm)	Be (ppm)	Bi (ppm)	Ca (ppm)	Cd (ppm)	Ce (ppm)
4000037	OnZaP-3	5.02	47.29	MSP0001	Carbonate	0.06		36.6	2			181,300	1.53	0.49
4000955	OnZaP-3	5.14	47.39	MSP0010	Mudstone		5,320	32.1	3			146,173	0.82	5.62
4000543	OnZaP-1	47.65	47.65	MSP0001	Carbonate	0.08		6.5	3			157,600	0.10	
4000944	OnZaP-1	47.90	47.90	MSP0010	Carbonate		38,220	407.1	24			18,436	2.79	4.53
4000045	OnZaP-3	5.89	48.16	MSP0001	Carbonate	0.03		6.8	2			179,700	0.04	0.07
4000956	OnZaP-3	6.01	48.26	MSP0010	Carbonate		424	8.8				227,171	0.16	1.65
4000945	OnZaP-1	48.40	48.40	MSP0010	Carbonate		26,565	665.2	31			41,200	8.61	19.24
4000553	OnZaP-1	48.61	48.61	MSP0001	Mudstone	0.11	700	14.4	2			600	0.37	0.36
4000053	OnZaP-3	6.67	48.94	MSP0001	Mudstone	0.05	200	3.3	1			1,000	0.11	0.14
4000957	OnZaP-3	6.84	49.09	MSP0010	Mudstone									
4000561	OnZaP-1	49.29	49.29	MSP0001	Carbonate	0.05	800	0.8	2			164,100	0.21	3.91
4000061	OnZaP-3	7.28	49.55	MSP0001	Carbonate	0.11		20.8	3			157,000	0.35	0.08
4000958	OnZaP-3	8.00	50.25	MSP0010	Mudstone									
4000563	OnZaP-1	50.43	50.43	MSP0001	Mudstone	0.15	1,500	10.3	2			2,800	0.03	0.09
4000946	OnZaP-1	50.58	50.58	MSP0010	Carbonate		1,606	5.6	1			190,444	1.37	9.00
4000959	OnZaP-3	8.40	50.65	MSP0010	Mudstone		5,778	108.7	5			1,245	2.37	1.92
4000065	OnZaP-3	8.44	50.71	MSP0001	Mudstone	2.47	10,400	234.8	11		0.43	3,100	7.13	1.69
4000571	OnZaP-1	50.77	50.77	MSP0001	Carbonate	0.04			1			160,800	0.15	0.03
4000947	OnZaP-1	51.13	51.13	MSP0010	Carbonate		69,964	694.2	249			2,132	8.49	19.70
4000575	OnZaP-1	51.41	51.41	MSP0001	Mudstone	4.76	29,000	1009.7	219	2	1.04	1,600	20.64	15.33
4000080	OnZaP-3	9.31	51.58	MSP0001	Carbonate	0.04		9.3	3			166,400	0.51	0.12
4000960	OnZaP-3	9.57	51.82	MSP0010	Carbonate		38,292	149.2	76			796	0.40	15.04
4000583	OnZaP-1	52.16	52.16	MSP0001	Carbonate	0.05			2			168,600	1.44	
4000090	OnZaP-3	10.14	52.41	MSP0001	Carbonate	0.05		3.2	2			184,600	0.44	0.04
4000592	OnZaP-1	52.92	52.92	MSP0001	Carbonate	0.05	2,300	1.4	1			217,700	1.50	4.46
4000098	OnZaP-3	10.70	52.97	MSP0001	Carbonate	0.05	700	9.5	3			216,800	0.17	6.22
4000948	OnZaP-1	53.12	53.12	MSP0010	Mudstone		46,930	252.9	89			117,977	5.71	70.29
4000961	OnZaP-3	11.00	53.25	MSP0010	Carbonate		42,830	276.4	148			7,802	1.78	41.92
4000949	OnZaP-1	53.50	53.50	MSP0010	Mudstone		60,172	411.7	445			31,092	6.40	41.10
4000962	OnZaP-3	11.33	53.58	MSP0010	Carbonate		29,457	284.6	256			234,107	2.98	103.47
4000100	OnZaP-3	11.33	53.60	MSP0001	Mudstone	3.37	22,500	845.9	167		0.68	41,800	13.21	28.77
4000593	OnZaP-1	53.70	53.70	MSP0001	Mudstone	1.19	20,600	343.9	166	2	0.51	2,200	2.90	46.24
4000963	OnZaP-3	11.70	53.95	MSP0010	Mudstone		74,849	1690.3	614			1,415	2.28	267.53
4000964	OnZaP-3	11.96	54.21	MSP0010	Mudstone		67,961		507			9,943		
4000102	OnZaP-3	12.16	54.43	MSP0001	Mudstone	1.46	19,700	701.3	149	1	0.80	1,100	9.68	29.20
4000965	OnZaP-3	12.67	54.92	MSP0010	Mudstone		88,428	402.0	815			1,566	2.51	109.25
4000594	OnZaP-1	55.14	55.14	MSP0001	Mudstone	0.93	15,500	277.0	126		0.35	1,000	3.16	29.99
4000966	OnZaP-3	13.11	55.36	MSP0010	Mudstone		54,411	381.0	379			3,192	1.80	52.25
4000597	OnZaP-1	55.51	55.51	MSP0001	Carbonate	0.33	3,300	30.2	7		0.14	222,900	0.41	7.58
4000103	OnZaP-3	13.29	55.56	MSP0001	Mudstone	1.25	17,800	512.3	123	2	0.38	1,400	5.53	43.83
4000601	OnZaP-1	55.68	55.68	MSP0001	Mudstone	1.65	17,800	351.4	141	1	0.43	800	8.70	25.58
4000950	OnZaP-1	55.80	55.80	MSP0010	Mudstone		52,774	323.7	446			1,511	5.05	74.99
4000967	OnZaP-3	13.82	56.07	MSP0010	Carbonate		51,046	285.9	202			28,665	2.74	63.85
4000602	OnZaP-1	56.17	56.17	MSP0001	Mudstone	1.61	15,800	277.3	136		0.47	800	8.04	28.75
4000968	OnZaP-3	14.25	56.50	MSP0010	Mudstone		41,259	178.1	55			121,907	2.26	151.43

Sample ID	Drill site	Core depth (m)	Comb. depth (m)	Sample set	Lithology	Ag (ppm)	Al (ppm)	As (ppm)	Ba (ppm)	Be (ppm)	Bi (ppm)	Ca (ppm)	Cd (ppm)	Ce (ppm)
4000108	OnZaP-3	14.31	56.58	MSP0001	Mudstone	0.58	22,300	121.6	25	2	0.13	127,900	1.16	124.20
4000605	OnZaP-1	56.89	56.89	MSP0001	Carbonate	0.21	1,400	24.2	5			253,200	0.45	7.58
4000969	OnZaP-3	14.69	56.94	MSP0010	Mudstone		64,832	517.5	577			2,262	1.98	107.52
4000113	OnZaP-3	14.85	57.12	MSP0001	Mudstone	1.11	16,200	326.6	118		0.28	1,600	6.24	22.11
4000614	OnZaP-1	57.64	57.64	MSP0001	Carbonate	0.37	4,700	18.7	15			183,600	0.13	6.88
4000951	OnZaP-1	57.93	57.93	MSP0010	Mudstone		78,340	263.7	642			1,492	6.65	69.27
4000970	OnZaP-3	15.72	57.97	MSP0010	Mudstone		34,346	1448.3	309			3,007	2.69	46.79
4000114	OnZaP-3	15.70	57.97	MSP0001	Mudstone	1.92	20,600	370.6	194	1	0.43	2,000	2.30	33.33
4000618	OnZaP-1	58.41	58.41	MSP0001	Mudstone	0.99	29,900	190.5	320	1	0.20	800	3.40	43.17
4000971	OnZaP-3	16.42	58.67	MSP0010	Mudstone		84,014	343.6	739			1,381	4.69	69.62
4000972	OnZaP-3	16.72	58.97	MSP0010	Mudstone		29,323	221.0	232			893	2.43	48.15
4000115	OnZaP-3	16.92	59.19	MSP0001	Mudstone	1.63	38,700	338.4	257	2	0.37	1,000	5.49	18.49
4000952	OnZaP-1	59.25	59.25	MSP0010	Mudstone		49,728		410			7,412		
4000619	OnZaP-1	59.67	59.67	MSP0001	Mudstone	0.96	39,100	102.9	256	1	0.19	29,800	1.61	25.98
4000122	OnZaP-3	17.55	59.82	MSP0001	Mudstone	1.6	16,800	267.7	67		0.32	500	2.90	16.08
4000973	OnZaP-3	17.89	60.14	MSP0010	Mudstone		24,173	163.6	19			45,731	2.06	33.20
4000623	OnZaP-1	60.18	60.18	MSP0001	Mudstone	0.67	26,200	41.2	44		0.06	164,400	0.57	12.64
4000128	OnZaP-3	18.65	60.92	MSP0001	Carbonate	0.73	5,000	37.2	21			209,700	0.13	8.20
4000129	OnZaP-3	18.97	61.24	MSP0001	Mudstone	2.23	30,000	309.0	195		0.28	500	5.22	17.08
4000974	OnZaP-3	19.27	61.52	MSP0010	Mudstone		57,477	305.3	451			833	3.20	60.73
4000975	OnZaP-3	20.07	62.32	MSP0010	Mudstone		57,687	136.4	477			4,533	2.13	70.16
4000130	OnZaP-3	20.13	62.40	MSP0001	Mudstone	1.57	31,800	97.3	150		0.26	78,700	1.60	25.28
4000132	OnZaP-3	20.90	63.17	MSP0001	Mudstone	0.99	23,400	225.2	202	1	0.15	400	1.59	28.30
4000976	OnZaP-3	21.12	63.37	MSP0010	Mudstone		45,359	127.3	358			564	1.82	71.27
4000133	OnZaP-3	21.96	64.23	MSP0001	Mudstone	1.27	35,500	98.4	331	1	0.21	1,000	1.56	41.91
4000977	OnZaP-3	22.36	64.61	MSP0010	Mudstone		43,004	144.4	435			1,062	1.71	89.61
4000978	OnZaP-3	22.96	65.21	MSP0010	Mudstone		79,681	238.1	781			614	2.97	179.84
4000134	OnZaP-3	23.12	65.39	MSP0001	Mudstone	1.59	43,100	180.0	403	2	0.29	700	1.66	27.01
4000979	OnZaP-3	23.59	65.84	MSP0010	Mudstone		48,642		417			1,803		
4000135	OnZaP-3	24.26	66.53	MSP0001	Carbonate	0.33	6,500	60.8	98			207,700	0.28	7.79
4000980	OnZaP-3	24.91	67.16	MSP0010	Mudstone		59,587	124.8	75			2,407	2.16	148.03
4000151	OnZaP-3	25.18	67.45	MSP0001	Carbonate	0.28	3,600	75.3	102			202,200	0.20	7.08
4000981	OnZaP-3	25.59	67.84	MSP0010	Mudstone		63,733	23.1	316			5,892	0.44	24.25
4000159	OnZaP-3	25.76	68.03	MSP0001	Mudstone	1.72	62,200	140.6	334	1	0.17	1,600	1.95	41.21
4000982	OnZaP-3	26.20	68.45	MSP0010	Mudstone		52,011	132.7	73			2,737	2.94	64.68
4000168	OnZaP-3	26.56	68.83	MSP0001	Mudstone	1.24	57,000	85.7	31	1	0.13	68,300	0.41	128.96
4000178	OnZaP-3	27.32	69.59	MSP0001	Carbonate	0.58	7,600	47.4	15		0.10	189,800	0.31	5.20
4000983	OnZaP-3	27.51	69.76	MSP0010	Carbonate		42,852	12.5	53			26,622	1.36	16.53
4000179	OnZaP-3	28.13	70.40	MSP0001	Mudstone	0.39	7,600	158.7	66		0.05	200	4.37	5.54
4000984	OnZaP-3	28.69	70.94	MSP0010	Mudstone		19,841	18.7	269			395	0.87	8.44
4000180	OnZaP-3	29.20	71.47	MSP0001	Mudstone	3.41	24,400	213.0	263	1	0.32	500	3.95	28.08
4000985	OnZaP-3	29.35	71.60	MSP0010	Mudstone		21,840	163.9	264			318	6.58	41.92
4000181	OnZaP-3	30.59	72.86	MSP0001	Mudstone	1.21	16,800	113.0	18	1	0.22	83,300	1.04	50.12
4000986	OnZaP-3	30.68	72.93	MSP0010	Mudstone		31,756	567.0	148			1,082	8.16	46.44
4000987	OnZaP-3	31.40	73.65	MSP0010	Mudstone		26,805	219.3	279			696	1.58	51.27

Sample ID	Drill site	Core depth (m)	Comb. depth (m)	Sample set	Lithology	Ag (ppm)	Al (ppm)	As (ppm)	Ba (ppm)	Be (ppm)	Bi (ppm)	Ca (ppm)	Cd (ppm)	Ce (ppm)
4000187	OnZaP-3	31.63	73.90	MSP0001	Mudstone	1.36	19,100	245.7	175		0.34	600	3.09	21.00
4000988	OnZaP-3	32.10	74.35	MSP0010	Mudstone		17,999	316.6	38			1,562	3.70	80.43
4000190	OnZaP-3	32.36	74.63	MSP0001	Carbonate	0.16	4,700	20.0	8			156,400	0.29	3.75
4000201	OnZaP-3	33.24	75.51	MSP0001	Mudstone	0.87	19,200	129.2	21		0.21	38,500	1.35	14.74
4000989	OnZaP-3	33.48	75.73	MSP0010	Mudstone		29,277	315.9	74			3,483	4.75	89.96
4000990	OnZaP-3	33.81	76.06	MSP0010	Mudstone		12,240		179			200		
4000202	OnZaP-3	34.29	76.56	MSP0001	Mudstone	0.86	27,700	42.6	409		0.20	700	0.40	25.66
4000203	OnZaP-3	34.96	77.23	MSP0001	Mudstone	0.28	27,200	8.6	292		0.10	400	0.39	21.68
4000214	OnZaP-3	36.54	78.81	MSP0001	Carbonate	0.19	11,300	9.3	39		0.05	159,200	0.98	16.95
4000216	OnZaP-3	37.30	79.57	MSP0001	Carbonate	0.21	8,700	13.1	35		0.08	133,700	0.46	6.29
4000225	OnZaP-3	38.42	80.69	MSP0001	Mudstone	0.26	15,200	11.8	40		0.07	126,200	0.08	14.16
4000231	OnZaP-3	39.25	81.52	MSP0001	Mudstone	0.35	23,100	15.6	32	1	0.10	134,100	0.02	24.14
4000239	OnZaP-3	40.20	82.47	MSP0001	Mudstone	0.45	43,500	15.2	175	1	0.13	20,000	0.03	49.63
4000244	OnZaP-3	41.09	83.36	MSP0001	Mudstone	0.19	19,400	6.3	34		0.05	141,100	0.03	35.35
4000251	OnZaP-3	42.32	84.59	MSP0001	Carbonate	0.42	11,100	11.6	17		0.08	144,500	0.09	14.49
4000256	OnZaP-3	43.12	85.39	MSP0001	Carbonate	0.13	3,200	4.5	6			179,700	0.07	5.66
4000264	OnZaP-3	44.02	86.29	MSP0001	Mudstone	0.8	34,600	22.0	226		0.17	26,300	0.29	34.14
4000265	OnZaP-3	44.82	87.09	MSP0001	Mudstone	0.86	26,300	22.8	249		0.18	3,300	0.20	23.10
4000266	OnZaP-3	45.87	88.14	MSP0001	Mudstone	0.9	26,500	24.8	338		0.12	800	0.81	20.64
4000991	OnZaP-3	46.11	88.36	MSP0010	Mudstone		32,266	49.1	463			1,287	1.65	46.22
4000992	OnZaP-3	46.51	88.76	MSP0010	Mudstone		39,091	78.8	551			535	5.87	56.13
4000267	OnZaP-3	46.59	88.86	MSP0001	Mudstone	1.58	33,900	52.2	470		0.17	1,500	2.13	27.74
4000993	OnZaP-3	47.86	90.11	MSP0010	Mudstone		26,118	90.5	352			485	10.17	45.19
4000268	OnZaP-3	48.02	90.29	MSP0001	Mudstone	1.57	28,400	41.7	427		0.16	1,200	1.84	23.31
4000994	OnZaP-3	48.94	91.19	MSP0010	Mudstone		32,873	74.0	463			4,221	3.61	41.85
4000269	OnZaP-3	49.00	91.27	MSP0001	Mudstone	1.17	18,600	35.3	268		0.11	900	0.64	19.38
4000270	OnZaP-3	49.68	91.95	MSP0001	Mudstone	2.04	23,400	65.8	253		0.35	2,100	0.97	25.87
4000271	OnZaP-3	50.28	92.55	MSP0001	Mudstone	0.83	32,000	23.6	365	1	0.16	2,900	0.27	18.20
4000273	OnZaP-3	50.99	93.26	MSP0001	Mudstone	0.61	25,800	12.7	204		0.08	12,800	1.59	9.87
4001000	OnZaP-1	51.57	93.82	MSP0010	Carbonate		2,417	3.1	1			237,126	0.74	14.10
4000279	OnZaP-3	52.53	94.80	MSP0001	Mudstone	1.35	34,100	33.7	442	1	0.22	5,700	0.35	7.41
4000280	OnZaP-3	53.02	95.29	MSP0001	Mudstone	1.06	31,400	28.7	414	1	0.11	600	0.75	15.10
4000995	OnZaP-3	53.75	96.00	MSP0010	Mudstone		31,147	38.7	403			388	3.39	37.82
4000281	OnZaP-3	54.02	96.29	MSP0001	Mudstone	1.44	27,300	43.5	276		0.13	500	3.17	22.27
4000288	OnZaP-3	55.01	97.28	MSP0001	Mudstone	0.33	10,400	14.2	13			181,300	2.11	7.29
4000289	OnZaP-3	55.60	97.87	MSP0001	Mudstone	2.26	32,300	52.5	418		0.15	600	5.09	24.05
4000996	OnZaP-3	55.76	98.01	MSP0010	Mudstone		40,047	43.5	590			698	2.71	49.17
4000290	OnZaP-3	56.52	98.79	MSP0001	Mudstone	1.04	23,800	23.3	343	1	0.16	2,300	2.64	16.06
4000997	OnZaP-3	57.27	99.52	MSP0010	Mudstone		27,162	173.5	386			646	6.64	33.00
4000998	OnZaP-3	58.06	100.31	MSP0010	Mudstone		49,145	210.1	667			591	6.44	61.00
4000291	OnZaP-3	58.24	100.51	MSP0001	Mudstone	2.57	32,200	481.7	519	1	0.34	600	3.51	24.59
4000299	OnZaP-3	58.87	101.14	MSP0001	Carbonate	0.25	3,400	20.5	5			207,200	0.05	16.89
4000999	OnZaP-3	59.88	102.13	MSP0010	Mudstone		52,440	227.5	624			841	9.77	73.43
4000306	OnZaP-3	59.95	102.22	MSP0001	Mudstone	4.3	55,800	183.6	458	1	0.55	700	16.48	19.85

Table A1b: Element concentration data for drill cores OnZaP-1 and OnZaP-3, continued.

Sample ID	Drill site	Core depth (m)	Comb. depth (m)	Sample set	Lithology	Co (ppm)	Cr (ppm)	Cs (ppm)	Cu (ppm)	Dy (ppm)	Er (ppm)	Eu (ppm)	Fe (ppm)	Ga (ppm)
4000319	OnZaP-1	1.96	1.96	MSP0001	Mudstone	13.3	118	2.8	15.1	1.3	0.8	0.3	53,800	15.93
4000921	OnZaP-1	2.08	2.08	MSP0010	Mudstone	23.0	155	4.3	28.6	5.7	3.3	2.0	70,330	19.02
4000320	OnZaP-1	2.85	2.85	MSP0001	Mudstone	17.6	102	3.7	31.8	1.4	0.9	0.4	75,600	16.48
4000321	OnZaP-1	3.92	3.92	MSP0001	Mudstone	32.9	118	4.8	40.6	1.0	0.7	0.3	74,600	19.69
4000922	OnZaP-1	5.28	5.28	MSP0010	Mudstone	9.0	60	2.4	5.9	2.0	1.2	0.7	65,246	9.19
4000322	OnZaP-1	5.31	5.31	MSP0001	Mudstone	15.0	117	3.7	9.8	1.1	0.7	0.3	68,500	19.09
4000323	OnZaP-1	6.50	6.50	MSP0001	Mudstone	20.8	108	5.0	44.2	0.9	0.6	0.2	68,600	17.12
4000923	OnZaP-1	6.60	6.60	MSP0010	Mudstone								98,308	
4000324	OnZaP-1	7.01	7.01	MSP0001	Mudstone	21.7	123	6.2	22.3	1.3	0.9	0.4	44,000	19.50
4000332	OnZaP-1	7.96	7.96	MSP0001	Mudstone	9.9	25	1.1	14.0	2.0	1.0	0.7	53,900	6.21
4000336	OnZaP-1	8.35	8.35	MSP0001	Mudstone	34.8	90	5.8	25.2	1.3	0.9	0.4	47,400	19.27
4000342	OnZaP-1	8.74	8.74	MSP0001	Mudstone	35.7	21	3.9	25.4	2.0	1.1	0.7	58,500	6.45
4000345	OnZaP-1	9.58	9.58	MSP0001	Mudstone	35.1	82	3.4	32.4	2.1	1.3	0.6	48,800	15.20
4000346	OnZaP-1	10.79	10.79	MSP0001	Mudstone	36.9	99	3.5	21.4	0.8	0.6	0.2	65,700	18.24
4000924	OnZaP-1	11.13	11.13	MSP0010	Mudstone	26.1	99	5.1	26.5	4.3	2.6	1.5	100,047	17.24
4000347	OnZaP-1	11.86	11.86	MSP0001	Mudstone	14.5	96	3.7	9.1	1.8	1.3	0.5	38,900	20.78
4000925	OnZaP-1	12.15	12.15	MSP0010	Mudstone	107.9	116	4.4	91.4	5.9	3.6	2.0	104,796	15.84
4000348	OnZaP-1	12.39	12.39	MSP0001	Mudstone	79.9	94	4.0	83.6	1.3	1.0	0.3	79,700	17.32
4000349	OnZaP-1	13.16	13.16	MSP0001	Mudstone	11.5	5	4.1	11.5	1.3	0.7	0.6	65,200	2.29
4000351	OnZaP-1	13.40	13.40	MSP0001	Mudstone	9.8	12	4.1	4.4	1.0	0.5	0.5	56,700	3.50
4000358	OnZaP-1	14.65	14.65	MSP0001	Mudstone	21.8	102	5.1	36.2	1.0	0.7	0.2	62,900	20.73
4000362	OnZaP-1	15.26	15.26	MSP0001	Mudstone	15.2	51	1.2	6.9	2.0	1.2	0.6	49,500	9.74
4000368	OnZaP-1	16.29	16.29	MSP0001	Mudstone	10.3	6	1.4	14.3	1.1	0.6	0.3	52,200	2.11
4000376	OnZaP-1	17.36	17.36	MSP0001	Mudstone	10.4	8	1.7	1.7	0.8	0.6	0.5	56,800	3.21
4000383	OnZaP-1	17.90	17.90	MSP0001	Mudstone	13.6	9	4.1	5.2	1.5	0.8	0.6	52,600	3.92
4000926	OnZaP-1	18.85	18.85	MSP0010	Mudstone	54.1	123	12.0	70.7	4.5	2.5	1.8	85,500	20.06
4000392	OnZaP-1	19.08	19.08	MSP0001	Mudstone	17.8	113	6.8	10.4	1.3	0.9	0.5	43,500	20.24
4000393	OnZaP-1	19.99	19.99	MSP0001	Mudstone	21.5	123	8.8	8.8	1.1	0.7	0.3	55,900	20.10
4000394	OnZaP-1	20.66	20.66	MSP0001	Mudstone	53.9	140	6.0	197.7	1.6	0.9	0.6	35,800	19.54
4000927	OnZaP-1	21.91	21.91	MSP0010	Mudstone	13.0	140	8.1	14.2	4.4	2.5	1.9	66,329	20.59
4000395	OnZaP-1	21.94	21.94	MSP0001	Mudstone	11.5	109	5.1	18.5	1.4	0.8	0.6	57,400	17.66
4000396	OnZaP-1	22.33	22.33	MSP0001	Mudstone	22.6	130	4.7	50.2	1.3	0.6	0.6	68,100	18.41
4000398	OnZaP-1	23.03	23.03	MSP0001	Mudstone	15.9	112	5.7	19.9	1.9	1.3	0.7	68,800	18.27
4000928	OnZaP-1	23.84	23.84	MSP0010	Mudstone	24.8	58	4.5	35.6	3.1	1.8	1.1	72,681	9.24
4000403	OnZaP-1	24.31	24.31	MSP0001	Mudstone	13.8	65	4.2	21.9	2.0	1.1	0.8	48,200	12.54
4000406	OnZaP-1	25.03	25.03	MSP0001	Mudstone	9.8	8	3.7	26.6	1.6	0.7	0.7	46,400	3.40
4000412	OnZaP-1	26.09	26.09	MSP0001	Mudstone	14.8	127	5.1	21.5	1.0	0.7	0.3	16,900	19.27
4000413	OnZaP-1	26.80	26.80	MSP0001	Mudstone	40.9	121	4.7	25.1	1.6	0.9	0.5	22,400	20.01
4000414	OnZaP-1	27.77	27.77	MSP0001	Mudstone	13.1	44	0.4	13.7	2.6	1.3	0.8	35,900	10.58
4000929	OnZaP-1	27.95	27.95	MSP0010	Mudstone	23.6	154	4.3	27.5	4.7	2.9	1.8	44,798	22.27
4000421	OnZaP-1	28.36	28.36	MSP0001	Mudstone	10.7	13	0.7	11.5	2.4	1.0	0.7	30,800	4.99
4000930	OnZaP-1	28.80	28.80	MSP0010	Mudstone	42.0	126	4.7	45.9	6.9	4.3	2.8	41,909	27.61

Sample ID	Drill site	Core depth (m)	Comb. depth (m)	Sample set	Lithology	Co (ppm)	Cr (ppm)	Cs (ppm)	Cu (ppm)	Dy (ppm)	Er (ppm)	Eu (ppm)	Fe (ppm)	Ga (ppm)
4000429	OnZaP-1	29.28	29.28	MSP0001	Carbonate	2.5	3	0.3	2.0	1.2	0.6	0.6	22,700	0.81
4000931	OnZaP-1	30.66	30.66	MSP0010	Mudstone	68.0	180	2.5	42.2	6.4	4.1	1.8	91,256	16.06
4000436	OnZaP-1	30.79	30.79	MSP0001	Mudstone	20.8	110	1.5	34.2	1.7	1.1	0.4	32,400	19.55
4000442	OnZaP-1	31.21	31.21	MSP0001	Carbonate	1.1	2	0.5	0.9	1.5	0.9	0.5	15,300	0.62
4000932	OnZaP-1	31.85	31.85	MSP0010	Mudstone	31.7	162	1.9	29.5	6.3	4.1	1.8	35,940	18.72
4000447	OnZaP-1	31.86	31.86	MSP0001	Mudstone	22.9	106	1.2	28.9	1.4	0.9	0.3	55,500	22.23
4000933	OnZaP-1	32.19	32.19	MSP0010	Mudstone	26.0	170	2.1	38.8	6.7	4.4	1.6	58,466	19.72
4000455	OnZaP-1	33.15	33.15	MSP0001	Carbonate	1.9	4	0.1	1.8	0.7	0.6	0.3	4,500	1.15
4000466	OnZaP-1	33.96	33.96	MSP0001	Carbonate	3.8	3	0.3	9.9	1.8	1.4	0.3	8,300	0.81
4000471	OnZaP-1	34.64	34.64	MSP0001	Carbonate	3.6	8	0.1	10.4	1.2	0.8	0.2	5,300	2.03
4000478	OnZaP-1	35.61	35.61	MSP0001	Mudstone	3.0	3	0.2	14.4	0.9	0.5	0.2	12,900	0.76
4000934	OnZaP-1	36.40	36.40	MSP0010	Mudstone	27.0	191	4.1	88.7	13.9	7.8	2.4	35,658	24.58
4000483	OnZaP-1	36.52	36.52	MSP0001	Mudstone	23.1	117	2.4	73.3	4.7	2.7	0.7	32,700	23.78
4000484	OnZaP-1	36.94	36.94	MSP0001	Carbonate	1.4	3	1.1	1.7	1.3	0.8	0.3	2,700	1.26
4000935	OnZaP-1	37.83	37.83	MSP0010	Mudstone	32.6	80	2.5	92.6	14.0	7.9	2.4	89,562	19.53
4000491	OnZaP-1	38.13	38.13	MSP0001	Mudstone	37.7	71	1.1	80.5	4.8	2.7	0.6	91,500	20.94
4000936	OnZaP-1	38.91	38.91	MSP0010	Mudstone	44.8	79	2.3	70.9	14.3	8.5	3.3	133,607	21.92
4000492	OnZaP-1	38.97	38.97	MSP0001	Mudstone	44.8	66	1.5	98.0	4.9	3.4	0.8	67,200	17.93
4000493	OnZaP-1	39.88	39.88	MSP0001	Mudstone	19.9	150	7.8	92.8	3.5	2.5	0.7	34,500	8.28
4000937	OnZaP-1	40.02	40.02	MSP0010	Carbonate	17.6	187	6.2	103.3	7.5	5.3	1.4	43,591	11.17
4000938	OnZaP-1	41.09	41.09	MSP0010	Mudstone	21.3	196	2.4	197.0	6.6	4.9	1.2	72,136	13.28
4000494	OnZaP-1	41.15	41.15	MSP0001	Mudstone	20.7	163	2.0	205.5	3.3	2.4	0.5	46,000	12.87
4000939	OnZaP-1	41.38	41.38	MSP0010	Mudstone	27.3	201	4.8	343.4	9.1	6.5	1.8	84,217	13.30
4000500	OnZaP-1	42.04	42.04	MSP0001	Carbonate	0.6	4	0.3	1.5	1.0	0.7	0.5	1,400	0.24
4000940	OnZaP-1	42.42	42.42	MSP0010	Mudstone	34.9	191	5.9	266.8	7.3	5.0	1.5	121,589	7.09
4000504	OnZaP-1	42.45	42.45	MSP0001	Mudstone	28.8	97	11.1	115.3	2.4	1.8	0.5	59,600	11.64
4000941	OnZaP-1	42.86	42.86	MSP0010	Carbonate	83.7	170	4.2	131.7	4.6	3.4	0.8	189,602	4.42
4000942	OnZaP-1	43.69	43.69	MSP0010	Carbonate								136,266	
4000516	OnZaP-1	43.94	43.94	MSP0001	Carbonate	0.4	2		0.9				300	0.05
4000005	OnZaP-3	2.10	44.37	MSP0001	Carbonate	0.7	10		2.4				800	0.10
4000521	OnZaP-1	44.53	44.53	MSP0001	Carbonate	0.4	2		1.1				300	0.05
4000953	OnZaP-3	2.68	44.93	MSP0010	Carbonate	2.7	49	2.9	147.9	11.6	8.6	3.5	6,992	3.46
4000954	OnZaP-3	2.77	45.02	MSP0010	Mudstone	3.3	245	8.5	97.1	1.2	1.2	0.3	14,381	11.21
4000015	OnZaP-3	3.12	45.39	MSP0001	Carbonate	0.6	5		4.0				600	
4000529	OnZaP-1	45.65	45.65	MSP0001	Carbonate	0.5	3		0.5				500	0.08
4000943	OnZaP-1	46.36	46.36	MSP0010	Mudstone	38.4	394	8.1	248.1	3.0	2.7	0.5	48,329	9.11
4000030	OnZaP-3	4.38	46.65	MSP0001	Carbonate	0.3	5		2.3				500	0.03
4000536	OnZaP-1	46.70	46.70	MSP0001	Mudstone	1.5	5	0.3	4.4				600	0.24
4000037	OnZaP-3	5.02	47.29	MSP0001	Carbonate	1.8	4	0.2	4.6				1,100	0.14
4000955	OnZaP-3	5.14	47.39	MSP0010	Mudstone	3.2	42	1.4	23.6	1.2	0.8	0.5	5,482	2.06
4000543	OnZaP-1	47.65	47.65	MSP0001	Carbonate	0.3	2		0.7				400	
4000944	OnZaP-1	47.90	47.90	MSP0010	Carbonate	42.6	217	5.9	70.6	3.2	3.0	0.3	59,583	12.21
4000045	OnZaP-3	5.89	48.16	MSP0001	Carbonate	2.5	2		1.9				500	0.15
4000956	OnZaP-3	6.01	48.26	MSP0010	Carbonate	0.3	3		20.9	0.3	0.2	0.1	283	0.10
4000945	OnZaP-1	48.40	48.40	MSP0010	Carbonate	32.4	272	4.2	243.0	3.5	2.8	0.5	62,991	6.54

Sample ID	Drill site	Core depth (m)	Comb. depth (m)	Sample set	Lithology	Co (ppm)	Cr (ppm)	Cs (ppm)	Cu (ppm)	Dy (ppm)	Er (ppm)	Eu (ppm)	Fe (ppm)	Ga (ppm)
4000553	OnZaP-1	48.61	48.61	MSP0001	Mudstone	3.2	7		12.3	0.1			6,600	0.14
4000053	OnZaP-3	6.67	48.94	MSP0001	Mudstone	0.9	184		13.9				6,700	0.17
4000957	OnZaP-3	6.84	49.09	MSP0010	Mudstone									
4000561	OnZaP-1	49.29	49.29	MSP0001	Carbonate	0.7	7	0.2	1.7	1.0	0.7	0.3	2,200	0.31
4000061	OnZaP-3	7.28	49.55	MSP0001	Carbonate	4.8	3		3.4				1,100	0.03
4000958	OnZaP-3	8.00	50.25	MSP0010	Mudstone									
4000563	OnZaP-1	50.43	50.43	MSP0001	Mudstone	2.2	2	0.4	4.7				1,200	0.37
4000946	OnZaP-1	50.58	50.58	MSP0010	Carbonate	0.6	12	0.3	9.5	1.8	1.4	0.4	1,669	0.62
4000959	OnZaP-3	8.40	50.65	MSP0010	Mudstone	7.4	70	1.3	138.1	0.4	0.3	0.1	8,108	1.92
4000065	OnZaP-3	8.44	50.71	MSP0001	Mudstone	9.1	213	2.5	152.6	0.6	0.4		16,100	3.36
4000571	OnZaP-1	50.77	50.77	MSP0001	Carbonate	0.4	4		0.6				1,700	0.15
4000947	OnZaP-1	51.13	51.13	MSP0010	Carbonate	27.7	286	6.3	213.9	4.5	3.7	0.5	82,175	10.16
4000575	OnZaP-1	51.41	51.41	MSP0001	Mudstone	36.3	247	2.4	624.4	3.7	2.7	0.4	36,900	10.02
4000080	OnZaP-3	9.31	51.58	MSP0001	Carbonate	4.9	4		8.3				1,200	0.09
4000960	OnZaP-3	9.57	51.82	MSP0010	Carbonate	1.8	69	1.2	14.7	1.6	1.5	0.2	37,330	2.38
4000583	OnZaP-1	52.16	52.16	MSP0001	Carbonate	0.7	5	0.1	0.7				800	0.12
4000090	OnZaP-3	10.14	52.41	MSP0001	Carbonate	0.6	8	0.1	4.6				1,100	0.22
4000592	OnZaP-1	52.92	52.92	MSP0001	Carbonate	1.0	6	1.6	0.8	0.7	0.7	0.2	1,700	1.01
4000098	OnZaP-3	10.70	52.97	MSP0001	Carbonate	6.9	8	0.3	1.9	0.8	0.7	0.3	2,300	0.41
4000948	OnZaP-1	53.12	53.12	MSP0010	Mudstone	8.6	253	11.8	189.2	20.7	15.3	4.9	29,000	8.91
4000961	OnZaP-3	11.00	53.25	MSP0010	Carbonate	6.8	114	4.9	51.2	6.0	5.5	0.7	56,291	7.52
4000949	OnZaP-1	53.50	53.50	MSP0010	Mudstone	39.0	150	1.1	239.3	7.2	5.3	1.4	69,565	7.45
4000962	OnZaP-3	11.33	53.58	MSP0010	Carbonate	3.7	177	2.4	109.4	22.6	17.7	8.9	16,812	5.98
4000100	OnZaP-3	11.33	53.60	MSP0001	Mudstone	8.3	269	1.6	579.3	7.1	5.4	1.6	19,200	6.68
4000593	OnZaP-1	53.70	53.70	MSP0001	Mudstone	37.0	87	1.1	117.6	6.7	4.8	1.1	27,700	8.91
4000963	OnZaP-3	11.70	53.95	MSP0010	Mudstone	32.4	313	1.4	107.9	18.9	10.9	4.3	153,603	21.26
4000964	OnZaP-3	11.96	54.21	MSP0010	Mudstone								56,716	
4000102	OnZaP-3	12.16	54.43	MSP0001	Mudstone	21.5	234	1.3	190.6	4.5	3.5	0.9	16,400	7.49
4000965	OnZaP-3	12.67	54.92	MSP0010	Mudstone	28.4	128	1.2	64.7	12.4	10.2	2.3	98,507	10.33
4000594	OnZaP-1	55.14	55.14	MSP0001	Mudstone	50.9	67	0.8	201.6	4.7	3.2	0.9	39,000	5.03
4000966	OnZaP-3	13.11	55.36	MSP0010	Mudstone	43.9	102	1.4	77.6	9.4	6.7	1.8	105,999	5.88
4000597	OnZaP-1	55.51	55.51	MSP0001	Carbonate	3.2	5	1.3	11.1	1.9	1.4	0.5	17,500	0.97
4000103	OnZaP-3	13.29	55.56	MSP0001	Mudstone	36.1	180	1.3	127.0	6.0	3.8	1.4	20,400	6.51
4000601	OnZaP-1	55.68	55.68	MSP0001	Mudstone	51.8	95	1.5	250.0	4.8	3.6	0.8	52,300	6.26
4000950	OnZaP-1	55.80	55.80	MSP0010	Mudstone	46.6	186	0.7	257.3	11.1	8.0	2.3	130,557	11.13
4000967	OnZaP-3	13.82	56.07	MSP0010	Carbonate	41.6	89	3.5	126.2	9.0	6.4	1.9	95,557	5.83
4000602	OnZaP-1	56.17	56.17	MSP0001	Mudstone	54.4	76	0.3	118.3	3.0	2.1	0.8	55,200	4.82
4000968	OnZaP-3	14.25	56.50	MSP0010	Mudstone	38.9	64	5.4	40.4	11.8	7.5	2.9	72,911	10.45
4000108	OnZaP-3	14.31	56.58	MSP0001	Mudstone	17.5	28	6.4	27.7	7.8	4.9	2.0	22,500	8.11
4000605	OnZaP-1	56.89	56.89	MSP0001	Carbonate	5.5	8	0.3	26.0	1.6	1.1	0.5	13,500	0.59
4000969	OnZaP-3	14.69	56.94	MSP0010	Mudstone	51.9	71	1.2	88.4	9.3	6.1	2.4	193,861	7.95
4000113	OnZaP-3	14.85	57.12	MSP0001	Mudstone	66.6	70	0.8	194.0	3.4	2.5	0.7	28,400	5.26
4000614	OnZaP-1	57.64	57.64	MSP0001	Carbonate	5.3	27	1.2	217.3	1.1	0.8	0.7	23,800	2.01
4000951	OnZaP-1	57.93	57.93	MSP0010	Mudstone	78.4	149	1.0	326.2	10.5	7.3	2.1	110,406	15.00
4000970	OnZaP-3	15.72	57.97	MSP0010	Mudstone	64.2	63	0.9	135.0	7.0	4.8	1.6	327,835	4.39

Sample ID	Drill site	Core depth (m)	Comb. depth (m)	Sample set	Lithology	Co (ppm)	Cr (ppm)	Cs (ppm)	Cu (ppm)	Dy (ppm)	Er (ppm)	Eu (ppm)	Fe (ppm)	Ga (ppm)
4000114	OnZaP-3	15.70	57.97	MSP0001	Mudstone	47.2	142	0.8	140.7	4.3	3.0	0.9	59,700	6.29
4000618	OnZaP-1	58.41	58.41	MSP0001	Mudstone	35.5	86	0.4	239.4	5.8	4.0	1.3	26,000	12.12
4000971	OnZaP-3	16.42	58.67	MSP0010	Mudstone	58.1	75	0.7	62.2	7.1	4.7	1.9	153,007	17.13
4000972	OnZaP-3	16.72	58.97	MSP0010	Mudstone	25.2	98	0.6	133.9	5.1	3.9	1.3	28,359	5.01
4000115	OnZaP-3	16.92	59.19	MSP0001	Mudstone	57.2	152	0.8	402.8	4.0	2.8	1.0	52,200	11.10
4000952	OnZaP-1	59.25	59.25	MSP0010	Mudstone								46,333	
4000619	OnZaP-1	59.67	59.67	MSP0001	Mudstone	38.9	46	1.2	149.7	6.7	4.4	1.1	24,500	11.61
4000122	OnZaP-3	17.55	59.82	MSP0001	Mudstone	54.7	98	3.0	198.0	2.2	1.6	0.6	54,300	4.80
4000973	OnZaP-3	17.89	60.14	MSP0010	Mudstone	25.6	100	6.3	111.0	5.0	3.7	1.0	42,016	6.20
4000623	OnZaP-1	60.18	60.18	MSP0001	Mudstone	18.0	58	5.1	47.4	3.4	2.3	0.5	27,100	7.98
4000128	OnZaP-3	18.65	60.92	MSP0001	Carbonate	3.1	40	1.4	77.0	2.0	1.3	0.5	34,300	1.24
4000129	OnZaP-3	18.97	61.24	MSP0001	Mudstone	54.1	190	0.8	316.8	3.5	2.2	0.7	72,400	9.76
4000974	OnZaP-3	19.27	61.52	MSP0010	Mudstone	62.7	86	0.9	240.6	8.7	5.7	2.0	137,786	13.65
4000975	OnZaP-3	20.07	62.32	MSP0010	Mudstone	46.9	193	1.5	323.7	12.2	8.1	2.1	104,727	12.58
4000130	OnZaP-3	20.13	62.40	MSP0001	Mudstone	28.0	168	2.1	170.3	3.9	2.6	0.7	81,500	8.24
4000132	OnZaP-3	20.90	63.17	MSP0001	Mudstone	17.1	95	0.5	178.2	4.4	3.1	0.9	17,000	10.94
4000976	OnZaP-3	21.12	63.37	MSP0010	Mudstone	23.2	72	0.8	150.1	10.3	6.9	2.1	38,998	10.72
4000133	OnZaP-3	21.96	64.23	MSP0001	Mudstone	22.3	161	1.0	87.5	4.9	3.1	1.1	35,200	12.88
4000977	OnZaP-3	22.36	64.61	MSP0010	Mudstone	29.6	204	0.8	113.0	11.0	6.6	2.4	55,274	9.37
4000978	OnZaP-3	22.96	65.21	MSP0010	Mudstone	67.7	112	1.0	137.8	18.4	11.4	4.3	87,405	24.94
4000134	OnZaP-3	23.12	65.39	MSP0001	Mudstone	44.3	134	0.6	103.7	3.6	2.2	0.9	51,000	21.70
4000979	OnZaP-3	23.59	65.84	MSP0010	Mudstone								120,112	
4000135	OnZaP-3	24.26	66.53	MSP0001	Carbonate	9.0	14	1.2	21.6	1.9	0.9	0.5	21,500	1.79
4000980	OnZaP-3	24.91	67.16	MSP0010	Mudstone	49.3	263	10.7	125.0	5.5	3.1	2.4	47,314	21.28
4000151	OnZaP-3	25.18	67.45	MSP0001	Carbonate	8.7	8	0.7	39.1	1.5	0.7	0.6	25,400	1.27
4000981	OnZaP-3	25.59	67.84	MSP0010	Mudstone	10.8	26	1.1	50.8	1.8	1.2	0.6	47,271	3.65
4000159	OnZaP-3	25.76	68.03	MSP0001	Mudstone	61.5	119	5.6	192.9	2.6	1.6	0.9	43,000	17.69
4000982	OnZaP-3	26.20	68.45	MSP0010	Mudstone	72.3	311	9.7	156.2	5.8	3.7	1.8	74,469	16.59
4000168	OnZaP-3	26.56	68.83	MSP0001	Mudstone	28.8	31	5.7	67.2	8.1	4.0	4.4	40,500	18.21
4000178	OnZaP-3	27.32	69.59	MSP0001	Carbonate	6.1	10	2.0	28.4	1.1	0.7	0.4	15,200	2.14
4000983	OnZaP-3	27.51	69.76	MSP0010	Carbonate	3.4	290	7.8	348.9	2.9	2.1	0.7	13,192	10.82
4000179	OnZaP-3	28.13	70.40	MSP0001	Mudstone	7.6	117	0.8	88.7	1.5	1.2	0.3	8,700	2.23
4000984	OnZaP-3	28.69	70.94	MSP0010	Mudstone	2.4	12	0.3	53.0	2.5	1.7	0.5	2,258	6.57
4000180	OnZaP-3	29.20	71.47	MSP0001	Mudstone	13.4	156	0.6	126.3	4.7	2.8	1.1	20,300	7.78
4000985	OnZaP-3	29.35	71.60	MSP0010	Mudstone	10.3	187	0.6	28.9	6.0	3.9	1.8	11,147	7.54
4000181	OnZaP-3	30.59	72.86	MSP0001	Mudstone	12.5	105	3.5	30.9	14.9	7.8	6.5	28,800	4.06
4000986	OnZaP-3	30.68	72.93	MSP0010	Mudstone	19.8	330	4.9	326.5	7.9	6.6	1.8	26,059	6.40
4000987	OnZaP-3	31.40	73.65	MSP0010	Mudstone	44.5	111	0.9	49.4	6.4	4.0	2.1	90,186	5.58
4000187	OnZaP-3	31.63	73.90	MSP0001	Mudstone	29.3	126	1.0	49.5	3.6	2.1	1.0	34,100	4.64
4000988	OnZaP-3	32.10	74.35	MSP0010	Mudstone	37.0	91	4.5	210.7	10.7	7.2	3.2	68,221	3.13
4000190	OnZaP-3	32.36	74.63	MSP0001	Carbonate	2.6	12	1.2	7.1	3.4	1.9	0.8	7,500	1.19
4000201	OnZaP-3	33.24	75.51	MSP0001	Mudstone	19.7	37	4.6	43.4	2.3	1.6	0.6	26,400	4.52
4000989	OnZaP-3	33.48	75.73	MSP0010	Mudstone	32.1	121	4.1	234.8	8.8	5.5	3.3	73,663	5.32
4000990	OnZaP-3	33.81	76.06	MSP0010	Mudstone								1,048	
4000202	OnZaP-3	34.29	76.56	MSP0001	Mudstone	12.1	123	0.8	87.6	2.8	1.8	0.7	16,900	6.94

Sample ID	Drill site	Core depth (m)	Comb. depth (m)	Sample set	Lithology	Co (ppm)	Cr (ppm)	Cs (ppm)	Cu (ppm)	Dy (ppm)	Er (ppm)	Eu (ppm)	Fe (ppm)	Ga (ppm)
4000203	OnZaP-3	34.96	77.23	MSP0001	Mudstone	6.6	87	1.6	28.2	0.9	0.6	0.4	9,500	6.49
4000214	OnZaP-3	36.54	78.81	MSP0001	Carbonate	7.2	35	2.3	16.1	1.9	1.2	0.7	9,400	3.08
4000216	OnZaP-3	37.30	79.57	MSP0001	Carbonate	8.1	13	1.6	19.4	1.4	0.8	0.6	11,100	2.22
4000225	OnZaP-3	38.42	80.69	MSP0001	Mudstone	11.4	22	2.3	24.1	1.8	1.0	0.7	16,800	3.69
4000231	OnZaP-3	39.25	81.52	MSP0001	Mudstone	16.4	21	3.1	33.7	1.8	0.9	0.6	21,800	5.87
4000239	OnZaP-3	40.20	82.47	MSP0001	Mudstone	20.4	46	2.3	56.7	1.5	0.8	0.6	22,900	12.93
4000244	OnZaP-3	41.09	83.36	MSP0001	Mudstone	6.5	15	3.2	19.3	2.0	1.0	0.8	9,400	4.91
4000251	OnZaP-3	42.32	84.59	MSP0001	Carbonate	14.0	8	2.0	27.7	1.5	1.0	0.7	16,800	2.76
4000256	OnZaP-3	43.12	85.39	MSP0001	Carbonate	2.8	6	0.6	10.9	1.4	0.7	0.7	6,800	0.99
4000264	OnZaP-3	44.02	86.29	MSP0001	Mudstone	16.9	60	3.7	37.9	1.4	0.7	0.4	19,700	7.27
4000265	OnZaP-3	44.82	87.09	MSP0001	Mudstone	25.8	39	1.8	30.3	1.1	0.5	0.5	16,900	6.28
4000266	OnZaP-3	45.87	88.14	MSP0001	Mudstone	7.9	79	1.7	133.6	2.0	1.0	0.5	10,900	5.58
4000991	OnZaP-3	46.11	88.36	MSP0010	Mudstone	10.5	84	1.9	248.4	4.6	3.0	1.4	17,217	6.73
4000992	OnZaP-3	46.51	88.76	MSP0010	Mudstone	17.5	142	1.8	542.8	5.7	3.7	1.9	24,564	8.60
4000267	OnZaP-3	46.59	88.86	MSP0001	Mudstone	9.5	96	1.7	254.1	2.4	1.6	0.7	12,600	7.30
4000993	OnZaP-3	47.86	90.11	MSP0010	Mudstone	10.7	121	1.0	762.2	4.7	3.1	1.5	16,838	4.67
4000268	OnZaP-3	48.02	90.29	MSP0001	Mudstone	8.8	126	0.9	380.6	2.1	1.4	0.7	15,400	9.85
4000994	OnZaP-3	48.94	91.19	MSP0010	Mudstone	10.4	161	1.6	478.9	4.4	2.9	1.4	15,152	8.44
4000269	OnZaP-3	49.00	91.27	MSP0001	Mudstone	8.4	111	0.9	171.4	1.9	1.1	0.6	9,500	5.33
4000270	OnZaP-3	49.68	91.95	MSP0001	Mudstone	21.2	139	1.3	111.5	1.7	0.8	0.7	28,500	6.11
4000271	OnZaP-3	50.28	92.55	MSP0001	Mudstone	11.5	101	1.2	78.2	1.6	1.0	0.5	14,200	9.29
4000273	OnZaP-3	50.99	93.26	MSP0001	Mudstone	10.2	83	2.2	34.5	1.0	0.8	0.4	11,400	6.02
4001000	OnZaP-1	51.57	93.82	MSP0010	Carbonate	0.2	12	0.5	6.6	3.3	2.8	0.8	1,444	0.88
4000279	OnZaP-3	52.53	94.80	MSP0001	Mudstone	14.2	117	1.5	129.4	1.2	0.7	0.3	19,600	13.79
4000280	OnZaP-3	53.02	95.29	MSP0001	Mudstone	11.2	131	1.3	258.8	1.4	1.0	0.5	10,200	9.26
4000995	OnZaP-3	53.75	96.00	MSP0010	Mudstone	9.3	105	2.4	304.0	3.8	2.4	1.4	12,571	7.48
4000281	OnZaP-3	54.02	96.29	MSP0001	Mudstone	9.4	112	2.6	307.2	2.2	1.5	0.7	12,400	5.96
4000288	OnZaP-3	55.01	97.28	MSP0001	Mudstone	4.9	12	2.6	27.8	1.4	1.0	0.5	4,700	3.40
4000289	OnZaP-3	55.60	97.87	MSP0001	Mudstone	8.5	114	2.0	409.2	2.3	1.3	0.7	11,300	7.88
4000996	OnZaP-3	55.76	98.01	MSP0010	Mudstone	11.3	154	1.9	519.0	4.6	2.9	1.6	10,987	10.62
4000290	OnZaP-3	56.52	98.79	MSP0001	Mudstone	7.0	118	0.9	129.0	1.5	1.0	0.6	10,700	9.17
4000997	OnZaP-3	57.27	99.52	MSP0010	Mudstone	10.1	103	1.4	291.4	4.1	2.8	1.3	16,039	6.33
4000998	OnZaP-3	58.06	100.31	MSP0010	Mudstone	14.4	149	1.5	463.7	7.1	4.6	2.3	15,554	10.45
4000291	OnZaP-3	58.24	100.51	MSP0001	Mudstone	17.5	135	1.0	531.0	3.4	2.3	0.9	14,000	9.50
4000299	OnZaP-3	58.87	101.14	MSP0001	Carbonate	3.4	8	1.1	9.8	2.5	1.5	1.0	6,800	1.26
4000999	OnZaP-3	59.88	102.13	MSP0010	Mudstone	16.2	226	1.7	446.3	9.1	5.9	2.9	26,508	10.51
4000306	OnZaP-3	59.95	102.22	MSP0001	Mudstone	14.6	194	1.2	488.4	3.0	2.3	0.9	20,600	11.04

Table A1c: Element concentration data for drill cores OnZaP-1 and OnZaP-3, continued.

Sample ID	Drill site	Core depth (m)	Comb. depth (m)	Sample set	Lithology	Gd (ppm)	Hf (ppm)	Ho (ppm)	In (ppm)	K (ppm)	La (ppm)	Li (ppm)	Lu (ppm)	Mg (ppm)
4000319	OnZaP-1	1.96	1.96	MSP0001	Mudstone	1.1	3.5	0.3	0.07	26,600	3.1	38.2	0.1	15,000
4000921	OnZaP-1	2.08	2.08	MSP0010	Mudstone	7.7	5.7	1.1		27,027	36.6	44.4	0.5	18,724
4000320	OnZaP-1	2.85	2.85	MSP0001	Mudstone	1.5	3.0	0.3	0.06	27,500	5.4	40.8	0.1	19,700
4000321	OnZaP-1	3.92	3.92	MSP0001	Mudstone	1.0	3.2	0.2	0.08	29,200	3.0	41.9	0.1	18,600
4000922	OnZaP-1	5.28	5.28	MSP0010	Mudstone	2.7	1.9	0.4		33,085	14.6	18.5	0.2	19,015
4000322	OnZaP-1	5.31	5.31	MSP0001	Mudstone	0.9	3.5	0.2	0.08	33,600	3.1	37.7	0.1	18,200
4000323	OnZaP-1	6.50	6.50	MSP0001	Mudstone	0.7	3.1	0.2	0.06	34,000	2.6	37.4		18,300
4000923	OnZaP-1	6.60	6.60	MSP0010	Mudstone					27,793				23,775
4000324	OnZaP-1	7.01	7.01	MSP0001	Mudstone	1.4	3.3	0.3	0.11	29,300	5.1	46.1	0.1	15,900
4000332	OnZaP-1	7.96	7.96	MSP0001	Mudstone	2.2	1.2	0.4	0.04	14,700	9.2	19.7	0.1	57,500
4000336	OnZaP-1	8.35	8.35	MSP0001	Mudstone	1.3	2.9	0.3	0.10	28,100	6.3	54.0	0.1	17,300
4000342	OnZaP-1	8.74	8.74	MSP0001	Mudstone	1.9	1.2	0.4	0.03	13,400	9.1	18.5	0.1	68,700
4000345	OnZaP-1	9.58	9.58	MSP0001	Mudstone	2.2	3.0	0.4	0.07	29,700	9.5	40.7	0.2	16,700
4000346	OnZaP-1	10.79	10.79	MSP0001	Mudstone	0.8	2.9	0.2	0.09	24,800	1.5	46.6	0.1	15,700
4000924	OnZaP-1	11.13	11.13	MSP0010	Mudstone	6.0	3.2	0.9		29,289	29.6	42.7	0.4	18,660
4000347	OnZaP-1	11.86	11.86	MSP0001	Mudstone	2.2	4.5	0.4	0.12	39,800	6.4	49.1	0.2	13,800
4000925	OnZaP-1	12.15	12.15	MSP0010	Mudstone	8.5	3.9	1.2		28,286	45.6	39.8	0.6	14,782
4000348	OnZaP-1	12.39	12.39	MSP0001	Mudstone	1.3	3.1	0.3	0.09	32,800	4.3	42.9	0.2	13,200
4000349	OnZaP-1	13.16	13.16	MSP0001	Mudstone	1.4	0.4	0.3	0.02	5,500	6.3	10.0		76,700
4000351	OnZaP-1	13.40	13.40	MSP0001	Mudstone	1.3	0.7	0.2	0.02	8,800	5.8	12.8		64,300
4000358	OnZaP-1	14.65	14.65	MSP0001	Mudstone	0.8	3.8	0.2	0.07	26,300	1.8	48.7	0.1	22,200
4000362	OnZaP-1	15.26	15.26	MSP0001	Mudstone	2.1	1.9	0.4	0.04	15,600	12.9	26.7	0.2	46,500
4000368	OnZaP-1	16.29	16.29	MSP0001	Mudstone	1.0	0.3	0.2	0.01	5,400	2.3	8.8		75,300
4000376	OnZaP-1	17.36	17.36	MSP0001	Mudstone	0.9	0.5	0.2	0.02	7,600	3.7	12.1		80,800
4000383	OnZaP-1	17.90	17.90	MSP0001	Mudstone	1.5	3.6	0.3	0.02	9,400	5.5	13.1		74,400
4000926	OnZaP-1	18.85	18.85	MSP0010	Mudstone	7.6	3.7	0.9		42,085	40.8	52.7	0.4	31,054
4000392	OnZaP-1	19.08	19.08	MSP0001	Mudstone	1.4	7.8	0.3	0.10	36,100	8.5	44.0	0.2	14,100
4000393	OnZaP-1	19.99	19.99	MSP0001	Mudstone	1.3	4.7	0.3	0.08	39,200	4.5	42.9	0.1	17,400
4000394	OnZaP-1	20.66	20.66	MSP0001	Mudstone	2.1	3.5	0.3	0.10	37,500	10.5	38.4	0.2	10,400
4000927	OnZaP-1	21.91	21.91	MSP0010	Mudstone	7.3	4.1	0.9		32,806	40.6	35.6	0.4	21,368
4000395	OnZaP-1	21.94	21.94	MSP0001	Mudstone	2.0	3.1	0.2	0.07	34,100	12.4	34.5	0.1	18,700
4000396	OnZaP-1	22.33	22.33	MSP0001	Mudstone	1.7	3.0	0.2	0.08	24,000	10.8	34.9	0.1	20,800
4000398	OnZaP-1	23.03	23.03	MSP0001	Mudstone	2.2	3.2	0.4	0.06	25,800	13.6	38.6	0.2	27,300
4000928	OnZaP-1	23.84	23.84	MSP0010	Mudstone	3.9	1.7	0.7		25,522	16.0	24.0	0.3	59,139
4000403	OnZaP-1	24.31	24.31	MSP0001	Mudstone	2.6	2.2	0.4	0.04	22,100	13.8	31.2	0.1	41,900
4000406	OnZaP-1	25.03	25.03	MSP0001	Mudstone	1.8	0.5	0.3	0.03	7,100	6.3	12.3	0.1	81,800
4000412	OnZaP-1	26.09	26.09	MSP0001	Mudstone	1.2	4.1	0.2	0.06	24,300	5.3	67.8	0.1	11,200
4000413	OnZaP-1	26.80	26.80	MSP0001	Mudstone	1.9	3.7	0.3	0.10	29,000	9.1	73.8	0.1	17,800
4000414	OnZaP-1	27.77	27.77	MSP0001	Mudstone	3.0	2.1	0.5	0.05	24,100	20.8	39.1	0.2	52,000
4000929	OnZaP-1	27.95	27.95	MSP0010	Mudstone	7.8	5.2	1.0		37,353	57.9	74.6	0.5	25,098
4000421	OnZaP-1	28.36	28.36	MSP0001	Mudstone	2.5	1.2	0.4	0.03	9,600	13.1	19.2	0.1	80,100
4000930	OnZaP-1	28.80	28.80	MSP0010	Mudstone	10.7	9.6	1.4		45,539	71.2	94.9	0.7	17,763

Sample ID	Drill site	Core depth (m)	Comb. depth (m)	Sample set	Lithology	Gd (ppm)	Hf (ppm)	Ho (ppm)	In (ppm)	K (ppm)	La (ppm)	Li (ppm)	Lu (ppm)	Mg (ppm)
4000429	OnZaP-1	29.28	29.28	MSP0001	Carbonate	1.6	0.3	0.2	0.01	2,200	3.8	7.2		99,500
4000931	OnZaP-1	30.66	30.66	MSP0010	Mudstone	9.8	6.4	1.3		39,133	61.6	59.5	0.7	10,998
4000436	OnZaP-1	30.79	30.79	MSP0001	Mudstone	1.8	3.2	0.4	0.10	38,000	8.1	65.2	0.2	8,800
4000442	OnZaP-1	31.21	31.21	MSP0001	Carbonate	1.5	0.2	0.3		2,400	3.0	9.2	0.1	98,000
4000932	OnZaP-1	31.85	31.85	MSP0010	Mudstone	9.4	5.1	1.3		47,637	60.5	56.9	0.7	9,340
4000447	OnZaP-1	31.86	31.86	MSP0001	Mudstone	1.4	3.2	0.3	0.07	28,300	4.9	62.1	0.2	8,200
4000933	OnZaP-1	32.19	32.19	MSP0010	Mudstone	8.3	4.4	1.4		48,299	57.4	69.0	0.7	11,045
4000455	OnZaP-1	33.15	33.15	MSP0001	Carbonate	1.0	0.2	0.2	0.03	2,000	2.9	1.7	0.1	68,200
4000466	OnZaP-1	33.96	33.96	MSP0001	Carbonate	1.9	0.1	0.5		1,800	5.7	1.4	0.2	62,600
4000471	OnZaP-1	34.64	34.64	MSP0001	Carbonate	1.2	0.3	0.2	0.03	2,900	3.4	3.2		73,900
4000478	OnZaP-1	35.61	35.61	MSP0001	Mudstone	0.7	0.1	0.2		1,100	2.6	1.5		72,900
4000934	OnZaP-1	36.40	36.40	MSP0010	Mudstone	17.0	8.7	2.7		52,438	99.1	58.4	1.1	23,707
4000483	OnZaP-1	36.52	36.52	MSP0001	Mudstone	4.5	10.2	1.0	0.04	41,300	13.7	56.9	0.4	17,800
4000484	OnZaP-1	36.94	36.94	MSP0001	Carbonate	1.1	0.5	0.3		5,500	4.8	4.5		63,100
4000935	OnZaP-1	37.83	37.83	MSP0010	Mudstone	16.5	9.0	2.8		42,782	99.3	47.4	1.1	15,627
4000491	OnZaP-1	38.13	38.13	MSP0001	Mudstone	4.0	12.7	0.9	0.03	33,500	16.9	38.8	0.5	9,500
4000936	OnZaP-1	38.91	38.91	MSP0010	Mudstone	21.1	12.6	2.9		49,127	146.3	53.7	1.2	22,963
4000492	OnZaP-1	38.97	38.97	MSP0001	Mudstone	4.1	9.3	1.0	0.02	34,000	16.0	50.2	0.6	16,000
4000493	OnZaP-1	39.88	39.88	MSP0001	Mudstone	3.3	2.8	0.6	0.05	24,000	21.8	68.9	0.4	42,300
4000937	OnZaP-1	40.02	40.02	MSP0010	Carbonate	8.4	4.8	1.7		29,088	38.9	68.4	0.9	44,369
4000938	OnZaP-1	41.09	41.09	MSP0010	Mudstone	6.5	3.4	1.5		32,205	31.7	37.7	0.9	27,528
4000494	OnZaP-1	41.15	41.15	MSP0001	Mudstone	3.0	2.8	0.8	0.08	23,800	11.7	41.2	0.5	11,600
4000939	OnZaP-1	41.38	41.38	MSP0010	Mudstone	9.8	5.0	2.0		42,377	42.4	46.9	1.1	28,960
4000500	OnZaP-1	42.04	42.04	MSP0001	Carbonate	1.1	0.0	0.2	0.01	800	3.3	2.1	0.1	81,700
4000940	OnZaP-1	42.42	42.42	MSP0010	Mudstone	8.6	5.7	1.6		25,591	38.2	42.7	0.7	41,228
4000504	OnZaP-1	42.45	42.45	MSP0001	Mudstone	2.8	2.8	0.6	0.05	28,600	21.8	89.6	0.3	57,400
4000941	OnZaP-1	42.86	42.86	MSP0010	Carbonate	5.2	1.6	1.0		12,397	27.6	36.2	0.5	59,258
4000942	OnZaP-1	43.69	43.69	MSP0010	Carbonate					28,454				64,557
4000516	OnZaP-1	43.94	43.94	MSP0001	Carbonate					200	0.1	1.8		79,800
4000005	OnZaP-3	2.10	44.37	MSP0001	Carbonate					200		1.1		75,200
4000521	OnZaP-1	44.53	44.53	MSP0001	Carbonate					200		2.0		78,400
4000953	OnZaP-3	2.68	44.93	MSP0010	Carbonate	11.4	0.6	2.8		8,589	22.4	31.3	0.9	79,522
4000954	OnZaP-3	2.77	45.02	MSP0010	Mudstone	0.8	1.7	0.3		23,946	0.6	95.2	0.2	55,983
4000015	OnZaP-3	3.12	45.39	MSP0001	Carbonate				0.01	200	0.2	2.7		77,800
4000529	OnZaP-1	45.65	45.65	MSP0001	Carbonate					300	0.1	3.4		81,700
4000943	OnZaP-1	46.36	46.36	MSP0010	Mudstone	2.7	2.9	0.8		28,959	11.4	106.4	0.5	77,740
4000030	OnZaP-3	4.38	46.65	MSP0001	Carbonate						0.2	1.7		70,100
4000536	OnZaP-1	46.70	46.70	MSP0001	Mudstone		0.1			700		2.1		1,600
4000037	OnZaP-3	5.02	47.29	MSP0001	Carbonate					600	0.4	1.6		67,400
4000955	OnZaP-3	5.14	47.39	MSP0010	Mudstone	1.2	0.3	0.3		4,729	3.7	13.3	0.1	83,140
4000543	OnZaP-1	47.65	47.65	MSP0001	Carbonate					200		1.6		82,400
4000944	OnZaP-1	47.90	47.90	MSP0010	Carbonate	1.7	2.5	0.9		27,177	2.3	113.6	0.5	96,832
4000045	OnZaP-3	5.89	48.16	MSP0001	Carbonate				0.01	400		1.8		73,000
4000956	OnZaP-3	6.01	48.26	MSP0010	Carbonate	0.3	0.1	0.1			1.2	3.8	0.0	98,552
4000945	OnZaP-1	48.40	48.40	MSP0010	Carbonate	3.0	2.0	0.9		17,317	12.4	108.0	0.4	89,876

Sample ID	Drill site	Core depth (m)	Comb. depth (m)	Sample set	Lithology	Gd (ppm)	Hf (ppm)	Ho (ppm)	In (ppm)	K (ppm)	La (ppm)	Li (ppm)	Lu (ppm)	Mg (ppm)
4000553	OnZaP-1	48.61	48.61	MSP0001	Mudstone	0.1	0.1			300	0.2	1.4		1,100
4000053	OnZaP-3	6.67	48.94	MSP0001	Mudstone		0.0					0.4		400
4000957	OnZaP-3	6.84	49.09	MSP0010	Mudstone									
4000561	OnZaP-1	49.29	49.29	MSP0001	Carbonate	0.9		0.2		800	2.8	37.8		72,400
4000061	OnZaP-3	7.28	49.55	MSP0001	Carbonate					200		1.2		78,800
4000958	OnZaP-3	8.00	50.25	MSP0010	Mudstone									
4000563	OnZaP-1	50.43	50.43	MSP0001	Mudstone		0.1			1,200		4.7		3,100
4000946	OnZaP-1	50.58	50.58	MSP0010	Carbonate	1.8	0.1	0.4		1,021	6.2	49.5	0.2	95,023
4000959	OnZaP-3	8.40	50.65	MSP0010	Mudstone	0.5	0.3	0.1		4,280	1.0	17.9	0.0	11,706
4000065	OnZaP-3	8.44	50.71	MSP0001	Mudstone	0.7	0.3	0.1	0.07	8,800	0.9	28.2		21,400
4000571	OnZaP-1	50.77	50.77	MSP0001	Carbonate					300	0.1	21.6		83,200
4000947	OnZaP-1	51.13	51.13	MSP0010	Carbonate	3.3	2.3	1.1		40,540	12.1	62.9	0.6	99,261
4000575	OnZaP-1	51.41	51.41	MSP0001	Mudstone	3.2	4.4	0.8	0.02	18,700	9.0	34.1	0.4	17,200
4000080	OnZaP-3	9.31	51.58	MSP0001	Carbonate					200		3.6		82,100
4000960	OnZaP-3	9.57	51.82	MSP0010	Carbonate	1.6	0.9	0.4		35,141	10.5	15.0	0.2	76,153
4000583	OnZaP-1	52.16	52.16	MSP0001	Carbonate					400		3.6		81,900
4000090	OnZaP-3	10.14	52.41	MSP0001	Carbonate					600		2.6		83,800
4000592	OnZaP-1	52.92	52.92	MSP0001	Carbonate	0.2	0.0	0.2	0.01	3,200	5.9	10.0	0.1	65,800
4000098	OnZaP-3	10.70	52.97	MSP0001	Carbonate	0.7	0.0	0.2		1,200	5.2	5.7		121,600
4000948	OnZaP-1	53.12	53.12	MSP0010	Mudstone	18.7	1.9	5.0		42,819	51.3	92.1	1.6	91,942
4000961	OnZaP-3	11.00	53.25	MSP0010	Carbonate	4.9	4.0	1.5		40,362	24.6	85.3	0.9	72,727
4000949	OnZaP-1	53.50	53.50	MSP0010	Mudstone	6.2	1.7	1.7		44,474	24.8	18.5	0.8	12,553
4000962	OnZaP-3	11.33	53.58	MSP0010	Carbonate	19.9	1.9	5.5		22,082	69.4	22.5	2.0	14,163
4000100	OnZaP-3	11.33	53.60	MSP0001	Mudstone	7.1	0.5	1.7	0.11	13,300	19.6	21.6	0.8	6,800
4000593	OnZaP-1	53.70	53.70	MSP0001	Mudstone	6.4	4.2	1.4		17,200	27.0	16.2	0.7	3,800
4000963	OnZaP-3	11.70	53.95	MSP0010	Mudstone	23.9	13.3	3.8		46,383	168.9	52.3	1.4	13,491
4000964	OnZaP-3	11.96	54.21	MSP0010	Mudstone					43,088				16,877
4000102	OnZaP-3	12.16	54.43	MSP0001	Mudstone	5.1	1.9	1.1		14,100	18.2	17.0	0.5	4,400
4000965	OnZaP-3	12.67	54.92	MSP0010	Mudstone	12.3	9.4	3.0		65,712	62.6	19.2	1.9	13,858
4000594	OnZaP-1	55.14	55.14	MSP0001	Mudstone	3.9	1.2	1.0		12,300	16.8	11.8	0.4	2,500
4000966	OnZaP-3	13.11	55.36	MSP0010	Mudstone	8.6	2.0	2.2		40,350	29.7	14.3	1.0	15,002
4000597	OnZaP-1	55.51	55.51	MSP0001	Carbonate	2.4	0.1	0.4		2,600	4.9	7.0	0.3	7,300
4000103	OnZaP-3	13.29	55.56	MSP0001	Mudstone	5.9	1.9	1.4	0.05	12,900	25.5	18.0	0.5	5,800
4000601	OnZaP-1	55.68	55.68	MSP0001	Mudstone	3.6	1.9	1.1	0.04	12,200	15.3	19.3	0.5	7,800
4000950	OnZaP-1	55.80	55.80	MSP0010	Mudstone	10.0	3.7	2.5		32,215	42.3	16.6	1.3	7,951
4000967	OnZaP-3	13.82	56.07	MSP0010	Carbonate	9.0	2.1	2.1		45,021	36.5	33.1	0.9	64,740
4000602	OnZaP-1	56.17	56.17	MSP0001	Mudstone	3.0	1.6	0.7	0.02	9,700	16.6	8.9	0.4	2,400
4000968	OnZaP-3	14.25	56.50	MSP0010	Mudstone	14.9	6.2	2.5		33,684	80.7	71.3	1.1	84,869
4000108	OnZaP-3	14.31	56.58	MSP0001	Mudstone	8.6	6.5	1.6	0.03	18,400	67.2	68.0	0.7	54,000
4000605	OnZaP-1	56.89	56.89	MSP0001	Carbonate	2.1	0.1	0.4		1,100	4.5	43.6	0.2	52,900
4000969	OnZaP-3	14.69	56.94	MSP0010	Mudstone	10.9	4.3	2.0		50,072	55.5	21.5	0.8	20,362
4000113	OnZaP-3	14.85	57.12	MSP0001	Mudstone	3.1	1.2	0.8	0.04	10,700	12.6	13.2	0.3	4,100
4000614	OnZaP-1	57.64	57.64	MSP0001	Carbonate	1.4	0.5	0.3	0.02	4,300	3.9	17.8	0.1	92,000
4000951	OnZaP-1	57.93	57.93	MSP0010	Mudstone	9.6	5.6	2.3		56,684	36.8	31.9	1.2	14,317
4000970	OnZaP-3	15.72	57.97	MSP0010	Mudstone	7.1	1.3	1.5		24,772	25.4	11.7	0.6	11,100

Sample ID	Drill site	Core depth (m)	Comb. depth (m)	Sample set	Lithology	Gd (ppm)	Hf (ppm)	Ho (ppm)	In (ppm)	K (ppm)	La (ppm)	Li (ppm)	Lu (ppm)	Mg (ppm)
4000114	OnZaP-3	15.70	57.97	MSP0001	Mudstone	4.2	1.7	1.0	0.01	12,300	19.3	16.4	0.4	4,800
4000618	OnZaP-1	58.41	58.41	MSP0001	Mudstone	6.1	4.9	1.3	0.07	26,000	20.2	19.4	0.6	4,200
4000971	OnZaP-3	16.42	58.67	MSP0010	Mudstone	8.9	3.4	1.5		47,219	36.1	24.7	0.8	11,924
4000972	OnZaP-3	16.72	58.97	MSP0010	Mudstone	5.4	2.1	1.2		17,806	26.6	12.7	0.6	5,743
4000115	OnZaP-3	16.92	59.19	MSP0001	Mudstone	3.6	2.4	0.9	0.06	17,600	8.9	30.3	0.3	8,100
4000952	OnZaP-1	59.25	59.25	MSP0010	Mudstone					40,800				9,040
4000619	OnZaP-1	59.67	59.67	MSP0001	Mudstone	5.7	5.3	1.6	0.06	42,600	11.9	31.8	0.8	11,700
4000122	OnZaP-3	17.55	59.82	MSP0001	Mudstone	2.4	1.3	0.5		10,900	8.9	35.5	0.3	20,700
4000973	OnZaP-3	17.89	60.14	MSP0010	Mudstone	4.3	2.6	1.2		22,144	18.8	49.7	0.5	52,926
4000623	OnZaP-1	60.18	60.18	MSP0001	Mudstone	3.1	2.9	0.8	0.03	21,800	6.6	67.3	0.4	44,600
4000128	OnZaP-3	18.65	60.92	MSP0001	Carbonate	2.3	0.4	0.4		4,800	5.2	15.2	0.3	72,300
4000129	OnZaP-3	18.97	61.24	MSP0001	Mudstone	2.8	3.5	0.7	0.16	15,800	8.0	20.2	0.3	5,400
4000974	OnZaP-3	19.27	61.52	MSP0010	Mudstone	9.0	4.8	1.9		39,986	33.2	22.0	0.9	8,738
4000975	OnZaP-3	20.07	62.32	MSP0010	Mudstone	11.0	5.6	2.6		45,358	36.6	28.6	1.2	13,275
4000130	OnZaP-3	20.13	62.40	MSP0001	Mudstone	3.9	2.4	0.8	0.05	22,000	13.1	34.4	0.4	17,400
4000132	OnZaP-3	20.90	63.17	MSP0001	Mudstone	3.6	3.4	0.9	0.04	15,500	14.5	16.4	0.5	4,400
4000976	OnZaP-3	21.12	63.37	MSP0010	Mudstone	9.1	5.6	2.2		32,081	37.3	18.3	1.0	9,063
4000133	OnZaP-3	21.96	64.23	MSP0001	Mudstone	4.8	4.1	1.0	0.05	18,800	19.5	23.1	0.5	7,200
4000977	OnZaP-3	22.36	64.61	MSP0010	Mudstone	11.5	6.0	2.3		30,096	46.8	15.3	0.9	5,854
4000978	OnZaP-3	22.96	65.21	MSP0010	Mudstone	20.2	11.7	3.8		48,001	88.2	47.2	1.7	12,483
4000134	OnZaP-3	23.12	65.39	MSP0001	Mudstone	3.8	6.1	0.7	0.03	21,600	10.9	36.6	0.3	8,900
4000979	OnZaP-3	23.59	65.84	MSP0010	Mudstone					40,956				20,854
4000135	OnZaP-3	24.26	66.53	MSP0001	Carbonate	2.1	0.3	0.4		6,100	3.8	12.8	0.1	65,700
4000980	OnZaP-3	24.91	67.16	MSP0010	Mudstone	10.7	6.7	1.1		45,755	71.9	111.5	0.4	118,247
4000151	OnZaP-3	25.18	67.45	MSP0001	Carbonate	1.6	0.3	0.3	0.01	3,400	3.3	8.3		95,100
4000981	OnZaP-3	25.59	67.84	MSP0010	Mudstone	2.5	1.8	0.4		49,367	11.8	14.2	0.2	85,622
4000159	OnZaP-3	25.76	68.03	MSP0001	Mudstone	3.2	5.0	0.5	0.08	40,200	19.7	69.3	0.2	69,900
4000982	OnZaP-3	26.20	68.45	MSP0010	Mudstone	7.1	5.7	1.2		35,157	33.1	79.8	0.5	101,051
4000168	OnZaP-3	26.56	68.83	MSP0001	Mudstone	12.1	5.1	1.4	0.02	27,100	60.5	98.8	0.4	104,700
4000178	OnZaP-3	27.32	69.59	MSP0001	Carbonate	1.5	0.5	0.3	0.01	6,000	3.6	15.2	0.1	89,000
4000983	OnZaP-3	27.51	69.76	MSP0010	Carbonate	3.2	1.9	0.7		33,966	13.0	54.9	0.3	81,256
4000179	OnZaP-3	28.13	70.40	MSP0001	Mudstone	1.5	0.5	0.4	0.02	4,200	4.1	8.1	0.2	5,000
4000984	OnZaP-3	28.69	70.94	MSP0010	Mudstone	2.1	0.5	0.6		10,147	5.3	12.0	0.3	3,705
4000180	OnZaP-3	29.20	71.47	MSP0001	Mudstone	5.6	1.1	0.9	0.07	13,300	22.7	16.7	0.4	4,900
4000985	OnZaP-3	29.35	71.60	MSP0010	Mudstone	7.7	0.9	1.3		11,441	34.7	15.7	0.6	4,812
4000181	OnZaP-3	30.59	72.86	MSP0001	Mudstone	22.3	0.4	2.8		11,800	39.2	61.6	0.9	33,900
4000986	OnZaP-3	30.68	72.93	MSP0010	Mudstone	7.1	2.5	2.0		23,410	36.7	37.4	1.1	38,351
4000987	OnZaP-3	31.40	73.65	MSP0010	Mudstone	8.3	1.4	1.4		19,231	37.5	15.4	0.6	6,310
4000187	OnZaP-3	31.63	73.90	MSP0001	Mudstone	3.8	1.1	0.7	0.05	12,500	15.1	15.4	0.3	5,800
4000988	OnZaP-3	32.10	74.35	MSP0010	Mudstone	13.6	1.3	2.4		12,407	63.5	34.2	1.0	33,469
4000190	OnZaP-3	32.36	74.63	MSP0001	Carbonate	3.9	0.1	0.7		4,000	2.7	11.7	0.4	81,800
4000201	OnZaP-3	33.24	75.51	MSP0001	Mudstone	2.2	0.4	0.5		12,000	13.9	37.8	0.3	37,500
4000989	OnZaP-3	33.48	75.73	MSP0010	Mudstone	12.9	1.4	1.9		24,205	83.7	41.1	0.8	50,549
4000990	OnZaP-3	33.81	76.06	MSP0010	Mudstone					6,286				2,868
4000202	OnZaP-3	34.29	76.56	MSP0001	Mudstone	3.1	1.9	0.6		15,400	20.3	15.3	0.3	6,200

Sample ID	Drill site	Core depth (m)	Comb. depth (m)	Sample set	Lithology	Gd (ppm)	Hf (ppm)	Ho (ppm)	In (ppm)	K (ppm)	La (ppm)	Li (ppm)	Lu (ppm)	Mg (ppm)
4000203	OnZaP-3	34.96	77.23	MSP0001	Mudstone	1.4	1.0	0.2		14,000	15.3	18.2		12,200
4000214	OnZaP-3	36.54	78.81	MSP0001	Carbonate	1.8	0.6	0.4	0.03	8,400	12.4	15.3	0.2	65,300
4000216	OnZaP-3	37.30	79.57	MSP0001	Carbonate	1.5	0.4	0.3		6,000	3.8	11.8	0.1	75,000
4000225	OnZaP-3	38.42	80.69	MSP0001	Mudstone	2.3	0.6	0.4	0.02	9,900	11.2	19.8	0.1	62,900
4000231	OnZaP-3	39.25	81.52	MSP0001	Mudstone	2.0	1.1	0.3	0.01	14,500	17.8	26.4	0.2	50,800
4000239	OnZaP-3	40.20	82.47	MSP0001	Mudstone	1.7	2.1	0.3	0.02	23,400	37.4	40.6	0.2	51,600
4000244	OnZaP-3	41.09	83.36	MSP0001	Mudstone	2.8	0.9	0.4	0.01	12,600	24.2	22.6	0.2	55,200
4000251	OnZaP-3	42.32	84.59	MSP0001	Carbonate	1.8	0.5	0.4		8,100	9.3	21.9	0.1	76,300
4000256	OnZaP-3	43.12	85.39	MSP0001	Carbonate	2.1	0.1	0.3		2,700	3.5	14.6		87,500
4000264	OnZaP-3	44.02	86.29	MSP0001	Mudstone	1.9	1.4	0.3	0.04	24,000	22.1	31.7	0.1	39,600
4000265	OnZaP-3	44.82	87.09	MSP0001	Mudstone	1.7	1.3	0.2		14,800	12.7	18.0	0.1	14,700
4000266	OnZaP-3	45.87	88.14	MSP0001	Mudstone	2.3	1.3	0.4	0.02	17,400	13.5	18.8	0.2	14,000
4000991	OnZaP-3	46.11	88.36	MSP0010	Mudstone	5.4	2.0	1.0		26,850	29.5	21.5	0.5	16,236
4000992	OnZaP-3	46.51	88.76	MSP0010	Mudstone	6.4	2.2	1.2		32,806	36.8	24.6	0.6	11,682
4000267	OnZaP-3	46.59	88.86	MSP0001	Mudstone	2.9	1.4	0.5	0.06	22,400	19.3	22.1	0.3	14,300
4000993	OnZaP-3	47.86	90.11	MSP0010	Mudstone	5.4	1.5	1.0		19,909	29.0	10.6	0.6	6,365
4000268	OnZaP-3	48.02	90.29	MSP0001	Mudstone	2.7	1.6	0.5		14,800	14.7	16.3	0.2	8,000
4000994	OnZaP-3	48.94	91.19	MSP0010	Mudstone	4.9	1.7	0.9		21,590	27.0	21.6	0.5	11,455
4000269	OnZaP-3	49.00	91.27	MSP0001	Mudstone	2.2	1.4	0.4		13,800	12.2	11.0	0.2	6,400
4000270	OnZaP-3	49.68	91.95	MSP0001	Mudstone	2.2	1.6	0.3	0.02	14,300	14.6	14.0	0.2	10,000
4000271	OnZaP-3	50.28	92.55	MSP0001	Mudstone	1.9	1.6	0.3		18,900	9.8	18.4	0.2	11,100
4000273	OnZaP-3	50.99	93.26	MSP0001	Mudstone	1.5	1.5	0.3	0.02	12,200	5.0	18.9	0.1	18,300
4001000	OnZaP-1	51.57	93.82	MSP0010	Carbonate	3.0	0.2	0.8		1,119	11.4	11.0	0.5	114,492
4000279	OnZaP-3	52.53	94.80	MSP0001	Mudstone	1.2	1.7	0.2		17,700	3.9	26.7	0.1	16,100
4000280	OnZaP-3	53.02	95.29	MSP0001	Mudstone	1.6	1.7	0.3		20,700	8.7	20.9	0.2	11,200
4000995	OnZaP-3	53.75	96.00	MSP0010	Mudstone	4.8	1.7	0.8		23,495	24.1	21.9	0.4	19,086
4000281	OnZaP-3	54.02	96.29	MSP0001	Mudstone	2.1	1.4	0.4	0.04	23,100	14.4	24.9	0.2	21,700
4000288	OnZaP-3	55.01	97.28	MSP0001	Mudstone	1.8	0.2	0.3	0.02	8,800	5.2	19.1	0.3	23,100
4000289	OnZaP-3	55.60	97.87	MSP0001	Mudstone	2.7	1.6	0.5	0.08	19,200	15.8	20.2	0.2	14,000
4000996	OnZaP-3	55.76	98.01	MSP0010	Mudstone	5.7	2.0	0.9		31,488	33.7	24.6	0.5	13,938
4000290	OnZaP-3	56.52	98.79	MSP0001	Mudstone	2.1	1.1	0.3	0.02	16,700	10.2	18.0	0.2	8,900
4000997	OnZaP-3	57.27	99.52	MSP0010	Mudstone	4.5	1.6	0.9		22,925	21.0	19.8	0.5	11,127
4000998	OnZaP-3	58.06	100.31	MSP0010	Mudstone	8.2	2.8	1.5		43,474	40.2	22.2	0.8	9,257
4000291	OnZaP-3	58.24	100.51	MSP0001	Mudstone	3.1	2.3	0.8	0.02	18,400	15.2	17.5	0.4	5,800
4000299	OnZaP-3	58.87	101.14	MSP0001	Carbonate	3.3	0.2	0.4		2,800	12.8	23.3	0.2	76,700
4000999	OnZaP-3	59.88	102.13	MSP0010	Mudstone	11.2	3.0	2.0		46,729	49.3	24.4	1.1	10,031
4000306	OnZaP-3	59.95	102.22	MSP0001	Mudstone	3.7	2.1	0.7	0.05	32,700	11.9	24.7	0.4	9,300

Table A1d: Element concentration data for drill cores OnZaP-1 and OnZaP-3, continued.

Sample ID	Drill site	Core depth (m)	Comb. depth (m)	Sample set	Lithology	Mn (ppm)	Mo (ppm)	Na (ppm)	Nb (ppm)	Nd (ppm)	Ni (ppm)	P (ppm)	Pb (ppm)	Pr (ppm)
4000319	OnZaP-1	1.96	1.96	MSP0001	Mudstone	631	0.13	9,810	11.96	4.7	26.3	430	3.01	1.1
4000921	OnZaP-1	2.08	2.08	MSP0010	Mudstone	800		9,562		39.3	48.8	622	4.80	10.1
4000320	OnZaP-1	2.85	2.85	MSP0001	Mudstone	965	0.18	8,080	11.67	6.9	35.4	390	3.42	1.7
4000321	OnZaP-1	3.92	3.92	MSP0001	Mudstone	1,017	0.29	9,650	12.80	4.1	65.4	390	2.63	1.0
4000922	OnZaP-1	5.28	5.28	MSP0010	Mudstone	842		8,852		14.9	21.0	223	0.77	4.0
4000322	OnZaP-1	5.31	5.31	MSP0001	Mudstone	659	0.17	11,320	13.40	4.8	29.9	340	1.80	1.1
4000323	OnZaP-1	6.50	6.50	MSP0001	Mudstone	656	0.14	9,250	12.06	3.7	42.8	340	3.01	0.9
4000923	OnZaP-1	6.60	6.60	MSP0010	Mudstone	984		5,487						
4000324	OnZaP-1	7.01	7.01	MSP0001	Mudstone	961	0.20	7,410	4.93	6.5	44.6	740	5.31	1.5
4000332	OnZaP-1	7.96	7.96	MSP0001	Mudstone	7,959	0.57	240	1.91	9.3	15.6	450	20.90	2.3
4000336	OnZaP-1	8.35	8.35	MSP0001	Mudstone	1,367	1.81	2,390	2.62	6.7	47.5	340	60.08	1.8
4000342	OnZaP-1	8.74	8.74	MSP0001	Mudstone	8,218	1.66	490	1.49	8.3	48.2	220	79.11	2.1
4000345	OnZaP-1	9.58	9.58	MSP0001	Mudstone	1,654	3.76	4,750	2.52	10.5	74.6	340	85.56	2.6
4000346	OnZaP-1	10.79	10.79	MSP0001	Mudstone	458	0.42	7,160	2.88	2.3	48.6	320	26.25	0.5
4000924	OnZaP-1	11.13	11.13	MSP0010	Mudstone	710		2,336		30.4	41.0	401	11.02	7.9
4000347	OnZaP-1	11.86	11.86	MSP0001	Mudstone	170	1.05	8,570	3.92	9.2	18.3	310	12.76	2.2
4000925	OnZaP-1	12.15	12.15	MSP0010	Mudstone	271		5,727		45.1	168.4	387	72.90	11.7
4000348	OnZaP-1	12.39	12.39	MSP0001	Mudstone	285	6.31	5,610	2.24	6.2	111.1	300	78.95	1.4
4000349	OnZaP-1	13.16	13.16	MSP0001	Mudstone	7,739	0.24	80	1.58	5.7	10.1	90	6.71	1.4
4000351	OnZaP-1	13.40	13.40	MSP0001	Mudstone	5,799	0.16	1,010	2.59	5.3	12.1	150	2.48	1.4
4000358	OnZaP-1	14.65	14.65	MSP0001	Mudstone	285	0.78	9,730	3.11	3.0	41.6	370	3.45	0.6
4000362	OnZaP-1	15.26	15.26	MSP0001	Mudstone	3,911	0.15	2,280	2.77	11.5	28.2	320	1.66	3.0
4000368	OnZaP-1	16.29	16.29	MSP0001	Mudstone	4,847	1.58	430	0.99	3.3	15.1	130	1.95	0.7
4000376	OnZaP-1	17.36	17.36	MSP0001	Mudstone	3,916	0.12	1,020	1.35	3.0	19.1	70	1.65	0.8
4000383	OnZaP-1	17.90	17.90	MSP0001	Mudstone	4,581	0.52	830	1.92	6.2	21.5	230	1.81	1.4
4000926	OnZaP-1	18.85	18.85	MSP0010	Mudstone	755		4,029		44.0	62.8	470	3.21	11.3
4000392	OnZaP-1	19.08	19.08	MSP0001	Mudstone	200	0.20	11,080	10.10	10.4	41.0	250	1.58	2.5
4000393	OnZaP-1	19.99	19.99	MSP0001	Mudstone	350	0.20	10,350	10.00	6.8	44.8	270	1.36	1.6
4000394	OnZaP-1	20.66	20.66	MSP0001	Mudstone	134	0.28	8,810	6.68	12.4	113.3	330	4.73	3.2
4000927	OnZaP-1	21.91	21.91	MSP0010	Mudstone	698		9,910		43.3	28.9	400	2.98	11.4
4000395	OnZaP-1	21.94	21.94	MSP0001	Mudstone	509	0.07	10,170	12.58	13.6	27.7	300	2.73	3.4
4000396	OnZaP-1	22.33	22.33	MSP0001	Mudstone	673	1.46	9,890	13.09	11.9	61.8	310	3.63	2.9
4000398	OnZaP-1	23.03	23.03	MSP0001	Mudstone	1,027	0.11	7,090	12.51	14.3	33.9	410	3.07	3.6
4000928	OnZaP-1	23.84	23.84	MSP0010	Mudstone	3,228		2,311		18.7	38.8	275		4.7
4000403	OnZaP-1	24.31	24.31	MSP0001	Mudstone	2,190	0.30	2,790	3.07	13.7	25.9	300	4.44	3.5
4000406	OnZaP-1	25.03	25.03	MSP0001	Mudstone	3,782	0.16	120	1.09	6.9	12.8	170	3.08	1.6
4000412	OnZaP-1	26.09	26.09	MSP0001	Mudstone	139	1.83	2,540	5.55	7.5	39.1	280	3.05	1.8
4000413	OnZaP-1	26.80	26.80	MSP0001	Mudstone	347	0.37	320	4.46	10.5	104.4	310	4.16	2.7
4000414	OnZaP-1	27.77	27.77	MSP0001	Mudstone	2,008	0.74	170	2.68	17.9	17.2	340	10.93	4.5
4000929	OnZaP-1	27.95	27.95	MSP0010	Mudstone	475				48.1	47.1	404	18.47	13.9
4000421	OnZaP-1	28.36	28.36	MSP0001	Mudstone	3,192	0.31	150	2.88	10.7	18.6	310	7.50	2.6
4000930	OnZaP-1	28.80	28.80	MSP0010	Mudstone	146		280		61.3	61.8	395	34.12	17.3

Sample ID	Drill site	Core depth (m)	Comb. depth (m)	Sample set	Lithology	Mn (ppm)	Mo (ppm)	Na (ppm)	Nb (ppm)	Nd (ppm)	Ni (ppm)	P (ppm)	Pb (ppm)	Pr (ppm)
4000429	OnZaP-1	29.28	29.28	MSP0001	Carbonate	3,056	0.17	1,420	1.66	4.7	4.9	170	1.78	1.1
4000931	OnZaP-1	30.66	30.66	MSP0010	Mudstone	43	9.96	2,177		61.2	154.7	253	58.29	14.8
4000436	OnZaP-1	30.79	30.79	MSP0001	Mudstone	33	0.57	3,450	2.86	10.5	40.0	240	31.32	2.6
4000442	OnZaP-1	31.21	31.21	MSP0001	Carbonate	2,249	0.16	70	0.65	3.8	4.5	60	1.15	0.7
4000932	OnZaP-1	31.85	31.85	MSP0010	Mudstone	22	21.30	2,710		54.5	106.1	322	22.39	13.6
4000447	OnZaP-1	31.86	31.86	MSP0001	Mudstone	19	17.04	3,440	5.73	6.7	125.8	260	40.15	1.5
4000933	OnZaP-1	32.19	32.19	MSP0010	Mudstone	23	28.88	2,026		46.8	181.0	372	29.77	12.1
4000455	OnZaP-1	33.15	33.15	MSP0001	Carbonate	824	0.37	590	1.32	3.6	5.5	150	1.67	0.9
4000466	OnZaP-1	33.96	33.96	MSP0001	Carbonate	672	1.34	300	1.61	5.1	9.0	80	4.35	1.1
4000471	OnZaP-1	34.64	34.64	MSP0001	Carbonate	850	0.39	1,670	5.01	4.2	5.6	320	1.75	0.9
4000478	OnZaP-1	35.61	35.61	MSP0001	Mudstone	854	1.24	200	1.81	3.1	7.4	40	4.98	0.6
4000934	OnZaP-1	36.40	36.40	MSP0010	Mudstone	33	53.13	1,185		88.2	223.3	488	16.49	23.7
4000483	OnZaP-1	36.52	36.52	MSP0001	Mudstone	38	68.74	1,030	28.48	21.6	190.0	450	25.41	4.5
4000484	OnZaP-1	36.94	36.94	MSP0001	Carbonate	1,106	2.04	440	1.12	5.0	8.3	50	1.08	1.4
4000935	OnZaP-1	37.83	37.83	MSP0010	Mudstone	27	68.53	321		81.0	161.9	350		22.4
4000491	OnZaP-1	38.13	38.13	MSP0001	Mudstone	24	41.05	890	39.66	21.6	150.7	240	43.11	5.3
4000936	OnZaP-1	38.91	38.91	MSP0010	Mudstone	58	187.17	103		113.6	400.5	736	44.77	32.3
4000492	OnZaP-1	38.97	38.97	MSP0001	Mudstone	64	138.19	1,160	35.00	17.5	344.5	420	44.85	4.5
4000493	OnZaP-1	39.88	39.88	MSP0001	Mudstone	259	38.98	2,620	3.28	19.0	184.6	400	33.57	4.7
4000937	OnZaP-1	40.02	40.02	MSP0010	Carbonate	145	119.66	609		35.1	270.4	287	26.06	9.3
4000938	OnZaP-1	41.09	41.09	MSP0010	Mudstone	64	108.33			30.4	372.7	347	41.59	8.0
4000494	OnZaP-1	41.15	41.15	MSP0001	Mudstone	35	117.91	700	4.44	14.6	452.5	690	58.97	3.3
4000939	OnZaP-1	41.38	41.38	MSP0010	Mudstone	44	131.00	454		44.3	397.6	841	57.95	11.0
4000500	OnZaP-1	42.04	42.04	MSP0001	Carbonate	818	2.18	220	0.37	4.0	6.1	1,950	2.05	0.9
4000940	OnZaP-1	42.42	42.42	MSP0010	Mudstone	42	149.19			39.6	447.7	580	73.18	9.5
4000504	OnZaP-1	42.45	42.45	MSP0001	Mudstone	116	101.95	190	2.89	19.9	328.6	270	49.80	5.2
4000941	OnZaP-1	42.86	42.86	MSP0010	Carbonate	510	209.00			28.9	449.8	192	79.82	7.2
4000942	OnZaP-1	43.69	43.69	MSP0010	Carbonate	94								
4000516	OnZaP-1	43.94	43.94	MSP0001	Carbonate	365	4.92	130	0.04		4.5	280	5.42	
4000005	OnZaP-3	2.10	44.37	MSP0001	Carbonate	275	1.19	130	0.15		5.9	680	0.75	
4000521	OnZaP-1	44.53	44.53	MSP0001	Carbonate	440	6.86	130	0.04		6.4	760	3.04	
4000953	OnZaP-3	2.68	44.93	MSP0010	Carbonate	573	172.89			39.1	119.7	27,097	16.82	8.0
4000954	OnZaP-3	2.77	45.02	MSP0010	Mudstone	30	486.82			1.8	246.7	341	17.48	0.3
4000015	OnZaP-3	3.12	45.39	MSP0001	Carbonate	274	2.52	110	0.06	0.2	7.3	400	0.90	
4000529	OnZaP-1	45.65	45.65	MSP0001	Carbonate	420	38.47	110	0.06		11.7	30	1.68	
4000943	OnZaP-1	46.36	46.36	MSP0010	Mudstone	51	1,009.31			9.9	1,383.0	146	46.01	2.4
4000030	OnZaP-3	4.38	46.65	MSP0001	Carbonate	226	1.33	90			3.8	240	1.33	0.4
4000536	OnZaP-1	46.70	46.70	MSP0001	Mudstone	2	18.21	90	0.05		16.8		1.13	
4000037	OnZaP-3	5.02	47.29	MSP0001	Carbonate	434	7.03	90	0.05	0.2	21.0	40	1.59	0.2
4000955	OnZaP-3	5.14	47.39	MSP0010	Mudstone	411	47.74			4.0	68.9	109	2.87	0.9
4000543	OnZaP-1	47.65	47.65	MSP0001	Carbonate	409	3.42	120			6.4	200	3.05	
4000944	OnZaP-1	47.90	47.90	MSP0010	Carbonate	208	368.03			3.7	590.5	130	28.51	0.8
4000045	OnZaP-3	5.89	48.16	MSP0001	Carbonate	141	4.96	90	0.04		8.3	160	0.98	
4000956	OnZaP-3	6.01	48.26	MSP0010	Carbonate	252				1.0	10.8	289	2.17	0.2
4000945	OnZaP-1	48.40	48.40	MSP0010	Carbonate	395	880.26			13.0	960.6	125	41.44	3.1

Sample ID	Drill site	Core depth (m)	Comb. depth (m)	Sample set	Lithology	Mn (ppm)	Mo (ppm)	Na (ppm)	Nb (ppm)	Nd (ppm)	Ni (ppm)	P (ppm)	Pb (ppm)	Pr (ppm)
4000553	OnZaP-1	48.61	48.61	MSP0001	Mudstone	74	8.99	90	0.28	0.2	20.0	10	2.48	
4000053	OnZaP-3	6.67	48.94	MSP0001	Mudstone	28	7.17	40	0.11	0.2	14.8		0.92	
4000957	OnZaP-3	6.84	49.09	MSP0010	Mudstone									
4000561	OnZaP-1	49.29	49.29	MSP0001	Carbonate	1,344	11.28	150	0.08	3.3	37.0	30	1.58	0.5
4000061	OnZaP-3	7.28	49.55	MSP0001	Carbonate	234	8.02	60			13.7	30	1.86	
4000958	OnZaP-3	8.00	50.25	MSP0010	Mudstone									
4000563	OnZaP-1	50.43	50.43	MSP0001	Mudstone	6	10.00	100	0.09	0.1	21.8		1.62	
4000946	OnZaP-1	50.58	50.58	MSP0010	Carbonate	1,050	11.05			6.3	90.9	118	1.19	1.4
4000959	OnZaP-3	8.40	50.65	MSP0010	Mudstone	21	99.39			1.6	184.2	140	6.51	0.3
4000065	OnZaP-3	8.44	50.71	MSP0001	Mudstone	33	134.90	90	0.20	1.7	285.5	300	15.29	0.3
4000571	OnZaP-1	50.77	50.77	MSP0001	Carbonate	2,412	2.41	150			14.5	460	1.20	
4000947	OnZaP-1	51.13	51.13	MSP0010	Carbonate	72	509.87			13.6	909.0	267	36.51	3.2
4000575	OnZaP-1	51.41	51.41	MSP0001	Mudstone	34	557.00	950	4.28	11.0	1,282.9	360	65.14	2.5
4000080	OnZaP-3	9.31	51.58	MSP0001	Carbonate	222	4.01	80	0.06	0.2	12.7	770	2.35	
4000960	OnZaP-3	9.57	51.82	MSP0010	Carbonate	35	169.73			10.4	96.0	225	18.18	2.6
4000583	OnZaP-1	52.16	52.16	MSP0001	Carbonate	723	2.24	70	0.08		9.7	900	0.76	
4000090	OnZaP-3	10.14	52.41	MSP0001	Carbonate	698	2.47	60	0.09		9.4	920	0.90	
4000592	OnZaP-1	52.92	52.92	MSP0001	Carbonate	2,232	1.68	100	0.08	2.2	31.7	270	0.62	0.6
4000098	OnZaP-3	10.70	52.97	MSP0001	Carbonate	2,007	2.94	90	0.18	3.3	19.3	1,430	1.25	0.7
4000948	OnZaP-1	53.12	53.12	MSP0010	Mudstone	116	202.36	593		59.0	564.2	36,255	21.16	12.2
4000961	OnZaP-3	11.00	53.25	MSP0010	Carbonate	53	350.17			23.0	159.3	2,172	41.00	5.7
4000949	OnZaP-1	53.50	53.50	MSP0010	Mudstone	272	416.39	6,044		25.5	571.1	192	23.09	5.9
4000962	OnZaP-3	11.33	53.58	MSP0010	Carbonate	27	153.15			68.5	273.1	79,156	22.03	16.2
4000100	OnZaP-3	11.33	53.60	MSP0001	Mudstone	24	181.78	860	1.98	22.0	770.6	18,320	73.92	4.8
4000593	OnZaP-1	53.70	53.70	MSP0001	Mudstone	52	268.90	2,260	19.12	27.8	411.7	410	32.33	6.3
4000963	OnZaP-3	11.70	53.95	MSP0010	Mudstone	26	21.57			138.6	344.9	888	60.02	38.1
4000964	OnZaP-3	11.96	54.21	MSP0010	Mudstone	129		5,332						
4000102	OnZaP-3	12.16	54.43	MSP0001	Mudstone	14	322.94	1,700	7.49	19.8	873.8	190	40.07	4.5
4000965	OnZaP-3	12.67	54.92	MSP0010	Mudstone	42	271.35	3,628		52.8	460.7	232	18.15	13.7
4000594	OnZaP-1	55.14	55.14	MSP0001	Mudstone	82	228.81	2,090	3.47	17.5	317.0	80	30.59	3.9
4000966	OnZaP-3	13.11	55.36	MSP0010	Mudstone	43	320.75	3,875		31.9	363.4	148	16.30	7.4
4000597	OnZaP-1	55.51	55.51	MSP0001	Carbonate	1,252	5.17	100	0.18	6.0	28.8	190	14.97	1.1
4000103	OnZaP-3	13.29	55.56	MSP0001	Mudstone	28	235.03	1,640	7.83	26.8	479.4	250	36.47	6.0
4000601	OnZaP-1	55.68	55.68	MSP0001	Mudstone	31	263.02	720	4.44	14.6	459.3	130	47.73	3.1
4000950	OnZaP-1	55.80	55.80	MSP0010	Mudstone	35	201.34	272		41.6	411.6	345	50.00	9.9
4000967	OnZaP-3	13.82	56.07	MSP0010	Carbonate	229	292.12	4,104		36.4	263.9	160	15.52	8.7
4000602	OnZaP-1	56.17	56.17	MSP0001	Mudstone	80	243.85	400	2.61	19.7	407.6	80	43.51	4.0
4000968	OnZaP-3	14.25	56.50	MSP0010	Mudstone	663	179.54	1,900		73.8	176.0	196	15.29	18.7
4000108	OnZaP-3	14.31	56.58	MSP0001	Mudstone	742	57.26	450	22.17	60.7	79.2	190	15.88	15.3
4000605	OnZaP-1	56.89	56.89	MSP0001	Carbonate	1,468	14.15	120	0.24	5.6	31.5	20	7.64	1.0
4000969	OnZaP-3	14.69	56.94	MSP0010	Mudstone	50	225.50	3,544		53.0	245.1	181	23.32	13.3
4000113	OnZaP-3	14.85	57.12	MSP0001	Mudstone	25	185.94	2,000	3.57	12.5	274.8	90	26.42	3.0
4000614	OnZaP-1	57.64	57.64	MSP0001	Carbonate	2,991	2.38	80	1.38	4.7	16.0	290	6.92	1.0
4000951	OnZaP-1	57.93	57.93	MSP0010	Mudstone	42	226.37	301		37.1	391.7	408	20.61	9.0
4000970	OnZaP-3	15.72	57.97	MSP0010	Mudstone	63	240.30	520		27.6	412.8	98	31.18	6.3

Sample ID	Drill site	Core depth (m)	Comb. depth (m)	Sample set	Lithology	Mn (ppm)	Mo (ppm)	Na (ppm)	Nb (ppm)	Nd (ppm)	Ni (ppm)	P (ppm)	Pb (ppm)	Pr (ppm)
4000114	OnZaP-3	15.70	57.97	MSP0001	Mudstone	39	195.63	860	2.86	19.2	294.9	190	38.01	4.3
4000618	OnZaP-1	58.41	58.41	MSP0001	Mudstone	21	131.87	550	6.60	26.0	365.3	190	20.12	5.7
4000971	OnZaP-3	16.42	58.67	MSP0010	Mudstone	41	221.97			41.9	295.1	146	23.90	9.5
4000972	OnZaP-3	16.72	58.97	MSP0010	Mudstone	22	141.00	450		27.1	166.3	137	8.26	6.8
4000115	OnZaP-3	16.92	59.19	MSP0001	Mudstone	36	169.01	1,050	3.06	11.5	326.0	250	30.16	2.7
4000952	OnZaP-1	59.25	59.25	MSP0010	Mudstone	98								
4000619	OnZaP-1	59.67	59.67	MSP0001	Mudstone	307	83.41	1,650	4.40	15.7	176.0	390	16.89	3.5
4000122	OnZaP-3	17.55	59.82	MSP0001	Mudstone	80	185.97	310	1.64	11.0	338.1	90	26.84	2.4
4000973	OnZaP-3	17.89	60.14	MSP0010	Mudstone	309	97.52			19.0	219.4	400	9.13	4.7
4000623	OnZaP-1	60.18	60.18	MSP0001	Mudstone	1,561	7.18	2,090	1.29	7.6	100.8	260	10.82	1.7
4000128	OnZaP-3	18.65	60.92	MSP0001	Carbonate	2,045	2.25	60	1.32	5.7	13.5	290	9.90	1.2
4000129	OnZaP-3	18.97	61.24	MSP0001	Mudstone	65	174.63	680	1.93	10.3	424.5	140	21.67	2.3
4000974	OnZaP-3	19.27	61.52	MSP0010	Mudstone	53	163.23	167		33.9	372.6	266	15.94	8.4
4000975	OnZaP-3	20.07	62.32	MSP0010	Mudstone	141	134.46	1,108		40.6	252.0	493	13.36	9.8
4000130	OnZaP-3	20.13	62.40	MSP0001	Mudstone	484	21.07	1,710	1.10	14.3	165.2	310	15.35	3.3
4000132	OnZaP-3	20.90	63.17	MSP0001	Mudstone	21	96.83	630	6.56	16.0	225.3	90	11.77	3.9
4000976	OnZaP-3	21.12	63.37	MSP0010	Mudstone	25	123.59	1,418		37.1	210.2	132		9.0
4000133	OnZaP-3	21.96	64.23	MSP0001	Mudstone	29	49.35	730	4.26	23.0	153.6	410	21.99	5.6
4000977	OnZaP-3	22.36	64.61	MSP0010	Mudstone	14	86.06	636		47.4	194.4	404	15.37	12.0
4000978	OnZaP-3	22.96	65.21	MSP0010	Mudstone	30	112.13	422		88.3	323.8	307	22.76	22.1
4000134	OnZaP-3	23.12	65.39	MSP0001	Mudstone	28	80.05	720	7.49	16.8	283.6	320	27.19	3.7
4000979	OnZaP-3	23.59	65.84	MSP0010	Mudstone	40								
4000135	OnZaP-3	24.26	66.53	MSP0001	Carbonate	1,351	13.31	100	0.57	4.8	75.4	520	5.18	1.2
4000980	OnZaP-3	24.91	67.16	MSP0010	Mudstone	123	62.19			76.8	312.3	1,150	11.28	18.6
4000151	OnZaP-3	25.18	67.45	MSP0001	Carbonate	1,240	3.14	110	0.54	4.7	17.2	1,090	4.21	1.1
4000981	OnZaP-3	25.59	67.84	MSP0010	Mudstone	113	8.54	171		13.8	35.8	401	3.86	3.4
4000159	OnZaP-3	25.76	68.03	MSP0001	Mudstone	93	38.37	1,190	6.21	22.0	247.7	640	22.84	5.3
4000982	OnZaP-3	26.20	68.45	MSP0010	Mudstone	122	71.14			34.4	319.5	745	25.67	8.7
4000168	OnZaP-3	26.56	68.83	MSP0001	Mudstone	290	7.61	290	2.84	74.0	63.8	10,550	26.84	17.0
4000178	OnZaP-3	27.32	69.59	MSP0001	Carbonate	634	13.51	130	1.04	3.9	46.3	100	5.76	0.9
4000983	OnZaP-3	27.51	69.76	MSP0010	Carbonate	129	22.49			14.0	55.3	94	2.23	3.5
4000179	OnZaP-3	28.13	70.40	MSP0001	Mudstone	21	73.99	350	1.38	4.3	320.9	60	3.80	1.0
4000984	OnZaP-3	28.69	70.94	MSP0010	Mudstone	5	33.11			5.9	49.3	43	0.93	1.4
4000180	OnZaP-3	29.20	71.47	MSP0001	Mudstone	16	124.51	430	1.91	25.6	573.7	200	13.28	5.9
4000985	OnZaP-3	29.35	71.60	MSP0010	Mudstone	6	105.76			41.4	391.2	179		9.6
4000181	OnZaP-3	30.59	72.86	MSP0001	Mudstone	139	62.33	160	0.52	58.4	262.6	18,560	23.14	11.0
4000986	OnZaP-3	30.68	72.93	MSP0010	Mudstone	36	265.65	13		33.3	952.0	316	7.85	8.4
4000987	OnZaP-3	31.40	73.65	MSP0010	Mudstone	12	124.19	1,022		42.5	374.3	216		9.0
4000187	OnZaP-3	31.63	73.90	MSP0001	Mudstone	15	99.09	1,580	1.44	17.4	454.8	190	17.30	3.9
4000988	OnZaP-3	32.10	74.35	MSP0010	Mudstone	42	291.29			65.7	425.0	462	14.98	15.0
4000190	OnZaP-3	32.36	74.63	MSP0001	Carbonate	769	9.02	180	0.06	5.6	62.3	1,010	3.37	0.9
4000201	OnZaP-3	33.24	75.51	MSP0001	Mudstone	137	99.49	100	0.32	12.0	397.3	210	10.76	2.7
4000989	OnZaP-3	33.48	75.73	MSP0010	Mudstone	49	229.84			72.5	803.0	888	11.07	17.4
4000990	OnZaP-3	33.81	76.06	MSP0010	Mudstone	5								
4000202	OnZaP-3	34.29	76.56	MSP0001	Mudstone	14	12.01	5,900	1.17	18.2	89.3	280	10.95	4.5

Sample ID	Drill site	Core depth (m)	Comb. depth (m)	Sample set	Lithology	Mn (ppm)	Mo (ppm)	Na (ppm)	Nb (ppm)	Nd (ppm)	Ni (ppm)	P (ppm)	Pb (ppm)	Pr (ppm)
4000203	OnZaP-3	34.96	77.23	MSP0001	Mudstone	23	1.05	3,760	1.68	10.7	27.6	120	5.80	3.0
4000214	OnZaP-3	36.54	78.81	MSP0001	Carbonate	1,011	0.35	470	1.00	9.5	11.9	90	3.40	2.8
4000216	OnZaP-3	37.30	79.57	MSP0001	Carbonate	1,020	0.66	410	0.48	5.9	11.7	420	3.07	1.2
4000225	OnZaP-3	38.42	80.69	MSP0001	Mudstone	877	0.29	210	0.86	11.4	16.9	860	3.92	2.5
4000231	OnZaP-3	39.25	81.52	MSP0001	Mudstone	757	0.55	190	1.32	14.2	21.3	320	5.94	4.0
4000239	OnZaP-3	40.20	82.47	MSP0001	Mudstone	186	0.56	7,000	2.19	20.8	38.1	440	8.09	6.6
4000244	OnZaP-3	41.09	83.36	MSP0001	Mudstone	981	0.30	260	1.09	21.9	14.4	340	3.90	5.8
4000251	OnZaP-3	42.32	84.59	MSP0001	Carbonate	1,017	5.62	160	1.09	10.6	19.7	220	6.51	2.4
4000256	OnZaP-3	43.12	85.39	MSP0001	Carbonate	1,341	0.13	80	0.27	4.7	4.9	220	2.78	1.0
4000264	OnZaP-3	44.02	86.29	MSP0001	Mudstone	204	4.33	2,620	1.48	15.4	37.7	150	10.17	4.2
4000265	OnZaP-3	44.82	87.09	MSP0001	Mudstone	45	2.25	4,560	1.46	15.3	58.1	160	9.72	3.6
4000266	OnZaP-3	45.87	88.14	MSP0001	Mudstone	39	11.72	2,130	2.30	12.8	98.9	150	7.23	3.0
4000991	OnZaP-3	46.11	88.36	MSP0010	Mudstone	41	26.70	2,226		28.5	174.9	188	9.44	7.4
4000992	OnZaP-3	46.51	88.76	MSP0010	Mudstone	31	47.72	2,359		32.9	269.0	205		8.7
4000267	OnZaP-3	46.59	88.86	MSP0001	Mudstone	43	33.42	2,430	2.21	15.3	174.9	140	11.31	4.0
4000993	OnZaP-3	47.86	90.11	MSP0010	Mudstone	19	73.56	3,255		28.6	180.1	194	18.32	7.3
4000268	OnZaP-3	48.02	90.29	MSP0001	Mudstone	30	14.20	4,940	2.24	13.5	105.4	170	15.04	3.2
4000994	OnZaP-3	48.94	91.19	MSP0010	Mudstone	45	38.72	3,505		25.0	204.4	154	10.63	6.6
4000269	OnZaP-3	49.00	91.27	MSP0001	Mudstone	26	11.04	4,310	1.70	11.2	103.3	110	7.86	2.9
4000270	OnZaP-3	49.68	91.95	MSP0001	Mudstone	42	10.76	5,520	1.02	14.1	139.5	170	22.39	3.7
4000271	OnZaP-3	50.28	92.55	MSP0001	Mudstone	43	3.08	9,060	1.73	10.0	66.2	150	10.32	2.6
4000273	OnZaP-3	50.99	93.26	MSP0001	Mudstone	106	2.98	5,250	1.53	7.1	34.6	150	8.28	1.4
4001000	OnZaP-1	51.57	93.82	MSP0010	Carbonate	1,730				9.7	15.3	3,762	0.78	2.2
4000279	OnZaP-3	52.53	94.80	MSP0001	Mudstone	70	4.95	6,100	1.93	4.6	121.0	170	11.27	1.2
4000280	OnZaP-3	53.02	95.29	MSP0001	Mudstone	32	12.79	4,680	2.50	9.0	119.4	170	15.68	2.2
4000995	OnZaP-3	53.75	96.00	MSP0010	Mudstone	44	34.38	2,116		24.1	185.5	157	9.74	6.3
4000281	OnZaP-3	54.02	96.29	MSP0001	Mudstone	60	27.03	1,730	3.40	12.6	188.0	160	9.95	3.1
4000288	OnZaP-3	55.01	97.28	MSP0001	Mudstone	952	2.62	60	0.15	4.9	35.7	200	2.99	1.1
4000289	OnZaP-3	55.60	97.87	MSP0001	Mudstone	40	21.63	2,340	3.59	12.9	163.8	170	12.18	3.4
4000996	OnZaP-3	55.76	98.01	MSP0010	Mudstone	38	31.75	2,658		28.4	148.7	246	9.57	7.7
4000290	OnZaP-3	56.52	98.79	MSP0001	Mudstone	40	5.78	3,050	1.52	9.7	89.1	140	6.61	2.3
4000997	OnZaP-3	57.27	99.52	MSP0010	Mudstone	30	44.49	785		21.5	296.4	149	7.50	5.5
4000998	OnZaP-3	58.06	100.31	MSP0010	Mudstone	25	68.20	1,313		37.2	408.4	254	14.72	9.7
4000291	OnZaP-3	58.24	100.51	MSP0001	Mudstone	21	66.18	1,800	4.10	13.9	549.5	250	18.69	3.6
4000299	OnZaP-3	58.87	101.14	MSP0001	Carbonate	2,075	1.63	90	0.41	14.2	15.7	810	3.53	2.8
4000999	OnZaP-3	59.88	102.13	MSP0010	Mudstone	30	95.04	1,224		49.6	520.8	369	25.93	12.3
4000306	OnZaP-3	59.95	102.22	MSP0001	Mudstone	31	48.84	1,070	3.00	13.8	331.1	250	31.56	3.4

Table A1e: Element concentration data for drill cores OnZaP-1 and OnZaP-3, continued.

Sample ID	Drill site	Core depth (m)	Comb. depth (m)	Sample set	Lithology	Rb (ppm)	Re (ppm)	Sb (ppm)	Sc (ppm)	Se (ppm)	Si (ppm)	Sm (ppm)	Sn (ppm)	Sr (ppm)
4000319	OnZaP-1	1.96	1.96	MSP0001	Mudstone	40.1		0.18	14.1			1.2	1.2	16
4000921	OnZaP-1	2.08	2.08	MSP0010	Mudstone	87.7			20.5		302,844	7.8		25
4000320	OnZaP-1	2.85	2.85	MSP0001	Mudstone	41.6		0.20	13.3			1.5	0.8	16
4000321	OnZaP-1	3.92	3.92	MSP0001	Mudstone	42.5		0.37	14.5			1.0	1.7	13
4000922	OnZaP-1	5.28	5.28	MSP0010	Mudstone	52.9			21.4		305,603	2.8		8
4000322	OnZaP-1	5.31	5.31	MSP0001	Mudstone	54.0		0.35	15.7			1.2	1.4	15
4000323	OnZaP-1	6.50	6.50	MSP0001	Mudstone	48.9		0.28	11.8			0.8	1.0	12
4000923	OnZaP-1	6.60	6.60	MSP0010	Mudstone				15.7		291,291			
4000324	OnZaP-1	7.01	7.01	MSP0001	Mudstone	51.7		0.29	17.1			1.4	3.7	16
4000332	OnZaP-1	7.96	7.96	MSP0001	Mudstone	24.5		0.20	5.0			2.2	0.6	154
4000336	OnZaP-1	8.35	8.35	MSP0001	Mudstone	34.5	0.002	0.89	14.2	0.40		1.4	2.0	42
4000342	OnZaP-1	8.74	8.74	MSP0001	Mudstone	44.1	0.004	0.94	9.1			1.9	0.6	171
4000345	OnZaP-1	9.58	9.58	MSP0001	Mudstone	31.9	0.009	1.42	15.3			2.3	1.5	49
4000346	OnZaP-1	10.79	10.79	MSP0001	Mudstone	29.0		0.85	12.8			0.6	1.3	10
4000924	OnZaP-1	11.13	11.13	MSP0010	Mudstone	101.5			18.9		277,665	6.0		12
4000347	OnZaP-1	11.86	11.86	MSP0001	Mudstone	60.9	0.004	0.77	18.0			2.2	1.9	12
4000925	OnZaP-1	12.15	12.15	MSP0010	Mudstone	94.4			19.8	1.50	276,660	8.6		17
4000348	OnZaP-1	12.39	12.39	MSP0001	Mudstone	57.0	0.005	2.83	16.7			1.3	1.5	10
4000349	OnZaP-1	13.16	13.16	MSP0001	Mudstone	36.8		0.09	3.9			1.3		211
4000351	OnZaP-1	13.40	13.40	MSP0001	Mudstone	47.0		0.10	4.4			1.2	0.2	138
4000358	OnZaP-1	14.65	14.65	MSP0001	Mudstone	35.5		0.33	12.6			0.8	1.5	10
4000362	OnZaP-1	15.26	15.26	MSP0001	Mudstone	37.7		0.14	11.7			2.3	0.7	87
4000368	OnZaP-1	16.29	16.29	MSP0001	Mudstone	22.2		0.12	5.3			1.0	0.3	105
4000376	OnZaP-1	17.36	17.36	MSP0001	Mudstone	30.2		0.15	6.1			0.9	0.2	145
4000383	OnZaP-1	17.90	17.90	MSP0001	Mudstone	41.2	0.003	0.13	6.5			1.6	0.3	103
4000926	OnZaP-1	18.85	18.85	MSP0010	Mudstone	174.9			22.9		260,174	8.3		12
4000392	OnZaP-1	19.08	19.08	MSP0001	Mudstone	79.4		0.18	19.2			2.0	1.7	8
4000393	OnZaP-1	19.99	19.99	MSP0001	Mudstone	85.6		0.19	18.6			1.5	1.5	7
4000394	OnZaP-1	20.66	20.66	MSP0001	Mudstone	82.8	0.004	0.24	18.2			2.4	1.9	7
4000927	OnZaP-1	21.91	21.91	MSP0010	Mudstone	144.3			20.7		293,618	7.7		23
4000395	OnZaP-1	21.94	21.94	MSP0001	Mudstone	76.5		0.15	14.8			2.4	1.5	12
4000396	OnZaP-1	22.33	22.33	MSP0001	Mudstone	42.3		0.26	15.5			2.1	1.7	10
4000398	OnZaP-1	23.03	23.03	MSP0001	Mudstone	46.9		0.18	15.7			2.7	1.3	17
4000928	OnZaP-1	23.84	23.84	MSP0010	Mudstone	69.9			20.3	1.69	150,518	4.0		42
4000403	OnZaP-1	24.31	24.31	MSP0001	Mudstone	62.3		0.32	12.6			3.3	1.0	59
4000406	OnZaP-1	25.03	25.03	MSP0001	Mudstone	29.5		0.09	6.2			1.8	0.3	114
4000412	OnZaP-1	26.09	26.09	MSP0001	Mudstone	29.1		0.22	14.1			1.4	1.7	8
4000413	OnZaP-1	26.80	26.80	MSP0001	Mudstone	30.8		0.38	17.3			2.1	1.6	14
4000414	OnZaP-1	27.77	27.77	MSP0001	Mudstone	20.9		1.53	9.9			3.3	1.0	96
4000929	OnZaP-1	27.95	27.95	MSP0010	Mudstone	131.8			19.9		271,505	7.4		34
4000421	OnZaP-1	28.36	28.36	MSP0001	Mudstone	27.1		1.50	5.8			2.3	0.5	130
4000930	OnZaP-1	28.80	28.80	MSP0010	Mudstone	152.4			21.1		289,015	10.3		21

Sample ID	Drill site	Core depth (m)	Comb. depth (m)	Sample set	Lithology	Rb (ppm)	Re (ppm)	Sb (ppm)	Sc (ppm)	Se (ppm)	Si (ppm)	Sm (ppm)	Sn (ppm)	Sr (ppm)
4000429	OnZaP-1	29.28	29.28	MSP0001	Carbonate	6.6		0.31	2.0			1.4		163
4000931	OnZaP-1	30.66	30.66	MSP0010	Mudstone	88.4	0.012		22.8	1.73	269,230	10.6		10
4000436	OnZaP-1	30.79	30.79	MSP0001	Mudstone	48.8		7.37	16.1			2.2	1.8	6
4000442	OnZaP-1	31.21	31.21	MSP0001	Carbonate	9.6		0.21	1.1			1.1		137
4000932	OnZaP-1	31.85	31.85	MSP0010	Mudstone	87.6	0.028		21.0	1.36	317,421	9.3		9
4000447	OnZaP-1	31.86	31.86	MSP0001	Mudstone	32.8	0.021	14.56	17.2			1.4	2.8	6
4000933	OnZaP-1	32.19	32.19	MSP0010	Mudstone	89.4	0.039		24.9	1.65	290,157	8.1		9
4000455	OnZaP-1	33.15	33.15	MSP0001	Carbonate	4.9		0.39	0.3			0.8	0.2	117
4000466	OnZaP-1	33.96	33.96	MSP0001	Carbonate	5.6	0.002	0.89	0.3			1.0	0.1	75
4000471	OnZaP-1	34.64	34.64	MSP0001	Carbonate	6.1	0.002	0.37	1.5			1.0	0.5	91
4000478	OnZaP-1	35.61	35.61	MSP0001	Mudstone	3.3		0.79	0.2			0.7	0.2	54
4000934	OnZaP-1	36.40	36.40	MSP0010	Mudstone	96.0	0.103		20.5		280,004	18.0		7
4000483	OnZaP-1	36.52	36.52	MSP0001	Mudstone	19.1	0.114	8.75	9.3			4.5	4.4	5
4000484	OnZaP-1	36.94	36.94	MSP0001	Carbonate	18.0	0.003	0.16	0.2			1.1		103
4000935	OnZaP-1	37.83	37.83	MSP0010	Mudstone	70.8	0.050		13.1	1.68	277,956	15.5		6
4000491	OnZaP-1	38.13	38.13	MSP0001	Mudstone	24.2	0.042	17.13	5.0			3.8	4.2	4
4000936	OnZaP-1	38.91	38.91	MSP0010	Mudstone	72.3	0.108		15.9	1.67	216,117	20.1		10
4000492	OnZaP-1	38.97	38.97	MSP0001	Mudstone	22.8	0.141	15.02	7.6	1.50		3.5	2.6	12
4000493	OnZaP-1	39.88	39.88	MSP0001	Mudstone	78.2	0.037	10.78	8.1	7.80		3.6	0.8	90
4000937	OnZaP-1	40.02	40.02	MSP0010	Carbonate	72.8	0.120		13.9	5.62	261,468	7.0		37
4000938	OnZaP-1	41.09	41.09	MSP0010	Mudstone	52.7	0.153		19.7	1.44	313,393	6.0		6
4000494	OnZaP-1	41.15	41.15	MSP0001	Mudstone	31.5	0.172	18.75	10.8			3.2	1.9	6
4000939	OnZaP-1	41.38	41.38	MSP0010	Mudstone	69.1	0.189		22.6	1.33	273,623	8.9		8
4000500	OnZaP-1	42.04	42.04	MSP0001	Carbonate	3.2	0.005	0.12				0.9		132
4000940	OnZaP-1	42.42	42.42	MSP0010	Mudstone	58.5	0.202		13.5	2.03	267,868	8.0		7
4000504	OnZaP-1	42.45	42.45	MSP0001	Mudstone	103.6	0.177	13.84	7.7	7.10		3.6	0.6	37
4000941	OnZaP-1	42.86	42.86	MSP0010	Carbonate	43.2	0.320		5.0	14.16	135,795	5.2		47
4000942	OnZaP-1	43.69	43.69	MSP0010	Carbonate				6.6		227,527			
4000516	OnZaP-1	43.94	43.94	MSP0001	Carbonate	0.4	0.003	0.37						51
4000005	OnZaP-3	2.10	44.37	MSP0001	Carbonate	0.6	0.017	0.10						53
4000521	OnZaP-1	44.53	44.53	MSP0001	Carbonate	0.7	0.003	0.30						54
4000953	OnZaP-3	2.68	44.93	MSP0010	Carbonate	34.7	0.312		3.3	2.44	114,994	9.3		112
4000954	OnZaP-3	2.77	45.02	MSP0010	Mudstone	105.6	0.389		2.3	3.65	340,574	0.7		2
4000015	OnZaP-3	3.12	45.39	MSP0001	Carbonate	0.8	0.011	0.13						59
4000529	OnZaP-1	45.65	45.65	MSP0001	Carbonate	0.9	0.009	0.40						73
4000943	OnZaP-1	46.36	46.36	MSP0010	Mudstone	77.4	0.468		7.9	4.11	280,028	2.2		5
4000030	OnZaP-3	4.38	46.65	MSP0001	Carbonate	0.8	0.003	0.12						35
4000536	OnZaP-1	46.70	46.70	MSP0001	Mudstone	2.3	0.007	0.46		0.80				
4000037	OnZaP-3	5.02	47.29	MSP0001	Carbonate	3.3	0.018	0.38					0.2	88
4000955	OnZaP-3	5.14	47.39	MSP0010	Mudstone	19.9	0.067		1.3	2.35	139,816	1.0		127
4000543	OnZaP-1	47.65	47.65	MSP0001	Carbonate	0.5	0.004	0.18						35
4000944	OnZaP-1	47.90	47.90	MSP0010	Carbonate	86.5	0.139		7.9	10.61	220,824	1.2		14
4000045	OnZaP-3	5.89	48.16	MSP0001	Carbonate	2.0	0.008	0.15					0.1	78
4000956	OnZaP-3	6.01	48.26	MSP0010	Carbonate	0.7			0.3		3,588	0.2		88
4000945	OnZaP-1	48.40	48.40	MSP0010	Carbonate	44.6	0.477		5.8	15.13	202,655	2.6		32

Sample ID	Drill site	Core depth (m)	Comb. depth (m)	Sample set	Lithology	Rb (ppm)	Re (ppm)	Sb (ppm)	Sc (ppm)	Se (ppm)	Si (ppm)	Sm (ppm)	Sn (ppm)	Sr (ppm)
4000553	OnZaP-1	48.61	48.61	MSP0001	Mudstone	0.8	0.007	0.35	0.1			0.1	0.3	
4000053	OnZaP-3	6.67	48.94	MSP0001	Mudstone	0.6	0.003	0.22					0.5	1
4000957	OnZaP-3	6.84	49.09	MSP0010	Mudstone									
4000561	OnZaP-1	49.29	49.29	MSP0001	Carbonate	2.7	0.011	0.26	0.8			0.9		96
4000061	OnZaP-3	7.28	49.55	MSP0001	Carbonate	1.1	0.009	0.54					0.2	58
4000958	OnZaP-3	8.00	50.25	MSP0010	Mudstone									
4000563	OnZaP-1	50.43	50.43	MSP0001	Mudstone	4.2	0.008	0.55	0.2	0.40				3
4000946	OnZaP-1	50.58	50.58	MSP0010	Carbonate	4.2			1.5		119,519	1.4		132
4000959	OnZaP-3	8.40	50.65	MSP0010	Mudstone	18.9	0.073		0.5	3.90	432,880	0.4		2
4000065	OnZaP-3	8.44	50.71	MSP0001	Mudstone	38.2	0.129	6.46	1.0	4.10		0.4	0.9	5
4000571	OnZaP-1	50.77	50.77	MSP0001	Carbonate	1.0	0.003	0.21						39
4000947	OnZaP-1	51.13	51.13	MSP0010	Carbonate	53.6	0.490		26.1	9.85	186,922	2.9		9
4000575	OnZaP-1	51.41	51.41	MSP0001	Mudstone	42.3	0.516	22.03	9.6	2.30		3.1	3.0	12
4000080	OnZaP-3	9.31	51.58	MSP0001	Carbonate	0.5	0.006	0.31					0.2	81
4000960	OnZaP-3	9.57	51.82	MSP0010	Carbonate	19.5	0.262		15.1	1.42	285,540	1.6		2
4000583	OnZaP-1	52.16	52.16	MSP0001	Carbonate	1.2	0.005	0.13						79
4000090	OnZaP-3	10.14	52.41	MSP0001	Carbonate	2.8	0.004	0.14						119
4000592	OnZaP-1	52.92	52.92	MSP0001	Carbonate	10.9	0.005	0.07	0.4			0.4		70
4000098	OnZaP-3	10.70	52.97	MSP0001	Carbonate	4.4	0.006	0.19	0.3			0.6		135
4000948	OnZaP-1	53.12	53.12	MSP0010	Mudstone	88.8	0.198		12.7	6.18	130,070	13.4		87
4000961	OnZaP-3	11.00	53.25	MSP0010	Carbonate	54.6	0.342		13.5	2.91	253,951	4.4		14
4000949	OnZaP-1	53.50	53.50	MSP0010	Mudstone	24.2	0.193		19.2	5.52	257,618	5.5		19
4000962	OnZaP-3	11.33	53.58	MSP0010	Carbonate	34.2	0.142		9.2	2.25	88,531	15.2		185
4000100	OnZaP-3	11.33	53.60	MSP0001	Mudstone	34.4	0.296	15.01	8.2	1.40		4.9	1.7	64
4000593	OnZaP-1	53.70	53.70	MSP0001	Mudstone	23.0	0.143	10.46	5.7			5.9	1.6	11
4000963	OnZaP-3	11.70	53.95	MSP0010	Mudstone	75.2			23.8	16.53	198,141	25.4		9
4000964	OnZaP-3	11.96	54.21	MSP0010	Mudstone				21.4		282,353			
4000102	OnZaP-3	12.16	54.43	MSP0001	Mudstone	27.0	0.221	15.09	6.0	0.50		4.6	1.5	8
4000965	OnZaP-3	12.67	54.92	MSP0010	Mudstone	35.7	0.213		20.2	4.56	245,825	10.6		9
4000594	OnZaP-1	55.14	55.14	MSP0001	Mudstone	16.3	0.081	7.83	4.9			3.8	1.0	10
4000966	OnZaP-3	13.11	55.36	MSP0010	Mudstone	22.7	0.114		17.3	1.01	301,331	7.3		8
4000597	OnZaP-1	55.51	55.51	MSP0001	Carbonate	9.0	0.007	4.88	2.9	2.40		1.7		189
4000103	OnZaP-3	13.29	55.56	MSP0001	Mudstone	24.4	0.140	10.83	5.5	1.40		5.8	1.6	11
4000601	OnZaP-1	55.68	55.68	MSP0001	Mudstone	25.5	0.189	10.08	8.7			3.0	0.7	10
4000950	OnZaP-1	55.80	55.80	MSP0010	Mudstone	30.2	0.143		26.1	2.67	283,066	8.5		10
4000967	OnZaP-3	13.82	56.07	MSP0010	Carbonate	35.2	0.108		13.3	1.29	210,926	7.9		13
4000602	OnZaP-1	56.17	56.17	MSP0001	Mudstone	16.5	0.156	9.18	7.1			3.1	1.0	9
4000968	OnZaP-3	14.25	56.50	MSP0010	Mudstone	67.7	0.100		9.9	4.94	120,727	15.0		79
4000108	OnZaP-3	14.31	56.58	MSP0001	Mudstone	76.0	0.048	4.71	6.0	4.50		10.7	0.5	139
4000605	OnZaP-1	56.89	56.89	MSP0001	Carbonate	3.5	0.009	1.23	2.2	1.20		1.5		228
4000969	OnZaP-3	14.69	56.94	MSP0010	Mudstone	29.8	0.072		12.4	0.96	213,795	10.6		8
4000113	OnZaP-3	14.85	57.12	MSP0001	Mudstone	20.6	0.077	8.96	4.1	0.50		2.9	1.3	7
4000614	OnZaP-1	57.64	57.64	MSP0001	Carbonate	13.1		1.26	3.2	2.40		1.1		99
4000951	OnZaP-1	57.93	57.93	MSP0010	Mudstone	45.5	0.166		40.0	0.95	236,760	8.2		7
4000970	OnZaP-3	15.72	57.97	MSP0010	Mudstone	18.8	0.079		9.3	8.07	176,109	5.9		13

Sample ID	Drill site	Core depth (m)	Comb. depth (m)	Sample set	Lithology	Rb (ppm)	Re (ppm)	Sb (ppm)	Sc (ppm)	Se (ppm)	Si (ppm)	Sm (ppm)	Sn (ppm)	Sr (ppm)
4000114	OnZaP-3	15.70	57.97	MSP0001	Mudstone	25.0	0.077	9.49	5.4	3.50		3.9	1.2	14
4000618	OnZaP-1	58.41	58.41	MSP0001	Mudstone	30.9	0.125	5.46	15.6			5.2	1.2	7
4000971	OnZaP-3	16.42	58.67	MSP0010	Mudstone	49.6	0.116		33.9	1.29	237,207	8.8		9
4000972	OnZaP-3	16.72	58.97	MSP0010	Mudstone	18.8	0.149		8.4	4.61	369,380	5.3		10
4000115	OnZaP-3	16.92	59.19	MSP0001	Mudstone	22.3	0.088	10.34	14.0			3.0	2.4	8
4000952	OnZaP-1	59.25	59.25	MSP0010	Mudstone				15.5		332,678			
4000619	OnZaP-1	59.67	59.67	MSP0001	Mudstone	24.5	0.070	4.71	16.1	3.00		4.1	1.1	39
4000122	OnZaP-3	17.55	59.82	MSP0001	Mudstone	34.6	0.105	8.67	5.1			2.0	0.9	5
4000973	OnZaP-3	17.89	60.14	MSP0010	Mudstone	63.0	0.151		9.2	3.80	296,284	3.8		41
4000623	OnZaP-1	60.18	60.18	MSP0001	Mudstone	63.5	0.013	2.07	14.3	3.20		2.9	0.4	170
4000128	OnZaP-3	18.65	60.92	MSP0001	Carbonate	15.6		2.40	5.8	3.60		1.6		149
4000129	OnZaP-3	18.97	61.24	MSP0001	Mudstone	21.2	0.131	10.41	12.4			2.4	1.5	5
4000974	OnZaP-3	19.27	61.52	MSP0010	Mudstone	43.0	0.034		25.2		266,275	7.7		6
4000975	OnZaP-3	20.07	62.32	MSP0010	Mudstone	48.1	0.101		34.3	2.98	283,005	9.4		11
4000130	OnZaP-3	20.13	62.40	MSP0001	Mudstone	42.3	0.024	8.24	26.5	4.30		3.2	1.1	100
4000132	OnZaP-3	20.90	63.17	MSP0001	Mudstone	22.7	0.095	5.61	6.0			3.3	2.1	5
4000976	OnZaP-3	21.12	63.37	MSP0010	Mudstone	28.0	0.087		12.7	1.23	368,813	8.3		6
4000133	OnZaP-3	21.96	64.23	MSP0001	Mudstone	20.9	0.041	7.32	10.1			4.9	2.1	6
4000977	OnZaP-3	22.36	64.61	MSP0010	Mudstone	32.7	0.053		10.2		355,812	10.1		7
4000978	OnZaP-3	22.96	65.21	MSP0010	Mudstone	64.0	0.019		25.6	1.48	265,591	19.5		7
4000134	OnZaP-3	23.12	65.39	MSP0001	Mudstone	15.1	0.037	9.95	14.3			3.9	3.9	5
4000979	OnZaP-3	23.59	65.84	MSP0010	Mudstone				12.4		264,330			
4000135	OnZaP-3	24.26	66.53	MSP0001	Carbonate	16.1	0.017	2.09	2.5	1.30		1.7	0.1	182
4000980	OnZaP-3	24.91	67.16	MSP0010	Mudstone	137.9	0.056		16.2	1.92	214,455	12.3		7
4000151	OnZaP-3	25.18	67.45	MSP0001	Carbonate	9.3	0.003	1.25	1.5			1.5		100
4000981	OnZaP-3	25.59	67.84	MSP0010	Mudstone	20.1			26.5		225,104	2.7		2
4000159	OnZaP-3	25.76	68.03	MSP0001	Mudstone	93.5	0.038	10.49	22.6			4.6	1.6	7
4000982	OnZaP-3	26.20	68.45	MSP0010	Mudstone	112.2	0.106		26.2	4.44	217,109	6.6		6
4000168	OnZaP-3	26.56	68.83	MSP0001	Mudstone	92.5	0.007	5.40	13.8	2.30		13.7	0.7	78
4000178	OnZaP-3	27.32	69.59	MSP0001	Carbonate	20.4	0.015	2.32	2.3	1.00		1.1	0.1	117
4000983	OnZaP-3	27.51	69.76	MSP0010	Carbonate	92.5	0.081		15.2	2.55	286,646	2.8		20
4000179	OnZaP-3	28.13	70.40	MSP0001	Mudstone	10.9	0.088	1.84	1.5			1.0	0.8	2
4000984	OnZaP-3	28.69	70.94	MSP0010	Mudstone	17.8	0.049		6.3		443,431	1.6		2
4000180	OnZaP-3	29.20	71.47	MSP0001	Mudstone	26.2	0.133	5.19	9.0			5.2	1.5	3
4000985	OnZaP-3	29.35	71.60	MSP0010	Mudstone	23.0	0.143		7.3	3.66	429,302	8.5		3
4000181	OnZaP-3	30.59	72.86	MSP0001	Mudstone	45.7	0.044	4.54	5.2	3.20		16.7	0.4	110
4000986	OnZaP-3	30.68	72.93	MSP0010	Mudstone	55.2	0.426		15.4		363,068	6.2		6
4000987	OnZaP-3	31.40	73.65	MSP0010	Mudstone	24.5	0.054		8.1	1.21	352,957	8.5		7
4000187	OnZaP-3	31.63	73.90	MSP0001	Mudstone	20.0	0.137	5.10	6.0			3.9	1.0	7
4000988	OnZaP-3	32.10	74.35	MSP0010	Mudstone	33.1	0.111		5.7		354,216	13.4		7
4000190	OnZaP-3	32.36	74.63	MSP0001	Carbonate	14.8	0.007	0.89	8.0	0.60		2.2	0.1	82
4000201	OnZaP-3	33.24	75.51	MSP0001	Mudstone	47.5	0.075	3.41	4.2	3.00		2.4	0.3	38
4000989	OnZaP-3	33.48	75.73	MSP0010	Mudstone	51.9	0.127		7.9	1.26	313,461	13.9		8
4000990	OnZaP-3	33.81	76.06	MSP0010	Mudstone				3.4		454,054			
4000202	OnZaP-3	34.29	76.56	MSP0001	Mudstone	25.6	0.049	2.47	8.4			3.4	1.2	7

Sample ID	Drill site	Core depth (m)	Comb. depth (m)	Sample set	Lithology	Rb (ppm)	Re (ppm)	Sb (ppm)	Sc (ppm)	Se (ppm)	Si (ppm)	Sm (ppm)	Sn (ppm)	Sr (ppm)
4000203	OnZaP-3	34.96	77.23	MSP0001	Mudstone	33.8		1.41	6.2	0.60		1.7	1.0	4
4000214	OnZaP-3	36.54	78.81	MSP0001	Carbonate	32.3	0.003	0.74	3.1			2.2	0.2	154
4000216	OnZaP-3	37.30	79.57	MSP0001	Carbonate	21.8		0.85	2.9			1.5	0.1	113
4000225	OnZaP-3	38.42	80.69	MSP0001	Mudstone	37.1		0.89	3.8			2.3	0.3	133
4000231	OnZaP-3	39.25	81.52	MSP0001	Mudstone	55.1		1.24	6.3			2.7	0.5	180
4000239	OnZaP-3	40.20	82.47	MSP0001	Mudstone	44.5		1.84	7.1	0.40		2.4	1.1	34
4000244	OnZaP-3	41.09	83.36	MSP0001	Mudstone	48.3		0.62	6.0			4.1	0.3	176
4000251	OnZaP-3	42.32	84.59	MSP0001	Carbonate	31.1	0.002	1.03	3.2			1.9		183
4000256	OnZaP-3	43.12	85.39	MSP0001	Carbonate	10.3		0.25	1.9			1.7		194
4000264	OnZaP-3	44.02	86.29	MSP0001	Mudstone	73.7	0.014	1.88	6.6	0.90		2.1	0.4	43
4000265	OnZaP-3	44.82	87.09	MSP0001	Mudstone	36.0	0.016	2.17	4.7	0.80		2.5	0.5	8
4000266	OnZaP-3	45.87	88.14	MSP0001	Mudstone	38.4	0.045	1.61	5.7			2.5	0.6	5
4000991	OnZaP-3	46.11	88.36	MSP0010	Mudstone	45.6	0.064		6.9	3.18	379,973	5.4		7
4000992	OnZaP-3	46.51	88.76	MSP0010	Mudstone	50.0	0.116		9.0	1.53	380,978	6.5		8
4000267	OnZaP-3	46.59	88.86	MSP0001	Mudstone	42.6	0.111	3.24	7.1			3.0	1.0	7
4000993	OnZaP-3	47.86	90.11	MSP0010	Mudstone	26.0	0.099		3.8	1.37	410,234	5.4		6
4000268	OnZaP-3	48.02	90.29	MSP0001	Mudstone	25.4	0.059	2.34	7.4	0.40		2.5	1.1	7
4000994	OnZaP-3	48.94	91.19	MSP0010	Mudstone	38.1	0.108		8.6	4.51	397,664	4.8		11
4000269	OnZaP-3	49.00	91.27	MSP0001	Mudstone	23.6	0.058	1.42	4.2			2.1	0.7	6
4000270	OnZaP-3	49.68	91.95	MSP0001	Mudstone	27.6	0.035	4.11	5.5	0.50		2.8	0.8	7
4000271	OnZaP-3	50.28	92.55	MSP0001	Mudstone	34.2	0.013	1.87	8.3	1.00		2.3	0.8	9
4000273	OnZaP-3	50.99	93.26	MSP0001	Mudstone	35.8	0.009	1.46	7.3	1.80		1.4	0.5	23
4001000	OnZaP-1	51.57	93.82	MSP0010	Carbonate	4.9			2.1	1.29	12,221	2.2		109
4000279	OnZaP-3	52.53	94.80	MSP0001	Mudstone	28.5	0.031	2.34	11.5	3.10		1.2	1.3	11
4000280	OnZaP-3	53.02	95.29	MSP0001	Mudstone	28.8	0.080	1.94	7.0			1.7	0.8	6
4000995	OnZaP-3	53.75	96.00	MSP0010	Mudstone	45.2	0.095		7.9		398,865	4.6		5
4000281	OnZaP-3	54.02	96.29	MSP0001	Mudstone	53.4	0.105	2.67	5.0			2.7	0.7	5
4000288	OnZaP-3	55.01	97.28	MSP0001	Mudstone	37.6	0.010	0.51	3.2	1.00		1.4	0.2	275
4000289	OnZaP-3	55.60	97.87	MSP0001	Mudstone	40.7	0.097	3.45	8.6			2.8	1.2	6
4000996	OnZaP-3	55.76	98.01	MSP0010	Mudstone	47.7	0.118		13.0		385,253	5.2		7
4000290	OnZaP-3	56.52	98.79	MSP0001	Mudstone	26.4	0.029	1.59	7.0	1.20		2.1	1.0	5
4000997	OnZaP-3	57.27	99.52	MSP0010	Mudstone	32.8	0.136		7.4	2.65	400,762	4.3		5
4000998	OnZaP-3	58.06	100.31	MSP0010	Mudstone	52.8	0.206		11.0	2.15	371,305	7.3		8
4000291	OnZaP-3	58.24	100.51	MSP0001	Mudstone	28.0	0.188	6.09	7.9			2.8	1.2	6
4000299	OnZaP-3	58.87	101.14	MSP0001	Carbonate	11.2	0.017	0.52	2.1	0.70		3.2		185
4000999	OnZaP-3	59.88	102.13	MSP0010	Mudstone	54.1	0.222		15.1	1.64	361,075	10.2		9
4000306	OnZaP-3	59.95	102.22	MSP0001	Mudstone	40.1	0.160	7.20	10.3			3.1	1.5	6

Table A1f: Element concentration data for drill cores OnZaP-1 and OnZaP-3, continued.

Sample ID	Drill site	Core depth (m)	Comb. depth (m)	Sample set	Lithology	Ta (ppm)	Tb (ppm)	Te (ppm)	Th (ppm)	Ti (ppm)	Tl (ppm)	Tm (ppm)	U (ppm)	V (ppm)
4000319	OnZaP-1	1.96	1.96	MSP0001	Mudstone	0.8	0.2	0.42	2.1	5,760	0.60	0.1	0.5	106
4000921	OnZaP-1	2.08	2.08	MSP0010	Mudstone		1.1		13.6	6,982	0.66	0.5	1.6	117
4000320	OnZaP-1	2.85	2.85	MSP0001	Mudstone	0.8	0.2	0.07	2.4	5,650	0.83	0.2	0.7	99
4000321	OnZaP-1	3.92	3.92	MSP0001	Mudstone	0.8	0.2	0.08	1.7	6,110	1.10	0.1	0.3	123
4000922	OnZaP-1	5.28	5.28	MSP0010	Mudstone		0.4		4.8	5,709	0.46	0.2	0.5	61
4000322	OnZaP-1	5.31	5.31	MSP0001	Mudstone	0.9	0.1	0.19	1.9	6,180	0.93	0.1	0.5	124
4000323	OnZaP-1	6.50	6.50	MSP0001	Mudstone	0.6	0.1	0.06	1.5	5,330	1.10		0.5	111
4000923	OnZaP-1	6.60	6.60	MSP0010	Mudstone					3,680				
4000324	OnZaP-1	7.01	7.01	MSP0001	Mudstone	1.0	0.2	0.51	1.8	4,170	0.94	0.1	0.5	152
4000332	OnZaP-1	7.96	7.96	MSP0001	Mudstone		0.3	0.68	1.1	1,510	0.45	0.1	3.6	56
4000336	OnZaP-1	8.35	8.35	MSP0001	Mudstone		0.2	0.21	2.4	2,460	0.80	0.1	2.0	130
4000342	OnZaP-1	8.74	8.74	MSP0001	Mudstone		0.3	1.01	1.9	1,250	0.44	0.2	0.8	62
4000345	OnZaP-1	9.58	9.58	MSP0001	Mudstone		0.3	0.31	2.9	2,220	0.65	0.2	1.6	139
4000346	OnZaP-1	10.79	10.79	MSP0001	Mudstone			0.12	1.0	3,240	0.87		0.6	140
4000924	OnZaP-1	11.13	11.13	MSP0010	Mudstone		0.9		9.0	4,326	0.74	0.4	1.4	124
4000347	OnZaP-1	11.86	11.86	MSP0001	Mudstone	0.2	0.3	0.08	2.4	2,880	0.73	0.2	1.6	169
4000925	OnZaP-1	12.15	12.15	MSP0010	Mudstone		1.2		10.9	5,517	1.02	0.5	2.2	129
4000348	OnZaP-1	12.39	12.39	MSP0001	Mudstone		0.2	0.79	2.2	2,500	0.96	0.1	1.2	142
4000349	OnZaP-1	13.16	13.16	MSP0001	Mudstone		0.2	0.95	0.9	640	0.37		0.2	19
4000351	OnZaP-1	13.40	13.40	MSP0001	Mudstone	0.2	0.1	0.87	1.5	1,310	0.51		0.2	26
4000358	OnZaP-1	14.65	14.65	MSP0001	Mudstone		0.1	0.82	1.4	5,030	1.45	0.1	1.0	168
4000362	OnZaP-1	15.26	15.26	MSP0001	Mudstone	0.1	0.3	0.56	3.0	2,530	0.87	0.2	0.7	68
4000368	OnZaP-1	16.29	16.29	MSP0001	Mudstone		0.1	1.07	0.6	650	0.25		0.1	24
4000376	OnZaP-1	17.36	17.36	MSP0001	Mudstone			1.25	1.1	1,090	0.36		0.2	27
4000383	OnZaP-1	17.90	17.90	MSP0001	Mudstone		0.2	0.75	1.3	1,200	0.46		0.2	29
4000926	OnZaP-1	18.85	18.85	MSP0010	Mudstone		1.0		10.4	6,246	1.69	0.4	0.7	128
4000392	OnZaP-1	19.08	19.08	MSP0001	Mudstone	0.5	0.2		3.2	5,110	1.22	0.1	0.7	185
4000393	OnZaP-1	19.99	19.99	MSP0001	Mudstone	0.6	0.1	0.41	2.4	6,270	1.46	0.1	0.5	157
4000394	OnZaP-1	20.66	20.66	MSP0001	Mudstone	0.2	0.2	0.23	3.2	3,740	1.00	0.1	2.8	184
4000927	OnZaP-1	21.91	21.91	MSP0010	Mudstone		1.0		13.3	5,289	1.48	0.4	0.8	134
4000395	OnZaP-1	21.94	21.94	MSP0001	Mudstone	0.8	0.2	0.08	3.3	5,420	1.44	0.1	0.5	115
4000396	OnZaP-1	22.33	22.33	MSP0001	Mudstone	0.8	0.2	0.10	2.7	5,910	1.59	0.1	0.5	113
4000398	OnZaP-1	23.03	23.03	MSP0001	Mudstone	0.8	0.3	0.14	3.3	5,530	1.79	0.2	0.7	93
4000928	OnZaP-1	23.84	23.84	MSP0010	Mudstone		0.6		4.3	3,337	0.66	0.3	0.4	58
4000403	OnZaP-1	24.31	24.31	MSP0001	Mudstone	0.2	0.3	0.44	3.6	2,530	1.02	0.2	0.5	63
4000406	OnZaP-1	25.03	25.03	MSP0001	Mudstone		0.2	1.20	1.0	590	0.28		0.3	32
4000412	OnZaP-1	26.09	26.09	MSP0001	Mudstone	1.4	0.1		2.4	2,860	0.87	0.1	0.4	152
4000413	OnZaP-1	26.80	26.80	MSP0001	Mudstone	0.2	0.2	0.10	3.1	2,630	0.90	0.1	0.5	116
4000414	OnZaP-1	27.77	27.77	MSP0001	Mudstone	0.1	0.4	0.82	2.8	1,390	0.54	0.2	0.9	75
4000929	OnZaP-1	27.95	27.95	MSP0010	Mudstone		1.0		13.3	5,161	0.77	0.4	1.1	127
4000421	OnZaP-1	28.36	28.36	MSP0001	Mudstone	0.1	0.3	1.17	1.8	690	0.19	0.2	0.3	32
4000930	OnZaP-1	28.80	28.80	MSP0010	Mudstone		1.4		19.8	5,183	1.06	0.6	6.9	220

Sample ID	Drill site	Core depth (m)	Comb. depth (m)	Sample set	Lithology	Ta (ppm)	Tb (ppm)	Te (ppm)	Th (ppm)	Ti (ppm)	Tl (ppm)	Tm (ppm)	U (ppm)	V (ppm)
4000429	OnZaP-1	29.28	29.28	MSP0001	Carbonate		0.1	1.12	0.4	210	0.08		0.7	13
4000931	OnZaP-1	30.66	30.66	MSP0010	Mudstone		1.3		15.1	7,083	1.07	0.6	4.5	181
4000436	OnZaP-1	30.79	30.79	MSP0001	Mudstone	0.1	0.2	0.17	2.4	1,820	0.79	0.2	1.9	187
4000442	OnZaP-1	31.21	31.21	MSP0001	Carbonate		0.2	1.47	0.1	140	0.12	0.1	0.6	13
4000932	OnZaP-1	31.85	31.85	MSP0010	Mudstone		1.3		13.3	5,546	0.92	0.6	4.9	255
4000447	OnZaP-1	31.86	31.86	MSP0001	Mudstone	0.2		0.10	1.9	1,680	1.07	0.1	2.9	289
4000933	OnZaP-1	32.19	32.19	MSP0010	Mudstone		1.2		10.7	5,763	0.99	0.7	4.7	340
4000455	OnZaP-1	33.15	33.15	MSP0001	Carbonate		0.2	1.37		200	0.06		0.6	13
4000466	OnZaP-1	33.96	33.96	MSP0001	Carbonate		0.2	1.88		300	0.15	0.2	0.5	12
4000471	OnZaP-1	34.64	34.64	MSP0001	Carbonate		0.2	1.16		440	0.11	0.1	0.4	28
4000478	OnZaP-1	35.61	35.61	MSP0001	Mudstone	0.3		2.38		110	0.16		0.5	8
4000934	OnZaP-1	36.40	36.40	MSP0010	Mudstone		2.6		21.3	6,311	1.61	1.1	16.0	587
4000483	OnZaP-1	36.52	36.52	MSP0001	Mudstone	1.6	0.7	0.11	3.4	2,330	2.35	0.5	20.8	603
4000484	OnZaP-1	36.94	36.94	MSP0001	Carbonate	0.2	0.2	1.92		170	0.60	0.1	1.8	31
4000935	OnZaP-1	37.83	37.83	MSP0010	Mudstone		2.6		16.1	4,133	2.16	1.1	16.2	520
4000491	OnZaP-1	38.13	38.13	MSP0001	Mudstone	2.0	0.6	0.58	4.2	1,170	2.77	0.4	9.9	338
4000936	OnZaP-1	38.91	38.91	MSP0010	Mudstone		2.9		22.1	4,755	3.46	1.2	17.8	1,016
4000492	OnZaP-1	38.97	38.97	MSP0001	Mudstone	0.9	0.6	0.46	2.9	1,760	3.13	0.5	11.8	857
4000493	OnZaP-1	39.88	39.88	MSP0001	Mudstone	0.2	0.5	1.39	3.8	1,350	2.88	0.4	17.8	579
4000937	OnZaP-1	40.02	40.02	MSP0010	Carbonate		1.3		10.4	4,719	2.47	0.8	25.0	686
4000938	OnZaP-1	41.09	41.09	MSP0010	Mudstone		1.1		7.8	7,579	1.96	0.7	17.8	1,422
4000494	OnZaP-1	41.15	41.15	MSP0001	Mudstone	0.2	0.5	0.77	3.6	1,620	2.68	0.4	22.2	1,557
4000939	OnZaP-1	41.38	41.38	MSP0010	Mudstone		1.5		11.1	10,172	2.49	1.0	16.7	1,329
4000500	OnZaP-1	42.04	42.04	MSP0001	Carbonate		0.2	1.63		120	0.19		4.2	41
4000940	OnZaP-1	42.42	42.42	MSP0010	Mudstone		1.3		12.2	10,680	3.02	0.7	19.9	926
4000504	OnZaP-1	42.45	42.45	MSP0001	Mudstone	0.2	0.4	0.66	4.5	1,620	5.15	0.3	17.3	1,251
4000941	OnZaP-1	42.86	42.86	MSP0010	Carbonate		0.8		4.1	5,546	5.45	0.5	39.7	628
4000942	OnZaP-1	43.69	43.69	MSP0010	Carbonate									
4000516	OnZaP-1	43.94	43.94	MSP0001	Carbonate			0.92					15.5	44
4000005	OnZaP-3	2.10	44.37	MSP0001	Carbonate			2.25		20			0.6	37
4000521	OnZaP-1	44.53	44.53	MSP0001	Carbonate			0.86		10	0.06		6.6	35
4000953	OnZaP-3	2.68	44.93	MSP0010	Carbonate		1.8		2.9	552	1.31	1.1	85.0	560
4000954	OnZaP-3	2.77	45.02	MSP0010	Mudstone		0.2		4.2	1,596	2.75	0.2	12.8	1,630
4000015	OnZaP-3	3.12	45.39	MSP0001	Carbonate			2.05					1.2	37
4000529	OnZaP-1	45.65	45.65	MSP0001	Carbonate			0.91			0.06		0.8	34
4000943	OnZaP-1	46.36	46.36	MSP0010	Mudstone		0.5		5.7	4,376	3.94	0.4	34.0	1,307
4000030	OnZaP-3	4.38	46.65	MSP0001	Carbonate		0.3	1.58					2.8	21
4000536	OnZaP-1	46.70	46.70	MSP0001	Mudstone			0.08		40	0.10		0.7	32
4000037	OnZaP-3	5.02	47.29	MSP0001	Carbonate		0.1	1.37		30	0.07		2.0	93
4000955	OnZaP-3	5.14	47.39	MSP0010	Mudstone		0.2		1.1	517	0.74	0.1	3.2	414
4000543	OnZaP-1	47.65	47.65	MSP0001	Carbonate			1.17					7.5	19
4000944	OnZaP-1	47.90	47.90	MSP0010	Carbonate		0.4		4.4	4,412	8.48	0.5	21.1	1,984
4000045	OnZaP-3	5.89	48.16	MSP0001	Carbonate			1.58		10			0.8	45
4000956	OnZaP-3	6.01	48.26	MSP0010	Carbonate		0.0		0.1	80		0.0	1.1	47
4000945	OnZaP-1	48.40	48.40	MSP0010	Carbonate		0.5		5.6	2,426	3.77	0.4	49.5	1,040

Sample ID	Drill site	Core depth (m)	Comb. depth (m)	Sample set	Lithology	Ta (ppm)	Tb (ppm)	Te (ppm)	Th (ppm)	Ti (ppm)	Tl (ppm)	Tm (ppm)	U (ppm)	V (ppm)
4000553	OnZaP-1	48.61	48.61	MSP0001	Mudstone					30	0.05		4.5	22
4000053	OnZaP-3	6.67	48.94	MSP0001	Mudstone					10			2.6	7
4000957	OnZaP-3	6.84	49.09	MSP0010	Mudstone									
4000561	OnZaP-1	49.29	49.29	MSP0001	Carbonate			1.73		40	0.15		4.1	127
4000061	OnZaP-3	7.28	49.55	MSP0001	Carbonate	0.2		1.15		10	0.08		1.7	75
4000958	OnZaP-3	8.00	50.25	MSP0010	Mudstone									
4000563	OnZaP-1	50.43	50.43	MSP0001	Mudstone					70	0.20		2.4	85
4000946	OnZaP-1	50.58	50.58	MSP0010	Carbonate		0.3		0.2	157		0.2	2.9	149
4000959	OnZaP-3	8.40	50.65	MSP0010	Mudstone		0.1		1.1	498	0.75	0.0	4.9	425
4000065	OnZaP-3	8.44	50.71	MSP0001	Mudstone		0.1	0.59	1.0	500	1.39		8.5	733
4000571	OnZaP-1	50.77	50.77	MSP0001	Carbonate			1.61		20			4.5	55
4000947	OnZaP-1	51.13	51.13	MSP0010	Carbonate		0.6		5.3	6,851	2.38	0.5	28.1	2,996
4000575	OnZaP-1	51.41	51.41	MSP0001	Mudstone	0.2	0.5	0.78	3.6	1,540	2.09	0.4	57.6	3,018
4000080	OnZaP-3	9.31	51.58	MSP0001	Carbonate	0.1		1.94		10			4.4	52
4000960	OnZaP-3	9.57	51.82	MSP0010	Carbonate		0.2		2.4	7,351	0.65	0.2	13.9	319
4000583	OnZaP-1	52.16	52.16	MSP0001	Carbonate			1.98		20			1.7	39
4000090	OnZaP-3	10.14	52.41	MSP0001	Carbonate			2.10		20	0.10		1.2	53
4000592	OnZaP-1	52.92	52.92	MSP0001	Carbonate			1.59		50	0.43		2.4	130
4000098	OnZaP-3	10.70	52.97	MSP0001	Carbonate	0.1		1.26		60	0.14		5.0	72
4000948	OnZaP-1	53.12	53.12	MSP0010	Mudstone		3.1		5.4	3,557	3.29	2.0	55.6	1,622
4000961	OnZaP-3	11.00	53.25	MSP0010	Carbonate		0.9		8.7	5,516	1.54	0.9	43.4	1,111
4000949	OnZaP-1	53.50	53.50	MSP0010	Mudstone		1.1		4.1	6,854	1.76	0.8	50.0	2,102
4000962	OnZaP-3	11.33	53.58	MSP0010	Carbonate		3.4		4.8	1,908	0.76	2.4	87.4	1,030
4000100	OnZaP-3	11.33	53.60	MSP0001	Mudstone		1.1	0.53	3.1	1,080	0.62	0.7	44.2	1,623
4000593	OnZaP-1	53.70	53.70	MSP0001	Mudstone	1.0	0.9	0.41	4.7	1,200	0.37	0.7	40.1	1,426
4000963	OnZaP-3	11.70	53.95	MSP0010	Mudstone		3.5		19.6	9,879	1.87	1.5	43.2	1,416
4000964	OnZaP-3	11.96	54.21	MSP0010	Mudstone					5,289				
4000102	OnZaP-3	12.16	54.43	MSP0001	Mudstone	0.5	0.7	0.51	3.4	1,540	0.44	0.5	46.1	2,309
4000965	OnZaP-3	12.67	54.92	MSP0010	Mudstone		2.0		9.7	6,380	1.25	1.6	48.5	1,316
4000594	OnZaP-1	55.14	55.14	MSP0001	Mudstone	0.2	0.6	0.35	2.5	790	0.25	0.5	41.4	1,178
4000966	OnZaP-3	13.11	55.36	MSP0010	Mudstone		1.5		5.3	4,512	1.34	1.0	41.9	1,278
4000597	OnZaP-1	55.51	55.51	MSP0001	Carbonate		0.2	1.52		70	0.57	0.2	5.4	133
4000103	OnZaP-3	13.29	55.56	MSP0001	Mudstone	0.6	0.9	0.48	3.3	1,210	0.44	0.6	52.5	1,422
4000601	OnZaP-1	55.68	55.68	MSP0001	Mudstone	0.3	0.6	0.41	3.2	910	2.36	0.5	42.6	1,422
4000950	OnZaP-1	55.80	55.80	MSP0010	Mudstone		1.8		7.8	6,866	3.10	1.2	49.2	1,462
4000967	OnZaP-3	13.82	56.07	MSP0010	Carbonate		1.5		5.3	4,578	1.38	0.9	39.6	1,259
4000602	OnZaP-1	56.17	56.17	MSP0001	Mudstone	0.2	0.5	0.46	3.2	670	3.57	0.3	36.9	1,089
4000968	OnZaP-3	14.25	56.50	MSP0010	Mudstone		2.2		9.6	2,918	2.25	1.1	24.2	812
4000108	OnZaP-3	14.31	56.58	MSP0001	Mudstone	1.8	1.3	1.19	6.4	1,260	2.36	0.8	18.8	603
4000605	OnZaP-1	56.89	56.89	MSP0001	Carbonate		0.2	2.21	0.2	70	0.44	0.2	3.7	70
4000969	OnZaP-3	14.69	56.94	MSP0010	Mudstone		1.6		8.2	4,767	1.38	0.9	39.1	1,230
4000113	OnZaP-3	14.85	57.12	MSP0001	Mudstone	0.4	0.5	0.33	2.3	970	0.31	0.4	36.8	1,189
4000614	OnZaP-1	57.64	57.64	MSP0001	Carbonate		0.2	2.37	0.4	500	0.54	0.1	1.5	64
4000951	OnZaP-1	57.93	57.93	MSP0010	Mudstone		1.7		9.7	9,865	2.81	1.1	24.4	1,058
4000970	OnZaP-3	15.72	57.97	MSP0010	Mudstone		1.2		4.2	2,732	1.42	0.7	39.9	952

Sample ID	Drill site	Core depth (m)	Comb. depth (m)	Sample set	Lithology	Ta (ppm)	Tb (ppm)	Te (ppm)	Th (ppm)	Ti (ppm)	Tl (ppm)	Tm (ppm)	U (ppm)	V (ppm)
4000114	OnZaP-3	15.70	57.97	MSP0001	Mudstone	0.2	0.7	0.44	2.9	870	0.96	0.5	43.7	1,284
4000618	OnZaP-1	58.41	58.41	MSP0001	Mudstone	0.5	0.7	0.12	6.7	1,280	1.32	0.6	33.2	959
4000971	OnZaP-3	16.42	58.67	MSP0010	Mudstone		1.3		5.6	5,041	2.65	0.7	24.5	904
4000972	OnZaP-3	16.72	58.97	MSP0010	Mudstone		0.8		6.1	2,743	0.64	0.6	24.5	943
4000115	OnZaP-3	16.92	59.19	MSP0001	Mudstone	0.1	0.6	0.38	2.0	1,500	3.05	0.4	44.7	1,534
4000952	OnZaP-1	59.25	59.25	MSP0010	Mudstone					3,915				
4000619	OnZaP-1	59.67	59.67	MSP0001	Mudstone	0.4	0.8	0.23	5.2	1,350	1.50	0.7	20.2	359
4000122	OnZaP-3	17.55	59.82	MSP0001	Mudstone	0.1	0.4	0.34	2.8	680	3.56	0.3	25.2	674
4000973	OnZaP-3	17.89	60.14	MSP0010	Mudstone		0.7		5.4	1,957	2.59	0.5	11.7	581
4000623	OnZaP-1	60.18	60.18	MSP0001	Mudstone	0.1	0.5	1.57	1.9	1,210	2.35	0.4	5.7	241
4000128	OnZaP-3	18.65	60.92	MSP0001	Carbonate		0.4	2.01	0.4	500	0.46	0.2	3.2	71
4000129	OnZaP-3	18.97	61.24	MSP0001	Mudstone	0.1	0.6	0.41	3.5	1,090	2.23	0.4	20.8	961
4000974	OnZaP-3	19.27	61.52	MSP0010	Mudstone		1.5		10.1	9,071	2.31	0.8	19.4	729
4000975	OnZaP-3	20.07	62.32	MSP0010	Mudstone		2.0		11.3	8,861	1.51	1.2	24.4	518
4000130	OnZaP-3	20.13	62.40	MSP0001	Mudstone		0.6	0.33	2.8	960	1.14	0.4	9.0	347
4000132	OnZaP-3	20.90	63.17	MSP0001	Mudstone	0.4	0.7	0.13	5.1	950	0.70	0.5	19.8	707
4000976	OnZaP-3	21.12	63.37	MSP0010	Mudstone		1.7		11.7	2,934	0.76	1.0	20.8	726
4000133	OnZaP-3	21.96	64.23	MSP0001	Mudstone	0.3	0.8	0.17	5.9	1,200	1.03	0.5	17.1	723
4000977	OnZaP-3	22.36	64.61	MSP0010	Mudstone		1.9		11.7	8,068	1.04	0.9	23.2	385
4000978	OnZaP-3	22.96	65.21	MSP0010	Mudstone		3.3		21.3	11,552	1.82	1.6	14.9	1,280
4000134	OnZaP-3	23.12	65.39	MSP0001	Mudstone	0.5	0.6	0.14	5.3	1,840	1.78	0.3	14.2	1,194
4000979	OnZaP-3	23.59	65.84	MSP0010	Mudstone					6,338				
4000135	OnZaP-3	24.26	66.53	MSP0001	Carbonate	0.2	0.3	2.19	0.3	320	0.59	0.1	1.2	79
4000980	OnZaP-3	24.91	67.16	MSP0010	Mudstone		1.3		10.1	11,562	4.18	0.4	9.7	599
4000151	OnZaP-3	25.18	67.45	MSP0001	Carbonate	0.4	0.3	1.41	0.2	290	0.38	0.1	1.4	40
4000981	OnZaP-3	25.59	67.84	MSP0010	Mudstone		0.4		1.8	18,158	0.61	0.2	2.2	109
4000159	OnZaP-3	25.76	68.03	MSP0001	Mudstone	0.4	0.5	0.52	3.8	3,990	3.10	0.2	7.0	559
4000982	OnZaP-3	26.20	68.45	MSP0010	Mudstone		1.1		8.7	10,805	3.97	0.5	11.6	456
4000168	OnZaP-3	26.56	68.83	MSP0001	Mudstone	0.2	1.6	0.54	4.7	2,470	3.28	0.5	39.6	332
4000178	OnZaP-3	27.32	69.59	MSP0001	Carbonate		0.2	1.68	0.4	750	0.72	0.1	3.0	56
4000983	OnZaP-3	27.51	69.76	MSP0010	Carbonate		0.5		2.7	2,067	2.38	0.3	4.7	412
4000179	OnZaP-3	28.13	70.40	MSP0001	Mudstone		0.2	0.09	0.9	390	0.29	0.2	10.9	249
4000984	OnZaP-3	28.69	70.94	MSP0010	Mudstone		0.4		1.1	652		0.2	4.8	473
4000180	OnZaP-3	29.20	71.47	MSP0001	Mudstone	0.1	0.8	0.18	2.1	1,050	0.74	0.4	27.2	1,052
4000985	OnZaP-3	29.35	71.60	MSP0010	Mudstone		1.1		2.8	1,264	0.49	0.6	17.5	1,061
4000181	OnZaP-3	30.59	72.86	MSP0001	Mudstone		2.7	1.22	1.0	760	1.62	1.0	81.3	764
4000986	OnZaP-3	30.68	72.93	MSP0010	Mudstone		1.2		8.2	3,866	1.52	1.0	29.1	1,075
4000987	OnZaP-3	31.40	73.65	MSP0010	Mudstone		1.2		5.3	2,563	0.71	0.6	22.7	825
4000187	OnZaP-3	31.63	73.90	MSP0001	Mudstone		0.6	0.18	2.6	680	0.62	0.3	22.4	703
4000988	OnZaP-3	32.10	74.35	MSP0010	Mudstone		1.9		5.4	1,806	3.50	1.0	50.5	394
4000190	OnZaP-3	32.36	74.63	MSP0001	Carbonate		0.5	1.39	0.2	130	0.47	0.3	7.4	424
4000201	OnZaP-3	33.24	75.51	MSP0001	Mudstone	0.2	0.4	1.02	1.2	760	1.90	0.2	10.8	956
4000989	OnZaP-3	33.48	75.73	MSP0010	Mudstone		1.7		6.3	2,300	1.73	0.8	36.7	1,079
4000990	OnZaP-3	33.81	76.06	MSP0010	Mudstone					457				
4000202	OnZaP-3	34.29	76.56	MSP0001	Mudstone		0.5	0.20	4.2	880	0.49	0.2	9.0	262

Sample ID	Drill site	Core depth (m)	Comb. depth (m)	Sample set	Lithology	Ta (ppm)	Tb (ppm)	Te (ppm)	Th (ppm)	Ti (ppm)	Tl (ppm)	Tm (ppm)	U (ppm)	V (ppm)
4000203	OnZaP-3	34.96	77.23	MSP0001	Mudstone	0.1	0.2	0.09	3.7	1,070	0.63	0.1	1.9	124
4000214	OnZaP-3	36.54	78.81	MSP0001	Carbonate		0.6	1.95	1.9	550	0.83	0.2	0.6	22
4000216	OnZaP-3	37.30	79.57	MSP0001	Carbonate		0.3	1.77	1.1	370	0.95	0.1	0.4	16
4000225	OnZaP-3	38.42	80.69	MSP0001	Mudstone		0.3	1.50	2.0	610	1.05	0.1	0.5	22
4000231	OnZaP-3	39.25	81.52	MSP0001	Mudstone	0.2	0.3	1.56	3.5	970	1.46	0.2	0.7	28
4000239	OnZaP-3	40.20	82.47	MSP0001	Mudstone	0.2	0.3	0.62	4.6	1,460	3.16	0.1	1.6	62
4000244	OnZaP-3	41.09	83.36	MSP0001	Mudstone		0.4	1.53	2.8	800	1.79	0.2	0.6	25
4000251	OnZaP-3	42.32	84.59	MSP0001	Carbonate	0.1	0.3	1.56	1.0	430	1.81	0.2	0.9	16
4000256	OnZaP-3	43.12	85.39	MSP0001	Carbonate		0.3	1.78	0.3	130	0.26	0.1	1.9	11
4000264	OnZaP-3	44.02	86.29	MSP0001	Mudstone	0.1	0.2	0.42	4.4	1,300	1.79	0.1	2.2	74
4000265	OnZaP-3	44.82	87.09	MSP0001	Mudstone	0.8	0.2	0.37	4.2	990	0.75		2.2	75
4000266	OnZaP-3	45.87	88.14	MSP0001	Mudstone	0.1	0.3	0.27	5.5	1,040	0.70	0.2	5.4	219
4000991	OnZaP-3	46.11	88.36	MSP0010	Mudstone		0.8		9.9	2,377	0.86	0.4	6.7	307
4000992	OnZaP-3	46.51	88.76	MSP0010	Mudstone		1.0		12.2	2,587	0.90	0.6	9.9	430
4000267	OnZaP-3	46.59	88.86	MSP0001	Mudstone	0.2	0.4	0.26	5.6	1,140	0.80	0.2	7.8	380
4000993	OnZaP-3	47.86	90.11	MSP0010	Mudstone		0.8		8.4	1,938	0.92	0.5	7.0	228
4000268	OnZaP-3	48.02	90.29	MSP0001	Mudstone	0.2	0.4	0.29	4.7	1,310	0.61	0.2	5.7	353
4000994	OnZaP-3	48.94	91.19	MSP0010	Mudstone		0.8		9.3	2,066	0.87	0.4	6.6	372
4000269	OnZaP-3	49.00	91.27	MSP0001	Mudstone	0.1	0.3	0.22	3.9	870	0.44	0.2	4.5	179
4000270	OnZaP-3	49.68	91.95	MSP0001	Mudstone		0.3	0.44	3.8	710	0.70	0.2	2.7	119
4000271	OnZaP-3	50.28	92.55	MSP0001	Mudstone	0.1	0.3	0.21	4.2	1,020	0.66	0.2	3.7	162
4000273	OnZaP-3	50.99	93.26	MSP0001	Mudstone		0.2	0.30	3.6	1,000	0.86	0.1	1.5	75
4001000	OnZaP-1	51.57	93.82	MSP0010	Carbonate		0.5		0.1	149		0.4	9.0	145
4000279	OnZaP-3	52.53	94.80	MSP0001	Mudstone	0.1	0.2	0.42	2.3	1,440	0.91	0.1	2.1	343
4000280	OnZaP-3	53.02	95.29	MSP0001	Mudstone	0.2	0.3	0.14	3.0	1,430	0.69	0.2	3.5	280
4000995	OnZaP-3	53.75	96.00	MSP0010	Mudstone		0.7		10.3	2,969	0.96	0.3	8.3	373
4000281	OnZaP-3	54.02	96.29	MSP0001	Mudstone	0.2	0.3	0.30	4.7	1,380	1.11	0.2	7.6	323
4000288	OnZaP-3	55.01	97.28	MSP0001	Mudstone	0.1	0.3	1.29	0.5	300	0.85	0.1	0.8	146
4000289	OnZaP-3	55.60	97.87	MSP0001	Mudstone	0.2	0.4	0.27	5.3	1,360	0.88	0.2	8.6	490
4000996	OnZaP-3	55.76	98.01	MSP0010	Mudstone		0.8		9.9	2,974	0.88	0.4	7.6	610
4000290	OnZaP-3	56.52	98.79	MSP0001	Mudstone		0.3	0.14	2.6	970	0.51	0.1	2.9	385
4000997	OnZaP-3	57.27	99.52	MSP0010	Mudstone		0.7		6.5	2,145	0.72	0.4	6.3	421
4000998	OnZaP-3	58.06	100.31	MSP0010	Mudstone		1.3		12.7	3,500	0.97	0.7	12.1	843
4000291	OnZaP-3	58.24	100.51	MSP0001	Mudstone	0.2	0.5	0.32	6.0	1,640	0.85	0.4	12.7	918
4000299	OnZaP-3	58.87	101.14	MSP0001	Carbonate		0.4	2.22	0.5	170	0.27	0.2	1.0	69
4000999	OnZaP-3	59.88	102.13	MSP0010	Mudstone		1.7		12.6	3,895	1.09	0.9	13.3	854
4000306	OnZaP-3	59.95	102.22	MSP0001	Mudstone	0.2	0.5	0.55	3.7	1,480	1.05	0.3	8.0	1,010

Table A1g: Element concentration data for drill cores OnZaP-1 and OnZaP-3, continued.

Sample ID	Drill site	Core depth (m)	Comb. depth (m)	Sample set	Lithology	W (ppm)	Y (ppm)	Yb (ppm)	Zn (ppm)	Zr (ppm)
4000319	OnZaP-1	1.96	1.96	MSP0001	Mudstone	1.3	5.1	0.8	77.7	132.3
4000921	OnZaP-1	2.08	2.08	MSP0010	Mudstone	1.9	28.9	3.2	96.2	180.9
4000320	OnZaP-1	2.85	2.85	MSP0001	Mudstone	1.5	6.7	0.9	101.7	116.4
4000321	OnZaP-1	3.92	3.92	MSP0001	Mudstone	2.2	4.1	0.7	117.7	115.1
4000922	OnZaP-1	5.28	5.28	MSP0010	Mudstone		11.4	1.1	54.4	69.4
4000322	OnZaP-1	5.31	5.31	MSP0001	Mudstone	1.1	4.3	0.8	72.7	125.6
4000323	OnZaP-1	6.50	6.50	MSP0001	Mudstone	2.1	3.5	0.7	145.6	114.4
4000923	OnZaP-1	6.60	6.60	MSP0010	Mudstone					
4000324	OnZaP-1	7.01	7.01	MSP0001	Mudstone	19.6	6.1	0.8	108.7	117.0
4000332	OnZaP-1	7.96	7.96	MSP0001	Mudstone	1.4	10.0	0.9	43.6	43.9
4000336	OnZaP-1	8.35	8.35	MSP0001	Mudstone	1.5	7.2	0.9	33.8	108.8
4000342	OnZaP-1	8.74	8.74	MSP0001	Mudstone	0.9	10.6	1.0	22.6	43.5
4000345	OnZaP-1	9.58	9.58	MSP0001	Mudstone	1.3	10.6	1.2	32.0	109.4
4000346	OnZaP-1	10.79	10.79	MSP0001	Mudstone	2.5	3.2	0.6	33.7	105.8
4000924	OnZaP-1	11.13	11.13	MSP0010	Mudstone	2.3	23.5	2.7	31.5	113.3
4000347	OnZaP-1	11.86	11.86	MSP0001	Mudstone	1.1	7.6	1.6	28.5	161.5
4000925	OnZaP-1	12.15	12.15	MSP0010	Mudstone	2.6	31.5	3.7	26.0	138.0
4000348	OnZaP-1	12.39	12.39	MSP0001	Mudstone	1.2	6.2	1.0	27.0	121.3
4000349	OnZaP-1	13.16	13.16	MSP0001	Mudstone	0.5	8.2	0.6	746.6	14.7
4000351	OnZaP-1	13.40	13.40	MSP0001	Mudstone	1.0	7.1	0.5	24.5	27.8
4000358	OnZaP-1	14.65	14.65	MSP0001	Mudstone	1.0	4.0	0.8	70.5	132.5
4000362	OnZaP-1	15.26	15.26	MSP0001	Mudstone	1.3	10.6	1.2	37.9	68.1
4000368	OnZaP-1	16.29	16.29	MSP0001	Mudstone	0.4	6.9	0.5	70.9	10.8
4000376	OnZaP-1	17.36	17.36	MSP0001	Mudstone	0.5	5.9	0.6	30.7	18.1
4000383	OnZaP-1	17.90	17.90	MSP0001	Mudstone	0.4	18.9	0.6	51.6	146.7
4000926	OnZaP-1	18.85	18.85	MSP0010	Mudstone		22.3	2.5	127.4	128.9
4000392	OnZaP-1	19.08	19.08	MSP0001	Mudstone	2.4	13.7	0.9	57.5	285.1
4000393	OnZaP-1	19.99	19.99	MSP0001	Mudstone	1.7	7.1	0.8	63.7	181.1
4000394	OnZaP-1	20.66	20.66	MSP0001	Mudstone	2.7	6.1	1.0	21.8	133.0
4000927	OnZaP-1	21.91	21.91	MSP0010	Mudstone		22.7	2.4	39.6	137.2
4000395	OnZaP-1	21.94	21.94	MSP0001	Mudstone	1.2	6.5	0.8	30.3	112.8
4000396	OnZaP-1	22.33	22.33	MSP0001	Mudstone	0.5	6.0	0.7	46.0	117.9
4000398	OnZaP-1	23.03	23.03	MSP0001	Mudstone	0.8	10.4	1.1	46.5	117.0
4000928	OnZaP-1	23.84	23.84	MSP0010	Mudstone		18.0	1.7	26.0	66.5
4000403	OnZaP-1	24.31	24.31	MSP0001	Mudstone	1.5	10.1	1.0	33.4	81.2
4000406	OnZaP-1	25.03	25.03	MSP0001	Mudstone	0.6	9.3	0.8	27.2	21.2
4000412	OnZaP-1	26.09	26.09	MSP0001	Mudstone	9.1	4.2	0.7	27.3	146.3
4000413	OnZaP-1	26.80	26.80	MSP0001	Mudstone	1.7	7.2	1.0	20.8	144.3
4000414	OnZaP-1	27.77	27.77	MSP0001	Mudstone	1.0	12.6	1.3	42.9	85.5
4000929	OnZaP-1	27.95	27.95	MSP0010	Mudstone	3.8	27.2	2.9	34.9	191.3
4000421	OnZaP-1	28.36	28.36	MSP0001	Mudstone	0.6	12.3	0.9	19.5	49.1
4000930	OnZaP-1	28.80	28.80	MSP0010	Mudstone	4.3	40.4	4.3	42.6	331.3

Sample ID	Drill site	Core depth (m)	Comb. depth (m)	Sample set	Lithology	W (ppm)	Y (ppm)	Yb (ppm)	Zn (ppm)	Zr (ppm)
4000429	OnZaP-1	29.28	29.28	MSP0001	Carbonate	0.5	7.0	0.5	11.9	15.8
4000931	OnZaP-1	30.66	30.66	MSP0010	Mudstone	6.3	35.3	4.2	113.0	217.2
4000436	OnZaP-1	30.79	30.79	MSP0001	Mudstone	2.1	6.4	1.1	80.0	124.8
4000442	OnZaP-1	31.21	31.21	MSP0001	Carbonate	0.4	9.9	0.8	12.5	11.0
4000932	OnZaP-1	31.85	31.85	MSP0010	Mudstone	7.4	43.0	4.2	101.1	196.8
4000447	OnZaP-1	31.86	31.86	MSP0001	Mudstone	1.3	5.5	1.0	82.6	128.6
4000933	OnZaP-1	32.19	32.19	MSP0010	Mudstone	5.8	45.7	4.5	110.2	189.9
4000455	OnZaP-1	33.15	33.15	MSP0001	Carbonate	0.6	5.6	0.5	9.3	5.8
4000466	OnZaP-1	33.96	33.96	MSP0001	Carbonate	0.6	13.3	1.4	17.5	5.0
4000471	OnZaP-1	34.64	34.64	MSP0001	Carbonate	0.6	7.7	0.6	10.9	9.6
4000478	OnZaP-1	35.61	35.61	MSP0001	Mudstone	14.8	5.9	0.6	12.2	4.7
4000934	OnZaP-1	36.40	36.40	MSP0010	Mudstone	9.4	72.9	7.0	247.3	372.9
4000483	OnZaP-1	36.52	36.52	MSP0001	Mudstone	3.9	14.3	2.6	162.0	344.0
4000484	OnZaP-1	36.94	36.94	MSP0001	Carbonate	0.7	6.8	0.6	22.6	12.0
4000935	OnZaP-1	37.83	37.83	MSP0010	Mudstone	6.1	78.7	7.0	117.3	462.8
4000491	OnZaP-1	38.13	38.13	MSP0001	Mudstone	2.0	15.0	3.1	200.0	476.5
4000936	OnZaP-1	38.91	38.91	MSP0010	Mudstone	14.2	79.6	7.7	337.1	413.6
4000492	OnZaP-1	38.97	38.97	MSP0001	Mudstone	6.1	23.7	3.3	263.0	404.3
4000493	OnZaP-1	39.88	39.88	MSP0001	Mudstone	36.2	25.4	2.5	270.9	139.9
4000937	OnZaP-1	40.02	40.02	MSP0010	Carbonate	11.3	52.0	5.2	325.4	189.7
4000938	OnZaP-1	41.09	41.09	MSP0010	Mudstone	11.5	44.9	5.2	219.0	143.3
4000494	OnZaP-1	41.15	41.15	MSP0001	Mudstone	5.5	19.5	2.6	437.4	124.4
4000939	OnZaP-1	41.38	41.38	MSP0010	Mudstone	15.9	63.2	6.5	263.6	205.5
4000500	OnZaP-1	42.04	42.04	MSP0001	Carbonate	0.6	8.1	0.5	13.6	2.7
4000940	OnZaP-1	42.42	42.42	MSP0010	Mudstone	17.4	57.6	4.8	193.3	226.7
4000504	OnZaP-1	42.45	42.45	MSP0001	Mudstone	5.1	19.9	1.6	209.2	101.0
4000941	OnZaP-1	42.86	42.86	MSP0010	Carbonate	13.3	34.2	3.2	312.1	62.5
4000942	OnZaP-1	43.69	43.69	MSP0010	Carbonate					
4000516	OnZaP-1	43.94	43.94	MSP0001	Carbonate	1.2			10.5	
4000005	OnZaP-3	2.10	44.37	MSP0001	Carbonate	0.5			14.1	
4000521	OnZaP-1	44.53	44.53	MSP0001	Carbonate	0.7			6.4	
4000953	OnZaP-3	2.68	44.93	MSP0010	Carbonate	10.3	103.9	6.2	168.2	23.7
4000954	OnZaP-3	2.77	45.02	MSP0010	Mudstone	29.8	12.2	1.4	131.7	57.1
4000015	OnZaP-3	3.12	45.39	MSP0001	Carbonate	0.3			15.2	
4000529	OnZaP-1	45.65	45.65	MSP0001	Carbonate	1.1	0.1		6.9	
4000943	OnZaP-1	46.36	46.36	MSP0010	Mudstone	45.7		3.0	765.8	101.9
4000030	OnZaP-3	4.38	46.65	MSP0001	Carbonate	0.2			15.5	
4000536	OnZaP-1	46.70	46.70	MSP0001	Mudstone	6.5	0.2		31.0	2.0
4000037	OnZaP-3	5.02	47.29	MSP0001	Carbonate	15.5			37.8	
4000955	OnZaP-3	5.14	47.39	MSP0010	Mudstone	3.3	8.6	0.7	58.8	9.2
4000543	OnZaP-1	47.65	47.65	MSP0001	Carbonate	0.5			10.7	
4000944	OnZaP-1	47.90	47.90	MSP0010	Carbonate	27.1	22.4	3.0	177.4	94.6
4000045	OnZaP-3	5.89	48.16	MSP0001	Carbonate	20.0			5.5	
4000956	OnZaP-3	6.01	48.26	MSP0010	Carbonate		2.4	0.2	16.6	1.4
4000945	OnZaP-1	48.40	48.40	MSP0010	Carbonate	38.0	23.7	2.6	502.7	73.7

Sample ID	Drill site	Core depth (m)	Comb. depth (m)	Sample set	Lithology	W (ppm)	Y (ppm)	Yb (ppm)	Zn (ppm)	Zr (ppm)
4000553	OnZaP-1	48.61	48.61	MSP0001	Mudstone	7.2	0.7	0.1	40.3	8.0
4000053	OnZaP-3	6.67	48.94	MSP0001	Mudstone	0.3	0.4		6.3	2.9
4000957	OnZaP-3	6.84	49.09	MSP0010	Mudstone					
4000561	OnZaP-1	49.29	49.29	MSP0001	Carbonate	1.2	7.1	0.7	25.6	1.0
4000061	OnZaP-3	7.28	49.55	MSP0001	Carbonate	61.8			29.2	
4000958	OnZaP-3	8.00	50.25	MSP0010	Mudstone					
4000563	OnZaP-1	50.43	50.43	MSP0001	Mudstone	5.5	0.7		5.9	2.7
4000946	OnZaP-1	50.58	50.58	MSP0010	Carbonate		15.3	1.3	122.9	2.9
4000959	OnZaP-3	8.40	50.65	MSP0010	Mudstone	6.5	3.4	0.3	189.4	12.1
4000065	OnZaP-3	8.44	50.71	MSP0001	Mudstone	4.9	4.5	0.3	642.2	12.8
4000571	OnZaP-1	50.77	50.77	MSP0001	Carbonate	0.3			22.6	
4000947	OnZaP-1	51.13	51.13	MSP0010	Carbonate	30.6	33.7	3.4	667.5	88.3
4000575	OnZaP-1	51.41	51.41	MSP0001	Mudstone	19.9	30.2	2.8	1,916.6	168.9
4000080	OnZaP-3	9.31	51.58	MSP0001	Carbonate	49.6	0.1		38.6	
4000960	OnZaP-3	9.57	51.82	MSP0010	Carbonate	13.1	10.9	1.5	8.9	31.7
4000583	OnZaP-1	52.16	52.16	MSP0001	Carbonate	0.4			119.6	
4000090	OnZaP-3	10.14	52.41	MSP0001	Carbonate	0.2			45.0	
4000592	OnZaP-1	52.92	52.92	MSP0001	Carbonate	0.7	6.8	0.7	127.2	1.8
4000098	OnZaP-3	10.70	52.97	MSP0001	Carbonate	81.0	6.8	0.6	24.3	2.0
4000948	OnZaP-1	53.12	53.12	MSP0010	Mudstone	22.5	206.8	10.9	385.8	90.2
4000961	OnZaP-3	11.00	53.25	MSP0010	Carbonate	23.8	50.1	5.8	112.0	164.7
4000949	OnZaP-1	53.50	53.50	MSP0010	Mudstone	30.1	53.0	4.8	448.3	89.0
4000962	OnZaP-3	11.33	53.58	MSP0010	Carbonate	14.7	235.3	14.1	162.1	88.6
4000100	OnZaP-3	11.33	53.60	MSP0001	Mudstone	10.7	63.7	4.6	1,115.2	43.4
4000593	OnZaP-1	53.70	53.70	MSP0001	Mudstone	8.8	43.2	4.6	216.1	156.6
4000963	OnZaP-3	11.70	53.95	MSP0010	Mudstone	13.0	114.9	9.2	158.3	495.5
4000964	OnZaP-3	11.96	54.21	MSP0010	Mudstone					
4000102	OnZaP-3	12.16	54.43	MSP0001	Mudstone	10.9	31.9	3.3	814.6	82.4
4000965	OnZaP-3	12.67	54.92	MSP0010	Mudstone	19.0	97.6	11.3	110.2	299.0
4000594	OnZaP-1	55.14	55.14	MSP0001	Mudstone	6.0	33.3	2.9	237.8	62.0
4000966	OnZaP-3	13.11	55.36	MSP0010	Mudstone	16.6	73.7	6.1	74.7	109.4
4000597	OnZaP-1	55.51	55.51	MSP0001	Carbonate	2.1	17.4	1.6	34.0	2.7
4000103	OnZaP-3	13.29	55.56	MSP0001	Mudstone	8.2	41.0	3.6	425.1	87.6
4000601	OnZaP-1	55.68	55.68	MSP0001	Mudstone	8.0	30.3	3.5	577.4	86.0
4000950	OnZaP-1	55.80	55.80	MSP0010	Mudstone	18.8	70.3	7.8	269.0	153.6
4000967	OnZaP-3	13.82	56.07	MSP0010	Carbonate	18.9	70.5	5.8	165.1	91.9
4000602	OnZaP-1	56.17	56.17	MSP0001	Mudstone	6.9	20.9	2.4	642.4	69.4
4000968	OnZaP-3	14.25	56.50	MSP0010	Mudstone	13.2	79.3	7.1	177.1	196.2
4000108	OnZaP-3	14.31	56.58	MSP0001	Mudstone	3.6	47.6	5.3	105.4	194.0
4000605	OnZaP-1	56.89	56.89	MSP0001	Carbonate	1.0	15.9	1.4	38.3	4.9
4000969	OnZaP-3	14.69	56.94	MSP0010	Mudstone	14.6	66.8	5.2	99.8	131.7
4000113	OnZaP-3	14.85	57.12	MSP0001	Mudstone		25.0	2.2	438.0	61.7
4000614	OnZaP-1	57.64	57.64	MSP0001	Carbonate	2.0	9.9	0.9	12.4	18.1
4000951	OnZaP-1	57.93	57.93	MSP0010	Mudstone	17.1	69.1	7.1	434.7	249.6
4000970	OnZaP-3	15.72	57.97	MSP0010	Mudstone	13.5	50.5	4.1	107.7	65.3

Sample ID	Drill site	Core depth (m)	Comb. depth (m)	Sample set	Lithology	W (ppm)	Y (ppm)	Yb (ppm)	Zn (ppm)	Zr (ppm)
4000114	OnZaP-3	15.70	57.97	MSP0001	Mudstone	6.6	29.6	2.7	153.3	78.8
4000618	OnZaP-1	58.41	58.41	MSP0001	Mudstone	4.1	27.8	3.7	265.6	171.6
4000971	OnZaP-3	16.42	58.67	MSP0010	Mudstone	16.4	39.7	4.8	269.9	138.0
4000972	OnZaP-3	16.72	58.97	MSP0010	Mudstone	11.7	34.4	3.9	124.6	86.3
4000115	OnZaP-3	16.92	59.19	MSP0001	Mudstone	6.7	22.5	2.4	390.3	107.0
4000952	OnZaP-1	59.25	59.25	MSP0010	Mudstone					
4000619	OnZaP-1	59.67	59.67	MSP0001	Mudstone	2.9	39.1	4.7	121.5	225.7
4000122	OnZaP-3	17.55	59.82	MSP0001	Mudstone	6.5	14.3	1.6	221.0	57.5
4000973	OnZaP-3	17.89	60.14	MSP0010	Mudstone	8.1	43.2	3.3	153.8	105.4
4000623	OnZaP-1	60.18	60.18	MSP0001	Mudstone	1.4	25.8	2.5	65.6	104.3
4000128	OnZaP-3	18.65	60.92	MSP0001	Carbonate	3.3	13.1	1.3	14.4	18.9
4000129	OnZaP-3	18.97	61.24	MSP0001	Mudstone	7.0	18.0	2.5	419.9	154.3
4000974	OnZaP-3	19.27	61.52	MSP0010	Mudstone	13.6	54.9	5.2	177.8	184.4
4000975	OnZaP-3	20.07	62.32	MSP0010	Mudstone	14.0	73.5	7.6	186.3	219.0
4000130	OnZaP-3	20.13	62.40	MSP0001	Mudstone	1.6	22.7	2.6	107.5	101.0
4000132	OnZaP-3	20.90	63.17	MSP0001	Mudstone	3.5	24.4	2.9	119.5	136.2
4000976	OnZaP-3	21.12	63.37	MSP0010	Mudstone	8.6	67.0	6.5	126.6	229.4
4000133	OnZaP-3	21.96	64.23	MSP0001	Mudstone	2.1	26.7	3.2	107.4	182.5
4000977	OnZaP-3	22.36	64.61	MSP0010	Mudstone	9.8	61.1	5.7	94.1	204.6
4000978	OnZaP-3	22.96	65.21	MSP0010	Mudstone	12.6	124.2	10.5	156.1	513.0
4000134	OnZaP-3	23.12	65.39	MSP0001	Mudstone	3.2	12.3	2.0	105.5	209.1
4000979	OnZaP-3	23.59	65.84	MSP0010	Mudstone					
4000135	OnZaP-3	24.26	66.53	MSP0001	Carbonate	41.8	10.7	0.7	19.7	12.5
4000980	OnZaP-3	24.91	67.16	MSP0010	Mudstone	11.6	27.6	2.6	205.5	242.5
4000151	OnZaP-3	25.18	67.45	MSP0001	Carbonate	63.0	8.7	0.7	15.2	10.8
4000981	OnZaP-3	25.59	67.84	MSP0010	Mudstone	3.7	11.5	1.1	45.7	69.7
4000159	OnZaP-3	25.76	68.03	MSP0001	Mudstone	3.9	15.6	1.5	198.2	198.9
4000982	OnZaP-3	26.20	68.45	MSP0010	Mudstone	12.1	33.3	3.3	258.7	202.9
4000168	OnZaP-3	26.56	68.83	MSP0001	Mudstone	1.1	39.7	3.1	86.5	210.2
4000178	OnZaP-3	27.32	69.59	MSP0001	Carbonate	1.2	8.9	0.8	31.1	19.5
4000983	OnZaP-3	27.51	69.76	MSP0010	Carbonate	2.7	21.1	2.1	141.9	73.4
4000179	OnZaP-3	28.13	70.40	MSP0001	Mudstone	2.5	11.1	1.0	398.4	32.8
4000984	OnZaP-3	28.69	70.94	MSP0010	Mudstone	3.3	17.5	1.6	62.9	35.1
4000180	OnZaP-3	29.20	71.47	MSP0001	Mudstone	5.6	29.6	2.8	364.6	46.4
4000985	OnZaP-3	29.35	71.60	MSP0010	Mudstone	9.7	41.7	3.5	506.8	39.0
4000181	OnZaP-3	30.59	72.86	MSP0001	Mudstone	2.8	106.6	6.0	105.0	15.6
4000986	OnZaP-3	30.68	72.93	MSP0010	Mudstone	23.9	65.5	6.7	616.1	87.3
4000987	OnZaP-3	31.40	73.65	MSP0010	Mudstone	11.2	43.8	3.7	115.5	56.2
4000187	OnZaP-3	31.63	73.90	MSP0001	Mudstone	4.2	20.5	1.9	277.9	45.2
4000988	OnZaP-3	32.10	74.35	MSP0010	Mudstone	20.1	78.1	6.5	257.6	55.9
4000190	OnZaP-3	32.36	74.63	MSP0001	Carbonate	0.6	30.7	2.1	40.4	3.3
4000201	OnZaP-3	33.24	75.51	MSP0001	Mudstone	95.5	15.8	1.5	151.4	20.2
4000989	OnZaP-3	33.48	75.73	MSP0010	Mudstone	18.7	58.5	4.9	393.2	54.6
4000990	OnZaP-3	33.81	76.06	MSP0010	Mudstone					
4000202	OnZaP-3	34.29	76.56	MSP0001	Mudstone	1.0	17.6	1.8	41.6	75.2

Sample ID	Drill site	Core depth (m)	Comb. depth (m)	Sample set	Lithology	W (ppm)	Y (ppm)	Yb (ppm)	Zn (ppm)	Zr (ppm)
4000203	OnZaP-3	34.96	77.23	MSP0001	Mudstone	0.8	7.2	0.7	49.3	42.7
4000214	OnZaP-3	36.54	78.81	MSP0001	Carbonate	0.3	11.9	1.2	129.6	24.9
4000216	OnZaP-3	37.30	79.57	MSP0001	Carbonate	0.3	10.5	0.8	57.2	15.1
4000225	OnZaP-3	38.42	80.69	MSP0001	Mudstone	0.2	13.7	1.1	26.3	24.1
4000231	OnZaP-3	39.25	81.52	MSP0001	Mudstone	16.9	10.5	1.0	30.3	47.3
4000239	OnZaP-3	40.20	82.47	MSP0001	Mudstone	55.9	8.8	1.0	30.2	75.7
4000244	OnZaP-3	41.09	83.36	MSP0001	Mudstone	0.2	12.4	1.1	20.6	34.4
4000251	OnZaP-3	42.32	84.59	MSP0001	Carbonate	31.4	10.3	0.9	41.3	18.2
4000256	OnZaP-3	43.12	85.39	MSP0001	Carbonate		10.5	0.7	25.9	4.4
4000264	OnZaP-3	44.02	86.29	MSP0001	Mudstone	0.7	7.5	0.8	80.5	53.1
4000265	OnZaP-3	44.82	87.09	MSP0001	Mudstone	160.7	6.2	0.8	46.3	48.8
4000266	OnZaP-3	45.87	88.14	MSP0001	Mudstone	1.1	11.5	1.3	185.2	51.5
4000991	OnZaP-3	46.11	88.36	MSP0010	Mudstone	5.2	27.4	3.0	311.0	73.5
4000992	OnZaP-3	46.51	88.76	MSP0010	Mudstone	7.5	34.7	3.8	962.9	87.6
4000267	OnZaP-3	46.59	88.86	MSP0001	Mudstone	2.0	13.9	1.7	464.6	54.0
4000993	OnZaP-3	47.86	90.11	MSP0010	Mudstone	7.2	28.6	3.1	1,880.8	61.9
4000268	OnZaP-3	48.02	90.29	MSP0001	Mudstone	1.1	13.7	1.5	388.9	65.1
4000994	OnZaP-3	48.94	91.19	MSP0010	Mudstone	5.7	27.0	3.0	631.3	68.9
4000269	OnZaP-3	49.00	91.27	MSP0001	Mudstone	0.6	11.5	1.2	127.2	53.6
4000270	OnZaP-3	49.68	91.95	MSP0001	Mudstone	0.9	9.0	0.9	211.8	62.0
4000271	OnZaP-3	50.28	92.55	MSP0001	Mudstone	0.7	8.6	1.0	45.4	64.1
4000273	OnZaP-3	50.99	93.26	MSP0001	Mudstone	0.8	7.4	0.9	327.0	50.2
4001000	OnZaP-1	51.57	93.82	MSP0010	Carbonate	1.1	29.2	3.0	72.9	3.9
4000279	OnZaP-3	52.53	94.80	MSP0001	Mudstone	1.2	6.5	0.8	62.0	63.7
4000280	OnZaP-3	53.02	95.29	MSP0001	Mudstone	1.3	8.0	1.0	103.1	69.1
4000995	OnZaP-3	53.75	96.00	MSP0010	Mudstone	6.2	20.2	2.3	464.5	60.7
4000281	OnZaP-3	54.02	96.29	MSP0001	Mudstone	1.9	12.0	1.3	561.0	55.7
4000288	OnZaP-3	55.01	97.28	MSP0001	Mudstone	72.3	11.6	1.4	343.2	8.4
4000289	OnZaP-3	55.60	97.87	MSP0001	Mudstone	1.8	14.0	1.5	879.6	60.1
4000996	OnZaP-3	55.76	98.01	MSP0010	Mudstone	6.7	26.9	2.8	410.6	77.3
4000290	OnZaP-3	56.52	98.79	MSP0001	Mudstone	1.0	8.8	0.9	432.6	47.8
4000997	OnZaP-3	57.27	99.52	MSP0010	Mudstone	6.7	24.6	2.8	937.2	58.6
4000998	OnZaP-3	58.06	100.31	MSP0010	Mudstone	10.7	42.6	4.6	849.6	102.4
4000291	OnZaP-3	58.24	100.51	MSP0001	Mudstone	3.8	19.7	2.1	623.5	94.2
4000299	OnZaP-3	58.87	101.14	MSP0001	Carbonate	12.2	17.6	1.1	24.9	7.7
4000999	OnZaP-3	59.88	102.13	MSP0010	Mudstone	10.1	57.2	6.0	1,112.9	110.6
4000306	OnZaP-3	59.95	102.22	MSP0001	Mudstone	2.6	16.8	2.2	1,178.6	82.4

Table A2: Total organic carbon (TOC) and sulphur (TS) for drill cores OnZaP-1 and OnZaP-3.

Sample ID	Drill site	Core depth (m)	Combined depth (m)	Sample set	Lithology	TS (wt.%)	TOC (wt.%)
4000319	OnZaP-1	1.96	1.96	MSP0001	Mudstone	0.05	0.5
4000921	OnZaP-1	2.08	2.08	MSP0010	Mudstone		1.3
4000320	OnZaP-1	2.85	2.85	MSP0001	Mudstone	0.27	0.3
4000321	OnZaP-1	3.92	3.92	MSP0001	Mudstone	0.29	0.3
4000922	OnZaP-1	5.28	5.28	MSP0010	Mudstone		0.9
4000322	OnZaP-1	5.31	5.31	MSP0001	Mudstone	0.32	0.5
4000323	OnZaP-1	6.50	6.50	MSP0001	Mudstone	0.51	0.2
4000923	OnZaP-1	6.60	6.60	MSP0010	Mudstone		1.5
4000324	OnZaP-1	7.01	7.01	MSP0001	Mudstone	0.27	0.2
4000332	OnZaP-1	7.96	7.96	MSP0001	Mudstone	0.54	2.9
4000336	OnZaP-1	8.35	8.35	MSP0001	Mudstone	2.06	0.3
4000342	OnZaP-1	8.74	8.74	MSP0001	Mudstone	1.11	1.2
4000345	OnZaP-1	9.58	9.58	MSP0001	Mudstone	2.21	1.4
4000346	OnZaP-1	10.79	10.79	MSP0001	Mudstone	2.23	0.7
4000924	OnZaP-1	11.13	11.13	MSP0010	Mudstone		3.1
4000347	OnZaP-1	11.86	11.86	MSP0001	Mudstone	0.92	2.4
4000925	OnZaP-1	12.15	12.15	MSP0010	Mudstone		5.6
4000348	OnZaP-1	12.39	12.39	MSP0001	Mudstone	4.35	2.3
4000349	OnZaP-1	13.16	13.16	MSP0001	Mudstone	0.13	2.9
4000351	OnZaP-1	13.40	13.40	MSP0001	Mudstone	0.03	1.0
4000358	OnZaP-1	14.65	14.65	MSP0001	Mudstone	0.23	1.1
4000362	OnZaP-1	15.26	15.26	MSP0001	Mudstone	0.04	0.2
4000376	OnZaP-1	17.36	17.36	MSP0001	Mudstone	0.02	3.3
4000383	OnZaP-1	17.90	17.90	MSP0001	Mudstone	0.02	1.1
4000926	OnZaP-1	18.85	18.85	MSP0010	Mudstone		0.8
4000392	OnZaP-1	19.08	19.08	MSP0001	Mudstone	0.07	0.4
4000393	OnZaP-1	19.99	19.99	MSP0001	Mudstone	0.08	0.4
4000394	OnZaP-1	20.66	20.66	MSP0001	Mudstone	0.79	0.4
4000927	OnZaP-1	21.91	21.91	MSP0010	Mudstone		0.9
4000395	OnZaP-1	21.94	21.94	MSP0001	Mudstone	0.16	0.6
4000396	OnZaP-1	22.33	22.33	MSP0001	Mudstone	0.48	0.7
4000398	OnZaP-1	23.03	23.03	MSP0001	Mudstone	0.22	0.5
4000928	OnZaP-1	23.84	23.84	MSP0010	Mudstone		2.0
4000403	OnZaP-1	24.31	24.31	MSP0001	Mudstone	0.91	0.2
4000406	OnZaP-1	25.03	25.03	MSP0001	Mudstone	0.37	1.1
4000412	OnZaP-1	26.09	26.09	MSP0001	Mudstone	0.90	0.5
4000413	OnZaP-1	26.80	26.80	MSP0001	Mudstone	0.51	0.2
4000414	OnZaP-1	27.77	27.77	MSP0001	Mudstone	1.84	0.1
4000929	OnZaP-1	27.95	27.95	MSP0010	Mudstone		2.0
4000421	OnZaP-1	28.36	28.36	MSP0001	Mudstone	1.46	0.5
4000930	OnZaP-1	28.80	28.80	MSP0010	Mudstone		2.4
4000429	OnZaP-1	29.28	29.28	MSP0001	Carbonate	0.14	0.7
4000931	OnZaP-1	30.66	30.66	MSP0010	Mudstone		9.2
4000436	OnZaP-1	30.79	30.79	MSP0001	Mudstone	3.11	2.1
4000442	OnZaP-1	31.21	31.21	MSP0001	Carbonate	0.09	3.3
4000932	OnZaP-1	31.85	31.85	MSP0010	Mudstone		11.7
4000447	OnZaP-1	31.86	31.86	MSP0001	Mudstone	5.18	6.2
4000933	OnZaP-1	32.19	32.19	MSP0010	Mudstone		12.6
4000455	OnZaP-1	33.15	33.15	MSP0001	Carbonate	0.10	4.0
4000466	OnZaP-1	33.96	33.96	MSP0001	Carbonate	0.62	4.0
4000471	OnZaP-1	34.64	34.64	MSP0001	Carbonate	0.36	2.2
4000478	OnZaP-1	35.61	35.61	MSP0001	Mudstone	0.81	1.7
4000934	OnZaP-1	36.40	36.40	MSP0010	Mudstone		17.0
4000483	OnZaP-1	36.52	36.52	MSP0001	Mudstone	3.66	12.5
4000484	OnZaP-1	36.94	36.94	MSP0001	Carbonate	0.03	2.7
4000935	OnZaP-1	37.83	37.83	MSP0010	Mudstone		23.1
4000491	OnZaP-1	38.13	38.13	MSP0001	Mudstone	10.90	12.8
4000936	OnZaP-1	38.91	38.91	MSP0010	Mudstone		27.2

Sample ID	Drill site	Core depth (m)	Combined depth (m)	Sample set	Lithology	TS (wt.%)	TOC (wt.%)
4000492	OnZaP-1	38.97	38.97	MSP0001	Mudstone	8.54	21.5
4000493	OnZaP-1	39.88	39.88	MSP0001	Mudstone	3.67	22.1
4000937	OnZaP-1	40.02	40.02	MSP0010	Carbonate		25.6
4000938	OnZaP-1	41.09	41.09	MSP0010	Mudstone		37.2
4000494	OnZaP-1	41.15	41.15	MSP0001	Mudstone	5.54	32.6
4000939	OnZaP-1	41.38	41.38	MSP0010	Mudstone		35.3
4000500	OnZaP-1	42.04	42.04	MSP0001	Carbonate	0.02	5.9
4000940	OnZaP-1	42.42	42.42	MSP0010	Mudstone		41.4
4000941	OnZaP-1	42.86	42.86	MSP0010	Carbonate		18.0
4000942	OnZaP-1	43.69	43.69	MSP0010	Carbonate		39.2
4000516	OnZaP-1	43.94	43.94	MSP0001	Carbonate	0.02	4.9
4000005	OnZaP-3	2.10	44.37	MSP0001	Carbonate	0.02	0.7
4000521	OnZaP-1	44.53	44.53	MSP0001	Carbonate	0.02	6.6
4000953	OnZaP-3	2.68	44.93	MSP0010	Carbonate		9.2
4000954	OnZaP-3	2.77	45.02	MSP0010	Mudstone		14.9
4000015	OnZaP-3	3.12	45.39	MSP0001	Carbonate	0.02	1.0
4000529	OnZaP-1	45.65	45.65	MSP0001	Carbonate	0.02	3.6
4000943	OnZaP-1	46.36	46.36	MSP0010	Mudstone		40.6
4000030	OnZaP-3	4.38	46.65	MSP0001	Carbonate	0.02	1.8
4000536	OnZaP-1	46.70	46.70	MSP0001	Mudstone	0.07	4.7
4000037	OnZaP-3	5.02	47.29	MSP0001	Carbonate	0.02	10.6
4000955	OnZaP-3	5.14	47.39	MSP0010	Mudstone		5.5
4000543	OnZaP-1	47.65	47.65	MSP0001	Carbonate	0.02	0.8
4000944	OnZaP-1	47.90	47.90	MSP0010	Carbonate		22.1
4000045	OnZaP-3	5.89	48.16	MSP0001	Carbonate	0.02	1.0
4000956	OnZaP-3	6.01	48.26	MSP0010	Carbonate		3.1
4000945	OnZaP-1	48.40	48.40	MSP0010	Carbonate		41.9
4000553	OnZaP-1	48.61	48.61	MSP0001	Mudstone	0.03	4.8
4000053	OnZaP-3	6.67	48.94	MSP0001	Mudstone	0.02	3.3
4000957	OnZaP-3	6.84	49.09	MSP0010	Mudstone		7.6
4000561	OnZaP-1	49.29	49.29	MSP0001	Carbonate	0.02	1.7
4000061	OnZaP-3	7.28	49.55	MSP0001	Carbonate	0.02	1.1
4000958	OnZaP-3	8.00	50.25	MSP0010	Mudstone		7.3
4000563	OnZaP-1	50.43	50.43	MSP0001	Mudstone	0.09	5.9
4000946	OnZaP-1	50.58	50.58	MSP0010	Carbonate		2.9
4000959	OnZaP-3	8.40	50.65	MSP0010	Mudstone		6.8
4000065	OnZaP-3	8.44	50.71	MSP0001	Mudstone	1.17	8.4
4000571	OnZaP-1	50.77	50.77	MSP0001	Carbonate	0.02	1.3
4000947	OnZaP-1	51.13	51.13	MSP0010	Carbonate		62.3
4000080	OnZaP-3	9.31	51.58	MSP0001	Carbonate	0.02	0.7
4000960	OnZaP-3	9.57	51.82	MSP0010	Carbonate		51.0
4000583	OnZaP-1	52.16	52.16	MSP0001	Carbonate	0.02	1.9
4000090	OnZaP-3	10.14	52.41	MSP0001	Carbonate	0.02	0.4
4000592	OnZaP-1	52.92	52.92	MSP0001	Carbonate	0.02	1.1
4000098	OnZaP-3	10.70	52.97	MSP0001	Carbonate	0.02	1.3
4000948	OnZaP-1	53.12	53.12	MSP0010	Mudstone		44.3
4000961	OnZaP-3	11.00	53.25	MSP0010	Carbonate		62.0
4000949	OnZaP-1	53.50	53.50	MSP0010	Mudstone		65.9
4000962	OnZaP-3	11.33	53.58	MSP0010	Carbonate		38.9
4000100	OnZaP-3	11.33	53.60	MSP0001	Mudstone	2.28	54.0
4000593	OnZaP-1	53.70	53.70	MSP0001	Mudstone	3.20	62.5
4000963	OnZaP-3	11.70	53.95	MSP0010	Mudstone		27.8
4000964	OnZaP-3	11.96	54.21	MSP0010	Mudstone		67.7
4000102	OnZaP-3	12.16	54.43	MSP0001	Mudstone	2.23	65.0
4000965	OnZaP-3	12.67	54.92	MSP0010	Mudstone		66.4
4000966	OnZaP-3	13.11	55.36	MSP0010	Mudstone		68.6
4000597	OnZaP-1	55.51	55.51	MSP0001	Carbonate	2.14	4.7
4000103	OnZaP-3	13.29	55.56	MSP0001	Mudstone	2.21	64.2
4000601	OnZaP-1	55.68	55.68	MSP0001	Mudstone	6.36	50.4
4000950	OnZaP-1	55.80	55.80	MSP0010	Mudstone		51.9
4000967	OnZaP-3	13.82	56.07	MSP0010	Carbonate		70.5
4000602	OnZaP-1	56.17	56.17	MSP0001	Mudstone	6.51	48.9
4000968	OnZaP-3	14.25	56.50	MSP0010	Mudstone		45.6
4000108	OnZaP-3	14.31	56.58	MSP0001	Mudstone	2.34	25.2
4000605	OnZaP-1	56.89	56.89	MSP0001	Carbonate	1.45	2.7

Sample ID	Drill site	Core depth (m)	Combined depth (m)	Sample set	Lithology	TS (wt.%)	TOC (wt.%)
4000969	OnZaP-3	14.69	56.94	MSP0010	Mudstone		63.7
4000113	OnZaP-3	14.85	57.12	MSP0001	Mudstone	3.44	59.8
4000614	OnZaP-1	57.64	57.64	MSP0001	Carbonate	1.82	1.0
4000951	OnZaP-1	57.93	57.93	MSP0010	Mudstone		43.0
4000970	OnZaP-3	15.72	57.97	MSP0010	Mudstone		60.7
4000114	OnZaP-3	15.70	57.97	MSP0001	Mudstone	7.34	54.1
4000618	OnZaP-1	58.41	58.41	MSP0001	Mudstone	3.34	36.9
4000971	OnZaP-3	16.42	58.67	MSP0010	Mudstone		44.0
4000972	OnZaP-3	16.72	58.97	MSP0010	Mudstone		46.9
4000115	OnZaP-3	16.92	59.19	MSP0001	Mudstone	5.90	30.9
4000952	OnZaP-1	59.25	59.25	MSP0010	Mudstone		39.3
4000619	OnZaP-1	59.67	59.67	MSP0001	Mudstone	2.95	21.7
4000122	OnZaP-3	17.55	59.82	MSP0001	Mudstone	5.59	32.5
4000973	OnZaP-3	17.89	60.14	MSP0010	Mudstone		23.3
4000623	OnZaP-1	60.18	60.18	MSP0001	Mudstone	3.06	7.1
4000128	OnZaP-3	18.65	60.92	MSP0001	Carbonate	2.81	0.7
4000129	OnZaP-3	18.97	61.24	MSP0001	Mudstone	9.01	29.2
4000974	OnZaP-3	19.27	61.52	MSP0010	Mudstone		36.0
4000975	OnZaP-3	20.07	62.32	MSP0010	Mudstone		30.5
4000130	OnZaP-3	20.13	62.40	MSP0001	Mudstone	10.70	10.0
4000132	OnZaP-3	20.90	63.17	MSP0001	Mudstone	1.62	25.7
4000976	OnZaP-3	21.12	63.37	MSP0010	Mudstone		37.0
4000133	OnZaP-3	21.96	64.23	MSP0001	Mudstone	3.54	19.0
4000977	OnZaP-3	22.36	64.61	MSP0010	Mudstone		28.1
4000978	OnZaP-3	22.96	65.21	MSP0010	Mudstone		20.7
4000134	OnZaP-3	23.12	65.39	MSP0001	Mudstone	5.87	16.9
4000979	OnZaP-3	23.59	65.84	MSP0010	Mudstone		26.3
4000135	OnZaP-3	24.26	66.53	MSP0001	Carbonate	2.07	7.4
4000980	OnZaP-3	24.91	67.16	MSP0010	Mudstone		20.4
4000151	OnZaP-3	25.18	67.45	MSP0001	Carbonate	1.52	2.5
4000981	OnZaP-3	25.59	67.84	MSP0010	Mudstone		19.0
4000159	OnZaP-3	25.76	68.03	MSP0001	Mudstone	4.31	14.8
4000982	OnZaP-3	26.20	68.45	MSP0010	Mudstone		19.1
4000168	OnZaP-3	26.56	68.83	MSP0001	Mudstone	3.82	1.2
4000178	OnZaP-3	27.32	69.59	MSP0001	Carbonate	1.53	1.1
4000983	OnZaP-3	27.51	69.76	MSP0010	Carbonate		12.9
4000179	OnZaP-3	28.13	70.40	MSP0001	Mudstone	0.53	19.7
4000984	OnZaP-3	28.69	70.94	MSP0010	Mudstone		7.1
4000180	OnZaP-3	29.20	71.47	MSP0001	Mudstone	1.92	9.4
4000985	OnZaP-3	29.35	71.60	MSP0010	Mudstone		9.0
4000181	OnZaP-3	30.59	72.86	MSP0001	Mudstone	2.77	13.6
4000986	OnZaP-3	30.68	72.93	MSP0010	Mudstone		33.3
4000987	OnZaP-3	31.40	73.65	MSP0010	Mudstone		33.3
4000187	OnZaP-3	31.63	73.90	MSP0001	Mudstone	3.48	26.6
4000988	OnZaP-3	32.10	74.35	MSP0010	Mudstone		40.4
4000190	OnZaP-3	32.36	74.63	MSP0001	Carbonate	0.49	9.8
4000201	OnZaP-3	33.24	75.51	MSP0001	Mudstone	1.34	11.7
4000989	OnZaP-3	33.48	75.73	MSP0010	Mudstone		38.1
4000990	OnZaP-3	33.81	76.06	MSP0010	Mudstone		12.6
4000202	OnZaP-3	34.29	76.56	MSP0001	Mudstone	1.62	9.2
4000203	OnZaP-3	34.96	77.23	MSP0001	Mudstone	0.80	9.0
4000214	OnZaP-3	36.54	78.81	MSP0001	Carbonate	0.80	2.0
4000216	OnZaP-3	37.30	79.57	MSP0001	Carbonate	1.08	2.6
4000225	OnZaP-3	38.42	80.69	MSP0001	Mudstone	1.77	1.9
4000231	OnZaP-3	39.25	81.52	MSP0001	Mudstone	1.72	0.0
4000239	OnZaP-3	40.20	82.47	MSP0001	Mudstone	2.58	0.2
4000244	OnZaP-3	41.09	83.36	MSP0001	Mudstone	0.68	0.0
4000251	OnZaP-3	42.32	84.59	MSP0001	Carbonate	1.26	1.6
4000256	OnZaP-3	43.12	85.39	MSP0001	Carbonate	0.37	0.0
4000264	OnZaP-3	44.02	86.29	MSP0001	Mudstone	1.66	4.3
4000265	OnZaP-3	44.82	87.09	MSP0001	Mudstone	1.78	4.8
4000266	OnZaP-3	45.87	88.14	MSP0001	Mudstone	0.81	13.9
4000991	OnZaP-3	46.11	88.36	MSP0010	Mudstone		12.1
4000992	OnZaP-3	46.51	88.76	MSP0010	Mudstone		17.9
4000267	OnZaP-3	46.59	88.86	MSP0001	Mudstone	1.11	13.0

Sample ID	Drill site	Core depth (m)	Combined depth (m)	Sample set	Lithology	TS (wt.%)	TOC (wt.%)
4000993	OnZaP-3	47.86	90.11	MSP0010	Mudstone		18.1
4000268	OnZaP-3	48.02	90.29	MSP0001	Mudstone	1.38	10.2
4000994	OnZaP-3	48.94	91.19	MSP0010	Mudstone		14.5
4000269	OnZaP-3	49.00	91.27	MSP0001	Mudstone	0.77	12.8
4000270	OnZaP-3	49.68	91.95	MSP0001	Mudstone	2.68	6.8
4000271	OnZaP-3	50.28	92.55	MSP0001	Mudstone	1.27	5.6
4000273	OnZaP-3	50.99	93.26	MSP0001	Mudstone	0.88	3.8
4001000	OnZaP-1	51.57	93.82	MSP0010	Carbonate		2.0
4000279	OnZaP-3	52.53	94.80	MSP0001	Mudstone	1.85	6.3
4000280	OnZaP-3	53.02	95.29	MSP0001	Mudstone	0.85	10.3
4000995	OnZaP-3	53.75	96.00	MSP0010	Mudstone		14.8
4000281	OnZaP-3	54.02	96.29	MSP0001	Mudstone	0.87	15.2
4000288	OnZaP-3	55.01	97.28	MSP0001	Mudstone	0.25	5.8
4000289	OnZaP-3	55.60	97.87	MSP0001	Mudstone	0.94	15.2
4000996	OnZaP-3	55.76	98.01	MSP0010	Mudstone		16.5
4000290	OnZaP-3	56.52	98.79	MSP0001	Mudstone	0.89	8.7
4000997	OnZaP-3	57.27	99.52	MSP0010	Mudstone		22.4
4000998	OnZaP-3	58.06	100.31	MSP0010	Mudstone		16.9
4000291	OnZaP-3	58.24	100.51	MSP0001	Mudstone	1.49	13.0
4000299	OnZaP-3	58.87	101.14	MSP0001	Carbonate	0.81	0.0
4000999	OnZaP-3	59.88	102.13	MSP0010	Mudstone		22.7
4000306	OnZaP-3	59.95	102.22	MSP0001	Mudstone	2.05	18.9

Table A3a: X-ray diffraction mineral abundances in drill cores OnZaP-1 and OnZaP-3.

Sample ID	Drill site	Core depth (m)	Comb. depth (m)	Sample set	Lithology	Quartz (wt.%)	K-feldspar (wt.%)	Plagoclase (wt.%)	Mica 2M1 (wt.%)	Mica 1M (wt.%)	Chlorite (wt.%)	Calcite (wt.%)	Dolomite (wt.%)	Pyrite (wt.%)
4000319	OnZaP-1	1.96	1.96	MSP0001	Mudstone	50.50	0.98	11.43				0.59	0.07	0.08
4000320	OnZaP-1	2.85	2.85	MSP0001	Mudstone	41.82	1.27	8.95				0.76	0.30	0.28
4000321	OnZaP-1	3.92	3.92	MSP0001	Mudstone	41.82	1.23	10.69				0.34	0.00	0.36
4000322	OnZaP-1	5.31	5.31	MSP0001	Mudstone	41.97	1.09	12.66				0.34	0.00	0.37
4000332	OnZaP-1	7.96	7.96	MSP0001	Mudstone	10.61	2.61	0.87				0.45	31.06	0.91
4000336	OnZaP-1	8.35	8.35	MSP0001	Mudstone	42.83	0.93	3.34				0.22	2.94	2.56
4000342	OnZaP-1	8.74	8.74	MSP0001	Mudstone	16.37	2.08	1.54				0.26	33.36	1.03
4000345	OnZaP-1	9.58	9.58	MSP0001	Mudstone	42.87	0.63	5.48				0.12	9.21	2.51
4000347	OnZaP-1	11.86	11.86	MSP0001	Mudstone	38.84	0.66	11.16				0.18	0.20	0.62
4000348	OnZaP-1	12.39	12.39	MSP0001	Mudstone	41.43	0.84	7.40				0.55	0.23	4.64
4000349	OnZaP-1	13.16	13.16	MSP0001	Mudstone	12.51	1.54	0.54				0.42	34.60	0.70
4000351	OnZaP-1	13.40	13.40	MSP0001	Mudstone	25.51	1.05	1.33				0.53	27.26	0.31
4000358	OnZaP-1	14.65	14.65	MSP0001	Mudstone	30.60	1.39	12.65				0.92	1.01	0.05
4000362	OnZaP-1	15.26	15.26	MSP0001	Mudstone	29.85	2.30	3.25				2.06	19.33	0.14
4000368	OnZaP-1	16.29	16.29	MSP0001	Mudstone	17.05	2.31	0.55				0.48	35.87	0.68
4000376	OnZaP-1	17.36	17.36	MSP0001	Mudstone	10.86	0.99	1.84				0.07	40.04	0.40
4000383	OnZaP-1	17.90	17.90	MSP0001	Mudstone	20.62	1.18	0.72				0.02	38.14	0.12
4000392	OnZaP-1	19.08	19.08	MSP0001	Mudstone	41.80	1.70	13.23				0.59	0.00	0.04
4000393	OnZaP-1	19.99	19.99	MSP0001	Mudstone	38.08	1.89	12.25				0.61	0.32	0.22
4000394	OnZaP-1	20.66	20.66	MSP0001	Mudstone	45.30	1.18	10.69				0.30	0.35	0.03
4000395	OnZaP-1	21.94	21.94	MSP0001	Mudstone	41.28	2.67	12.55				1.82	0.42	0.30
4000398	OnZaP-1	23.03	23.03	MSP0001	Mudstone	36.93	2.19	9.02				6.22	0.88	0.23
4000403	OnZaP-1	24.31	24.31	MSP0001	Mudstone	27.26	1.66	4.10				2.37	17.14	0.95
4000406	OnZaP-1	25.03	25.03	MSP0001	Mudstone	16.11	2.05	0.62				1.08	43.62	0.53
4000413	OnZaP-1	26.80	26.80	MSP0001	Mudstone	46.26	1.14	0.54				0.84	2.41	0.57
4000414	OnZaP-1	27.77	27.77	MSP0001	Mudstone	24.29	1.05	0.82				0.39	28.69	1.90
4000429	OnZaP-1	29.28	29.28	MSP0001	Carbonate	11.51	1.25	1.92				0.28	51.51	0.33
4000436	OnZaP-1	30.79	30.79	MSP0001	Mudstone	46.16	1.42	4.22				0.54	1.17	3.98
4000442	OnZaP-1	31.21	31.21	MSP0001	Carbonate	14.67	0.95	1.09				0.79	60.17	0.28
4000447	OnZaP-1	31.86	31.86	MSP0001	Mudstone	34.02	7.10	4.02				0.73	0.88	8.17
4000933	OnZaP-1	32.19	32.19	MSP0010	Mudstone	34.00	12.90	2.60	35.10	1.90		trace		6.10
4000455	OnZaP-1	33.15	33.15	MSP0001	Carbonate	9.44	1.44	0.69				0.27	70.59	0.22
4000466	OnZaP-1	33.96	33.96	MSP0001	Carbonate	0.60	1.17	0.63				0.91	80.59	0.84
4000471	OnZaP-1	34.64	34.64	MSP0001	Carbonate	7.22	2.09	2.30				0.91	74.60	0.42
4000483	OnZaP-1	36.52	36.52	MSP0001	Mudstone	25.70	11.45	3.55				0.00	1.25	5.65
4000484	OnZaP-1	36.94	36.94	MSP0001	Carbonate	5.19	2.15	1.05				2.12	68.75	0.21
4000491	OnZaP-1	38.13	38.13	MSP0001	Mudstone	26.54	2.71	1.05				0.58	0.00	16.53
4000936	OnZaP-1	38.91	38.91	MSP0010	Mudstone	15.40	6.00	0.30	43.70	5.70		trace	trace	12.50
4000492	OnZaP-1	38.97	38.97	MSP0001	Mudstone	19.27	5.00	1.29				2.44	0.09	13.38
4000494	OnZaP-1	41.15	41.15	MSP0001	Mudstone	27.81	2.35	0.78				0.71	0.11	8.45
4000500	OnZaP-1	42.04	42.04	MSP0001	Carbonate	1.07	0.86	0.52				0.50	76.80	0.07

Sample ID	Drill site	Core depth (m)	Comb. depth (m)	Sample set	Lithology	Quartz (wt.%)	K-feldspar (wt.%)	Plagoclase (wt.%)	Mica 2M1 (wt.%)	Mica 1M (wt.%)	Chlorite (wt.%)	Calcite (wt.%)	Dolomite (wt.%)	Pyrite (wt.%)
4000504	OnZaP-1	42.45	42.45	MSP0001	Mudstone	23.76	4.49	0.26				9.57	0.00	12.87
4000516	OnZaP-1	43.94	43.94	MSP0001	Carbonate	1.95	0.88	0.17				1.31	80.69	0.17
4000005	OnZaP-3	2.10	44.35	MSP0001	Carbonate	10.92	0.38	0.02				0.21	76.66	0.04
4000521	OnZaP-1	44.53	44.53	MSP0001	Carbonate	1.53	1.11	0.44				0.55	81.49	0.15
4000015	OnZaP-3	3.12	45.37	MSP0001	Carbonate	1.71	0.37	0.08				0.76	84.10	0.00
4000529	OnZaP-1	45.65	45.65	MSP0001	Carbonate	1.56	1.67	0.65				2.19	80.48	0.13
4000030	OnZaP-3	4.38	46.63	MSP0001	Carbonate	3.11	0.55	0.29				0.31	81.34	0.02
4000536	OnZaP-1	46.70	46.70	MSP0001	Mudstone	94.29	0.00	0.00				0.00	0.00	0.13
4000037	OnZaP-3	5.02	47.27	MSP0001	Carbonate	0.69	1.13	0.23				0.36	77.58	0.04
4000543	OnZaP-1	47.65	47.65	MSP0001	Carbonate	3.12	0.42	0.74				0.56	83.10	0.16
4000045	OnZaP-3	5.89	48.14	MSP0001	Carbonate	0.23	0.72	0.25				1.66	88.17	0.06
4000553	OnZaP-1	48.61	48.61	MSP0001	Mudstone	93.41	0.10	0.37				0.11	0.00	0.10
4000053	OnZaP-3	6.67	48.92	MSP0001	Mudstone	96.32	0.00	0.00				0.14	0.00	0.02
4000561	OnZaP-1	49.29	49.29	MSP0001	Carbonate	19.68	0.66	0.72				17.19	37.52	0.16
4000061	OnZaP-3	7.28	49.53	MSP0001	Carbonate	8.96	0.61	0.06				2.02	78.88	0.07
4000563	OnZaP-1	50.43	50.43	MSP0001	Mudstone	92.32	0.00	0.19				0.00	0.00	0.15
4000065	OnZaP-3	8.44	50.69	MSP0001	Mudstone	74.41	2.53	0.26				0.24	0.43	1.51
4000571	OnZaP-1	50.77	50.77	MSP0001	Carbonate	0.99	2.15	0.41				1.57	77.43	0.11
4000575	OnZaP-1	51.41	51.41	MSP0001	Mudstone	9.72	8.76	3.57				0.14	0.00	11.12
4000080	OnZaP-3	9.31	51.56	MSP0001	Carbonate	3.54	0.29	0.00				5.31	78.74	0.06
4000583	OnZaP-1	52.16	52.16	MSP0001	Carbonate	0.51	1.53	0.83				1.80	84.43	0.12
4000090	OnZaP-3	10.14	52.39	MSP0001	Carbonate	2.68	0.85	0.09				6.42	75.46	0.01
4000592	OnZaP-1	52.92	52.92	MSP0001	Carbonate	2.83	1.84	0.73				10.03	71.15	0.38
4000098	OnZaP-3	10.70	52.95	MSP0001	Carbonate	5.61	0.85	0.06				12.79	67.84	0.17
4000948	OnZaP-1	53.12	53.12	MSP0010	Mudstone	2.30	3.00	0.70	6.70	35.70		trace		2.60
4000100	OnZaP-3	11.33	53.58	MSP0001	Mudstone	10.94	2.83	0.87				0.00	0.00	2.73
4000593	OnZaP-1	53.70	53.70	MSP0001	Mudstone	8.19	10.15	1.32				0.44	0.00	5.20
4000102	OnZaP-3	12.16	54.41	MSP0001	Mudstone	9.86	5.71	1.21				0.21	0.00	2.68
4000594	OnZaP-1	55.14	55.14	MSP0001	Mudstone	19.08	9.32	1.84				0.64	0.00	7.73
4000966	OnZaP-3	13.11	55.36	MSP0010	Mudstone									
4000597	OnZaP-1	55.51	55.51	MSP0001	Carbonate	36.12	0.35	0.24				51.50	0.07	3.53
4000103	OnZaP-3	13.29	55.54	MSP0001	Mudstone	12.73	5.90	1.00				0.10	0.00	3.62
4000601	OnZaP-1	55.68	55.68	MSP0001	Mudstone	22.49	1.90	1.15				0.62	0.00	9.98
4000950	OnZaP-1	55.80	55.80	MSP0010	Mudstone	31.50	3.20	0.00	18.30	4.70				11.00
4000602	OnZaP-1	56.17	56.17	MSP0001	Mudstone	28.72	2.00	0.58				0.30	0.00	8.32
4000108	OnZaP-3	14.31	56.56	MSP0001	Mudstone	2.40	1.19	0.00				31.55	6.80	3.99
4000605	OnZaP-1	56.89	56.89	MSP0001	Carbonate	1.76	0.50	0.77				62.90	8.58	2.33
4000969	OnZaP-3	14.69	56.94	MSP0010	Mudstone	10.20	8.50	0.60	11.10	5.30				10.70
4000113	OnZaP-3	14.85	57.10	MSP0001	Mudstone	18.80	5.21	1.35				0.25	0.00	4.95
4000614	OnZaP-1	57.64	57.64	MSP0001	Carbonate	4.70	2.02	0.54				6.01	59.36	2.11
4000618	OnZaP-1	58.41	58.41	MSP0001	Mudstone	30.86	6.98	0.00				0.72	0.32	4.02
4000115	OnZaP-3	16.92	59.17	MSP0001	Mudstone	23.51	6.88	0.68				0.11	0.00	9.01
4000619	OnZaP-1	59.67	59.67	MSP0001	Mudstone	23.56	24.55	0.99				7.24	0.00	3.92
4000122	OnZaP-3	17.55	59.80	MSP0001	Mudstone	41.98	1.55	0.00				0.11	0.00	8.61

Sample ID	Drill site	Core depth (m)	Comb. depth (m)	Sample set	Lithology	Quartz (wt.%)	K-feldspar (wt.%)	Plagoclase (wt.%)	Mica 2M1 (wt.%)	Mica 1M (wt.%)	Chlorite (wt.%)	Calcite (wt.%)	Dolomite (wt.%)	Pyrite (wt.%)
4000623	OnZaP-1	60.18	60.18	MSP0001	Mudstone	17.47	1.09	3.09				43.27	0.05	4.02
4000128	OnZaP-3	18.65	60.90	MSP0001	Carbonate	4.79	0.55	0.15				20.65	49.39	3.63
4000129	OnZaP-3	18.97	61.22	MSP0001	Mudstone	26.63	8.87	0.19				0.34	0.00	11.49
4000130	OnZaP-3	20.13	62.38	MSP0001	Mudstone	25.51	4.22	1.68				20.15	0.00	13.84
4000132	OnZaP-3	20.90	63.15	MSP0001	Mudstone	53.17	3.92	0.41				0.07	0.00	1.75
4000976	OnZaP-3	21.12	63.37	MSP0010	Mudstone	48.90	10.40	1.40	16.70	3.40				2.70
4000133	OnZaP-3	21.96	64.21	MSP0001	Mudstone	39.59	14.50	0.23				0.23	0.00	4.97
4000134	OnZaP-3	23.12	65.37	MSP0001	Mudstone	24.37	8.68	0.46				0.49	0.00	8.83
4000135	OnZaP-3	24.26	66.51	MSP0001	Carbonate	6.42	3.72	0.14				16.10	45.14	2.97
4000980	OnZaP-3	24.91	67.16	MSP0010	Mudstone	14.70	1.80	0.50	5.10	47.10	12.40	0.80		5.30
4000151	OnZaP-3	25.18	67.43	MSP0001	Carbonate	0.50	1.45	0.00				1.64	74.23	1.82
4000981	OnZaP-3	25.59	67.84	MSP0010	Mudstone	16.20	16.70	0.10	10.10	33.50	8.60	trace		5.50
4000159	OnZaP-3	25.76	68.01	MSP0001	Mudstone	6.52	19.89	1.08				0.15	0.00	8.06
4000168	OnZaP-3	26.56	68.81	MSP0001	Mudstone	1.12	2.56	1.12				12.78	0.19	6.89
4000178	OnZaP-3	27.32	69.57	MSP0001	Carbonate	4.70	1.03	0.21				9.52	67.14	1.99
4000179	OnZaP-3	28.13	70.38	MSP0001	Mudstone	71.64	1.67	0.72				0.03	0.00	0.66
4000180	OnZaP-3	29.20	71.45	MSP0001	Mudstone	69.78	2.02	0.47				0.09	0.00	2.67
4000181	OnZaP-3	30.59	72.84	MSP0001	Mudstone	38.81	1.96	0.07				8.62	0.03	4.46
4000187	OnZaP-3	31.63	73.88	MSP0001	Mudstone	51.17	5.29	1.24				0.03	0.03	4.94
4000190	OnZaP-3	32.36	74.61	MSP0001	Carbonate	15.46	2.18	0.00				3.08	59.58	0.73
4000201	OnZaP-3	33.24	75.49	MSP0001	Mudstone	34.99	1.30	0.08				29.35	0.62	2.18
4000202	OnZaP-3	34.29	76.54	MSP0001	Mudstone	62.36	4.29	5.71				0.06	0.05	2.35
4000203	OnZaP-3	34.96	77.21	MSP0001	Mudstone	67.82	1.37	3.50				0.18	0.00	0.99
4000214	OnZaP-3	36.54	78.79	MSP0001	Carbonate	24.02	1.46	0.22				16.43	38.99	0.92
4000216	OnZaP-3	37.30	79.55	MSP0001	Carbonate	26.92	1.89	0.22				3.24	52.18	1.10
4000225	OnZaP-3	38.42	80.67	MSP0001	Mudstone	31.14	2.09	0.08				13.05	31.91	1.92
4000231	OnZaP-3	39.25	81.50	MSP0001	Mudstone	40.66	2.40	0.14				14.31	7.73	2.12
4000239	OnZaP-3	40.20	82.45	MSP0001	Mudstone	48.18	4.50	11.71				4.01	0.15	3.06
4000244	OnZaP-3	41.09	83.34	MSP0001	Mudstone	30.26	2.01	0.37				23.75	17.00	0.83
4000251	OnZaP-3	42.32	84.57	MSP0001	Carbonate	20.53	0.75	0.10				27.21	23.51	1.29
4000256	OnZaP-3	43.12	85.37	MSP0001	Carbonate	2.23	1.43	0.12				24.79	44.63	0.30
4000264	OnZaP-3	44.02	86.27	MSP0001	Mudstone	54.13	6.16	2.75				6.45	0.00	2.65
4000265	OnZaP-3	44.82	87.07	MSP0001	Mudstone	61.03	3.37	7.00				0.64	0.00	2.58
4000266	OnZaP-3	45.87	88.12	MSP0001	Mudstone	62.59	6.97	1.98				0.17	0.00	1.17
4000991	OnZaP-3	46.11	88.36	MSP0010	Mudstone	62.20	11.00	2.40	8.70	6.30				1.90
4000267	OnZaP-3	46.59	88.84	MSP0001	Mudstone	55.52	11.05	2.37				0.30	0.00	1.54
4000993	OnZaP-3	47.86	90.11	MSP0010	Mudstone	70.30	9.10	3.50	5.20	3.90				1.80
4000268	OnZaP-3	48.02	90.27	MSP0001	Mudstone	59.62	6.17	5.12				0.33	0.00	1.94
4000269	OnZaP-3	49.00	91.25	MSP0001	Mudstone	66.10	5.87	4.51				0.22	0.00	1.10
4000270	OnZaP-3	49.68	91.93	MSP0001	Mudstone	65.28	4.00	5.74				0.58	0.04	4.01
4000271	OnZaP-3	50.28	92.53	MSP0001	Mudstone	59.48	4.60	9.53				0.59	0.00	1.86
4000273	OnZaP-3	50.99	93.24	MSP0001	Mudstone	71.34	3.03	6.44				2.50	0.00	1.24
4000279	OnZaP-3	52.53	94.78	MSP0001	Mudstone	53.68	4.77	7.03				1.07	0.00	2.53
4000280	OnZaP-3	53.02	95.27	MSP0001	Mudstone	56.52	9.00	4.93				0.19	0.00	1.16

Sample ID	Drill site	Core depth (m)	Comb. depth (m)	Sample set	Lithology	Quartz (wt.%)	K-feldspar (wt.%)	Plagoclase (wt.%)	Mica 2M1 (wt.%)	Mica 1M (wt.%)	Chlorite (wt.%)	Calcite (wt.%)	Dolomite (wt.%)	Pyrite (wt.%)
4000281	OnZaP-3	54.02	96.27	MSP0001	Mudstone	57.93	8.35	1.38				0.20	0.00	1.18
4000288	OnZaP-3	55.01	97.26	MSP0001	Mudstone	40.70	0.25	0.00				34.89	0.15	0.59
4000289	OnZaP-3	55.60	97.85	MSP0001	Mudstone	56.75	10.16	2.29				0.20	0.00	1.32
4000290	OnZaP-3	56.52	98.77	MSP0001	Mudstone	65.27	3.74	3.35				0.43	0.00	1.34
4000291	OnZaP-3	58.24	100.49	MSP0001	Mudstone	50.21	16.31	1.28				0.18	0.00	2.05
4000299	OnZaP-3	58.87	101.12	MSP0001	Carbonate	3.70	0.59	0.00				44.29	25.27	1.05
4000306	OnZaP-3	59.95	102.20	MSP0001	Mudstone	41.08	15.79	1.40				0.33	0.34	2.86

Table A3b: X-ray diffraction mineral abundances in drill cores OnZaP-1 and OnZaP-3, continued.

Sample ID	Drill site	Core depth (m)	Comb. depth (m)	Sample set	Lithology	Apatite (wt.%)	Rutile (wt.%)	Anastase (wt.%)	Graphite (wt.%)	Hematite (wt.%)	Talc (wt.%)	Hornblende (wt.%)	Biotite (wt.%)	Phlogopite (wt.%)
4000319	OnZaP-1	1.96	1.96	MSP0001	Mudstone	0.28		0.00		0.00	0.00	0.00	0.00	0.00
4000320	OnZaP-1	2.85	2.85	MSP0001	Mudstone	0.32		0.00		0.00	0.00	0.00	13.35	0.00
4000321	OnZaP-1	3.92	3.92	MSP0001	Mudstone	0.40		0.00		0.00	0.00	0.00	13.38	0.00
4000322	OnZaP-1	5.31	5.31	MSP0001	Mudstone	0.27		0.00		0.00	0.00	0.00	12.43	0.00
4000332	OnZaP-1	7.96	7.96	MSP0001	Mudstone	0.47		0.00		0.00	0.00	0.00	4.11	0.00
4000336	OnZaP-1	8.35	8.35	MSP0001	Mudstone	0.22		0.00		0.00	0.00	0.00	2.94	0.00
4000342	OnZaP-1	8.74	8.74	MSP0001	Mudstone	0.13		0.00		0.00	0.00	0.00	3.04	0.00
4000345	OnZaP-1	9.58	9.58	MSP0001	Mudstone	0.51		0.00		0.00	0.00	0.00	2.97	0.00
4000347	OnZaP-1	11.86	11.86	MSP0001	Mudstone	0.13		0.00		0.00	0.00	0.00	5.03	0.00
4000348	OnZaP-1	12.39	12.39	MSP0001	Mudstone	0.39		0.00		0.00	0.00	0.00	5.05	0.00
4000349	OnZaP-1	13.16	13.16	MSP0001	Mudstone	0.23		0.00		0.00	0.00	0.00	6.54	0.00
4000351	OnZaP-1	13.40	13.40	MSP0001	Mudstone	0.10		0.00		0.00	0.00	0.00	10.81	0.00
4000358	OnZaP-1	14.65	14.65	MSP0001	Mudstone	0.23		0.00		0.00	0.00	0.00	29.19	0.00
4000362	OnZaP-1	15.26	15.26	MSP0001	Mudstone	0.28		0.00		0.00	0.00	0.00	14.09	0.00
4000368	OnZaP-1	16.29	16.29	MSP0001	Mudstone	0.21		0.00		0.00	0.00	0.00	6.92	0.00
4000376	OnZaP-1	17.36	17.36	MSP0001	Mudstone	0.04		0.00		0.00	0.00	0.00	8.92	0.00
4000383	OnZaP-1	17.90	17.90	MSP0001	Mudstone	0.13		0.00		0.00	0.00	0.00	6.96	0.00
4000392	OnZaP-1	19.08	19.08	MSP0001	Mudstone	0.14		0.00		0.00	0.00	0.00	16.46	0.00
4000393	OnZaP-1	19.99	19.99	MSP0001	Mudstone	0.36		0.00		0.00	0.00	0.00	21.84	0.00
4000394	OnZaP-1	20.66	20.66	MSP0001	Mudstone	0.52		0.00		0.00	0.00	0.00	9.95	0.00
4000395	OnZaP-1	21.94	21.94	MSP0001	Mudstone	0.25		0.00		0.00	0.00	0.00	24.06	0.00
4000398	OnZaP-1	23.03	23.03	MSP0001	Mudstone	0.50		0.00		0.00	0.00	0.00	30.67	0.00
4000403	OnZaP-1	24.31	24.31	MSP0001	Mudstone	0.23		0.00		0.00	0.00	0.00	15.68	0.00
4000406	OnZaP-1	25.03	25.03	MSP0001	Mudstone	0.45		0.00		0.00	0.00	0.00	3.72	0.00
4000413	OnZaP-1	26.80	26.80	MSP0001	Mudstone	0.27		0.00		0.00	0.00	0.00	4.54	0.00
4000414	OnZaP-1	27.77	27.77	MSP0001	Mudstone	0.31		0.00		0.00	0.00	0.00	3.51	0.00
4000429	OnZaP-1	29.28	29.28	MSP0001	Carbonate	0.47		0.00		0.00	0.00	0.00	2.09	0.00
4000436	OnZaP-1	30.79	30.79	MSP0001	Mudstone	0.21		0.00		0.00	0.00	0.00	4.67	0.00
4000442	OnZaP-1	31.21	31.21	MSP0001	Carbonate	0.64		0.00		0.00	0.00	0.00	4.90	0.00
4000447	OnZaP-1	31.86	31.86	MSP0001	Mudstone	0.09		0.00		0.00	0.00	0.00	6.52	0.00
4000933	OnZaP-1	32.19	32.19	MSP0010	Mudstone		0.80		5.80					
4000455	OnZaP-1	33.15	33.15	MSP0001	Carbonate	0.06		0.00		0.00	0.00	0.00	0.00	2.64
4000466	OnZaP-1	33.96	33.96	MSP0001	Carbonate	0.01		0.00		0.00	0.00	0.00	0.00	1.79
4000471	OnZaP-1	34.64	34.64	MSP0001	Carbonate	0.36		0.00		0.00	0.36	0.00	0.00	1.72
4000483	OnZaP-1	36.52	36.52	MSP0001	Mudstone	0.38		0.00		0.00	0.00	0.00	0.00	15.31
4000484	OnZaP-1	36.94	36.94	MSP0001	Carbonate	0.01		0.00		0.00	0.00	0.00	0.00	5.53
4000491	OnZaP-1	38.13	38.13	MSP0001	Mudstone	0.00		0.00		0.00	0.00	0.00	0.00	7.61
4000936	OnZaP-1	38.91	38.91	MSP0010	Mudstone	0.50			15.20					
4000492	OnZaP-1	38.97	38.97	MSP0001	Mudstone	0.00		0.00		0.00	0.00	0.00	0.00	7.55
4000494	OnZaP-1	41.15	41.15	MSP0001	Mudstone	0.00		0.00		0.00	0.00	0.00	0.00	6.87
4000500	OnZaP-1	42.04	42.04	MSP0001	Carbonate	0.96		0.00		0.00	0.00	0.00	0.00	0.81
4000504	OnZaP-1	42.45	42.45	MSP0001	Mudstone	0.38		0.00		0.00	0.00	0.00	0.00	26.58

Sample ID	Drill site	Core depth (m)	Comb. depth (m)	Sample set	Lithology	Apatite (wt.%)	Rutile (wt.%)	Anastase (wt.%)	Graphite (wt.%)	Hematite (wt.%)	Talc (wt.%)	Hornblende (wt.%)	Biotite (wt.%)	Phlogopite (wt.%)
4000516	OnZaP-1	43.94	43.94	MSP0001	Carbonate	0.20		0.00		0.00	0.00	0.00	0.00	1.81
4000005	OnZaP-3	2.10	44.35	MSP0001	Carbonate	0.95		0.00		0.00	0.00	0.00	0.00	2.61
4000521	OnZaP-1	44.53	44.53	MSP0001	Carbonate	0.58		0.00		0.00	0.00	0.00	0.00	1.66
4000015	OnZaP-3	3.12	45.37	MSP0001	Carbonate	0.93		0.00		0.00	0.00	0.00	0.00	1.64
4000529	OnZaP-1	45.65	45.65	MSP0001	Carbonate	0.39		0.00		0.00	0.64	0.00	0.00	1.51
4000030	OnZaP-3	4.38	46.63	MSP0001	Carbonate	0.71		0.00		0.00	0.00	0.00	0.00	2.43
4000536	OnZaP-1	46.70	46.70	MSP0001	Mudstone	0.00		0.00		0.00	0.00	0.00	0.00	0.93
4000037	OnZaP-3	5.02	47.27	MSP0001	Carbonate	0.65		0.00		0.00	0.00	0.00	0.00	3.33
4000543	OnZaP-1	47.65	47.65	MSP0001	Carbonate	0.00		0.00		0.00	0.00	0.00	0.00	2.69
4000045	OnZaP-3	5.89	48.14	MSP0001	Carbonate	0.80		0.00		0.00	0.00	0.00	0.00	2.63
4000553	OnZaP-1	48.61	48.61	MSP0001	Mudstone	0.00		0.00		0.00	0.00	0.00	0.00	0.68
4000053	OnZaP-3	6.67	48.92	MSP0001	Mudstone	0.00		0.00		0.00	0.00	0.00	0.00	0.27
4000561	OnZaP-1	49.29	49.29	MSP0001	Carbonate	0.00		0.00		0.00	11.92	0.00	0.00	4.91
4000061	OnZaP-3	7.28	49.53	MSP0001	Carbonate	0.52		0.00		0.00	0.00	0.00	0.00	2.57
4000563	OnZaP-1	50.43	50.43	MSP0001	Mudstone	0.00		0.00		0.00	0.00	0.00	0.00	1.05
4000065	OnZaP-3	8.44	50.69	MSP0001	Mudstone	0.15		0.00		0.00	0.00	0.00	0.00	9.71
4000571	OnZaP-1	50.77	50.77	MSP0001	Carbonate	0.00		0.00		0.00	6.25	0.00	0.00	4.50
4000575	OnZaP-1	51.41	51.41	MSP0001	Mudstone	0.32		0.00		0.00	0.00	0.00	0.00	0.00
4000080	OnZaP-3	9.31	51.56	MSP0001	Carbonate	0.52		0.00		0.00	0.95	0.00	0.00	2.23
4000583	OnZaP-1	52.16	52.16	MSP0001	Carbonate	0.47		0.00		0.00	1.42	0.00	0.00	3.75
4000090	OnZaP-3	10.14	52.39	MSP0001	Carbonate	1.37		0.00		0.00	1.13	0.00	0.00	3.23
4000592	OnZaP-1	52.92	52.92	MSP0001	Carbonate	0.18		0.00		0.00	2.88	0.00	0.00	3.77
4000098	OnZaP-3	10.70	52.95	MSP0001	Carbonate	0.71		0.00		0.00	1.55	0.00	0.00	3.35
4000948	OnZaP-1	53.12	53.12	MSP0010	Mudstone	18.30			30.20					
4000100	OnZaP-3	11.33	53.58	MSP0001	Mudstone	11.20		0.00		0.00	0.00	0.00	0.00	5.58
4000593	OnZaP-1	53.70	53.70	MSP0001	Mudstone	0.32		0.00		0.00	0.00	0.00	0.00	2.41
4000102	OnZaP-3	12.16	54.41	MSP0001	Mudstone	0.02		0.00		0.00	0.00	0.00	0.00	2.98
4000594	OnZaP-1	55.14	55.14	MSP0001	Mudstone	0.19		0.00		0.00	0.00	0.00	0.00	3.43
4000966	OnZaP-3	13.11	55.36	MSP0010	Mudstone									
4000597	OnZaP-1	55.51	55.51	MSP0001	Carbonate	0.31		0.00		0.00	0.00	0.00	0.00	3.20
4000103	OnZaP-3	13.29	55.54	MSP0001	Mudstone	0.14		0.00		0.00	0.00	0.00	0.00	3.50
4000601	OnZaP-1	55.68	55.68	MSP0001	Mudstone	0.26		0.00		0.00	0.00	0.00	0.00	5.13
4000950	OnZaP-1	55.80	55.80	MSP0010	Mudstone				31.30					
4000602	OnZaP-1	56.17	56.17	MSP0001	Mudstone	0.46		0.00		0.00	0.00	0.00	0.00	2.56
4000108	OnZaP-3	14.31	56.56	MSP0001	Mudstone	0.10		0.00		0.00	0.00	0.00	0.00	24.44
4000605	OnZaP-1	56.89	56.89	MSP0001	Carbonate	0.23		0.00		0.00	11.65	0.00	0.00	4.08
4000969	OnZaP-3	14.69	56.94	MSP0010	Mudstone				53.50					
4000113	OnZaP-3	14.85	57.10	MSP0001	Mudstone	0.18		0.00		0.00	0.00	0.00	0.00	2.68
4000614	OnZaP-1	57.64	57.64	MSP0001	Carbonate	0.16		0.00		0.00	3.98	0.00	0.00	6.55
4000618	OnZaP-1	58.41	58.41	MSP0001	Mudstone	0.24		0.00		0.00	0.00	0.00	0.00	3.81
4000115	OnZaP-3	16.92	59.17	MSP0001	Mudstone	0.15		0.00		0.00	0.00	0.00	0.00	4.63
4000619	OnZaP-1	59.67	59.67	MSP0001	Mudstone	0.12		0.00		0.00	0.00	0.00	0.00	6.01
4000122	OnZaP-3	17.55	59.80	MSP0001	Mudstone	0.05		0.00		0.00	0.00	0.00	0.00	11.58
4000623	OnZaP-1	60.18	60.18	MSP0001	Mudstone	0.23		0.00		0.00	0.00	0.00	0.00	21.70
4000128	OnZaP-3	18.65	60.90	MSP0001	Carbonate	0.86		0.00		0.00	2.06	0.00	0.00	4.84

Sample ID	Drill site	Core depth (m)	Comb. depth (m)	Sample set	Lithology	Apatite (wt.%)	Rutile (wt.%)	Anastase (wt.%)	Graphite (wt.%)	Hematite (wt.%)	Talc (wt.%)	Hornblende (wt.%)	Biotite (wt.%)	Phlogopite (wt.%)
4000129	OnZaP-3	18.97	61.22	MSP0001	Mudstone	0.00		0.00		0.00	0.00	0.00	0.00	4.04
4000130	OnZaP-3	20.13	62.38	MSP0001	Mudstone	0.16		0.00		0.00	0.00	0.00	0.00	9.64
4000132	OnZaP-3	20.90	63.15	MSP0001	Mudstone	0.00		0.00		0.00	0.00	0.00	0.00	2.69
4000976	OnZaP-3	21.12	63.37	MSP0010	Mudstone				16.30					
4000133	OnZaP-3	21.96	64.21	MSP0001	Mudstone	0.08		0.00		0.00	0.00	0.00	0.00	4.80
4000134	OnZaP-3	23.12	65.37	MSP0001	Mudstone	0.00		0.00		0.00	0.00	0.00	0.00	5.84
4000135	OnZaP-3	24.26	66.51	MSP0001	Carbonate	0.36		0.00		0.00	0.00	0.00	0.00	7.72
4000980	OnZaP-3	24.91	67.16	MSP0010	Mudstone	0.50	1.90		9.60					
4000151	OnZaP-3	25.18	67.43	MSP0001	Carbonate	0.82		0.00		0.00	0.00	0.00	0.00	4.18
4000981	OnZaP-3	25.59	67.84	MSP0010	Mudstone	0.80	2.50		5.40					
4000159	OnZaP-3	25.76	68.01	MSP0001	Mudstone	0.00		0.00		0.00	0.00	0.00	0.00	32.57
4000168	OnZaP-3	26.56	68.81	MSP0001	Mudstone	7.40		0.00		0.00	0.00	0.00	0.00	49.94
4000178	OnZaP-3	27.32	69.57	MSP0001	Carbonate	0.59		0.00		0.00	1.96	0.00	0.00	7.34
4000179	OnZaP-3	28.13	70.38	MSP0001	Mudstone	0.04		0.00		0.00	0.00	0.00	0.00	2.71
4000180	OnZaP-3	29.20	71.45	MSP0001	Mudstone	0.05		0.00		0.00	0.00	0.00	0.00	2.69
4000181	OnZaP-3	30.59	72.84	MSP0001	Mudstone	10.73		0.00		0.00	0.00	0.00	0.00	16.52
4000187	OnZaP-3	31.63	73.88	MSP0001	Mudstone	0.13		0.00		0.00	0.00	0.00	0.00	3.52
4000190	OnZaP-3	32.36	74.61	MSP0001	Carbonate	0.73		0.00		0.00	0.00	0.00	0.00	5.29
4000201	OnZaP-3	33.24	75.49	MSP0001	Mudstone	0.04		0.00		0.00	0.00	0.00	0.00	17.52
4000202	OnZaP-3	34.29	76.54	MSP0001	Mudstone	0.08		0.00		0.00	0.00	0.00	0.00	3.28
4000203	OnZaP-3	34.96	77.21	MSP0001	Mudstone	0.00		0.00		0.00	0.00	0.00	0.00	6.16
4000214	OnZaP-3	36.54	78.79	MSP0001	Carbonate	0.15		0.00		0.00	1.99	0.00	0.00	8.56
4000216	OnZaP-3	37.30	79.55	MSP0001	Carbonate	0.33		0.00		0.00	1.35	0.00	0.00	5.91
4000225	OnZaP-3	38.42	80.67	MSP0001	Mudstone	0.58		0.00		0.00	0.00	0.00	0.00	12.88
4000231	OnZaP-3	39.25	81.50	MSP0001	Mudstone	0.00		0.00		0.00	0.00	0.00	0.00	26.98
4000239	OnZaP-3	40.20	82.45	MSP0001	Mudstone	0.00		0.00		0.00	0.00	0.00	0.00	21.14
4000244	OnZaP-3	41.09	83.34	MSP0001	Mudstone	0.24		0.00		0.00	3.60	0.00	0.00	16.09
4000251	OnZaP-3	42.32	84.57	MSP0001	Carbonate	0.21		0.00		0.00	6.57	0.00	0.00	13.64
4000256	OnZaP-3	43.12	85.37	MSP0001	Carbonate	0.35		0.00		0.00	15.15	0.00	0.00	9.55
4000264	OnZaP-3	44.02	86.27	MSP0001	Mudstone	0.00		0.00		0.00	0.00	0.00	0.00	20.19
4000265	OnZaP-3	44.82	87.07	MSP0001	Mudstone	0.00		0.00		0.00	0.00	0.00	0.00	7.45
4000266	OnZaP-3	45.87	88.12	MSP0001	Mudstone	0.00		0.00		0.00	0.00	0.00	0.00	7.41
4000991	OnZaP-3	46.11	88.36	MSP0010	Mudstone				6.90					
4000267	OnZaP-3	46.59	88.84	MSP0001	Mudstone	0.00		0.00		0.00	0.00	0.00	0.00	7.41
4000993	OnZaP-3	47.86	90.11	MSP0010	Mudstone				6.40					
4000268	OnZaP-3	48.02	90.27	MSP0001	Mudstone	0.06		0.00		0.00	0.00	0.00	0.00	4.38
4000269	OnZaP-3	49.00	91.25	MSP0001	Mudstone	0.00		0.00		0.00	0.00	0.00	0.00	3.65
4000270	OnZaP-3	49.68	91.93	MSP0001	Mudstone	0.13		0.00		0.00	0.00	0.00	0.00	6.22
4000271	OnZaP-3	50.28	92.53	MSP0001	Mudstone	0.00		0.00		0.00	0.00	0.00	0.00	5.66
4000273	OnZaP-3	50.99	93.24	MSP0001	Mudstone	0.02		0.00		0.00	0.00	0.00	0.00	7.35
4000279	OnZaP-3	52.53	94.78	MSP0001	Mudstone	0.00		0.00		0.00	0.00	0.00	0.00	8.10
4000280	OnZaP-3	53.02	95.27	MSP0001	Mudstone	0.00		0.00		0.00	0.00	0.00	0.00	6.27
4000281	OnZaP-3	54.02	96.27	MSP0001	Mudstone	0.00		0.00		0.00	0.00	0.00	0.00	12.05
4000288	OnZaP-3	55.01	97.26	MSP0001	Mudstone	0.24		0.00		0.00	0.00	0.00	0.00	13.96
4000289	OnZaP-3	55.60	97.85	MSP0001	Mudstone	0.05		0.00		0.00	0.00	0.00	0.00	7.05

Sample ID	Drill site	Core depth (m)	Comb. depth (m)	Sample set	Lithology	Apatite (wt.%)	Rutile (wt.%)	Anastase (wt.%)	Graphite (wt.%)	Hematite (wt.%)	Talc (wt.%)	Hornblende (wt.%)	Biotite (wt.%)	Phlogopite (wt.%)
4000290	OnZaP-3	56.52	98.77	MSP0001	Mudstone	0.00		0.00		0.00	0.00	0.00	0.00	5.24
4000291	OnZaP-3	58.24	100.49	MSP0001	Mudstone	0.00		0.00		0.00	0.00	0.00	0.00	4.15
4000299	OnZaP-3	58.87	101.12	MSP0001	Carbonate	0.96		0.00		0.00	10.30	0.00	0.00	9.58
4000306	OnZaP-3	59.95	102.20	MSP0001	Mudstone	0.31		0.00		0.00	0.00	0.00	0.00	5.13

Table A3c: X-ray diffraction mineral abundances in drill cores OnZaP-1 and OnZaP-3, continued.

Sample ID	Drill site	Depth (m)	Combined depth (m)	Sample set	Lithology	Ankerite (wt.%)	Annite (wt.%)	Kaolinite (wt.%)	Illite/ muscovite (wt.%)	Illite-smectite (wt.%)	Chlorite (wt.%)
4000319	OnZaP-1	1.96	1.96	MSP0001	Mudstone	0.33	15.36	0.00	18.04	0.00	1.90
4000320	OnZaP-1	2.85	2.85	MSP0001	Mudstone	0.36	13.35	0.00	16.47	0.00	2.44
4000321	OnZaP-1	3.92	3.92	MSP0001	Mudstone	0.59	13.38	0.00	17.48	0.00	0.00
4000322	OnZaP-1	5.31	5.31	MSP0001	Mudstone	0.51	12.43	0.00	16.72	0.00	0.70
4000332	OnZaP-1	7.96	7.96	MSP0001	Mudstone	30.14	4.11	0.00	9.65	0.00	2.09
4000336	OnZaP-1	8.35	8.35	MSP0001	Mudstone	3.80	2.94	0.00	32.98	0.00	4.02
4000342	OnZaP-1	8.74	8.74	MSP0001	Mudstone	34.08	0.00	0.00	6.92	0.00	0.00
4000345	OnZaP-1	9.58	9.58	MSP0001	Mudstone	4.98	2.97	0.00	25.90	0.00	0.43
4000347	OnZaP-1	11.86	11.86	MSP0001	Mudstone	0.40	5.03	0.00	33.39	0.00	1.93
4000348	OnZaP-1	12.39	12.39	MSP0001	Mudstone	0.27	5.03	0.00	28.29	0.00	3.56
4000349	OnZaP-1	13.16	13.16	MSP0001	Mudstone	38.47	0.00	0.00	1.54	0.00	0.00
4000351	OnZaP-1	13.4	13.4	MSP0001	Mudstone	30.28	0.00	0.00	1.82	0.00	0.00
4000358	OnZaP-1	14.65	14.65	MSP0001	Mudstone	0.43	0.00	0.00	22.44	0.00	0.00
4000362	OnZaP-1	15.26	15.26	MSP0001	Mudstone	19.16	0.00	0.00	9.36	0.00	0.00
4000368	OnZaP-1	16.29	16.29	MSP0001	Mudstone	33.30	0.00	0.00	0.33	0.00	0.00
4000376	OnZaP-1	17.36	17.36	MSP0001	Mudstone	32.71	0.00	0.00	0.85	0.00	0.00
4000383	OnZaP-1	17.9	17.9	MSP0001	Mudstone	29.07	0.00	0.00	1.94	0.00	0.00
4000392	OnZaP-1	19.08	19.08	MSP0001	Mudstone	0.00	0.00	0.00	25.60	0.00	0.00
4000393	OnZaP-1	19.99	19.99	MSP0001	Mudstone	0.62	0.00	0.00	23.41	0.00	0.00
4000394	OnZaP-1	20.66	20.66	MSP0001	Mudstone	0.18	0.00	0.00	31.14	0.00	0.00
4000395	OnZaP-1	21.94	21.94	MSP0001	Mudstone	0.39	0.00	0.00	15.63	0.00	0.00
4000398	OnZaP-1	23.03	23.03	MSP0001	Mudstone	0.19	0.00	0.00	12.63	0.00	0.00
4000403	OnZaP-1	24.31	24.31	MSP0001	Mudstone	15.33	0.00	0.00	15.05	0.00	0.00
4000406	OnZaP-1	25.03	25.03	MSP0001	Mudstone	27.13	0.00	0.00	3.64	0.00	0.00
4000413	OnZaP-1	26.8	26.8	MSP0001	Mudstone	3.07	0.00	0.00	40.15	0.00	0.00
4000414	OnZaP-1	27.77	27.77	MSP0001	Mudstone	16.42	0.00	0.00	22.49	0.00	0.00
4000429	OnZaP-1	29.28	29.28	MSP0001	Carbonate	29.47	0.00	0.00	0.44	0.00	0.00
4000436	OnZaP-1	30.79	30.79	MSP0001	Mudstone	0.00	0.00	0.00	35.56	0.00	0.00
4000442	OnZaP-1	31.21	31.21	MSP0001	Carbonate	12.92	0.00	0.00	0.29	0.00	0.00
4000447	OnZaP-1	31.86	31.86	MSP0001	Mudstone	0.00	0.00	0.00	32.27	0.00	0.00
4000933	OnZaP-1	32.19	32.19	MSP0010	Mudstone						
4000455	OnZaP-1	33.15	33.15	MSP0001	Carbonate	8.89	0.00	0.00	1.77	0.00	0.00
4000466	OnZaP-1	33.96	33.96	MSP0001	Carbonate	9.28	0.00	0.00	0.21	0.00	0.00
4000471	OnZaP-1	34.64	34.64	MSP0001	Carbonate	6.84	0.00	0.00	1.03	0.00	0.00
4000483	OnZaP-1	36.52	36.52	MSP0001	Mudstone	0.00	0.00	0.00	24.21	0.00	0.00
4000484	OnZaP-1	36.94	36.94	MSP0001	Carbonate	11.57	0.00	0.00	0.71	0.00	0.00
4000491	OnZaP-1	38.13	38.13	MSP0001	Mudstone	0.71	0.00	0.00	31.47	0.00	0.00
4000936	OnZaP-1	38.91	38.91	MSP0010	Mudstone						
4000492	OnZaP-1	38.97	38.97	MSP0001	Mudstone	0.85	0.00	0.00	28.63	0.00	0.00
4000494	OnZaP-1	41.15	41.15	MSP0001	Mudstone	0.06	0.00	0.00	20.26	0.00	0.00
4000500	OnZaP-1	42.04	42.04	MSP0001	Carbonate	12.52	0.00	0.00	0.03	0.00	0.00

Sample ID	Drill site	Depth (m)	Combined depth (m)	Sample set	Lithology	Ankerite (wt.%)	Annite (wt.%)	Kaolinite (wt.%)	Illite/ muscovite (wt.%)	Illite-smectite (wt.%)	Chlorite (wt.%)
4000504	OnZaP-1	42.45	42.45	MSP0001	Mudstone	0.00	0.00	0.00	8.05	0.00	1.52
4000516	OnZaP-1	43.94	43.94	MSP0001	Carbonate	7.47	0.00	0.00	0.41	0.00	0.00
4000005	OnZaP-3	2.1	44.35	MSP0001	Carbonate	6.57	0.00	0.00	0.95	0.00	0.00
4000521	OnZaP-1	44.53	44.53	MSP0001	Carbonate	5.23	0.00	0.00	0.67	0.00	0.00
4000015	OnZaP-3	3.12	45.37	MSP0001	Carbonate	8.65	0.00	0.00	0.72	0.00	0.00
4000529	OnZaP-1	45.65	45.65	MSP0001	Carbonate	5.93	0.00	0.00	1.23	0.00	0.00
4000030	OnZaP-3	4.38	46.63	MSP0001	Carbonate	9.08	0.00	0.00	0.41	0.00	0.00
4000536	OnZaP-1	46.7	46.7	MSP0001	Mudstone	0.00	0.00	0.00	0.00	0.00	0.00
4000037	OnZaP-3	5.02	47.27	MSP0001	Carbonate	4.81	0.00	0.00	0.58	0.00	0.00
4000543	OnZaP-1	47.65	47.65	MSP0001	Carbonate	7.62	0.00	0.00	0.84	0.00	0.00
4000045	OnZaP-3	5.89	48.14	MSP0001	Carbonate	4.02	0.00	0.00	0.41	0.00	0.00
4000553	OnZaP-1	48.61	48.61	MSP0001	Mudstone	0.00	0.00	0.00	0.47	0.00	0.00
4000053	OnZaP-3	6.67	48.92	MSP0001	Mudstone	0.00	0.00	0.00	0.00	0.00	0.00
4000561	OnZaP-1	49.29	49.29	MSP0001	Carbonate	3.28	0.00	0.00	2.26	0.00	0.00
4000061	OnZaP-3	7.28	49.53	MSP0001	Carbonate	4.91	0.00	0.00	0.35	0.00	0.00
4000563	OnZaP-1	50.43	50.43	MSP0001	Mudstone	0.00	0.00	0.00	0.41	0.00	0.00
4000065	OnZaP-3	8.44	50.69	MSP0001	Mudstone	0.22	0.00	0.00	2.14	0.00	0.00
4000571	OnZaP-1	50.77	50.77	MSP0001	Carbonate	3.22	0.00	0.00	2.06	0.00	0.00
4000575	OnZaP-1	51.41	51.41	MSP0001	Mudstone	0.00	0.00	0.00	24.62	0.00	2.27
4000080	OnZaP-3	9.31	51.56	MSP0001	Carbonate	7.26	0.00	0.00	0.36	0.00	0.00
4000583	OnZaP-1	52.16	52.16	MSP0001	Carbonate	3.14	0.00	0.00	0.10	0.00	0.00
4000090	OnZaP-3	10.14	52.39	MSP0001	Carbonate	7.40	0.00	0.00	0.92	0.00	0.00
4000592	OnZaP-1	52.92	52.92	MSP0001	Carbonate	4.70	0.00	0.00	0.38	0.00	0.00
4000098	OnZaP-3	10.7	52.95	MSP0001	Carbonate	5.23	0.00	0.00	0.57	0.00	0.00
4000948	OnZaP-1	53.12	53.12	MSP0010	Mudstone						
4000100	OnZaP-3	11.33	53.58	MSP0001	Mudstone	0.00	0.00	0.00	11.85	0.00	0.00
4000593	OnZaP-1	53.7	53.7	MSP0001	Mudstone	0.04	0.00	0.00	9.43	0.00	0.00
4000102	OnZaP-3	12.16	54.41	MSP0001	Mudstone	0.00	0.00	0.00	12.33	0.00	0.00
4000594	OnZaP-1	55.14	55.14	MSP0001	Mudstone	0.00	0.00	0.00	5.98	0.00	0.00
4000966	OnZaP-3	13.11	55.36	MSP0010	Mudstone						
4000597	OnZaP-1	55.51	55.51	MSP0001	Carbonate	0.00	0.00	0.00	0.00	0.00	0.00
4000103	OnZaP-3	13.29	55.54	MSP0001	Mudstone	0.00	0.00	0.00	8.83	0.00	0.00
4000601	OnZaP-1	55.68	55.68	MSP0001	Mudstone	0.00	0.00	0.00	8.07	0.00	0.00
4000950	OnZaP-1	55.8	55.8	MSP0010	Mudstone						
4000602	OnZaP-1	56.17	56.17	MSP0001	Mudstone	0.00	0.00	0.00	8.15	0.00	0.00
4000108	OnZaP-3	14.31	56.56	MSP0001	Mudstone	0.47	0.00	0.00	3.86	0.00	0.00
4000605	OnZaP-1	56.89	56.89	MSP0001	Carbonate	1.19	0.00	0.00	3.30	0.00	0.00
4000969	OnZaP-3	14.69	56.94	MSP0010	Mudstone						
4000113	OnZaP-3	14.85	57.1	MSP0001	Mudstone	0.00	0.00	0.00	6.79	0.00	0.00
4000614	OnZaP-1	57.64	57.64	MSP0001	Carbonate	12.85	0.00	0.00	0.72	0.00	0.00
4000618	OnZaP-1	58.41	58.41	MSP0001	Mudstone	0.00	0.00	0.00	16.14	0.00	0.00
4000115	OnZaP-3	16.92	59.17	MSP0001	Mudstone	0.07	0.00	0.00	24.06	0.00	0.00
4000619	OnZaP-1	59.67	59.67	MSP0001	Mudstone	0.01	0.00	0.00	11.89	0.00	0.00
4000122	OnZaP-3	17.55	59.8	MSP0001	Mudstone	0.00	0.00	0.00	3.63	0.00	0.00

Sample ID	Drill site	Depth (m)	Combined depth (m)	Sample set	Lithology	Ankerite (wt.%)	Annite (wt.%)	Kaolinite (wt.%)	Illite/ muscovite (wt.%)	Illite-smectite (wt.%)	Chlorite (wt.%)
4000623	OnZaP-1	60.18	60.18	MSP0001	Mudstone	0.07	0.00	0.00	1.88	0.00	0.00
4000128	OnZaP-3	18.65	60.9	MSP0001	Carbonate	11.32	0.00	0.00	1.05	0.00	0.00
4000129	OnZaP-3	18.97	61.22	MSP0001	Mudstone	0.00	0.00	0.00	19.24	0.00	0.00
4000130	OnZaP-3	20.13	62.38	MSP0001	Mudstone	0.00	0.00	0.00	14.82	0.00	0.00
4000132	OnZaP-3	20.9	63.15	MSP0001	Mudstone	0.00	0.00	0.00	12.29	0.00	0.00
4000976	OnZaP-3	21.12	63.37	MSP0010	Mudstone						
4000133	OnZaP-3	21.96	64.21	MSP0001	Mudstone	0.12	0.00	0.00	16.48	0.00	0.00
4000134	OnZaP-3	23.12	65.37	MSP0001	Mudstone	0.14	0.00	0.00	34.28	0.00	0.00
4000135	OnZaP-3	24.26	66.51	MSP0001	Carbonate	9.27	0.00	0.00	0.81	0.00	0.00
4000980	OnZaP-3	24.91	67.16	MSP0010	Mudstone						
4000151	OnZaP-3	25.18	67.43	MSP0001	Carbonate	12.64	0.00	0.00	0.25	0.00	0.00
4000981	OnZaP-3	25.59	67.84	MSP0010	Mudstone						
4000159	OnZaP-3	25.76	68.01	MSP0001	Mudstone	0.00	0.00	0.00	3.62	0.00	13.31
4000168	OnZaP-3	26.56	68.81	MSP0001	Mudstone	0.00	0.00	0.00	5.33	0.00	11.48
4000178	OnZaP-3	27.32	69.57	MSP0001	Carbonate	2.60	0.00	0.00	0.59	0.00	1.25
4000179	OnZaP-3	28.13	70.38	MSP0001	Mudstone	0.00	0.00	0.00	2.12	0.00	0.70
4000180	OnZaP-3	29.2	71.45	MSP0001	Mudstone	0.06	0.00	0.00	12.76	0.00	0.00
4000181	OnZaP-3	30.59	72.84	MSP0001	Mudstone	0.01	0.00	0.00	5.19	0.00	0.00
4000187	OnZaP-3	31.63	73.88	MSP0001	Mudstone	0.00	0.00	0.00	7.05	0.00	0.00
4000190	OnZaP-3	32.36	74.61	MSP0001	Carbonate	2.69	0.00	0.00	0.47	0.00	0.00
4000201	OnZaP-3	33.24	75.49	MSP0001	Mudstone	0.00	0.00	0.00	2.23	0.00	0.00
4000202	OnZaP-3	34.29	76.54	MSP0001	Mudstone	0.00	0.00	0.00	12.60	0.00	0.00
4000203	OnZaP-3	34.96	77.21	MSP0001	Mudstone	0.07	0.00	0.00	10.93	0.00	0.00
4000214	OnZaP-3	36.54	78.79	MSP0001	Carbonate	1.93	0.00	0.00	0.62	0.00	2.73
4000216	OnZaP-3	37.3	79.55	MSP0001	Carbonate	2.39	0.00	0.00	0.41	0.00	1.49
4000225	OnZaP-3	38.42	80.67	MSP0001	Mudstone	1.79	0.00	0.00	0.83	0.00	1.86
4000231	OnZaP-3	39.25	81.5	MSP0001	Mudstone	0.36	0.00	0.00	2.21	0.00	2.52
4000239	OnZaP-3	40.2	82.45	MSP0001	Mudstone	0.00	0.00	0.00	3.48	0.00	3.62
4000244	OnZaP-3	41.09	83.34	MSP0001	Mudstone	1.23	0.00	0.00	1.14	0.00	2.98
4000251	OnZaP-3	42.32	84.57	MSP0001	Carbonate	0.77	0.00	0.00	0.97	0.00	2.81
4000256	OnZaP-3	43.12	85.37	MSP0001	Carbonate	0.60	0.00	0.00	0.86	0.00	0.00
4000264	OnZaP-3	44.02	86.27	MSP0001	Mudstone	0.00	0.00	0.00	3.32	0.00	0.00
4000265	OnZaP-3	44.82	87.07	MSP0001	Mudstone	0.07	0.00	0.00	13.10	0.00	0.00
4000266	OnZaP-3	45.87	88.12	MSP0001	Mudstone	0.05	0.00	0.00	5.76	0.00	0.00
4000991	OnZaP-3	46.11	88.36	MSP0010	Mudstone						
4000267	OnZaP-3	46.59	88.84	MSP0001	Mudstone	0.04	0.00	0.00	8.77	0.00	0.00
4000993	OnZaP-3	47.86	90.11	MSP0010	Mudstone						
4000268	OnZaP-3	48.02	90.27	MSP0001	Mudstone	0.05	0.00	0.00	12.12	0.00	0.00
4000269	OnZaP-3	49	91.25	MSP0001	Mudstone	0.03	0.00	0.00	5.73	0.00	0.00
4000270	OnZaP-3	49.68	91.93	MSP0001	Mudstone	0.03	0.00	0.00	7.13	0.00	0.00
4000271	OnZaP-3	50.28	92.53	MSP0001	Mudstone	0.00	0.00	0.00	12.65	0.00	0.00
4000273	OnZaP-3	50.99	93.24	MSP0001	Mudstone	0.00	0.00	0.00	4.25	0.00	0.00
4000279	OnZaP-3	52.53	94.78	MSP0001	Mudstone	0.09	0.00	0.00	16.47	0.00	0.00
4000280	OnZaP-3	53.02	95.27	MSP0001	Mudstone	0.01	0.00	0.00	11.63	0.00	0.00

Sample ID	Drill site	Depth (m)	Combined depth (m)	Sample set	Lithology	Ankerite (wt.%)	Annite (wt.%)	Kaolinite (wt.%)	Illite/ muscovite (wt.%)	Illite-smectite (wt.%)	Chlorite (wt.%)
4000281	OnZaP-3	54.02	96.27	MSP0001	Mudstone	0.00	0.00	0.00	3.71	0.00	0.00
4000288	OnZaP-3	55.01	97.26	MSP0001	Mudstone	0.00	0.00	0.00	3.44	0.00	0.00
4000289	OnZaP-3	55.6	97.85	MSP0001	Mudstone	0.00	0.00	0.00	6.97	0.00	0.00
4000290	OnZaP-3	56.52	98.77	MSP0001	Mudstone	0.02	0.00	0.00	11.88	0.00	0.00
4000291	OnZaP-3	58.24	100.49	MSP0001	Mudstone	0.02	0.00	0.00	12.79	0.00	0.00
4000299	OnZaP-3	58.87	101.12	MSP0001	Carbonate	2.55	0.00	0.00	1.70	0.00	0.00
4000306	OnZaP-3	59.95	102.2	MSP0001	Mudstone	0.00	0.00	0.00	13.87	0.00	0.00

Table A4: Isotope ratios in drill cores OnZaP-1 and OnZaP-3.

Sample ID	Drill site	Core depth (m)	Combined depth (m)	Sample set	Lithology	δ56Fe	δ56Fe 2SD	δ57Fe	δ98Mo	δ98Mo 2SD
4000925	OnZaP-1	12.15	12.15	MSP0010	Mudstone	-0.18	0.08	-0.28		
4000928	OnZaP-1	23.84	23.84	MSP0010	Mudstone	0.18	0.08	0.29		
4000931	OnZaP-1	30.66	30.66	MSP0010	Mudstone	0.07	0.07	0.11	0.28	0.09
4000933	OnZaP-1	32.19	32.19	MSP0010	Mudstone	0.10	0.08	0.14		
4000934	OnZaP-1	36.40	36.40	MSP0010	Mudstone	-0.16	0.08	-0.28		
4000935	OnZaP-1	37.83	37.83	MSP0010	Mudstone	-0.36	0.08	-0.52		
4000936	OnZaP-1	38.91	38.91	MSP0010	Mudstone	-0.33	0.07	-0.51	0.81	0.10
4000940	OnZaP-1	42.42	42.42	MSP0010	Mudstone	-0.11	0.07	-0.20	0.77	0.09
4000943	OnZaP-1	46.36	46.36	MSP0010	Mudstone	-0.53	0.08	-0.80	1.49	0.14
4000955	OnZaP-3	5.14	47.39	MSP0010	Mudstone	-0.37	0.08	-0.53	0.98	0.08
4000959	OnZaP-3	8.40	50.65	MSP0010	Mudstone	-0.22	0.07	-0.32		
4000948	OnZaP-1	53.12	53.12	MSP0010	Mudstone	-0.19	0.07	-0.27	1.11	0.07
4000963	OnZaP-3	11.70	53.95	MSP0010	Mudstone	0.27	0.08	0.39		
4000966	OnZaP-3	13.11	55.36	MSP0010	Mudstone	-0.26	0.07	-0.38	0.82	0.09
4000950	OnZaP-1	55.80	55.80	MSP0010	Mudstone	-0.58	0.07	-0.79	0.67	0.06
4000968	OnZaP-3	14.25	56.50	MSP0010	Mudstone	0.13	0.08	0.17		
4000969	OnZaP-3	14.69	56.94	MSP0010	Mudstone	0.51	0.08	0.66		
4000951	OnZaP-1	57.93	57.93	MSP0010	Mudstone	-0.48	0.08	-0.72		
4000970	OnZaP-3	15.72	57.97	MSP0010	Mudstone	0.60	0.07	0.92	0.54	0.10
4000971	OnZaP-3	16.42	58.67	MSP0010	Mudstone	-0.49	0.07	-0.71		
4000972	OnZaP-3	16.72	58.97	MSP0010	Mudstone	-0.01	0.07	-0.01	0.78	0.11
4000973	OnZaP-3	17.89	60.14	MSP0010	Mudstone	-0.18	0.07	-0.31	0.36	0.08
4000975	OnZaP-3	20.07	62.32	MSP0010	Mudstone	-0.12	0.07	-0.14	0.71	0.07
4000976	OnZaP-3	21.12	63.37	MSP0010	Mudstone	-0.06	0.08	-0.07		
4000978	OnZaP-3	22.96	65.21	MSP0010	Mudstone	-0.02	0.08	-0.02		
4000980	OnZaP-3	24.91	67.16	MSP0010	Mudstone	-0.39	0.08	-0.58		
4000981	OnZaP-3	25.59	67.84	MSP0010	Mudstone	-0.10	0.08	-0.14		
4000982	OnZaP-3	26.20	68.45	MSP0010	Mudstone	-0.13	0.07	-0.18	-0.04	0.08
4000985	OnZaP-3	29.35	71.60	MSP0010	Mudstone	-0.39	0.08	-0.58		
4000987	OnZaP-3	31.40	73.65	MSP0010	Mudstone	-0.36	0.08	-0.54		
4000988	OnZaP-3	32.10	74.35	MSP0010	Mudstone				0.82	0.07
4000989	OnZaP-3	33.48	75.73	MSP0010	Mudstone	-0.43	0.07	-0.66		
4000991	OnZaP-3	46.11	88.36	MSP0010	Mudstone	0.00	0.08	0.00		
4000992	OnZaP-3	46.51	88.76	MSP0010	Mudstone	-0.10	0.08	-0.15		
4000993	OnZaP-3	47.86	90.11	MSP0010	Mudstone	0.10	0.08	0.15		
4000994	OnZaP-3	48.94	91.19	MSP0010	Mudstone	0.01	0.08	0.04		
4000996	OnZaP-3	55.76	98.01	MSP0010	Mudstone	0.08	0.08	0.12		
4000997	OnZaP-3	57.27	99.52	MSP0010	Mudstone	-0.10	0.08	-0.17		
4000998	OnZaP-3	58.06	100.31	MSP0010	Mudstone	0.13	0.07	0.19	-0.02	0.11

Table A5a: Element concentration data for drill core OPH.

Sample ID	Depth (m)	Sample set	Lithology	Ag (ppm)	Al (ppm)	As (ppm)	Ba (ppm)	Be (ppm)	Bi (ppm)	Ca (ppm)	Cd (ppm)	Ce (ppm)	Cl (ppm)	Co (ppm)
OPH-10	530.39	NGU	Mudstone		73,037		159			20,512		50		36.9
OPH-73	542.63	Yale2	Mudstone		61,728					15,951				
OPH-73	542.63	Yale2	Mudstone		61,728					15,951				
OPH-73	542.72	NGU	Mudstone		78,329		208			16,295		32		56.2
OPH-73	542.72	NGU	Mudstone		78,329		208			16,295		32		56.2
OPH-80	543.68	NGU	Mudstone		74,095		185			20,440		48		51.0
OPH-83	544.22	NGU	Mudstone		75,683		265			12,936		44		55.0
OPH-121	552.43	NGU	Mudstone		52,025		16			24,800		24		36.5
OPH-284	591.30	NGU	Mudstone		85,739		295			19,225		47		32.1
OPH-306	594.85	Yale2	Mudstone		61,346					18,565				
OPH-306	594.85	Yale2	Mudstone		61,346					18,565				
OPH-306	594.93	NGU	Mudstone		93,148		554			19,297		54		30.1
OPH-306	594.93	NGU	Mudstone		93,148		554			19,297		54		30.1
OPH-507	636.42	NGU	Mudstone		79,917		365			15,294		31		45.8
OPH-515	637.85	NGU	Mudstone		70,920		222			78,616		46		32.4
OPH-523	638.53	Yale2	Mudstone		39,861					52,852				
OPH-523	638.53	Yale2	Mudstone		39,861					52,852				
OPH-523	638.63	NGU	Mudstone		69,332		249			56,175		45		21.0
OPH-523	638.63	NGU	Mudstone		69,332		249			56,175		45		21.0
OPH-844	890.22	Yale2	Mudstone		35,908					11,589				
OPH-844	890.22	Yale2	Mudstone		35,908					11,589				
OPH-844	890.22	NGU	Mudstone		34,243	39	319			8,934		30	720	8.7
OPH-844	890.22	NGU	Mudstone		34,243	39	319			8,934		30	720	8.7
OPH-849	891.17	Yale1	Mudstone		22,790		373	0.51	0.41	4,737	5.25	15		39.9
OPH-849	891.17	Yale1	Mudstone		22,790		373	0.51	0.41	4,737	5.25	15		39.9
OPH-849	891.17	NGU	Mudstone		22,493	262	272			3,230			1,510	29.9
OPH-849	891.17	NGU	Mudstone		22,493	262	272			3,230			1,510	29.9
OPH-858	892.79	NGU	Mudstone		23,605	238	226			2,823		20	1,080	28.9
OPH-862	893.38	NGU	Mudstone		10,532	414	38			1,394			1,700	37.1
OPH-867	894.16	NGU	Mudstone		41,864	113	373			3,988		62	810	12.9
OPH-875	894.98	NGU	Carbonate		16,513	271	81			89,336			1,140	35.6
OPH-879	895.49	NGU	Carbonate		3,694	107				110,777			290	8.8
OPH-885	896.12	NGU												
OPH-903	897.58	NGU			28,738					10,006				
OPH-924	899.15	NGU	Carbonate		28,368		150			134,362		26	430	52.9
OPH-925	899.25	NGU	Carbonate		29,532	254	250			212,263		16	320	46.9
OPH-938	900.23	NGU	Carbonate		39,429		527			122,927		18	440	9.5
OPH-945	901.96	NGU				84	961				20.00			66.9
OPH-955	903.08	NGU	Mudstone		71,449	22	789			9,934			310	41.0
OPH-970	904.30	NGU	Mudstone		80,975	37	726			14,723		18	280	35.9
OPH-975	912.04	Yale2	Mudstone		58,241					35,443				
OPH-975	912.04	Yale2	Mudstone		58,241					35,443				

Sample ID	Depth (m)	Sample set	Lithology	Ag (ppm)	Al (ppm)	As (ppm)	Ba (ppm)	Be (ppm)	Bi (ppm)	Ca (ppm)	Cd (ppm)	Ce (ppm)	Cl (ppm)	Co (ppm)
OPH-975	912.04	Yale2	Mudstone		58,241					35,443				
OPH-975	912.19	Yale1	Mudstone		63,955		47	1.30	0.07	65,685	1.55	185		74.6
OPH-975	912.19	Yale1	Mudstone		63,955		47	1.30	0.07	65,685	1.55	185		74.6
OPH-975	912.19	Yale1	Mudstone		63,955		47	1.30	0.07	65,685	1.55	185		74.6
OPH-975	912.19	NGU	Mudstone		74,095	12	34			42,024		40	300	11.7
OPH-975	912.19	NGU	Mudstone		74,095	12	34			42,024		40	300	11.7
OPH-975	912.19	NGU	Mudstone		74,095	12	34			42,024		40	300	11.7
OPH-979	912.70	NGU	Mudstone		66,686	19	50			41,166		34		26.1
OPH-1361	1,080.00	NGU	Carbonate		12,702	13				250,856		20	640	8.8
OPH-1364	1,080.57	Acme	Carbonate	0.144	6,100	<0.2	3	<1	<0.04	193,800	0.09	5		0.4
OPH-1364	1,080.57	Yale2	Carbonate		3,353					182,335				
OPH-1364	1,080.57	Acme	Carbonate	0.144	6,100	<0.2	3	<1	<0.04	193,800	0.09	5		0.4
OPH-1364	1,080.57	Yale2	Carbonate		3,353					182,335				
OPH-1366	1,081.11	NGU	Carbonate		3,498	10				222,269			430	
OPH-1368	1,081.36	Acme	Carbonate	0.130	14,500	3	6	<1	<0.04	167,500	0.12	6		3.4
OPH-1372	1,081.93	Acme	Carbonate	0.148	11,200	2	8	<1	0.06	204,900	0.18	9		1.3
OPH-1373	1,082.28	NGU	Carbonate		11,644					237,277			1,330	
OPH-1376	1,082.71	NGU	Carbonate		3,223	18	36			219,410			760	10.0
OPH-1383	1,083.49	NGU	Carbonate		6,827		24			220,839			640	
OPH-1390	1,084.18	NGU	Carbonate		2,408		10			223,698			360	
OPH-1393	1,084.47	Yale1	Carbonate		4,172		10	0.56	-0.03	304,563	0.09	4		10.6
OPH-1393	1,084.47	Yale1	Carbonate		4,172		10	0.56	-0.03	304,563	0.09	4		10.6
OPH-1393	1,084.47	Acme	Carbonate	0.119	3,600	2	8	<1	<0.04	197,500	0.12	3		1.5
OPH-1393	1,084.47	Acme	Carbonate	0.119	3,600	2	8	<1	<0.04	197,500	0.12	3		1.5
OPH-1398	1,085.13	Acme	Carbonate	0.215	3,300	1	7	<1	<0.04	183,200	0.10	3		1.7
OPH-1400	1,085.42	Acme	Carbonate	0.124	3,000	4	9	<1	<0.04	180,100	<0.02	2		2.3
OPH-1403	1,086.33	NGU	Carbonate		3,387		18			220,839			440	
OPH-1405	1,086.52	Acme	Carbonate	0.129	3,000	<0.2	6	<1	<0.04	208,600	0.08	3		1.4
OPH-1405	1,086.52	Yale2	Carbonate		1,227					162,505				
OPH-1405	1,086.52	Yale2	Carbonate		1,227					162,505				
OPH-1405	1,086.52	Acme	Carbonate	0.129	3,000	<0.2	6	<1	<0.04	208,600	0.08	3		1.4
OPH-1412	1,087.73	Acme	Carbonate	0.114	5,600	3	6	<1	<0.04	212,400	0.04	4		1.9
OPH-1421	1,089.09	NGU	Carbonate		11,273	21				226,557		20		27.0
OPH-1426	1,089.67	Acme	Carbonate	0.199	10,700	11	5	<1	0.21	234,900	0.31	14		22.8
OPH-1434	1,090.51	NGU	Carbonate		68,803		11			55,531		50	670	21.3
OPH-1436	1,090.80	Acme	Carbonate	0.152	11,400	6	6	<1	0.22	227,900	0.03	19		12.1
OPH-1442	1,091.87	NGU	Carbonate		4,329					197,969			430	
OPH-1444	1,092.14	Acme	Carbonate	0.132	3,800	<0.2	4	<1	<0.04	189,400	0.06	4		3.0
OPH-1449	1,093.39	Yale2	Carbonate		940					157,393				
OPH-1449	1,093.39	Yale2	Carbonate		940					157,393				
OPH-1449	1,093.39	Acme	Carbonate	0.142	2,800	10	14	<1	<0.04	209,500	0.10	5		0.9
OPH-1449	1,093.39	Acme	Carbonate	0.142	2,800	10	14	<1	<0.04	209,500	0.10	5		0.9
OPH-1452	1,093.90	NGU	Carbonate		22,652		13			60,463		50	10,300	
OPH-1461	1,094.89	Acme	Carbonate	0.075	3,400	3	13	<1	<0.04	202,900	0.06	3		1.4
OPH-1464	1,095.45	Acme	Carbonate	0.139	2,400	6	39	<1	<0.04	196,500	0.03	4		0.8

Sample ID	Depth (m)	Sample set	Lithology	Ag (ppm)	Al (ppm)	As (ppm)	Ba (ppm)	Be (ppm)	Bi (ppm)	Ca (ppm)	Cd (ppm)	Ce (ppm)	Cl (ppm)	Co (ppm)
OPH-1464	1,095.45	Yale1	Carbonate		2,361		75	0.88	-0.03	246,267	0.11	4		12.0
OPH-1464	1,095.45	Acme	Carbonate	0.139	2,400	6	39	<1	<0.04	196,500	0.03	4		0.8
OPH-1464	1,095.45	Yale1	Carbonate		2,361		75	0.88	-0.03	246,267	0.11	4		12.0
OPH-1466	1,095.74	Acme	Carbonate	0.196	10,700	11	16	<1	<0.04	186,700	0.34	13		2.3
OPH-1468	1,096.29	NGU	Carbonate		32,020		29			196,540		76	980	
OPH-1469	1,096.31	Acme	Carbonate	0.144	7,300	3	19	3.00	<0.04	200,300	0.09	8		1.4
OPH-1470	1,096.57	Acme	Carbonate	0.103	3,700	2	16	<1	<0.04	188,700	0.08	8		1.6
OPH-1472	1,096.82	Acme	Carbonate	0.102	2,800	2	36	<1	<0.04	198,500	0.07	5		0.9
OPH-1479	1,098.06	Acme	Carbonate	0.203	3,200	1	19	<1	<0.04	199,200	0.09	5		1.4
OPH-1483	1,098.66	NGU	Carbonate		3,414		27			212,263			210	
OPH-1486	1,099.04	Acme	Carbonate	0.158	1,000	0	46	<1	<0.04	213,000	0.19	2		0.6
OPH-1488	1,099.51	NGU					11						270	
OPH-1491	1,099.98	Acme	Carbonate	0.166	1,400	2	7	<1	<0.04	210,400	0.17	1		0.6
OPH-1491	1,099.98	Yale1	Carbonate		865		4	0.17	-0.02	326,909	0.12	1		9.1
OPH-1491	1,099.98	Yale1	Carbonate		865		4	0.17	-0.02	326,909	0.12	1		9.1
OPH-1491	1,099.98	Acme	Carbonate	0.166	1,400	2	7	<1	<0.04	210,400	0.17	1		0.6
OPH-1499	1,101.27	Yale2	Carbonate		302					146,585				
OPH-1499	1,101.27	Yale2	Carbonate		302					146,585				
OPH-1501	1,101.45	NGU	Mudstone		73,037	79	236			1,701		150	1,150	11.5
OPH-1509	1,102.06	NGU	Mudstone		27,415	225	213			1,329		42	2,050	28.3
OPH-1516	1,102.74	NGU	Mudstone		45,145	348	431			1,365		90	1,630	45.8
OPH-1519	1,103.35	NGU	Mudstone		24,134	292	233			736		36	1,010	11.1
OPH-1527	1,104.69	Yale1	Carbonate		1,912		31	0.33	-0.03	253,039	0.28	3		14.3
OPH-1533	1,106.00	NGU	Carbonate		2,064		15			226,557			270	
OPH-1542	1,106.99	NGU	Mudstone		37,788	132	443			1,901		68	2,480	23.1
OPH-1556	1,109.44	NGU	Carbonate		5,118	21	19			187,964		34	440	
OPH-1557	1,109.57	NGU	Carbonate		794	11				205,831			400	
OPH-1557	1,109.57	Yale1	Carbonate		1,655		6	0.42	-0.01	297,322	0.26	3		17.8
OPH-1557	1,109.57	Yale1	Carbonate		1,655		6	0.42	-0.01	297,322	0.26	3		17.8
OPH-1557	1,109.57	NGU	Carbonate		794	11				205,831			400	
OPH-1560	1,109.96	Yale1	Carbonate		806		12	0.17	-0.04	119,964	0.04	1		2.5
OPH-1560	1,109.96	NGU	Carbonate		667	11	23			247,998			470	
OPH-1560	1,109.96	Yale1	Carbonate		806		12	0.17	-0.04	119,964	0.04	1		2.5
OPH-1560	1,109.96	NGU	Carbonate		667	11	23			247,998			470	
OPH-1561	1,110.18	NGU	Carbonate		900	37	28			249,427	18.00	32	430	
OPH-1499	1,110.27	Acme	Carbonate	0.148	1,400	8	27	<1	<0.04	224,400	0.10	3		0.4
OPH-1499	1,110.27	Acme	Carbonate	0.148	1,400	8	27	<1	<0.04	224,400	0.10	3		0.4
OPH-1564	1,110.79	Yale1	Carbonate		718		6	0.18	-0.02	303,807	0.10	1		10.7
OPH-1564	1,110.79	NGU	Carbonate		524	18	10			225,128			810	
OPH-1567	1,111.40	NGU	Carbonate		720	13	13			191,537			1,030	
OPH-1568	1,111.60	NGU	Carbonate		826	25	21			207,260	12.00		960	
OPH-1569	1,111.80	NGU	Carbonate		4,440	27	18			195,111		20	1,210	
OPH-1571	1,112.02	NGU	Carbonate		13,284	73	57			240,136		129	1,200	8.9
OPH-1572	1,112.08	Yale1	Mudstone		31,000		221	2.30	0.78	2,862	6.10	104		94.2
OPH-1572	1,112.08	NGU	Mudstone		33,660	573	116			2,073		74	4,870	74.1

Sample ID	Depth (m)	Sample set	Lithology	Ag (ppm)	Al (ppm)	As (ppm)	Ba (ppm)	Be (ppm)	Bi (ppm)	Ca (ppm)	Cd (ppm)	Ce (ppm)	Cl (ppm)	Co (ppm)
OPH-1572	1,112.08	Acme	Mudstone	3.976	39,800	589	23	2.00	0.79	3,100	8.18	84		59.7
OPH-1572	1,112.08	NGU	Mudstone		33,660	573	116			2,073		74	4,870	74.1
OPH-1572	1,112.08	Acme	Mudstone	3.976	39,800	589	23	2.00	0.79	3,100	8.18	84		59.7
OPH-1572	1,112.08	Yale1	Mudstone		31,000		221	2.30	0.78	2,862	6.10	104		94.2
OPH-1572	1,112.08	Yale1	Mudstone		31,000		221	2.30	0.78	2,862	6.10	104		94.2
OPH-1572	1,112.08	NGU	Mudstone		33,660	573	116			2,073		74	4,870	74.1
OPH-1572	1,112.08	Acme	Mudstone	3.976	39,800	589	23	2.00	0.79	3,100	8.18	84		59.7
OPH-1573	1,112.27	Yale1	Mudstone		28,966		238	2.26	0.88	3,882	4.65	77		127.2
OPH-1573	1,112.27	Acme	Mudstone	3.521	33,000	424	48	2.00	0.79	1,700	3.69	63		55.0
OPH-1573	1,112.27	Yale1	Mudstone		28,966		238	2.26	0.88	3,882	4.65	77		127.2
OPH-1573	1,112.27	Acme	Mudstone	3.521	33,000	424	48	2.00	0.79	1,700	3.69	63		55.0
OPH-1575	1,112.65	Acme	Mudstone	3.011	33,900	342	66	2.00	0.77	1,700	4.59	56		49.6
OPH-1575	1,112.65	Yale1	Mudstone		23,854		204	1.67	0.77	2,462	4.15	70		115.3
OPH-1575	1,112.65	Yale1	Mudstone		23,854		204	1.67	0.77	2,462	4.15	70		115.3
OPH-1575	1,112.65	Acme	Mudstone	3.011	33,900	342	66	2.00	0.77	1,700	4.59	56		49.6
OPH-1578	1,113.28	Yale1	Mudstone		34,778		305	2.37	0.68	6,699	6.39	122		61.7
OPH-1578	1,113.28	Acme	Mudstone	2.424	38,800	344	21	2.00	0.52	3,500	7.06	96		40.6
OPH-1578	1,113.28	Acme	Mudstone	2.424	38,800	344	21	2.00	0.52	3,500	7.06	96		40.6
OPH-1578	1,113.28	Yale1	Mudstone		34,778		305	2.37	0.68	6,699	6.39	122		61.7
OPH-1579	1,113.58	NGU	Mudstone		40,541	487	343			14,151		149	2,120	50.4
OPH-1580	1,113.63	Acme	Mudstone	2.732	39,200	281	16	1.00	0.73	1,100	5.61	81		56.9
OPH-1580	1,113.63	Yale1	Mudstone		32,849		290	1.87	0.82	2,310	4.25	105		84.4
OPH-1580	1,113.63	Acme	Mudstone	2.732	39,200	281	16	1.00	0.73	1,100	5.61	81		56.9
OPH-1580	1,113.63	Yale1	Mudstone		32,849		290	1.87	0.82	2,310	4.25	105		84.4
OPH-1581	1,113.83	Yale1	Mudstone		28,097		248	1.50	0.63	2,880	3.27	90		62.9
OPH-1581	1,113.83	Acme	Mudstone	2.421	32,600	299	113	1.00	0.73	2,000	3.52	72		55.1
OPH-1581	1,113.83	Acme	Mudstone	2.421	32,600	299	113	1.00	0.73	2,000	3.52	72		55.1
OPH-1581	1,113.83	Yale1	Mudstone		28,097		248	1.50	0.63	2,880	3.27	90		62.9
OPH-1582	1,113.92	NGU	Mudstone		35,513	337	292			4,617		83	2,270	72.9
OPH-1584	1,114.20	Yale1	Mudstone		20,515		173	1.02	0.27	3,248	2.96	36		74.7
OPH-1584	1,114.20	Acme	Mudstone	1.669	22,200	226	100	1.00	0.44	1,500	5.67	41		39.7
OPH-1584	1,114.20	Acme	Mudstone	1.669	22,200	226	100	1.00	0.44	1,500	5.67	41		39.7
OPH-1584	1,114.20	Yale1	Mudstone		20,515		173	1.02	0.27	3,248	2.96	36		74.7
OPH-1585	1,114.34	Yale1	Mudstone		24,317		190	1.41	0.38	3,748	3.27	39		100.9
OPH-1585	1,114.34	Yale2	Mudstone		24,590					29,813				
OPH-1585	1,114.34	Yale2	Mudstone		24,590					29,813				
OPH-1585	1,114.34	Yale2	Mudstone		24,590					29,813				
OPH-1585	1,114.34	Acme	Mudstone	1.815	26,900	343	38	1.00	0.48	1,300	4.15	36		55.2
OPH-1585	1,114.34	Acme	Mudstone	1.815	26,900	343	38	1.00	0.48	1,300	4.15	36		55.2
OPH-1585	1,114.34	Acme	Mudstone	1.815	26,900	343	38	1.00	0.48	1,300	4.15	36		55.2
OPH-1585	1,114.34	Yale1	Mudstone		24,317		190	1.41	0.38	3,748	3.27	39		100.9
OPH-1585	1,114.34	Yale1	Mudstone		24,317		190	1.41	0.38	3,748	3.27	39		100.9
OPH-1586	1,114.62	NGU	Mudstone		40,435	342	359			1,079		66	3,730	72.1
OPH-1587	1,114.77	Acme	Mudstone	1.672	50,800	255	23	1.00	0.34	1,200	2.48	41		58.9
OPH-1587	1,114.77	Yale1	Mudstone		52,569		359	2.34	0.28	2,914	2.47	38		138.0

Sample ID	Depth (m)	Sample set	Lithology	Ag (ppm)	Al (ppm)	As (ppm)	Ba (ppm)	Be (ppm)	Bi (ppm)	Ca (ppm)	Cd (ppm)	Ce (ppm)	Cl (ppm)	Co (ppm)
OPH-1587	1,114.77	Yale1	Mudstone		52,569		359	2.34	0.28	2,914	2.47	38		138.0
OPH-1587	1,114.77	Acme	Mudstone	1.672	50,800	255	23	1.00	0.34	1,200	2.48	41		58.9
OPH-1588	1,115.02	Yale1	Mudstone		22,134		171	0.84	0.33	2,317	2.00	27		99.9
OPH-1588	1,115.02	Yale1	Mudstone		22,134		171	0.84	0.33	2,317	2.00	27		99.9
OPH-1588	1,115.02	Acme	Mudstone	0.457	7,400	101	55	<1	0.10	300	0.48	8		21.5
OPH-1588	1,115.02	Acme	Mudstone	0.457	7,400	101	55	<1	0.10	300	0.48	8		21.5
OPH-1589	1,115.21	NGU	Mudstone		38,529	353	341			1,043		77	4,000	78.3
OPH-1590	1,115.59	NGU	Carbonate		519	29	14			222,269			280	
OPH-1592	1,115.87	NGU	Mudstone		33,766	262	155			1,651		62	4,010	60.4
OPH-1596	1,116.61	NGU	Carbonate		450	18	14			220,125				
OPH-1596	1,116.65	Yale1	Carbonate		239		9	0.15	-0.05	111,970	0.09	2		7.0
OPH-1599	1,117.43	NGU	Carbonate		22,917	275	168			822		19	2,570	64.9
OPH-1601	1,117.48	Acme	Mudstone	2.299	66,100	274	24	4.00	0.23	10,400	3.74	44		54.2
OPH-1606	1,118.27	Yale1	Mudstone		31,387		242	1.43	0.32	2,609	1.96	47		110.9
OPH-1606	1,118.27	Yale1	Mudstone		31,387		242	1.43	0.32	2,609	1.96	47		110.9
OPH-1606	1,118.27	Acme	Mudstone	2.067	30,500	290	29	<1	0.33	1,500	1.12	48		70.9
OPH-1606	1,118.27	Acme	Mudstone	2.067	30,500	290	29	<1	0.33	1,500	1.12	48		70.9
OPH-1608	1,118.59	NGU	Mudstone		32,866	201	267			2,037		76	4,500	42.8
OPH-1613	1,119.54	NGU	Mudstone		84,151	79	572			1,787		36	4,370	44.1
OPH-1647	1,120.31	Yale2	Mudstone		33,055					2,285				
OPH-1647	1,120.31	Yale2	Mudstone		33,055					2,285				
OPH-1647	1,120.31	Yale2	Mudstone		33,055					2,285				
OPH-1617	1,120.31	Acme	Mudstone	0.371	77,100	38	243	4.00	<0.04	1,700	2.61	6		13.7
OPH-1617	1,120.31	Yale1	Mudstone		97,813		653	4.44	-0.01	4,322	2.34	11		48.5
OPH-1617	1,120.31	Yale1	Mudstone		97,813		653	4.44	-0.01	4,322	2.34	11		48.5
OPH-1617	1,120.31	Acme	Mudstone	0.371	77,100	38	243	4.00	<0.04	1,700	2.61	6		13.7
OPH-1621	1,120.77	NGU	Mudstone		70,920	63	417			7,140		30	2,750	28.9
OPH-1624	1,121.15	NGU	Mudstone		61,922	59	502			3,481		34	2,490	40.5
OPH-1625	1,121.37	Acme	Mudstone	1.268	30,000	206	26	2.00	0.31	4,000	1.63	45		23.2
OPH-1625	1,121.37	Yale1	Mudstone		27,071		211	1.18	0.29	3,552	1.78	48		55.2
OPH-1625	1,121.37	Yale1	Mudstone		27,071		211	1.18	0.29	3,552	1.78	48		55.2
OPH-1625	1,121.37	Acme	Mudstone	1.268	30,000	206	26	2.00	0.31	4,000	1.63	45		23.2
OPH-1626	1,121.70	NGU	Mudstone		52,396	134	398			1,286		117	3,040	22.9
OPH-1634	1,123.13	NGU	Mudstone		50,543	101	111			26,444		19	320	26.4
OPH-1640	1,123.62	NGU	Mudstone		36,042	280	311			1,858		44	3,310	68.8
OPH-1647	1,124.27	Yale1	Mudstone		62,016		521	2.77	0.16	3,716	3.54	235		93.1
OPH-1647	1,124.27	Yale1	Mudstone		62,016		521	2.77	0.16	3,716	3.54	235		93.1
OPH-1647	1,124.27	Yale1	Mudstone		62,016		521	2.77	0.16	3,716	3.54	235		93.1
OPH-1647	1,124.27	Acme	Mudstone	0.910	119,300	82	333	6.00	0.24	1,900	4.67	373		8.6
OPH-1647	1,124.27	Acme	Mudstone	0.910	119,300	82	333	6.00	0.24	1,900	4.67	373		8.6
OPH-1647	1,124.27	Acme	Mudstone	0.910	119,300	82	333	6.00	0.24	1,900	4.67	373		8.6
OPH-1651	1,124.55	NGU	Mudstone		24,928	185	238			1,222		44	2,040	49.5
OPH-1655	1,125.02	NGU	Mudstone		21,329	135	28			173,670		23	250	13.0
OPH-1676	1,127.22	NGU	Mudstone		22,229	117	219			1,294		19	1,880	19.5
OPH-1683	1,135.64	NGU	Carbonate		8,098		41			170,811			630	10.0

Sample ID	Depth (m)	Sample set	Lithology	Ag (ppm)	Al (ppm)	As (ppm)	Ba (ppm)	Be (ppm)	Bi (ppm)	Ca (ppm)	Cd (ppm)	Ce (ppm)	Cl (ppm)	Co (ppm)
OPH-1697	1,136.81	Yale2	Mudstone		19,781					105,555				
OPH-1697	1,136.81	Yale2	Mudstone		19,781					105,555				
OPH-1697	1,137.01	NGU	Mudstone		28,685		107			125,071		30	250	14.6
OPH-1697	1,137.01	NGU	Mudstone		28,685		107			125,071		30	250	14.6
OPH-1704	1,137.78	NGU	Carbonate		24,293		104			104,345		26	250	4.4
OPH-1709	1,138.18	NGU	Carbonate		34,666		124			102,915		33		14.7
OPH-1729	1,145.99	NGU	Mudstone		27,468	26	298			9,863		18	1,340	6.8
OPH-1746	1,159.50	NGU	Mudstone		29,532	167	283			1,429	15.00	25	720	7.6
OPH-1752	1,160.27	NGU	Mudstone		29,638	149	276			3,702		26	680	11.9
OPH-1761	1,161.32	Yale2	Mudstone		32,570					1,306				
OPH-1761	1,161.32	Yale2	Mudstone		32,570					1,306				
OPH-1761	1,161.32	NGU	Mudstone		35,089	111	310			2,451		28	640	7.6
OPH-1761	1,161.32	NGU	Mudstone		35,089	111	310			2,451		28	640	7.6
OPH-1765	1,161.95	NGU	Mudstone		30,273	88	168			50,386	23.00	24		9.4
OPH-1768	1,162.23	NGU	Mudstone		33,607	243	305			3,945	11.00	37	970	10.1
OPH-1779	1,166.13	NGU	Mudstone		38,688		210			85,763		96		5.2
OPH-1796	1,175.69	NGU	Mudstone		51,708	110	607			3,516		65	1,070	24.0
OPH-1809	1,187.30	NGU	Mudstone		48,744	40	469			24,299		44	800	16.6
OPH-1809	1,187.30	Yale2	Mudstone		48,124					7,752				
OPH-1809	1,187.30	Yale2	Mudstone		48,124					7,752				
OPH-1809	1,187.30	NGU	Mudstone		48,744	40	469			24,299		44	800	16.6
OPH-1814	1,187.91	NGU	Mudstone		40,329	26	349			57,533		42	680	16.4
OPH-1823	1,188.90	NGU	Mudstone		28,580	28	150			92,910		36	280	32.6
OPH-1831	1,190.01	NGU	Carbonate		35,354		258			103,630		34	280	21.2
OPH-1835	1,190.75	NGU	Carbonate		58,747		324			80,760		20	450	29.5
OPH-1849	1,198.41	NGU	Mudstone		79,388	39	857			4,831		37	1,110	44.9
OPH-1856	1,199.56	NGU	Carbonate		28,791		133			146,512		28	640	
OPH-1862	1,200.64	NGU	Carbonate		36,518		244			143,653		42	250	
OPH-1865	1,201.25	NGU	Carbonate		56,630		474			125,786		100	500	
OPH-1871	1,202.50	NGU	Carbonate		22,969		79			152,229		34	710	
OPH-1879	1,203.59	NGU	Mudstone		50,861		681			45,597		151	1,300	6.9
OPH-1885	1,204.44	NGU	Mudstone		73,566	10	994			10,935		35	1,310	18.0
OPH-1892	1,205.03	NGU	Mudstone		76,212		1,330			4,624		38	2,400	15.0
OPH-1904	1,206.20	NGU	Mudstone		49,009	14	586			2,108		31	1,960	23.9
OPH-1918	1,207.63	Yale2	Mudstone		58,332					2,408				
OPH-1918	1,207.63	Yale2	Mudstone		58,332					2,408				
OPH-1918	1,207.63	NGU	Mudstone		60,335		939			3,623		72	1,890	10.8
OPH-1918	1,207.63	NGU	Mudstone		60,335		939			3,623		72	1,890	10.8
OPH-1924	1,208.96	NGU	Carbonate		34,719		623			136,506		42	2,550	
OPH-1927	1,209.45	NGU	Carbonate		42,763	35	767			117,209		46	950	12.7
OPH-1939	1,211.12	NGU	Mudstone		45,251		726			5,282		51	2,380	13.3
OPH-1942	1,211.51	NGU	Mudstone		45,886		687			2,166		39	3,270	8.8
OPH-1948	1,212.51	NGU	Carbonate		8,468		27			323,755		64	700	4.2
OPH-1960	1,214.11	NGU	Mudstone		55,571		896			23,370		18	420	12.6
OPH-1962	1,214.28	NGU	Mudstone		71,449		1,360			53,888		80	610	36.1

Sample ID	Depth (m)	Sample set	Lithology	Ag (ppm)	Al (ppm)	As (ppm)	Ba (ppm)	Be (ppm)	Bi (ppm)	Ca (ppm)	Cd (ppm)	Ce (ppm)	Cl (ppm)	Co (ppm)
OPH-1975	1,215.53	NGU	Carbonate		6,404		18			257,289			760	4.5
OPH-1984	1,216.89	NGU	Mudstone		26,939		328			32,804		62	310	6.7
OPH-1994	1,217.74	NGU	Mudstone		47,421		694			3,531		37	460	8.4
OPH-2001	1,218.36	NGU	Carbonate		6,827		17			333,046		17	370	7.1
OPH-2001	1,218.36	Yale2	Carbonate		5,708					185,829				
OPH-2001	1,218.36	NGU	Carbonate		6,827		17			333,046		17	370	7.1
OPH-2001	1,218.36	Yale2	Carbonate		5,708					185,829				
OPH-2010	1,219.18	NGU	Carbonate		9,262		1,640			453,829			550	30.4
OPH-2027	1,220.85	NGU	Mudstone		32,655		398			7,862		21	330	4.2
OPH-2040	1,221.72	NGU	Mudstone		64,569		1,670			10,863		25		16.3
OPH-2052	1,223.79	NGU	Mudstone		49,538	11	696			3,273		135		25.4
OPH-2061	1,225.13	Yale2	Mudstone		41,589					8,287				
OPH-2061	1,225.13	Yale2	Mudstone		41,589					8,287				
OPH-2061	1,225.13	NGU	Mudstone		76,212		79			9,148		20	220	36.6
OPH-2061	1,225.13	NGU	Mudstone		76,212		79			9,148		20	220	36.6
OPH-2068	1,226.04	NGU	Mudstone		39,906	31	12			10,863		29	260	11.8
OPH-2069	1,226.21	NGU	Carbonate		30,591	24	18			96,483		52	220	28.4
OPH-2397	1,426.19	NGU	Mudstone		40,752		355			17,796			10,700	19.5
OPH-2406	1,427.09	Yale2	Mudstone		37,035					10,782				
OPH-2406	1,427.09	Yale2	Mudstone		37,035					10,782				
OPH-2406	1,427.16	NGU	Mudstone		36,730		460			12,721			8,780	31.0
OPH-2406	1,427.16	NGU	Mudstone		36,730		460			12,721			8,780	31.0
OPH-2413	1,427.81	NGU	Mudstone		44,298		513			18,653			8,230	27.8
OPH-2423	1,437.13	NGU	Mudstone		67,215	66	21			37,736				95.6
OPH-2426	1,437.68	NGU	Mudstone		49,114		31			30,446				20.3
OPH-2993	1,765.27	NGU	Carbonate		42,181					158,661			370	21.3
OPH-3009	1,767.41	NGU	Carbonate		32,655	76	25			142,938			600	62.9
OPH-3016	1,777.38	Yale2	Mudstone		25,129					5,997				
OPH-3016	1,777.38	Yale2	Mudstone		25,129					5,997				
OPH-3016	1,777.46	NGU	Mudstone		39,535	35	513			22,227		132	2,890	34.4
OPH-3016	1,777.46	NGU	Mudstone		39,535	35	513			22,227		132	2,890	34.4
OPH-3057	1,792.05	NGU			51,602					8,576				
OPH-3112	1,868.46	NGU	Mudstone		62,452		79			6,897			4,500	16.0
OPH-3117	1,869.18	NGU	Mudstone		73,566		64			4,874			2,120	8.7
OPH-3132	1,871.00	Yale2	Mudstone		50,428					6,225				
OPH-3132	1,871.00	Yale2	Mudstone		50,428					6,225				
OPH-3132	1,871.00	NGU	Mudstone		60,864		395			6,511			4,660	13.9
OPH-3132	1,871.00	NGU	Mudstone		60,864		395			6,511			4,660	13.9
OPH-3141	1,871.27	NGU	Mudstone		57,159		546			6,053		267	4,750	27.8
OPH-3137	1,871.47	NGU	Mudstone		62,452	36	425			6,103		15	3,200	32.2
OPH-3161	1,881.50	NGU	Mudstone		76,741	36	2,300			5,746		50	1,850	18.0
OPH-3168	1,887.61	NGU	Mudstone		77,271		3,150			5,918		45	1,100	
OPH-3179	1,888.77	NGU	Carbonate		2,678	18	30			205,831				5.1
OPH-3182	1,889.14	NGU			40,858					81,475				
OPH-3191	1,902.61	Yale2	Mudstone		62,643					30,114				

Sample ID	Depth (m)	Sample set	Lithology	Ag (ppm)	Al (ppm)	As (ppm)	Ba (ppm)	Be (ppm)	Bi (ppm)	Ca (ppm)	Cd (ppm)	Ce (ppm)	Cl (ppm)	Co (ppm)
OPH-3194	1,902.88	NGU	Mudstone		74,624		779			26,444		50		11.6
OPH-3229	1,915.60	NGU	Mudstone		76,741					33,876				
OPH-3256	1,926.73	Yale2	Mudstone		55,669					20,653				
OPH-3256	1,926.73	Yale2	Mudstone		55,669					20,653				
OPH-3256	1,926.80	NGU	Mudstone		73,566		473			20,011	11.00	39		28.9
OPH-3256	1,926.80	NGU	Mudstone		73,566		473			20,011	11.00	39		28.9
OPH-3272	1,935.31	NGU	Mudstone		74,624		370			21,012		54		39.6
OPH-3275	1,935.54	NGU	Mudstone		71,978		352			28,230		55		36.8
OPH-3295	1,946.55	NGU	Mudstone		59,805		310			53,316		52		24.6
OPH-3324	1,957.85	NGU	Mudstone		74,624		327			21,012		57		20.8
OPH-3331	1,958.63	NGU	Mudstone		83,092		400			18,868		49		9.0
OPH-3355	1,970.85	Yale2	Mudstone		62,974					5,143				
OPH-3355	1,970.85	Yale2	Mudstone		62,974					5,143				
OPH-3355	1,970.85	NGU	Mudstone		86,268		471			4,667		62		19.9
OPH-3355	1,970.85	NGU	Mudstone		86,268		471			4,667		62		19.9
OPH-3386	1,980.42	NGU	Carbonate		50,279		300			87,907		52		14.0
OPH-3411	1,991.90	NGU			50,067					90,051				
OPH-3463	2,011.35	Yale2	Mudstone		54,204					79,892				
OPH-3589	2,052.57	Yale2	Mudstone		47,882					50,809				
OPH-3707	2,103.47	Yale2	Mudstone		20,064					102,109				
OPH-3736	2,205.38	Yale1	Carbonate		1,245		48		0.09	-0.01	172,110	0.04	2	16.7
OPH-3904	2,252.09	Yale1	Carbonate		203		281		0.05	-0.04	80,748	0.04	0	7.0
OPH-4022	2,285.28	Yale2	Carbonate		1,985						130,353			
OPH-4081	2,305.25	Yale1	Carbonate		136		1,917		0.09	-0.03	45,674	0.02	0	15.3
OPH-4142	2,324.43	Yale1	Carbonate		544		261		0.07	-0.01	260,586	0.29	1	2.5
OPH-4178	2,328.55	Yale1	Carbonate		339		4		0.27	-0.02	7,723	0.04	1	9.3
OPH-4178	2,328.55	Acme	Carbonate	0.078	300	3	15	<1		<0.04	2,300	0.04	0	3.9
OPH-4183	2,329.14	Acme	Carbonate	0.094	5,300	2	3	<1		<0.04	180,700	0.31	3	1.1
OPH-4185	2,329.34	Acme		0.057		0	8	<1		<0.04	185,400	0.27	0	0.3
OPH-4187	2,329.62	Acme		0.050		4	62	<1		<0.04	181,700	0.31	0	0.3
OPH-4193	2,330.28	Yale2	Evaporite		56						39,091			
OPH-4194	2,330.34	Yale1	Carbonate		469		7		0.25	-0.02	51,843	0.03	1	3.2
OPH-4194	2,330.34	Acme	Carbonate	0.109	100	4	1	<1		<0.04	25,900	0.06	0	2.0
OPH-4194	2,330.34	Acme	Carbonate	0.109	100	4	1	<1		<0.04	25,900	0.06	0	2.0
OPH-4194	2,330.34	Yale1	Carbonate		469		7		0.25	-0.02	51,843	0.03	1	3.2
OPH-4199	2,330.85	Acme	Evaporite	0.058	300	3	3	<1		<0.04	128,900	0.11	1	0.2
OPH-4211	2,509.02	Yale1	Evaporite		65		1		0.03		33,653	0.01	0	0.5
OPH-4257	2,517.36	Yale1	Evaporite		8,102		5		0.18	-0.03	240,787	0.01	2	11.0
OPH-4310	2,526.68	Yale1	Evaporite		5,063		3		0.14	-0.01	1,785	0.02	10	29.3
OPH-4366	2,547.78	Yale1	Evaporite		12,700		81		0.38	-0.01	65,266	0.03	1	5.8
OPH-4383	2,549.45	Yale2	Mudstone		25,891						49,724			
OPH-4440	2,570.15	Yale1	Evaporite		139		1		0.02	-0.02	119,128	0.02	1	0.7
OPH-4537	2,700.97	Yale1	Evaporite		35		1			-0.03	24,466		0	0.5
OPH-4582	2,724.31	Yale2	Evaporite		6,400						112,107			
OPH-4635	2,833.79	Yale1	Evaporite		603		77		0.02	-0.03	109,161		11	2.9

Sample ID	Depth (m)	Sample set	Lithology	Ag (ppm)	Al (ppm)	As (ppm)	Ba (ppm)	Be (ppm)	Bi (ppm)	Ca (ppm)	Cd (ppm)	Ce (ppm)	Cl (ppm)	Co (ppm)
OPH-4620	2,838.14	Yale2	Evaporite		1,076					117,603				
OPH-4683	2,850.46	Yale1	Evaporite		3,289		129	0.08	-0.03	70,433	0.19	5		1.5
OPH-4683	2,850.46	Yale1	Evaporite		3,289		129	0.08	-0.03	70,433	0.19	5		1.5
OPH-4683	2,850.46	Yale2	Evaporite		583					6,926				
OPH-4683	2,850.46	Yale2	Evaporite		583					6,926				
OPH-4774	2,878.31	Yale1	Evaporite		2,092		32	0.03	-0.03	174,874	0.01	11		2.9
OPH-4813	2,896.20	Yale1	Evaporite		3,202		21	0.07	-0.03	38,673	0.01	2		0.5
OPH-4853	2,904.34	Yale1	Evaporite		1,562		15	0.04	-0.02	32,572	0.01	2		0.4

Table A5b: Element concentration data for drill core OPH, continued.

Sample ID	Depth (m)	Sample set	Lithology	Cr (ppm)	Cs (ppm)	Cu (ppm)	Dy (ppm)	Er (ppm)	Eu (ppm)	F (ppm)	Fe (ppm)	Ga (ppm)	Gd (ppm)	Hf (ppm)
OPH-10	530.39	NGU	Mudstone	270.0		78.0					74,839	16.7		
OPH-73	542.63	Yale2	Mudstone	719.0							107,394			
OPH-73	542.63	Yale2	Mudstone	719.0							107,394			
OPH-73	542.72	NGU	Mudstone	767.0		99.4					107,712	26.3		5.6
OPH-73	542.72	NGU	Mudstone	767.0		99.4					107,712	26.3		5.6
OPH-80	543.68	NGU	Mudstone	495.0		99.8					86,029	19.6		
OPH-83	544.22	NGU	Mudstone	1,120.0		157.0					104,914	26.6		
OPH-121	552.43	NGU	Mudstone	408.0		70.2					65,047	14.1		
OPH-284	591.30	NGU	Mudstone	117.0		41.7					73,440	20.2		5.9
OPH-306	594.85	Yale2	Mudstone	95.5							80,187			
OPH-306	594.85	Yale2	Mudstone	95.5							80,187			
OPH-306	594.93	NGU	Mudstone	90.0		11.1					77,636	22.2		7.9
OPH-306	594.93	NGU	Mudstone	90.0		11.1					77,636	22.2		7.9
OPH-507	636.42	NGU	Mudstone	157.0		208.0					69,943	15.8		5.5
OPH-515	637.85	NGU	Mudstone	270.0		66.9					73,440	15.5		
OPH-523	638.53	Yale2	Mudstone	119.6							54,554			
OPH-523	638.53	Yale2	Mudstone	119.6							54,554			
OPH-523	638.63	NGU	Mudstone	146.0		54.7					54,695	12.8		
OPH-523	638.63	NGU	Mudstone	146.0		54.7					54,695	12.8		
OPH-844	890.22	Yale2	Mudstone	45.6							27,910			
OPH-844	890.22	Yale2	Mudstone	45.6							27,910			
OPH-844	890.22	NGU	Mudstone	80.9		10.3					34,761	9.2		
OPH-844	890.22	NGU	Mudstone	80.9		10.3					34,761	9.2		
OPH-849	891.17	Yale1	Mudstone	41.9		70.1	3.8	2.2	1.0		164,945		3.7	2.0
OPH-849	891.17	Yale1	Mudstone	41.9		70.1	3.8	2.2	1.0		164,945		3.7	2.0
OPH-849	891.17	NGU	Mudstone	66.6		75.6					190,943	4.4		
OPH-849	891.17	NGU	Mudstone	66.6		75.6					190,943	4.4		
OPH-858	892.79	NGU	Mudstone	54.9		49.2					185,348	5.0		
OPH-862	893.38	NGU	Mudstone	66.3		109.0					285,366	4.8		
OPH-867	894.16	NGU	Mudstone	105.0		63.1					109,110	10.6		
OPH-875	894.98	NGU	Carbonate	92.2		138.0					217,521	4.9		
OPH-879	895.49	NGU	Carbonate	10.9		67.7					214,024			
OPH-885	896.12	NGU												
OPH-903	897.58	NGU									164,365			
OPH-924	899.15	NGU	Carbonate	53.2		258.0					156,671	12.4		
OPH-925	899.25	NGU	Carbonate	46.8	14.0	509.0					149,677	10.7		
OPH-938	900.23	NGU	Carbonate	147.0		17.3					36,300	11.9		
OPH-945	901.96	NGU		1,020.0		80.5						15.8		
OPH-955	903.08	NGU	Mudstone	128.0		223.0					79,735	15.4		
OPH-970	904.30	NGU	Mudstone	191.0		60.3					79,035	16.7		
OPH-975	912.04	Yale2	Mudstone	60.2							48,183			
OPH-975	912.04	Yale2	Mudstone	60.2							48,183			

Sample ID	Depth (m)	Sample set	Lithology	Cr (ppm)	Cs (ppm)	Cu (ppm)	Dy (ppm)	Er (ppm)	Eu (ppm)	F (ppm)	Fe (ppm)	Ga (ppm)	Gd (ppm)	Hf (ppm)
OPH-975	912.04	Yale2	Mudstone	60.2							48,183			
OPH-975	912.19	Yale1	Mudstone	145.7		30.6	8.7	5.4	1.9		48,065		8.8	5.1
OPH-975	912.19	Yale1	Mudstone	145.7		30.6	8.7	5.4	1.9		48,065		8.8	5.1
OPH-975	912.19	Yale1	Mudstone	145.7		30.6	8.7	5.4	1.9		48,065		8.8	5.1
OPH-975	912.19	NGU	Mudstone	87.6		55.9					48,610	22.6		6.2
OPH-975	912.19	NGU	Mudstone	87.6		55.9					48,610	22.6		6.2
OPH-975	912.19	NGU	Mudstone	87.6		55.9					48,610	22.6		6.2
OPH-979	912.70	NGU	Mudstone	134.0		92.0					63,927	21.7		
OPH-1361	1,080.00	NGU	Carbonate	16.5							21,612	4.1		
OPH-1364	1,080.57	Acme	Carbonate	6.0	<0.1		0.6	0.6	0.5	0.2	4,800	1.9	0.5	0.5
OPH-1364	1,080.57	Yale2	Carbonate	5.2							5,179			
OPH-1364	1,080.57	Acme	Carbonate	6.0	<0.1		0.6	0.6	0.5	0.2	4,800	1.9	0.5	0.5
OPH-1364	1,080.57	Yale2	Carbonate	5.2							5,179			
OPH-1366	1,081.11	NGU	Carbonate	12.3							3,812			
OPH-1368	1,081.36	Acme	Carbonate	7.0		0.1	1.2	0.7	0.5	0.1	8,200	4.1	0.9	1.3
OPH-1372	1,081.93	Acme	Carbonate	15.0		0.1	1.1	0.8	0.6	0.3	7,000	3.4	0.9	0.6
OPH-1373	1,082.28	NGU	Carbonate	28.2							6,379	3.6		
OPH-1376	1,082.71	NGU	Carbonate	27.5		12.0					11,051			
OPH-1383	1,083.49	NGU	Carbonate	35.7		10.1					10,351			
OPH-1390	1,084.18	NGU	Carbonate	13.4							3,980			
OPH-1393	1,084.47	Yale1	Carbonate	13.2		5.5	0.3	0.2	0.2		5,166		0.4	0.3
OPH-1393	1,084.47	Yale1	Carbonate	13.2		5.5	0.3	0.2	0.2		5,166		0.4	0.3
OPH-1393	1,084.47	Acme	Carbonate	10.0	<0.1	4.1	0.3	0.1	0.1		3,700	1.3	0.3	0.2
OPH-1393	1,084.47	Acme	Carbonate	10.0	<0.1	4.1	0.3	0.1	0.1		3,700	1.3	0.3	0.2
OPH-1398	1,085.13	Acme	Carbonate	8.0	<0.1	4.2	0.1	0.1	<0.1		6,200	1.0	0.1	0.2
OPH-1400	1,085.42	Acme	Carbonate	7.0	<0.1	5.9	0.2	0.1	<0.1		10,100	0.9	0.2	0.1
OPH-1403	1,086.33	NGU	Carbonate	14.0							6,882			
OPH-1405	1,086.52	Acme	Carbonate	7.0	<0.1	1.9	0.1	0.1	0.2		4,300	1.0	0.1	0.2
OPH-1405	1,086.52	Yale2	Carbonate	5.1							3,275			
OPH-1405	1,086.52	Yale2	Carbonate	5.1							3,275			
OPH-1405	1,086.52	Acme	Carbonate	7.0	<0.1	1.9	0.1	0.1	0.2		4,300	1.0	0.1	0.2
OPH-1412	1,087.73	Acme	Carbonate	10.0	<0.1	2.3	0.2	0.2	0.2		6,400	1.8	0.2	0.3
OPH-1421	1,089.09	NGU	Carbonate	23.0		12.1				2,100	13,849			
OPH-1426	1,089.67	Acme	Carbonate	34.0	<0.1	23.9	1.7	0.8	0.3		41,200	3.0	2.0	1.5
OPH-1434	1,090.51	NGU	Carbonate	140.0		14.7				3,600	46,931	19.4		
OPH-1436	1,090.80	Acme	Carbonate	35.0		0.1	15.0	3.7	1.8	0.6	17,800	3.4	3.9	1.2
OPH-1442	1,091.87	NGU	Carbonate	9.3						2,000	6,449			
OPH-1444	1,092.14	Acme	Carbonate	9.0	<0.1	5.2	1.2	0.6	0.1		7,700	1.3	1.0	0.3
OPH-1449	1,093.39	Yale2	Carbonate	4.3							4,190			
OPH-1449	1,093.39	Yale2	Carbonate	4.3							4,190			
OPH-1449	1,093.39	Acme	Carbonate	7.0	<0.1	3.6	0.4	0.2	0.1		5,100	1.0	0.2	0.2
OPH-1449	1,093.39	Acme	Carbonate	7.0	<0.1	3.6	0.4	0.2	0.1		5,100	1.0	0.2	0.2
OPH-1452	1,093.90	NGU	Carbonate	76.7						2,300	12,450	11.6		
OPH-1461	1,094.89	Acme	Carbonate	9.0		0.4	2.7	0.2	0.1	<0.1	4,100	0.9	0.2	0.2
OPH-1464	1,095.45	Acme	Carbonate	5.0		0.2	3.5	1.0	0.7	0.2	3,900	0.7	1.1	0.1

Sample ID	Depth (m)	Sample set	Lithology	Cr (ppm)	Cs (ppm)	Cu (ppm)	Dy (ppm)	Er (ppm)	Eu (ppm)	F (ppm)	Fe (ppm)	Ga (ppm)	Gd (ppm)	Hf (ppm)
OPH-1464	1,095.45	Yale1	Carbonate	4.7		4.3	1.9	1.5	0.4		3,776		1.6	0.2
OPH-1464	1,095.45	Acme	Carbonate	5.0	0.2	3.5	1.0	0.7	0.2		3,900	0.7	1.1	0.1
OPH-1464	1,095.45	Yale1	Carbonate	4.7		4.3	1.9	1.5	0.4		3,776		1.6	0.2
OPH-1466	1,095.74	Acme	Carbonate	15.0	1.5	8.3	2.3	1.5	0.4		7,000	4.5	2.7	0.4
OPH-1468	1,096.29	NGU	Carbonate	11.4						2,900	8,253	23.4		5.2
OPH-1469	1,096.31	Acme	Carbonate	14.0	1.1	4.5	2.3	2.0	0.2		4,000	3.4	2.3	0.4
OPH-1470	1,096.57	Acme	Carbonate	7.0	0.5	3.1	0.5	0.3	0.1		3,900	1.4	0.7	0.3
OPH-1472	1,096.82	Acme	Carbonate	7.0	0.3	3.3	0.7	0.6	0.1		2,300	1.0	0.7	0.2
OPH-1479	1,098.06	Acme	Carbonate	7.0	0.7	2.6	0.3	0.2	0.1		3,500	1.2	0.5	0.2
OPH-1483	1,098.66	NGU	Carbonate	11.0						2,100	4,301			
OPH-1486	1,099.04	Acme	Carbonate	5.0	0.2	1.6	0.3	0.3	<0.1		800	0.3	0.5	0.0
OPH-1488	1,099.51	NGU		7.0						2,200				
OPH-1491	1,099.98	Acme	Carbonate	6.0	0.3	2.5	0.2	0.1	<0.1		800	0.4	0.2	0.1
OPH-1491	1,099.98	Yale1	Carbonate	4.0		2.9	0.2	0.1	0.1		1,192		0.2	0.1
OPH-1491	1,099.98	Yale1	Carbonate	4.0		2.9	0.2	0.1	0.1		1,192		0.2	0.1
OPH-1491	1,099.98	Acme	Carbonate	6.0	0.3	2.5	0.2	0.1	<0.1		800	0.4	0.2	0.1
OPH-1499	1,101.27	Yale2	Carbonate	2.5							2,303			
OPH-1499	1,101.27	Yale2	Carbonate	2.5							2,303			
OPH-1501	1,101.45	NGU	Mudstone	41.7	12.0	51.3					50,778	12.0		15.4
OPH-1509	1,102.06	NGU	Mudstone	138.0		154.0					55,115	11.2		5.9
OPH-1516	1,102.74	NGU	Mudstone	164.0		113.0					97,220	12.6		5.5
OPH-1519	1,103.35	NGU	Mudstone	147.0		121.0					24,200	5.1		
OPH-1527	1,104.69	Yale1	Carbonate	4.4		5.4	0.5	0.4	0.1		1,033		0.5	0.2
OPH-1533	1,106.00	NGU	Carbonate	13.5							1,455			
OPH-1542	1,106.99	NGU	Mudstone	97.8		82.1					45,463	11.5		7.6
OPH-1556	1,109.44	NGU	Carbonate	68.0						4,400	1,476			
OPH-1557	1,109.57	NGU	Carbonate	19.3						2,200	629			
OPH-1557	1,109.57	Yale1	Carbonate	22.4		5.9	0.8	0.6	0.2		1,071		0.6	0.1
OPH-1557	1,109.57	Yale1	Carbonate	22.4		5.9	0.8	0.6	0.2		1,071		0.6	0.1
OPH-1557	1,109.57	NGU	Carbonate	19.3						2,200	629			
OPH-1560	1,109.96	Yale1	Carbonate	5.6		3.3	0.1	0.1	0.1		396		0.1	0.1
OPH-1560	1,109.96	NGU	Carbonate	14.1						2,600	581			
OPH-1560	1,109.96	Yale1	Carbonate	5.6		3.3	0.1	0.1	0.1		396		0.1	0.1
OPH-1560	1,109.96	NGU	Carbonate	14.1						2,600	581			
OPH-1561	1,110.18	NGU	Carbonate	17.5		5.9				4,700	2,028			
OPH-1499	1,110.27	Acme	Carbonate	4.0	<0.1	3.1	0.2	0.1	<0.1		5,400	0.5	0.3	0.1
OPH-1499	1,110.27	Acme	Carbonate	4.0	<0.1	3.1	0.2	0.1	<0.1		5,400	0.5	0.3	0.1
OPH-1564	1,110.79	Yale1	Carbonate	10.0		3.3	0.2	0.2	0.2		777		0.2	0.1
OPH-1564	1,110.79	NGU	Carbonate	19.5						2,200	622			
OPH-1567	1,111.40	NGU	Carbonate	21.4		6.5				2,900	860			
OPH-1568	1,111.60	NGU	Carbonate	22.6		81.3				3,600	986			
OPH-1569	1,111.80	NGU	Carbonate	54.2		8.9				4,600	5,686			
OPH-1571	1,112.02	NGU	Carbonate	155.0		32.3				14,400	8,883	4.8		
OPH-1572	1,112.08	Yale1	Mudstone	264.1		562.0	11.2	7.8	2.1		58,699		10.2	6.5
OPH-1572	1,112.08	NGU	Mudstone	553.0		433.0				3,500	50,568	18.1		7.0

Sample ID	Depth (m)	Sample set	Lithology	Cr (ppm)	Cs (ppm)	Cu (ppm)	Dy (ppm)	Er (ppm)	Eu (ppm)	F (ppm)	Fe (ppm)	Ga (ppm)	Gd (ppm)	Hf (ppm)
OPH-1572	1,112.08	Acme	Mudstone	268.0	3.2	401.3	10.9	7.0	2.1		51,200	13.4	9.8	5.4
OPH-1572	1,112.08	NGU	Mudstone	553.0		433.0				3,500	50,568	18.1		7.0
OPH-1572	1,112.08	Acme	Mudstone	268.0	3.2	401.3	10.9	7.0	2.1		51,200	13.4	9.8	5.4
OPH-1572	1,112.08	Yale1	Mudstone	264.1		562.0	11.2	7.8	2.1		58,699		10.2	6.5
OPH-1572	1,112.08	Yale1	Mudstone	264.1		562.0	11.2	7.8	2.1		58,699		10.2	6.5
OPH-1572	1,112.08	NGU	Mudstone	553.0		433.0				3,500	50,568	18.1		7.0
OPH-1572	1,112.08	Acme	Mudstone	268.0	3.2	401.3	10.9	7.0	2.1		51,200	13.4	9.8	5.4
OPH-1573	1,112.27	Yale1	Mudstone	251.8		156.3	9.3	6.7	1.6		61,688		8.2	4.7
OPH-1573	1,112.27	Acme	Mudstone	193.0	1.8	165.6	8.4	6.2	1.3		46,400	10.3	8.0	4.5
OPH-1573	1,112.27	Yale1	Mudstone	251.8		156.3	9.3	6.7	1.6		61,688		8.2	4.7
OPH-1573	1,112.27	Acme	Mudstone	193.0	1.8	165.6	8.4	6.2	1.3		46,400	10.3	8.0	4.5
OPH-1575	1,112.65	Acme	Mudstone	202.0	1.5	115.9	8.4	6.1	1.1		40,900	11.1	7.1	4.5
OPH-1575	1,112.65	Yale1	Mudstone	193.2		100.4	8.0	5.7	1.3		60,557		7.1	4.0
OPH-1575	1,112.65	Yale1	Mudstone	193.2		100.4	8.0	5.7	1.3		60,557		7.1	4.0
OPH-1575	1,112.65	Acme	Mudstone	202.0	1.5	115.9	8.4	6.1	1.1		40,900	11.1	7.1	4.5
OPH-1578	1,113.28	Yale1	Mudstone	283.0		328.2	13.6	8.9	2.6		54,692		13.1	6.4
OPH-1578	1,113.28	Acme	Mudstone	200.0	1.3	218.5	14.1	9.1	2.5		38,500	14.2	13.0	6.1
OPH-1578	1,113.28	Acme	Mudstone	200.0	1.3	218.5	14.1	9.1	2.5		38,500	14.2	13.0	6.1
OPH-1578	1,113.28	Yale1	Mudstone	283.0		328.2	13.6	8.9	2.6		54,692		13.1	6.4
OPH-1579	1,113.58	NGU	Mudstone	361.0		233.0					43,714	15.9		8.1
OPH-1580	1,113.63	Acme	Mudstone	143.0	1.0	122.8	8.4	5.6	1.6		62,200	11.8	7.0	5.9
OPH-1580	1,113.63	Yale1	Mudstone	168.8		172.5	8.7	5.9	1.7		82,680		8.7	6.1
OPH-1580	1,113.63	Acme	Mudstone	143.0	1.0	122.8	8.4	5.6	1.6		62,200	11.8	7.0	5.9
OPH-1580	1,113.63	Yale1	Mudstone	168.8		172.5	8.7	5.9	1.7		82,680		8.7	6.1
OPH-1581	1,113.83	Yale1	Mudstone	155.1		142.3	7.8	5.3	1.6		62,172		7.9	4.8
OPH-1581	1,113.83	Acme	Mudstone	117.0	1.0	116.4	7.7	5.7	1.6		57,000	8.9	8.0	4.9
OPH-1581	1,113.83	Acme	Mudstone	117.0	1.0	116.4	7.7	5.7	1.6		57,000	8.9	8.0	4.9
OPH-1581	1,113.83	Yale1	Mudstone	155.1		142.3	7.8	5.3	1.6		62,172		7.9	4.8
OPH-1582	1,113.92	NGU	Mudstone	252.0		179.0					76,937	12.7		5.0
OPH-1584	1,114.20	Yale1	Mudstone	114.8		111.4	3.5	2.2	0.7		28,449		3.5	2.0
OPH-1584	1,114.20	Acme	Mudstone	106.0	0.7	96.0	4.9	3.2	1.0		34,800	6.7	4.9	3.0
OPH-1584	1,114.20	Acme	Mudstone	106.0	0.7	96.0	4.9	3.2	1.0		34,800	6.7	4.9	3.0
OPH-1584	1,114.20	Yale1	Mudstone	114.8		111.4	3.5	2.2	0.7		28,449		3.5	2.0
OPH-1585	1,114.34	Yale1	Mudstone	158.5		188.5	4.9	3.4	0.8		50,924		3.9	3.2
OPH-1585	1,114.34	Yale2	Mudstone	114.0							45,397			
OPH-1585	1,114.34	Yale2	Mudstone	114.0							45,397			
OPH-1585	1,114.34	Yale2	Mudstone	114.0							45,397			
OPH-1585	1,114.34	Acme	Mudstone	114.0	0.9	146.5	5.3	3.7	0.8		45,100	9.0	4.1	3.5
OPH-1585	1,114.34	Acme	Mudstone	114.0	0.9	146.5	5.3	3.7	0.8		45,100	9.0	4.1	3.5
OPH-1585	1,114.34	Acme	Mudstone	114.0	0.9	146.5	5.3	3.7	0.8		45,100	9.0	4.1	3.5
OPH-1585	1,114.34	Yale1	Mudstone	158.5		188.5	4.9	3.4	0.8		50,924		3.9	3.2
OPH-1585	1,114.34	Yale1	Mudstone	158.5		188.5	4.9	3.4	0.8		50,924		3.9	3.2
OPH-1586	1,114.62	NGU	Mudstone	222.0		275.0					72,740	19.1		9.8
OPH-1587	1,114.77	Acme	Mudstone	86.0	0.6	205.0	7.4	6.0	1.4		52,300	14.8	6.4	8.5
OPH-1587	1,114.77	Yale1	Mudstone	119.9		268.8	6.9	5.7	1.2		64,065		5.3	8.2

Sample ID	Depth (m)	Sample set	Lithology	Cr (ppm)	Cs (ppm)	Cu (ppm)	Dy (ppm)	Er (ppm)	Eu (ppm)	F (ppm)	Fe (ppm)	Ga (ppm)	Gd (ppm)	Hf (ppm)
OPH-1587	1,114.77	Yale1	Mudstone	119.9		268.8	6.9	5.7	1.2		64,065		5.3	8.2
OPH-1587	1,114.77	Acme	Mudstone	86.0	0.6	205.0	7.4	6.0	1.4		52,300	14.8	6.4	8.5
OPH-1588	1,115.02	Yale1	Mudstone	108.5		199.1	3.9	2.9	0.7		75,127		3.1	2.8
OPH-1588	1,115.02	Yale1	Mudstone	108.5		199.1	3.9	2.9	0.7		75,127		3.1	2.8
OPH-1588	1,115.02	Acme	Mudstone	32.0	0.2	49.1	1.6	1.2	0.2		22,300	3.8	1.2	1.2
OPH-1588	1,115.02	Acme	Mudstone	32.0	0.2	49.1	1.6	1.2	0.2		22,300	3.8	1.2	1.2
OPH-1589	1,115.21	NGU	Mudstone	242.0		162.0					53,436	16.6		7.3
OPH-1590	1,115.59	NGU	Carbonate	8.0							4,504			
OPH-1592	1,115.87	NGU	Mudstone	244.0		105.0				3,100	47,211	16.7		7.5
OPH-1596	1,116.61	NGU	Carbonate	11.2		10.7					12,380			
OPH-1596	1,116.65	Yale1	Carbonate	2.0		4.4	0.3	0.2	0.2		6,132		0.3	0.1
OPH-1599	1,117.43	NGU	Carbonate	154.0		113.0					52,107	7.9		
OPH-1601	1,117.48	Acme	Mudstone	54.0	2.4	66.5	10.0	6.5	2.3		51,500	18.9	9.1	7.5
OPH-1606	1,118.27	Yale1	Mudstone	80.7		243.7	4.2	3.0	1.0		57,068		4.0	4.5
OPH-1606	1,118.27	Yale1	Mudstone	80.7		243.7	4.2	3.0	1.0		57,068		4.0	4.5
OPH-1606	1,118.27	Acme	Mudstone	90.0	0.7	85.9	3.7	3.6	0.9		58,100	10.9	3.6	4.3
OPH-1606	1,118.27	Acme	Mudstone	90.0	0.7	85.9	3.7	3.6	0.9		58,100	10.9	3.6	4.3
OPH-1608	1,118.59	NGU	Mudstone	158.0		203.0					21,542	15.3		6.2
OPH-1613	1,119.54	NGU	Mudstone	158.0		326.0					20,143	30.8		5.2
OPH-1647	1,120.31	Yale2	Mudstone	106.4							70,760			
OPH-1647	1,120.31	Yale2	Mudstone	106.4							70,760			
OPH-1647	1,120.31	Yale2	Mudstone	106.4							70,760			
OPH-1617	1,120.31	Acme	Mudstone	87.0	1.1	346.4	3.9	3.0	0.7		10,500	31.7	3.6	8.0
OPH-1617	1,120.31	Yale1	Mudstone	114.0		502.1	5.9	3.7	1.3		15,060		5.2	9.2
OPH-1617	1,120.31	Yale1	Mudstone	114.0		502.1	5.9	3.7	1.3		15,060		5.2	9.2
OPH-1617	1,120.31	Acme	Mudstone	87.0	1.1	346.4	3.9	3.0	0.7		10,500	31.7	3.6	8.0
OPH-1621	1,120.77	NGU	Mudstone	197.0		265.0					71,341	24.1		
OPH-1624	1,121.15	NGU	Mudstone	101.0		348.0					47,841	18.5		
OPH-1625	1,121.37	Acme	Mudstone	71.0	1.0	135.8	6.7	5.4	1.5		29,400	11.2	5.5	7.1
OPH-1625	1,121.37	Yale1	Mudstone	91.0		155.5	6.0	4.7	1.4		35,531		4.7	6.2
OPH-1625	1,121.37	Yale1	Mudstone	91.0		155.5	6.0	4.7	1.4		35,531		4.7	6.2
OPH-1625	1,121.37	Acme	Mudstone	71.0	1.0	135.8	6.7	5.4	1.5		29,400	11.2	5.5	7.1
OPH-1626	1,121.70	NGU	Mudstone	120.0		129.0					25,179	20.9		12.0
OPH-1634	1,123.13	NGU	Mudstone	151.0		119.0				4,900	53,716	17.4		
OPH-1640	1,123.62	NGU	Mudstone	229.0		199.0					63,718	12.3		
OPH-1647	1,124.27	Yale1	Mudstone	117.6		127.8	16.1	8.0	3.6		42,947		17.7	11.7
OPH-1647	1,124.27	Yale1	Mudstone	117.6		127.8	16.1	8.0	3.6		42,947		17.7	11.7
OPH-1647	1,124.27	Yale1	Mudstone	117.6		127.8	16.1	8.0	3.6		42,947		17.7	11.7
OPH-1647	1,124.27	Acme	Mudstone	89.0	1.5	29.0	17.5	5.3	6.1		9,200	40.6	29.5	20.3
OPH-1647	1,124.27	Acme	Mudstone	89.0	1.5	29.0	17.5	5.3	6.1		9,200	40.6	29.5	20.3
OPH-1647	1,124.27	Acme	Mudstone	89.0	1.5	29.0	17.5	5.3	6.1		9,200	40.6	29.5	20.3
OPH-1651	1,124.55	NGU	Mudstone	106.0		121.0					67,075	8.1		7.8
OPH-1655	1,125.02	NGU	Mudstone	71.7		45.5				2,500	66,026	7.6		
OPH-1676	1,127.22	NGU	Mudstone	131.0		38.8					35,671	4.4		
OPH-1683	1,135.64	NGU	Carbonate	17.8		10.8					13,849			

Sample ID	Depth (m)	Sample set	Lithology	Cr (ppm)	Cs (ppm)	Cu (ppm)	Dy (ppm)	Er (ppm)	Eu (ppm)	F (ppm)	Fe (ppm)	Ga (ppm)	Gd (ppm)	Hf (ppm)
OPH-1697	1,136.81	Yale2	Mudstone	32.3							9,822			
OPH-1697	1,136.81	Yale2	Mudstone	32.3							9,822			
OPH-1697	1,137.01	NGU	Mudstone	64.0		23.1					12,660	7.5		
OPH-1697	1,137.01	NGU	Mudstone	64.0		23.1					12,660	7.5		
OPH-1704	1,137.78	NGU	Carbonate	39.5		11.5					9,932	6.7		
OPH-1709	1,138.18	NGU	Carbonate	51.2		22.8					19,024	8.1		
OPH-1729	1,145.99	NGU	Mudstone	72.0		128.0					10,282	6.9		
OPH-1746	1,159.50	NGU	Mudstone	220.0		472.0					12,520	8.5		
OPH-1752	1,160.27	NGU	Mudstone	189.0		1,220.0					14,758	9.2		
OPH-1761	1,161.32	Yale2	Mudstone	275.8							13,498			
OPH-1761	1,161.32	Yale2	Mudstone	275.8							13,498			
OPH-1761	1,161.32	NGU	Mudstone	355.0		644.0					13,499	10.4		
OPH-1761	1,161.32	NGU	Mudstone	355.0		644.0					13,499	10.4		
OPH-1765	1,161.95	NGU	Mudstone	121.0		143.0					28,816	7.9		
OPH-1768	1,162.23	NGU	Mudstone	582.0		670.0					16,716	10.9		
OPH-1779	1,166.13	NGU	Mudstone	44.7		17.4				2,400	22,242	11.5		
OPH-1796	1,175.69	NGU	Mudstone	184.0		292.0					26,019	14.8		5.5
OPH-1809	1,187.30	NGU	Mudstone	181.0		44.5					45,882	14.4		
OPH-1809	1,187.30	Yale2	Mudstone	122.0							31,726			
OPH-1809	1,187.30	Yale2	Mudstone	122.0							31,726			
OPH-1809	1,187.30	NGU	Mudstone	181.0		44.5					45,882	14.4		
OPH-1814	1,187.91	NGU	Mudstone	94.6		68.3					42,105	11.4		
OPH-1823	1,188.90	NGU	Mudstone	62.5		129.0					61,060	8.0		
OPH-1831	1,190.01	NGU	Carbonate	63.3		111.0					75,538	11.1		
OPH-1835	1,190.75	NGU	Carbonate	85.6		130.0					72,740	19.1		
OPH-1849	1,198.41	NGU	Mudstone	151.0		15.2					32,174	18.9		
OPH-1856	1,199.56	NGU	Carbonate	47.7							35,881	9.7		
OPH-1862	1,200.64	NGU	Carbonate	54.8							33,433	11.5		
OPH-1865	1,201.25	NGU	Carbonate	33.5							47,351	17.5		10.1
OPH-1871	1,202.50	NGU	Carbonate	49.4							26,019	7.7		
OPH-1879	1,203.59	NGU	Mudstone	89.9		91.1					41,196	13.6		
OPH-1885	1,204.44	NGU	Mudstone	173.0		16.6					37,629	20.4		5.5
OPH-1892	1,205.03	NGU	Mudstone	126.0		38.6					24,550	20.9		5.6
OPH-1904	1,206.20	NGU	Mudstone	82.4		38.7					46,931	14.6		
OPH-1918	1,207.63	Yale2	Mudstone	99.3							25,806			
OPH-1918	1,207.63	Yale2	Mudstone	99.3							25,806			
OPH-1918	1,207.63	NGU	Mudstone	118.0		251.0					26,089	17.8		8.8
OPH-1918	1,207.63	NGU	Mudstone	118.0		251.0					26,089	17.8		8.8
OPH-1924	1,208.96	NGU	Carbonate	104.0		46.0					24,060	10.2		5.6
OPH-1927	1,209.45	NGU	Carbonate	133.0		22.6					28,746	10.4		
OPH-1939	1,211.12	NGU	Mudstone	127.0		15.0					28,956	12.3		
OPH-1942	1,211.51	NGU	Mudstone	152.0		47.7					23,501	15.0		
OPH-1948	1,212.51	NGU	Carbonate	25.6		168.0					18,954	4.4		
OPH-1960	1,214.11	NGU	Mudstone	108.0		6.2					24,060	13.2		
OPH-1962	1,214.28	NGU	Mudstone	155.0		160.0					54,066	15.6		6.6

Sample ID	Depth (m)	Sample set	Lithology	Cr (ppm)	Cs (ppm)	Cu (ppm)	Dy (ppm)	Er (ppm)	Eu (ppm)	F (ppm)	Fe (ppm)	Ga (ppm)	Gd (ppm)	Hf (ppm)
OPH-1975	1,215.53	NGU	Carbonate	22.5		12.8					44,344	3.3		
OPH-1984	1,216.89	NGU	Mudstone	60.3		43.2					17,486	6.8		
OPH-1994	1,217.74	NGU	Mudstone	86.5		19.9					29,026	15.7		
OPH-2001	1,218.36	NGU	Carbonate	23.7		256.0					44,973	3.9		
OPH-2001	1,218.36	Yale2	Carbonate	12.2							32,290			
OPH-2001	1,218.36	NGU	Carbonate	23.7		256.0					44,973	3.9		
OPH-2001	1,218.36	Yale2	Carbonate	12.2							32,290			
OPH-2010	1,219.18	NGU	Carbonate	153.0		40.5					61,270	16.2		
OPH-2027	1,220.85	NGU	Mudstone	83.2							23,850	7.9		
OPH-2040	1,221.72	NGU	Mudstone	137.0		29.7					45,113	15.9		
OPH-2052	1,223.79	NGU	Mudstone	46.0		77.7					54,625	14.0		20.6
OPH-2061	1,225.13	Yale2	Mudstone	145.5							94,753			
OPH-2061	1,225.13	Yale2	Mudstone	145.5							94,753			
OPH-2061	1,225.13	NGU	Mudstone	174.0		50.9					88,827	20.9		
OPH-2061	1,225.13	NGU	Mudstone	174.0		50.9					88,827	20.9		
OPH-2068	1,226.04	NGU	Mudstone	118.0							41,406	14.3		6.4
OPH-2069	1,226.21	NGU	Carbonate	88.1		463.0					60,710	12.4		
OPH-2397	1,426.19	NGU	Mudstone	201.0		15.0					47,491	14.2		
OPH-2406	1,427.09	Yale2	Mudstone	91.4							36,700			
OPH-2406	1,427.09	Yale2	Mudstone	91.4							36,700			
OPH-2406	1,427.16	NGU	Mudstone	191.0		16.9					42,875	9.6		
OPH-2406	1,427.16	NGU	Mudstone	191.0		16.9					42,875	9.6		
OPH-2413	1,427.81	NGU	Mudstone	178.0		42.1					46,372	13.0		
OPH-2423	1,437.13	NGU	Mudstone	219.0		169.0					111,209	17.5		
OPH-2426	1,437.68	NGU	Mudstone	86.1		261.0					53,086	7.9		
OPH-2993	1,765.27	NGU	Carbonate	174.0		29.2					95,122	11.4		
OPH-3009	1,767.41	NGU	Carbonate	67.1		64.1					22,312	4.3		
OPH-3016	1,777.38	Yale2	Mudstone	169.8							31,631			
OPH-3016	1,777.38	Yale2	Mudstone	169.8							31,631			
OPH-3016	1,777.46	NGU	Mudstone	239.0		70.8					42,245	10.3		
OPH-3016	1,777.46	NGU	Mudstone	239.0		70.8					42,245	10.3		
OPH-3057	1,792.05	NGU									40,777			
OPH-3112	1,868.46	NGU	Mudstone	141.0		8.0					41,196	12.8		5.2
OPH-3117	1,869.18	NGU	Mudstone	122.0							21,892	13.7		
OPH-3132	1,871.00	Yale2	Mudstone	123.7							25,030			
OPH-3132	1,871.00	Yale2	Mudstone	123.7							25,030			
OPH-3132	1,871.00	NGU	Mudstone	171.0							26,858	20.2		
OPH-3132	1,871.00	NGU	Mudstone	171.0							26,858	20.2		
OPH-3141	1,871.27	NGU	Mudstone	150.0	11.0	242.0					72,041	18.7		
OPH-3137	1,871.47	NGU	Mudstone	144.0		36.0					26,578	18.3		
OPH-3161	1,881.50	NGU	Mudstone	148.0							13,989	21.5		
OPH-3168	1,887.61	NGU	Mudstone	137.0							8,603	17.4		
OPH-3179	1,888.77	NGU	Carbonate	40.6		191.0					4,064			
OPH-3182	1,889.14	NGU									26,089			
OPH-3191	1,902.61	Yale2	Mudstone	115.4							46,756			

Sample ID	Depth (m)	Sample set	Lithology	Cr (ppm)	Cs (ppm)	Cu (ppm)	Dy (ppm)	Er (ppm)	Eu (ppm)	F (ppm)	Fe (ppm)	Ga (ppm)	Gd (ppm)	Hf (ppm)	
OPH-3194	1,902.88	NGU	Mudstone	102.0		78.3					48,190	19.0			
OPH-3229	1,915.60	NGU	Mudstone								37,349				
OPH-3256	1,926.73	Yale2	Mudstone	163.1							51,732				
OPH-3256	1,926.73	Yale2	Mudstone	163.1							51,732				
OPH-3256	1,926.80	NGU	Mudstone	174.0							47,771	19.8			
OPH-3256	1,926.80	NGU	Mudstone	174.0							47,771	19.8			
OPH-3272	1,935.31	NGU	Mudstone	153.0							52,527	20.4			
OPH-3275	1,935.54	NGU	Mudstone	144.0							50,079	21.2			
OPH-3295	1,946.55	NGU	Mudstone	102.0							50,359	16.4			
OPH-3324	1,957.85	NGU	Mudstone	147.0							49,799	19.4			
OPH-3331	1,958.63	NGU	Mudstone	151.0		6.5					34,412	21.7			
OPH-3355	1,970.85	Yale2	Mudstone	147.8							53,398				
OPH-3355	1,970.85	Yale2	Mudstone	147.8							53,398				
OPH-3355	1,970.85	NGU	Mudstone	146.0							55,534	23.1			
OPH-3355	1,970.85	NGU	Mudstone	146.0							55,534	23.1			
OPH-3386	1,980.42	NGU	Carbonate	54.4							28,327	12.5			
OPH-3411	1,991.90	NGU									23,850				
OPH-3463	2,011.35	Yale2	Mudstone	57.8							35,106				
OPH-3589	2,052.57	Yale2	Mudstone	80.8							30,762				
OPH-3707	2,103.47	Yale2	Mudstone	48.6							24,960				
OPH-3736	2,205.38	Yale1	Carbonate	14.3		11.5	0.1	0.1	0.1		1,240		0.2	0.0	
OPH-3904	2,252.09	Yale1	Carbonate	4.8		19.3	0.1	0.1	0.2		215		0.1		
OPH-4022	2,285.28	Yale2	Carbonate	10.5							2,149				
OPH-4081	2,305.25	Yale1	Carbonate	5.5		40.2	0.1	0.1	0.7		201		0.2		
OPH-4142	2,324.43	Yale1	Carbonate	2.8		16.1	0.1	0.1	0.1		239		0.1	0.1	
OPH-4178	2,328.55	Yale1	Carbonate	2.7		66.1	0.1	0.1	0.1		188		0.2	0.0	
OPH-4178	2,328.55	Acme	Carbonate	2.0	<0.1	34.9	<0.1	<0.1	<0.1		200	0.1	<0.1	<0.02	
OPH-4183	2,329.14	Acme	Carbonate	10.0	0.4	53.8	0.2	0.2	<0.1		1,000	1.9	0.3	0.0	
OPH-4185	2,329.34	Acme		1.0	<0.1	5.3	<0.1	<0.1	<0.1			<0.02	<0.1	<0.02	
OPH-4187	2,329.62	Acme		1.0	<0.1	23.3	<0.1	<0.1	<0.1			0.0	<0.1	<0.02	
OPH-4193	2,330.28	Yale2	Evaporite	0.8							39				
OPH-4194	2,330.34	Yale1	Carbonate	1.9		43.6	0.1	0.1	0.0		429		0.1	0.1	
OPH-4194	2,330.34	Acme	Carbonate	2.0	<0.1	31.4	<0.1	<0.1	<0.1		400	0.1	<0.1	<0.02	
OPH-4194	2,330.34	Acme	Carbonate	2.0	<0.1	31.4	<0.1	<0.1	<0.1		400	0.1	<0.1	<0.02	
OPH-4194	2,330.34	Yale1	Carbonate	1.9		43.6	0.1	0.1	0.0		429		0.1	0.1	
OPH-4199	2,330.85	Acme	Evaporite	2.0	<0.1	5.7	<0.1	<0.1	<0.1		200	0.1	<0.1	<0.02	
OPH-4211	2,509.02	Yale1	Evaporite	1.3		2.2	0.1	0.0	0.1		51		0.1		
OPH-4257	2,517.36	Yale1	Evaporite	13.5		42.0	0.9	0.2	0.6		3,667		1.8	0.1	
OPH-4310	2,526.68	Yale1	Evaporite	8.8		22.8	0.4	0.4	0.1		3,148		0.2	0.1	
OPH-4366	2,547.78	Yale1	Evaporite	20.7		68.2	0.4	0.1	0.2		5,544		0.5	0.1	
OPH-4383	2,549.45	Yale2	Mudstone	17.0							11,343				
OPH-4440	2,570.15	Yale1	Evaporite	1.9		12.8	0.2	0.1	0.1		179		0.3	0.0	
OPH-4537	2,700.97	Yale1	Evaporite	0.3		1.0	0.1	0.0	0.1		67		0.1		
OPH-4582	2,724.31	Yale2	Evaporite	6.5							1,720				
OPH-4635	2,833.79	Yale1	Evaporite	3.1		11.7	0.8	0.4	0.3		513		0.9		

Sample ID	Depth (m)	Sample set	Lithology	Cr (ppm)	Cs (ppm)	Cu (ppm)	Dy (ppm)	Er (ppm)	Eu (ppm)	F (ppm)	Fe (ppm)	Ga (ppm)	Gd (ppm)	Hf (ppm)
OPH-4620	2,838.14	Yale2	Evaporite	3.2							484			
OPH-4683	2,850.46	Yale1	Evaporite	13.0		33.9	0.4	0.2	0.2		2,295		0.5	0.2
OPH-4683	2,850.46	Yale1	Evaporite	13.0		33.9	0.4	0.2	0.2		2,295		0.5	0.2
OPH-4683	2,850.46	Yale2	Evaporite	1.5							888			
OPH-4683	2,850.46	Yale2	Evaporite	1.5							888			
OPH-4774	2,878.31	Yale1	Evaporite	2.7		32.0	0.5	0.3	0.2		3,911		0.7	0.1
OPH-4813	2,896.20	Yale1	Evaporite	2.8		12.5	0.2	0.1	0.1		1,276		0.2	0.1
OPH-4853	2,904.34	Yale1	Evaporite	2.2		8.9	0.2	0.1	0.1		1,071		0.2	0.0

Table A5c: Element concentration data for drill core OPH, continued.

Sample ID	Depth (m)	Sample set	Lithology	Ho (ppm)	In (ppm)	K (ppm)	La (ppm)	Li (ppm)	Lu (ppm)	Mg (ppm)	Mn (ppm)	Mo (ppm)	Na (ppm)	Nb (ppm)
OPH-10	530.39	NGU	Mudstone			8,551	28.0			47,700	697		26,929	16.7
OPH-73	542.63	Yale2	Mudstone							58,235		0.5		
OPH-73	542.63	Yale2	Mudstone							58,235		0.5		
OPH-73	542.72	NGU	Mudstone			8,077	16.0			66,937	999		13,873	18.1
OPH-73	542.72	NGU	Mudstone			8,077	16.0			66,937	999		13,873	18.1
OPH-80	543.68	NGU	Mudstone			7,969	19.0			56,022	829		20,920	17.7
OPH-83	544.22	NGU	Mudstone			12,120	16.0			65,731	999	6.8	7,715	19.1
OPH-121	552.43	NGU	Mudstone			357				52,283	829		18,621	12.9
OPH-284	591.30	NGU	Mudstone			10,128	22.0			12,362	612		43,547	20.5
OPH-306	594.85	Yale2	Mudstone							8,118		2.0		
OPH-306	594.85	Yale2	Mudstone							8,118		2.0		
OPH-306	594.93	NGU	Mudstone			17,350	20.0			10,071	550		44,289	21.5
OPH-306	594.93	NGU	Mudstone			17,350	20.0			10,071	550		44,289	21.5
OPH-507	636.42	NGU	Mudstone			10,709				16,403	798		35,683	19.8
OPH-515	637.85	NGU	Mudstone			8,966	20.0			19,840	2,896		19,956	17.6
OPH-523	638.53	Yale2	Mudstone							10,546		0.6		
OPH-523	638.53	Yale2	Mudstone							10,546		0.6		
OPH-523	638.63	NGU	Mudstone			9,464	21.0			13,568	2,168		26,781	16.7
OPH-523	638.63	NGU	Mudstone			9,464	21.0			13,568	2,168		26,781	16.7
OPH-844	890.22	Yale2	Mudstone							5,881		49.5		
OPH-844	890.22	Yale2	Mudstone							5,881		49.5		
OPH-844	890.22	NGU	Mudstone			21,169				5,439	124	58.5	6,380	5.4
OPH-844	890.22	NGU	Mudstone			21,169				5,439	124	58.5	6,380	5.4
OPH-849	891.17	Yale1	Mudstone	0.8	1.47		7.7	8.5	0.38	5,683	123		2,164	
OPH-849	891.17	Yale1	Mudstone	0.8	1.47		7.7	8.5	0.38	5,683	123		2,164	
OPH-849	891.17	NGU	Mudstone			18,512				4,698	93	102.0	2,003	3.1
OPH-849	891.17	NGU	Mudstone			18,512				4,698	93	102.0	2,003	3.1
OPH-858	892.79	NGU	Mudstone			17,599				5,849	124	90.2	2,077	3.1
OPH-862	893.38	NGU	Mudstone			4,881				4,137	77	126.0		
OPH-867	894.16	NGU	Mudstone			27,063	36.0			7,598	139	82.1	6,454	4.6
OPH-875	894.98	NGU	Carbonate			6,649				7,960	341	156.0	1,780	
OPH-879	895.49	NGU	Carbonate			282				1,779	256	14.5		
OPH-885	896.12	NGU												
OPH-903	897.58	NGU				10,211				15,257	318		3,561	
OPH-924	899.15	NGU	Carbonate			11,954				10,553	867	45.2	3,487	4.2
OPH-925	899.25	NGU	Carbonate			16,437				8,865	1,278	26.7	3,264	5.6
OPH-938	900.23	NGU	Carbonate			25,818				10,794	1,076	39.0	4,080	10.1
OPH-945	901.96	NGU										3.3		5.2
OPH-955	903.08	NGU	Mudstone			40,594				16,222	349	17.7	14,763	2.6
OPH-970	904.30	NGU	Mudstone			40,760				29,609	627	11.9	13,576	7.7
OPH-975	912.04	Yale2	Mudstone							31,787		20.1		
OPH-975	912.04	Yale2	Mudstone							31,787		20.1		

Sample ID	Depth (m)	Sample set	Lithology	Ho (ppm)	In (ppm)	K (ppm)	La (ppm)	Li (ppm)	Lu (ppm)	Mg (ppm)	Mn (ppm)	Mo (ppm)	Na (ppm)	Nb (ppm)
OPH-975	912.04	Yale2	Mudstone							31,787		20.1		
OPH-975	912.19	Yale1	Mudstone	1.9	2.53		92.0	15.5	0.69	17,685	556		14,666	
OPH-975	912.19	Yale1	Mudstone	1.9	2.53		92.0	15.5	0.69	17,685	556		14,666	
OPH-975	912.19	Yale1	Mudstone	1.9	2.53		92.0	15.5	0.69	17,685	556		14,666	
OPH-975	912.19	NGU	Mudstone			3,636				31,720	805	33.2	25,742	17.9
OPH-975	912.19	NGU	Mudstone			3,636				31,720	805	33.2	25,742	17.9
OPH-975	912.19	NGU	Mudstone			3,636				31,720	805	33.2	25,742	17.9
OPH-979	912.70	NGU	Mudstone			3,744				22,493	596	55.9	23,591	17.1
OPH-1361	1,080.00	NGU	Carbonate			100				74,173	604			7.9
OPH-1364	1,080.57	Acme	Carbonate	0.2	0.03		2.7	6.1	<0.1	78,800	416	6.3	330	2.3
OPH-1364	1,080.57	Yale2	Carbonate							83,145		5.0		
OPH-1364	1,080.57	Acme	Carbonate	0.2	0.03		2.7	6.1	<0.1	78,800	416	6.3	330	2.3
OPH-1364	1,080.57	Yale2	Carbonate							83,145		5.0		
OPH-1366	1,081.11	NGU	Carbonate			83				71,761	1,123			3.7
OPH-1368	1,081.36	Acme	Carbonate	0.2	0.02	200	3.4	10.4	<0.1	103,300	382	0.6	310	1.2
OPH-1372	1,081.93	Acme	Carbonate	0.2	0.02		4.7	9.9	<0.1	78,600	446	3.1	370	1.3
OPH-1373	1,082.28	NGU	Carbonate							79,601	372			4.2
OPH-1376	1,082.71	NGU	Carbonate							99,501	565			2.5
OPH-1383	1,083.49	NGU	Carbonate			125				109,753	488			4.4
OPH-1390	1,084.18	NGU	Carbonate							118,195	287			2.7
OPH-1393	1,084.47	Yale1	Carbonate	0.2	3.15		2.3	4.8	0.03	158,373	427		303	
OPH-1393	1,084.47	Yale1	Carbonate	0.2	3.15		2.3	4.8	0.03	158,373	427		303	
OPH-1393	1,084.47	Acme	Carbonate	<0.1	<0.01	200	1.6	3.1	<0.1	102,600	290	0.3	240	0.8
OPH-1393	1,084.47	Acme	Carbonate	<0.1	<0.01	200	1.6	3.1	<0.1	102,600	290	0.3	240	0.8
OPH-1398	1,085.13	Acme	Carbonate	<0.1	<0.01	200	1.6	4.4	<0.1	103,000	379	0.2	180	0.7
OPH-1400	1,085.42	Acme	Carbonate	<0.1	0.01	200	1.1	4.6	<0.1	104,700	368	0.1	170	0.8
OPH-1403	1,086.33	NGU	Carbonate							112,768	318			
OPH-1405	1,086.52	Acme	Carbonate	<0.1	0.01	100	2.4	2.1	<0.1	95,400	373	0.3	140	0.5
OPH-1405	1,086.52	Yale2	Carbonate							74,591		0.5		
OPH-1405	1,086.52	Yale2	Carbonate							74,591		0.5		
OPH-1405	1,086.52	Acme	Carbonate	<0.1	0.01	100	2.4	2.1	<0.1	95,400	373	0.3	140	0.5
OPH-1412	1,087.73	Acme	Carbonate	<0.1	<0.01	100	2.4	4.4	<0.1	86,600	385	0.3	170	0.8
OPH-1421	1,089.09	NGU	Carbonate			108				79,601	658			3.7
OPH-1426	1,089.67	Acme	Carbonate	0.3	0.06	100	6.2	12.2	<0.1	36,300	619	0.6	120	0.9
OPH-1434	1,090.51	NGU	Carbonate			8,966	21.0			147,141	356			16.8
OPH-1436	1,090.80	Acme	Carbonate	0.7	0.02	200	11.1	15.4	0.10	48,100	655	1.3	190	1.6
OPH-1442	1,091.87	NGU	Carbonate			149				95,280	480			5.7
OPH-1444	1,092.14	Acme	Carbonate	0.2	0.01		2.0	8.6	<0.1	77,300	535	0.1	110	0.8
OPH-1449	1,093.39	Yale2	Carbonate							82,008		0.7		
OPH-1449	1,093.39	Yale2	Carbonate							82,008		0.7		
OPH-1449	1,093.39	Acme	Carbonate	<0.1	<0.01	200	2.6	2.5	<0.1	104,800	439	0.6	130	2.0
OPH-1449	1,093.39	Acme	Carbonate	<0.1	<0.01	200	2.6	2.5	<0.1	104,800	439	0.6	130	2.0
OPH-1452	1,093.90	NGU	Carbonate			1,461	28.0			95,883	93		890	29.5
OPH-1461	1,094.89	Acme	Carbonate	<0.1	0.01	1,100	2.3	5.9	<0.1	96,600	321	0.2	100	0.6
OPH-1464	1,095.45	Acme	Carbonate	0.2	<0.01	900	4.8	2.9	<0.1	105,300	209	0.7	180	0.5

Sample ID	Depth (m)	Sample set	Lithology	Ho (ppm)	In (ppm)	K (ppm)	La (ppm)	Li (ppm)	Lu (ppm)	Mg (ppm)	Mn (ppm)	Mo (ppm)	Na (ppm)	Nb (ppm)
OPH-1464	1,095.45	Yale1	Carbonate	0.6	3.22		5.7	3.8	0.23	139,121	290			
OPH-1464	1,095.45	Acme	Carbonate	0.2	<0.01	900	4.8	2.9	<0.1	105,300	209	0.7	180	0.5
OPH-1464	1,095.45	Yale1	Carbonate	0.6	3.22		5.7	3.8	0.23	139,121	290			
OPH-1466	1,095.74	Acme	Carbonate	0.5	0.04	4,400	13.2	11.1	0.20	106,600	336	1.1	150	4.0
OPH-1468	1,096.29	NGU	Carbonate			5,703	35.0			78,998	240			413.0
OPH-1469	1,096.31	Acme	Carbonate	0.6	0.01	2,800	4.6	6.9	0.30	103,700	276	0.2	170	10.5
OPH-1470	1,096.57	Acme	Carbonate	0.1	0.01	1,300	4.2	3.6	<0.1	112,700	276	0.3	180	3.4
OPH-1472	1,096.82	Acme	Carbonate	0.2	<0.01	1,200	3.6	3.7	<0.1	106,500	203	0.2	160	0.7
OPH-1479	1,098.06	Acme	Carbonate	<0.1	<0.01	2,100	2.7	3.4	<0.1	112,000	260	0.3	130	1.3
OPH-1483	1,098.66	NGU	Carbonate			1,685				119,401	410			5.7
OPH-1486	1,099.04	Acme	Carbonate	0.1	<0.01	600	1.8	3.2	<0.1	98,000	162	0.3	220	0.4
OPH-1488	1,099.51	NGU												
OPH-1491	1,099.98	Acme	Carbonate	<0.1	<0.01	900	0.9	3.7	<0.1	120,200	77	4.6	110	0.5
OPH-1491	1,099.98	Yale1	Carbonate	0.1	2.20		0.9	3.8	0.02	133,232	91			
OPH-1491	1,099.98	Yale1	Carbonate	0.1	2.20		0.9	3.8	0.02	133,232	91			
OPH-1491	1,099.98	Acme	Carbonate	<0.1	<0.01	900	0.9	3.7	<0.1	120,200	77	4.6	110	0.5
OPH-1499	1,101.27	Yale2	Carbonate							69,733		1.2		
OPH-1499	1,101.27	Yale2	Carbonate							69,733		1.2		
OPH-1501	1,101.45	NGU	Mudstone			17,018	84.0			10,433		24.3	40,728	50.6
OPH-1509	1,102.06	NGU	Mudstone			20,007	27.0			25,750		141.0		19.8
OPH-1516	1,102.74	NGU	Mudstone			38,353	58.0			8,563		112.0	2,226	17.1
OPH-1519	1,103.35	NGU	Mudstone			17,931				5,222		45.4	3,413	18.9
OPH-1527	1,104.69	Yale1	Carbonate	0.2	3.09		2.3	5.0	0.06	108,645	161			
OPH-1533	1,106.00	NGU	Carbonate			1,046				103,119	232	5.1		3.1
OPH-1542	1,106.99	NGU	Mudstone			30,965	35.0			11,337		62.5	890	39.5
OPH-1556	1,109.44	NGU	Carbonate			2,632	19.0			54,394	132	3.4		
OPH-1557	1,109.57	NGU	Carbonate			332				120,004	124	14.4		
OPH-1557	1,109.57	Yale1	Carbonate	0.3	2.29		2.3	15.3	0.10	164,660	240		396	
OPH-1557	1,109.57	Yale1	Carbonate	0.3	2.29		2.3	15.3	0.10	164,660	240		396	
OPH-1557	1,109.57	NGU	Carbonate			332				120,004	124	14.4		
OPH-1560	1,109.96	Yale1	Carbonate	0.1	3.20		0.4	4.3	0.01	59,515	59			
OPH-1560	1,109.96	NGU	Carbonate			241				97,692	116			3.0
OPH-1560	1,109.96	Yale1	Carbonate	0.1	3.20		0.4	4.3	0.01	59,515	59			
OPH-1560	1,109.96	NGU	Carbonate			241				97,692	116			3.0
OPH-1561	1,110.18	NGU	Carbonate			357				89,249	124	20.8		
OPH-1499	1,110.27	Acme	Carbonate	<0.1	<0.01	300	1.7	2.8	<0.1	94,500	129	0.2	150	0.5
OPH-1499	1,110.27	Acme	Carbonate	<0.1	<0.01	300	1.7	2.8	<0.1	94,500	129	0.2	150	0.5
OPH-1564	1,110.79	Yale1	Carbonate	0.1	2.36		0.9	9.5	0.04	130,682	324		316	
OPH-1564	1,110.79	NGU	Carbonate			191				98,295	217	19.0		
OPH-1567	1,111.40	NGU	Carbonate			241				110,959	279	13.4		
OPH-1568	1,111.60	NGU	Carbonate			274				107,340	287	31.1		
OPH-1569	1,111.80	NGU	Carbonate			1,959	17.0			85,631	256	18.0		
OPH-1571	1,112.02	NGU	Carbonate			8,468	98.0			34,192		71.6	1,632	
OPH-1572	1,112.08	Yale1	Mudstone	2.6	2.04		58.7	66.0	1.16	26,313	17		1,885	
OPH-1572	1,112.08	NGU	Mudstone			22,082	55.0			56,746		464.0	3,042	5.1

Sample ID	Depth (m)	Sample set	Lithology	Ho (ppm)	In (ppm)	K (ppm)	La (ppm)	Li (ppm)	Lu (ppm)	Mg (ppm)	Mn (ppm)	Mo (ppm)	Na (ppm)	Nb (ppm)
OPH-1572	1,112.08	Acme	Mudstone	2.2	0.11	31,200	47.9	59.9	1.10	22,100	22	408.2	2,030	32.0
OPH-1572	1,112.08	NGU	Mudstone			22,082	55.0			56,746		464.0	3,042	5.1
OPH-1572	1,112.08	Acme	Mudstone	2.2	0.11	31,200	47.9	59.9	1.10	22,100	22	408.2	2,030	32.0
OPH-1572	1,112.08	Yale1	Mudstone	2.6	2.04		58.7	66.0	1.16	26,313	17		1,885	
OPH-1572	1,112.08	Yale1	Mudstone	2.6	2.04		58.7	66.0	1.16	26,313	17		1,885	
OPH-1572	1,112.08	NGU	Mudstone			22,082	55.0			56,746		464.0	3,042	5.1
OPH-1572	1,112.08	Acme	Mudstone	2.2	0.11	31,200	47.9	59.9	1.10	22,100	22	408.2	2,030	32.0
OPH-1573	1,112.27	Yale1	Mudstone	2.2	2.08		44.9	36.5	0.96	13,015	9		1,976	
OPH-1573	1,112.27	Acme	Mudstone	2.1	0.06	26,300	34.0	30.5	0.90	10,900	12	408.1	1,490	23.4
OPH-1573	1,112.27	Yale1	Mudstone	2.2	2.08		44.9	36.5	0.96	13,015	9		1,976	
OPH-1573	1,112.27	Acme	Mudstone	2.1	0.06	26,300	34.0	30.5	0.90	10,900	12	408.1	1,490	23.4
OPH-1575	1,112.65	Acme	Mudstone	2.2	0.07	25,500	33.0	31.8	0.70	10,100	11	353.7	1,830	23.3
OPH-1575	1,112.65	Yale1	Mudstone	1.9	1.64		39.4	24.7	0.81	8,092	6		1,472	
OPH-1575	1,112.65	Yale1	Mudstone	1.9	1.64		39.4	24.7	0.81	8,092	6		1,472	
OPH-1575	1,112.65	Acme	Mudstone	2.2	0.07	25,500	33.0	31.8	0.70	10,100	11	353.7	1,830	23.3
OPH-1578	1,113.28	Yale1	Mudstone	3.0	2.41		68.1	32.7	1.19	11,183	12		1,232	
OPH-1578	1,113.28	Acme	Mudstone	2.9	0.12	28,100	54.9	30.9	1.30	9,000	13	216.6	1,140	37.6
OPH-1578	1,113.28	Acme	Mudstone	2.9	0.12	28,100	54.9	30.9	1.30	9,000	13	216.6	1,140	37.6
OPH-1578	1,113.28	Yale1	Mudstone	3.0	2.41		68.1	32.7	1.19	11,183	12		1,232	
OPH-1579	1,113.58	NGU	Mudstone			29,719	86.0			9,347		254.0	2,151	33.4
OPH-1580	1,113.63	Acme	Mudstone	1.8	0.11	33,000	41.0	19.6	0.80	6,100	7	214.2	2,430	29.4
OPH-1580	1,113.63	Yale1	Mudstone	2.0	1.53		54.6	20.1	0.84	6,733	5		1,874	
OPH-1580	1,113.63	Acme	Mudstone	1.8	0.11	33,000	41.0	19.6	0.80	6,100	7	214.2	2,430	29.4
OPH-1580	1,113.63	Yale1	Mudstone	2.0	1.53		54.6	20.1	0.84	6,733	5		1,874	
OPH-1581	1,113.83	Yale1	Mudstone	1.8	1.88		46.5	15.9	0.71	6,085	4		1,470	
OPH-1581	1,113.83	Acme	Mudstone	1.8	0.07	28,200	37.7	15.1	0.80	4,900	6	253.3	1,290	19.6
OPH-1581	1,113.83	Acme	Mudstone	1.8	0.07	28,200	37.7	15.1	0.80	4,900	6	253.3	1,290	19.6
OPH-1581	1,113.83	Yale1	Mudstone	1.8	1.88		46.5	15.9	0.71	6,085	4		1,470	
OPH-1582	1,113.92	NGU	Mudstone			29,719	50.0			6,754		244.0	1,558	11.3
OPH-1584	1,114.20	Yale1	Mudstone	0.8	2.28		18.9	10.0	0.31	4,541	1		1,302	
OPH-1584	1,114.20	Acme	Mudstone	1.1	0.15	18,800	21.7	10.3	0.40	3,600	5	172.4	1,230	11.8
OPH-1584	1,114.20	Acme	Mudstone	1.1	0.15	18,800	21.7	10.3	0.40	3,600	5	172.4	1,230	11.8
OPH-1584	1,114.20	Yale1	Mudstone	0.8	2.28		18.9	10.0	0.31	4,541	1		1,302	
OPH-1585	1,114.34	Yale1	Mudstone	1.2	2.14		21.0	14.6	0.46	5,757	3		1,529	
OPH-1585	1,114.34	Yale2	Mudstone							4,889		109.5		
OPH-1585	1,114.34	Yale2	Mudstone							4,889		109.5		
OPH-1585	1,114.34	Yale2	Mudstone							4,889		109.5		
OPH-1585	1,114.34	Acme	Mudstone	1.2	0.10	21,100	18.9	14.2	0.60	4,400	5	236.5	1,420	15.0
OPH-1585	1,114.34	Acme	Mudstone	1.2	0.10	21,100	18.9	14.2	0.60	4,400	5	236.5	1,420	15.0
OPH-1585	1,114.34	Acme	Mudstone	1.2	0.10	21,100	18.9	14.2	0.60	4,400	5	236.5	1,420	15.0
OPH-1585	1,114.34	Yale1	Mudstone	1.2	2.14		21.0	14.6	0.46	5,757	3		1,529	
OPH-1585	1,114.34	Yale1	Mudstone	1.2	2.14		21.0	14.6	0.46	5,757	3		1,529	
OPH-1586	1,114.62	NGU	Mudstone			32,044	25.0			5,898		272.0	4,525	87.9
OPH-1587	1,114.77	Acme	Mudstone	1.9	0.10	37,800	18.8	17.4	1.00	5,100	7	169.2	11,090	82.6
OPH-1587	1,114.77	Yale1	Mudstone	1.8	1.65		17.3	19.1	0.88	7,094	5		13,502	

Sample ID	Depth (m)	Sample set	Lithology	Ho (ppm)	In (ppm)	K (ppm)	La (ppm)	Li (ppm)	Lu (ppm)	Mg (ppm)	Mn (ppm)	Mo (ppm)	Na (ppm)	Nb (ppm)
OPH-1587	1,114.77	Yale1	Mudstone	1.8	1.65		17.3	19.1	0.88	7,094	5		13,502	
OPH-1587	1,114.77	Acme	Mudstone	1.9	0.10	37,800	18.8	17.4	1.00	5,100	7	169.2	11,090	82.6
OPH-1588	1,115.02	Yale1	Mudstone	1.0	1.38		15.5	10.0	0.41	4,311	4		3,420	
OPH-1588	1,115.02	Yale1	Mudstone	1.0	1.38		15.5	10.0	0.41	4,311	4		3,420	
OPH-1588	1,115.02	Acme	Mudstone	0.4	0.01	6,000	4.8	3.3	0.20	1,300	2	97.7	830	5.8
OPH-1588	1,115.02	Acme	Mudstone	0.4	0.01	6,000	4.8	3.3	0.20	1,300	2	97.7	830	5.8
OPH-1589	1,115.21	NGU	Mudstone			32,957	33.0			6,633		231.0	2,893	30.9
OPH-1590	1,115.59	NGU	Carbonate			282				108,546	612	3.3		2.0
OPH-1592	1,115.87	NGU	Mudstone			22,414	35.0			47,700		235.0	1,706	22.8
OPH-1596	1,116.61	NGU	Carbonate			199				112,768	891	6.1		2.2
OPH-1596	1,116.65	Yale1	Carbonate	0.2	4.04		1.3	3.4	0.02	62,708	527			
OPH-1599	1,117.43	NGU	Carbonate			17,350				23,458		193.0	1,410	2.6
OPH-1601	1,117.48	Acme	Mudstone	2.2	0.08	40,300	18.2	58.9	0.90	18,300	38	64.7	1,210	26.2
OPH-1606	1,118.27	Yale1	Mudstone	1.0	1.85		24.0	19.1	0.50	6,345	14		2,270	
OPH-1606	1,118.27	Yale1	Mudstone	1.0	1.85		24.0	19.1	0.50	6,345	14		2,270	
OPH-1606	1,118.27	Acme	Mudstone	1.0	<0.01	21,800	25.0	12.2	0.70	4,200	14	162.6	2,260	6.0
OPH-1606	1,118.27	Acme	Mudstone	1.0	<0.01	21,800	25.0	12.2	0.70	4,200	14	162.6	2,260	6.0
OPH-1608	1,118.59	NGU	Mudstone			24,323	39.0			4,722		110.0	2,151	10.7
OPH-1613	1,119.54	NGU	Mudstone			56,284	17.0			12,664		45.4	3,561	11.4
OPH-1647	1,120.31	Yale2	Mudstone							5,826		79.8		
OPH-1647	1,120.31	Yale2	Mudstone							5,826		79.8		
OPH-1647	1,120.31	Yale2	Mudstone							5,826		79.8		
OPH-1617	1,120.31	Acme	Mudstone	0.9	0.07	45,400	2.3	54.4	0.40	14,600	61	9.1	8,490	16.0
OPH-1617	1,120.31	Yale1	Mudstone	1.3	2.76		4.1	72.2	0.56	23,144	79		8,182	
OPH-1617	1,120.31	Yale1	Mudstone	1.3	2.76		4.1	72.2	0.56	23,144	79		8,182	
OPH-1617	1,120.31	Acme	Mudstone	0.9	0.07	45,400	2.3	54.4	0.40	14,600	61	9.1	8,490	16.0
OPH-1621	1,120.77	NGU	Mudstone			43,168				17,609	147	27.4	6,603	11.3
OPH-1624	1,121.15	NGU	Mudstone			49,975	20.0			9,347		26.4	3,413	20.5
OPH-1625	1,121.37	Acme	Mudstone	1.5	0.15	24,800	23.3	13.1	0.90	4,200	96	94.0	3,200	22.5
OPH-1625	1,121.37	Yale1	Mudstone	1.5	1.67		25.2	14.6	0.73	5,445	39		3,635	
OPH-1625	1,121.37	Yale1	Mudstone	1.5	1.67		25.2	14.6	0.73	5,445	39		3,635	
OPH-1625	1,121.37	Acme	Mudstone	1.5	0.15	24,800	23.3	13.1	0.90	4,200	96	94.0	3,200	22.5
OPH-1626	1,121.70	NGU	Mudstone			37,274	67.0			6,814		98.6	3,190	53.4
OPH-1634	1,123.13	NGU	Mudstone			30,217				74,173	333	32.2	1,335	16.8
OPH-1640	1,123.62	NGU	Mudstone			26,565	22.0			6,633		128.0	2,745	11.5
OPH-1647	1,124.27	Yale1	Mudstone	3.0	2.62		115.8	39.4	0.85	12,664	31		1,380	
OPH-1647	1,124.27	Yale1	Mudstone	3.0	2.62		115.8	39.4	0.85	12,664	31		1,380	
OPH-1647	1,124.27	Yale1	Mudstone	3.0	2.62		115.8	39.4	0.85	12,664	31		1,380	
OPH-1647	1,124.27	Acme	Mudstone	2.5	0.11	52,000	151.9	68.5	0.40	16,500	45	10.5	1,360	61.0
OPH-1647	1,124.27	Acme	Mudstone	2.5	0.11	52,000	151.9	68.5	0.40	16,500	45	10.5	1,360	61.0
OPH-1647	1,124.27	Acme	Mudstone	2.5	0.11	52,000	151.9	68.5	0.40	16,500	45	10.5	1,360	61.0
OPH-1651	1,124.55	NGU	Mudstone			21,584	19.0			3,431		104.0	1,706	20.5
OPH-1655	1,125.02	NGU	Mudstone			9,215				101,310	1,549	7.9	890	4.5
OPH-1676	1,127.22	NGU	Mudstone			18,761	20.0			5,349		47.2	890	3.7
OPH-1683	1,135.64	NGU	Carbonate			3,287				87,440	1,967	5.0		

Sample ID	Depth (m)	Sample set	Lithology	Ho (ppm)	In (ppm)	K (ppm)	La (ppm)	Li (ppm)	Lu (ppm)	Mg (ppm)	Mn (ppm)	Mo (ppm)	Na (ppm)	Nb (ppm)
OPH-1697	1,136.81	Yale2	Mudstone							62,946		0.6		
OPH-1697	1,136.81	Yale2	Mudstone							62,946		0.6		
OPH-1697	1,137.01	NGU	Mudstone			11,539	16.0			59,399	1,394		2,967	8.1
OPH-1697	1,137.01	NGU	Mudstone			11,539	16.0			59,399	1,394		2,967	8.1
OPH-1704	1,137.78	NGU	Carbonate			11,539	19.0			52,464	1,270		1,410	5.4
OPH-1709	1,138.18	NGU	Carbonate			13,863	19.0			45,770	1,084		5,861	7.0
OPH-1729	1,145.99	NGU	Mudstone			20,256				11,397	93	15.7	1,335	5.2
OPH-1746	1,159.50	NGU	Mudstone			21,916				6,814		58.7	890	5.5
OPH-1752	1,160.27	NGU	Mudstone			20,173	19.0			6,030		61.5		5.1
OPH-1761	1,161.32	Yale2	Mudstone							6,390		71.8		
OPH-1761	1,161.32	Yale2	Mudstone							6,390		71.8		
OPH-1761	1,161.32	NGU	Mudstone			23,410	18.0			7,056		64.9		5.1
OPH-1761	1,161.32	NGU	Mudstone			23,410	18.0			7,056		64.9		5.1
OPH-1765	1,161.95	NGU	Mudstone			13,282				5,524	426	11.0	5,861	5.1
OPH-1768	1,162.23	NGU	Mudstone			22,331	23.0			6,935		103.0	742	5.3
OPH-1779	1,166.13	NGU	Mudstone			22,248	51.0			36,303	1,301		3,264	40.3
OPH-1796	1,175.69	NGU	Mudstone			37,191	34.0			11,820	147	60.6	4,303	21.0
OPH-1809	1,187.30	NGU	Mudstone			27,312	32.0			25,508	480	17.4	7,122	14.9
OPH-1809	1,187.30	Yale2	Mudstone							17,982		11.8		
OPH-1809	1,187.30	Yale2	Mudstone							17,982		11.8		
OPH-1809	1,187.30	NGU	Mudstone			27,312	32.0			25,508	480	17.4	7,122	14.9
OPH-1814	1,187.91	NGU	Mudstone			19,342	17.0			14,835	813	7.6	9,125	7.4
OPH-1823	1,188.90	NGU	Mudstone			12,618				18,332	1,286	3.4	6,009	6.8
OPH-1831	1,190.01	NGU	Carbonate			15,690				16,764	1,317	3.8	4,970	7.6
OPH-1835	1,190.75	NGU	Carbonate			21,501				40,645	1,456	4.5	3,932	13.9
OPH-1849	1,198.41	NGU	Mudstone			30,632	17.0			13,990	101	7.9	27,523	17.8
OPH-1856	1,199.56	NGU	Carbonate			13,697				36,423	1,440			12.0
OPH-1862	1,200.64	NGU	Carbonate			20,090	18.0			38,655	1,386		816	13.7
OPH-1865	1,201.25	NGU	Carbonate			25,652	57.0			59,942	1,355		964	47.7
OPH-1871	1,202.50	NGU	Carbonate			7,272	17.0			32,805	1,231			8.2
OPH-1879	1,203.59	NGU	Mudstone			26,399	110.0			26,594	457	5.4	9,125	16.1
OPH-1885	1,204.44	NGU	Mudstone			36,776				32,745	240	8.4	13,353	31.5
OPH-1892	1,205.03	NGU	Mudstone			42,338	24.0			22,011	139	20.2	13,724	26.2
OPH-1904	1,206.20	NGU	Mudstone			22,497	16.0			20,925	147	8.8	10,312	16.3
OPH-1918	1,207.63	Yale2	Mudstone							22,694		11.5		
OPH-1918	1,207.63	Yale2	Mudstone							22,694		11.5		
OPH-1918	1,207.63	NGU	Mudstone			36,028	36.0			23,157	147	13.3	6,973	31.1
OPH-1918	1,207.63	NGU	Mudstone			36,028	36.0			23,157	147	13.3	6,973	31.1
OPH-1924	1,208.96	NGU	Carbonate			23,161	15.0			22,976	1,076	21.7	2,077	14.0
OPH-1927	1,209.45	NGU	Carbonate			27,644	25.0			13,026	565	9.4	8,012	14.4
OPH-1939	1,211.12	NGU	Mudstone			29,470	34.0			20,744	139	27.9	4,229	11.0
OPH-1942	1,211.51	NGU	Mudstone			27,312	17.0			20,081	116	31.4	4,080	12.7
OPH-1948	1,212.51	NGU	Carbonate			2,507	40.0			16,945	2,409	4.0		2.9
OPH-1960	1,214.11	NGU	Mudstone			32,127				10,734	186	3.1	12,092	16.1
OPH-1962	1,214.28	NGU	Mudstone			43,334	40.0			25,328	410		10,534	28.2

Sample ID	Depth (m)	Sample set	Lithology	Ho (ppm)	In (ppm)	K (ppm)	La (ppm)	Li (ppm)	Lu (ppm)	Mg (ppm)	Mn (ppm)	Mo (ppm)	Na (ppm)	Nb (ppm)
OPH-1975	1,215.53	NGU	Carbonate			141				53,670	1,673			4.2
OPH-1984	1,216.89	NGU	Mudstone			15,358	32.0			13,810	271	5.4	5,193	11.9
OPH-1994	1,217.74	NGU	Mudstone			27,395	15.0			18,935	139	12.1	8,680	66.1
OPH-2001	1,218.36	NGU	Carbonate			2,300	17.0			18,151	2,982			4.8
OPH-2001	1,218.36	Yale2	Carbonate							18,148		1.1		
OPH-2001	1,218.36	NGU	Carbonate			2,300	17.0			18,151	2,982			4.8
OPH-2001	1,218.36	Yale2	Carbonate							18,148		1.1		
OPH-2010	1,219.18	NGU	Carbonate			3,171				24,724	4,074	10.8		10.0
OPH-2027	1,220.85	NGU	Mudstone			18,014				18,574	186	17.6	5,638	8.7
OPH-2040	1,221.72	NGU	Mudstone			40,677	19.0			39,619	356	13.5	1,929	20.5
OPH-2052	1,223.79	NGU	Mudstone			19,591	70.0			40,886	372	8.4	3,338	86.0
OPH-2061	1,225.13	Yale2	Mudstone							47,185		4.6		
OPH-2061	1,225.13	Yale2	Mudstone							47,185		4.6		
OPH-2061	1,225.13	NGU	Mudstone			6,708				65,128	612	5.3	22,701	12.3
OPH-2061	1,225.13	NGU	Mudstone			6,708				65,128	612	5.3	22,701	12.3
OPH-2068	1,226.04	NGU	Mudstone			365	15.0			46,494	573	51.6	4,525	34.9
OPH-2069	1,226.21	NGU	Carbonate			291	33.0			41,851	1,417	21.8	1,039	26.6
OPH-2397	1,426.19	NGU	Mudstone			3,702				23,760	651	16.7	22,033	5.8
OPH-2406	1,427.09	Yale2	Mudstone							8,157		14.4		
OPH-2406	1,427.09	Yale2	Mudstone							8,157		14.4		
OPH-2406	1,427.16	NGU	Mudstone			6,093				15,438	410	15.9	20,475	5.4
OPH-2406	1,427.16	NGU	Mudstone			6,093				15,438	410	15.9	20,475	5.4
OPH-2413	1,427.81	NGU	Mudstone			7,073				14,774	379	10.7	25,446	4.9
OPH-2423	1,437.13	NGU	Mudstone			830				40,765	1,193		34,941	7.2
OPH-2426	1,437.68	NGU	Mudstone			1,469				23,639	627	5.5	37,538	4.8
OPH-2993	1,765.27	NGU	Carbonate			191				63,319	2,881			2.8
OPH-3009	1,767.41	NGU	Carbonate			996				15,739	805		24,926	3.2
OPH-3016	1,777.38	Yale2	Mudstone							3,259		22.0		
OPH-3016	1,777.38	Yale2	Mudstone							3,259		22.0		
OPH-3016	1,777.46	NGU	Mudstone			4,134	79.0			17,247	418	13.8	25,817	6.2
OPH-3016	1,777.46	NGU	Mudstone			4,134	79.0			17,247	418	13.8	25,817	6.2
OPH-3057	1,792.05	NGU				3,694				14,171	310		33,829	
OPH-3112	1,868.46	NGU	Mudstone			1,278				14,835	248	13.6	43,844	11.0
OPH-3117	1,869.18	NGU	Mudstone			955				14,654	256	4.6	52,820	9.0
OPH-3132	1,871.00	Yale2	Mudstone							26,402		0.6		
OPH-3132	1,871.00	Yale2	Mudstone							26,402		0.6		
OPH-3132	1,871.00	NGU	Mudstone			5,977				27,921	488		30,194	11.0
OPH-3132	1,871.00	NGU	Mudstone			5,977				27,921	488		30,194	11.0
OPH-3141	1,871.27	NGU	Mudstone			7,936	154.0			22,554	395	17.8	27,300	8.7
OPH-3137	1,871.47	NGU	Mudstone			7,006				25,810	434		31,381	10.6
OPH-3161	1,881.50	NGU	Mudstone			19,841	30.0			13,086	225		34,422	11.6
OPH-3168	1,887.61	NGU	Mudstone			20,090	20.0			10,071	163		38,206	11.8
OPH-3179	1,888.77	NGU	Carbonate			473				120,607	1,030		1,410	
OPH-3182	1,889.14	NGU				13,780				51,740	1,301		12,760	
OPH-3191	1,902.61	Yale2	Mudstone							36,909		0.3		

Sample ID	Depth (m)	Sample set	Lithology	Ho (ppm)	In (ppm)	K (ppm)	La (ppm)	Li (ppm)	Lu (ppm)	Mg (ppm)	Mn (ppm)	Mo (ppm)	Na (ppm)	Nb (ppm)
OPH-3194	1,902.88	NGU	Mudstone			22,082	27.0			33,649	465		15,060	15.4
OPH-3229	1,915.60	NGU	Mudstone			38,021				28,162	488		10,312	
OPH-3256	1,926.73	Yale2	Mudstone							23,621		0.5		
OPH-3256	1,926.73	Yale2	Mudstone							23,621		0.5		
OPH-3256	1,926.80	NGU	Mudstone			31,629	18.0			24,061	364		12,537	16.3
OPH-3256	1,926.80	NGU	Mudstone			31,629	18.0			24,061	364		12,537	16.3
OPH-3272	1,935.31	NGU	Mudstone			23,410	29.0			34,192	496		12,537	15.3
OPH-3275	1,935.54	NGU	Mudstone			23,244	27.0			37,690	689		11,721	15.4
OPH-3295	1,946.55	NGU	Mudstone			22,497	32.0			42,273	1,193		7,344	9.7
OPH-3324	1,957.85	NGU	Mudstone			25,153	31.0			34,132	573		12,166	18.2
OPH-3331	1,958.63	NGU	Mudstone			35,032	29.0			20,925	310		14,615	13.0
OPH-3355	1,970.85	Yale2	Mudstone							20,880		0.4		
OPH-3355	1,970.85	Yale2	Mudstone							20,880		0.4		
OPH-3355	1,970.85	NGU	Mudstone			36,194	32.0			21,890	101		13,428	12.6
OPH-3355	1,970.85	NGU	Mudstone			36,194	32.0			21,890	101		13,428	12.6
OPH-3386	1,980.42	NGU	Carbonate			22,165	19.0			56,384	1,092		8,754	7.0
OPH-3411	1,991.90	NGU				24,821				58,314	604		6,083	
OPH-3463	2,011.35	Yale2	Mudstone							49,255		0.2		
OPH-3589	2,052.57	Yale2	Mudstone							41,182		0.5		
OPH-3707	2,103.47	Yale2	Mudstone							48,973		0.2		
OPH-3736	2,205.38	Yale1	Carbonate		0.1	1.37		0.7	3.3	0.01	195,669	790			
OPH-3904	2,252.09	Yale1	Carbonate		0.1	3.70		0.3	8.1	0.00	49,699	1,522			
OPH-4022	2,285.28	Yale2	Carbonate							87,421		0.3		
OPH-4081	2,305.25	Yale1	Carbonate		0.1	2.82		0.5	1.7	0.01	42,677	248		501	
OPH-4142	2,324.43	Yale1	Carbonate		0.1	2.22		1.4	4.1	0.01	162,134	523		272	
OPH-4178	2,328.55	Yale1	Carbonate		0.1	1.79		1.4	7.1	0.01	269,966	525			
OPH-4178	2,328.55	Acme	Carbonate	<0.1	<0.01	400	0.7	3.4	<0.1	176,300	342	2.1	130	<0.04	
OPH-4183	2,329.14	Acme	Carbonate	<0.1	<0.01	3,300	2.6	50.6	<0.1	123,100	228	0.0	60	0.1	
OPH-4185	2,329.34	Acme		<0.1	<0.01		0.2	2.5	<0.1	89,100	153	0.1	90	0.7	
OPH-4187	2,329.62	Acme		<0.1	<0.01		0.1	2.4	<0.1	79,900	419	0.1	60	0.1	
OPH-4193	2,330.28	Yale2	Evaporite							136,544		0.7		
OPH-4194	2,330.34	Yale1	Carbonate		0.1	1.98		0.6	8.3	0.01	330,177	557		248	
OPH-4194	2,330.34	Acme	Carbonate	<0.1	0.01	400	0.6	8.1	<0.1	175,000	313	0.5	120	0.1	
OPH-4194	2,330.34	Acme	Carbonate	<0.1	0.01	400	0.6	8.1	<0.1	175,000	313	0.5	120	0.1	
OPH-4194	2,330.34	Yale1	Carbonate		0.1	1.98		0.6	8.3	0.01	330,177	557		248	
OPH-4199	2,330.85	Acme	Evaporite	<0.1	<0.01	300	0.4	6.8	<0.1	44,700	74	0.1	60	1.7	
OPH-4211	2,509.02	Yale1	Evaporite		0.1	1.85		0.2	6.2	0.00	68,402	32			
OPH-4257	2,517.36	Yale1	Evaporite		0.2	2.96		1.1	13.8	0.01	90,815	85		2,118	
OPH-4310	2,526.68	Yale1	Evaporite		0.2	1.52		1.2	7.8	0.05	328,190	376		781	
OPH-4366	2,547.78	Yale1	Evaporite		0.1	1.69		0.6	72.6	0.01	325,676	314		211	
OPH-4383	2,549.45	Yale2	Mudstone							53,599		0.8		
OPH-4440	2,570.15	Yale1	Evaporite		0.1	1.85		1.1	4.3	0.01	201,132	212		451	
OPH-4537	2,700.97	Yale1	Evaporite		0.1	2.30		0.2	0.6	0.00	49,903	34		4,779	
OPH-4582	2,724.31	Yale2	Evaporite							43,310		0.2		
OPH-4635	2,833.79	Yale1	Evaporite		0.2	2.07		3.2	15.6	0.04	137,383	73		22,200	

Sample ID	Depth (m)	Sample set	Lithology	Ho (ppm)	In (ppm)	K (ppm)	La (ppm)	Li (ppm)	Lu (ppm)	Mg (ppm)	Mn (ppm)	Mo (ppm)	Na (ppm)	Nb (ppm)
OPH-4620	2,838.14	Yale2	Evaporite							44,606		1.1		
OPH-4683	2,850.46	Yale1	Evaporite	0.2	2.94		2.8	21.7	0.03	63,919	31		236,899	
OPH-4683	2,850.46	Yale1	Evaporite	0.2	2.94		2.8	21.7	0.03	63,919	31		236,899	
OPH-4683	2,850.46	Yale2	Evaporite							30,060		0.0		
OPH-4683	2,850.46	Yale2	Evaporite							30,060		0.0		
OPH-4774	2,878.31	Yale1	Evaporite	0.2	2.17		5.5	6.9	0.03	68,394	245		75,925	
OPH-4813	2,896.20	Yale1	Evaporite	0.1	2.43		1.1	29.6	0.01	35,732	16		302,679	
OPH-4853	2,904.34	Yale1	Evaporite	0.1	2.07		0.7	18.9	0.01	38,261	20		200,999	

Table A5d: Element concentration data for drill core OPH, continued.

Sample ID	Depth (m)	Sample set	Lithology	Nd (ppm)	Ni (ppm)	P (ppm)	Pb (ppm)	Pr (ppm)	Rb (ppm)	Re (ppm)	Sb (ppm)	Sc (ppm)	Se (ppm)	Sm (ppm)
OPH-10	530.39	NGU	Mudstone	24.0	201.0	1,004			15.1			20.2		
OPH-73	542.63	Yale2	Mudstone											
OPH-73	542.63	Yale2	Mudstone											
OPH-73	542.72	NGU	Mudstone	14.0	286.0	786			16.1			23.2		
OPH-73	542.72	NGU	Mudstone	14.0	286.0	786			16.1			23.2		
OPH-80	543.68	NGU	Mudstone	24.0	255.0	956			15.2			24.5		
OPH-83	544.22	NGU	Mudstone	24.0	332.0	633			23.9			21.3		
OPH-121	552.43	NGU	Mudstone		202.0	611	5.1					15.0		
OPH-284	591.30	NGU	Mudstone	22.0	86.9	1,034			21.7			20.4		
OPH-306	594.85	Yale2	Mudstone											
OPH-306	594.85	Yale2	Mudstone											
OPH-306	594.93	NGU	Mudstone	23.0	76.1	1,030			35.2			20.7		
OPH-306	594.93	NGU	Mudstone	23.0	76.1	1,030			35.2			20.7		
OPH-507	636.42	NGU	Mudstone	23.0	205.0	1,039	19.9		23.3			20.5		
OPH-515	637.85	NGU	Mudstone	19.0	173.0	847	24.4		19.3			24.5		
OPH-523	638.53	Yale2	Mudstone											
OPH-523	638.53	Yale2	Mudstone											
OPH-523	638.63	NGU	Mudstone	21.0	96.2	864	6.6		19.9			19.2		
OPH-523	638.63	NGU	Mudstone	21.0	96.2	864	6.6		19.9			19.2		
OPH-844	890.22	Yale2	Mudstone											
OPH-844	890.22	Yale2	Mudstone											
OPH-844	890.22	NGU	Mudstone	16.0	80.3	153	17.9		74.0			9.8		
OPH-844	890.22	NGU	Mudstone	16.0	80.3	153	17.9		74.0			9.8		
OPH-849	891.17	Yale1	Mudstone	9.8	290.5		41.1	2.32	63.4					3.3
OPH-849	891.17	Yale1	Mudstone	9.8	290.5		41.1	2.32	63.4					3.3
OPH-849	891.17	NGU	Mudstone	18.0	238.0	127	55.5		43.5			6.4		
OPH-849	891.17	NGU	Mudstone	18.0	238.0	127	55.5		43.5			6.4		
OPH-858	892.79	NGU	Mudstone		212.0	127	53.1		44.2			7.7		
OPH-862	893.38	NGU	Mudstone		410.0	96	108.0		27.1		26.00			
OPH-867	894.16	NGU	Mudstone	39.0	250.0	201	30.3		81.2			15.7		
OPH-875	894.98	NGU	Carbonate		436.0	140	47.5		26.1			8.9		
OPH-879	895.49	NGU	Carbonate		163.0		23.6							
OPH-885	896.12	NGU												
OPH-903	897.58	NGU				144								
OPH-924	899.15	NGU	Carbonate		156.0	340	28.7		45.5			12.1		
OPH-925	899.25	NGU	Carbonate		128.0	175			45.4			5.9		
OPH-938	900.23	NGU	Carbonate		59.8	371	7.0		71.3			23.5		
OPH-945	901.96	NGU			221.0				132.0			56.0		
OPH-955	903.08	NGU	Mudstone		161.0	305			104.0			25.9		
OPH-970	904.30	NGU	Mudstone	15.0	78.2	436			119.0			45.1		
OPH-975	912.04	Yale2	Mudstone											
OPH-975	912.04	Yale2	Mudstone											

Sample ID	Depth (m)	Sample set	Lithology	Nd (ppm)	Ni (ppm)	P (ppm)	Pb (ppm)	Pr (ppm)	Rb (ppm)	Re (ppm)	Sb (ppm)	Sc (ppm)	Se (ppm)	Sm (ppm)
OPH-975	912.04	Yale2	Mudstone											
OPH-975	912.19	Yale1	Mudstone	62.3	101.5		2.9	17.77	20.8					10.3
OPH-975	912.19	Yale1	Mudstone	62.3	101.5		2.9	17.77	20.8					10.3
OPH-975	912.19	Yale1	Mudstone	62.3	101.5		2.9	17.77	20.8					10.3
OPH-975	912.19	NGU	Mudstone	23.0	41.4	305	7.4		15.1			17.8		
OPH-975	912.19	NGU	Mudstone	23.0	41.4	305	7.4		15.1			17.8		
OPH-975	912.19	NGU	Mudstone	23.0	41.4	305	7.4		15.1			17.8		
OPH-979	912.70	NGU	Mudstone	23.0	119.0	345	8.7		11.9			21.6		
OPH-1361	1,080.00	NGU	Carbonate	13.0	15.8	301								
OPH-1364	1,080.57	Acme	Carbonate	2.7	23.9	50	0.5	1.10	0.3	0.010	0.11	1.6	0.5	0.5
OPH-1364	1,080.57	Yale2	Carbonate											
OPH-1364	1,080.57	Acme	Carbonate	2.7	23.9	50	0.5	1.10	0.3	0.010	0.11	1.6	0.5	0.5
OPH-1364	1,080.57	Yale2	Carbonate											
OPH-1366	1,081.11	NGU	Carbonate		10.1	83								
OPH-1368	1,081.36	Acme	Carbonate	3.5	16.2	320	1.0	0.80	1.1	<0.002	0.08	3.5	<0.3	0.9
OPH-1372	1,081.93	Acme	Carbonate	4.7	17.9	180	1.0	1.10	0.5	0.003	0.16	4.5	<0.3	0.9
OPH-1373	1,082.28	NGU	Carbonate		12.0	96	15.1							
OPH-1376	1,082.71	NGU	Carbonate	12.0	33.3	83	15.2							
OPH-1383	1,083.49	NGU	Carbonate		11.2	61								
OPH-1390	1,084.18	NGU	Carbonate			92								
OPH-1393	1,084.47	Yale1	Carbonate	2.1	7.4		1.3	0.61	1.0					0.4
OPH-1393	1,084.47	Yale1	Carbonate	2.1	7.4		1.3	0.61	1.0					0.4
OPH-1393	1,084.47	Acme	Carbonate	1.4	5.5	170	1.1	0.30	0.7	<0.002	0.19	1.0	<0.3	0.3
OPH-1393	1,084.47	Acme	Carbonate	1.4	5.5	170	1.1	0.30	0.7	<0.002	0.19	1.0	<0.3	0.3
OPH-1398	1,085.13	Acme	Carbonate	1.3	6.3	70	1.1	0.30	0.7	<0.002	0.21	1.0	<0.3	0.2
OPH-1400	1,085.42	Acme	Carbonate	1.1	10.3	70	2.0	0.30	0.7	<0.002	0.45	0.9	<0.3	0.2
OPH-1403	1,086.33	NGU	Carbonate		9.6	79								
OPH-1405	1,086.52	Acme	Carbonate	1.3	7.9	90	1.0	0.30	0.5	<0.002	0.19	1.1	<0.3	0.3
OPH-1405	1,086.52	Yale2	Carbonate											
OPH-1405	1,086.52	Yale2	Carbonate											
OPH-1405	1,086.52	Acme	Carbonate	1.3	7.9	90	1.0	0.30	0.5	<0.002	0.19	1.1	<0.3	0.3
OPH-1412	1,087.73	Acme	Carbonate	1.9	8.8	90	2.0	0.40	0.6	<0.002	0.34	1.8	0.5	0.3
OPH-1421	1,089.09	NGU	Carbonate		20.1	476	13.5							
OPH-1426	1,089.67	Acme	Carbonate	7.8	39.9	500	24.7	1.90	1.1	<0.002	2.97	6.2	<0.3	1.8
OPH-1434	1,090.51	NGU	Carbonate	18.0	59.3	380	11.4		59.9			21.3		
OPH-1436	1,090.80	Acme	Carbonate	12.4	20.0	6,040	3.7	2.90	1.5	0.004	0.89	4.7	1.7	4.4
OPH-1442	1,091.87	NGU	Carbonate		19.3	607								
OPH-1444	1,092.14	Acme	Carbonate	2.2	9.9	110	1.9	0.50	0.5	<0.002	0.40	2.3	0.9	0.6
OPH-1449	1,093.39	Yale2	Carbonate											
OPH-1449	1,093.39	Yale2	Carbonate											
OPH-1449	1,093.39	Acme	Carbonate	2.2	4.4	60	2.8	0.60	0.9	<0.002	0.46	1.0	0.3	0.3
OPH-1449	1,093.39	Acme	Carbonate	2.2	4.4	60	2.8	0.60	0.9	<0.002	0.46	1.0	0.3	0.3
OPH-1452	1,093.90	NGU	Carbonate	18.0	52.5	122	8.1		48.8			8.8		
OPH-1461	1,094.89	Acme	Carbonate	1.6	4.8	210	2.2	0.30	8.5	0.004	0.28	1.1	<0.3	0.3
OPH-1464	1,095.45	Acme	Carbonate	5.0	4.7	110	1.4	1.10	4.0	<0.002	0.34	1.2	<0.3	0.9

Sample ID	Depth (m)	Sample set	Lithology	Nd (ppm)	Ni (ppm)	P (ppm)	Pb (ppm)	Pr (ppm)	Rb (ppm)	Re (ppm)	Sb (ppm)	Sc (ppm)	Se (ppm)	Sm (ppm)
OPH-1464	1,095.45	Yale1	Carbonate	5.4	5.7		1.4	1.31	3.9					1.2
OPH-1464	1,095.45	Acme	Carbonate	5.0	4.7	110	1.4	1.10	4.0	<0.002	0.34	1.2	<0.3	0.9
OPH-1464	1,095.45	Yale1	Carbonate	5.4	5.7		1.4	1.31	3.9					1.2
OPH-1466	1,095.74	Acme	Carbonate	12.7	16.5	330	3.0	3.20	33.3	0.003	0.54	4.4	0.8	2.8
OPH-1468	1,096.29	NGU	Carbonate	41.0	8.6	240	15.9		67.2					12.0
OPH-1469	1,096.31	Acme	Carbonate	5.2	4.7	120	1.7	1.20	22.1	<0.002	0.24	1.6	0.4	1.7
OPH-1470	1,096.57	Acme	Carbonate	3.3	4.5	200	2.0	1.00	9.4	<0.002	0.30	0.9	<0.3	0.5
OPH-1472	1,096.82	Acme	Carbonate	3.6	3.3	180	0.7	0.90	7.9	<0.002	0.23	1.3	<0.3	0.8
OPH-1479	1,098.06	Acme	Carbonate	2.5	4.0	130	1.1	0.80	13.0	<0.002	0.20	1.1	0.4	0.7
OPH-1483	1,098.66	NGU	Carbonate			140			16.0					
OPH-1486	1,099.04	Acme	Carbonate	1.7	3.5	140	3.9	0.30	2.9	0.003	0.06	0.3	<0.3	0.4
OPH-1488	1,099.51	NGU												
OPH-1491	1,099.98	Acme	Carbonate	0.7	6.8	90	0.8	<0.1	5.1	0.003	0.16	0.4	<0.3	0.1
OPH-1491	1,099.98	Yale1	Carbonate	1.0	10.9		0.8	0.29	7.4					0.2
OPH-1491	1,099.98	Yale1	Carbonate	1.0	10.9		0.8	0.29	7.4					0.2
OPH-1491	1,099.98	Acme	Carbonate	0.7	6.8	90	0.8	<0.1	5.1	0.003	0.16	0.4	<0.3	0.1
OPH-1499	1,101.27	Yale2	Carbonate											
OPH-1499	1,101.27	Yale2	Carbonate											
OPH-1501	1,101.45	NGU	Mudstone	53.0	53.5	327	19.8		35.1					
OPH-1509	1,102.06	NGU	Mudstone	29.0	397.0	253	26.1		67.2			9.5		
OPH-1516	1,102.74	NGU	Mudstone	46.0	310.0	349	33.5		61.7			16.7		10.0
OPH-1519	1,103.35	NGU	Mudstone	14.0	166.0	179	13.8		31.6			5.3		
OPH-1527	1,104.69	Yale1	Carbonate	1.9	2.4		0.5	0.57	2.1					0.4
OPH-1533	1,106.00	NGU	Carbonate		18.2	57	6.5		8.1					
OPH-1542	1,106.99	NGU	Mudstone	28.0	118.0	288	21.7		59.9			8.6		
OPH-1556	1,109.44	NGU	Carbonate	21.0	35.1	21,908	9.3		20.3					
OPH-1557	1,109.57	NGU	Carbonate		17.8	3,190	8.8							
OPH-1557	1,109.57	Yale1	Carbonate	1.9	30.0		0.7	0.51	5.9					0.5
OPH-1557	1,109.57	Yale1	Carbonate	1.9	30.0		0.7	0.51	5.9					0.5
OPH-1557	1,109.57	NGU	Carbonate		17.8	3,190	8.8							
OPH-1560	1,109.96	Yale1	Carbonate	0.3	10.0		0.2	0.17	2.1					0.1
OPH-1560	1,109.96	NGU	Carbonate		12.3	13,704								
OPH-1560	1,109.96	Yale1	Carbonate	0.3	10.0		0.2	0.17	2.1					0.1
OPH-1560	1,109.96	NGU	Carbonate		12.3	13,704								
OPH-1561	1,110.18	NGU	Carbonate	25.0	19.1	30,942	8.0		5.1					
OPH-1499	1,110.27	Acme	Carbonate	1.0	3.2	60	2.1	0.50	1.2	<0.002	0.45	0.3	<0.3	0.3
OPH-1499	1,110.27	Acme	Carbonate	1.0	3.2	60	2.1	0.50	1.2	<0.002	0.45	0.3	<0.3	0.3
OPH-1564	1,110.79	Yale1	Carbonate	0.6	34.1		0.2	0.22	2.1					0.1
OPH-1564	1,110.79	NGU	Carbonate		38.2	4,364								
OPH-1567	1,111.40	NGU	Carbonate		41.4	7,812								
OPH-1568	1,111.60	NGU	Carbonate		44.7	14,358	10.7		6.0					
OPH-1569	1,111.80	NGU	Carbonate	12.0	84.7	15,842	5.7		17.6					
OPH-1571	1,112.02	NGU	Carbonate	83.0	166.0	107,796	42.7		56.0					32.0
OPH-1572	1,112.08	Yale1	Mudstone	51.5	675.4		23.3	12.75	73.1					10.5
OPH-1572	1,112.08	NGU	Mudstone	43.0	692.0	511	67.8		127.0			15.5		12.0

Sample ID	Depth (m)	Sample set	Lithology	Nd (ppm)	Ni (ppm)	P (ppm)	Pb (ppm)	Pr (ppm)	Rb (ppm)	Re (ppm)	Sb (ppm)	Sc (ppm)	Se (ppm)	Sm (ppm)
OPH-1572	1,112.08	Acme	Mudstone	51.7	616.5	970	61.0	11.80	69.0	0.232	13.95	11.9	16.2	9.8
OPH-1572	1,112.08	NGU	Mudstone	43.0	692.0	511	67.8		127.0			15.5		12.0
OPH-1572	1,112.08	Acme	Mudstone	51.7	616.5	970	61.0	11.80	69.0	0.232	13.95	11.9	16.2	9.8
OPH-1572	1,112.08	Yale1	Mudstone	51.5	675.4		23.3	12.75	73.1					10.5
OPH-1572	1,112.08	Yale1	Mudstone	51.5	675.4		23.3	12.75	73.1					10.5
OPH-1572	1,112.08	NGU	Mudstone	43.0	692.0	511	67.8		127.0			15.5		12.0
OPH-1572	1,112.08	Acme	Mudstone	51.7	616.5	970	61.0	11.80	69.0	0.232	13.95	11.9	16.2	9.8
OPH-1573	1,112.27	Yale1	Mudstone	40.1	588.9		30.2	9.91	57.4					8.3
OPH-1573	1,112.27	Acme	Mudstone	32.8	438.5	480	59.8	8.80	48.9	0.221	13.49	9.8	16.6	7.1
OPH-1573	1,112.27	Yale1	Mudstone	40.1	588.9		30.2	9.91	57.4					8.3
OPH-1573	1,112.27	Acme	Mudstone	32.8	438.5	480	59.8	8.80	48.9	0.221	13.49	9.8	16.6	7.1
OPH-1575	1,112.65	Acme	Mudstone	33.1	381.4	520	58.6	8.10	48.2	0.212	12.59	10.1	14.3	6.7
OPH-1575	1,112.65	Yale1	Mudstone	35.7	431.1		27.2	8.83	45.2					7.1
OPH-1575	1,112.65	Yale1	Mudstone	35.7	431.1		27.2	8.83	45.2					7.1
OPH-1575	1,112.65	Acme	Mudstone	33.1	381.4	520	58.6	8.10	48.2	0.212	12.59	10.1	14.3	6.7
OPH-1578	1,113.28	Yale1	Mudstone	61.9	521.2		23.6	15.31	63.3					13.1
OPH-1578	1,113.28	Acme	Mudstone	56.2	366.6	1,480	45.5	13.60	50.5	0.139	9.69	10.4	13.6	12.9
OPH-1578	1,113.28	Acme	Mudstone	56.2	366.6	1,480	45.5	13.60	50.5	0.139	9.69	10.4	13.6	12.9
OPH-1578	1,113.28	Yale1	Mudstone	61.9	521.2		23.6	15.31	63.3					13.1
OPH-1579	1,113.58	NGU	Mudstone	79.0	401.0	6,284	46.0		65.5			15.3		19.0
OPH-1580	1,113.63	Acme	Mudstone	44.8	304.8	270	65.6	11.50	49.6	0.176	15.03	13.1	12.4	8.9
OPH-1580	1,113.63	Yale1	Mudstone	49.7	402.3		36.8	12.22	56.0					9.7
OPH-1580	1,113.63	Acme	Mudstone	44.8	304.8	270	65.6	11.50	49.6	0.176	15.03	13.1	12.4	8.9
OPH-1580	1,113.63	Yale1	Mudstone	49.7	402.3		36.8	12.22	56.0					9.7
OPH-1581	1,113.83	Yale1	Mudstone	43.0	322.2		29.7	10.56	48.0					8.6
OPH-1581	1,113.83	Acme	Mudstone	38.6	265.4	660	58.2	9.80	42.0	0.170	13.49	10.3	9.4	8.7
OPH-1581	1,113.83	Acme	Mudstone	38.6	265.4	660	58.2	9.80	42.0	0.170	13.49	10.3	9.4	8.7
OPH-1581	1,113.83	Yale1	Mudstone	43.0	322.2		29.7	10.56	48.0					8.6
OPH-1582	1,113.92	NGU	Mudstone	42.0	296.0	1,872	62.2		56.0			16.8		10.0
OPH-1584	1,114.20	Yale1	Mudstone	18.2	204.7		15.6	4.56	30.4					3.8
OPH-1584	1,114.20	Acme	Mudstone	22.1	192.4	390	43.1	5.90	29.3	0.171	9.95	6.2	7.3	5.0
OPH-1584	1,114.20	Acme	Mudstone	22.1	192.4	390	43.1	5.90	29.3	0.171	9.95	6.2	7.3	5.0
OPH-1584	1,114.20	Yale1	Mudstone	18.2	204.7		15.6	4.56	30.4					3.8
OPH-1585	1,114.34	Yale1	Mudstone	19.1	364.9		18.5	4.79	39.2					4.1
OPH-1585	1,114.34	Yale2	Mudstone											
OPH-1585	1,114.34	Yale2	Mudstone											
OPH-1585	1,114.34	Yale2	Mudstone											
OPH-1585	1,114.34	Acme	Mudstone	18.6	286.6	350	45.1	4.80	34.3	0.183	11.50	9.1	8.5	4.2
OPH-1585	1,114.34	Acme	Mudstone	18.6	286.6	350	45.1	4.80	34.3	0.183	11.50	9.1	8.5	4.2
OPH-1585	1,114.34	Acme	Mudstone	18.6	286.6	350	45.1	4.80	34.3	0.183	11.50	9.1	8.5	4.2
OPH-1585	1,114.34	Yale1	Mudstone	19.1	364.9		18.5	4.79	39.2					4.1
OPH-1585	1,114.34	Yale1	Mudstone	19.1	364.9		18.5	4.79	39.2					4.1
OPH-1586	1,114.62	NGU	Mudstone	38.0	294.0	284	61.6		59.7			21.6		11.0
OPH-1587	1,114.77	Acme	Mudstone	24.9	191.7	310	38.9	5.90	49.0	0.099	9.30	12.6	9.5	5.4
OPH-1587	1,114.77	Yale1	Mudstone	21.7	254.5		18.1	4.92	43.1					4.8

Sample ID	Depth (m)	Sample set	Lithology	Nd (ppm)	Ni (ppm)	P (ppm)	Pb (ppm)	Pr (ppm)	Rb (ppm)	Re (ppm)	Sb (ppm)	Sc (ppm)	Se (ppm)	Sm (ppm)
OPH-1587	1,114.77	Yale1	Mudstone	21.7	254.5		18.1	4.92	43.1					4.8
OPH-1587	1,114.77	Acme	Mudstone	24.9	191.7	310	38.9	5.90	49.0	0.099	9.30	12.6	9.5	5.4
OPH-1588	1,115.02	Yale1	Mudstone	13.3	326.5		15.4	3.34	33.0					2.9
OPH-1588	1,115.02	Yale1	Mudstone	13.3	326.5		15.4	3.34	33.0					2.9
OPH-1588	1,115.02	Acme	Mudstone	4.6	86.9	40	8.3	1.10	7.7	0.017	3.48	3.3	3.0	0.8
OPH-1588	1,115.02	Acme	Mudstone	4.6	86.9	40	8.3	1.10	7.7	0.017	3.48	3.3	3.0	0.8
OPH-1589	1,115.21	NGU	Mudstone	41.0	302.0	223	50.4		63.2			18.3		
OPH-1590	1,115.59	NGU	Carbonate		6.3	92	6.0							
OPH-1592	1,115.87	NGU	Mudstone	36.0	406.0	305	36.3		107.0			13.3		
OPH-1596	1,116.61	NGU	Carbonate		13.7									
OPH-1596	1,116.65	Yale1	Carbonate	1.0	8.0		0.5	0.36	0.7					0.2
OPH-1599	1,117.43	NGU	Carbonate	12.0	423.0	87	23.8		59.1			7.0		
OPH-1601	1,117.48	Acme	Mudstone	34.0	256.7	4,130	39.6	7.10	65.7	0.054	7.23	17.6	13.5	8.9
OPH-1606	1,118.27	Yale1	Mudstone	23.1	422.8		50.9	5.84	46.3					4.5
OPH-1606	1,118.27	Yale1	Mudstone	23.1	422.8		50.9	5.84	46.3					4.5
OPH-1606	1,118.27	Acme	Mudstone	23.0	376.5	170	23.2	6.10	35.3	0.175	11.49	19.5	7.8	4.5
OPH-1606	1,118.27	Acme	Mudstone	23.0	376.5	170	23.2	6.10	35.3	0.175	11.49	19.5	7.8	4.5
OPH-1608	1,118.59	NGU	Mudstone	37.0	288.0	463	23.6		56.5			18.1		
OPH-1613	1,119.54	NGU	Mudstone	26.0	163.0	218	14.2		107.0			22.9		
OPH-1647	1,120.31	Yale2	Mudstone											
OPH-1647	1,120.31	Yale2	Mudstone											
OPH-1647	1,120.31	Yale2	Mudstone											
OPH-1617	1,120.31	Acme	Mudstone	5.6	59.4	310	5.9	1.00	60.0	0.014	2.16	27.6	1.3	2.1
OPH-1617	1,120.31	Yale1	Mudstone	8.8	81.7		2.3	1.72	114.9					3.5
OPH-1617	1,120.31	Yale1	Mudstone	8.8	81.7		2.3	1.72	114.9					3.5
OPH-1617	1,120.31	Acme	Mudstone	5.6	59.4	310	5.9	1.00	60.0	0.014	2.16	27.6	1.3	2.1
OPH-1621	1,120.77	NGU	Mudstone	20.0	128.0	423	13.0		70.7			32.4		
OPH-1624	1,121.15	NGU	Mudstone	30.0	121.0	375	15.6		70.0			19.0		
OPH-1625	1,121.37	Acme	Mudstone	21.2	237.4	120	20.5	5.60	36.4	0.125	9.15	8.6	6.3	4.7
OPH-1625	1,121.37	Yale1	Mudstone	21.4	285.8		9.7	5.63	41.6					4.7
OPH-1625	1,121.37	Yale1	Mudstone	21.4	285.8		9.7	5.63	41.6					4.7
OPH-1625	1,121.37	Acme	Mudstone	21.2	237.4	120	20.5	5.60	36.4	0.125	9.15	8.6	6.3	4.7
OPH-1626	1,121.70	NGU	Mudstone	67.0	210.0	284	23.0		64.9			9.6		16.0
OPH-1634	1,123.13	NGU	Mudstone	11.0	233.0	550	10.0		97.8			19.0		
OPH-1640	1,123.62	NGU	Mudstone	25.0	543.0	384	23.7		47.1			11.8		
OPH-1647	1,124.27	Yale1	Mudstone	111.5	314.3		14.5	28.93	57.5					21.7
OPH-1647	1,124.27	Yale1	Mudstone	111.5	314.3		14.5	28.93	57.5					21.7
OPH-1647	1,124.27	Yale1	Mudstone	111.5	314.3		14.5	28.93	57.5					21.7
OPH-1647	1,124.27	Acme	Mudstone	218.4	100.4	470	17.6	50.90	48.4	0.010	2.15	22.4	2.4	43.0
OPH-1647	1,124.27	Acme	Mudstone	218.4	100.4	470	17.6	50.90	48.4	0.010	2.15	22.4	2.4	43.0
OPH-1647	1,124.27	Acme	Mudstone	218.4	100.4	470	17.6	50.90	48.4	0.010	2.15	22.4	2.4	43.0
OPH-1651	1,124.55	NGU	Mudstone	22.0	246.0	240	35.2		33.5			7.6		
OPH-1655	1,125.02	NGU	Mudstone	11.0	48.0	1,261	11.2		44.6					
OPH-1676	1,127.22	NGU	Mudstone	22.0	191.0	183	12.1		34.3			7.3		
OPH-1683	1,135.64	NGU	Carbonate		28.6	131			23.4					

Sample ID	Depth (m)	Sample set	Lithology	Nd (ppm)	Ni (ppm)	P (ppm)	Pb (ppm)	Pr (ppm)	Rb (ppm)	Re (ppm)	Sb (ppm)	Sc (ppm)	Se (ppm)	Sm (ppm)
OPH-1697	1,136.81	Yale2	Mudstone											
OPH-1697	1,136.81	Yale2	Mudstone											
OPH-1697	1,137.01	NGU	Mudstone	21.0	18.4	1,187	6.7		46.5			6.5		
OPH-1697	1,137.01	NGU	Mudstone	21.0	18.4	1,187	6.7		46.5			6.5		
OPH-1704	1,137.78	NGU	Carbonate	15.0	8.3	1,506			49.2			6.9		
OPH-1709	1,138.18	NGU	Carbonate	25.0	23.0	838	5.9		50.5			10.3		
OPH-1729	1,145.99	NGU	Mudstone	13.0	114.0	170	6.8		43.4			7.3		
OPH-1746	1,159.50	NGU	Mudstone	17.0	304.0	201	17.5		45.3			10.3		
OPH-1752	1,160.27	NGU	Mudstone	21.0	257.0	192	13.2		41.9			7.2		
OPH-1761	1,161.32	Yale2	Mudstone											
OPH-1761	1,161.32	Yale2	Mudstone											
OPH-1761	1,161.32	NGU	Mudstone	21.0	232.0	244	15.2		49.5			9.9		
OPH-1761	1,161.32	NGU	Mudstone	21.0	232.0	244	15.2		49.5			9.9		
OPH-1765	1,161.95	NGU	Mudstone	24.0	112.0	205	10.7		27.5			12.3		
OPH-1768	1,162.23	NGU	Mudstone	32.0	324.0	1,078	24.5		52.4			10.2		
OPH-1779	1,166.13	NGU	Mudstone	47.0	24.5	275	17.8		69.4			13.2		
OPH-1796	1,175.69	NGU	Mudstone	38.0	425.0	305	24.0		76.0			10.7		
OPH-1809	1,187.30	NGU	Mudstone	18.0	121.0	292	20.6		79.5			14.4		
OPH-1809	1,187.30	Yale2	Mudstone											
OPH-1809	1,187.30	Yale2	Mudstone											
OPH-1809	1,187.30	NGU	Mudstone	18.0	121.0	292	20.6		79.5			14.4		
OPH-1814	1,187.91	NGU	Mudstone	15.0	85.0	205	16.7		51.2			17.5		
OPH-1823	1,188.90	NGU	Mudstone	10.0	59.6	183	14.1		48.0			15.4		
OPH-1831	1,190.01	NGU	Carbonate		47.0	253			45.2			17.9		
OPH-1835	1,190.75	NGU	Carbonate		79.3	563			70.1			36.8		
OPH-1849	1,198.41	NGU	Mudstone	23.0	103.0	493	32.3		54.3			19.2		
OPH-1856	1,199.56	NGU	Carbonate	14.0	16.3	467			62.9					
OPH-1862	1,200.64	NGU	Carbonate	17.0	11.3	751			72.3			10.2		
OPH-1865	1,201.25	NGU	Carbonate	46.0	15.8	598			88.1			14.0		
OPH-1871	1,202.50	NGU	Carbonate	20.0	20.8	231			36.3			5.6		
OPH-1879	1,203.59	NGU	Mudstone	47.0	67.1	388	5.9		50.8			14.4		
OPH-1885	1,204.44	NGU	Mudstone	31.0	74.4	594	8.3		71.8			18.0		
OPH-1892	1,205.03	NGU	Mudstone	25.0	89.4	633	11.6		72.3			23.3		
OPH-1904	1,206.20	NGU	Mudstone	10.0	72.0	262	12.1		46.9			10.5		
OPH-1918	1,207.63	Yale2	Mudstone											
OPH-1918	1,207.63	Yale2	Mudstone											
OPH-1918	1,207.63	NGU	Mudstone	35.0	110.0	532	6.1		61.7			16.4		
OPH-1918	1,207.63	NGU	Mudstone	35.0	110.0	532	6.1		61.7			16.4		
OPH-1924	1,208.96	NGU	Carbonate	24.0	91.2	262	6.6		62.5			9.6		
OPH-1927	1,209.45	NGU	Carbonate	22.0	51.3	419	6.1		45.1			11.4		
OPH-1939	1,211.12	NGU	Mudstone	24.0	113.0	279	9.4		45.9			10.0		
OPH-1942	1,211.51	NGU	Mudstone	18.0	137.0	310	9.7		51.0			18.6		
OPH-1948	1,212.51	NGU	Carbonate	31.0	21.3	388			21.1					
OPH-1960	1,214.11	NGU	Mudstone		71.9	681			32.8			18.0		
OPH-1962	1,214.28	NGU	Mudstone	32.0	130.0	1,113	13.3		43.7			33.1		

Sample ID	Depth (m)	Sample set	Lithology	Nd (ppm)	Ni (ppm)	P (ppm)	Pb (ppm)	Pr (ppm)	Rb (ppm)	Re (ppm)	Sb (ppm)	Sc (ppm)	Se (ppm)	Sm (ppm)
OPH-1975	1,215.53	NGU	Carbonate		9.0	327								
OPH-1984	1,216.89	NGU	Mudstone	20.0	43.8	196			21.9			9.6		
OPH-1994	1,217.74	NGU	Mudstone	19.0	44.0	345			25.1			8.5		
OPH-2001	1,218.36	NGU	Carbonate		8.6	668			11.2					
OPH-2001	1,218.36	Yale2	Carbonate											
OPH-2001	1,218.36	NGU	Carbonate		8.6	668			11.2					
OPH-2001	1,218.36	Yale2	Carbonate											
OPH-2010	1,219.18	NGU	Carbonate		63.0	912	7.4		57.6			30.4		
OPH-2027	1,220.85	NGU	Mudstone	13.0	25.4	227			30.9			12.2		
OPH-2040	1,221.72	NGU	Mudstone	23.0	76.9	524			38.3			33.1		
OPH-2052	1,223.79	NGU	Mudstone	54.0	55.9	284	5.0		16.6			27.6		11.0
OPH-2061	1,225.13	Yale2	Mudstone											
OPH-2061	1,225.13	Yale2	Mudstone											
OPH-2061	1,225.13	NGU	Mudstone		57.9	467			28.2			41.0		
OPH-2061	1,225.13	NGU	Mudstone		57.9	467			28.2			41.0		
OPH-2068	1,226.04	NGU	Mudstone	20.0	162.0	388						12.0		
OPH-2069	1,226.21	NGU	Carbonate	21.0	158.0	498						13.5		
OPH-2397	1,426.19	NGU	Mudstone		176.0	79			8.7			20.5		
OPH-2406	1,427.09	Yale2	Mudstone											
OPH-2406	1,427.09	Yale2	Mudstone											
OPH-2406	1,427.16	NGU	Mudstone		232.0	380	16.7		12.0			23.7		
OPH-2406	1,427.16	NGU	Mudstone		232.0	380	16.7		12.0			23.7		
OPH-2413	1,427.81	NGU	Mudstone		229.0	179			11.4			22.2		
OPH-2423	1,437.13	NGU	Mudstone		207.0	877						43.4		
OPH-2426	1,437.68	NGU	Mudstone		75.1	236						24.1		
OPH-2993	1,765.27	NGU	Carbonate		65.0	201						14.3		
OPH-3009	1,767.41	NGU	Carbonate		48.2									
OPH-3016	1,777.38	Yale2	Mudstone											
OPH-3016	1,777.38	Yale2	Mudstone											
OPH-3016	1,777.46	NGU	Mudstone	50.0	739.0	131	11.4		10.3			14.3		
OPH-3016	1,777.46	NGU	Mudstone	50.0	739.0	131	11.4		10.3			14.3		
OPH-3057	1,792.05	NGU				196								
OPH-3112	1,868.46	NGU	Mudstone	17.0	117.0	183			7.8			7.6		
OPH-3117	1,869.18	NGU	Mudstone		55.7	144						7.4		
OPH-3132	1,871.00	Yale2	Mudstone											
OPH-3132	1,871.00	Yale2	Mudstone											
OPH-3132	1,871.00	NGU	Mudstone	19.0	51.3	257	6.5		24.3			11.0		
OPH-3132	1,871.00	NGU	Mudstone	19.0	51.3	257	6.5		24.3			11.0		
OPH-3141	1,871.27	NGU	Mudstone	92.0	177.0	188	82.2		30.4			17.9		14.0
OPH-3137	1,871.47	NGU	Mudstone	13.0	65.5	201	11.9		28.7			11.5		
OPH-3161	1,881.50	NGU	Mudstone	27.0	37.4	201			68.0			14.1		
OPH-3168	1,887.61	NGU	Mudstone	24.0	8.5	205	12.4		58.1			14.4		
OPH-3179	1,888.77	NGU	Carbonate		9.7	746	12.1							
OPH-3182	1,889.14	NGU				288								
OPH-3191	1,902.61	Yale2	Mudstone											

Sample ID	Depth (m)	Sample set	Lithology	Nd (ppm)	Ni (ppm)	P (ppm)	Pb (ppm)	Pr (ppm)	Rb (ppm)	Re (ppm)	Sb (ppm)	Sc (ppm)	Se (ppm)	Sm (ppm)
OPH-3194	1,902.88	NGU	Mudstone	25.0	33.9	607	5.4		88.9			15.5		
OPH-3229	1,915.60	NGU	Mudstone			642								
OPH-3256	1,926.73	Yale2	Mudstone											
OPH-3256	1,926.73	Yale2	Mudstone											
OPH-3256	1,926.80	NGU	Mudstone	22.0	82.9	964			143.0			14.4		
OPH-3256	1,926.80	NGU	Mudstone	22.0	82.9	964			143.0			14.4		
OPH-3272	1,935.31	NGU	Mudstone	24.0	78.6	690			104.0			16.1		
OPH-3275	1,935.54	NGU	Mudstone	21.0	71.6	738			103.0			16.4		
OPH-3295	1,946.55	NGU	Mudstone	21.0	61.8	519			99.6			12.6		
OPH-3324	1,957.85	NGU	Mudstone	28.0	74.0	637			112.0			13.4		
OPH-3331	1,958.63	NGU	Mudstone	23.0	45.0	423			152.0			21.1		
OPH-3355	1,970.85	Yale2	Mudstone											
OPH-3355	1,970.85	Yale2	Mudstone											
OPH-3355	1,970.85	NGU	Mudstone	25.0	71.2	380			156.0			18.9		
OPH-3355	1,970.85	NGU	Mudstone	25.0	71.2	380			156.0			18.9		
OPH-3386	1,980.42	NGU	Carbonate	22.0	42.1	916			101.0					
OPH-3411	1,991.90	NGU				772								
OPH-3463	2,011.35	Yale2	Mudstone											
OPH-3589	2,052.57	Yale2	Mudstone											
OPH-3707	2,103.47	Yale2	Mudstone											
OPH-3736	2,205.38	Yale1	Carbonate	0.7	9.5		1.3	0.21	2.4					0.1
OPH-3904	2,252.09	Yale1	Carbonate	0.4	0.9		1.9	0.19	1.6					0.1
OPH-4022	2,285.28	Yale2	Carbonate											
OPH-4081	2,305.25	Yale1	Carbonate	0.6	1.4		3.0	0.20	0.3					0.2
OPH-4142	2,324.43	Yale1	Carbonate	0.8	1.7		10.7	0.27	1.4					0.1
OPH-4178	2,328.55	Yale1	Carbonate	1.0	7.3		0.5	0.33	1.7					0.2
OPH-4178	2,328.55	Acme	Carbonate	0.7	4.5	100	1.3	0.10	1.2	<0.002	0.05	0.2	<0.3	0.1
OPH-4183	2,329.14	Acme	Carbonate	1.5	2.7	20	11.8	0.40	15.2	<0.002	0.02	0.8	<0.3	0.2
OPH-4185	2,329.34	Acme		0.1	0.9	70	5.6	<0.1	0.2	<0.002	<0.02	<0.1	0.4	<0.1
OPH-4187	2,329.62	Acme		0.2	1.6	320	5.4	<0.1	0.2	<0.002	<0.02	<0.1	<0.3	<0.1
OPH-4193	2,330.28	Yale2	Evaporite											
OPH-4194	2,330.34	Yale1	Carbonate	0.4	6.1		0.8	0.16	1.6					0.1
OPH-4194	2,330.34	Acme	Carbonate	0.3	4.5	140	1.3	<0.1	1.8	<0.002	<0.02	<0.1	<0.3	<0.1
OPH-4194	2,330.34	Acme	Carbonate	0.3	4.5	140	1.3	<0.1	1.8	<0.002	<0.02	<0.1	<0.3	<0.1
OPH-4194	2,330.34	Yale1	Carbonate	0.4	6.1		0.8	0.16	1.6					0.1
OPH-4199	2,330.85	Acme	Evaporite	0.3	<0.1	100	2.9	<0.1	1.7	<0.002	<0.02	<0.1	<0.3	<0.1
OPH-4211	2,509.02	Yale1	Evaporite	0.5	0.9		0.3	0.17	0.7					0.1
OPH-4257	2,517.36	Yale1	Evaporite	6.2	45.9		1.8	1.03	18.0					2.4
OPH-4310	2,526.68	Yale1	Evaporite	0.6	37.3		1.0	0.23	4.2					0.2
OPH-4366	2,547.78	Yale1	Evaporite	2.9	14.0		1.1	0.59	73.0					0.7
OPH-4383	2,549.45	Yale2	Mudstone											
OPH-4440	2,570.15	Yale1	Evaporite	1.7	1.4		1.0	0.49	1.2					0.3
OPH-4537	2,700.97	Yale1	Evaporite	0.5	0.3		0.1	0.16	0.1					0.2
OPH-4582	2,724.31	Yale2	Evaporite											
OPH-4635	2,833.79	Yale1	Evaporite	6.2	4.2		0.0	1.44	9.1					1.2

Sample ID	Depth (m)	Sample set	Lithology	Nd (ppm)	Ni (ppm)	P (ppm)	Pb (ppm)	Pr (ppm)	Rb (ppm)	Re (ppm)	Sb (ppm)	Sc (ppm)	Se (ppm)	Sm (ppm)
OPH-4620	2,838.14	Yale2	Evaporite											
OPH-4683	2,850.46	Yale1	Evaporite	3.1	9.0		0.3	0.82	95.2					0.6
OPH-4683	2,850.46	Yale1	Evaporite	3.1	9.0		0.3	0.82	95.2					0.6
OPH-4683	2,850.46	Yale2	Evaporite											
OPH-4683	2,850.46	Yale2	Evaporite											
OPH-4774	2,878.31	Yale1	Evaporite	4.6	4.0		0.1	1.33	8.3					0.8
OPH-4813	2,896.20	Yale1	Evaporite	1.2	1.8		0.0	0.36	4.7					0.2
OPH-4853	2,904.34	Yale1	Evaporite	0.9	1.6		0.1	0.27	20.9					0.2

Table A5e: Element concentration data for drill core OPH, continued.

Sample ID	Depth (m)	Sample set	Lithology	Sn (ppm)	Sr (ppm)	Ta (ppm)	Tb (ppm)	Te (ppm)	Th (ppm)	Ti (ppm)	Tl (ppm)	Tm (ppm)	U (ppm)	V (ppm)
OPH-10	530.39	NGU	Mudstone		48.9					9,470				215
OPH-73	542.63	Yale2	Mudstone							10,283			0.4	232
OPH-73	542.63	Yale2	Mudstone							10,283			0.4	232
OPH-73	542.72	NGU	Mudstone		43.5					10,369				267
OPH-73	542.72	NGU	Mudstone		43.5					10,369				267
OPH-80	543.68	NGU	Mudstone		53.5					9,949				234
OPH-83	544.22	NGU	Mudstone		37.8					11,627				304
OPH-121	552.43	NGU	Mudstone		19.8					8,151				199
OPH-284	591.30	NGU	Mudstone	6.9	106.0					11,328				241
OPH-306	594.85	Yale2	Mudstone							12,887			0.4	205
OPH-306	594.85	Yale2	Mudstone							12,887			0.4	205
OPH-306	594.93	NGU	Mudstone		172.0				4.6	11,447				227
OPH-306	594.93	NGU	Mudstone		172.0				4.6	11,447				227
OPH-507	636.42	NGU	Mudstone		80.8				4.5	10,069				237
OPH-515	637.85	NGU	Mudstone		97.2				3.0	9,649				227
OPH-523	638.53	Yale2	Mudstone							7,923			0.5	166
OPH-523	638.53	Yale2	Mudstone							7,923			0.5	166
OPH-523	638.63	NGU	Mudstone		78.0				4.0	7,971				184
OPH-523	638.63	NGU	Mudstone		78.0				4.0	7,971				184
OPH-844	890.22	Yale2	Mudstone							1,656			10.9	542
OPH-844	890.22	Yale2	Mudstone							1,656			10.9	542
OPH-844	890.22	NGU	Mudstone		22.9				7.4	1,678			22.4	611
OPH-844	890.22	NGU	Mudstone		22.9				7.4	1,678			22.4	611
OPH-849	891.17	Yale1	Mudstone		15.7				5.0	1,891	4.99	0.34	26.2	512
OPH-849	891.17	Yale1	Mudstone		15.7				5.0	1,891	4.99	0.34	26.2	512
OPH-849	891.17	NGU	Mudstone		7.0				5.0	1,456			27.9	455
OPH-849	891.17	NGU	Mudstone		7.0				5.0	1,456			27.9	455
OPH-858	892.79	NGU	Mudstone		5.1				4.5	1,510			27.8	420
OPH-862	893.38	NGU	Mudstone							671			26.5	808
OPH-867	894.16	NGU	Mudstone		14.6				8.5	2,415			32.7	863
OPH-875	894.98	NGU	Carbonate		45.4				3.7	1,181			45.2	978
OPH-879	895.49	NGU	Carbonate		58.0					90			12.3	102
OPH-885	896.12	NGU												
OPH-903	897.58	NGU								2,068				
OPH-924	899.15	NGU	Carbonate		109.0					2,415			5.6	356
OPH-925	899.25	NGU	Carbonate		141.0					4,297				337
OPH-938	900.23	NGU	Carbonate	9.1	102.0					6,053				495
OPH-945	901.96	NGU			68.5									394
OPH-955	903.08	NGU	Mudstone		30.1					7,791			13.0	428
OPH-970	904.30	NGU	Mudstone		37.1					11,807			5.0	537
OPH-975	912.04	Yale2	Mudstone							3,782			14.1	253
OPH-975	912.04	Yale2	Mudstone							3,782			14.1	253

Sample ID	Depth (m)	Sample set	Lithology	Sn (ppm)	Sr (ppm)	Ta (ppm)	Tb (ppm)	Te (ppm)	Th (ppm)	Ti (ppm)	Tl (ppm)	Tm (ppm)	U (ppm)	V (ppm)
OPH-975	912.04	Yale2	Mudstone							3,782			14.1	253
OPH-975	912.19	Yale1	Mudstone		598.3				6.6	6,419	0.40	0.77	18.0	739
OPH-975	912.19	Yale1	Mudstone		598.3				6.6	6,419	0.40	0.77	18.0	739
OPH-975	912.19	Yale1	Mudstone		598.3				6.6	6,419	0.40	0.77	18.0	739
OPH-975	912.19	NGU	Mudstone		203.0				19.8	4,549			20.1	293
OPH-975	912.19	NGU	Mudstone		203.0				19.8	4,549			20.1	293
OPH-975	912.19	NGU	Mudstone		203.0				19.8	4,549			20.1	293
OPH-979	912.70	NGU	Mudstone		187.0				8.4	5,892			20.8	406
OPH-1361	1,080.00	NGU	Carbonate		154.0					1,960				55
OPH-1364	1,080.57	Acme	Carbonate	0.1	112.0	0.1	0.2	5.34	0.6	230	0.05	<0.1	0.1	35
OPH-1364	1,080.57	Yale2	Carbonate							349			0.1	41
OPH-1364	1,080.57	Acme	Carbonate	0.1	112.0	0.1	0.2	5.34	0.6	230	0.05	<0.1	0.1	35
OPH-1364	1,080.57	Yale2	Carbonate							349			0.1	41
OPH-1366	1,081.11	NGU	Carbonate		96.9					491				29
OPH-1368	1,081.36	Acme	Carbonate	0.2	63.0	0.2	0.2	6.43	3.4	510	<0.05	<0.1	0.2	38
OPH-1372	1,081.93	Acme	Carbonate	0.2	152.0	<0.1	0.1	4.04	1.3	510	0.08	<0.1	0.2	32
OPH-1373	1,082.28	NGU	Carbonate		218.0					1,199			6.2	70
OPH-1376	1,082.71	NGU	Carbonate	10.1	98.7				9.2	485			6.7	60
OPH-1383	1,083.49	NGU	Carbonate		101.0					839				50
OPH-1390	1,084.18	NGU	Carbonate		78.6					354				14
OPH-1393	1,084.47	Yale1	Carbonate		91.0				0.5	410	0.22	0.05	0.2	11
OPH-1393	1,084.47	Yale1	Carbonate		91.0				0.5	410	0.22	0.05	0.2	11
OPH-1393	1,084.47	Acme	Carbonate	<0.1	69.0	<0.1	<0.1	6.29	0.4	270	0.18	<0.1	0.1	8
OPH-1393	1,084.47	Acme	Carbonate	<0.1	69.0	<0.1	<0.1	6.29	0.4	270	0.18	<0.1	0.1	8
OPH-1398	1,085.13	Acme	Carbonate	<0.1	53.0	<0.1	<0.1	8.27	0.4	280	0.05	<0.1	0.3	10
OPH-1400	1,085.42	Acme	Carbonate	<0.1	53.0	<0.1	<0.1	4.33	0.3	260	0.07	<0.1	0.3	15
OPH-1403	1,086.33	NGU	Carbonate		115.0					264				27
OPH-1405	1,086.52	Acme	Carbonate	<0.1	166.0	<0.1	<0.1	5.52	0.3	180	<0.05	<0.1	0.1	9
OPH-1405	1,086.52	Yale2	Carbonate							187			0.1	9
OPH-1405	1,086.52	Yale2	Carbonate							187			0.1	9
OPH-1405	1,086.52	Acme	Carbonate	<0.1	166.0	<0.1	<0.1	5.52	0.3	180	<0.05	<0.1	0.1	9
OPH-1412	1,087.73	Acme	Carbonate	<0.1	141.0	<0.1	<0.1	2.05	0.5	290	<0.05	<0.1	0.2	16
OPH-1421	1,089.09	NGU	Carbonate		267.0					1,115				32
OPH-1426	1,089.67	Acme	Carbonate	0.3	346.0	<0.1	0.2	2.59	2.5	300	0.15	0.10	0.6	17
OPH-1434	1,090.51	NGU	Carbonate		70.1				6.8	5,724				139
OPH-1436	1,090.80	Acme	Carbonate	0.3	440.0	<0.1	0.7	4.02	3.5	350	0.09	0.20	0.5	22
OPH-1442	1,091.87	NGU	Carbonate		254.0					336				31
OPH-1444	1,092.14	Acme	Carbonate	<0.1	324.0	<0.1	0.2	3.39	0.3	170	0.05	<0.1	0.2	10
OPH-1449	1,093.39	Yale2	Carbonate							126			0.2	8
OPH-1449	1,093.39	Yale2	Carbonate							126			0.2	8
OPH-1449	1,093.39	Acme	Carbonate	0.1	118.0	<0.1	<0.1	5.54	0.3	160	0.06	<0.1	0.2	9
OPH-1449	1,093.39	Acme	Carbonate	0.1	118.0	<0.1	<0.1	5.54	0.3	160	0.06	<0.1	0.2	9
OPH-1452	1,093.90	NGU	Carbonate		187.0				3.6	1,372				294
OPH-1461	1,094.89	Acme	Carbonate	0.1	205.0	0.7	<0.1	5.78	0.4	190	0.34	<0.1	1.7	5
OPH-1464	1,095.45	Acme	Carbonate	0.1	62.0	<0.1	0.1	6.87	0.2	140	0.12	<0.1	0.1	4

Sample ID	Depth (m)	Sample set	Lithology	Sn (ppm)	Sr (ppm)	Ta (ppm)	Tb (ppm)	Te (ppm)	Th (ppm)	Ti (ppm)	Tl (ppm)	Tm (ppm)	U (ppm)	V (ppm)
OPH-1464	1,095.45	Yale1	Carbonate		71.6				0.3	178	0.13	0.24	0.2	10
OPH-1464	1,095.45	Acme	Carbonate	0.1	62.0	<0.1	0.1	6.87	0.2	140	0.12	<0.1	0.1	4
OPH-1464	1,095.45	Yale1	Carbonate		71.6				0.3	178	0.13	0.24	0.2	10
OPH-1466	1,095.74	Acme	Carbonate	0.6	126.0	<0.1	0.4	5.77	0.6	410	1.11	0.20	1.1	61
OPH-1468	1,096.29	NGU	Carbonate		324.0	19.6			35.7	300			29.8	15
OPH-1469	1,096.31	Acme	Carbonate	1.1	166.0	0.7	0.3	7.21	0.7	360	0.70	0.30	0.2	8
OPH-1470	1,096.57	Acme	Carbonate	0.3	56.0	0.1	<0.1	6.41	0.8	220	0.29	<0.1	0.2	4
OPH-1472	1,096.82	Acme	Carbonate	0.3	149.0	<0.1	<0.1	3.91	0.4	180	0.23	<0.1	0.1	4
OPH-1479	1,098.06	Acme	Carbonate	0.2	78.0	0.6	<0.1	8.99	0.4	210	0.44	<0.1	0.2	7
OPH-1483	1,098.66	NGU	Carbonate		70.8					258				19
OPH-1486	1,099.04	Acme	Carbonate	<0.1	97.0	<0.1	<0.1	6.19	<0.1	80	0.09	<0.1	11.0	30
OPH-1488	1,099.51	NGU			69.2								6.3	27
OPH-1491	1,099.98	Acme	Carbonate	<0.1	51.0	<0.1	<0.1	7.11	0.2	90	0.23	<0.1	0.7	27
OPH-1491	1,099.98	Yale1	Carbonate		69.4				0.1	129	0.28	0.03	0.9	37
OPH-1491	1,099.98	Yale1	Carbonate		69.4				0.1	129	0.28	0.03	0.9	37
OPH-1491	1,099.98	Acme	Carbonate	<0.1	51.0	<0.1	<0.1	7.11	0.2	90	0.23	<0.1	0.7	27
OPH-1499	1,101.27	Yale2	Carbonate							69			0.5	30
OPH-1499	1,101.27	Yale2	Carbonate							69			0.5	30
OPH-1501	1,101.45	NGU	Mudstone		32.3				12.5	2,421			10.1	288
OPH-1509	1,102.06	NGU	Mudstone		18.4				5.7	2,254			20.1	1,060
OPH-1516	1,102.74	NGU	Mudstone		15.1				8.9	3,165			24.2	1,200
OPH-1519	1,103.35	NGU	Mudstone		6.2					2,589				698
OPH-1527	1,104.69	Yale1	Carbonate		110.9				0.3	122	0.08	0.08	12.1	46
OPH-1533	1,106.00	NGU	Carbonate		190.0					156				68
OPH-1542	1,106.99	NGU	Mudstone		24.3				7.3	2,571			20.3	483
OPH-1556	1,109.44	NGU	Carbonate		150.0					246			44.3	333
OPH-1557	1,109.57	NGU	Carbonate		60.2					60			15.3	121
OPH-1557	1,109.57	Yale1	Carbonate		93.0				0.2	119	0.26	0.11	6.8	217
OPH-1557	1,109.57	Yale1	Carbonate		93.0				0.2	119	0.26	0.11	6.8	217
OPH-1557	1,109.57	NGU	Carbonate		60.2					60			15.3	121
OPH-1560	1,109.96	Yale1	Carbonate		56.9				0.1	48	0.11	0.04	0.7	25
OPH-1560	1,109.96	NGU	Carbonate		173.0					78				50
OPH-1560	1,109.96	Yale1	Carbonate		56.9				0.1	48	0.11	0.04	0.7	25
OPH-1560	1,109.96	NGU	Carbonate		173.0					78				50
OPH-1561	1,110.18	NGU	Carbonate	5.9	182.0					144			44.6	101
OPH-1499	1,110.27	Acme	Carbonate	<0.1	85.0	0.4	<0.1	9.16	0.2	90	0.07	<0.1	0.6	19
OPH-1499	1,110.27	Acme	Carbonate	<0.1	85.0	0.4	<0.1	9.16	0.2	90	0.07	<0.1	0.6	19
OPH-1564	1,110.79	Yale1	Carbonate		176.5				0.1	57	0.09	0.05	0.6	77
OPH-1564	1,110.79	NGU	Carbonate		156.0								6.2	79
OPH-1567	1,111.40	NGU	Carbonate		122.0					84			12.9	137
OPH-1568	1,111.60	NGU	Carbonate		135.0					78			41.0	154
OPH-1569	1,111.80	NGU	Carbonate		191.0					336			29.0	259
OPH-1571	1,112.02	NGU	Carbonate		279.0				12.6	1,241			238.0	603
OPH-1572	1,112.08	Yale1	Mudstone		19.0				6.9	3,654	2.62	1.16	100.7	2,542
OPH-1572	1,112.08	NGU	Mudstone		15.8				17.2	2,925			202.0	3,790

Sample ID	Depth (m)	Sample set	Lithology	Sn (ppm)	Sr (ppm)	Ta (ppm)	Tb (ppm)	Te (ppm)	Th (ppm)	Ti (ppm)	Tl (ppm)	Tm (ppm)	U (ppm)	V (ppm)
OPH-1572	1,112.08	Acme	Mudstone	2.7	27.0	2.0	1.6	0.78	6.9	3,240	3.97	1.10	105.5	2,656
OPH-1572	1,112.08	NGU	Mudstone		15.8				17.2	2,925			202.0	3,790
OPH-1572	1,112.08	Acme	Mudstone	2.7	27.0	2.0	1.6	0.78	6.9	3,240	3.97	1.10	105.5	2,656
OPH-1572	1,112.08	Yale1	Mudstone		19.0				6.9	3,654	2.62	1.16	100.7	2,542
OPH-1572	1,112.08	Yale1	Mudstone		19.0				6.9	3,654	2.62	1.16	100.7	2,542
OPH-1572	1,112.08	NGU	Mudstone		15.8				17.2	2,925			202.0	3,790
OPH-1572	1,112.08	Acme	Mudstone	2.7	27.0	2.0	1.6	0.78	6.9	3,240	3.97	1.10	105.5	2,656
OPH-1573	1,112.27	Yale1	Mudstone		24.7				6.0	3,159	1.80	0.98	97.1	2,560
OPH-1573	1,112.27	Acme	Mudstone	2.5	22.0	1.2	1.3	0.78	5.8	2,730	2.91	1.00	80.6	2,133
OPH-1573	1,112.27	Yale1	Mudstone		24.7				6.0	3,159	1.80	0.98	97.1	2,560
OPH-1573	1,112.27	Acme	Mudstone	2.5	22.0	1.2	1.3	0.78	5.8	2,730	2.91	1.00	80.6	2,133
OPH-1575	1,112.65	Acme	Mudstone	2.5	23.0	1.4	1.2	0.79	5.3	2,720	2.88	1.00	86.5	2,162
OPH-1575	1,112.65	Yale1	Mudstone		18.6				5.3	2,958	1.39	0.84	86.9	1,923
OPH-1575	1,112.65	Yale1	Mudstone		18.6				5.3	2,958	1.39	0.84	86.9	1,923
OPH-1575	1,112.65	Acme	Mudstone	2.5	23.0	1.4	1.2	0.79	5.3	2,720	2.88	1.00	86.5	2,162
OPH-1578	1,113.28	Yale1	Mudstone		31.1				7.1	4,375	2.07	1.27	90.1	2,539
OPH-1578	1,113.28	Acme	Mudstone	2.9	26.0	2.1	2.2	0.65	6.0	3,020	2.57	1.30	77.5	2,276
OPH-1578	1,113.28	Acme	Mudstone	2.9	26.0	2.1	2.2	0.65	6.0	3,020	2.57	1.30	77.5	2,276
OPH-1578	1,113.28	Yale1	Mudstone		31.1				7.1	4,375	2.07	1.27	90.1	2,539
OPH-1579	1,113.58	NGU	Mudstone		53.5				12.7	3,602			111.0	2,270
OPH-1580	1,113.63	Acme	Mudstone	2.3	23.0	1.4	1.3	0.76	4.8	5,330	2.91	0.80	72.6	1,502
OPH-1580	1,113.63	Yale1	Mudstone		21.4				6.3	5,025	1.95	0.88	77.7	1,529
OPH-1580	1,113.63	Acme	Mudstone	2.3	23.0	1.4	1.3	0.76	4.8	5,330	2.91	0.80	72.6	1,502
OPH-1580	1,113.63	Yale1	Mudstone		21.4				6.3	5,025	1.95	0.88	77.7	1,529
OPH-1581	1,113.83	Yale1	Mudstone		23.7				5.7	3,751	1.46	0.77	64.9	1,248
OPH-1581	1,113.83	Acme	Mudstone	1.7	22.0	1.2	1.3	0.65	5.1	2,970	3.03	0.80	63.4	1,095
OPH-1581	1,113.83	Acme	Mudstone	1.7	22.0	1.2	1.3	0.65	5.1	2,970	3.03	0.80	63.4	1,095
OPH-1581	1,113.83	Yale1	Mudstone		23.7				5.7	3,751	1.46	0.77	64.9	1,248
OPH-1582	1,113.92	NGU	Mudstone		22.4				11.1	3,230			97.9	1,820
OPH-1584	1,114.20	Yale1	Mudstone		16.8				2.6	2,096	0.70	0.33	26.7	842
OPH-1584	1,114.20	Acme	Mudstone	1.7	21.0	0.7	0.8	0.45	3.9	1,990	2.53	0.40	42.6	710
OPH-1584	1,114.20	Acme	Mudstone	1.7	21.0	0.7	0.8	0.45	3.9	1,990	2.53	0.40	42.6	710
OPH-1584	1,114.20	Yale1	Mudstone		16.8				2.6	2,096	0.70	0.33	26.7	842
OPH-1585	1,114.34	Yale1	Mudstone		21.9				2.8	3,421	0.99	0.51	37.9	1,416
OPH-1585	1,114.34	Yale2	Mudstone							2,210			78.5	1,074
OPH-1585	1,114.34	Yale2	Mudstone							2,210			78.5	1,074
OPH-1585	1,114.34	Yale2	Mudstone							2,210			78.5	1,074
OPH-1585	1,114.34	Acme	Mudstone	1.8	20.0	0.7	0.8	0.62	3.3	2,830	3.44	0.60	55.3	1,165
OPH-1585	1,114.34	Acme	Mudstone	1.8	20.0	0.7	0.8	0.62	3.3	2,830	3.44	0.60	55.3	1,165
OPH-1585	1,114.34	Acme	Mudstone	1.8	20.0	0.7	0.8	0.62	3.3	2,830	3.44	0.60	55.3	1,165
OPH-1585	1,114.34	Yale1	Mudstone		21.9				2.8	3,421	0.99	0.51	37.9	1,416
OPH-1585	1,114.34	Yale1	Mudstone		21.9				2.8	3,421	0.99	0.51	37.9	1,416
OPH-1586	1,114.62	NGU	Mudstone		11.4	5.5			7.8	5,604			66.3	1,880
OPH-1587	1,114.77	Acme	Mudstone	2.9	19.0	1.1	1.1	0.64	2.7	9,390	2.23	1.00	40.8	958
OPH-1587	1,114.77	Yale1	Mudstone		30.4				2.0	13,784	1.16	0.88	31.9	1,331

Sample ID	Depth (m)	Sample set	Lithology	Sn (ppm)	Sr (ppm)	Ta (ppm)	Tb (ppm)	Te (ppm)	Th (ppm)	Ti (ppm)	Tl (ppm)	Tm (ppm)	U (ppm)	V (ppm)
OPH-1587	1,114.77	Yale1	Mudstone		30.4				2.0	13,784	1.16	0.88	31.9	1,331
OPH-1587	1,114.77	Acme	Mudstone	2.9	19.0	1.1	1.1	0.64	2.7	9,390	2.23	1.00	40.8	958
OPH-1588	1,115.02	Yale1	Mudstone		10.2				1.7	2,631	0.55	0.44	19.8	1,061
OPH-1588	1,115.02	Yale1	Mudstone		10.2				1.7	2,631	0.55	0.44	19.8	1,061
OPH-1588	1,115.02	Acme	Mudstone	0.5	3.0	0.2	0.2	0.19	0.7	1,070	0.46	0.20	11.2	369
OPH-1588	1,115.02	Acme	Mudstone	0.5	3.0	0.2	0.2	0.19	0.7	1,070	0.46	0.20	11.2	369
OPH-1589	1,115.21	NGU	Mudstone		10.0				7.9	8,151			93.6	2,010
OPH-1590	1,115.59	NGU	Carbonate		146.0					66			5.0	57
OPH-1592	1,115.87	NGU	Mudstone		16.7				12.5	4,034			75.9	1,620
OPH-1596	1,116.61	NGU	Carbonate		136.0									81
OPH-1596	1,116.65	Yale1	Carbonate		53.4				0.1	19	0.08	0.06	0.5	29
OPH-1599	1,117.43	NGU	Carbonate		10.7				4.7	2,008			39.4	1,040
OPH-1601	1,117.48	Acme	Mudstone	3.5	44.0	1.4	1.5	0.32	4.5	17,280	2.35	0.80	70.3	2,252
OPH-1606	1,118.27	Yale1	Mudstone		27.8				4.6	4,558	1.19	0.47	19.0	832
OPH-1606	1,118.27	Yale1	Mudstone		27.8				4.6	4,558	1.19	0.47	19.0	832
OPH-1606	1,118.27	Acme	Mudstone	1.0	24.0	0.7	0.6	0.47	4.8	1,800	3.62	0.60	17.8	777
OPH-1606	1,118.27	Acme	Mudstone	1.0	24.0	0.7	0.6	0.47	4.8	1,800	3.62	0.60	17.8	777
OPH-1608	1,118.59	NGU	Mudstone		28.8				9.9	2,859			50.7	1,250
OPH-1613	1,119.54	NGU	Mudstone		32.3				3.5	10,788			35.5	1,410
OPH-1647	1,120.31	Yale2	Mudstone							4,727			7.8	492
OPH-1647	1,120.31	Yale2	Mudstone							4,727			7.8	492
OPH-1647	1,120.31	Yale2	Mudstone							4,727			7.8	492
OPH-1617	1,120.31	Acme	Mudstone	4.4	24.0	0.5	0.6	0.09	1.6	11,200	1.57	0.40	9.1	1,047
OPH-1617	1,120.31	Yale1	Mudstone		29.5				2.2	17,257	1.69	0.57	8.4	1,441
OPH-1617	1,120.31	Yale1	Mudstone		29.5				2.2	17,257	1.69	0.57	8.4	1,441
OPH-1617	1,120.31	Acme	Mudstone	4.4	24.0	0.5	0.6	0.09	1.6	11,200	1.57	0.40	9.1	1,047
OPH-1621	1,120.77	NGU	Mudstone		28.1				3.3	12,107			17.9	802
OPH-1624	1,121.15	NGU	Mudstone		21.7				5.0	11,687			15.4	827
OPH-1625	1,121.37	Acme	Mudstone	1.4	21.0	0.9	0.9	0.34	6.6	1,880	1.11	0.70	25.1	600
OPH-1625	1,121.37	Yale1	Mudstone		25.6				5.8	2,523	0.46	0.74	18.6	775
OPH-1625	1,121.37	Yale1	Mudstone		25.6				5.8	2,523	0.46	0.74	18.6	775
OPH-1625	1,121.37	Acme	Mudstone	1.4	21.0	0.9	0.9	0.34	6.6	1,880	1.11	0.70	25.1	600
OPH-1626	1,121.70	NGU	Mudstone		19.7				22.6	3,153			43.2	822
OPH-1634	1,123.13	NGU	Mudstone		33.6				3.6	7,252			10.2	525
OPH-1640	1,123.62	NGU	Mudstone		23.4				4.5	5,058			20.6	934
OPH-1647	1,124.27	Yale1	Mudstone		31.8				20.3	4,753	1.35	1.06	21.4	1,307
OPH-1647	1,124.27	Yale1	Mudstone		31.8				20.3	4,753	1.35	1.06	21.4	1,307
OPH-1647	1,124.27	Yale1	Mudstone		31.8				20.3	4,753	1.35	1.06	21.4	1,307
OPH-1647	1,124.27	Acme	Mudstone	8.7	52.0	14.4	3.8	0.06	112.4	3,700	1.77	0.70	94.2	1,717
OPH-1647	1,124.27	Acme	Mudstone	8.7	52.0	14.4	3.8	0.06	112.4	3,700	1.77	0.70	94.2	1,717
OPH-1647	1,124.27	Acme	Mudstone	8.7	52.0	14.4	3.8	0.06	112.4	3,700	1.77	0.70	94.2	1,717
OPH-1651	1,124.55	NGU	Mudstone		13.7				5.2	2,583			22.3	524
OPH-1655	1,125.02	NGU	Mudstone		96.8					2,577			7.7	183
OPH-1676	1,127.22	NGU	Mudstone		10.8				3.5	1,924			21.5	771
OPH-1683	1,135.64	NGU	Carbonate		125.0					438				39

Sample ID	Depth (m)	Sample set	Lithology	Sn (ppm)	Sr (ppm)	Ta (ppm)	Tb (ppm)	Te (ppm)	Th (ppm)	Ti (ppm)	Tl (ppm)	Tm (ppm)	U (ppm)	V (ppm)
OPH-1697	1,136.81	Yale2	Mudstone							1,505			0.5	37
OPH-1697	1,136.81	Yale2	Mudstone							1,505			0.5	37
OPH-1697	1,137.01	NGU	Mudstone		124.0				4.8	2,697				47
OPH-1697	1,137.01	NGU	Mudstone		124.0				4.8	2,697				47
OPH-1704	1,137.78	NGU	Carbonate		108.0				4.3	1,708				38
OPH-1709	1,138.18	NGU	Carbonate		87.4				4.4	2,343				54
OPH-1729	1,145.99	NGU	Mudstone		20.7				3.0	1,606			5.9	257
OPH-1746	1,159.50	NGU	Mudstone		6.4				6.0	1,786			15.2	894
OPH-1752	1,160.27	NGU	Mudstone		8.7	7.3			4.2	1,750			9.6	836
OPH-1761	1,161.32	Yale2	Mudstone							1,649			9.6	960
OPH-1761	1,161.32	Yale2	Mudstone							1,649			9.6	960
OPH-1761	1,161.32	NGU	Mudstone		7.9				7.1	2,116			17.4	1,210
OPH-1761	1,161.32	NGU	Mudstone		7.9				7.1	2,116			17.4	1,210
OPH-1765	1,161.95	NGU	Mudstone		55.1				3.7	1,618			7.2	436
OPH-1768	1,162.23	NGU	Mudstone		16.0				7.7	2,038			26.0	1,250
OPH-1779	1,166.13	NGU	Mudstone		94.6				7.1	2,128				75
OPH-1796	1,175.69	NGU	Mudstone		17.0				11.6	3,189			14.6	1,030
OPH-1809	1,187.30	NGU	Mudstone		42.4				6.6	5,304			6.0	404
OPH-1809	1,187.30	Yale2	Mudstone							3,673			3.6	324
OPH-1809	1,187.30	Yale2	Mudstone							3,673			3.6	324
OPH-1809	1,187.30	NGU	Mudstone		42.4				6.6	5,304			6.0	404
OPH-1814	1,187.91	NGU	Mudstone		76.4				4.3	2,781				269
OPH-1823	1,188.90	NGU	Mudstone		96.0					2,853				99
OPH-1831	1,190.01	NGU	Carbonate		87.3				3.3	3,770				202
OPH-1835	1,190.75	NGU	Carbonate		91.8				4.0	10,429				355
OPH-1849	1,198.41	NGU	Mudstone		26.0				6.2	7,971			7.9	224
OPH-1856	1,199.56	NGU	Carbonate		106.0				3.1	3,141				55
OPH-1862	1,200.64	NGU	Carbonate		87.6				3.6	4,891				72
OPH-1865	1,201.25	NGU	Carbonate		88.6				22.1	3,506				58
OPH-1871	1,202.50	NGU	Carbonate		114.0				3.1	2,625				68
OPH-1879	1,203.59	NGU	Mudstone		42.4				7.2	5,232				165
OPH-1885	1,204.44	NGU	Mudstone		19.4				8.0	12,406				259
OPH-1892	1,205.03	NGU	Mudstone		28.8				9.3	9,170			5.5	365
OPH-1904	1,206.20	NGU	Mudstone		15.3				4.0	2,451				209
OPH-1918	1,207.63	Yale2	Mudstone							4,587			2.5	294
OPH-1918	1,207.63	Yale2	Mudstone							4,587			2.5	294
OPH-1918	1,207.63	NGU	Mudstone		20.2				14.0	5,442			8.5	357
OPH-1918	1,207.63	NGU	Mudstone		20.2				14.0	5,442			8.5	357
OPH-1924	1,208.96	NGU	Carbonate		156.0				8.3	2,775			7.1	503
OPH-1927	1,209.45	NGU	Carbonate		71.4				8.1	4,022				286
OPH-1939	1,211.12	NGU	Mudstone		24.7				14.4	3,554			12.1	418
OPH-1942	1,211.51	NGU	Mudstone		28.0				11.5	3,878			6.6	642
OPH-1948	1,212.51	NGU	Carbonate		380.0					611				97
OPH-1960	1,214.11	NGU	Mudstone		28.3				3.6	8,331				266
OPH-1962	1,214.28	NGU	Mudstone		41.7					20,917				359

Sample ID	Depth (m)	Sample set	Lithology	Sn (ppm)	Sr (ppm)	Ta (ppm)	Tb (ppm)	Te (ppm)	Th (ppm)	Ti (ppm)	Tl (ppm)	Tm (ppm)	U (ppm)	V (ppm)
OPH-1975	1,215.53	NGU	Carbonate		192.0					1,013				47
OPH-1984	1,216.89	NGU	Mudstone		35.0				3.3	2,140				145
OPH-1994	1,217.74	NGU	Mudstone		9.1				5.5	3,932				204
OPH-2001	1,218.36	NGU	Carbonate		241.0					719				92
OPH-2001	1,218.36	Yale2	Carbonate							632			0.5	69
OPH-2001	1,218.36	NGU	Carbonate		241.0					719				92
OPH-2001	1,218.36	Yale2	Carbonate							632			0.5	69
OPH-2010	1,219.18	NGU	Carbonate		9.6					977				442
OPH-2027	1,220.85	NGU	Mudstone		6.9				3.8	2,403				290
OPH-2040	1,221.72	NGU	Mudstone						3.4	10,788				546
OPH-2052	1,223.79	NGU	Mudstone						26.4	2,793				230
OPH-2061	1,225.13	Yale2	Mudstone							8,608			0.7	376
OPH-2061	1,225.13	Yale2	Mudstone							8,608			0.7	376
OPH-2061	1,225.13	NGU	Mudstone		11.4					9,230				431
OPH-2061	1,225.13	NGU	Mudstone		11.4					9,230				431
OPH-2068	1,226.04	NGU	Mudstone		8.0				6.3	2,913			8.7	620
OPH-2069	1,226.21	NGU	Carbonate		54.7				3.8	2,224			7.9	422
OPH-2397	1,426.19	NGU	Mudstone		82.1					2,505				394
OPH-2406	1,427.09	Yale2	Mudstone							3,586			4.0	264
OPH-2406	1,427.09	Yale2	Mudstone							3,586			4.0	264
OPH-2406	1,427.16	NGU	Mudstone		82.2					2,925				525
OPH-2406	1,427.16	NGU	Mudstone		82.2					2,925				525
OPH-2413	1,427.81	NGU	Mudstone		89.5					3,087				491
OPH-2423	1,437.13	NGU	Mudstone		19.0					10,668				471
OPH-2426	1,437.68	NGU	Mudstone		8.0					4,621				277
OPH-2993	1,765.27	NGU	Carbonate		31.7					2,559				160
OPH-3009	1,767.41	NGU	Carbonate		78.8					497				134
OPH-3016	1,777.38	Yale2	Mudstone							3,243			15.4	212
OPH-3016	1,777.38	Yale2	Mudstone							3,243			15.4	212
OPH-3016	1,777.46	NGU	Mudstone		75.8				10.0	2,913			32.1	395
OPH-3016	1,777.46	NGU	Mudstone		75.8				10.0	2,913			32.1	395
OPH-3057	1,792.05	NGU								3,015				
OPH-3112	1,868.46	NGU	Mudstone		48.7				4.5	4,225			5.7	197
OPH-3117	1,869.18	NGU	Mudstone		42.7				6.4	3,470				162
OPH-3132	1,871.00	Yale2	Mudstone							4,184			2.9	179
OPH-3132	1,871.00	Yale2	Mudstone							4,184			2.9	179
OPH-3132	1,871.00	NGU	Mudstone		65.8				8.5	4,207				246
OPH-3132	1,871.00	NGU	Mudstone		65.8				8.5	4,207				246
OPH-3141	1,871.27	NGU	Mudstone		59.8				12.7	3,614			9.6	232
OPH-3137	1,871.47	NGU	Mudstone		62.7				11.1	3,806				176
OPH-3161	1,881.50	NGU	Mudstone		62.5				13.9	4,016				123
OPH-3168	1,887.61	NGU	Mudstone		65.6				18.1	4,327				112
OPH-3179	1,888.77	NGU	Carbonate		172.0					144				10
OPH-3182	1,889.14	NGU								2,433				
OPH-3191	1,902.61	Yale2	Mudstone							4,890			1.0	67

Sample ID	Depth (m)	Sample set	Lithology	Sn (ppm)	Sr (ppm)	Ta (ppm)	Tb (ppm)	Te (ppm)	Th (ppm)	Ti (ppm)	Tl (ppm)	Tm (ppm)	U (ppm)	V (ppm)
OPH-3194	1,902.88	NGU	Mudstone		38.0				7.0	6,293				71
OPH-3229	1,915.60	NGU	Mudstone							6,353				
OPH-3256	1,926.73	Yale2	Mudstone							7,788			0.8	66
OPH-3256	1,926.73	Yale2	Mudstone							7,788			0.8	66
OPH-3256	1,926.80	NGU	Mudstone		39.7				9.2	7,732				82
OPH-3256	1,926.80	NGU	Mudstone		39.7				9.2	7,732				82
OPH-3272	1,935.31	NGU	Mudstone		44.3				7.3	7,492				141
OPH-3275	1,935.54	NGU	Mudstone		42.6				7.2	7,732				141
OPH-3295	1,946.55	NGU	Mudstone		54.9				5.6	4,094				90
OPH-3324	1,957.85	NGU	Mudstone		36.3				9.6	7,552				126
OPH-3331	1,958.63	NGU	Mudstone		42.3				8.2	6,473				140
OPH-3355	1,970.85	Yale2	Mudstone							4,483			0.8	93
OPH-3355	1,970.85	Yale2	Mudstone							4,483			0.8	93
OPH-3355	1,970.85	NGU	Mudstone		23.0				10.6	4,879				107
OPH-3355	1,970.85	NGU	Mudstone		23.0				10.6	4,879				107
OPH-3386	1,980.42	NGU	Carbonate		72.3				8.4	1,924				46
OPH-3411	1,991.90	NGU								1,990				
OPH-3463	2,011.35	Yale2	Mudstone							2,131			0.8	41
OPH-3589	2,052.57	Yale2	Mudstone							2,463			1.2	58
OPH-3707	2,103.47	Yale2	Mudstone							1,788			1.0	33
OPH-3736	2,205.38	Yale1	Carbonate		541.3				0.2	52	0.01	0.02	0.2	8
OPH-3904	2,252.09	Yale1	Carbonate		45.2				0.1	18	0.00	0.03	0.1	1
OPH-4022	2,285.28	Yale2	Carbonate							82			0.2	3
OPH-4081	2,305.25	Yale1	Carbonate		151.8				0.1	8	0.01	0.03	0.3	1
OPH-4142	2,324.43	Yale1	Carbonate		236.1				0.1	56	0.00	0.02	0.1	4
OPH-4178	2,328.55	Yale1	Carbonate		8.4				0.1	19	0.01	0.03	0.3	2
OPH-4178	2,328.55	Acme	Carbonate	<0.1	36.0	<0.1	<0.1	2.94	<0.1		<0.05	<0.1	2.0	2
OPH-4183	2,329.14	Acme	Carbonate	0.1	157.0	<0.1	<0.1	3.18	0.5	100	0.05	<0.1	0.3	2
OPH-4185	2,329.34	Acme		<0.1	487.0	<0.1	<0.1	3.45	<0.1		<0.05	<0.1	0.1	<1
OPH-4187	2,329.62	Acme		<0.1	656.0	<0.1	<0.1	2.57	<0.1		<0.05	<0.1	0.1	<1
OPH-4193	2,330.28	Yale2	Evaporite							482			0.3	1
OPH-4194	2,330.34	Yale1	Carbonate		449.2				0.2	20	0.02	0.02	0.7	1
OPH-4194	2,330.34	Acme	Carbonate	<0.1	224.0	<0.1	<0.1	3.46	<0.1	10	<0.05	<0.1	0.5	1
OPH-4194	2,330.34	Acme	Carbonate	<0.1	224.0	<0.1	<0.1	3.46	<0.1	10	<0.05	<0.1	0.5	1
OPH-4194	2,330.34	Yale1	Carbonate		449.2				0.2	20	0.02	0.02	0.7	1
OPH-4199	2,330.85	Acme	Evaporite	<0.1	866.0	<0.1	<0.1	2.18	<0.1	300	<0.05	<0.1	0.2	<1
OPH-4211	2,509.02	Yale1	Evaporite		124.0				0.0	5	0.00	0.02	0.0	0
OPH-4257	2,517.36	Yale1	Evaporite		1,075.3				0.2	181	0.14	0.04	0.1	9
OPH-4310	2,526.68	Yale1	Evaporite		3.5				0.9	183	0.06	0.07	0.9	18
OPH-4366	2,547.78	Yale1	Evaporite		212.1				0.1	272	0.28	0.03	0.2	9
OPH-4383	2,549.45	Yale2	Mudstone							1,115			0.2	46
OPH-4440	2,570.15	Yale1	Evaporite		476.8				0.0	8	0.02	0.02	0.0	1
OPH-4537	2,700.97	Yale1	Evaporite		124.8				0.0	3	0.00	0.02		0
OPH-4582	2,724.31	Yale2	Evaporite							221			0.1	3
OPH-4635	2,833.79	Yale1	Evaporite		475.5				0.1	8	0.00	0.07	0.0	1

Sample ID	Depth (m)	Sample set	Lithology	Sn (ppm)	Sr (ppm)	Ta (ppm)	Tb (ppm)	Te (ppm)	Th (ppm)	Ti (ppm)	Tl (ppm)	Tm (ppm)	U (ppm)	V (ppm)
OPH-4620	2,838.14	Yale2	Evaporite							62			3.0	92
OPH-4683	2,850.46	Yale1	Evaporite		343.1				0.2	119	0.05	0.05	0.9	33
OPH-4683	2,850.46	Yale1	Evaporite		343.1				0.2	119	0.05	0.05	0.9	33
OPH-4683	2,850.46	Yale2	Evaporite							64			0.0	1
OPH-4683	2,850.46	Yale2	Evaporite							64			0.0	1
OPH-4774	2,878.31	Yale1	Evaporite		805.2				0.1	32	0.00	0.06	0.0	5
OPH-4813	2,896.20	Yale1	Evaporite		150.7				0.1	35	0.01	0.03	0.1	3
OPH-4853	2,904.34	Yale1	Evaporite		145.2				0.2	39	0.01	0.03	0.0	2

Table A5f: Element concentration data for drill core OPH, continued.

Sample ID	Depth (m)	Sample set	Lithology	W (ppm)	Y (ppm)	Yb (ppm)	Zn (ppm)	Zr (ppm)
OPH-10	530.39	NGU	Mudstone		21.7		92.6	157.0
OPH-73	542.63	Yale2	Mudstone					
OPH-73	542.63	Yale2	Mudstone					
OPH-73	542.72	NGU	Mudstone	6.6	24.4		116.0	173.0
OPH-73	542.72	NGU	Mudstone	6.6	24.4		116.0	173.0
OPH-80	543.68	NGU	Mudstone		23.5		91.6	172.0
OPH-83	544.22	NGU	Mudstone		22.6		117.0	174.0
OPH-121	552.43	NGU	Mudstone	6.3	15.8		67.2	110.0
OPH-284	591.30	NGU	Mudstone		24.4		48.4	212.0
OPH-306	594.85	Yale2	Mudstone					
OPH-306	594.85	Yale2	Mudstone					
OPH-306	594.93	NGU	Mudstone		24.5		61.5	237.0
OPH-306	594.93	NGU	Mudstone		24.5		61.5	237.0
OPH-507	636.42	NGU	Mudstone		22.8		302.0	192.0
OPH-515	637.85	NGU	Mudstone		21.3		194.0	151.0
OPH-523	638.53	Yale2	Mudstone					
OPH-523	638.53	Yale2	Mudstone					
OPH-523	638.63	NGU	Mudstone		21.7		90.8	155.0
OPH-523	638.63	NGU	Mudstone		21.7		90.8	155.0
OPH-844	890.22	Yale2	Mudstone					
OPH-844	890.22	Yale2	Mudstone					
OPH-844	890.22	NGU	Mudstone		31.0		396.0	94.1
OPH-844	890.22	NGU	Mudstone		31.0		396.0	94.1
OPH-849	891.17	Yale1	Mudstone		24.6	2.2	981.3	84.7
OPH-849	891.17	Yale1	Mudstone		24.6	2.2	981.3	84.7
OPH-849	891.17	NGU	Mudstone		19.0		427.0	67.2
OPH-849	891.17	NGU	Mudstone		19.0		427.0	67.2
OPH-858	892.79	NGU	Mudstone		20.8		290.0	70.3
OPH-862	893.38	NGU	Mudstone		19.0		534.0	32.7
OPH-867	894.16	NGU	Mudstone		33.7		216.0	101.0
OPH-875	894.98	NGU	Carbonate		26.0		1,170.0	51.6
OPH-879	895.49	NGU	Carbonate		12.0		20.4	12.9
OPH-885	896.12	NGU						
OPH-903	897.58	NGU						
OPH-924	899.15	NGU	Carbonate		10.8		94.1	41.1
OPH-925	899.25	NGU	Carbonate		15.1		20.7	42.6
OPH-938	900.23	NGU	Carbonate	7.1	12.3		182.0	95.2
OPH-945	901.96	NGU		5.9	14.4		87.0	56.8
OPH-955	903.08	NGU	Mudstone		8.3		188.0	57.4
OPH-970	904.30	NGU	Mudstone		27.3		124.0	101.0
OPH-975	912.04	Yale2	Mudstone					
OPH-975	912.04	Yale2	Mudstone					
OPH-975	912.04	Yale2	Mudstone					

Sample ID	Depth (m)	Sample set	Lithology	W (ppm)	Y (ppm)	Yb (ppm)	Zn (ppm)	Zr (ppm)
OPH-975	912.19	Yale1	Mudstone		53.0	4.8	188.5	197.7
OPH-975	912.19	Yale1	Mudstone		53.0	4.8	188.5	197.7
OPH-975	912.19	Yale1	Mudstone		53.0	4.8	188.5	197.7
OPH-975	912.19	NGU	Mudstone		36.4		199.0	184.0
OPH-975	912.19	NGU	Mudstone		36.4		199.0	184.0
OPH-975	912.19	NGU	Mudstone		36.4		199.0	184.0
OPH-979	912.70	NGU	Mudstone	6.4	30.5		144.0	163.0
OPH-1361	1,080.00	NGU	Carbonate		10.9		42.4	48.1
OPH-1364	1,080.57	Acme	Carbonate	0.2	4.7	0.6	13.7	15.9
OPH-1364	1,080.57	Yale2	Carbonate					
OPH-1364	1,080.57	Acme	Carbonate	0.2	4.7	0.6	13.7	15.9
OPH-1364	1,080.57	Yale2	Carbonate					
OPH-1366	1,081.11	NGU	Carbonate		10.1		20.7	15.1
OPH-1368	1,081.36	Acme	Carbonate	0.3	6.1	0.5	30.0	35.9
OPH-1372	1,081.93	Acme	Carbonate	0.4	5.8	0.4	26.2	23.5
OPH-1373	1,082.28	NGU	Carbonate		5.5		29.5	19.1
OPH-1376	1,082.71	NGU	Carbonate		29.6		56.5	15.6
OPH-1383	1,083.49	NGU	Carbonate		8.7		43.8	11.0
OPH-1390	1,084.18	NGU	Carbonate		3.0		13.3	8.7
OPH-1393	1,084.47	Yale1	Carbonate		2.1	0.2	26.9	10.4
OPH-1393	1,084.47	Yale1	Carbonate		2.1	0.2	26.9	10.4
OPH-1393	1,084.47	Acme	Carbonate	0.2	1.5	<0.1	12.2	7.7
OPH-1393	1,084.47	Acme	Carbonate	0.2	1.5	<0.1	12.2	7.7
OPH-1398	1,085.13	Acme	Carbonate	0.4	1.6	0.1	10.3	6.8
OPH-1400	1,085.42	Acme	Carbonate	0.4	1.6	<0.1	7.8	6.7
OPH-1403	1,086.33	NGU	Carbonate					10.4
OPH-1405	1,086.52	Acme	Carbonate	0.2	1.3	<0.1	9.2	5.3
OPH-1405	1,086.52	Yale2	Carbonate					
OPH-1405	1,086.52	Yale2	Carbonate					
OPH-1405	1,086.52	Acme	Carbonate	0.2	1.3	<0.1	9.2	5.3
OPH-1412	1,087.73	Acme	Carbonate	0.3	1.7	0.1	13.5	9.2
OPH-1421	1,089.09	NGU	Carbonate		6.3		32.6	26.5
OPH-1426	1,089.67	Acme	Carbonate	0.3	8.6	0.6	64.1	49.7
OPH-1434	1,090.51	NGU	Carbonate	5.0	12.4		93.2	129.0
OPH-1436	1,090.80	Acme	Carbonate	0.4	23.9	1.2	22.9	46.0
OPH-1442	1,091.87	NGU	Carbonate		5.8		26.6	17.7
OPH-1444	1,092.14	Acme	Carbonate	0.2	7.5	0.3	34.9	9.2
OPH-1449	1,093.39	Yale2	Carbonate					
OPH-1449	1,093.39	Yale2	Carbonate					
OPH-1449	1,093.39	Acme	Carbonate	0.2	2.1	0.1	11.1	7.7
OPH-1449	1,093.39	Acme	Carbonate	0.2	2.1	0.1	11.1	7.7
OPH-1452	1,093.90	NGU	Carbonate	8.7	19.8		58.3	82.3
OPH-1461	1,094.89	Acme	Carbonate	0.2	1.8	<0.1	9.7	7.3
OPH-1464	1,095.45	Acme	Carbonate	0.2	7.2	0.5	10.6	5.0
OPH-1464	1,095.45	Yale1	Carbonate		22.8	1.5	59.5	5.6
OPH-1464	1,095.45	Acme	Carbonate	0.2	7.2	0.5	10.6	5.0

Sample ID	Depth (m)	Sample set	Lithology	W (ppm)	Y (ppm)	Yb (ppm)	Zn (ppm)	Zr (ppm)
OPH-1464	1,095.45	Yale1	Carbonate		22.8	1.5	59.5	5.6
OPH-1466	1,095.74	Acme	Carbonate	0.2	24.0	1.4	45.3	12.8
OPH-1468	1,096.29	NGU	Carbonate	115.0	118.0	10.9	67.4	85.3
OPH-1469	1,096.31	Acme	Carbonate	0.4	25.2	2.0	22.6	15.6
OPH-1470	1,096.57	Acme	Carbonate	0.5	4.8	0.2	12.1	17.2
OPH-1472	1,096.82	Acme	Carbonate	0.3	7.4	0.5	15.1	7.3
OPH-1479	1,098.06	Acme	Carbonate	0.3	2.1	0.2	9.8	9.1
OPH-1483	1,098.66	NGU	Carbonate		9.9		18.0	18.4
OPH-1486	1,099.04	Acme	Carbonate	0.2	5.8	0.5	41.2	3.0
OPH-1488	1,099.51	NGU			10.5			7.1
OPH-1491	1,099.98	Acme	Carbonate	0.2	1.2	<0.1	16.4	3.6
OPH-1491	1,099.98	Yale1	Carbonate		1.2	0.1	21.5	2.8
OPH-1491	1,099.98	Yale1	Carbonate		1.2	0.1	21.5	2.8
OPH-1491	1,099.98	Acme	Carbonate	0.2	1.2	<0.1	16.4	3.6
OPH-1499	1,101.27	Yale2	Carbonate					
OPH-1499	1,101.27	Yale2	Carbonate					
OPH-1501	1,101.45	NGU	Mudstone	13.7	53.8		55.9	508.0
OPH-1509	1,102.06	NGU	Mudstone	11.5	43.4		383.0	201.0
OPH-1516	1,102.74	NGU	Mudstone	8.6	47.4		220.0	173.0
OPH-1519	1,103.35	NGU	Mudstone	9.0	19.5		359.0	89.4
OPH-1527	1,104.69	Yale1	Carbonate		5.0	0.4	68.0	6.0
OPH-1533	1,106.00	NGU	Carbonate		3.6		35.8	9.2
OPH-1542	1,106.99	NGU	Mudstone	9.9	40.3		185.0	313.0
OPH-1556	1,109.44	NGU	Carbonate		77.2	6.5	77.0	31.4
OPH-1557	1,109.57	NGU	Carbonate		11.7		10.4	8.5
OPH-1557	1,109.57	Yale1	Carbonate		7.8	0.6	23.3	5.2
OPH-1557	1,109.57	Yale1	Carbonate		7.8	0.6	23.3	5.2
OPH-1557	1,109.57	NGU	Carbonate		11.7		10.4	8.5
OPH-1560	1,109.96	Yale1	Carbonate		0.8	0.1	17.7	0.9
OPH-1560	1,109.96	NGU	Carbonate		13.3		24.3	
OPH-1560	1,109.96	Yale1	Carbonate		0.8	0.1	17.7	0.9
OPH-1560	1,109.96	NGU	Carbonate		13.3		24.3	
OPH-1561	1,110.18	NGU	Carbonate		66.1	5.3	65.5	23.5
OPH-1499	1,110.27	Acme	Carbonate	0.2	1.9	0.1	8.7	3.5
OPH-1499	1,110.27	Acme	Carbonate	0.2	1.9	0.1	8.7	3.5
OPH-1564	1,110.79	Yale1	Carbonate		2.4	0.3	17.6	1.9
OPH-1564	1,110.79	NGU	Carbonate		7.5		16.4	7.4
OPH-1567	1,111.40	NGU	Carbonate		18.9		39.3	14.0
OPH-1568	1,111.60	NGU	Carbonate		32.0		611.0	25.0
OPH-1569	1,111.80	NGU	Carbonate		50.9		128.0	30.7
OPH-1571	1,112.02	NGU	Carbonate		440.0	42.2	324.0	198.0
OPH-1572	1,112.08	Yale1	Mudstone		80.6	7.4	657.9	314.4
OPH-1572	1,112.08	NGU	Mudstone	19.8	95.7	10.8	520.0	311.0
OPH-1572	1,112.08	Acme	Mudstone	25.3	67.7	6.8	610.7	228.3
OPH-1572	1,112.08	NGU	Mudstone	19.8	95.7	10.8	520.0	311.0
OPH-1572	1,112.08	Acme	Mudstone	25.3	67.7	6.8	610.7	228.3

Sample ID	Depth (m)	Sample set	Lithology	W (ppm)	Y (ppm)	Yb (ppm)	Zn (ppm)	Zr (ppm)
OPH-1572	1,112.08	Yale1	Mudstone		80.6	7.4	657.9	314.4
OPH-1572	1,112.08	Yale1	Mudstone		80.6	7.4	657.9	314.4
OPH-1572	1,112.08	NGU	Mudstone	19.8	95.7	10.8	520.0	311.0
OPH-1572	1,112.08	Acme	Mudstone	25.3	67.7	6.8	610.7	228.3
OPH-1573	1,112.27	Yale1	Mudstone		70.6	6.1	407.2	216.9
OPH-1573	1,112.27	Acme	Mudstone	22.7	61.6	6.2	286.4	181.0
OPH-1573	1,112.27	Yale1	Mudstone		70.6	6.1	407.2	216.9
OPH-1573	1,112.27	Acme	Mudstone	22.7	61.6	6.2	286.4	181.0
OPH-1575	1,112.65	Acme	Mudstone	20.0	61.8	5.9	349.9	179.6
OPH-1575	1,112.65	Yale1	Mudstone		60.8	5.4	308.4	194.9
OPH-1575	1,112.65	Yale1	Mudstone		60.8	5.4	308.4	194.9
OPH-1575	1,112.65	Acme	Mudstone	20.0	61.8	5.9	349.9	179.6
OPH-1578	1,113.28	Yale1	Mudstone		95.1	7.9	672.1	299.4
OPH-1578	1,113.28	Acme	Mudstone	16.2	84.6	8.4	542.3	282.1
OPH-1578	1,113.28	Acme	Mudstone	16.2	84.6	8.4	542.3	282.1
OPH-1578	1,113.28	Yale1	Mudstone		95.1	7.9	672.1	299.4
OPH-1579	1,113.58	NGU	Mudstone	13.1	123.0	11.4	635.0	293.0
OPH-1580	1,113.63	Acme	Mudstone	17.3	51.9	5.4	419.5	236.7
OPH-1580	1,113.63	Yale1	Mudstone		61.5	5.6	379.5	297.8
OPH-1580	1,113.63	Acme	Mudstone	17.3	51.9	5.4	419.5	236.7
OPH-1580	1,113.63	Yale1	Mudstone		61.5	5.6	379.5	297.8
OPH-1581	1,113.83	Yale1	Mudstone		56.1	4.8	278.5	247.7
OPH-1581	1,113.83	Acme	Mudstone	14.7	50.5	5.2	255.6	193.9
OPH-1581	1,113.83	Acme	Mudstone	14.7	50.5	5.2	255.6	193.9
OPH-1581	1,113.83	Yale1	Mudstone		56.1	4.8	278.5	247.7
OPH-1582	1,113.92	NGU	Mudstone	12.4	69.2	5.8	562.0	228.0
OPH-1584	1,114.20	Yale1	Mudstone		26.4	2.1	313.7	117.8
OPH-1584	1,114.20	Acme	Mudstone	9.7	30.0	3.0	422.3	128.0
OPH-1584	1,114.20	Acme	Mudstone	9.7	30.0	3.0	422.3	128.0
OPH-1584	1,114.20	Yale1	Mudstone		26.4	2.1	313.7	117.8
OPH-1585	1,114.34	Yale1	Mudstone		40.9	3.1	326.8	186.7
OPH-1585	1,114.34	Yale2	Mudstone					
OPH-1585	1,114.34	Yale2	Mudstone					
OPH-1585	1,114.34	Yale2	Mudstone					
OPH-1585	1,114.34	Acme	Mudstone	13.9	36.0	3.7	305.1	151.6
OPH-1585	1,114.34	Acme	Mudstone	13.9	36.0	3.7	305.1	151.6
OPH-1585	1,114.34	Acme	Mudstone	13.9	36.0	3.7	305.1	151.6
OPH-1585	1,114.34	Yale1	Mudstone		40.9	3.1	326.8	186.7
OPH-1585	1,114.34	Yale1	Mudstone		40.9	3.1	326.8	186.7
OPH-1586	1,114.62	NGU	Mudstone	34.8	102.0	11.4	371.0	416.0
OPH-1587	1,114.77	Acme	Mudstone	22.1	57.9	6.7	197.5	363.5
OPH-1587	1,114.77	Yale1	Mudstone		63.1	5.9	215.4	477.9
OPH-1587	1,114.77	Yale1	Mudstone		63.1	5.9	215.4	477.9
OPH-1587	1,114.77	Acme	Mudstone	22.1	57.9	6.7	197.5	363.5
OPH-1588	1,115.02	Yale1	Mudstone		35.5	2.7	120.5	174.5
OPH-1588	1,115.02	Yale1	Mudstone		35.5	2.7	120.5	174.5

Sample ID	Depth (m)	Sample set	Lithology	W (ppm)	Y (ppm)	Yb (ppm)	Zn (ppm)	Zr (ppm)
OPH-1588	1,115.02	Acme	Mudstone	6.3	11.8	1.2	40.5	57.9
OPH-1588	1,115.02	Acme	Mudstone	6.3	11.8	1.2	40.5	57.9
OPH-1589	1,115.21	NGU	Mudstone	27.2	61.1	6.9	173.0	318.0
OPH-1590	1,115.59	NGU	Carbonate		10.9		41.7	6.6
OPH-1592	1,115.87	NGU	Mudstone	17.1	47.8		256.0	245.0
OPH-1596	1,116.61	NGU	Carbonate		7.0		14.1	
OPH-1596	1,116.65	Yale1	Carbonate		2.6	0.2	11.8	1.1
OPH-1599	1,117.43	NGU	Carbonate	12.3	15.6		146.0	114.0
OPH-1601	1,117.48	Acme	Mudstone	24.0	61.3	5.4	268.0	252.4
OPH-1606	1,118.27	Yale1	Mudstone		27.1	3.2	150.0	205.2
OPH-1606	1,118.27	Yale1	Mudstone		27.1	3.2	150.0	205.2
OPH-1606	1,118.27	Acme	Mudstone	4.5	27.4	4.1	82.7	196.4
OPH-1606	1,118.27	Acme	Mudstone	4.5	27.4	4.1	82.7	196.4
OPH-1608	1,118.59	NGU	Mudstone		50.2		134.0	227.0
OPH-1613	1,119.54	NGU	Mudstone	7.5	42.9		172.0	183.0
OPH-1647	1,120.31	Yale2	Mudstone					
OPH-1647	1,120.31	Yale2	Mudstone					
OPH-1647	1,120.31	Yale2	Mudstone					
OPH-1617	1,120.31	Acme	Mudstone	7.5	21.1	2.9	200.5	215.3
OPH-1617	1,120.31	Yale1	Mudstone		41.1	3.6	281.3	273.4
OPH-1617	1,120.31	Yale1	Mudstone		41.1	3.6	281.3	273.4
OPH-1617	1,120.31	Acme	Mudstone	7.5	21.1	2.9	200.5	215.3
OPH-1621	1,120.77	NGU	Mudstone		49.3		155.0	204.0
OPH-1624	1,121.15	NGU	Mudstone	9.6	48.8		259.0	202.0
OPH-1625	1,121.37	Acme	Mudstone	2.3	49.3	5.8	121.1	276.2
OPH-1625	1,121.37	Yale1	Mudstone		56.4	4.8	153.5	336.2
OPH-1625	1,121.37	Yale1	Mudstone		56.4	4.8	153.5	336.2
OPH-1625	1,121.37	Acme	Mudstone	2.3	49.3	5.8	121.1	276.2
OPH-1626	1,121.70	NGU	Mudstone	10.3	78.9	6.7	183.0	415.0
OPH-1634	1,123.13	NGU	Mudstone	14.2	13.7		319.0	142.0
OPH-1640	1,123.62	NGU	Mudstone	8.2	25.1		290.0	147.0
OPH-1647	1,124.27	Yale1	Mudstone		67.5	6.0	380.1	425.5
OPH-1647	1,124.27	Yale1	Mudstone		67.5	6.0	380.1	425.5
OPH-1647	1,124.27	Yale1	Mudstone		67.5	6.0	380.1	425.5
OPH-1647	1,124.27	Acme	Mudstone	2.8	33.2	4.0	410.7	187.0
OPH-1647	1,124.27	Acme	Mudstone	2.8	33.2	4.0	410.7	187.0
OPH-1647	1,124.27	Acme	Mudstone	2.8	33.2	4.0	410.7	187.0
OPH-1651	1,124.55	NGU	Mudstone	5.7	50.8		88.5	246.0
OPH-1655	1,125.02	NGU	Mudstone		14.8		51.0	45.1
OPH-1676	1,127.22	NGU	Mudstone		31.3		42.7	55.0
OPH-1683	1,135.64	NGU	Carbonate		13.1		44.4	20.3
OPH-1697	1,136.81	Yale2	Mudstone					
OPH-1697	1,136.81	Yale2	Mudstone					
OPH-1697	1,137.01	NGU	Mudstone		29.3		56.9	82.4
OPH-1697	1,137.01	NGU	Mudstone		29.3		56.9	82.4
OPH-1704	1,137.78	NGU	Carbonate		27.7		32.0	56.3

Sample ID	Depth (m)	Sample set	Lithology	W (ppm)	Y (ppm)	Yb (ppm)	Zn (ppm)	Zr (ppm)
OPH-1709	1,138.18	NGU	Carbonate		21.0		44.6	70.3
OPH-1729	1,145.99	NGU	Mudstone		14.6		536.0	56.0
OPH-1746	1,159.50	NGU	Mudstone		38.1		2,040.0	74.6
OPH-1752	1,160.27	NGU	Mudstone		32.2		924.0	60.3
OPH-1761	1,161.32	Yale2	Mudstone					
OPH-1761	1,161.32	Yale2	Mudstone					
OPH-1761	1,161.32	NGU	Mudstone		45.0		912.0	74.4
OPH-1761	1,161.32	NGU	Mudstone		45.0		912.0	74.4
OPH-1765	1,161.95	NGU	Mudstone		41.3		2,660.0	42.2
OPH-1768	1,162.23	NGU	Mudstone		79.0	7.9	1,320.0	82.6
OPH-1779	1,166.13	NGU	Mudstone	8.5	43.9		178.0	164.0
OPH-1796	1,175.69	NGU	Mudstone		48.0		1,380.0	219.0
OPH-1809	1,187.30	NGU	Mudstone		26.1		308.0	117.0
OPH-1809	1,187.30	Yale2	Mudstone					
OPH-1809	1,187.30	Yale2	Mudstone					
OPH-1809	1,187.30	NGU	Mudstone		26.1		308.0	117.0
OPH-1814	1,187.91	NGU	Mudstone		19.2		227.0	77.3
OPH-1823	1,188.90	NGU	Mudstone		19.1		187.0	53.1
OPH-1831	1,190.01	NGU	Carbonate		16.3		64.4	77.8
OPH-1835	1,190.75	NGU	Carbonate		25.7		93.0	158.0
OPH-1849	1,198.41	NGU	Mudstone	7.9	27.9		79.7	171.0
OPH-1856	1,199.56	NGU	Carbonate		20.1		45.0	110.0
OPH-1862	1,200.64	NGU	Carbonate		22.1		52.7	114.0
OPH-1865	1,201.25	NGU	Carbonate	7.9	42.7		82.5	352.0
OPH-1871	1,202.50	NGU	Carbonate		27.8		42.8	79.4
OPH-1879	1,203.59	NGU	Mudstone		32.7		321.0	148.0
OPH-1885	1,204.44	NGU	Mudstone	5.3	37.9		328.0	193.0
OPH-1892	1,205.03	NGU	Mudstone	12.8	22.5		73.2	200.0
OPH-1904	1,206.20	NGU	Mudstone	5.7	8.6		62.4	87.8
OPH-1918	1,207.63	Yale2	Mudstone					
OPH-1918	1,207.63	Yale2	Mudstone					
OPH-1918	1,207.63	NGU	Mudstone	6.9	35.5		210.0	349.0
OPH-1918	1,207.63	NGU	Mudstone	6.9	35.5		210.0	349.0
OPH-1924	1,208.96	NGU	Carbonate		37.4		492.0	174.0
OPH-1927	1,209.45	NGU	Carbonate		35.1		704.0	118.0
OPH-1939	1,211.12	NGU	Mudstone		19.3		222.0	167.0
OPH-1942	1,211.51	NGU	Mudstone	6.8	10.3		467.0	125.0
OPH-1948	1,212.51	NGU	Carbonate		34.8		31.1	25.4
OPH-1960	1,214.11	NGU	Mudstone	7.8	17.3		83.4	132.0
OPH-1962	1,214.28	NGU	Mudstone	5.8	49.7		54.2	239.0
OPH-1975	1,215.53	NGU	Carbonate		18.4		35.1	21.9
OPH-1984	1,216.89	NGU	Mudstone		14.5		18.0	66.7
OPH-1994	1,217.74	NGU	Mudstone	18.1	28.2		54.3	107.0
OPH-2001	1,218.36	NGU	Carbonate		24.4		83.5	22.1
OPH-2001	1,218.36	Yale2	Carbonate					
OPH-2001	1,218.36	NGU	Carbonate		24.4		83.5	22.1

Sample ID	Depth (m)	Sample set	Lithology	W (ppm)	Y (ppm)	Yb (ppm)	Zn (ppm)	Zr (ppm)
OPH-2001	1,218.36	Yale2	Carbonate					
OPH-2010	1,219.18	NGU	Carbonate		19.9		230.0	121.0
OPH-2027	1,220.85	NGU	Mudstone		17.9		25.3	89.4
OPH-2040	1,221.72	NGU	Mudstone	5.6	37.5		80.9	172.0
OPH-2052	1,223.79	NGU	Mudstone	20.8	78.4	7.1	63.2	742.0
OPH-2061	1,225.13	Yale2	Mudstone					
OPH-2061	1,225.13	Yale2	Mudstone					
OPH-2061	1,225.13	NGU	Mudstone		40.0		101.0	160.0
OPH-2061	1,225.13	NGU	Mudstone		40.0		101.0	160.0
OPH-2068	1,226.04	NGU	Mudstone	9.0	46.6		104.0	209.0
OPH-2069	1,226.21	NGU	Carbonate	5.0	46.2		165.0	122.0
OPH-2397	1,426.19	NGU	Mudstone		21.5		95.3	61.5
OPH-2406	1,427.09	Yale2	Mudstone					
OPH-2406	1,427.09	Yale2	Mudstone					
OPH-2406	1,427.16	NGU	Mudstone		28.4		44.1	64.6
OPH-2406	1,427.16	NGU	Mudstone		28.4		44.1	64.6
OPH-2413	1,427.81	NGU	Mudstone		21.4		29.2	56.0
OPH-2423	1,437.13	NGU	Mudstone		38.7		89.1	91.2
OPH-2426	1,437.68	NGU	Mudstone		8.2		96.6	48.8
OPH-2993	1,765.27	NGU	Carbonate		16.5		260.0	22.4
OPH-3009	1,767.41	NGU	Carbonate		4.9		60.7	14.6
OPH-3016	1,777.38	Yale2	Mudstone					
OPH-3016	1,777.38	Yale2	Mudstone					
OPH-3016	1,777.46	NGU	Mudstone	5.1	45.9	5.2	44.0	129.0
OPH-3016	1,777.46	NGU	Mudstone	5.1	45.9	5.2	44.0	129.0
OPH-3057	1,792.05	NGU						
OPH-3112	1,868.46	NGU	Mudstone		29.6		19.5	138.0
OPH-3117	1,869.18	NGU	Mudstone		24.0		13.7	121.0
OPH-3132	1,871.00	Yale2	Mudstone					
OPH-3132	1,871.00	Yale2	Mudstone					
OPH-3132	1,871.00	NGU	Mudstone		29.9		29.0	146.0
OPH-3132	1,871.00	NGU	Mudstone		29.9		29.0	146.0
OPH-3141	1,871.27	NGU	Mudstone		26.4		26.5	120.0
OPH-3137	1,871.47	NGU	Mudstone		28.9		23.9	144.0
OPH-3161	1,881.50	NGU	Mudstone		22.8		71.2	124.0
OPH-3168	1,887.61	NGU	Mudstone		25.4		39.7	137.0
OPH-3179	1,888.77	NGU	Carbonate		3.0		153.0	6.3
OPH-3182	1,889.14	NGU						
OPH-3191	1,902.61	Yale2	Mudstone					
OPH-3194	1,902.88	NGU	Mudstone		19.4		51.9	150.0
OPH-3229	1,915.60	NGU	Mudstone					
OPH-3256	1,926.73	Yale2	Mudstone					
OPH-3256	1,926.73	Yale2	Mudstone					
OPH-3256	1,926.80	NGU	Mudstone		14.7		52.4	143.0
OPH-3256	1,926.80	NGU	Mudstone		14.7		52.4	143.0
OPH-3272	1,935.31	NGU	Mudstone		22.2		97.8	137.0

Sample ID	Depth (m)	Sample set	Lithology	W (ppm)	Y (ppm)	Yb (ppm)	Zn (ppm)	Zr (ppm)
OPH-3275	1,935.54	NGU	Mudstone	6.7	19.4		87.2	139.0
OPH-3295	1,946.55	NGU	Mudstone		14.3		74.4	85.9
OPH-3324	1,957.85	NGU	Mudstone	5.3	17.1		87.5	157.0
OPH-3331	1,958.63	NGU	Mudstone		14.5		48.9	137.0
OPH-3355	1,970.85	Yale2	Mudstone					
OPH-3355	1,970.85	Yale2	Mudstone					
OPH-3355	1,970.85	NGU	Mudstone		12.8		66.9	121.0
OPH-3355	1,970.85	NGU	Mudstone		12.8		66.9	121.0
OPH-3386	1,980.42	NGU	Carbonate		14.3		32.3	88.8
OPH-3411	1,991.90	NGU						
OPH-3463	2,011.35	Yale2	Mudstone					
OPH-3589	2,052.57	Yale2	Mudstone					
OPH-3707	2,103.47	Yale2	Mudstone					
OPH-3736	2,205.38	Yale1	Carbonate		0.7	0.1	72.2	0.8
OPH-3904	2,252.09	Yale1	Carbonate		0.3	0.0	6.1	
OPH-4022	2,285.28	Yale2	Carbonate					
OPH-4081	2,305.25	Yale1	Carbonate		0.6	0.1	99.0	
OPH-4142	2,324.43	Yale1	Carbonate		0.5	0.0	17.9	1.0
OPH-4178	2,328.55	Yale1	Carbonate		0.7	0.1	81.2	0.7
OPH-4178	2,328.55	Acme	Carbonate	0.8	0.5	0.1	49.2	0.5
OPH-4183	2,329.14	Acme	Carbonate	<0.1	1.3	<0.1	23.0	2.3
OPH-4185	2,329.34	Acme		0.1 <0.1		<0.1	14.4	<0.2
OPH-4187	2,329.62	Acme		<0.1	0.1	<0.1	9.4	<0.2
OPH-4193	2,330.28	Yale2	Evaporite					
OPH-4194	2,330.34	Yale1	Carbonate		0.3	0.1	85.1	1.0
OPH-4194	2,330.34	Acme	Carbonate	<0.1	0.1	<0.1	51.4	0.4
OPH-4194	2,330.34	Acme	Carbonate	<0.1	0.1	<0.1	51.4	0.4
OPH-4194	2,330.34	Yale1	Carbonate		0.3	0.1	85.1	1.0
OPH-4199	2,330.85	Acme	Evaporite	<0.1	0.1	<0.1	8.1	0.4
OPH-4211	2,509.02	Yale1	Evaporite		0.3	0.0	13.0	
OPH-4257	2,517.36	Yale1	Evaporite		2.9	0.1	50.6	3.9
OPH-4310	2,526.68	Yale1	Evaporite		3.4	0.4	95.7	1.6
OPH-4366	2,547.78	Yale1	Evaporite		1.5	0.1	93.2	2.4
OPH-4383	2,549.45	Yale2	Mudstone					
OPH-4440	2,570.15	Yale1	Evaporite		1.1	0.1	73.5	0.3
OPH-4537	2,700.97	Yale1	Evaporite		0.3	0.0	17.3	
OPH-4582	2,724.31	Yale2	Evaporite					
OPH-4635	2,833.79	Yale1	Evaporite		4.4	0.3		0.3
OPH-4620	2,838.14	Yale2	Evaporite					
OPH-4683	2,850.46	Yale1	Evaporite		2.2	0.2	8.1	5.2
OPH-4683	2,850.46	Yale1	Evaporite		2.2	0.2	8.1	5.2
OPH-4683	2,850.46	Yale2	Evaporite					
OPH-4683	2,850.46	Yale2	Evaporite					
OPH-4774	2,878.31	Yale1	Evaporite		3.0	0.3	1.3	1.4
OPH-4813	2,896.20	Yale1	Evaporite		0.8	0.1	1.9	1.0
OPH-4853	2,904.34	Yale1	Evaporite		0.8	0.1		0.9

Table A6: Total organic carbon (TOC) and sulphur (TS) for drill core OPH.

Sample ID	Depth (m)	Sample set	Lithology	TC (wt.%)	TOC (wt.%)	TS (wt.%)
OPH-10	530.39	NGU	Mudstone	0.2	0.1	0.1
OPH-73	542.63	Yale	Mudstone		0.0	
OPH-73	542.63	Yale	Mudstone		0.0	
OPH-73	542.72	NGU	Mudstone	0.1		0.1
OPH-73	542.72	NGU	Mudstone	0.1		0.1
OPH-80	543.68	NGU	Mudstone	0.2		0.1
OPH-83	544.22	NGU	Mudstone	0.6	0.6	0.0
OPH-121	552.43	NGU	Mudstone	0.1	0.1	
OPH-284	591.30	NGU	Mudstone	0.4	0.2	0.0
OPH-306	594.85	Yale	Mudstone		0.0	
OPH-306	594.85	Yale	Mudstone		0.0	
OPH-306	594.93	NGU	Mudstone	0.4	0.2	0.0
OPH-306	594.93	NGU	Mudstone	0.4	0.2	0.0
OPH-507	636.42	NGU	Mudstone	0.7	0.7	0.3
OPH-515	637.85	NGU	Mudstone	2.5	0.8	0.1
OPH-523	638.53	Yale	Mudstone		0.0	
OPH-523	638.53	Yale	Mudstone		0.0	
OPH-523	638.63	NGU	Mudstone	2.4	1.4	0.1
OPH-523	638.63	NGU	Mudstone	2.4	1.4	0.1
OPH-844	890.22	NGU	Mudstone	19.2	18.8	2.9
OPH-844	890.22	NGU	Mudstone	19.2	18.8	2.9
OPH-844	890.22	Yale	Mudstone		0.2	
OPH-844	890.22	Yale	Mudstone		0.2	
OPH-849	891.17	NGU	Mudstone	17.8	17.8	18.9
OPH-849	891.17	NGU	Mudstone	17.8	17.8	18.9
OPH-849	891.17	Yale	Mudstone		27.8	
OPH-849	891.17	Yale	Mudstone		27.8	
OPH-858	892.79	NGU	Mudstone	17.9	17.4	17.9
OPH-862	893.38	NGU	Mudstone	22.5	22.3	29.1
OPH-867	894.16	NGU	Mudstone			
OPH-875	894.98	NGU	Carbonate			
OPH-879	895.49	NGU	Carbonate			
OPH-885	896.12	NGU		2.7	2.7	7.0
OPH-903	897.58	NGU		21.1	20.1	13.2
OPH-924	899.15	NGU	Carbonate	10.0	6.4	8.8
OPH-925	899.25	NGU	Carbonate	9.5	3.8	7.7
OPH-938	900.23	NGU	Carbonate	10.3	6.6	1.7
OPH-945	901.96	NGU		1.5		3.1
OPH-955	903.08	NGU	Mudstone	2.3	2.3	4.6
OPH-970	904.30	NGU	Mudstone	1.2	1.1	3.5
OPH-975	912.04	Yale	Mudstone		0.0	
OPH-975	912.04	Yale	Mudstone		0.0	
OPH-975	912.04	Yale	Mudstone		0.0	
OPH-975	912.19	NGU	Mudstone	2.3	1.5	0.7
OPH-975	912.19	NGU	Mudstone	2.3	1.5	0.7
OPH-975	912.19	NGU	Mudstone	2.3	1.5	0.7
OPH-975	912.19	Yale	Mudstone		2.1	
OPH-975	912.19	Yale	Mudstone		2.1	
OPH-975	912.19	Yale	Mudstone		2.1	
OPH-979	912.70	NGU	Mudstone	1.4	0.8	2.2
OPH-1361	1,080.00	NGU	Carbonate	11.8	2.6	1.0
OPH-1364	1,080.57	Yale	Carbonate		0.1	
OPH-1364	1,080.57	Yale	Carbonate		0.1	
OPH-1366	1,081.11	NGU	Carbonate			
OPH-1373	1,082.28	NGU	Carbonate	14.2	4.9	
OPH-1376	1,082.71	NGU	Carbonate	16.7	6.5	1.0
OPH-1383	1,083.49	NGU	Carbonate	13.1	1.2	0.5
OPH-1390	1,084.18	NGU	Carbonate	12.5	0.2	
OPH-1393	1,084.47	Yale	Carbonate		5.7	
OPH-1393	1,084.47	Yale	Carbonate		5.7	
OPH-1403	1,086.33	NGU	Carbonate	12.4	0.7	0.2
OPH-1405	1,086.52	Yale	Carbonate		0.0	

OPH-1405	1,086.52	Yale	Carbonate		0.0	
OPH-1421	1,089.09	NGU	Carbonate	8.2	0.7	1.0
OPH-1434	1,090.51	NGU	Carbonate	2.7	1.0	3.3
OPH-1442	1,091.87	NGU	Carbonate	13.7	6.3	0.2
OPH-1449	1,093.39	Yale	Carbonate		0.0	
OPH-1449	1,093.39	Yale	Carbonate		0.0	
OPH-1452	1,093.90	NGU	Carbonate	31.9	27.4	0.8
OPH-1464	1,095.45	Yale	Carbonate		3.5	
OPH-1464	1,095.45	Yale	Carbonate		3.5	
OPH-1468	1,096.29	NGU	Carbonate	14.2	7.7	0.3
OPH-1483	1,098.66	NGU	Carbonate	13.0	0.6	0.1
OPH-1488	1,099.51	NGU		12.9		
OPH-1491	1,099.98	Yale	Carbonate		10.4	
OPH-1491	1,099.98	Yale	Carbonate		10.4	
OPH-1499	1,101.27	Yale	Carbonate		0.0	
OPH-1499	1,101.27	Yale	Carbonate		0.0	
OPH-1501	1,101.45	NGU	Mudstone	7.2	7.8	5.6
OPH-1509	1,102.06	NGU	Mudstone	24.9	25.9	6.1
OPH-1516	1,102.74	NGU	Mudstone	16.7	15.7	10.7
OPH-1519	1,103.35	NGU	Mudstone	14.1	14.4	2.9
OPH-1527	1,104.69	Yale	Carbonate		5.6	
OPH-1533	1,106.00	NGU	Carbonate	7.0	3.1	
OPH-1542	1,106.99	NGU	Mudstone	16.3	16.7	5.2
OPH-1556	1,109.44	NGU	Carbonate	9.2	2.3	0.1
OPH-1557	1,109.57	NGU	Carbonate	14.1	2.3	
OPH-1557	1,109.57	NGU	Carbonate	14.1	2.3	
OPH-1557	1,109.57	Yale	Carbonate		9.4	
OPH-1557	1,109.57	Yale	Carbonate		9.4	
OPH-1560	1,109.96	Yale	Carbonate		7.6	
OPH-1560	1,109.96	NGU	Carbonate	13.8	1.2	
OPH-1560	1,109.96	NGU	Carbonate	13.8	1.2	
OPH-1560	1,109.96	Yale	Carbonate		7.6	
OPH-1561	1,110.18	NGU	Carbonate	12.0	1.5	0.0
OPH-1564	1,110.79	NGU	Carbonate	18.0	6.2	
OPH-1564	1,110.79	Yale	Carbonate		16.2	
OPH-1567	1,111.40	NGU	Carbonate	18.8	7.4	
OPH-1568	1,111.60	NGU	Carbonate	16.4	5.5	
OPH-1569	1,111.80	NGU	Carbonate	17.7	9.7	0.5
OPH-1571	1,112.02	NGU	Carbonate	13.3	13.3	0.9
OPH-1572	1,112.08	NGU	Mudstone	33.9	33.5	5.4
OPH-1572	1,112.08	NGU	Mudstone	33.9	33.5	5.4
OPH-1572	1,112.08	NGU	Mudstone	33.9	33.5	5.4
OPH-1572	1,112.08	Yale	Mudstone		35.1	
OPH-1572	1,112.08	Yale	Mudstone		35.1	
OPH-1572	1,112.08	Yale	Mudstone		35.1	
OPH-1573	1,112.27	Yale	Mudstone		33.9	
OPH-1573	1,112.27	Yale	Mudstone		33.9	
OPH-1575	1,112.65	Yale	Mudstone		36.3	
OPH-1575	1,112.65	Yale	Mudstone		36.3	
OPH-1578	1,113.28	Yale	Mudstone		26.9	
OPH-1578	1,113.28	Yale	Mudstone		26.9	
OPH-1579	1,113.58	NGU	Mudstone	23.6	23.2	5.0
OPH-1580	1,113.63	Yale	Mudstone		30.7	
OPH-1580	1,113.63	Yale	Mudstone		30.7	
OPH-1581	1,113.83	Yale	Mudstone		32.4	
OPH-1581	1,113.83	Yale	Mudstone		32.4	
OPH-1582	1,113.92	NGU	Mudstone	26.8	25.6	8.7
OPH-1584	1,114.20	Yale	Mudstone		33.1	
OPH-1584	1,114.20	Yale	Mudstone		33.1	
OPH-1585	1,114.34	Yale	Mudstone		0.4	
OPH-1585	1,114.34	Yale	Mudstone		38.6	
OPH-1585	1,114.34	Yale	Mudstone		38.6	
OPH-1585	1,114.34	Yale	Mudstone		38.6	
OPH-1585	1,114.34	Yale	Mudstone		0.4	
OPH-1585	1,114.34	Yale	Mudstone		0.4	
OPH-1586	1,114.62	NGU	Mudstone	34.1	33.4	8.3
OPH-1587	1,114.77	Yale	Mudstone		33.5	

OPH-1587	1,114.77	Yale	Mudstone		33.5	
OPH-1588	1,115.02	Yale	Mudstone		57.1	
OPH-1588	1,115.02	Yale	Mudstone		57.1	
OPH-1589	1,115.21	NGU	Mudstone	41.6	40.7	6.8
OPH-1590	1,115.59	NGU	Carbonate	15.6	2.5	0.1
OPH-1592	1,115.87	NGU	Mudstone	38.0	33.3	5.6
OPH-1596	1,116.61	NGU	Carbonate	14.2	1.0	0.3
OPH-1596	1,116.65	Yale	Carbonate		3.9	
OPH-1599	1,117.43	NGU	Carbonate	28.7	27.8	6.0
OPH-1606	1,118.27	Yale	Mudstone		42.1	
OPH-1606	1,118.27	Yale	Mudstone		42.1	
OPH-1608	1,118.59	NGU	Mudstone	37.2	38.1	2.7
OPH-1613	1,119.54	NGU	Mudstone	23.5	24.0	2.3
OPH-1647	1,120.31	Yale	Mudstone		0.3	
OPH-1647	1,120.31	Yale	Mudstone		0.3	
OPH-1647	1,120.31	Yale	Mudstone		0.3	
OPH-1617	1,120.31	Yale	Mudstone		16.4	
OPH-1617	1,120.31	Yale	Mudstone		16.4	
OPH-1621	1,120.77	NGU	Mudstone	14.2	15.0	8.0
OPH-1624	1,121.15	NGU	Mudstone	15.6	15.2	5.8
OPH-1625	1,121.37	Yale	Mudstone		44.5	
OPH-1625	1,121.37	Yale	Mudstone		44.5	
OPH-1626	1,121.70	NGU	Mudstone	25.9	26.0	3.1
OPH-1634	1,123.13	NGU	Mudstone	3.4	2.6	5.5
OPH-1640	1,123.62	NGU	Mudstone	22.6	22.5	7.5
OPH-1647	1,124.27	Yale	Mudstone		23.4	
OPH-1647	1,124.27	Yale	Mudstone		23.4	
OPH-1647	1,124.27	Yale	Mudstone		23.4	
OPH-1651	1,124.55	NGU	Mudstone	20.5	20.9	7.8
OPH-1655	1,125.02	NGU	Mudstone	8.9	0.7	4.0
OPH-1676	1,127.22	NGU	Mudstone	16.6	16.7	4.2
OPH-1683	1,135.64	NGU	Carbonate	14.0	5.3	0.3
OPH-1697	1,136.81	Yale	Mudstone		0.0	
OPH-1697	1,136.81	Yale	Mudstone		0.0	
OPH-1697	1,137.01	NGU	Mudstone	5.3	0.7	0.7
OPH-1697	1,137.01	NGU	Mudstone	5.3	0.7	0.7
OPH-1704	1,137.78	NGU	Carbonate	4.8	0.9	0.3
OPH-1709	1,138.18	NGU	Carbonate	3.4	0.2	1.6
OPH-1729	1,145.99	NGU	Mudstone	8.6	8.9	1.0
OPH-1746	1,159.50	NGU	Mudstone	18.4	19.1	1.5
OPH-1752	1,160.27	NGU	Mudstone	17.4	17.4	1.9
OPH-1761	1,161.32	NGU	Mudstone	16.2	16.0	1.7
OPH-1761	1,161.32	NGU	Mudstone	16.2	16.0	1.7
OPH-1761	1,161.32	Yale	Mudstone		0.2	
OPH-1761	1,161.32	Yale	Mudstone		0.2	
OPH-1765	1,161.95	NGU	Mudstone	2.3	0.8	3.4
OPH-1768	1,162.23	NGU	Mudstone	21.7	22.1	2.1
OPH-1779	1,166.13	NGU	Mudstone	2.9	0.3	1.9
OPH-1796	1,175.69	NGU	Mudstone	20.1	19.8	2.7
OPH-1809	1,187.30	NGU	Mudstone	12.7	12.9	2.9
OPH-1809	1,187.30	NGU	Mudstone	12.7	12.9	2.9
OPH-1809	1,187.30	Yale	Mudstone		0.2	
OPH-1809	1,187.30	Yale	Mudstone		0.2	
OPH-1814	1,187.91	NGU	Mudstone	10.3	8.7	2.9
OPH-1823	1,188.90	NGU	Mudstone	5.5	2.7	4.4
OPH-1831	1,190.01	NGU	Carbonate	6.4	3.3	4.8
OPH-1835	1,190.75	NGU	Carbonate	5.2	2.7	0.7
OPH-1849	1,198.41	NGU	Mudstone	6.4	6.4	2.5
OPH-1856	1,199.56	NGU	Carbonate	9.5	5.0	
OPH-1862	1,200.64	NGU	Carbonate	5.1	0.8	0.1
OPH-1865	1,201.25	NGU	Carbonate	6.0	2.2	
OPH-1871	1,202.50	NGU	Carbonate	12.0	7.5	0.0
OPH-1879	1,203.59	NGU	Mudstone	8.4	7.4	2.1
OPH-1885	1,204.44	NGU	Mudstone	6.8	6.9	1.2
OPH-1892	1,205.03	NGU	Mudstone	11.9	12.8	0.9
OPH-1904	1,206.20	NGU	Mudstone	8.6	9.1	3.1
OPH-1918	1,207.63	NGU	Mudstone	11.4	12.1	0.1

OPH-1918	1,207.63	NGU	Mudstone	11.4	12.1	0.1
OPH-1918	1,207.63	Yale	Mudstone		0.1	
OPH-1918	1,207.63	Yale	Mudstone		0.1	
OPH-1924	1,208.96	NGU	Carbonate	18.2	14.3	0.1
OPH-1927	1,209.45	NGU	Carbonate	9.7	6.7	1.8
OPH-1939	1,211.12	NGU	Mudstone	15.0	15.4	0.5
OPH-1942	1,211.51	NGU	Mudstone	15.7	16.1	0.3
OPH-1948	1,212.51	NGU	Carbonate	14.1	4.4	0.3
OPH-1960	1,214.11	NGU	Mudstone	3.7	3.1	1.7
OPH-1962	1,214.28	NGU	Mudstone	3.8	2.5	3.2
OPH-1975	1,215.53	NGU	Carbonate	8.4	0.6	3.7
OPH-1984	1,216.89	NGU	Mudstone	4.3	3.4	0.1
OPH-1994	1,217.74	NGU	Mudstone	4.7	4.9	0.7
OPH-2001	1,218.36	Yale	Carbonate		0.0	
OPH-2001	1,218.36	NGU	Carbonate	10.6	0.8	2.5
OPH-2001	1,218.36	Yale	Carbonate		0.0	
OPH-2001	1,218.36	NGU	Carbonate	10.6	0.8	2.5
OPH-2010	1,219.18	NGU	Carbonate	3.8	3.9	2.0
OPH-2027	1,220.85	NGU	Mudstone	2.3	2.2	0.1
OPH-2040	1,221.72	NGU	Mudstone	0.2	0.2	0.7
OPH-2052	1,223.79	NGU	Mudstone	0.1		1.6
OPH-2061	1,225.13	Yale	Mudstone		0.0	
OPH-2061	1,225.13	Yale	Mudstone		0.0	
OPH-2061	1,225.13	NGU	Mudstone	0.4	0.4	1.9
OPH-2061	1,225.13	NGU	Mudstone	0.4	0.4	1.9
OPH-2068	1,226.04	NGU	Mudstone	8.3	8.5	
OPH-2069	1,226.21	NGU	Carbonate	7.6	4.7	1.5
OPH-2397	1,426.19	NGU	Mudstone	37.8	39.4	1.5
OPH-2406	1,427.09	Yale	Mudstone		0.4	
OPH-2406	1,427.09	Yale	Mudstone		0.4	
OPH-2406	1,427.16	NGU	Mudstone	40.0	39.8	1.7
OPH-2406	1,427.16	NGU	Mudstone	40.0	39.8	1.7
OPH-2413	1,427.81	NGU	Mudstone	32.2	31.6	2.0
OPH-2423	1,437.13	NGU	Mudstone	0.1		2.7
OPH-2426	1,437.68	NGU	Mudstone	0.2	0.1	1.2
OPH-2993	1,765.27	NGU	Carbonate	6.9	2.5	0.4
OPH-3009	1,767.41	NGU	Carbonate	14.5	10.3	0.4
OPH-3016	1,777.38	Yale	Mudstone		0.4	
OPH-3016	1,777.38	Yale	Mudstone		0.4	
OPH-3016	1,777.46	NGU	Mudstone	41.3	41.2	1.9
OPH-3016	1,777.46	NGU	Mudstone	41.3	41.2	1.9
OPH-3057	1,792.05	NGU		37.7	37.1	1.8
OPH-3112	1,868.46	NGU	Mudstone	16.4	16.6	2.0
OPH-3117	1,869.18	NGU	Mudstone	9.2	9.7	0.8
OPH-3132	1,871.00	NGU	Mudstone	19.4	19.8	0.5
OPH-3132	1,871.00	NGU	Mudstone	19.4	19.8	0.5
OPH-3132	1,871.00	Yale	Mudstone		0.2	
OPH-3132	1,871.00	Yale	Mudstone		0.2	
OPH-3141	1,871.27	NGU	Mudstone	15.2	15.2	0.6
OPH-3137	1,871.47	NGU	Mudstone	16.9	17.3	3.7
OPH-3161	1,881.50	NGU	Mudstone	10.1	10.0	0.3
OPH-3168	1,887.61	NGU	Mudstone	7.2	7.7	0.0
OPH-3179	1,888.77	NGU	Carbonate	12.3		0.1
OPH-3182	1,889.14	NGU		5.0		0.1
OPH-3191	1,902.61	Yale	Mudstone		0.0	
OPH-3194	1,902.88	NGU	Mudstone	1.4		0.0
OPH-3229	1,915.60	NGU	Mudstone	2.0		
OPH-3256	1,926.73	Yale	Mudstone		0.0	
OPH-3256	1,926.73	Yale	Mudstone		0.0	
OPH-3256	1,926.80	NGU	Mudstone	1.1		
OPH-3256	1,926.80	NGU	Mudstone	1.1		
OPH-3272	1,935.31	NGU	Mudstone	1.0		
OPH-3275	1,935.54	NGU	Mudstone	1.6		
OPH-3295	1,946.55	NGU	Mudstone	3.0		
OPH-3324	1,957.85	NGU	Mudstone	1.2		
OPH-3331	1,958.63	NGU	Mudstone	0.9		
OPH-3355	1,970.85	NGU	Mudstone	0.2		

OPH-3355	1,970.85	Yale	Mudstone		0.0
OPH-3355	1,970.85	Yale	Mudstone		0.0
OPH-3355	1,970.85	NGU	Mudstone	0.2	
OPH-3386	1,980.42	NGU	Carbonate	5.2	
OPH-3411	1,991.90	NGU		5.4	
OPH-3463	2,011.35	Yale	Mudstone		0.0
OPH-3589	2,052.57	Yale	Mudstone		0.0
OPH-3707	2,103.47	Yale	Mudstone		0.0
OPH-3736	2,205.38	Yale	Carbonate		21.0
OPH-3904	2,252.09	Yale	Carbonate		15.1
OPH-4022	2,285.28	Yale	Carbonate		0.0
OPH-4081	2,305.25	Yale	Carbonate		6.6
OPH-4142	2,324.43	Yale	Carbonate		9.9
OPH-4178	2,328.55	Yale	Carbonate		44.1
OPH-4194	2,330.34	Yale	Carbonate		40.0
OPH-4194	2,330.34	Yale	Carbonate		40.0
OPH-4211	2,509.02	Yale	Evaporite		32.6
OPH-4257	2,517.36	Yale	Evaporite		5.1
OPH-4310	2,526.68	Yale	Evaporite		46.5
OPH-4366	2,547.78	Yale	Evaporite		35.3
OPH-4440	2,570.15	Yale	Evaporite		26.2
OPH-4537	2,700.97	Yale	Evaporite		24.2
OPH-4635	2,833.79	Yale	Evaporite		25.8
OPH-4683	2,850.46	Yale	Evaporite		6.5
OPH-4683	2,850.46	Yale	Evaporite		6.5
OPH-4774	2,878.31	Yale	Evaporite		11.5
OPH-4813	2,896.20	Yale	Evaporite		6.3
OPH-4853	2,904.34	Yale	Evaporite		8.5

Table A7a: X-ray diffraction mineral abundances in drill core OPH.

Sample ID	Depth (m)	Lithology	Amphibole (wt.%)	Anatase (wt.%)	Anhydrite (wt.%)	Apatite (wt.%)	Aragonite (wt.%)	Axinite (wt.%)	Bassanite (wt.%)	Bloedite (wt.%)	Calcite (wt.%)	Chlorite (wt.%)	Clinozoizite (wt.%)	Dolomite (wt.%)
OPH-10	530.39	Mudstone												
OPH-73	542.63	Mudstone	5.8								1.0	54.1		
OPH-80	543.68	Mudstone												
OPH-83	544.22	Mudstone												
OPH-121	552.43	Mudstone												
OPH-284	591.30	Mudstone												
OPH-306	594.85	Mudstone									1.4	23.7		
OPH-507	636.42	Mudstone												
OPH-515	637.85	Mudstone												
OPH-523	638.53	Mudstone						25.4			11.5	6.9		
OPH-844	890.22	Mudstone									3.3	4.1		
OPH-849	891.17	Mudstone												
OPH-858	892.79	Mudstone												
OPH-862	893.38	Mudstone												
OPH-867	894.16	Mudstone												
OPH-875	894.98	Carbonate												
OPH-879	895.49	Carbonate												
OPH-924	899.15	Carbonate												
OPH-925	899.25	Carbonate												
OPH-938	900.23	Carbonate												
OPH-945	901.96													
OPH-955	903.08	Mudstone												
OPH-970	904.30	Mudstone												
OPH-975	912.04	Mudstone									5.2	16.5		0.4
OPH-979	912.70	Mudstone												
OPH-1361	1,080.00	Carbonate												
OPH-1364	1,080.57	Carbonate									29.3	4.3		53.1
OPH-1364	1,080.57	Carbonate												53.1
OPH-1366	1,081.11	Carbonate												
OPH-1368	1,081.36	Carbonate												62.3
OPH-1372	1,081.93	Carbonate												37.9
OPH-1373	1,082.28	Carbonate												
OPH-1376	1,082.71	Carbonate												
OPH-1383	1,083.49	Carbonate												
OPH-1390	1,084.18	Carbonate												
OPH-1393	1,084.47	Carbonate												86.3
OPH-1398	1,085.13	Carbonate												89.6
OPH-1400	1,085.42	Carbonate												91.6
OPH-1403	1,086.33	Carbonate												
OPH-1405	1,086.52	Carbonate												75.0
OPH-1405	1,086.52	Carbonate									17.3	3.0		75.0
OPH-1412	1,087.73	Carbonate												60.7

Sample ID	Depth (m)	Lithology	Amphibole (wt.%)	Anatase (wt.%)	Anhydrite (wt.%)	Apatite (wt.%)	Aragonite (wt.%)	Axinite (wt.%)	Bassanite (wt.%)	Bloedite (wt.%)	Calcite (wt.%)	Chlorite (wt.%)	Clinozoizite (wt.%)	Dolomite (wt.%)
OPH-1421	1,089.09	Carbonate												
OPH-1426	1,089.67	Carbonate												2.4
OPH-1434	1,090.51	Carbonate												
OPH-1436	1,090.80	Carbonate												
OPH-1442	1,091.87	Carbonate												
OPH-1444	1,092.14	Carbonate												2.7
OPH-1449	1,093.39	Carbonate												85.7
OPH-1449	1,093.39	Carbonate									6.2	5.0		85.7
OPH-1452	1,093.90	Carbonate												
OPH-1461	1,094.89	Carbonate												75.3
OPH-1464	1,095.45	Carbonate												93.5
OPH-1466	1,095.74	Carbonate												73.4
OPH-1468	1,096.29	Carbonate												
OPH-1469	1,096.31	Carbonate												64.0
OPH-1470	1,096.57	Carbonate												69.1
OPH-1472	1,096.82	Carbonate												86.6
OPH-1479	1,098.06	Carbonate												92.7
OPH-1483	1,098.66	Carbonate												
OPH-1486	1,099.04	Carbonate												85.1
OPH-1488	1,099.51													81.7
OPH-1491	1,099.98	Carbonate												96.9
OPH-1499	1,101.27	Carbonate												83.1
OPH-1499	1,101.27	Carbonate									13.2			85.9
OPH-1501	1,101.45	Mudstone												
OPH-1509	1,102.06	Mudstone												
OPH-1516	1,102.74	Mudstone												
OPH-1519	1,103.35	Mudstone												
OPH-1527	1,104.69	Carbonate												88.8
OPH-1533	1,106.00	Carbonate												82.6
OPH-1542	1,106.99	Mudstone												
OPH-1556	1,109.44	Carbonate												84.8
OPH-1557	1,109.57	Carbonate												81.5
OPH-1560	1,109.96	Carbonate												78.9
OPH-1561	1,110.18	Carbonate												78.8
OPH-1564	1,110.79	Carbonate												76.9
OPH-1567	1,111.40	Carbonate												85.0
OPH-1568	1,111.60	Carbonate												71.5
OPH-1569	1,111.80	Carbonate												40.4
OPH-1571	1,112.02	Carbonate												
OPH-1572	1,112.08	Mudstone		1.5										
OPH-1573	1,112.27	Mudstone		1.1										0.3
OPH-1575	1,112.65	Mudstone		1.1										0.3
OPH-1578	1,113.28	Mudstone		0.8										
OPH-1579	1,113.58	Mudstone												
OPH-1580	1,113.63	Mudstone		1.8										

Sample ID	Depth (m)	Lithology	Amphibole (wt.%)	Anatase (wt.%)	Anhydrite (wt.%)	Apatite (wt.%)	Aragonite (wt.%)	Axinite (wt.%)	Bassanite (wt.%)	Bloedite (wt.%)	Calcite (wt.%)	Chlorite (wt.%)	Clinozoizite (wt.%)	Dolomite (wt.%)
OPH-1581	1,113.83	Mudstone		1.3										
OPH-1582	1,113.92	Mudstone												
OPH-1584	1,114.20	Mudstone		0.9										
OPH-1585	1,114.34	Mudstone		1.3										
OPH-1585	1,114.34	Mudstone		1.3										
OPH-1586	1,114.62	Mudstone												
OPH-1587	1,114.77	Mudstone		2.7										
OPH-1588	1,115.02	Mudstone		2.2										
OPH-1589	1,115.21	Mudstone												
OPH-1590	1,115.59	Carbonate												39.4
OPH-1592	1,115.87	Mudstone												
OPH-1596	1,116.61	Carbonate												89.6
OPH-1599	1,117.43	Carbonate												56.3
OPH-1601	1,117.48	Mudstone		3.4										
OPH-1606	1,118.27	Mudstone		1.6										
OPH-1608	1,118.59	Mudstone												
OPH-1613	1,119.54	Mudstone												
OPH-1647	1,120.31	Mudstone									0.6			0.9
OPH-1617	1,120.31	Mudstone		1.0										0.4
OPH-1647	1,120.31	Mudstone		1.5										0.9
OPH-1621	1,120.77	Mudstone												
OPH-1624	1,121.15	Mudstone												
OPH-1625	1,121.37	Mudstone		1.2										
OPH-1626	1,121.70	Mudstone												
OPH-1634	1,123.13	Mudstone												7.7
OPH-1640	1,123.62	Mudstone												
OPH-1651	1,124.55	Mudstone												
OPH-1655	1,125.02	Mudstone												24.9
OPH-1676	1,127.22	Mudstone												
OPH-1683	1,135.64	Carbonate												
OPH-1697	1,136.81	Mudstone				0.7					14.1	5.4		16.0
OPH-1697	1,136.81	Mudstone												0.9
OPH-1704	1,137.78	Carbonate												
OPH-1709	1,138.18	Carbonate												
OPH-1729	1,145.99	Mudstone												
OPH-1746	1,159.50	Mudstone												
OPH-1752	1,160.27	Mudstone												
OPH-1761	1,161.32	Mudstone									0.7			
OPH-1765	1,161.95	Mudstone												
OPH-1768	1,162.23	Mudstone												
OPH-1779	1,166.13	Mudstone												
OPH-1796	1,175.69	Mudstone												
OPH-1809	1,187.30	Mudstone									2.9	trace		0.6
OPH-1814	1,187.91	Mudstone												
OPH-1823	1,188.90	Mudstone												

Sample ID	Depth (m)	Lithology	Amphibole (wt.%)	Anatase (wt.%)	Anhydrite (wt.%)	Apatite (wt.%)	Aragonite (wt.%)	Axinite (wt.%)	Bassanite (wt.%)	Bloedite (wt.%)	Calcite (wt.%)	Chlorite (wt.%)	Clinozoizite (wt.%)	Dolomite (wt.%)
OPH-1831	1,190.01	Carbonate												
OPH-1835	1,190.75	Carbonate												
OPH-1849	1,198.41	Mudstone												
OPH-1856	1,199.56	Carbonate												
OPH-1862	1,200.64	Carbonate												
OPH-1865	1,201.25	Carbonate												
OPH-1871	1,202.50	Carbonate												
OPH-1879	1,203.59	Mudstone												
OPH-1885	1,204.44	Mudstone												
OPH-1892	1,205.03	Mudstone												
OPH-1904	1,206.20	Mudstone												
OPH-1918	1,207.63	Mudstone									0.5	8.3		0.7
OPH-1924	1,208.96	Carbonate												
OPH-1927	1,209.45	Carbonate												
OPH-1939	1,211.12	Mudstone												
OPH-1942	1,211.51	Mudstone												
OPH-1948	1,212.51	Carbonate												
OPH-1960	1,214.11	Mudstone												
OPH-1962	1,214.28	Mudstone												
OPH-1975	1,215.53	Carbonate												
OPH-1984	1,216.89	Mudstone												
OPH-1994	1,217.74	Mudstone												
OPH-2001	1,218.36	Carbonate									73.5			8.1
OPH-2010	1,219.18	Carbonate												
OPH-2027	1,220.85	Mudstone												
OPH-2040	1,221.72	Mudstone												
OPH-2052	1,223.79	Mudstone												0.0
OPH-2061	1,225.13	Mudstone									1.1	16.9		0.0
OPH-2068	1,226.04	Mudstone												
OPH-2069	1,226.21	Carbonate												
OPH-2397	1,426.19	Mudstone												
OPH-2406	1,427.09	Mudstone	3.1									9.5		
OPH-2413	1,427.81	Mudstone												
OPH-2423	1,437.13	Mudstone												
OPH-2426	1,437.68	Mudstone												
OPH-2993	1,765.27	Carbonate												
OPH-3009	1,767.41	Carbonate												
OPH-3016	1,777.38	Mudstone	0.5									12.8		
OPH-3112	1,868.46	Mudstone												
OPH-3117	1,869.18	Mudstone												
OPH-3132	1,871.00	Mudstone									trace	18.8		
OPH-3141	1,871.27	Mudstone												
OPH-3137	1,871.47	Mudstone												
OPH-3161	1,881.50	Mudstone												
OPH-3168	1,887.61	Mudstone												

Sample ID	Depth (m)	Lithology	Amphibole (wt.%)	Anatase (wt.%)	Anhydrite (wt.%)	Apatite (wt.%)	Aragonite (wt.%)	Axinite (wt.%)	Bassanite (wt.%)	Bloedite (wt.%)	Calcite (wt.%)	Chlorite (wt.%)	Clinozoizite (wt.%)	Dolomite (wt.%)
OPH-3179	1,888.77	Carbonate												92.5
OPH-3182	1,889.14													41.4
OPH-3191	1,902.61	Mudstone												17.7
OPH-3191	1,902.61	Mudstone									trace	12.6		17.7
OPH-3194	1,902.88	Mudstone												
OPH-3229	1,915.60	Mudstone												33.1
OPH-3256	1,926.73	Mudstone												5.9
OPH-3256	1,926.73	Mudstone									trace	7.7		9.1
OPH-3272	1,935.31	Mudstone												
OPH-3275	1,935.54	Mudstone												7.6
OPH-3295	1,946.55	Mudstone												
OPH-3324	1,957.85	Mudstone												
OPH-3331	1,958.63	Mudstone												
OPH-3355	1,970.85	Mudstone									1.7	5.7		1.5
OPH-3386	1,980.42	Carbonate												
OPH-3463	2,011.35	Mudstone												36.4
OPH-3589	2,052.57	Mudstone												42.2
OPH-3589	2,052.57	Mudstone										7.2		42.2
OPH-3707	2,103.47	Mudstone												48.1
OPH-3707	2,103.47	Mudstone										1.6		48.1
OPH-3736	2,205.38	Carbonate												60.4
OPH-3904	2,252.09	Carbonate												76.3
OPH-4022	2,285.28	Carbonate										1.1		61.6
OPH-4081	2,305.25	Carbonate												32.6
OPH-4142	2,324.43	Carbonate												89.8
OPH-4178	2,328.55	Carbonate			0.4									
OPH-4183	2,329.14	Carbonate												86.1
OPH-4185	2,329.34				15.0									70.2
OPH-4187	2,329.62				24.4									69.8
OPH-4193	2,330.28	Evaporite			60.9									1.5
OPH-4193	2,330.28	Evaporite			60.9									1.5
OPH-4194	2,330.34	Carbonate			6.3									
OPH-4199	2,330.85	Evaporite			43.4									39.9
OPH-4211	2,509.02	Evaporite			18.0									
OPH-4257	2,517.36	Evaporite			14.9									
OPH-4310	2,526.68	Evaporite			52.7									
OPH-4366	2,547.78	Evaporite			34.3									1.0
OPH-4383	2,549.45	Mudstone			6.4									
OPH-4383	2,549.45	Mudstone			6.4									
OPH-4440	2,570.15	Evaporite			22.2									
OPH-4537	2,700.97	Evaporite			12.0				1.2					
OPH-4582	2,724.31	Evaporite			33.5									1.1
OPH-4582	2,724.31	Evaporite			33.5									1.1
OPH-4635	2,833.79	Evaporite			38.8					2.1				0.8
OPH-4620	2,838.14	Evaporite			70.9							3.3		

Sample ID	Depth (m)	Lithology	Amphibole (wt.%)	Anatase (wt.%)	Anhydrite (wt.%)	Apatite (wt.%)	Aragonite (wt.%)	Axinite (wt.%)	Bassanite (wt.%)	Bloedite (wt.%)	Calcite (wt.%)	Chlorite (wt.%)	Clinozoizite (wt.%)	Dolomite (wt.%)
OPH-4683	2,850.46	Evaporite			13.4									1.3
OPH-4683	2,850.46	Evaporite			13.4							2.6		1.3
OPH-4774	2,878.31	Evaporite			32.7					0.8				
OPH-4813	2,896.20	Evaporite			4.2									
OPH-4853	2,904.34	Evaporite			10.1									

Table A7b: X-ray diffraction mineral abundances in drill core OPH, continued.

Sample ID	Depth (m)	Lithology	Glauberite (wt.%)	Gypsum (wt.%)	Halite (wt.%)	Hematite (wt.%)	Hexahydrite (wt.%)	K-feldspar (wt.%)	Kainite (wt.%)	Kaolinite (wt.%)	Kieserite (wt.%)	Langbeinite (wt.%)	Leonite (wt.%)	Magnesite (wt.%)
OPH-10	530.39	Mudstone												
OPH-73	542.63	Mudstone						3.9						
OPH-80	543.68	Mudstone												
OPH-83	544.22	Mudstone												
OPH-121	552.43	Mudstone												
OPH-284	591.30	Mudstone												
OPH-306	594.85	Mudstone						11.9						
OPH-507	636.42	Mudstone												
OPH-515	637.85	Mudstone												
OPH-523	638.53	Mudstone						8.5						
OPH-844	890.22	Mudstone						12.8						
OPH-849	891.17	Mudstone												
OPH-858	892.79	Mudstone												
OPH-862	893.38	Mudstone												
OPH-867	894.16	Mudstone												
OPH-875	894.98	Carbonate												
OPH-879	895.49	Carbonate												
OPH-924	899.15	Carbonate												
OPH-925	899.25	Carbonate												
OPH-938	900.23	Carbonate												
OPH-945	901.96													
OPH-955	903.08	Mudstone												
OPH-970	904.30	Mudstone												
OPH-975	912.04	Mudstone						2.6						
OPH-979	912.70	Mudstone												
OPH-1361	1,080.00	Carbonate												
OPH-1364	1,080.57	Carbonate						0.4						
OPH-1364	1,080.57	Carbonate												
OPH-1366	1,081.11	Carbonate												
OPH-1368	1,081.36	Carbonate												
OPH-1372	1,081.93	Carbonate												
OPH-1373	1,082.28	Carbonate												
OPH-1376	1,082.71	Carbonate												
OPH-1383	1,083.49	Carbonate												
OPH-1390	1,084.18	Carbonate												
OPH-1393	1,084.47	Carbonate												
OPH-1398	1,085.13	Carbonate												
OPH-1400	1,085.42	Carbonate												
OPH-1403	1,086.33	Carbonate												
OPH-1405	1,086.52	Carbonate												
OPH-1405	1,086.52	Carbonate												
OPH-1412	1,087.73	Carbonate												

Sample ID	Depth (m)	Lithology	Glauberite (wt.%)	Gypsum (wt.%)	Halite (wt.%)	Hematite (wt.%)	Hexahydrite (wt.%)	K-feldspar (wt.%)	Kainite (wt.%)	Kaolinite (wt.%)	Kieserite (wt.%)	Langbeinite (wt.%)	Leonite (wt.%)	Magnesite (wt.%)
OPH-1421	1,089.09	Carbonate												
OPH-1426	1,089.67	Carbonate												
OPH-1434	1,090.51	Carbonate												
OPH-1436	1,090.80	Carbonate												
OPH-1442	1,091.87	Carbonate												
OPH-1444	1,092.14	Carbonate												
OPH-1449	1,093.39	Carbonate												
OPH-1449	1,093.39	Carbonate												
OPH-1452	1,093.90	Carbonate												
OPH-1461	1,094.89	Carbonate												
OPH-1464	1,095.45	Carbonate												
OPH-1466	1,095.74	Carbonate												
OPH-1468	1,096.29	Carbonate												
OPH-1469	1,096.31	Carbonate								0.3				
OPH-1470	1,096.57	Carbonate												
OPH-1472	1,096.82	Carbonate												
OPH-1479	1,098.06	Carbonate												
OPH-1483	1,098.66	Carbonate												
OPH-1486	1,099.04	Carbonate												
OPH-1488	1,099.51													
OPH-1491	1,099.98	Carbonate												
OPH-1499	1,101.27	Carbonate												
OPH-1499	1,101.27	Carbonate												
OPH-1501	1,101.45	Mudstone												
OPH-1509	1,102.06	Mudstone												
OPH-1516	1,102.74	Mudstone												
OPH-1519	1,103.35	Mudstone												
OPH-1527	1,104.69	Carbonate												
OPH-1533	1,106.00	Carbonate												
OPH-1542	1,106.99	Mudstone												
OPH-1556	1,109.44	Carbonate												
OPH-1557	1,109.57	Carbonate												
OPH-1560	1,109.96	Carbonate												
OPH-1561	1,110.18	Carbonate												
OPH-1564	1,110.79	Carbonate												
OPH-1567	1,111.40	Carbonate												
OPH-1568	1,111.60	Carbonate												
OPH-1569	1,111.80	Carbonate												
OPH-1571	1,112.02	Carbonate												
OPH-1572	1,112.08	Mudstone												
OPH-1573	1,112.27	Mudstone												
OPH-1575	1,112.65	Mudstone												
OPH-1578	1,113.28	Mudstone												
OPH-1579	1,113.58	Mudstone												
OPH-1580	1,113.63	Mudstone												

Sample ID	Depth (m)	Lithology	Glauberite (wt.%)	Gypsum (wt.%)	Halite (wt.%)	Hematite (wt.%)	Hexahydrite (wt.%)	K-feldspar (wt.%)	Kainite (wt.%)	Kaolinite (wt.%)	Kieserite (wt.%)	Langbeinite (wt.%)	Leonite (wt.%)	Magnesite (wt.%)
OPH-1581	1,113.83	Mudstone												
OPH-1582	1,113.92	Mudstone												
OPH-1584	1,114.20	Mudstone												
OPH-1585	1,114.34	Mudstone												
OPH-1585	1,114.34	Mudstone						19.8						
OPH-1586	1,114.62	Mudstone												
OPH-1587	1,114.77	Mudstone												
OPH-1588	1,115.02	Mudstone												
OPH-1589	1,115.21	Mudstone												
OPH-1590	1,115.59	Carbonate												
OPH-1592	1,115.87	Mudstone												
OPH-1596	1,116.61	Carbonate												
OPH-1599	1,117.43	Carbonate												
OPH-1601	1,117.48	Mudstone												
OPH-1606	1,118.27	Mudstone												
OPH-1608	1,118.59	Mudstone												
OPH-1613	1,119.54	Mudstone												
OPH-1647	1,120.31	Mudstone						8.6						
OPH-1617	1,120.31	Mudstone												
OPH-1647	1,120.31	Mudstone												
OPH-1621	1,120.77	Mudstone												
OPH-1624	1,121.15	Mudstone												
OPH-1625	1,121.37	Mudstone												
OPH-1626	1,121.70	Mudstone												
OPH-1634	1,123.13	Mudstone												
OPH-1640	1,123.62	Mudstone												
OPH-1651	1,124.55	Mudstone												
OPH-1655	1,125.02	Mudstone												
OPH-1676	1,127.22	Mudstone												
OPH-1683	1,135.64	Carbonate												
OPH-1697	1,136.81	Mudstone						2.8						
OPH-1697	1,136.81	Mudstone												
OPH-1704	1,137.78	Carbonate												
OPH-1709	1,138.18	Carbonate												
OPH-1729	1,145.99	Mudstone												
OPH-1746	1,159.50	Mudstone												
OPH-1752	1,160.27	Mudstone												
OPH-1761	1,161.32	Mudstone						7.2						
OPH-1765	1,161.95	Mudstone												
OPH-1768	1,162.23	Mudstone												
OPH-1779	1,166.13	Mudstone												
OPH-1796	1,175.69	Mudstone												
OPH-1809	1,187.30	Mudstone						9.7						
OPH-1814	1,187.91	Mudstone												
OPH-1823	1,188.90	Mudstone												

Sample ID	Depth (m)	Lithology	Glauberite (wt.%)	Gypsum (wt.%)	Halite (wt.%)	Hematite (wt.%)	Hexahydrite (wt.%)	K-feldspar (wt.%)	Kainite (wt.%)	Kaolinite (wt.%)	Kieserite (wt.%)	Langbeinite (wt.%)	Leonite (wt.%)	Magnesite (wt.%)
OPH-1831	1,190.01	Carbonate												
OPH-1835	1,190.75	Carbonate												
OPH-1849	1,198.41	Mudstone												
OPH-1856	1,199.56	Carbonate												
OPH-1862	1,200.64	Carbonate												
OPH-1865	1,201.25	Carbonate												
OPH-1871	1,202.50	Carbonate												
OPH-1879	1,203.59	Mudstone												
OPH-1885	1,204.44	Mudstone												
OPH-1892	1,205.03	Mudstone												
OPH-1904	1,206.20	Mudstone												
OPH-1918	1,207.63	Mudstone						23.1						
OPH-1924	1,208.96	Carbonate												
OPH-1927	1,209.45	Carbonate												
OPH-1939	1,211.12	Mudstone												
OPH-1942	1,211.51	Mudstone												
OPH-1948	1,212.51	Carbonate												
OPH-1960	1,214.11	Mudstone												
OPH-1962	1,214.28	Mudstone												
OPH-1975	1,215.53	Carbonate												
OPH-1984	1,216.89	Mudstone												
OPH-1994	1,217.74	Mudstone												
OPH-2001	1,218.36	Carbonate						2.5						
OPH-2010	1,219.18	Carbonate												
OPH-2027	1,220.85	Mudstone												
OPH-2040	1,221.72	Mudstone												
OPH-2052	1,223.79	Mudstone												
OPH-2061	1,225.13	Mudstone						2.0						
OPH-2068	1,226.04	Mudstone												
OPH-2069	1,226.21	Carbonate												
OPH-2397	1,426.19	Mudstone												
OPH-2406	1,427.09	Mudstone						10.5						
OPH-2413	1,427.81	Mudstone												
OPH-2423	1,437.13	Mudstone												
OPH-2426	1,437.68	Mudstone												
OPH-2993	1,765.27	Carbonate												
OPH-3009	1,767.41	Carbonate												
OPH-3016	1,777.38	Mudstone						9.7						
OPH-3112	1,868.46	Mudstone												
OPH-3117	1,869.18	Mudstone												
OPH-3132	1,871.00	Mudstone						4.2						
OPH-3141	1,871.27	Mudstone												
OPH-3137	1,871.47	Mudstone												
OPH-3161	1,881.50	Mudstone												
OPH-3168	1,887.61	Mudstone												

Sample ID	Depth (m)	Lithology	Glauberite (wt.%)	Gypsum (wt.%)	Halite (wt.%)	Hematite (wt.%)	Hexahydrite (wt.%)	K-feldspar (wt.%)	Kainite (wt.%)	Kaolinite (wt.%)	Kieserite (wt.%)	Langbeinite (wt.%)	Leonite (wt.%)	Magnesite (wt.%)
OPH-3179	1,888.77	Carbonate												
OPH-3182	1,889.14													
OPH-3191	1,902.61	Mudstone												
OPH-3191	1,902.61	Mudstone						1.9						
OPH-3194	1,902.88	Mudstone												
OPH-3229	1,915.60	Mudstone												
OPH-3256	1,926.73	Mudstone												
OPH-3256	1,926.73	Mudstone				2.0		1.3						
OPH-3272	1,935.31	Mudstone												
OPH-3275	1,935.54	Mudstone												
OPH-3295	1,946.55	Mudstone												
OPH-3324	1,957.85	Mudstone												
OPH-3331	1,958.63	Mudstone												
OPH-3355	1,970.85	Mudstone				2.3		5.9						
OPH-3386	1,980.42	Carbonate												
OPH-3463	2,011.35	Mudstone						0.7						
OPH-3589	2,052.57	Mudstone												
OPH-3589	2,052.57	Mudstone				trace		0.9						
OPH-3707	2,103.47	Mudstone												
OPH-3707	2,103.47	Mudstone						13.4						
OPH-3736	2,205.38	Carbonate												38.4
OPH-3904	2,252.09	Carbonate												
OPH-4022	2,285.28	Carbonate				0.8								
OPH-4081	2,305.25	Carbonate												47.2
OPH-4142	2,324.43	Carbonate												0.5
OPH-4178	2,328.55	Carbonate												68.1
OPH-4183	2,329.14	Carbonate												
OPH-4185	2,329.34													
OPH-4187	2,329.62													24.4
OPH-4193	2,330.28	Evaporite												34.8
OPH-4193	2,330.28	Evaporite						0.8						34.8
OPH-4194	2,330.34	Carbonate												82.6
OPH-4199	2,330.85	Evaporite												
OPH-4211	2,509.02	Evaporite												77.4
OPH-4257	2,517.36	Evaporite												30.9
OPH-4310	2,526.68	Evaporite		1.2										40.6
OPH-4366	2,547.78	Evaporite	0.6											45.0
OPH-4383	2,549.45	Mudstone	10.7	3.8				0.8						29.0
OPH-4383	2,549.45	Mudstone	10.7	3.8										29.0
OPH-4440	2,570.15	Evaporite												64.8
OPH-4537	2,700.97	Evaporite	0.9	13.3	0.5		0.5							42.5
OPH-4582	2,724.31	Evaporite	54.2	5.4			0.7							2.0
OPH-4582	2,724.31	Evaporite	54.2	5.4			0.7							2.0
OPH-4635	2,833.79	Evaporite			7.2		4.0		0.8				2.8	34.6
OPH-4620	2,838.14	Evaporite			10.7									7.3

Sample ID	Depth (m)	Lithology	Glauberite (wt.%)	Gypsum (wt.%)	Halite (wt.%)	Hematite (wt.%)	Hexahydrite (wt.%)	K-feldspar (wt.%)	Kainite (wt.%)	Kaolinite (wt.%)	Kieserite (wt.%)	Langbeinite (wt.%)	Leonite (wt.%)	Magnesite (wt.%)
OPH-4683	2,850.46	Evaporite			77.4									5.3
OPH-4683	2,850.46	Evaporite			77.4									5.3
OPH-4774	2,878.31	Evaporite			31.6									23.4
OPH-4813	2,896.20	Evaporite			74.1		1.2				2.1			4.0
OPH-4853	2,904.34	Evaporite			65.7		0.9				1.6		2.0	3.8

Table A7c: X-ray diffraction mineral abundances in drill core OPH, continued.

Sample ID	Depth (m)	Lithology	Magnetite (wt.%)	Mica (wt.%)	Olivine (wt.%)	Pentahydrite (wt.%)	Picromerite (wt.%)	Plagioclase (wt.%)	Pyrite (wt.%)	Pyrrhotite (wt.%)	Quartz (wt.%)	Rutile (wt.%)	Siderite (wt.%)	Starkeyite (wt.%)
OPH-10	530.39	Mudstone												
OPH-73	542.63	Mudstone		1.8				16.7			9.9			
OPH-80	543.68	Mudstone												
OPH-83	544.22	Mudstone												
OPH-121	552.43	Mudstone												
OPH-284	591.30	Mudstone												
OPH-306	594.85	Mudstone		1.0				53.2			1.7			
OPH-507	636.42	Mudstone												
OPH-515	637.85	Mudstone												
OPH-523	638.53	Mudstone		3.6				25.8	0.4		17.4			
OPH-844	890.22	Mudstone		7.8				9.2	2.8	0.6	59.3			
OPH-849	891.17	Mudstone												
OPH-858	892.79	Mudstone												
OPH-862	893.38	Mudstone												
OPH-867	894.16	Mudstone												
OPH-875	894.98	Carbonate												
OPH-879	895.49	Carbonate												
OPH-924	899.15	Carbonate												
OPH-925	899.25	Carbonate												
OPH-938	900.23	Carbonate												
OPH-945	901.96			16.6							1.8			
OPH-955	903.08	Mudstone												
OPH-970	904.30	Mudstone												
OPH-975	912.04	Mudstone		6.5				40.3	trace		28.1			
OPH-979	912.70	Mudstone												
OPH-1361	1,080.00	Carbonate												
OPH-1364	1,080.57	Carbonate		2.4				0.6	0.3		0.4			
OPH-1364	1,080.57	Carbonate		2.4							0.4			
OPH-1366	1,081.11	Carbonate												
OPH-1368	1,081.36	Carbonate		4.2										
OPH-1372	1,081.93	Carbonate		4.5										
OPH-1373	1,082.28	Carbonate												
OPH-1376	1,082.71	Carbonate												
OPH-1383	1,083.49	Carbonate												
OPH-1390	1,084.18	Carbonate												
OPH-1393	1,084.47	Carbonate		1.5										
OPH-1398	1,085.13	Carbonate		1.3										
OPH-1400	1,085.42	Carbonate		1.3										
OPH-1403	1,086.33	Carbonate												
OPH-1405	1,086.52	Carbonate		0.6										
OPH-1405	1,086.52	Carbonate		0.6										

Sample ID	Depth (m)	Lithology	Magnetite (wt.%)	Mica (wt.%)	Olivine (wt.%)	Pentahydrite (wt.%)	Picromerite (wt.%)	Plagioclase (wt.%)	Pyrite (wt.%)	Pyrrhotite (wt.%)	Quartz (wt.%)	Rutile (wt.%)	Siderite (wt.%)	Starkeyite (wt.%)
OPH-1412	1,087.73	Carbonate												
OPH-1421	1,089.09	Carbonate												
OPH-1426	1,089.67	Carbonate		0.9										
OPH-1434	1,090.51	Carbonate												
OPH-1436	1,090.80	Carbonate		0.4										
OPH-1442	1,091.87	Carbonate												
OPH-1444	1,092.14	Carbonate		1.2										
OPH-1449	1,093.39	Carbonate												
OPH-1449	1,093.39	Carbonate							0.4					
OPH-1452	1,093.90	Carbonate												
OPH-1461	1,094.89	Carbonate		0.3							1.3			
OPH-1464	1,095.45	Carbonate									0.5			
OPH-1466	1,095.74	Carbonate		1.8							0.3			
OPH-1468	1,096.29	Carbonate												
OPH-1469	1,096.31	Carbonate		1.7							9.7			
OPH-1470	1,096.57	Carbonate		2.4							0.8			
OPH-1472	1,096.82	Carbonate		0.5							1.2			
OPH-1479	1,098.06	Carbonate		2.6							0.2			
OPH-1483	1,098.66	Carbonate												
OPH-1486	1,099.04	Carbonate		9.9							0.5			
OPH-1488	1,099.51			1.1										
OPH-1491	1,099.98	Carbonate		1.3										
OPH-1499	1,101.27	Carbonate		0.4										
OPH-1499	1,101.27	Carbonate		trace					0.5		0.2			
OPH-1501	1,101.45	Mudstone												
OPH-1509	1,102.06	Mudstone												
OPH-1516	1,102.74	Mudstone												
OPH-1519	1,103.35	Mudstone												
OPH-1527	1,104.69	Carbonate		2.7							0.5		0.7	
OPH-1533	1,106.00	Carbonate		4.5							0.4			
OPH-1542	1,106.99	Mudstone												
OPH-1556	1,109.44	Carbonate		4.9							5.8			
OPH-1557	1,109.57	Carbonate		3.7							6.1			
OPH-1560	1,109.96	Carbonate		3.9							0.6			
OPH-1561	1,110.18	Carbonate		5.1							0.4			
OPH-1564	1,110.79	Carbonate		4.2							0.3			
OPH-1567	1,111.40	Carbonate		4.9							1.3			
OPH-1568	1,111.60	Carbonate		5.0							1.8			
OPH-1569	1,111.80	Carbonate		10.6							2.4		0.4	
OPH-1571	1,112.02	Carbonate												
OPH-1572	1,112.08	Mudstone		34.2							26.9			
OPH-1573	1,112.27	Mudstone		26.3							42.7			
OPH-1575	1,112.65	Mudstone		26.1							43.1			
OPH-1578	1,113.28	Mudstone		28.1							46.5			

Sample ID	Depth (m)	Lithology	Magnetite (wt.%)	Mica (wt. %)	Olivine (wt.%)	Pentahydrite (wt.%)	Picromerite (wt.%)	Plagioclase (wt.%)	Pyrite (wt.%)	Pyrrhotite (wt.%)	Quartz (wt.%)	Rutile (wt.%)	Siderite (wt.%)	Starkeyite (wt.%)
OPH-1579	1,113.58	Mudstone												
OPH-1580	1,113.63	Mudstone		21.7							31.2			
OPH-1581	1,113.83	Mudstone		17.9							42.4			
OPH-1582	1,113.92	Mudstone												
OPH-1584	1,114.20	Mudstone		13.1							61.7			
OPH-1585	1,114.34	Mudstone		18.5							49.0			
OPH-1585	1,114.34	Mudstone		18.5					11.2		49.1			
OPH-1586	1,114.62	Mudstone												
OPH-1587	1,114.77	Mudstone		20.4							6.4			
OPH-1588	1,115.02	Mudstone		18.2							20.4			
OPH-1589	1,115.21	Mudstone												
OPH-1590	1,115.59	Carbonate		11.5							20.8		0.4	
OPH-1592	1,115.87	Mudstone												
OPH-1596	1,116.61	Carbonate		3.7							0.6			
OPH-1599	1,117.43	Carbonate		6.6							12.0			
OPH-1601	1,117.48	Mudstone		48.5							14.0			
OPH-1606	1,118.27	Mudstone		25.9							35.2			
OPH-1608	1,118.59	Mudstone												
OPH-1613	1,119.54	Mudstone												
OPH-1647	1,120.31	Mudstone		85.6				2.6	1.4		0.2			
OPH-1617	1,120.31	Mudstone		56.6								3.2		
OPH-1647	1,120.31	Mudstone		84.4										
OPH-1621	1,120.77	Mudstone												
OPH-1624	1,121.15	Mudstone												
OPH-1625	1,121.37	Mudstone		17.2							41.7			
OPH-1626	1,121.70	Mudstone												
OPH-1634	1,123.13	Mudstone		23.7							29.1			
OPH-1640	1,123.62	Mudstone												
OPH-1651	1,124.55	Mudstone												
OPH-1655	1,125.02	Mudstone		37.9							1.1			
OPH-1676	1,127.22	Mudstone												
OPH-1683	1,135.64	Carbonate												
OPH-1697	1,136.81	Mudstone		21.5				2.1	0.4		1.2			
OPH-1697	1,136.81	Mudstone		15.5							20.5			
OPH-1704	1,137.78	Carbonate												
OPH-1709	1,138.18	Carbonate												
OPH-1729	1,145.99	Mudstone												
OPH-1746	1,159.50	Mudstone												
OPH-1752	1,160.27	Mudstone												
OPH-1761	1,161.32	Mudstone		26.2				0.3	2.1		2.2			
OPH-1765	1,161.95	Mudstone												
OPH-1768	1,162.23	Mudstone												
OPH-1779	1,166.13	Mudstone												
OPH-1796	1,175.69	Mudstone												

Sample ID	Depth (m)	Lithology	Magnetite (wt.%)	Mica (wt.%)	Olivine (wt.%)	Pentahydrite (wt.%)	Picromerite (wt.%)	Plagioclase (wt.%)	Pyrite (wt.%)	Pyrrhotite (wt.%)	Quartz (wt.%)	Rutile (wt.%)	Siderite (wt.%)	Starkeyite (wt.%)
OPH-1809	1,187.30	Mudstone		32.7				11.5	2.9		3.2			
OPH-1814	1,187.91	Mudstone												
OPH-1823	1,188.90	Mudstone												
OPH-1831	1,190.01	Carbonate												
OPH-1835	1,190.75	Carbonate												
OPH-1849	1,198.41	Mudstone												
OPH-1856	1,199.56	Carbonate												
OPH-1862	1,200.64	Carbonate												
OPH-1865	1,201.25	Carbonate												
OPH-1871	1,202.50	Carbonate												
OPH-1879	1,203.59	Mudstone												
OPH-1885	1,204.44	Mudstone												
OPH-1892	1,205.03	Mudstone												
OPH-1904	1,206.20	Mudstone												
OPH-1918	1,207.63	Mudstone		20.5				8.4	trace		4.2			
OPH-1924	1,208.96	Carbonate												
OPH-1927	1,209.45	Carbonate												
OPH-1939	1,211.12	Mudstone												
OPH-1942	1,211.51	Mudstone												
OPH-1948	1,212.51	Carbonate												
OPH-1960	1,214.11	Mudstone												
OPH-1962	1,214.28	Mudstone												
OPH-1975	1,215.53	Carbonate												
OPH-1984	1,216.89	Mudstone												
OPH-1994	1,217.74	Mudstone												
OPH-2001	1,218.36	Carbonate		4.7				1.4	1.2	6.9	5.2			
OPH-2010	1,219.18	Carbonate												
OPH-2027	1,220.85	Mudstone												
OPH-2040	1,221.72	Mudstone												
OPH-2052	1,223.79	Mudstone		20.4							7.1			
OPH-2061	1,225.13	Mudstone		25.3				31.4		6.7	6.2			
OPH-2068	1,226.04	Mudstone									9.3			
OPH-2069	1,226.21	Carbonate		2.7							6.5			
OPH-2397	1,426.19	Mudstone												
OPH-2406	1,427.09	Mudstone		4.6				51.4		4.2	7.2			
OPH-2413	1,427.81	Mudstone												
OPH-2423	1,437.13	Mudstone												
OPH-2426	1,437.68	Mudstone												
OPH-2993	1,765.27	Carbonate												
OPH-3009	1,767.41	Carbonate												
OPH-3016	1,777.38	Mudstone						69.8		6.8	8.2			
OPH-3112	1,868.46	Mudstone												
OPH-3117	1,869.18	Mudstone												
OPH-3132	1,871.00	Mudstone		5.8				48.7			9.2			

Sample ID	Depth (m)	Lithology	Magnetite (wt.%)	Mica (wt.%)	Olivine (wt.%)	Pentahydrite (wt.%)	Picromerite (wt.%)	Plagioclase (wt.%)	Pyrite (wt.%)	Pyrrhotite (wt.%)	Quartz (wt.%)	Rutile (wt.%)	Siderite (wt.%)	Starkeyite (wt.%)
OPH-3141	1,871.27	Mudstone												
OPH-3137	1,871.47	Mudstone												
OPH-3161	1,881.50	Mudstone												
OPH-3168	1,887.61	Mudstone												
OPH-3179	1,888.77	Carbonate		2.2							1.5			
OPH-3182	1,889.14			7.5							29.5			
OPH-3191	1,902.61	Mudstone		33.2							21.0			
OPH-3191	1,902.61	Mudstone		33.2				13.3			10.2			
OPH-3194	1,902.88	Mudstone												
OPH-3229	1,915.60	Mudstone		23.2							22.5			
OPH-3256	1,926.73	Mudstone		38.4							27.1			
OPH-3256	1,926.73	Mudstone		34.0				15.7			11.2			
OPH-3272	1,935.31	Mudstone												
OPH-3275	1,935.54	Mudstone		35.9							24.5			
OPH-3295	1,946.55	Mudstone												
OPH-3324	1,957.85	Mudstone												
OPH-3331	1,958.63	Mudstone												
OPH-3355	1,970.85	Mudstone		30.5				17.0			12.2			
OPH-3386	1,980.42	Carbonate												
OPH-3463	2,011.35	Mudstone		35.2				3.3	0.6		13.2			
OPH-3589	2,052.57	Mudstone		12.8							29.3			
OPH-3589	2,052.57	Mudstone		12.8				7.2			14.2			
OPH-3707	2,103.47	Mudstone		5.2										
OPH-3707	2,103.47	Mudstone		5.2				31.5			15.2			
OPH-3736	2,205.38	Carbonate		1.2										
OPH-3904	2,252.09	Carbonate		0.6							22.5			
OPH-4022	2,285.28	Carbonate		2.7				1.2			16.2			
OPH-4081	2,305.25	Carbonate									16.5			
OPH-4142	2,324.43	Carbonate		2.2							7.1			
OPH-4178	2,328.55	Carbonate		0.6							28.1			
OPH-4183	2,329.14	Carbonate		3.7							5.2			
OPH-4185	2,329.34			0.5							14.0			
OPH-4187	2,329.62			0.9							2.3			
OPH-4193	2,330.28	Evaporite									1.2			
OPH-4193	2,330.28	Evaporite						0.8			17.2			
OPH-4194	2,330.34	Carbonate		0.3							8.1			
OPH-4199	2,330.85	Evaporite		0.8							14.9			
OPH-4211	2,509.02	Evaporite												
OPH-4257	2,517.36	Evaporite		13.4							3.4			
OPH-4310	2,526.68	Evaporite		1.3							2.4			
OPH-4366	2,547.78	Evaporite		8.1							3.3			
OPH-4383	2,549.45	Mudstone		5.5				20.6			18.2			
OPH-4383	2,549.45	Mudstone		5.5							22.5			
OPH-4440	2,570.15	Evaporite		1.1							8.4			

Sample ID	Depth (m)	Lithology	Magnetite (wt.%)	Mica (wt.%)	Olivine (wt.%)	Pentahydrite (wt.%)	Picromerite (wt.%)	Plagioclase (wt.%)	Pyrite (wt.%)	Pyrrhotite (wt.%)	Quartz (wt.%)	Rutile (wt.%)	Siderite (wt.%)	Starkeyite (wt.%)
OPH-4537	2,700.97	Evaporite		0.8							24.1			
OPH-4582	2,724.31	Evaporite									1.7			
OPH-4582	2,724.31	Evaporite									19.2			
OPH-4635	2,833.79	Evaporite									7.1			
OPH-4620	2,838.14	Evaporite									20.2			
OPH-4683	2,850.46	Evaporite												
OPH-4683	2,850.46	Evaporite									21.2			
OPH-4774	2,878.31	Evaporite				1.5					2.4			
OPH-4813	2,896.20	Evaporite				1.2								7.7
OPH-4853	2,904.34	Evaporite									0.9			9.9

Table A7d: X-ray diffraction mineral abundances in drill core OPH, continued.

Sample ID	Depth (m)	Lithology	Stilpnomelane (wt.%)	Sylvite (wt.%)	Talc (wt.%)	Titanite (wt.%)	Wagnerite (wt.%)
OPH-10	530.39	Mudstone					
OPH-73	542.63	Mudstone				5.8	
OPH-80	543.68	Mudstone					
OPH-83	544.22	Mudstone					
OPH-121	552.43	Mudstone					
OPH-284	591.30	Mudstone					
OPH-306	594.85	Mudstone	1.0			5.5	
OPH-507	636.42	Mudstone					
OPH-515	637.85	Mudstone					
OPH-523	638.53	Mudstone					
OPH-844	890.22	Mudstone					
OPH-849	891.17	Mudstone					
OPH-858	892.79	Mudstone					
OPH-862	893.38	Mudstone					
OPH-867	894.16	Mudstone					
OPH-875	894.98	Carbonate					
OPH-879	895.49	Carbonate					
OPH-924	899.15	Carbonate					
OPH-925	899.25	Carbonate					
OPH-938	900.23	Carbonate					
OPH-945	901.96						
OPH-955	903.08	Mudstone					
OPH-970	904.30	Mudstone					
OPH-975	912.04	Mudstone					
OPH-979	912.70	Mudstone					
OPH-1361	1,080.00	Carbonate					
OPH-1364	1,080.57	Carbonate			9.2		
OPH-1364	1,080.57	Carbonate					
OPH-1366	1,081.11	Carbonate					
OPH-1368	1,081.36	Carbonate					
OPH-1372	1,081.93	Carbonate					
OPH-1373	1,082.28	Carbonate					
OPH-1376	1,082.71	Carbonate					
OPH-1383	1,083.49	Carbonate					
OPH-1390	1,084.18	Carbonate					
OPH-1393	1,084.47	Carbonate					
OPH-1398	1,085.13	Carbonate					
OPH-1400	1,085.42	Carbonate					
OPH-1403	1,086.33	Carbonate					
OPH-1405	1,086.52	Carbonate					
OPH-1405	1,086.52	Carbonate			3.8		
OPH-1412	1,087.73	Carbonate					
OPH-1421	1,089.09	Carbonate					

Sample ID	Depth (m)	Lithology	Stilpnomelane (wt.%)	Sylvite (wt.%)	Talc (wt.%)	Titanite (wt.%)	Wagnerite (wt.%)
OPH-1426	1,089.67	Carbonate					
OPH-1434	1,090.51	Carbonate					
OPH-1436	1,090.80	Carbonate					
OPH-1442	1,091.87	Carbonate					
OPH-1444	1,092.14	Carbonate					
OPH-1449	1,093.39	Carbonate					
OPH-1449	1,093.39	Carbonate			2.4		
OPH-1452	1,093.90	Carbonate					
OPH-1461	1,094.89	Carbonate					
OPH-1464	1,095.45	Carbonate					
OPH-1466	1,095.74	Carbonate					
OPH-1468	1,096.29	Carbonate					
OPH-1469	1,096.31	Carbonate					
OPH-1470	1,096.57	Carbonate					
OPH-1472	1,096.82	Carbonate					
OPH-1479	1,098.06	Carbonate					
OPH-1483	1,098.66	Carbonate					
OPH-1486	1,099.04	Carbonate					
OPH-1488	1,099.51						
OPH-1491	1,099.98	Carbonate					
OPH-1499	1,101.27	Carbonate					
OPH-1499	1,101.27	Carbonate					
OPH-1501	1,101.45	Mudstone					
OPH-1509	1,102.06	Mudstone					
OPH-1516	1,102.74	Mudstone					
OPH-1519	1,103.35	Mudstone					
OPH-1527	1,104.69	Carbonate					
OPH-1533	1,106.00	Carbonate					
OPH-1542	1,106.99	Mudstone					
OPH-1556	1,109.44	Carbonate					
OPH-1557	1,109.57	Carbonate					
OPH-1560	1,109.96	Carbonate					
OPH-1561	1,110.18	Carbonate					
OPH-1564	1,110.79	Carbonate					
OPH-1567	1,111.40	Carbonate					
OPH-1568	1,111.60	Carbonate					
OPH-1569	1,111.80	Carbonate					
OPH-1571	1,112.02	Carbonate					
OPH-1572	1,112.08	Mudstone					
OPH-1573	1,112.27	Mudstone					
OPH-1575	1,112.65	Mudstone					
OPH-1578	1,113.28	Mudstone					
OPH-1579	1,113.58	Mudstone					
OPH-1580	1,113.63	Mudstone					
OPH-1581	1,113.83	Mudstone					
OPH-1582	1,113.92	Mudstone					

Sample ID	Depth (m)	Lithology	Stilpnomelane (wt.%)	Sylvite (wt.%)	Talc (wt.%)	Titanite (wt.%)	Wagnerite (wt.%)
OPH-1584	1,114.20	Mudstone					
OPH-1585	1,114.34	Mudstone					
OPH-1585	1,114.34	Mudstone					
OPH-1586	1,114.62	Mudstone					
OPH-1587	1,114.77	Mudstone					
OPH-1588	1,115.02	Mudstone					
OPH-1589	1,115.21	Mudstone					
OPH-1590	1,115.59	Carbonate					
OPH-1592	1,115.87	Mudstone					
OPH-1596	1,116.61	Carbonate					
OPH-1599	1,117.43	Carbonate					
OPH-1601	1,117.48	Mudstone					
OPH-1606	1,118.27	Mudstone					
OPH-1608	1,118.59	Mudstone					
OPH-1613	1,119.54	Mudstone					
OPH-1647	1,120.31	Mudstone					
OPH-1617	1,120.31	Mudstone					
OPH-1647	1,120.31	Mudstone					
OPH-1621	1,120.77	Mudstone					
OPH-1624	1,121.15	Mudstone					
OPH-1625	1,121.37	Mudstone					
OPH-1626	1,121.70	Mudstone					
OPH-1634	1,123.13	Mudstone					
OPH-1640	1,123.62	Mudstone					
OPH-1651	1,124.55	Mudstone					
OPH-1655	1,125.02	Mudstone					
OPH-1676	1,127.22	Mudstone					
OPH-1683	1,135.64	Carbonate					
OPH-1697	1,136.81	Mudstone					
OPH-1697	1,136.81	Mudstone					
OPH-1704	1,137.78	Carbonate					
OPH-1709	1,138.18	Carbonate					
OPH-1729	1,145.99	Mudstone					
OPH-1746	1,159.50	Mudstone					
OPH-1752	1,160.27	Mudstone					
OPH-1761	1,161.32	Mudstone					
OPH-1765	1,161.95	Mudstone					
OPH-1768	1,162.23	Mudstone					
OPH-1779	1,166.13	Mudstone					
OPH-1796	1,175.69	Mudstone					
OPH-1809	1,187.30	Mudstone					
OPH-1814	1,187.91	Mudstone					
OPH-1823	1,188.90	Mudstone					
OPH-1831	1,190.01	Carbonate					
OPH-1835	1,190.75	Carbonate					
OPH-1849	1,198.41	Mudstone					

Sample ID	Depth (m)	Lithology	Stilpnomelane (wt.%)	Sylvite (wt.%)	Talc (wt.%)	Titanite (wt.%)	Wagnerite (wt.%)
OPH-1856	1,199.56	Carbonate					
OPH-1862	1,200.64	Carbonate					
OPH-1865	1,201.25	Carbonate					
OPH-1871	1,202.50	Carbonate					
OPH-1879	1,203.59	Mudstone					
OPH-1885	1,204.44	Mudstone					
OPH-1892	1,205.03	Mudstone					
OPH-1904	1,206.20	Mudstone					
OPH-1918	1,207.63	Mudstone					
OPH-1924	1,208.96	Carbonate					
OPH-1927	1,209.45	Carbonate					
OPH-1939	1,211.12	Mudstone					
OPH-1942	1,211.51	Mudstone					
OPH-1948	1,212.51	Carbonate					
OPH-1960	1,214.11	Mudstone					
OPH-1962	1,214.28	Mudstone					
OPH-1975	1,215.53	Carbonate					
OPH-1984	1,216.89	Mudstone					
OPH-1994	1,217.74	Mudstone					
OPH-2001	1,218.36	Carbonate					
OPH-2010	1,219.18	Carbonate					
OPH-2027	1,220.85	Mudstone					
OPH-2040	1,221.72	Mudstone					
OPH-2052	1,223.79	Mudstone					
OPH-2061	1,225.13	Mudstone					
OPH-2068	1,226.04	Mudstone					
OPH-2069	1,226.21	Carbonate					
OPH-2397	1,426.19	Mudstone					
OPH-2406	1,427.09	Mudstone					
OPH-2413	1,427.81	Mudstone					
OPH-2423	1,437.13	Mudstone					
OPH-2426	1,437.68	Mudstone					
OPH-2993	1,765.27	Carbonate					
OPH-3009	1,767.41	Carbonate					
OPH-3016	1,777.38	Mudstone					
OPH-3112	1,868.46	Mudstone					
OPH-3117	1,869.18	Mudstone					
OPH-3132	1,871.00	Mudstone					
OPH-3141	1,871.27	Mudstone					
OPH-3137	1,871.47	Mudstone					
OPH-3161	1,881.50	Mudstone					
OPH-3168	1,887.61	Mudstone					
OPH-3179	1,888.77	Carbonate					
OPH-3182	1,889.14						
OPH-3191	1,902.61	Mudstone					
OPH-3191	1,902.61	Mudstone					

Sample ID	Depth (m)	Lithology	Stilpnomelane (wt.%)	Sylvite (wt.%)	Talc (wt.%)	Titanite (wt.%)	Wagnerite (wt.%)
OPH-3194	1,902.88	Mudstone					
OPH-3229	1,915.60	Mudstone					
OPH-3256	1,926.73	Mudstone					
OPH-3256	1,926.73	Mudstone					
OPH-3272	1,935.31	Mudstone					
OPH-3275	1,935.54	Mudstone					
OPH-3295	1,946.55	Mudstone					
OPH-3324	1,957.85	Mudstone					
OPH-3331	1,958.63	Mudstone					
OPH-3355	1,970.85	Mudstone					
OPH-3386	1,980.42	Carbonate					
OPH-3463	2,011.35	Mudstone					
OPH-3589	2,052.57	Mudstone					
OPH-3589	2,052.57	Mudstone					
OPH-3707	2,103.47	Mudstone					
OPH-3707	2,103.47	Mudstone					
OPH-3736	2,205.38	Carbonate					
OPH-3904	2,252.09	Carbonate					
OPH-4022	2,285.28	Carbonate					
OPH-4081	2,305.25	Carbonate					
OPH-4142	2,324.43	Carbonate					
OPH-4178	2,328.55	Carbonate					
OPH-4183	2,329.14	Carbonate					
OPH-4185	2,329.34						
OPH-4187	2,329.62						
OPH-4193	2,330.28	Evaporite					
OPH-4193	2,330.28	Evaporite					
OPH-4194	2,330.34	Carbonate					
OPH-4199	2,330.85	Evaporite					
OPH-4211	2,509.02	Evaporite					
OPH-4257	2,517.36	Evaporite					
OPH-4310	2,526.68	Evaporite					
OPH-4366	2,547.78	Evaporite					
OPH-4383	2,549.45	Mudstone			0.7		
OPH-4383	2,549.45	Mudstone					
OPH-4440	2,570.15	Evaporite					
OPH-4537	2,700.97	Evaporite					
OPH-4582	2,724.31	Evaporite					
OPH-4582	2,724.31	Evaporite			1.4		
OPH-4635	2,833.79	Evaporite					
OPH-4620	2,838.14	Evaporite			7.2		
OPH-4683	2,850.46	Evaporite					
OPH-4683	2,850.46	Evaporite					
OPH-4774	2,878.31	Evaporite					
OPH-4813	2,896.20	Evaporite					
OPH-4853	2,904.34	Evaporite					

Table A8: Isotope ratios in drill core OPH.

Sample ID	Depth (m)	Lithology	δ13C	δ18O	δ234U	δ238U	δ238U 2SE	δ53Cr	δ53Cr 2SE
OPH-73	542.63	Mudstone						-0.12	0.03
OPH-306	594.85	Mudstone						-0.24	0.04
OPH-523	638.53	Mudstone						-0.21	0.03
OPH-844	890.22	Mudstone						0.08	0.04
OPH-849	891.17	Mudstone			48.67	0.32	0.18		
OPH-945	901.96		-10.40	-20.56					
OPH-975	912.04	Mudstone						-0.05	0.04
OPH-1364	1,080.57	Carbonate						-0.07	0.04
OPH-1405	1,086.52	Carbonate						-0.20	0.03
OPH-1449	1,093.39	Carbonate						-0.02	0.04
OPH-1469	1,096.31	Carbonate	-2.69	-11.08					
OPH-1470	1,096.57	Carbonate	-2.27	-12.82					
OPH-1472	1,096.82	Carbonate	-1.51	-11.91					
OPH-1479	1,098.06	Carbonate	-1.25	-9.03					
OPH-1486	1,099.04	Carbonate	-1.28	-10.02					
OPH-1488	1,099.51		-1.47	-12.10					
OPH-1499	1,101.27	Carbonate						-0.01	0.05
OPH-1527	1,104.69	Carbonate	0.22	-10.33	40.17	0.17	0.14		
OPH-1533	1,106.00	Carbonate	-4.13	-9.66					
OPH-1556	1,109.44	Carbonate	-2.25	-4.79					
OPH-1557	1,109.57	Carbonate	-3.34	-6.48	34.98	-0.03	0.12		
OPH-1560	1,109.96	Carbonate	-1.92	-12.02				1.17	0.07
OPH-1561	1,110.18	Carbonate	-2.25	-11.72					
OPH-1564	1,110.79	Carbonate	-5.63	-11.76					
OPH-1567	1,111.40	Carbonate	-6.18	-11.43					
OPH-1568	1,111.60	Carbonate	-7.59	-12.06					
OPH-1569	1,111.80	Carbonate	-8.30	-13.16					
OPH-1572	1,112.08	Mudstone			46.80	0.40	0.14	1.63	0.11
OPH-1573	1,112.27	Mudstone			46.28	0.63	0.10	0.41	0.08
OPH-1575	1,112.65	Mudstone			45.05	0.79	0.09		
OPH-1584	1,114.20	Mudstone			43.79	0.74	0.08		
OPH-1585	1,114.34	Mudstone						0.73	0.03
OPH-1588	1,115.02	Mudstone			41.08	0.45	0.11		
OPH-1590	1,115.59	Carbonate	-7.52	-11.83					
OPH-1596	1,116.65	Carbonate	-4.46	-9.80				0.62	0.10
OPH-1599	1,117.43	Carbonate	-8.82	-10.95					
OPH-1606	1,118.27	Mudstone						1.22	0.04
OPH-1617	1,120.31	Mudstone			45.18	0.45	0.11		
OPH-1634	1,123.13	Mudstone	-9.95	-14.05					
OPH-1647	1,124.27	Mudstone			40.21	0.74	0.13	0.10	0.03
OPH-1655	1,125.02	Mudstone	-8.52	-13.19					
OPH-1697	1,136.81	Mudstone	-13.02	-14.46				-0.19	0.03
OPH-1761	1,161.32	Mudstone						0.94	0.03

Sample ID	Depth (m)	Lithology	δ13C	δ18O	δ234U	δ238U	δ238U 2SE	δ53Cr	δ53Cr 2SE
OPH-1809	1,187.30	Mudstone						0.11	0.03
OPH-1918	1,207.63	Mudstone						0.00	0.03
OPH-2001	1,218.36	Carbonate						0.00	0.03
OPH-2061	1,225.13	Mudstone						-0.16	0.03
OPH-2068	1,226.04	Mudstone	-15.38	-14.77					
OPH-2069	1,226.21	Carbonate	-21.39	-15.26					
OPH-2406	1,427.09	Mudstone						0.28	0.03
OPH-3016	1,777.38	Mudstone						0.48	0.03
OPH-3132	1,871.00	Mudstone						-0.07	0.03
OPH-3179	1,888.77	Carbonate	-0.39	-7.15					
OPH-3182	1,889.14		-0.39	-11.80					
OPH-3191	1,902.61	Mudstone	1.58	-11.28				0.30	0.03
OPH-3229	1,915.60	Mudstone	4.21	-13.21					
OPH-3256	1,926.73	Mudstone						-0.43	0.03
OPH-3275	1,935.54	Mudstone	5.21	-11.01					
OPH-3355	1,970.85	Mudstone						-0.16	0.03
OPH-3463	2,011.35	Mudstone						-0.16	0.02
OPH-3589	2,052.57	Mudstone	5.20	-13.40				-0.13	0.02
OPH-3707	2,103.47	Mudstone	5.64	-12.57				-0.17	0.03
OPH-3736	2,205.38	Carbonate	12.19	-7.61					
OPH-3904	2,252.09	Carbonate	11.39	-10.44				0.72	0.11
OPH-4022	2,285.28	Carbonate						0.12	0.03
OPH-4081	2,305.25	Carbonate	9.17	-7.00				1.16	0.08
OPH-4142	2,324.43	Carbonate	8.59	-9.04					
OPH-4193	2,330.28	Evaporite	8.43	-6.55				0.14	0.03
OPH-4211	2,509.02	Evaporite	11.58	-8.14				1.17	0.11
OPH-4310	2,526.68	Evaporite	11.74	-9.50					
OPH-4366	2,547.78	Evaporite	12.18	-10.50					
OPH-4383	2,549.45	Mudstone	12.32	-10.03				-0.17	0.02
OPH-4440	2,570.15	Evaporite	12.69	-10.76					
OPH-4537	2,700.97	Evaporite	18.80	-9.63					
OPH-4582	2,724.31	Evaporite						-0.34	0.03
OPH-4635	2,833.79	Evaporite	12.84	-16.65					
OPH-4620	2,838.14	Evaporite						0.40	0.03
OPH-4683	2,850.46	Evaporite						0.24	0.03
OPH-4774	2,878.31	Evaporite	11.82	-17.17					
OPH-4853	2,904.34	Evaporite						0.92	0.05